Synthesis and Photophysics of Liquid-Crystalline Complexes of Gold(III) and Platinum(IV)

Rachel Roberta Parker

PhD

University of York

Chemistry

September 2019

Abstract

Phosphorescent metal complexes are of great potential interest in optoelectronic applications, for example as emitters in organic light emitting diodes (OLEDs), due to the ability of such materials to emit from the triplet excited state. Through the combination of liquid-crystalline properties with triplet emission, these materials can form structures with long-range order that can display increased charge-transport abilities and show polarised emission.

It has been shown that the platinum(IV) complex [Pt(*p*-tolpy)$_2$Cl$_2$] can be prepared through a microwave-assisted, one-pot procedure. Alkoxyphenyl-functionalised analogues showed lamellar mesophases, which is remarkable given the low level of alkoxy-functionalisation and octahedral metal geometry. All of the platinum(IV) complexes were emissive in solution, showing moderate quantum yields of ≈10% and long lifetimes of up to 230 μs.

A large family of liquid-crystalline bis-cyclometallated gold(III) alkynyl complexes of the general formula [Au(C^N^C)(C≡CR)] has been synthesised, where C^N^C is an alkoxy-functionalised, 2,6-diphenylpyridine ligand and C≡CR is an alkoxy-functionalised phenylalkynyl ligand. The majority of complexes form columnar mesophases, with phase stability and symmetry tuneable through the number and length of the alkoxy substituents. The introduction of semi-perfluorinated chains appended on the phenylalkynyl ligand modified the liquid-crystallinity of the materials significantly owing to requirement for spatial separation between fluorocarbon and hydrocarbon chains. Consequences of this substitution are the increased incidence of Col$_r$ phases, observation of a re-entrant nematic phase, and generally increased stability of the mesophases. Complexes also showed a tendency to aggregate in concentrated solution, as well as form supramolecular networks in the form of metallogels.

All gold(III) alkynyl complexes were luminescent in solution, showing green and yellow emission with quantum yields of up to 34% and lifetimes ranging from 6 to 177 μs. Utilisation of the complexes as emitters in OLED devices showed external quantum efficiencies of up to 7.14% which proved to be competitive with similar reported compounds.

For Emily

Table of Contents

List of Figures

List of Schemes

List of Tables

Acknowledgements

Firstly, I would like to thank both of my supervisors, Prof. Duncan Bruce and Dr. Jason Lynam, for their support and encouragement over the past four years, as well as for the opportunities they have given me, including attending conferences, workshops and other institutions for collaboration. I am also grateful to Jason for performing the computational chemistry included in this thesis.

Thank you to Prof. J. A. Gareth Williams at the University of Durham for his assistance with the characterisation of the photophysical properties of the complexes included in this thesis, and for hosting me to allow me to contribute to these measurements.

Thank you to Prof. Yafei Wang and Dr. Bin Zhang from Changzhou University, China, who hosted me for two weeks in Changzhou in a collaboration to fabricate OLED devices, as well as Denghui Liu who worked tirelessly to construct a great many devices and teach me how to do so along the way. Sincere thanks also go to all of the students who took me under their wing and looked after me, it is thanks to them that my trip was so enjoyable and we shall remain fast friends.

This work would not be possible without funding from the University of York and their X-ray crystallography technicianship, and I will always be very grateful.

Thank you to Dr. Adrian Whitwood for being an excellent and patient teacher of all things crystallography, as well as for his assistance in my own crystal structures, along with Dr. Sam Hart. Thank you to Dr. Graeme McAllister for elemental analyses, Heather Fish for assistance with NMR spectroscopy, and Karl Heaton and Rosaria Cercola for mass spectrometry.

Thank you to the Materials Group at York, past and present members, for being great office- and lab-mates, especially to Dr. Richard Mandle and Dr. Julia Sarju for their assistance and friendship at the start of my PhD and ever since, and Jordan Herod and James Brailey-Partridge. Thanks also go to all past and present members of the Lynam group, especially as they let me drift in for the fun bits and go back upstairs to escape the grunt work.

Thank you to my family for their support over the past four years; my mum and dad and brother, Craig, as well as Helen and Harry, and everyone else too numerous to mention. Thank you to the all the friends I have made in York, especially to Knit Club and partners for being the most excellent friends. To Peter, for being the most loving and lovable cat, even though sitting on the computer is not conducive to thesis writing.

And most importantly, thank you to my wife, Emily, without whom nothing in my life would be possible.

Author's Declaration

The research contained within this thesis was carried out in the Department of Chemistry at the University of York between October 2015 and September 2019. To the best of my knowledge, this research is original and my own, except where reference has been made to the work of others, as summarised below. All sources have been acknowledged as references. This work has not previously been presented for an award at this, or any other, University.

Significant contributions from other researchers:

- Computational calculations were performed by Dr. Jason Lynam
- Final photophysical measurements were performed by Prof. J. A. Gareth Williams
- OLED devices were fabricated by Denghui Liu, or under his tutelage
- Ligands **HL5-12** and **HL5-14** were synthesised by MChem student Rebecca Howarth
- Complexes **11-*n***, **14-8** and **14-12** and ligands **HL-7-*n*** were synthesised by MChem student Rachel Stracey
- Complex **Au4-BODIPY** was synthesised by visiting researcher Olga Vodianova
- Crystal structures of **Pt-1** and **Au4-BODIPY** were collected and solved by Dr. Adrian Whitwood

Some of the material presented within this thesis has previously been published in:

R. R. Parker, J. P. Sarju, A. C. Whitwood, J. A. G. Williams, J. M. Lynam, D. W. Bruce, *Chem. Eur. J.* **2018**, *24*, 19010

Chapter 1: Introduction to Liquid Crystals, Emissive Transition Metal Complexes and their Application in OLED Devices

1.1 Introduction to Liquid Crystals

Liquid-crystalline materials are those which show a state of matter between a 3D crystalline solid and an isotropic liquid, in that they show fluidity while retaining some long-range orientational order of the molecules. Liquid-crystalline materials were discovered in the observations of Reinitzer,[1, 2] in which cholesteryl benzoate was observed to melt at 145 °C into an opaque fluid phase (the liquid-crystal state), which then became clear at 178 °C. The liquid-crystalline state (so-called by Lehmann[3]), also known as a mesophase, was described fully by Vorländer in 1907 in terms of molecular shape, namely the observation that the molecules showing mesomorphism were linear, rod-like materials (calamitic materials).[4] This definition was expanded upon 70 years later in the work of Chandrasekhar *et al.*,[5] who reported liquid-crystallinity in planar, disc-like molecules (discotic materials), which had been predicted previously but never observed experimentally.[6-8]

Liquid crystals can be classified by the stimulus responsible for the induction of the phase. In *lyotropic* liquid crystals, the mesophases are induced through the introduction of solvent; such systems are found in cell membranes, while DNA can also form liquid-crystalline phases,[9] as well as in most common surfactant based systems such as detergents.[10] Lyotropic liquid crystals are, however, outwith the scope of this thesis, and will therefore not be discussed further. In *thermotropic* liquid crystals, the mesophase is induced through the application of heat, *i.e.* the phase behaviour is temperature dependent.[11, 12] It is thermotropic liquid crystals that have found success in optoelectronic devices, such as LCD displays, and in thermochromic applications.[13, 14]

The research presented in this thesis concerns only thermotropic liquid crystals, subsections and properties of which are expanded on in the following section.

1.1.1 Thermotropic Liquid Crystals

Thermotropic liquid crystals can be further categorised by the molecular geometry of the materials in question and whether they are rod-like (calamitic) or disc-like (discotic) (Figure 1-1). These sub-divisions lie in the category of low-molecular weight materials, in contrast to high-molecular weight materials, in which liquid-crystalline polymers[15, 16] and dendrimers[17-19] are classified.

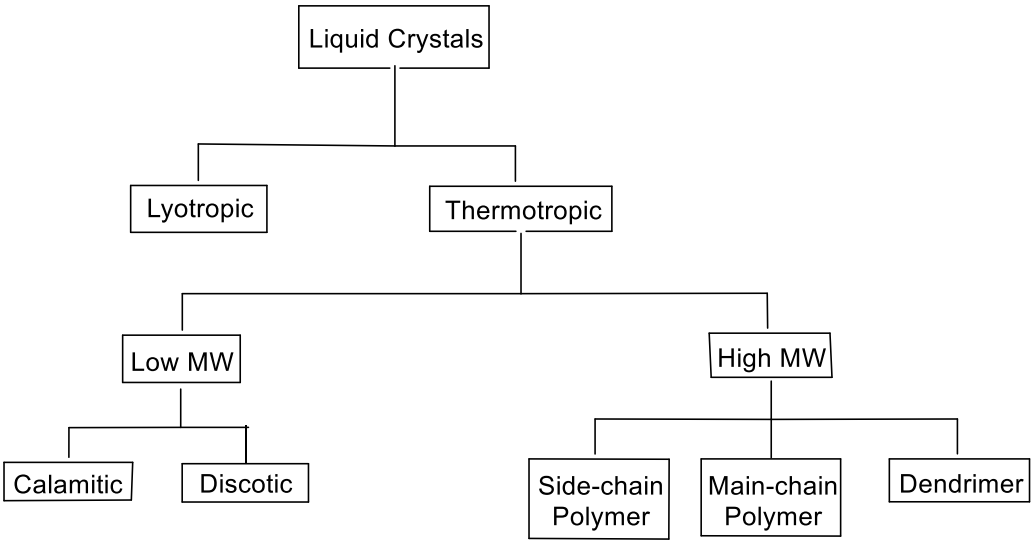

Figure 1-1: Categorisation of liquid-crystalline materials

The commonality in all low-molecular weight liquid crystals is the presence of a high degree of anisotropy. In rod-like materials, this is present in the form of two short axes and one substantially longer axis, while in disc-like materials, two axes are substantially longer than the other (Figure 1-2). For both classifications, in the mesophases, the unique molecular axis is correlated about a specific axis, termed the director, **n**.

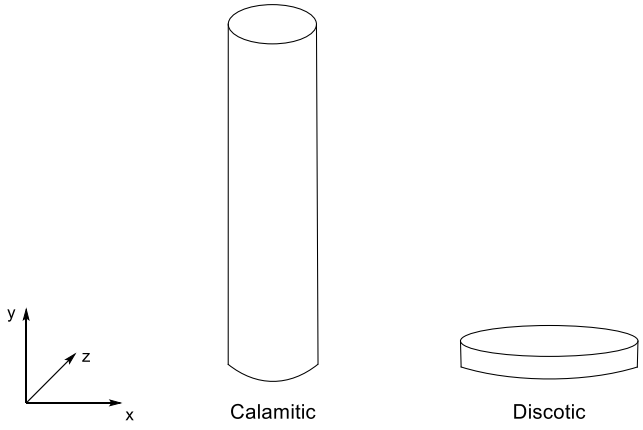

Figure 1-2: Molecular arrangement of calamitic and discotic mesogens with the unique molecular axis for both orientated along the y-axis.

1.1.1.1 Calamitic Systems

Calamitic liquid-crystalline materials orientate with the long axis approximately along the director to form a range of mesophases with varying levels of order. The most common of these phases are the nematic phase (N) and a large number of smectic phases (Sm) which are lamellar and defined by the relationship between the molecules in the layers (Figure 1-3).

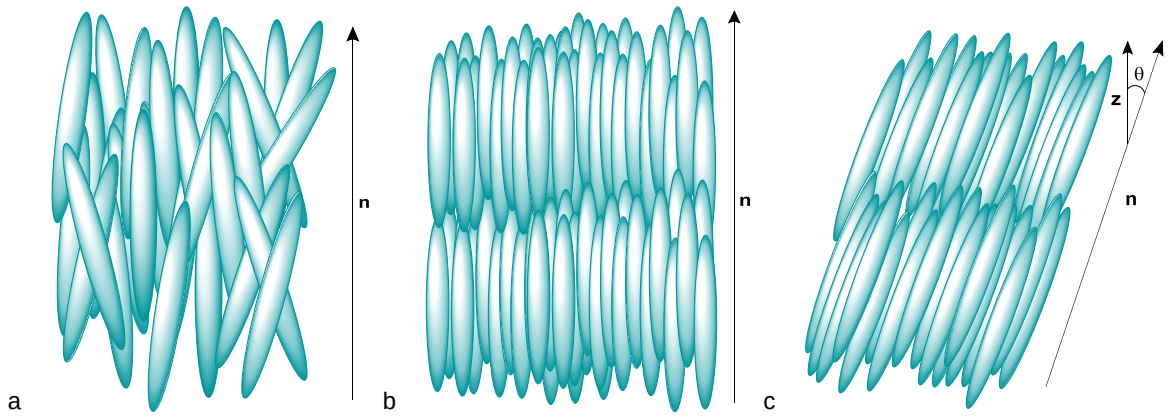

Figure 1-3: Arrangement of molecules in a) the nematic phase; b) the smectic A phase; c) the smectic C phase. Definition of smectic layers are exaggerated for clarity.

In the nematic phase the molecules are oriented, on average, parallel to the director; this is the most disorganised mesophase and displays no positional order. The degree to which the molecules align with the director is given by the order parameter, *S* (Equation 1-1) which, in a nematic phase, is typically between 0.4 and 0.7; for crystalline materials, *S* = 1 and for isotropic liquids, *S* = 0, as there is no order at all.

$$S = \frac{1}{2}\langle 3\cos^2\theta - 1\rangle$$ Equation 1-1

where *S* is the order parameter and θ is the average angle between the long molecular axis and the director, **n**.

The nematic phase is typically identified through a high level of fluidity and Brownian motion when observed by polarising optical microscopy (POM; this technique will be outlined in Section 1.1.3.1), as well as the presence of Schlieren defects in the texture (Figure 1-4a[20]).

Smectic phases are formed through the introduction of positional order within the phase, which takes the form of a layered structure; the two most common phases, smectic A (SmA) and smectic C (SmC) will be discussed, but many other smectic phases are known, such as SmB, SmF, SmI, *etc*.

In the smectic A phase, the molecules are aligned along the director, but also form layers perpendicular to **n**; they have partial positional order in one dimension. The layers typically equate to a single molecular length (monolayer) or two molecular lengths (formation of a bilayer), which can be measured through small-angle X-ray scattering (SAXS) experiments. Textures observed by POM for the SmA phase typically show focal-conic defects (Figure 1-4b[20]).

In the SmC phase, the same layered structure is observed, however the molecules are tilted with respect to the layer, resulting in a tilt angle (θ in Figure 1-3) between the director and the layer. POM textures of the SmC phase tend to show focal conic and/or Schlieren defects (Figure 1-4c[20]).

a 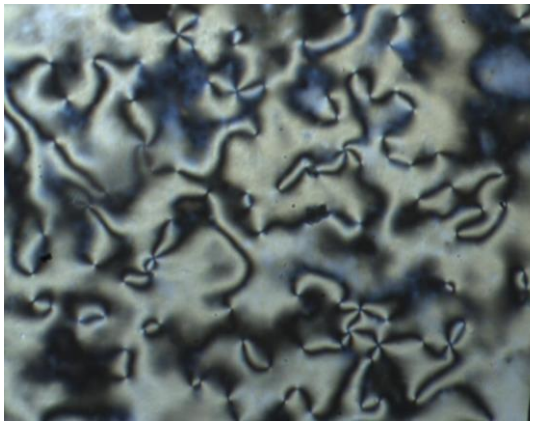 b 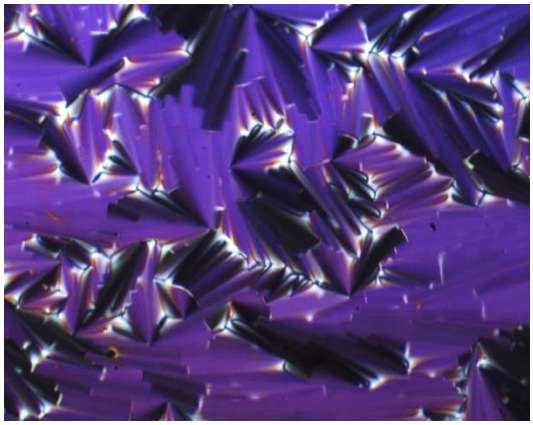

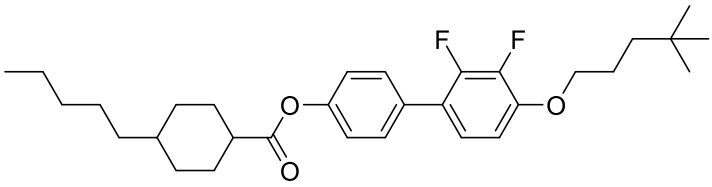

c 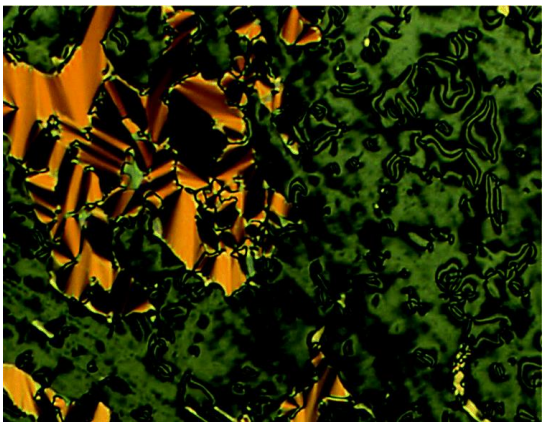

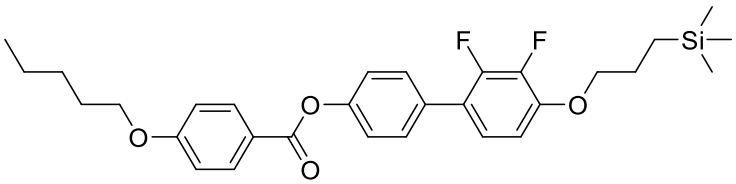

Figure 1-4: Structure and photomicrograph of microscopy texture of a) nematogen showing Schlieren defects; b) SmA phase of same showing focal-conic defects; c) SmC phase showing both focal-conic and Schlieren defects.[20]

1.1.1.2 Discotic Systems

For disc-like molecules, anisotropy is realised through the formation of planar molecules in which two directional axes are significantly longer than the third. For organic systems, they tend to be composed of multiple, rigid aromatic rings decorated on the periphery with multiple alkyl or alkoxy chains, such as substituted triphenylene or hexakis(phenylethynyl)benzene (Figure 1-5).[21, 22]

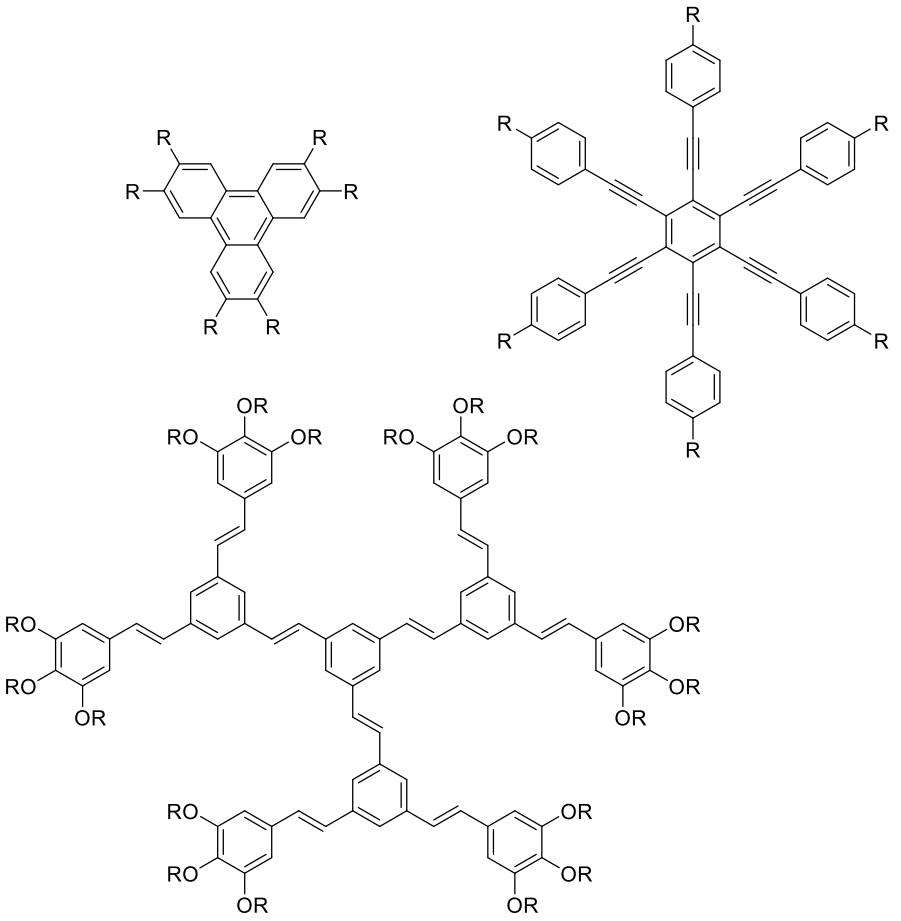

Figure 1-5: Examples of discotic molecules typically showing columnar phases, where R is an extended alkyl or alkoxy chain.[22]

Discotic mesogens tend to form columnar mesophases, in which the individual molecules stack atop one another to form one-dimensional columns, which then self-organise to form a two-dimensional lattice. The symmetry of the lattice formed is what defines the designation of the mesophases, with columnar hexagonal (Col_h) and columnar rectangular (Col_r) phases the most common. Also possible is the columnar oblique phase, Col_{ob}, although observations are less common than of Col_h and Col_r phases. While only a single plane group is possible for the Col_h phase (*p*6*mm*) and Col_{ob} (*p*1), the Col_r phase has three possible plane groups depending on the orientation of the columns with respect to each other (*p*2*gg*, *p*2*mg* and *c*2*mm*) (Figure 1-6). In columnar rectangular and oblique phases, the molecules are tilted with respect to the column axis (represented by ellipses in the lattice diagrams).[22]

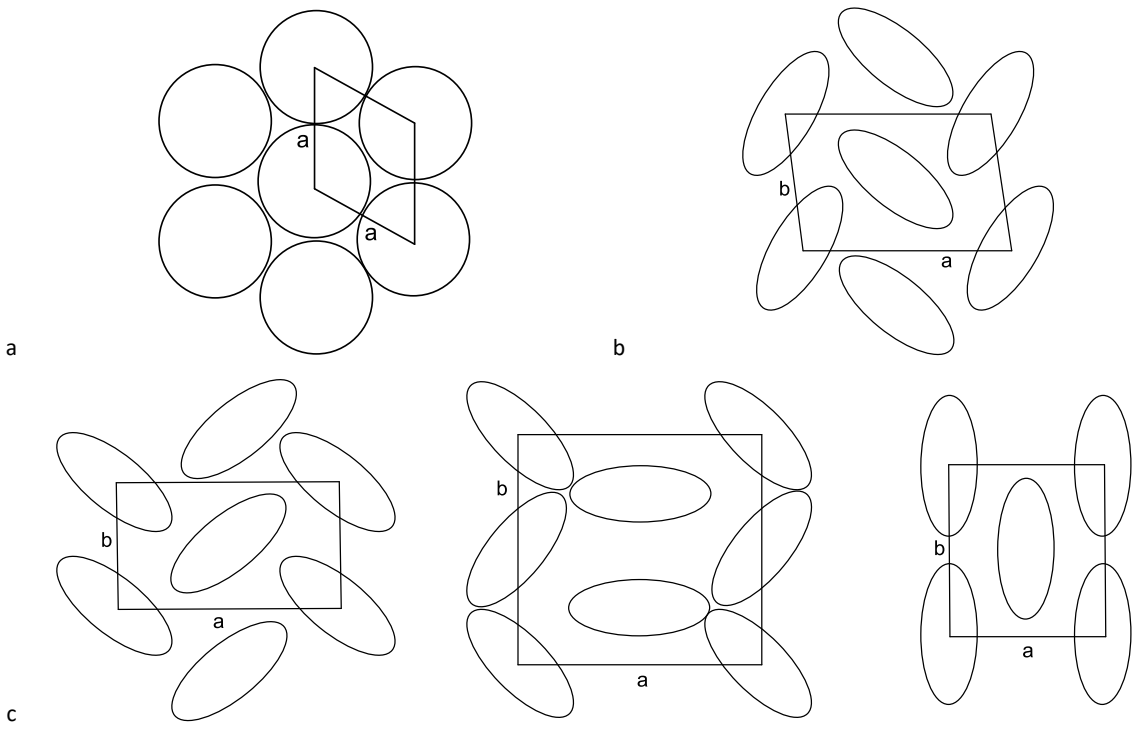

Figure 1-6: 2D lattices of a) Col_h (*p*6*mm*); b) Col_{ob} (*p*1); c) Col_r mesophases (*p*2*gg*, *p*2*mg* and *c*2*mm* from left to right).

Also observed for discotic mesogens are the discotic nematic (N_D) phase and the columnar nematic (N_{Col}) phase. These are both similar to the nematic phase discussed above for calamitic mesogens, in which there is no positional order of the molecules in the phase, with the molecular short-axis orientated along the director. In the N_{Col} phase, the integrity of the columns is preserved, but they do not form a two-dimensional lattice, but rather function as free columns. Thus, the N_{col} phase is a nematic phase of columnar aggregation (Figure 1-7). The symmetry of the N, N_D and N_{Col} phases is the same ($D_{\infty h}$), and as such textures observed for the N_D and N_{Col} phases also typically show Schlieren defects.[22]

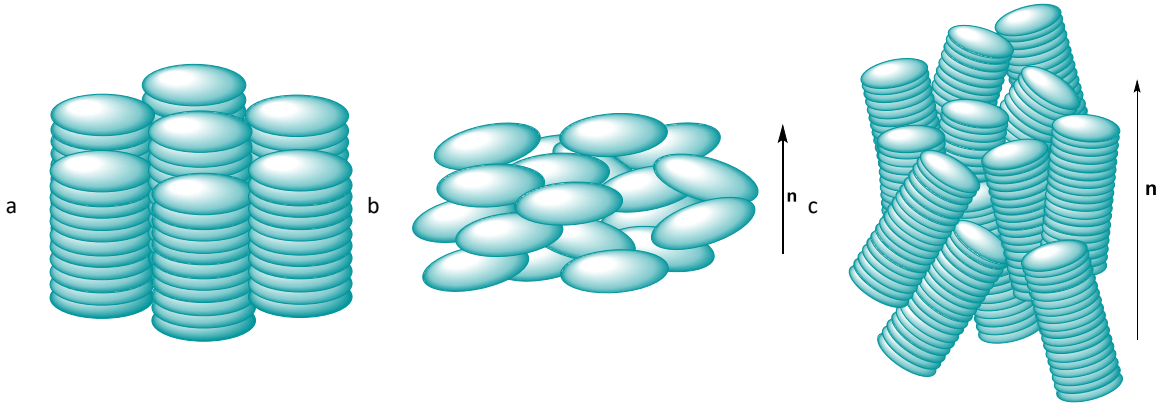

Figure 1-7: Orientation of molecules in the a) Col_h phase; b) N_D phase; c) N_{col} phase.

1.1.2 Metallomesogens

As the name suggests, metallomesogens are liquid-crystalline compounds in which a metal is included in the molecular structure. The inclusion of a metal centre offers the possibility of a wide variety of molecular geometries that are unavailable to purely organic systems, especially when considering complexes with high coordination numbers, such as lanthanide[23-27] and octahedral transition metal complexes.[23, 28-35] Phase behaviour can also be affected through a range of specific intermolecular interactions, including metal-metal and metal-ligand associations, which can have an impact on the self-assembly of the materials.

In addition to the novel and interesting liquid-crystalline properties of metallomesogens, several physical properties can also be realised, resulting in the formation of multi-functional materials, including magnetism, conduction and electronic properties. Most relevant to this thesis is the synthesis of metallomesogens with enhanced photophysical properties which can show phosphorescence.[36] The use of such materials in optoelectronic devices is explored further in Section 1.3.2

The first metallomesogens were reported by Vorländer in 1923 and were Schiff-base complexes of diarylmercury(II) showing smectic behaviour.[37] However, interest in metallic liquid crystals did not start to become prominent until the mid-1970s with simuntaneous publication of liquid-crystalline ferrocene derivatives by Malthête and Billard[38] and of dithiolene complexes of nickel(II) and platinum(II) by Giroud and Mueller-Westerhoff.[39]

Traditionally, metallomesogens have been designed around linear or square-planar metal centres, as from these architechtures, anisotropy is easily introduced to form both calamitic and discotic mesogens. The inclusion of anisotropy in more 3D geometries, such as octahedral, is less straightforward but many successful stratgies have been reported.

1.1.2.1 Strategies to Induce Liquid-Crystallinity in High Coordination Number Systems

With the knowledge that high levels of molecular anisotropy are required for materials to form liquid-crystalline phases, it is perhaps counter-intuitive to design such materials based on metals in which high coordination numbers are required, such as octahedral geometries for transition metals and coordination geometries with up to 12 coordination sites for metallomesogens based on lanthanides.

However, two main strategies have emerged to counteract the lack of anisotropy at the core metal centre. The first is to utilise a single, highly anisotropic ligand, typically rod-like in nature, combined

with smaller ancillary ligands, and the second to include a large number of ligands decorated with many extended alkyl or alkoxy chains in which a disc-like geometry emerges, overcoming the anisotropy of the metal centre. Both strategies will be expanded on below, using octahedral transition metal mesogens as examples due to their increased relevance to the material in this thesis. As may be expected, there are exceptions to these rules in which octahedral species have been reported that conform to neither strategy; such cases are discussed in the introductory section to Chapter 2.

Strategy One: A Single Anisotropic Ligand

Unsurprisingly, the resultant phases from these complexes are those observed for calamitic mesogens, such as nematic and smectic phases. This strategy has been utilised in the work of Bruce and colleagues over many years in the study of manganese and rhenium metallomesogens, often with carbonyl ancillary ligands, but others are known (Figure 1-8).[30-35, 40-42] This strategy has also been used for complexes of platinum(IV);[43, 44] these will be expanded on in Chapter 2.

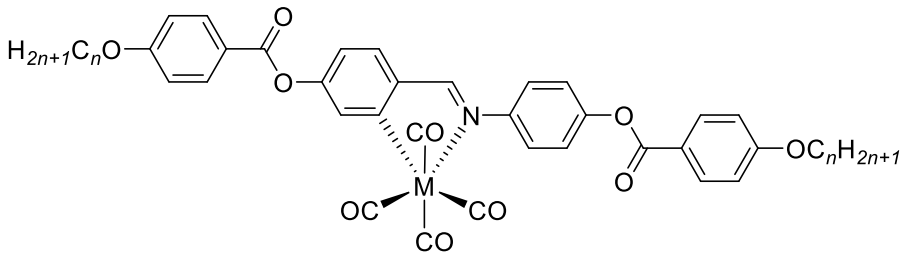

Figure 1-8: Example of complexes with octahedral geometries which show liquid-crystallinity through molecular design utilising strategy one, where M = Mn, Re.

Strategy Two: A Many Highly Functionalised Ligands

Strategy two is common in the work of Swager and co-workers, primarily for complexes of iron, chromium and manganese with multiple chelating ligands (Figure 1-9).[28, 29, 45] These complexes tend to form phases observed for discotic systems; columnar phases are dominant for many of these systems.

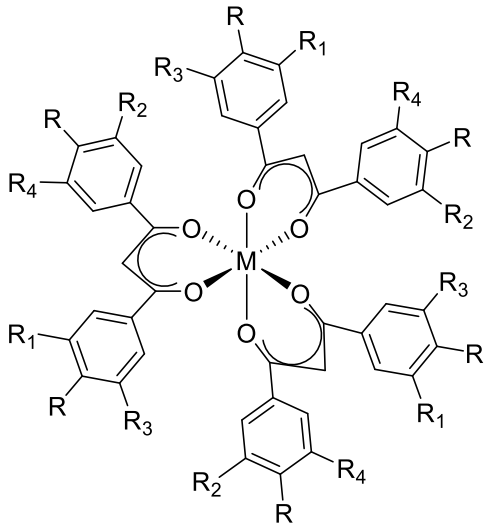

Figure 1-9: Example of complexes with octahedral geometries which show liquid-crystallinity through molecular design utilising strategy two, where M = Fe, Mn, Cr.

1.1.3 Characterisation of Liquid-Crystalline Phases

To assign the phase present in any liquid-crystalline compound, and extract relevant thermodynamic data about the transitions, or structural parameters about the phase organisation, the complementary techniques of polarising optical microscopy (POM), differential scanning calorimetry (DSC) and small-angle X-ray scattering (SAXS) are utilised. The premise behind each of these techniques and their application to liquid crystals is discussed.

1.1.3.1 Polarising Optical Microscopy (POM)

The most widely used technique for the characterisation of mesophases is polarising optical microscopy (POM), in which the sample is observed under crossed polarisers on a temperature-controllable hot stage. This technique is useful due to the anisotropy observed in liquid-crystalline phases, as they exhibit birefringence.

Birefringence is the phenomenon in which light incident on an anisotropic sample is split into two waves due to the presence of two refractive indexes within the sample.[46] These waves travel through the sample at different speeds and angles; the first travels perpendicular to the director, termed the ordinary ray, $n_{\perp}$ or n_o, and the other parallel to the director, termed the extraordinary ray, $n_{\parallel}$ or n_e. The difference between the rays results in optical birefringence, which can be assigned as positive when $n_{\parallel} - n_{\perp} > 0$ and negative when $n_{\parallel} - n_{\perp} < 0$ (Figure 1-10).

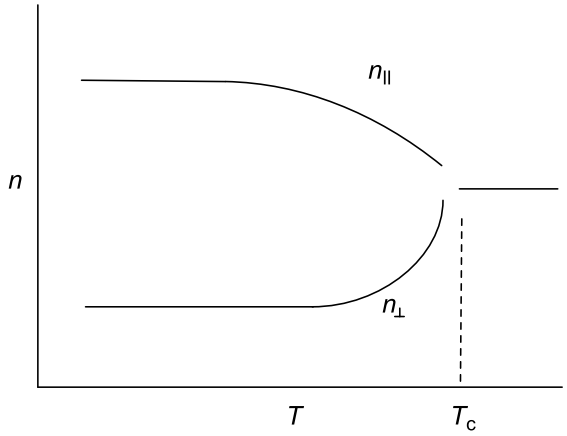

Figure 1-10: Birefringence as a function of temperature, showing the difference in ordinary ray, $n_{\perp}$, and extraordinary ray, $n_{\parallel}$, which become 0 as the sample becomes isotropic (at T_c).

In polarising optical microscopy, the sample is placed between two polarisers. The unpolarised incident light is polarised by the first polariser, which then passes through the sample, and then the second polariser which is orientated at 90° to the first. When the sample is isotropic in nature, or a homeotropically aligned mesophase, *i.e.* the director of the sample is the same as the optical axis, there is only one refractive index present in the sample, and so the light is not retarded by the sample and is extinguished by the second polariser. However, in an anisotropic crystal or an unaligned liquid crystal, the polarised light is split, due to the birefringence of the sample. The polarisation of the light is lost and the light is therefore able to pass through the second polariser, where an interference pattern between the ordinary and extraordinary rays can be observed (Figure 1-11).

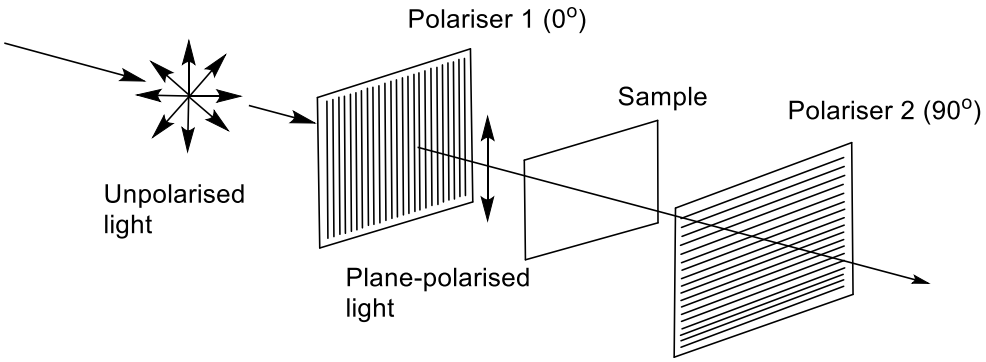

Figure 1-11: Schematic diagram of a sample between crossed polarisers and the effect on the incident light.

The interference pattern observed is fully dependent on the mesophase of the material; different phases show different textures when observed by POM, which was briefly touched upon in section 1.1.1.1 with the textures of nematic and smectic phases shown in Figure 1-4. These characteristic textures arise from symmetry-dependent elasticity of the phase and defects within the sample, typically in the meeting of different domains. Domains arise from localised changes in the orientation of the director throughout the bulk of the sample. When these meet, the overall order

of the phase is disrupted resulting in point defects (observed as black spots) or disclination defects (observed as line defects in the sample).

Most relevant to this work is the formation of defects in columnar phases, which commonly show fan-like structures or straight-line (spine) defects (Figure 1-12). The former are formed by confocal structures, where the layer thickness is constant throughout the sample but the columnar structure is curved over the scale of the sample without deformation of the two-dimensional lattice to form circular domains. [47] The latter is formed through optical extinction when the domain is orientated with the optical axis perpendicular to the axis of the column.

The combination of textures and defects are often key to identifying the mesophase.

a 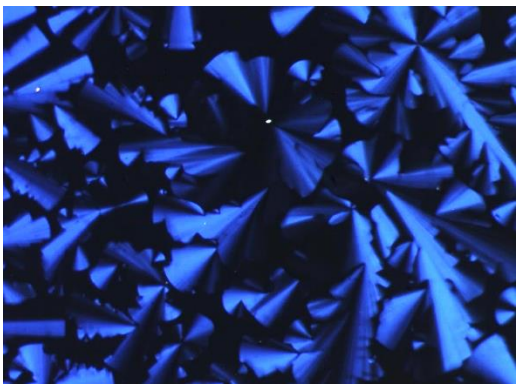 b 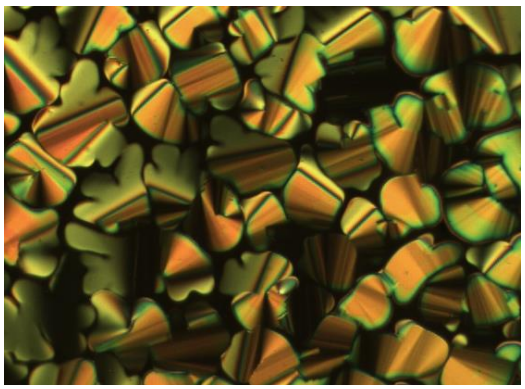

Figure 1-12: Texture of a) **12-8** (complex shown in Chapter 3) showing fan-like defects and; b) **10-N** showing straight-line defects.

1.1.3.2 Differential Scanning Calorimetry (DSC)

Complementary to POM is differential scanning calorimetry, in which the change in enthalpy for any phase transitions can be measured, as well as precise transition temperatures. It may be that phase changes are not observed in microscopy due to a minor change in texture, but an enthalpy change is observed by DSC, and *vice versa*, in which a second-order transition may not be observed in the DSC trace, but is very clearly defined when observed on the microscope.

Calibrated against a known indium standard, the power required to steadily heat a sample is recorded over a defined temperature range. Within the furnace, there is an empty, sealed pan in one chamber, and a pan of the same weight with the addition of a sample of the material in question in the other (Figure 1-13). Throughout the measurement, as the temperature is adjusted, the power required to keep both pans at the same temperature fluctuates due to the phase transitions.

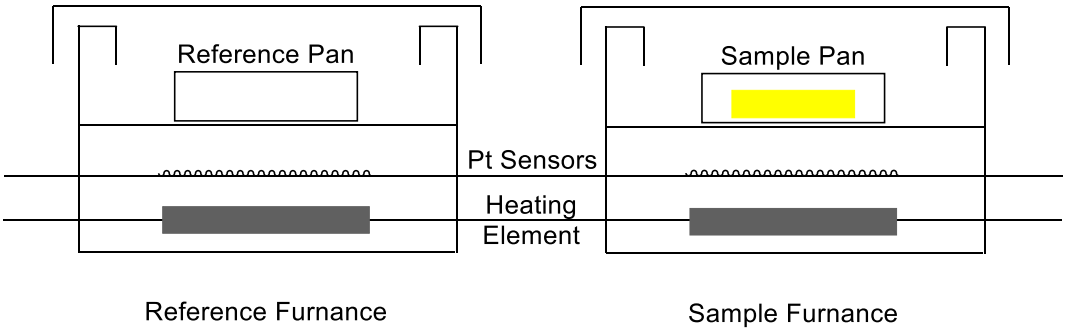

Figure 1-13: Schematic diagram of the dual-furnace experimental set-up of a differential scanning calorimeter (DSC).

On heating, any endothermic or exothermic transitions, *i.e.* transitions between crystalline and mesophase, between mesophases, or between the mesophase and isotropic liquid, requires increased power to keep both pans at the same temperature. This change in power can be plotted in what is referred to as a DSC trace (example shown in Figure 1-14) in which the area under the peaks can be integrated to give the enthalpy change for the transition. The magnitude of the enthalpy change of the transition can yield important information about changes in molecular order and arrangement in the molecules over the transition. The entropy change can also be calculated by assuming the system is at equilibrium at the transition.

In this example, the sample (**8-14**, as introduced in Chapter 3), which is crystalline at room temperature, is heated and melts at 89 °C in a sharp transition into the Col_h phase where it exists until it clears into the isotropic liquid at 166.0 °C. On cooling, the reverse transitions are observed, with some measure of supercooling for the crystallisation transition. This trace is typical of a sample with a wide-ranging, single mesophase. Typically, the heating and cooling cycles are repeated in order to investigate the reproducibility of the transitions and any degradation in the sample.

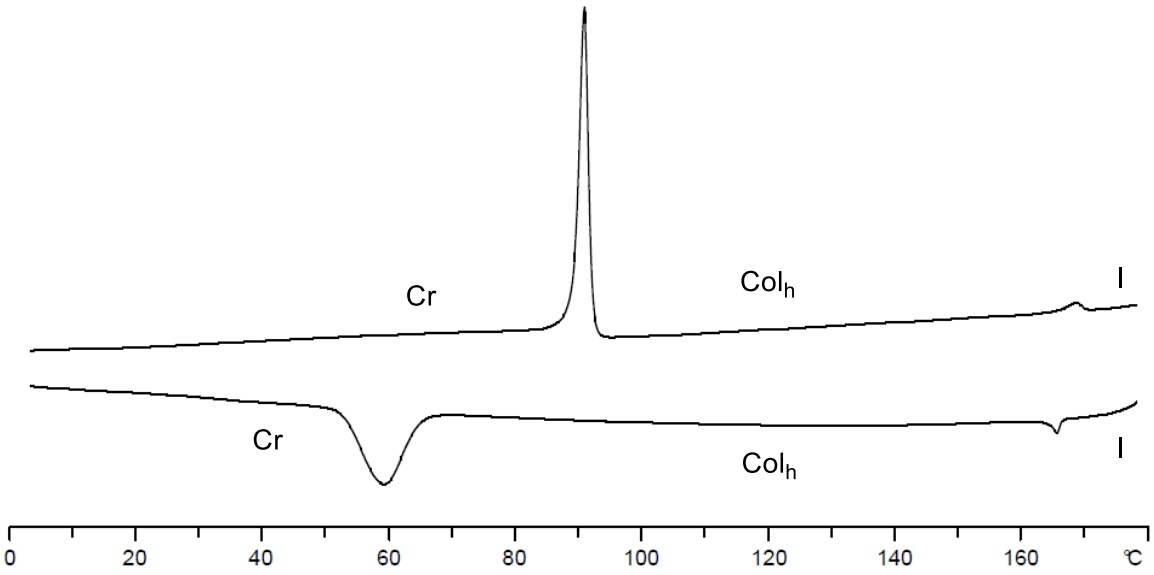

Figure 1-14: Example DSC trace of **8-14**, showing first heating and cooling cycles.

1.1.3.3 Small-angle X-ray Scatting (SAXS)

The third technique utilised in the identification and quantification of liquid-crystalline phases is small-angle X-ray diffraction (SAXS), a key technique from which structural parameters may be extracted. Due to the periodicity of a liquid-crystalline phase, when an X-ray beam is incident on the sample, the rays are scattered and, with application of Bragg's Law (Equation 1-2), a two-dimensional diffraction pattern can be produced. The application of Bragg's Law is the same as that for crystalline samples, in which the incident X-ray beam of wavelength λ is scattered from successive lattice planes resulting in an interaction between the scattered waves which results in constructive interference, and therefore a detectable reflection in the pattern, or destructive interference, which results in an absence of reflection, when the distance travelled by the waves is an integer multiple of λ ($n\lambda$) (Figure 1-15).

$$n\lambda = 2d\sin\theta \qquad \text{Equation 1-2}$$

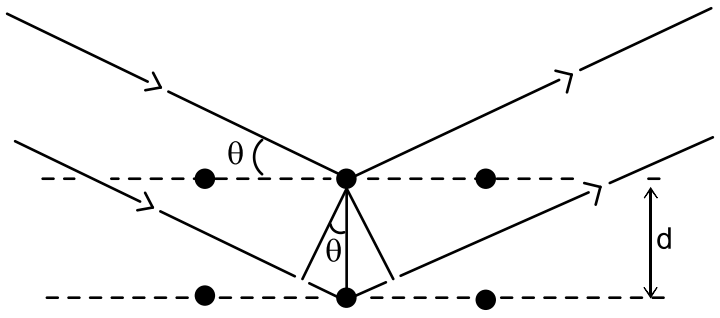

Figure 1-15: Illustration of Bragg's Law with incident X-ray beams and successive planes within an ordered sample.

Practically, the sample is loaded in a 0.9 mm diameter capillary tube, which is placed in a temperature-controlled furnace flanked by a magnet on either side which can give alignment to phases with high fluidity, such as nematic phases. The magnetic field applied from the 1 T magnets generates a magnetic field in the direction of the sample, which is insufficiently strong to align more viscous samples, such as smectic and columnar mesophases. The X-ray beam passes through the sample at a specified temperature and a diffraction pattern is collected (Figure 1-16).

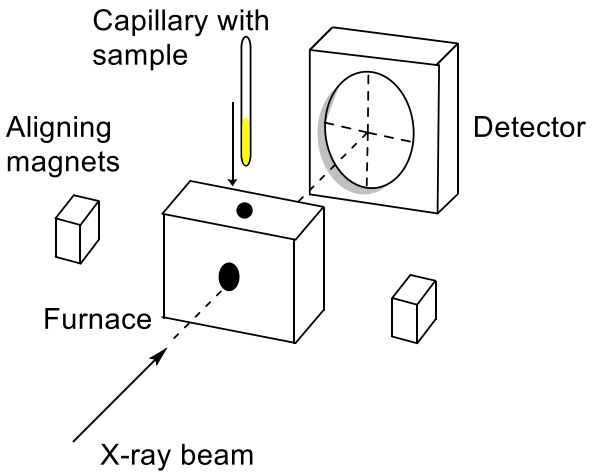

Figure 1-16: Schematic representation of SAXS experimental setup for the analysis of liquid crystals.

In an amorphous, unaligned sample (is often the case), a two-dimensional circular pattern is observed, which is radially integrated to give a diffraction pattern as a function of 2θ (°) or *d*-spacing (Å). An example of this is shown in Figure 1-17, in which the raw, circular diffraction pattern is shown in *a* and the integrated spectrum in *b* of a columnar hexagonal mesophase (of sample **8-14**, Chapter 3). As the majority of mesophases observed for the complexes reported in this thesis show columnar phases, special attention will be paid to the interpretation of SAXS of columnar phases.

a

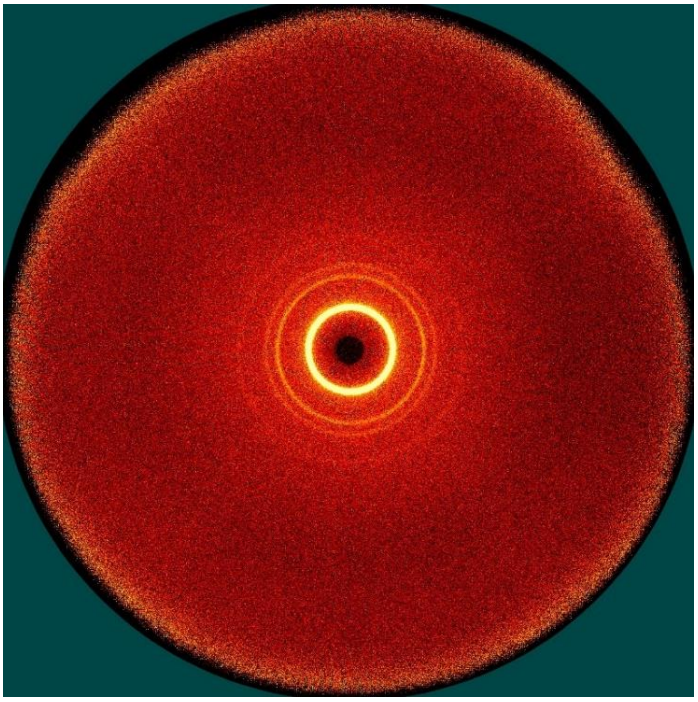

b

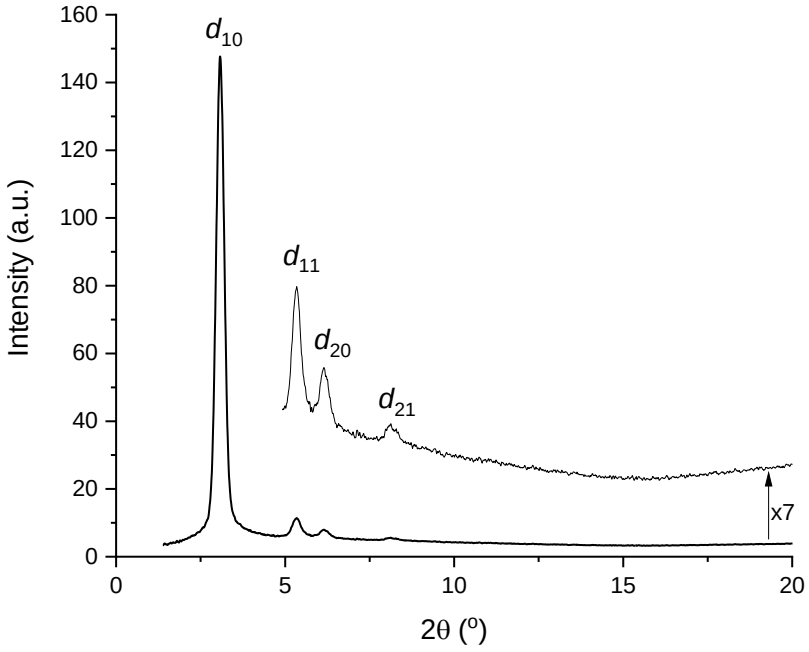

Figure 1-17: a) Raw diffraction pattern and b) integrated diffraction pattern of a Col_h mesophase of **8-14**.

Due to the symmetry of the columnar hexagonal phase, the reflections in the SAXS pattern always occur at a *d*-spacing of 1:√3:√4:√7 for the d_{10}, d_{11}, d_{20} and d_{21} reflections, respectively, according to Equation 1-3, which can be expanded upon for further reflections.[22] From the d_{10} reflection, it is also possible to calculate the lattice parameter, *a*, which is a measure of the inter-columnar distance, as defined in Figure 1-6, through the application of Equation 1-4. The origin of the reflections within the hexagonal lattice is shown in Figure 1-18. Accordingly, the SAXS pattern of the Col_h phase is characteristic and is indispensable in assigning phase symmetry, as it is sometimes not easy to distinguish textures of Col_h and Col_r phases.

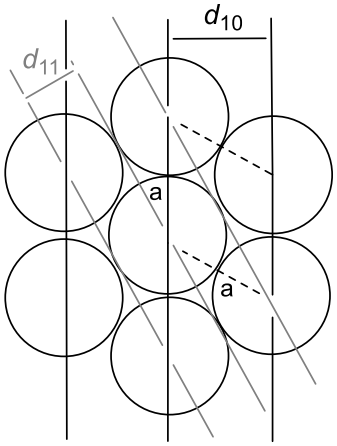

Figure 1-18: *d*-spacings and *a* parameter of the hexagonal lattice in the Col_h phase. Adapted from reference.[22]

For the Col_r phases of all three symmetries, indexation of the diffraction pattern is non-trivial. Typically observed in the small-angle region are the d_{11} and d_{20} reflections, although if two reflections are observed it is not always known which is which and it can be difficult to assign these without a large number of further reflections, which are often not observed. Assignment of the space group requires a fairly large number of observed reflections with accompanying systematic absences, and therefore space group assignment if often not definitive.

As columnar rectangular phases have lower symmetry than hexagonal columnar phases, the single lattice parameter (*a*) observed for Col_h phases is not-applicable; two lattice parameters, *a* and *b*, are required to describe the columnar arrangement, as shown diagrammatically in Figure 1-6 and calculated through the application of Equation 1-5.

$$d_{11} = \frac{d_{10}}{2\cos 30°} = \frac{d_{10}}{\sqrt{3}}$$ Equation 1-3

$$\frac{1}{d_{\mathrm{hk}}^2} = \frac{4}{3}\frac{h^2 + k^2 + hk}{a^2}$$ Equation 1-4

$$\frac{1}{d_{\mathrm{hk}}^2} = \frac{h^2}{a^2} + \frac{k^2}{b^2}$$ Equation 1-5

1.2 Introduction to Emissive Metal Complexes

Emissive compounds have a variety of uses in electronics,[48, 49] optical devices[50-53] and medicine, specifically in bioimaging.[54-58] Many emissive molecules are organic in nature, with fluorescence arising from aromatic moieties in the structure. This is a wide field of study and outwith the interest of the research presented in this thesis. What is relevant is research into the emissive behaviour

of transition metal complexes which show phosphorescence for uses primarily in optoelectronics such as organic light emitting diodes (OLEDs), the workings of which will be discussed in Section 1.3

1.2.1 The Heavy-Atom Effect and Inclusion of Spin-Orbit Coupling

As mentioned above, most emissive organic molecules typically show fluorescent emission; common electronic and emissive processes are shown by the simplified Jabłoński diagram in Figure 1-19. Fluorescent emission occurs through excitation from the singlet ground state (S_0) to the singlet excited state (S_1), followed by radiative emission from the same to return to the ground state; in both transitions there is a retention of electron spin. In this scenario, the triplet excited state, T_1 is not involved, due to the change in electron spin required to transition from S_1 to T_1, which is formally spin-forbidden with respect to spin selection rules as $\Delta S \neq 0$.[59]

Heavy metal elements such as those in the 2nd and 3rd row of the transition metal series have an increased level of spin-orbit coupling (SOC), which is a relativistic interaction between the spin angular momentum and the orbital angular momentum, which increases due to the larger nuclear charge (Z) being proportional to Z^4.[60] Consequently, in complexes of heavy metal elements, the $\Delta S = 0$ selection rule that formally forbids the transition between S_1 and T_1 becomes invalid as more quantum numbers are involved in the process, allowing the population of T_1 from S_1 *via* a process known as intersystem crossing (ISC). Subsequent radiative decay from the triplet excited state to the singlet ground state is then possible (phosphorescent emission), which is longer lived that fluorescence (10^{-9}-10^{-7} s for fluorescence compared to 10^{-3}-10^{2} s for phosphorescence) due to the accommodation of the required electron spin-flip.

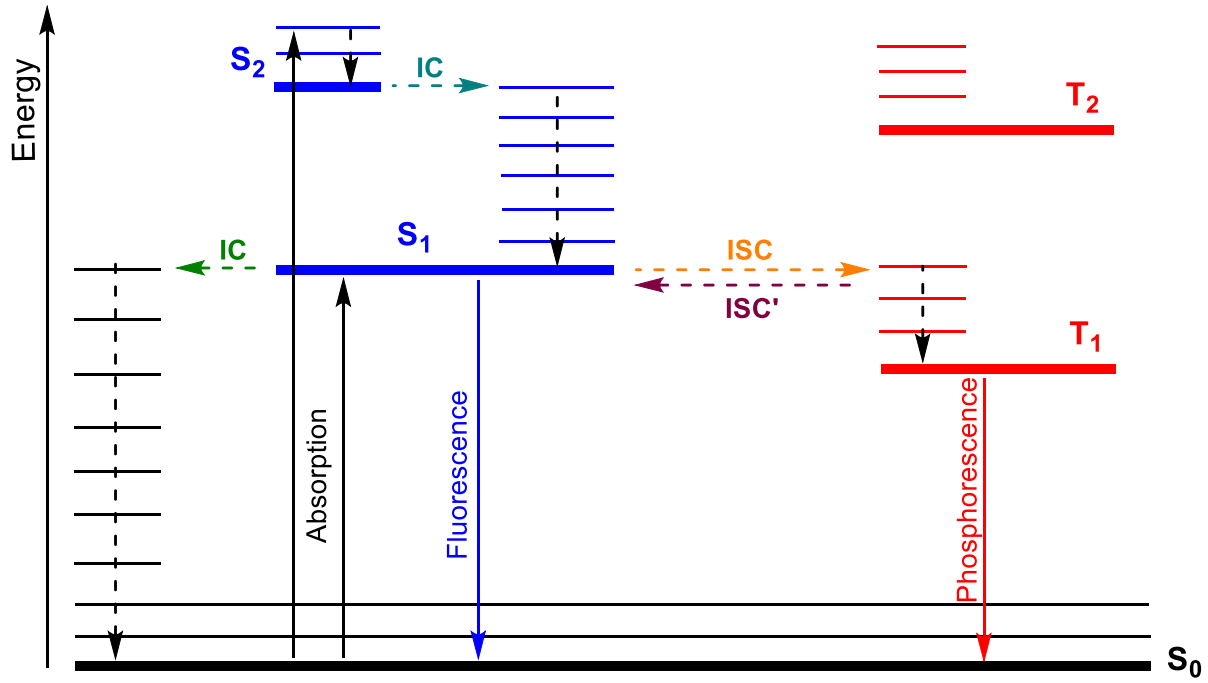

Figure 1-19: Simplified Jabłoński diagram showing absorption (black), fluorescence (blue) and phosphorescent (red) processes, as well as internal conversion (IC), intersystem crossing (ISC), reverse intersystem crossing (ISC'). Dashed arrows show vibrational relaxation.

1.2.2 Triplet Emission in Metal Complexes

As triplet and singlet excited states are statistically formed in a 3:1 ratio, access to the triplet manifold is a vital function for many applications, including those in OLEDs as discussed in Section 1.3.2. However, inclusion of a metal centre is not a guarantee of emission, as multiple factors contribute to the method of relaxation from the excited state to the ground state, many of which are non-radiative.

From experimental measurements, the radiative rate constant of emission, k_r, and the non-radiative rate constant of emission, k_{nr}, can be calculated. The radiative rate constant accounts for the energy that is dissipated as emitted light, and the non-radiative rate constant accounts for the loss of energy through all other pathways, including through internal conversion, intersystem crossing, bimolecular quenching, deactivating *d-d* states *etc*. The balance of these rate constants results in the magnitudes of the photoluminescence quantum yield (PLQY, ϕ), which is a measure of the efficiency of emission and is given by the number of photons emitted as a function of those absorbed, and the lifetime of emission, τ.

One major pathway for non-radiative emission is deactivation *via* energetically low-lying *d-d* states which, if thermally accessible, act as a sink for the excited state energy which is dissipated through

thermal equilibration or energy transfer. The presence of these states at low energies is responsible for the lack of luminescence in the 1st row transition metals, as they are easily accessible, as well as in 2nd and 3rd row complexes with weak-field ligands. This problem can be overcome in multiple ways, for example through the introduction of rigid, chelating ligands, the most common of which are bipyridine derivatives; the emissive species $[Ru(bpy)_3]^{2+}$ is ubiquitous in luminescence studies and photochemistry, showing red emission and readily accessible redox potentials.[61, 62] The introduction of chelating ligands leads to a smaller deformation of the excited state and a reduction in the overlap of the vibrational wavefunctions and therefore lower non-radiative rate constants as energy transfer to deactivating states (such as *d-d* states) is less efficient (Figure 1-20).

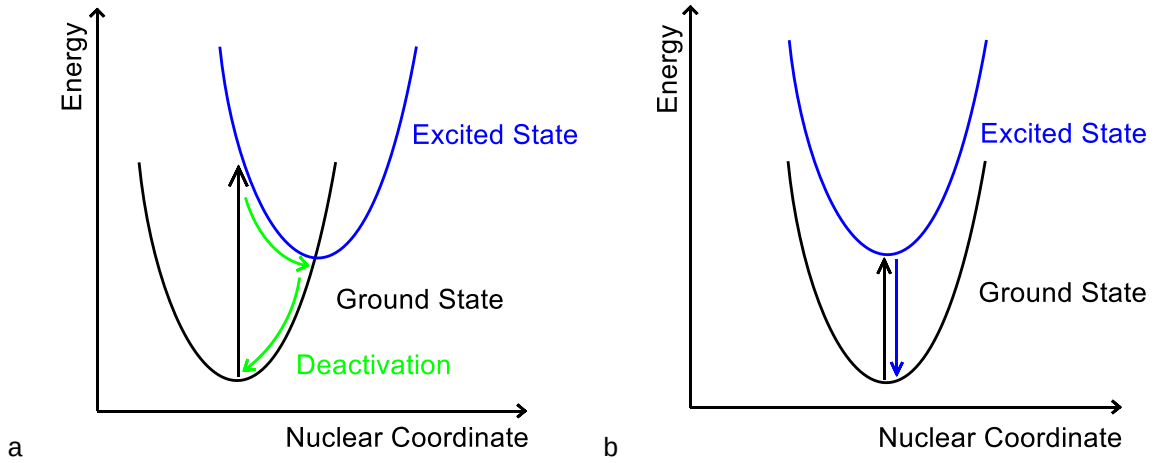

Figure 1-20: Displacement of the potential energy surface in species with a) thermally accessible deactivating states due to distortion between the ground and excited states and b) rigid chelating ligands resulting in minimal distortion between the group and excited states.

Both the position of the metal in the periodic table and the oxidation state can contribute to the magnitudes of k_r and k_{nr} as they affect the amount of metal character present in the excited state which in turn effects the efficiency of ISC due to the reduced level of SOC.

The inclusion of cyclometallating ligands in emissive metal complexes, such as the phenylpyridine derivatives utilised in this work, can increase the radiative rate constant of emissive systems as they are strong-field, σ-donating, π-accepting ligands. The use of a powerful σ-donating ligand increases the covalency in the metal-ligand bond which raises the energy of the 5*d* orbitals based on the metal centre which can increase the metal character in the excited state, resulting in more effective SOC. Cyclometallating ligands also increase the energy of deactivating *d-d* states, thereby reducing the non-radiative rate constant.

1.2.2.1 Platinum(IV) and Gold(III)

The two metals utilised in this research were platinum and gold in their +4 and +3 oxidation states, respectively. The fundamental properties of each will be addressed individually below, with discussion of recent literature on the emission of platinum(IV) complexes found in Chapter 2 and of gold(III) found in Chapter 4.

Platinum(IV) complexes have a d^6 electronic configuration and adopt an octahedral geometry; 2nd and 3rd row transition metals in the d^6 conformation always adopt an octahedral geometry when the coordination number is equal to six. This is a result of the ligand field and resultant crystal field splitting in which the e_g ($2e_g$) orbitals (dz^2, dx^2-y^2) are degenerate and found at higher energy than the t_{2g} orbitals ($d$xy, $d$xz, $d$yz), which are also degenerate (Figure 1-21).

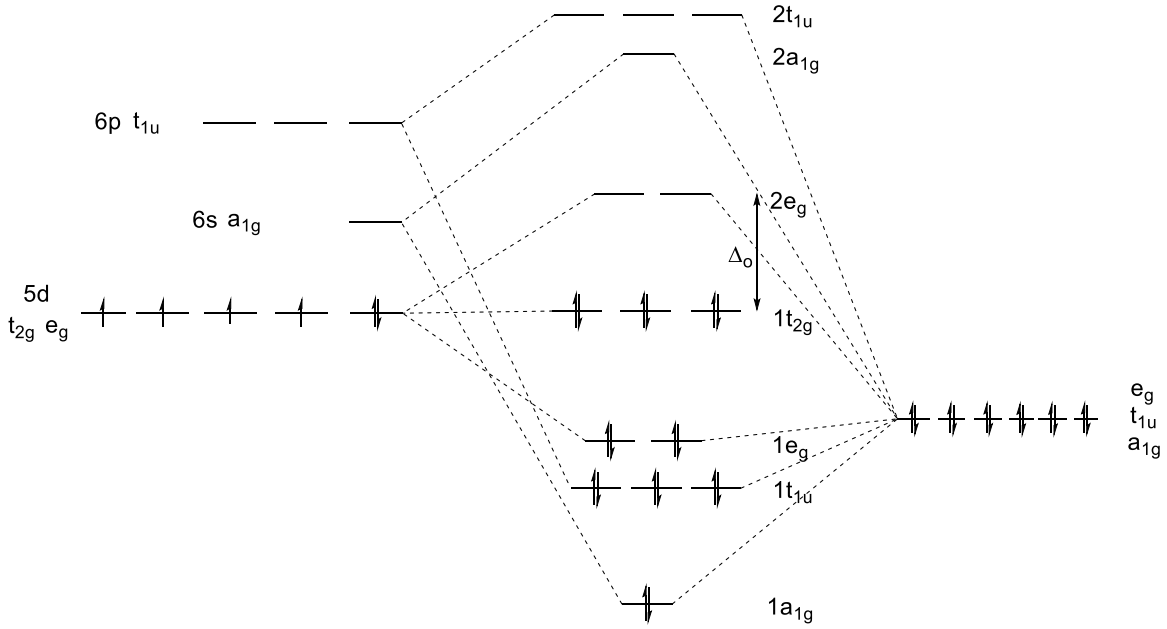

Figure 1-21: Molecular orbital energy-level diagram of an octahedral, d^6 metal complex such as those formed with platinum(IV); σ-bonding only.

Platinum(IV) complexes can be compared to the ubiquitous platinum(II) system, for which many room-temperature phosphorescent complexes are known. Generally, platinum(II) complexes have low-lying *d-d* states, but with the inclusion of chelating or cyclometallating ligands, these are raised in energy and emission is favoured.[53] This emission tends to be metal-ligand charge transfer (^{3}MLCT) in nature, giving broad, featureless emission bands. The square-planar nature of platinum(II) also allows for the formation of aggregates due to favourable π-π stacking and, the resulting Pt···Pt interactions can have an influence on the photophysical behaviour of the complexes; the associations can result in aggregation-induced emission (AIE)[63-65] and formation of excimers (excited dimers).[66-70]

In the octahedral platinum(IV), the higher oxidation state results in a contraction of the *d*-orbitals, which are lower in energy due to the higher positive charge. Accordingly, the lowest-energy excited state (from which the emission must originate, according to Kasha's rule[71]) becomes ligand-based, and therefore the emission observed is often a $\pi \rightarrow \pi^*$ transition with a smaller amount of metal character (^{3}LC), which results in poorer efficiencies. This reduction in efficiency can be combated through the use of multiple cyclometallating ligands, resulting in complexes with the general structure $[Pt(ppy)_2X_2]$, where ppy is a phenylpyridine derivative and X represents ancillary ligands, which are often halogens,[72, 73] a further chelating ligand such as bipyridine[74] or a further cyclometallating ligand to form charged complexes.[75, 76] Accordingly, reports of platinum(IV) emitters have lagged behind the well-explored platinum(II) derivatives, although in recent years, interest in the photophysical properties of platinum(IV) has increased (Chapter 2).

In contrast to platinum(IV), gold(III) is a d^8 metal and adopts a square-planar geometry. This conformation results in a decrease in the energy of the orbitals with a *z*-component, and an increase in the energy of the dx^2-y^2 orbital (Figure 1-22). This conformation is thermodynamically favoured and always present for 2nd and 3rd row transition metals with a coordination number of four.

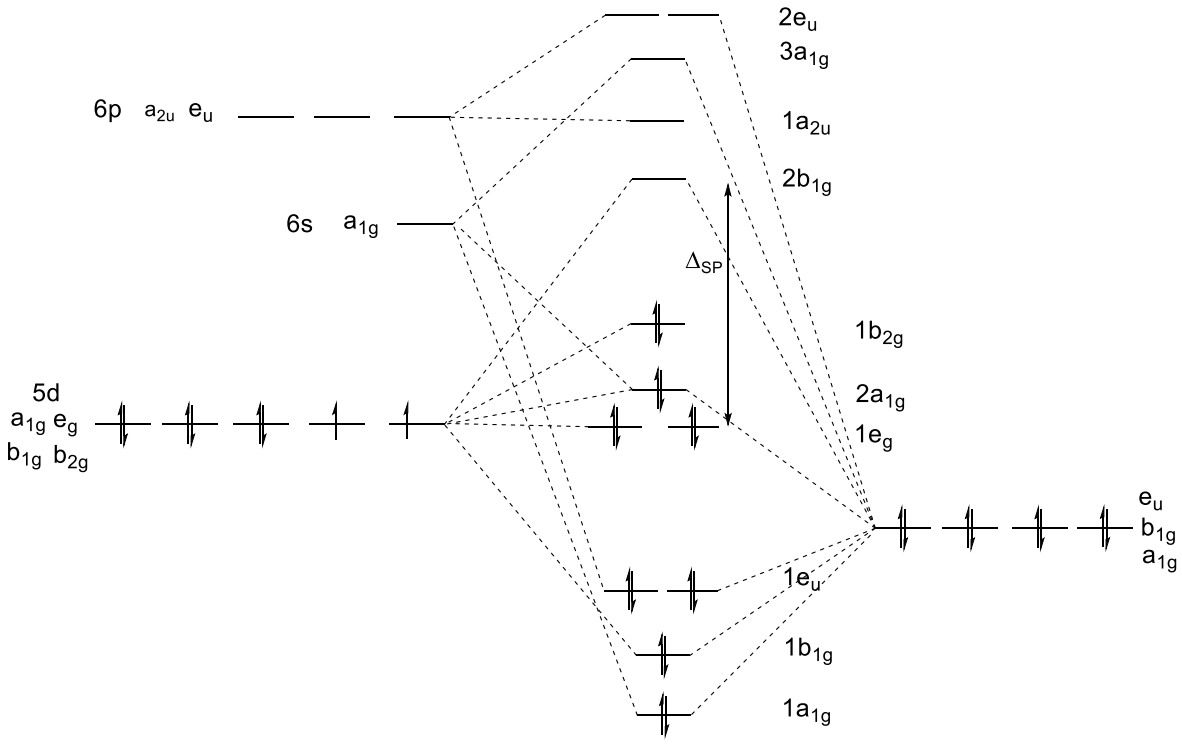

Figure 1-22: Molecular orbital energy-level diagram of a square-planar, d^8 metal complex such as those formed with gold(III); σ-bonding only.

Gold(III) complexes were not known to be emissive until recently, as they have very low-lying *d-d* states which lead to non-radiative emission that cannot be as easily overcome through the use of

chelating or cyclometallating ligands alone, as is successful for platinum(II). In order for room-temperature phosphorescence to be observed, a further strongly σ-donating ligand is required in the fourth coordination position to raise the *d*-*d* states and render the metal centre more electron rich. This is often an alkynyl,[77] alkyl[78] or aryl[79] ligand.

Compared to the isoelectronic platinum(II), the greater nuclear charge of the gold(III) centre results in a lowering of the energy of the metal *d*-orbitals. Consequently, unlike the predominantly ^{3}MLCT emission character observed for platinum(II), gold(III) emitters tend to show ligand-centred phosphorescence (^{3}LC), although this can be tuned to show ligand-ligand charge transfer (^{3}LLCT) through functionalisation of the ligands. The expanding field of luminescent gold(III) complexes is outlined and discussed in Chapter 4.

1.3 Introduction to Organic Light Emitting Diode (OLED) Devices

One of the main functions of phosphorescent complexes is as the emissive layer in organic light emitting diodes (OLEDs), which function on the principle of electroluminescence (EL), in which light in generated through the application of electricity.

Electroluminescence was first observed from silicon carbide (SiC) in 1907, with observations of EL from organic systems reported almost 50 years later in 1955 by Bernanose in the study of acridine orange and similar compounds, which were found to show fluorescence when an alternating-current (AC) was applied.[80] Electroluminescent materials were incorporated into many preliminary device structures,[81-83] but power requirements were large and unfeasible, until reports by Tang and VanSlyke of a bilayer-based device with thin-film materials which show appropriate drive voltages based on the emissive tris(8-hydroxyquinolato)aluminium(III), Alq_3 (shown later in Figure 1-25).[84]

OLED devices fabricated with electroluminescent materials show many advantages over the more traditionally used liquid crystal displays (LCDs), including faster response times, better contrast ratios and wider viewing angles. In addition, in an OLED device there is no requirement for a permanent backlight and consequently their power consumption is lower, as individual pixels can be illuminated and power is not used for those which are inactive. The lack of backlight also means that the devices are thinner and lighter compared to LCD equivalents and they can be incorporated into flexible substrates and portable devices. However, OLED screens are more expensive to manufacture and have a shorter operational lifetime, although as their commercial use becomes more popular, the cost gap is slowly closing. At the time of writing, OLED devices such as televisions are available commercially, many of which utilise iridium(III) complexes in the emissive layer,[85] although they still represent the high-end and state-of-the-art of the market.

There are, of course, still challenges to overcome within the field of OLED devices, especially within the design of emissive materials. In particular, it is more difficult to design blue emitters than those that emit red or green light, as blue emitters have inherently shorter usage lifetimes as they degrade more quickly due to the high-energy nature of the emission. Long-term stability of the emissive molecule must also be extended, as well as a reduction in the cost of production and an increase in viewing resolution.

1.3.1 Device Structure and Characterisation

The simplest OLED device structure consists of a thin emissive layer sandwiched between a cathode and an anode to form a circuit which is attached to a transparent substrate, often glass or a polymeric material, the latter of which can facilitate the formation of flexible devices (Figure 1-23).

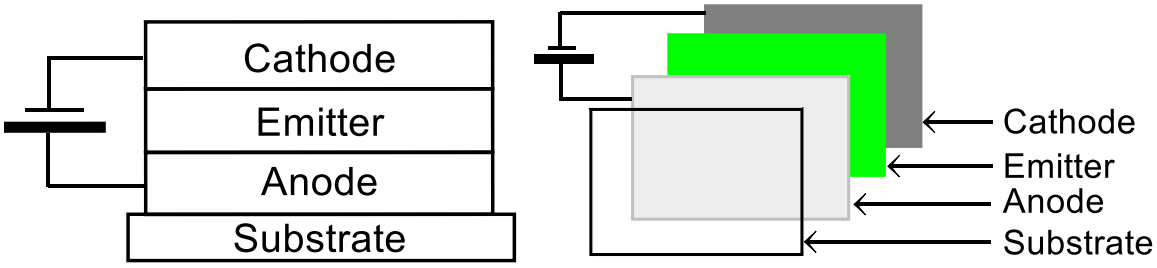

Figure 1-23: Device structure of simplest OLED, showing substrate, anode, emissive layer and cathode.

The working premise of electroluminescence in the device is analogous to that of photoluminescent excitation, in which an electron is excited from the singlet ground state to the singlet excited state (where it may cross to T_1, dependent on the material) through the application of light of an appropriate wavelength. In the device, when an electric field is applied, electrons are injected into the lowest unoccupied molecular orbital (LUMO) of the emissive material from the cathode and holes are injected into the highest occupied molecular orbital (HOMO) of the same from the anode. The recombination of the holes and electrons generates an exciton, from which light is emitted from the device.

However, this device configuration is rarely used and in reality, OLED devices are designed as a multi-layered structure to enhance the transport of holes and electrons through the matching of work functions and energy levels of the constituent materials (Figure 1-24). If there is poor compatibility between the anode or cathode and the emitter (Figure 1-24b, red arrows), the injection of charge carriers is significantly poorer. To combat this, hole and electron transport layers (HTL and ETL, respectively) are included in the device structure to minimise the gap and provide an easier pathway for the movement of charge carriers (Figure 1-24b, green arrows).

Hole/electron/exciton blocking layers (HBL and EBL, respectively) are often utilised to confine the recombination of charge carriers to within the emissive layer.

In the majority of devices (exceptions will be outlined in subsequent sections) the emitter exists as a dopant within a polymer matrix, forming the emissive layer (EML). Compatibility of energy levels between the host and emitter is also required as oftentimes the charge carrier is trapped on the host rather than the emissive dopant when it reaches the EML, especially at low dopant concentrations, which is followed by energy transfer to the emitter.

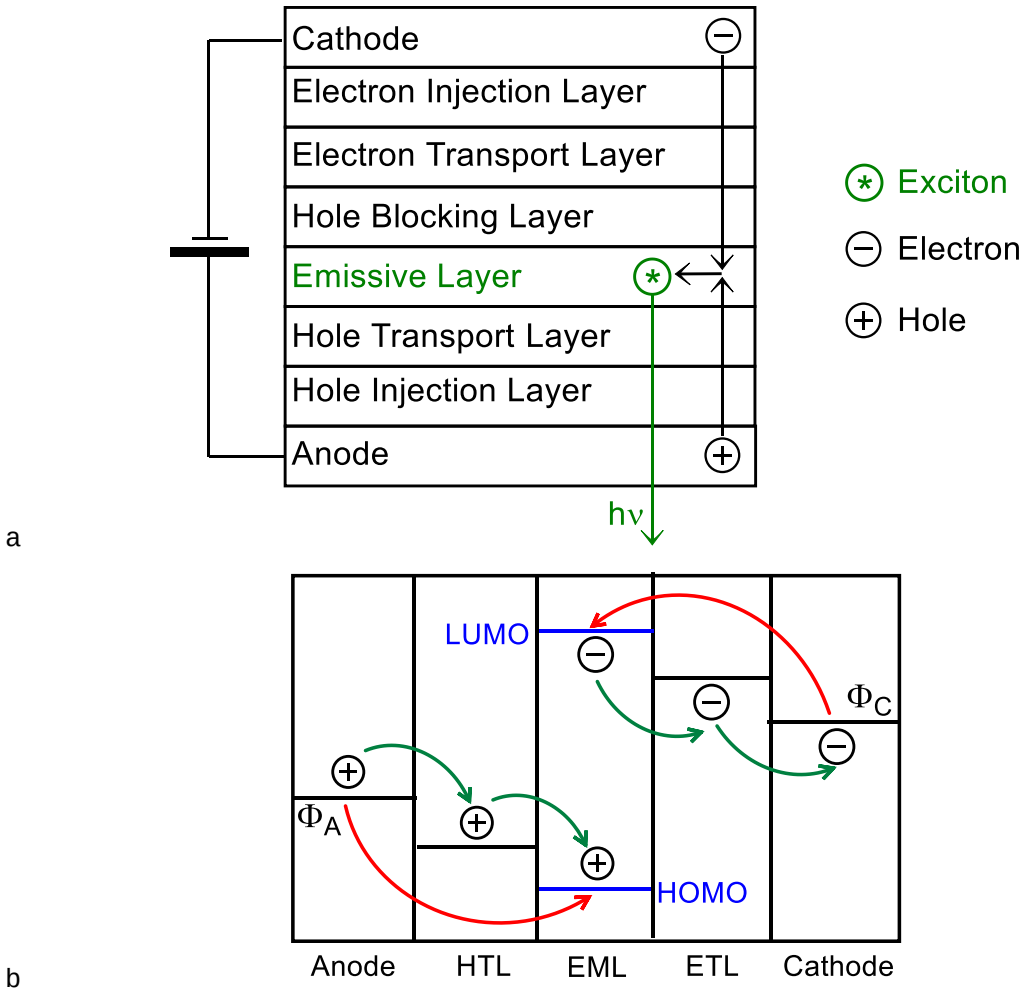

Figure 1-24: Schematic diagram a) of a typical multi-layered OLED structure, showing; b) pathways of the charge carriers as a function of work functions (Φ_A and Φ_C) and energy levels (HOMO/LUMO).

The use of indium tin oxide (ITO) as an anode is ubiquitous in the fabrication of OLED devices, as is the use of poly(3,4-ethylenedioxythiophene) polystyrene sulfonate (PEDOT:PSS) as the hole injection layer (HIL). A metallic cathode, such as aluminium or calcium, is used due to the presence of a low work function, or an alloy with the same property, such as Li/Al. The electron injection layer (EIL) tends to be composed of an inorganic salt, such as caesium fluoride (CsF) or zinc oxide (ZnO). The materials utilised as ETLs and HTLs as well as HBL/EBL and hosts for the EML are more varied. The materials which showed the highest compatibility with the emissive materials

presented in this thesis are outlined and discussed further in Chapter 4, however commonly used materials will be addressed below.

Commonly used electron-transport layer materials include tris(8-hydroxyquinolato)aluminium(III) (Alq_3), as utilised by Tang and Van Slyke and described above, as well as 3-(biphenyl-4-yl)-5-(4-tert-butylphenyl)-4-phenyl-4H-1,2,4-triazole (TAZ) and 1,3,5-tris(3-pyridyl-3-phenyl)benzene (TmPyPB); all three can also function as hole-blocking materials (Figure 1-25).[86] Specific-hole blocking materials include tris(2,4,6-trimethyl-3-(pyridin-3-yl)phenyl)borane (3TPYMB) and bis[2-(diphenylphosphino)phenyl] ether oxide (DPEPO) (structures shown in Chapter 4).

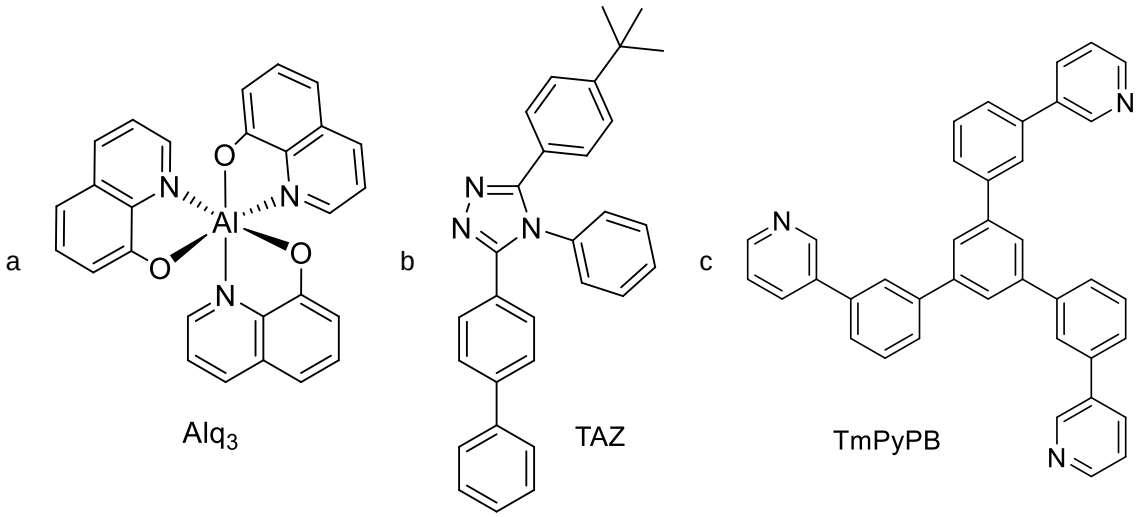

Figure 1-25: Structure of common ETL materials

Commonly used hole-transport materials, which typically include electron-donating groups such as carbazoles, include 4,4'-bis[*N*-(1-naphthyl)-*N*-phenylamino]biphenyl (NPB), tris(4-carbazoyl-9-ylphenyl)amine (TCTA) and poly(9-vinylcarbazole) (PVK) (Figure 1-26).[87]

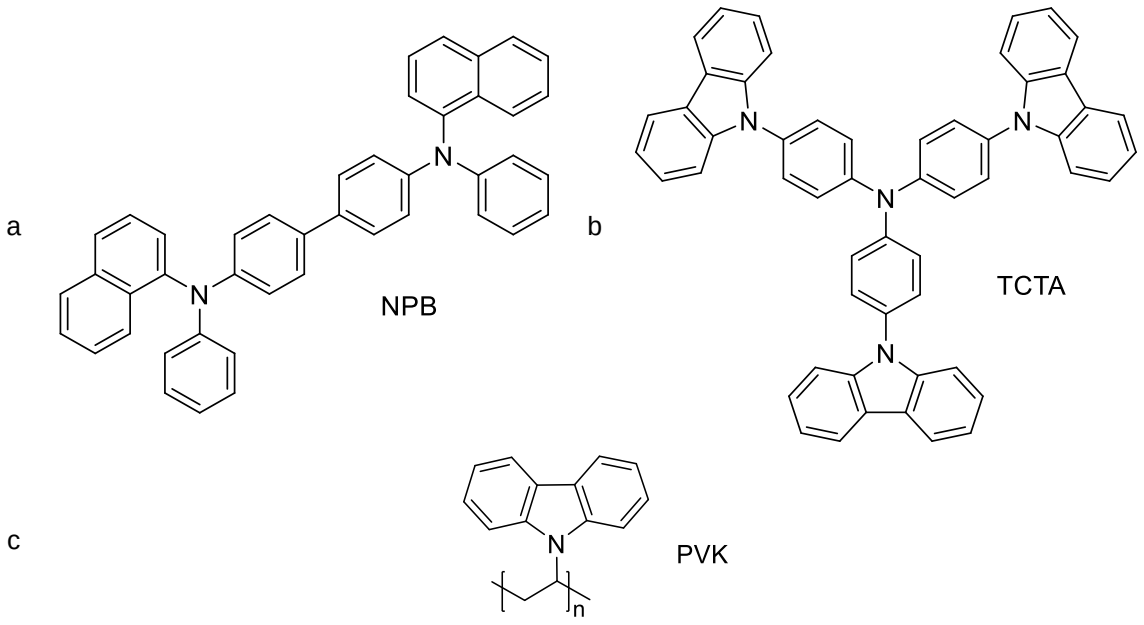

Figure 1-26: Structure of common HTL materials

Successive deposition of the layers is achieved through either spin-coating from a solution of a defined concentration, commonly used for PEDOT:PSS layers and emitters with high molecular weights, or vacuum deposition by resistive heating methods, used for low MW emitters and ETL, EIL and the metallic cathode.

The performance of the fabricated device is defined primarily through its efficiency parameters, including current efficiency, power efficiency and, most importantly, external quantum efficiency; the last of these is a measure of the number of output photons compared to the number of charge carriers injected. Although the *internal* quantum efficiency of a device can reach a theoretical 100% maximum with triplet emitters (*vide infra*), the *external* quantum yield (EQE) of a device is always significantly lower due to losses incurred upon charge carrier injection and mobility, limitations from the PLQY of the emissive material and the ability of photons to effectively exit the device, with light lost due to internal reflection. The internal (η_{int}) and external (η_{ext}) quantum efficiencies are related *via* the equations shown in Equation 1-6 to Equation 1-8.[88]

$$\eta_{ext} = \eta_{int}\eta_{ph} \qquad \text{Equation 1-6}$$

$$\eta_{ext} = \gamma\eta_{ex}\phi_P\eta_{ph} \qquad \text{Equation 1-7}$$

$$\eta_{ext} = \frac{\eta_{int}}{2n^2} \qquad \text{Equation 1-8}$$

where η_{ph} is the light-out coupling efficiency, η_{ex} is the fraction of formed excitons that result in a radiative transition, γ is the ratio of electrons to holes injected into the device (this must always be <1; to satisfy this, the reverse ratio can also be used), ϕ_P is the quantum yield of the emitter and *n* is the refractive index of the medium.

In addition to the EQE, device performance is characterised through the measurement of:

- Current efficiency, reported in cd A^{-1} and a measure of the maximum luminous intensity as a function of the current inputted to the device.
- Power efficiency, reported in lm W^{-1} and a measure of the maximum amount of visible light (as perceived by the human eye) as a function of the amount of power inputted to the device.
- Luminescence, reported in cd m^{-2} and a measure of the maximum brightness per unit area.
- Turn-on voltage, a measure of the minimum voltage at which emission can be experimentally detected from the device.
- Commission Internationale d'Eclairage (CIE) chromaticity coordinates, which are two-dimensional *x*,*y*-coordinates which can be plotted in CIE 1931 colour space to give an accurate measure of emission colour.

1.3.2 Phosphorescent OLEDs (PhOLEDs) Utilising Emissive Metal Complexes

Singlet excited states are statistically formed in a ratio of 1:3 compared to triplet excited states. As such, in using a fluorescent emitter in an OLED device, the internal quantum efficiency is limited to 25%, as only recombination from the singlet excited state is allowed. In comparison, when a triplet emitter is used, access to the triplet manifold means that the device can achieve a theoretical 100% internal efficiency, as recombination from both singlet and triplet excited states is allowed, although it should be noted that for phosphorescent emitters, all emission is triplet in nature due to ISC. The 100% theoretical efficiency arises due to the fact that the charge carriers injected into the OLED device originate from separate electrodes and are not coupled; as such there are no constraints on the spin of the injected charge carriers. To show respectable performance in an OLED device, a triplet emitter must ideally:

- Have a lifetime of emission of approximately 1 μs to avoid self-quenching;[89]
- Show a high PLQY (approaching 100%);
- Be resistant to aggregation to avoid self-quenching *via* triplet-triplet annihilation;
- Be charge neutral to avoid migration when the electric field is applied;
- Be able to undergo sublimation (for vacuum-deposition) or readily soluble in organic solvents (for solution-processing).

Deviation from these conditions, especially the first three, can result in a substantial reduction of device performance compared to the theoretical maximum.

From both a commercial point of view and in fundamental research, cyclometallated complexes of iridium(III) match these criteria. Colour tunability and improvements in quantum yield and lifetimes are achievable through modification and substitution of the cyclometallating and chelating ligands. These modifications can alter the energies of the orbitals involved in the emission, which may change the energy of emission, or alter the orbitals involved in the emission entirely, which has the ability to change the nature of the emission, for example, from intraligand $\pi \rightarrow \pi^*$ (^{3}IL) based, to charge-transfer based.

1.3.3 Liquid-Crystalline Materials for (Ph)OLEDs and Polarised Emission

The intrinsic ability of liquid-crystalline compounds to form an ordered material can be very beneficial to the fabrication of many types of devices, including thin-film transistors and photovoltaic devices.[22, 90-93]

The ordered nature of a liquid-crystalline device component can lead to lower drive voltages due the reduction in power needed to move charge carriers through an ordered material in comparison to one which is amorphous; materials which show columnar phases have been shown to have excellent hole-mobility along the columnar axis, essentially functioning as one-dimensional molecular wires.[22] The peripheral alkyl/alkoxy chains present in such systems are also of beneficial in doped emissive layers, acting as spacers between molecules and providing steric hindrance to mitigate self-quenching effects.

One of the main benefits of using a liquid-crystalline material in an OLED device is the comparative ease of molecular alignment due to the arrangement within the mesophase. From this, the emissive layer, whether doped in a polymer matrix or a neat-film of the emissive complex, can be aligned, and for certain emitters and device structures, this can lead to polarised emission.[94, 95]

The main application of polarised emission is in liquid crystal display (LCD) technology; the device structure of a typical LCD is shown in Figure 1-27. The source of light in an LCD display originates from a backlight, often LED or electroluminescent panel (ELP) based, which is unpolarised and passes through a polarising film. The polarised light then passes through the liquid-crystalline layer of the device, which is typically a nematic material although smectic mesogens are also used,[96] which is aligned by the transparent electrodes between which is it sandwiched. There is then a second polariser orientated at 90° to the first, as well as a colour filter for selection of the required wavelength of light. Glass substrates both on the front and back of the device are not shown in Figure 1-27 for the sake of clarity.

The forced surface alignment of the liquid-crystalline layer is given by two electrodes which are arranged perpendicular to each other, giving the liquid-crystalline layer a helically twisted conformation when little or no voltage is applied to the cell. When the layer is twisted, the incident polarised light is rotated and able to pass through the second polariser and escape the device, resulting in an illuminated pixel of the designated colour. When a large voltage is applied to the device, the molecules are rotated so that the helical structure is destroyed, thus the incident polarised light is not twisted and is extinguished by the second polariser, resulting in the pixel appearing black.

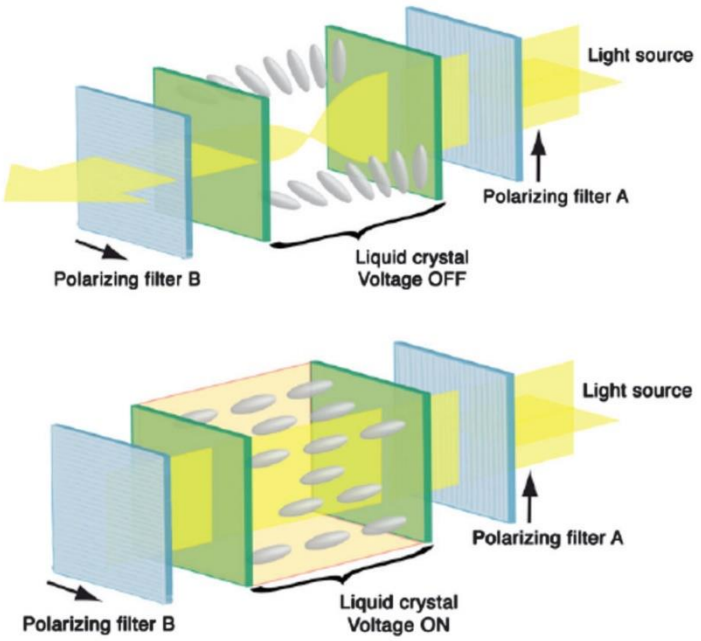

Figure 1-27: Device structure and working principle of LCD display. The top image shows the device with little to no voltage applied, with the helical LC alignment twisting the polarised light and allowing light to escape the device. The bottom image shows the non-twisted alignment of the LC when voltage is applied, resulting in the extinguishment of light by the second polariser. Image taken directly from source.[94]

This device structure has some obvious drawbacks, most relevant of which is the requirement for a backlight and multiple polarising layers; the backlight of the device is bulky and cumbersome, and its output of unpolarised light which then must be polarised by a filter is wasteful, as approximately 50% of the light produced by the backlight is lost in the polarisation process.[94] Herein lies the advantage of polarised emitters. An emitter which has the ability to emit polarised light has the potential to be used as a more efficient backlight in an LCD device and would render the first polariser redundant. This would result in a reduction of manufacturing costs, as well as operational costs, as all the light produced by the backlight would pass through the device, resulting in improved energy efficiency.

An overview of metallomesogens which exhibit polarised emission both in thin films and OLED devices is given in Chapter 4.

1.4 Thesis Objectives

The research outlined in this thesis concerns the synthesis and characterisation of emissive, liquid-crystalline organometallic complexes based on platinum(IV) and gold(III). The complexes and all

associated ligands have been synthesised from commercial starting materials through both established and novel synthetic methodology. Extensive materials characterisation will be outlined for all metal complexes, focussing on self-organisation behaviour, including thermotropic liquid-crystalline properties, concentration-dependent aggregation, and the formation of metallogels, and emissive properties. Proof-of-concept OLED devices with many of the novel gold(III) complexes will be presented, showing competitive device performance when compared to the literature.

1.4.1 A Comment on Nomenclature

It is appropriate here to give a brief comment on the nomenclature used throughout this thesis for the synthesised compounds. Within the body of the text (Chapters 2-5), final ligands and complexes are referred to by a naming structure devised during the writing up of results, *e.g.* **HL-1**, **Pt-1**, **1-8** *etc*. This was done for ease of reference for complex molecules and consistency between in-text references and figures. Shorthand organic nomenclature, *e.g.* 'two-chain C^N^C ligand', is also used within the text to refer to specific complexes and ligands, again for clarity. Naming systems for platinum complexes (Chapter 2) are kept separate from gold complexes (Chapters 3 and 4) due to the contained nature of each set of complexes. Nomenclature of platinum complexes has been retained (with slight modification) from the published version of this work to aid in consistency. In Chapter 6, which details all the experimental details relevant to this work, compounds are named according to IUPAC guidelines.

1.5 References

1. F. Reinitzer, *Monatsh. Chem.*, 1888, **9**, 421-441.
2. F. Reinitzer, *Liq. Cryst.*, 1989, **5**, 7-18.
3. O. Lehmann, *Z. Phys. Chem.*, 1889, **4**, 462.
4. D. Vorländer, *Ber. Dtsch. Chem. Ges.*, 1907, **40**, 1970-1972.
5. S. Chandrasekhar, B. K. Sadashiva and K. A. Suresh, *Pramana*, 1977, **9**, 471-480.
6. A. Isihara, *J. Chem. Phys.*, 1951, **19**, 1142-1147.
7. R. Alben, *Phys. Rev. Lett.*, 1973, **30**, 778-781.
8. J. P. Straley, *Phys. Rev. A*, 1974, **10**, 1881-1887.
9. T. E. Strzelecka, M. W. Davidson and R. L. Rill, *Nature*, 1988, **331**, 457-460.
10. G. J. T. Tiddy, *Phys. Rep.*, 1980, **57**, 1-46.
11. A. J. Leadbetter, *Thermotropic Liquid Crystals* Wiley, Chichester, New York, 1987.
12. D. Demus, *Liq. Cryst.*, 1989, **5**, 75-110.
13. B. Bahadur, *Liquid Crystals: Applications and Uses*, World Scientific, 1990.
14. G. Meier, E. Sackmann and J. G. Grabmaier, *Applications of Liquid Crystals*, Springer Berlin Heidelberg, 2012.
15. A. M. Donald, A. H. Windle and S. Hanna, *Liquid Crystalline Polymers*, Cambridge University Press, 2006.
16. L. L. Chapoy, *Recent Advances in Liquid Crystalline Polymers*, Springer Netherlands, 2012.
17. D. Bertrand, S. Buathong, I. Bury and D. Guillon, *Chem. Soc. Rev.*, 2007, **36**, 1495-1513.
18. S. Ponomarenko, N. Boiko and V. Shibaev, *Polym. Sci. Ser. C.*, 2001, **43**, 1-45.
19. D. Guillon and R. Deschenaux, *Curr. Opin. Solid State Mater. Sci.*, 2002, **6**, 515-525.
20. R. J. Mandle, E. J. Davis, J. P. Sarju, N. Stock, M. S. Cooke, S. A. Lobato, S. J. Cowling and J. W. Goodby, *J. Mat. Chem. C.*, 2015, **3**, 4333-4344.
21. S. Chandrasekhar, *Liq. Cryst.*, 1993, **14**, 3-14.
22. S. Laschat, A. Baro, N. Steinke, F. Giesselmann, C. Hägele, G. Scalia, R. Judele, E. Kapatsina, S. Sauer, A. Schreivogel and M. Tosoni, *Angew. Chem. Int. Ed.*, 2007, **46**, 4832-4887.
23. R. W. Date, E. F. Iglesias, K. E. Rowe, J. M. Elliott and D. W. Bruce, *Dalton Trans.*, 2003, 1914-1931.
24. K. Binnemans and K. Lodewyckx, *Angew. Chem. Int. Ed.*, 2001, **40**, 242-244.
25. K. Binnemans and C. Görller-Walrand, *Chem. Rev.*, 2002, **102**, 2303-2346.
26. T. Cardinaels, K. Driesen, T. N. Parac-Vogt, B. Heinrich, C. Bourgogne, D. Guillon, B. Donnio and K. Binnemans, *Chem. Mater.*, 2005, **17**, 6589-6598.
27. S. R. Collinson, F. Martin, K. Binnemans, R. V. Deun and D. W. Bruce, *Mol. Cryst. Liq. Cryst.*, 2001, **364**, 745-752.
28. T. M. Swager and H. Zheng, *Mol. Cryst. Liq. Cryst.*, 1995, **260**, 301-306.
29. H. Zheng and T. M. Swager, *J. Am. Chem. Soc.*, 1994, **116**, 761-762.
30. D. W. Bruce, *Adv. Mater.*, 1994, **6**, 699-701.
31. D. W. Bruce and X.-H. Liu, *Liq. Cryst.*, 1995, **18**, 165-166.
32. M.-A. Guillevic and D. W. Bruce, *Liq. Cryst.*, 2000, **27**, 153-156.
33. M.-A. Guillevic, M. J. Danks, S. K. Harries, S. R. Collinson, A. D. Pidwell and D. W. Bruce, *Polyhedron*, 2000, **19**, 249-257.
34. M.-A. Guillevic, M. E. Light, S. J. Coles, T. Gelbrich, M. B. Hursthouse and D. W. Bruce, *J. Chem. Soc., Dalton Trans.*, 2000, 1437-1445.
35. X.-H. Liu, B. Henirich, I. Manners, D. Guillon and D. W. Bruce, *J. Mater. Chem.*, 2000, **10**, 637-644.
36. D. Pucci and B. Donnio, in *Handbook of Liquid Crystals*, eds. J. W. Goodby, C. Tschierske, R. Peter, H. F. Gleeson, T. Kato and P. J. Collings, Wiley, 2014, pp. 1-67.
37. D. Vorländer, *Z. Phys. Chem.*, 1923, **105**, 211.
38. J. Malthete and J. Billard, *Mol. Cryst. Liq. Cryst.*, 1976, **34**, 117-121.
39. A. M. Giroud and U. T. Mueller-westewoff, *Mol. Cryst. Liq. Cryst.*, 1977, **41**, 11-13.
40. X.-h. Liu, I. Manners and D. W. Bruce, *J. Mater. Chem.*, 1998, **8**, 1555-1560.

41. X.-H. Liu, M. Nurul Abser and D. W. Bruce, *J. Organomet. Chem.*, 1998, **551**, 271-280.
42. K. E. Rowe and D. W. Bruce, *J. Chem. Soc., Dalton Trans.*, 1996, 3913-3915.
43. M. Ghedini, D. Pucci and G. Barberio, *Liq. Cryst.*, 2000, **27**, 1277-1283.
44. M. Ghedini, D. Pucci, A. Crispini and G. Barberio, *Organometallics*, 1999, **18**, 2116-2124.
45. S. T. Trzaska, H.-F. Hsu and T. M. Swager, *J. Am. Chem. Soc.*, 1999, **121**, 4518-4519.
46. R. W. Boyd, *Nonlinear Optics*, Elsevier Science, 2003.
47. P. Oswald and P. Pieranski, *Smectic and columnar liquid crystals: Concepts and physical properties illustrated by experiments*, Taylor & Francis, Boca Raton, Florida, USA, 2006.
48. R. Visbal and M. C. Gimeno, *Chem. Soc. Rev.*, 2014, **43**, 3551-3574.
49. J. Zhao, S. Ji, W. Wu, W. Wu, H. Guo, J. Sun, H. Sun, Y. Liu, Q. Li and L. Huang, *RSC Adv.*, 2012, **2**, 1712-1728.
50. Y. Chi and P.-T. Chou, *Chem. Soc. Rev.*, 2010, **39**, 638-655.
51. J. A. Gareth Williams, S. Develay, D. L. Rochester and L. Murphy, *Coord. Chem. Rev.*, 2008, **252**, 2596-2611.
52. Y. Chi, T.-K. Chang, P. Ganesan and P. Rajakannu, *Coord. Chem. Rev.*, 2017, **346**, 91-100.
53. V. W.-W. Yam and K. M.-C. Wong, *Chem. Commun.*, 2011, **47**, 11579-11592.
54. S. Faulkner, S. J. A. Pope and B. P. Burton-Pye, *Appl. Spectrosc. Rev.*, 2005, **40**, 1-31.
55. V. Fernández-Moreira, F. L. Thorp-Greenwood and M. P. Coogan, *Chem. Commun.*, 2010, **46**, 186-202.
56. K. K.-W. Lo, A. W.-T. Choi and W. H.-T. Law, *Dalton Trans.*, 2012, **41**, 6021-6047.
57. Q. Zhao, C. Huang and F. Li, *Chem. Soc. Rev.*, 2011, **40**, 2508-2524.
58. A. J. Amoroso and S. J. A. Pope, *Chem. Soc. Rev.*, 2015, **44**, 4723-4742.
59. R. P. Wayne, *Principles and Applications of Photochemistry*, Oxford University Press, Oxford, UK, 1988.
60. W. G. Richards and P. R. Scott, *Energy Levels in Atoms and Molecules*, Oxford University Press, Oxford, UK, 1995.
61. D. M. Roundhill, in *Photochemistry and Photophysics of Metal Complexes*, ed. D. M. Roundhill, Springer US, Boston, MA, 1994, pp. 165-215.
62. K. Kalyanasundaram, *Coord. Chem. Rev.*, 1982, **46**, 159-244.
63. J. Mei, N. L. C. Leung, R. T. K. Kwok, J. W. Y. Lam and B. Z. Tang, *Chem. Rev.*, 2015, **115**, 11718-11940.
64. Y. Hong, J. W. Y. Lam and B. Z. Tang, *Chem. Soc. Rev.*, 2011, **40**, 5361-5388.
65. Y. Chen, J. W. Y. Lam, R. T. K. Kwok, B. Liu and B. Z. Tang, *Materials Horizons*, 2019, **6**, 428-433.
66. M. T. Walden, P. Pander, D. S. Yufit, F. B. Dias and J. A. G. Williams, *J. Mat. Chem. C.*, 2019, **7**, 6592-6606.
67. M. Z. Shafikov, A. F. Suleymanova, D. N. Kozhevnikov and B. König, *Inorg. Chem.*, 2017, **56**, 4885-4897.
68. L. Murphy, P. Brulatti, V. Fattori, M. Cocchi and J. A. G. Williams, *Chem. Commun.*, 2012, **48**, 5817-5819.
69. W. Mróz, C. Botta, U. Giovanella, E. Rossi, A. Colombo, C. Dragonetti, D. Roberto, R. Ugo, A. Valore and J. A. G. Williams, *J. Mater. Chem.*, 2011, **21**, 8653-8661.
70. E. Rossi, L. Murphy, P. L. Brothwood, A. Colombo, C. Dragonetti, D. Roberto, R. Ugo, M. Cocchi and J. A. G. Williams, *J. Mater. Chem.*, 2011, **21**, 15501-15510.
71. M. Kasha, *Discussions of the Faraday Society*, 1950, **9**, 14-19.
72. F. Juliá, D. Bautista and P. Gonzalez-Herrero, *Chem. Commun.*, 2016, **52**, 1657-1660.
73. F. Juliá, M.-D. García-Legaz, D. Bautista and P. González-Herrero, *Inorg. Chem.*, 2016, **55**, 7647-7660.
74. D. M. Jenkins and S. Bernhard, *Inorg. Chem.*, 2010, **49**, 11297-11308.
75. F. Julia, D. Bautista, J. M. Fernandez-Hernandez and P. Gonzalez-Herrero, *Chem. Sci.*, 2014, **5**, 1875-1880.
76. F. Juliá and P. González-Herrero, *Dalton Trans.*, 2016, **45**, 10599-10608.
77. K. M.-C. Wong, L.-L. Hung, W. H. Lam, N. Zhu and V. W.-W. Yam, *J. Am. Chem. Soc.*, 2007, **129**, 4350-4365.

78. W.-P. To, G. S. M. Tong, C.-W. Cheung, C. Yang, D. Zhou and C.-M. Che, *Inorg. Chem.*, 2017, **56**, 5046-5059.
79. W.-P. To, D. Zhou, G. S. M. Tong, G. Cheng, C. Yang and C.-M. Che, *Angew. Chem. Int. Ed.*, 2017, **56**, 14036-14041.
80. A. Bernanose, *Br. J. Appl.*, 1955, **6**, S54-S55.
81. W. Helfrich and W. G. Schneider, *Phys. Rev. Lett.*, 1965, **14**, 229-231.
82. J. Dresner, *RCA Rev.*, 1969, **30**, 332-333.
83. D. F. Williams and M. Schadt, *Proc. IEEE*, 1970, **58**, 476-476.
84. C. W. Tang and S. A. VanSlyke, *Appl. Phys. Lett.*, 1987, **51**, 913-915.
85. E. Longhi and L. De Cola, *Iridium(III) Complexes for OLED Application. In Iridium(III) in Optoelectronic and Photonics Applications*, Wiley, 2017.
86. A. P. Kulkarni, C. J. Tonzola, A. Babel and S. A. Jenekhe, *Chem. Mater.*, 2004, **16**, 4556-4573.
87. Shahnawaz, S. Sudheendran Swayamprabha, M. R. Nagar, R. A. K. Yadav, S. Gull, D. K. Dubey and J.-H. Jou, *J. Mat. Chem. C.*, 2019, **7**, 7144-7158.
88. D. F. O'Brien, M. A. Baldo, M. E. Thompson and S. R. Forrest, *Appl. Phys. Lett.*, 1999, **74**, 442-444.
89. T. Hofbeck and H. Yersin, *Inorg. Chem.*, 2010, **49**, 9290-9299.
90. S. R. Forrest, *Nature*, 2004, **428**, 911.
91. J. Nelson, *Science*, 2001, **293**, 1059-1060.
92. L. Schmidt-Mende, A. Fechtenkötter, K. Müllen, E. Moons, R. H. Friend and J. D. MacKenzie, *Science*, 2001, **293**, 1119-1122.
93. S. Xiao, M. Myers, Q. Miao, S. Sanaur, K. Pang, M. L. Steigerwald and C. Nuckolls, *Angew. Chem. Int. Ed.*, 2005, **44**, 7390-7394.
94. Y. Wang, J. Shi, J. Chen, W. Zhu and E. Baranoff, *J. Mat. Chem. C.*, 2015, **3**, 7993-8005.
95. X. Wu, G. Xie, C. P. Cabry, X. Xu, S. J. Cowling, D. W. Bruce, W. Zhu, E. Baranoff and Y. Wang, *J. Mat. Chem. C.*, 2018, **6**, 3298-3309.
96. D. J. Gardiner and H. J. Coles, *J. Phys. D: Appl. Phys.*, 2006, **39**, 4948-4955.

Chapter 2: Synthesis and Characterisation of Luminescent, Liquid-Crystalline Complexes of Platinum(IV)

2.1 Introduction

As outlined in Chapter 1, emissive metal complexes have enormous potential for application in devices, such as thin-film transistors[1-3], solar cells,[4] photovoltaic devices[5] and, perhaps most relevant to this research, organic light emitting devices (OLEDs). The current commercial utilisation of iridium metal complexes in OLEDs is only a single example of how beneficial their inclusion is, and can be considered very much an indicator of the potential of phosphorescent materials in commercial OLED applications.[6-9]

2.1.1 Research Background

2.1.1.1 Initial Observation of [Pt(*p*-tolpy)$_2$Cl$_2$], (Pt-1)

The observation of an unknown, colourless platinum species was first observed in the PhD studies of Dr Julia Sarju on the topic of decarbonylation using platinum(II) complexes with 2-*p*-tolylpyridine ligands.[10] This species appeared as a side product in many of her reactions, indicated by distinctive resonances in the ^{1}H NMR spectra at 10.00 and 5.83 ppm (Figure 2-1).

These resonances showed distinctive platinum satellites, with the signal at 10.0 ppm appearing as a doublet with platinum satellites ($^3J_{HH}$ = 6.0 Hz, $^3J_{HPt}$ = 29.0 Hz) significantly downfield from any of the signals observed for her targeted platinum(II) complexes. There was also a noted upfield shift of the resonance at 5.83 ppm compared to the same. The $^3J_{HPt}$ coupling constant of 29 Hz is smaller than those observed for platinum(II) species, which typically exceed 30 Hz, and is more common for platinum(IV) species.[11]

This species proved to be highly insoluble in common organic solvents, although a small amount could be dissolved in dichloromethane or chloroform with heating. From a mixture of $CHCl_3$ and hexane, *via* a vapour diffusion set-up, single crystals of this species were grown and analysed by X-ray diffraction. The structure was shown to be [Pt(*p*-tolpy)$_2$Cl$_2$], herein denoted as **Pt-1**, where *p*-tolpy is 2-*p*-tolylpyridine (Figure 2-2). **Pt-1** is a known complex,[12] but has always been synthesised by a multi-step, targeted procedure (as discussed in Section 2.3.2.2); it has never been reported as being synthesised in a single step.

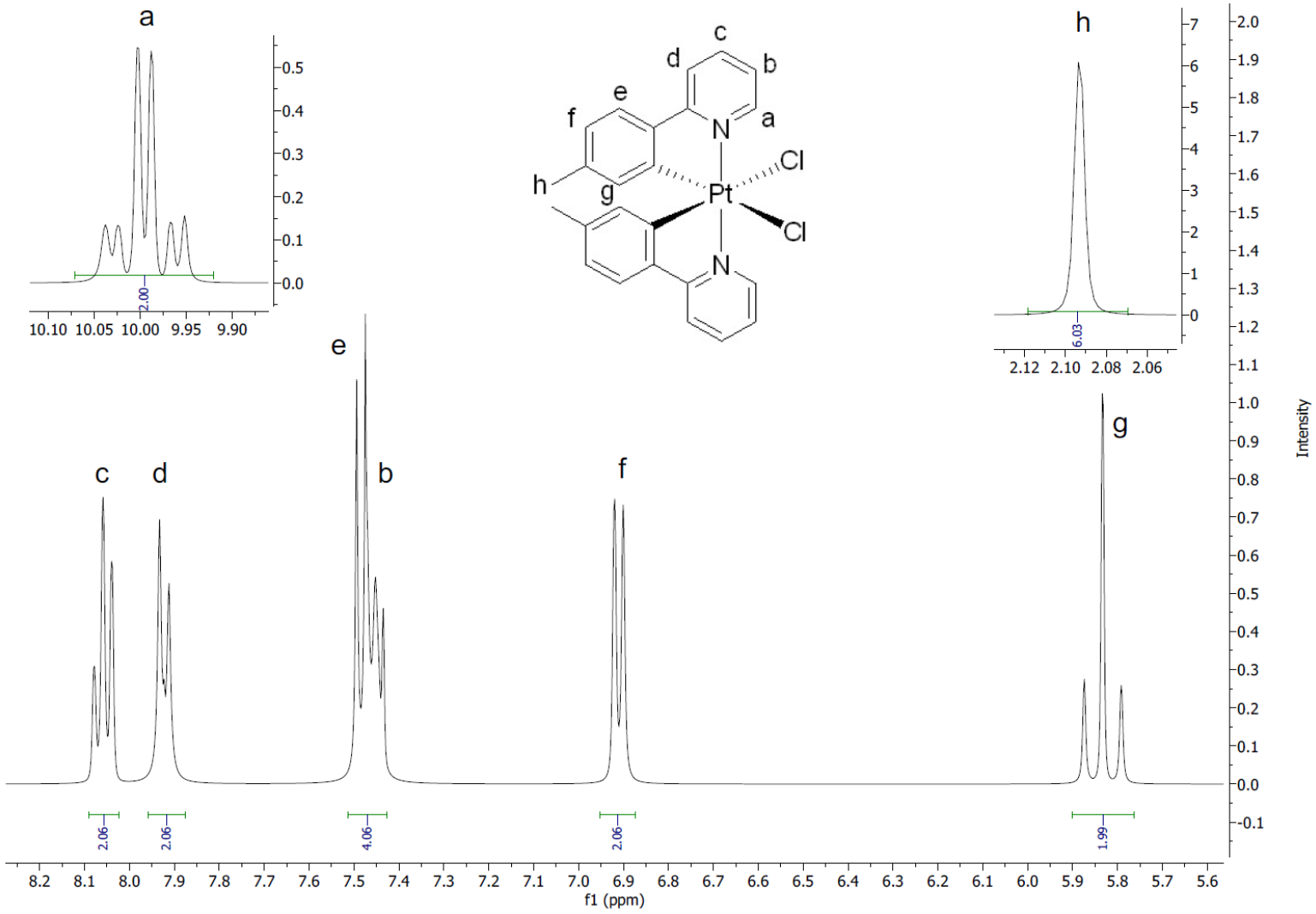

Figure 2-1: ^{1}H NMR spectrum of the aromatic region of the unknown platinum species

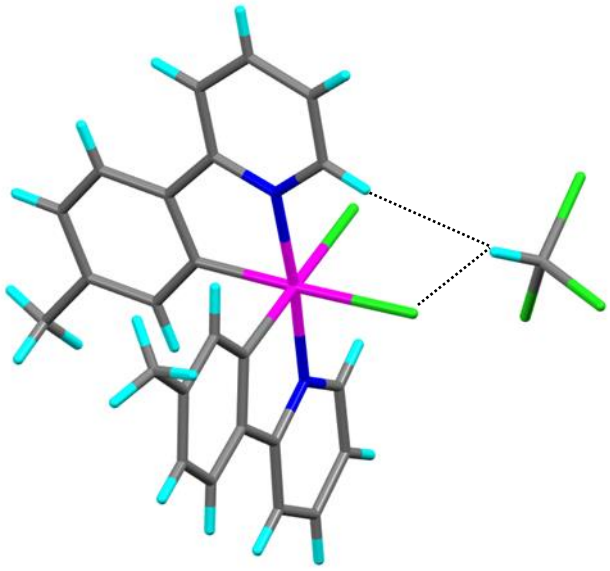

Figure 2-2: Single crystal structure of **Pt-1**, with one molecule of $CHCl_3$ as a solvent of crystallisation. Carbon atoms are shown in grey, hydrogen in cyan, chlorine in green, nitrogen in dark blue, and platinum in magenta.

The crystal structure shows mutually *trans N*-donor atoms and chloride ligands *trans* to the platinated carbons. The *p*-tolylpyridine ligands are identical, with the same Pt–N and Pt–C bond lengths (2.031(2) and 2.032(2) Å for Pt–N and 2.005(3) and 2.012(3) Å for Pt–C) and N–Pt–C bond angles (81.37(10) and 81.36(10)°); the bond angles deviate from 90° due to the prearranged bite angle of the cyclometallating tolpy ligand. The Pt–Cl distances also show the chloride ligands to be equivalent (2.4365(6) and 2.4489(7) Å).

The bis-cyclometallated nature of this complex was reminiscent of research into iridium(III) complexes by Santoro *et al.*[13, 14] with similar ligands which were extended and functionalised with alkoxyphenyl substituents.

2.1.1.2 Similarity to Iridium(III) Complexes in Literature

The iridium(III) species reported by Santoro *et al.* are a surprising but promising indication that the strategies outlined in Chapter 1, Section 1.1.2.1 to induce liquid-crystallinity in octahedral systems are not exclusively effective (Figure 2-3).[14] These complexes, taken at face-value, may not be expected to by liquid-crystalline; there is no obvious molecular anisotropy to form 'rods' or 'discs'. However, these octahedral complexes show columnar mesophases, even with relatively low levels of ligand functionalisation, *i.e.* only two chains per cyclometallating ligand. Alteration of the ancillary ligands also showed a profound effect; when the chloride and DMSO ligands shown in the

complex in Figure 2-3a were replaced by an acetate ligand, any liquid-crystalline behaviour was lost.

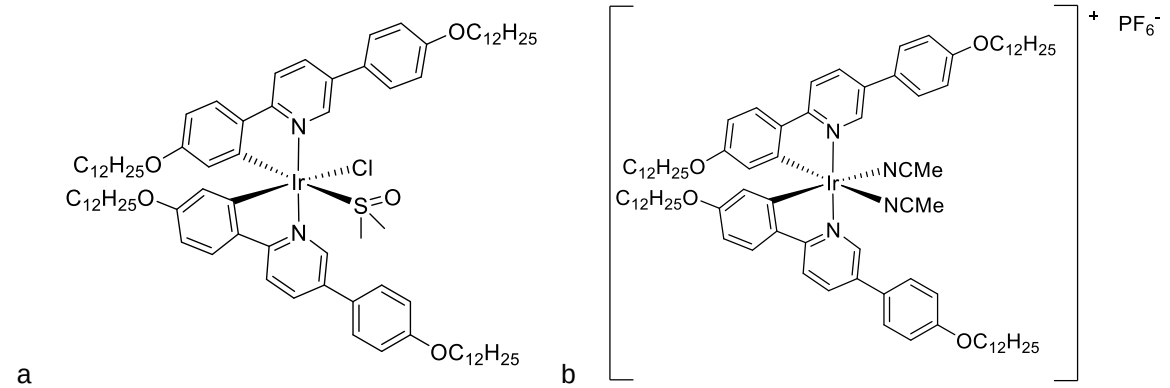

Figure 2-3: Liquid-crystalline iridium(III) complexes reported by Santoro *et al*. showing a) a neutral complex which shows both lamellar and columnar rectangular or ribbon phases, but poor stability over time and, b) a cationic complex which displays a columnar phase and is stable over time[14]

Increasing the level of ligand functionalisation, *i.e.* increasing the number of alkoxy chains per ligand, proved effective in the tuning of the phase behaviour, as would be expected (Figure 2-4). However, due to the unprecedented molecular geometry in these species, this change is not easy to predict.

For the species shown, first the di-μ-chloro bridged dimer is formed, and is subsequently cleaved using sodium acetylacetonate. Thus, with four dodecyloxy chains on each cyclometallating ligand, neither the di-μ-chloro dimer nor the monomeric acac species show any liquid crystalline behaviour. For the unsymmetric species with five chains, the dimeric species shows a room temperature columnar hexagonal phase, and again no liquid-crystalline behaviour was observed for the monomer. This behaviour was in accordance with the two-chain species, in which the acac monomer showed no interesting phase behaviour (Figure 2-3a). Conversely, with six chains on the C^N ligand no liquid-crystalline behaviour is observed for the dimer, but a columnar hexagonal phase is observed for the monomeric acac species.

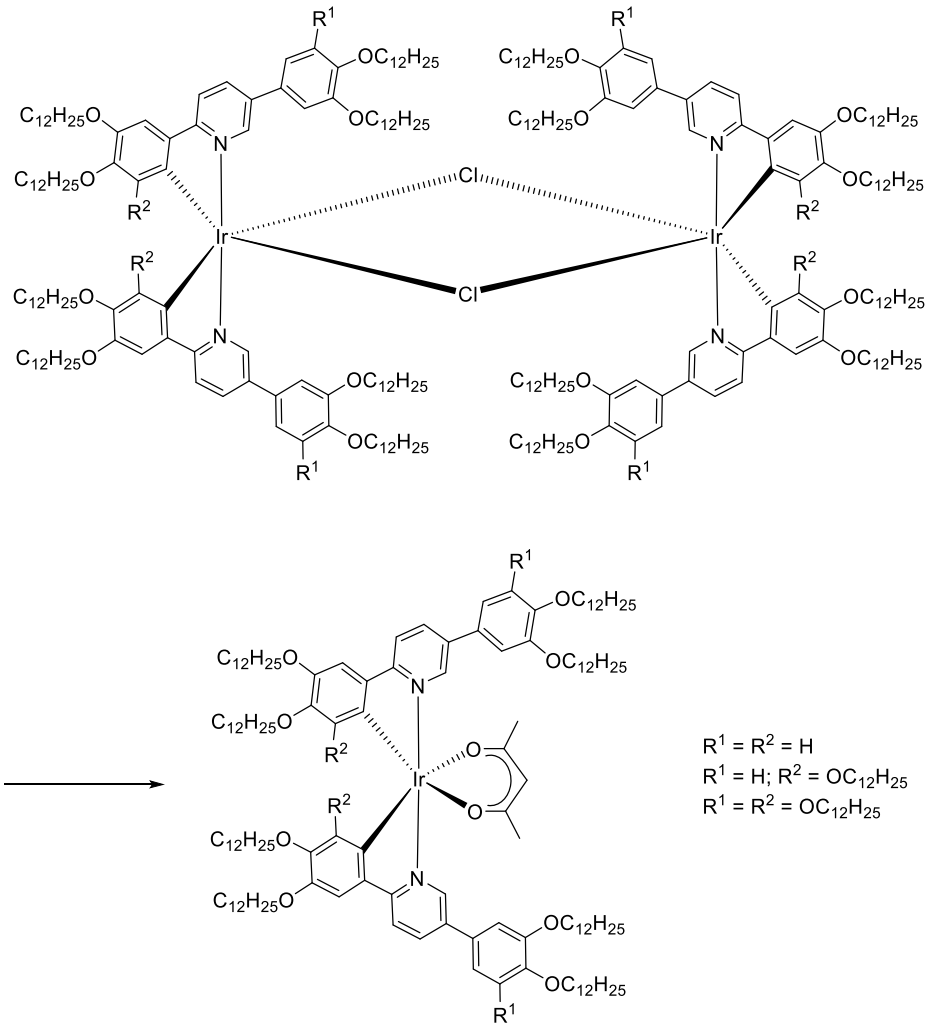

Figure 2-4: Further functionalised iridium(III) complexes reported by Santoro *et al.*; in each case, the di-μ-chloro bridged dimer is cleaved to form the monomeric acac complex. With four chains on each ligand, neither dimer not monomer were liquid-crystalline; with five chains, the dimer shows a room-temperature columnar hexagonal phase, but the monomer shows no liquid-crystalline behaviour; with six chains, the dimer is non-liquid-crystalline, but the monomeric species shows a columnar hexagonal phase.

Given the novel one-pot synthetic strategy to **Pt-1**, and the similar ligands and molecular geometry to that of established iridium(III) metallomesogens, it was proposed that investigating octahedral platinum(IV) systems further was promising, due to the potential to produce emissive, liquid-crystalline species.

2.1.2 Luminescent Platinum(II) and Platinum(IV) Complexes

Luminescent complexes of platinum(II) are ubiquitous in the literature and are very well known and established, especially for cyclometallated systems. An extensive review is out-with the remit of this thesis, but a brief overview will be given, and readers are directed to the thorough reviews of Williams,[15] Yam[16-18] and others.[19]

The first examples of platinum(II) species showing room-temperature phosphorescence were reported in the late 1980s (Figure 2-5).[20, 21] Subsequently, there have been numerous reports of a variety of emissive species, a large subset of which are based on cyclometallated systems, with bi- and tri-dentate phenylpyridine (ppy) derivatives showing bright, long-lived triplet emission.[14, 22-29] The luminescence shown in these systems can be coupled with other favourable properties, such as electoluminescence,[30-32] the ability to act as chemosensors[18] and, most relevant to this research, liquid-crystalline behaviour.[23, 24, 33, 34]

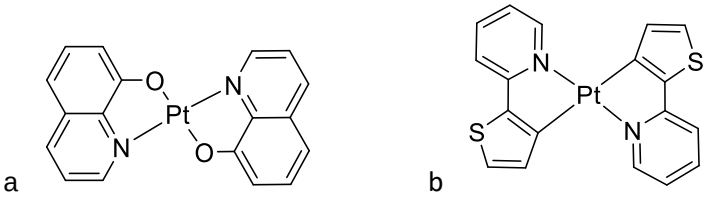

Figure 2-5: Structures of phosphorescent platinum(II) complexes as reported by a) Ballardini *et al.*[20] and b) Sandrini *et al.*[21]

In contrast, studies of emissive platinum(IV) complexes are comparatively rare, for reasons outlined in Chapter 1. There has been a recent interest in the emissive properties of cyclometallated platinum(IV) complexes, with reports more frequent and systematic studies into the effects of substitution well established.

The first report of room-temperature emission of platinum(IV) compounds was by Chassot *et al.* in the mid-1980s, with complexes based on functionalised phenylpyridine (ppy) and 2-(2-thienyl)pyridine ligands (Figure 2-7a).[35] These complexes showed structured emission bands in the blue-green region of the spectrum at room temperature in CH_2Cl_2 solution with luminescence lifetimes in the 100s of μs range.

Research published in 2010 by Jenkins and Bernhard details an extensive study into the effect of functionalisation of the ppy and bipyridine (bpy) ligands of complexes with the general formula $[Pt(ppy)_2(bpy)_2][PF_6]_2$ (Figure 2-6b).[36] These complexes were synthesised *via* a *bis*-chloride intermediate (of the type shown for later work in Figure 2-7b), in which the chloride ligands are displaced by the bpy and, although it is expected that the *bis*-chloride complexes could show interesting emissive behaviour based on subsequent literature,[37, 38] they are not characterised. The $[Pt(ppy)_2(bpy)_2][PF_6]_2$ complexes show a structured emission band in the blue region of the spectrum when ppy = 2-phenylpyridine and 5-methyl-2-(4'-fluorophenyl)pyridine, but no emission was observed when ppy = 5-methyl-2-(4'-methoxyphenyl)pyridine, with negligible variation with alteration of the bpy ligand. The emission in all cases was very weak, with the highest reported photoluminescence quantum yield (PLQY) only 1%.

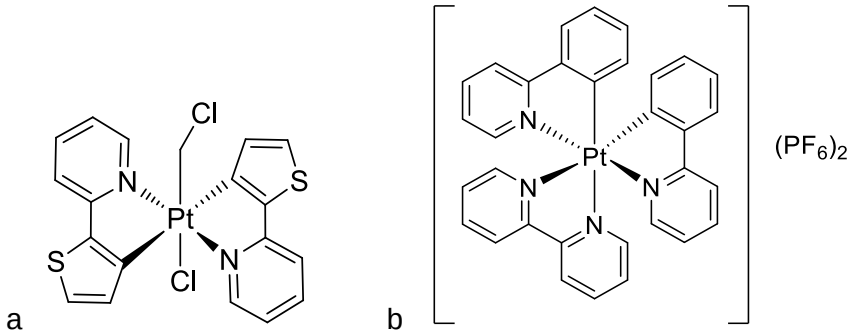

Figure 2-6: Model structures from a) Chassot *et al.*[35] who reported a platinum(IV) system with 2-(2-thienyl)pyridine) ligands after the oxidative addition of CH_2Cl_2; b) Jenkins and Bernhard[36] showing the $[Pt(C^N)2(N^N)]^+$ base unit, with reported functionalisation of both the C^N and N^N rings with fluorine and methoxy groups.

A series of papers by Juliá *et. al* report the effects of both the molecular configuration with respect to different isomers (Figure 2-7a) and ancillary ligands (Figure 2-7b and c) on the photophysical behaviour of a series of platinum(IV) complexes.[37-40] They report the difference between facial and meridional isomers, with *mer* isomers displaying only weak luminescence in solution at room temperature, but strong emission at 77 K in frozen butyronitrile glasses. They observe that room-temperature measurements may not be reliable, as the *mer* isomer partially isomerises to the *fac* isomer. In contrast, the *fac* isomers are strongly emitting at room temperature in the blue region of the spectrum, with 75% of the complexes showing a PQLY (ϕ) of 0.41 and above, the highest reported for a platinum(IV) complex at the time of publishing.[39]

Their observations on the impact of the nature of the ancillary ligands on the photophysical behaviour of a series of both symmetric and unsymmetric *bis*-cyclometallated phenylpyridine platinum(IV) complexes are striking. Symmetrical species (Figure 2-7b), where X = F, Cl, Br, OAc, TFA are all luminescent in deaerated CH_2Cl_2 solution. The intensity of the emission, *i.e.* the PLQY was strongly dependent on the nature of this ancillary ligand; when X= F, ϕ was calculated to be 40%, but X = I shows no measurable emission. There is also a significant impact on the lifetime of emission when altering the halogen, however, the wavelength of emission and emissive character (*i.e.* the vibronically structured band arising from a ^{3}LC(ppy) excited state) remain identical. This is rationalised through time-dependent density functional theory (TD-DFT) calculations, which indicated that the nature of the ancillary ligand contributed to the energy of deactivating non-radiative states, such as ligand-to-ligand charge-transfer (LLCT) or ligand-to-metal charge-transfer (LMCT) states.

The unsymmetrical equivalent $[Pt(ppy)_2X_2]$ complexes (Figure 2-7c) did not show any detectable emission in solution at room temperature due to low-lying, deactivating LMCT states. The

unsymmetrical complexes with both and X and Me ligands (Figure 2-7c) all show strong emission at room temperature when X = F, Cl, Br, OAc, TFA, but show none of the drastic ligand-dependent changes observed above. The exception to this is [Pt(ppy)$_2$I(Me)], which shows only weak emission due to low-lying LLCT states between p(I) and π*(ppy).[38]

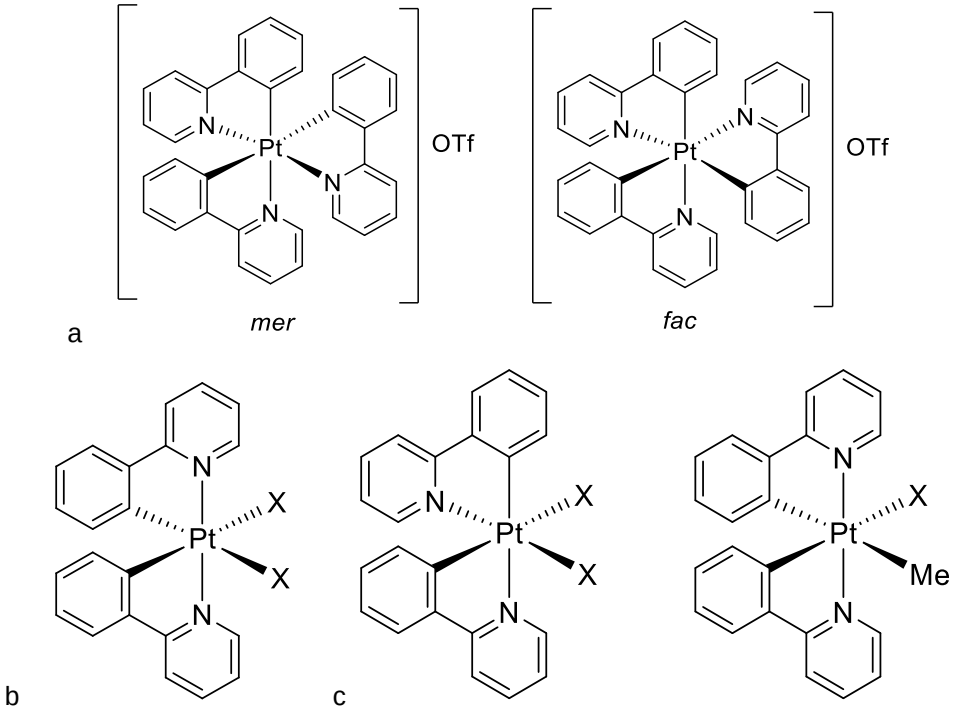

Figure 2-7: Model structures of a) the *mer* and *fac* isomers of the base unit of tris(cyclometallated)platinum(IV) complexes reported by Juliá *et al.*[39], with reported functionalisation of the C^N rings with fluorine and methyl groups, as well as systems where the pyridyl ring is replaced with pyrazole; Juliá *et al.*[38] showing b) symmetric and c) unsymmetric bis-cyclometallated 2-phenylpyridine systems, where X = F, Cl, Br, I, OTf, OAc, TFA.

More recently, work by Vivancos *et al.* reported two platinum(IV) species with 1,2,3-triazolylidene cyclometallating ligands and either bi- or tri-dentate 2,6-di(*p*-tolyl)pyridine ligands (Figure 2-8a and b).[41] Both the bi- and tri-dentate species show blue triplet emission at room temperature in CH_2Cl_2, and significant enhancements in PLQY are observed in poly(methyl methacrylate) (PMMA) films (2 wt%) due to a drastic decrease in the non-radiative rate constant, k_{nr}.

Further work into the effects of the cyclometallating ligand has been reported this year (2019) by Giménez *et al.*, where, rather than functionalise the 2-phenylpyridine, a range of substantially different heterocycles are utilised as cyclometallating ligands, as well as a supporting cyclometallated benzoquinolinyl ligand (Figure 2-8c).[42]

Heterocycles investigated as cyclometallating ligands include 2-(2,4-difluorophenyl)pyridine (dfppy), 2-phenylbenzothiazole (pbt), 2-(4-bromophenyl)benzothiazole (Br-pbt),

2-phenylquinoline (pq), 2-(2-thienyl)pyridine (thpy), 1-(2-pyridyl)pyrene (pypy). As with most of the platinum(IV) complexes highlighted in this brief introduction, the complexes show a structured emission band and long lifetimes. However, the emission wavelength is red-shifted compared to the previous examples, with the majority of complexes showing emission in the green region of the spectrum. Again, a significant increase in PLQY is observed when the complex is doped into films, with an absolute quantum yield of 85% for the complex with the cyclometallating pq ligand in a 5% by weight film of polystyrene (PS).

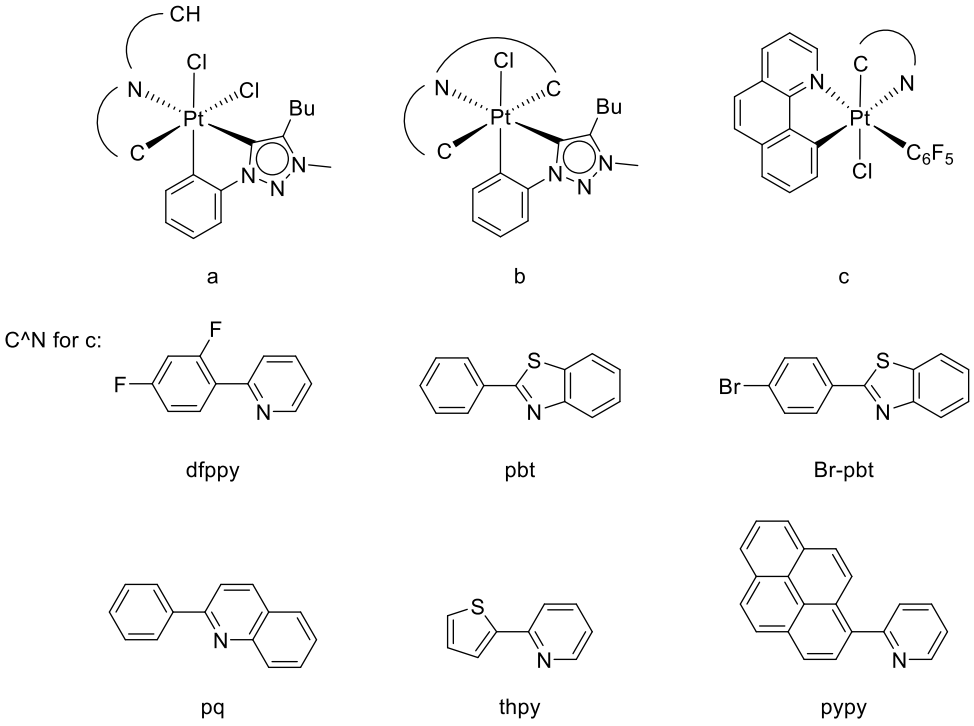

Figure 2-8: Two complexes reported by Vivancos *et al.*,[41] where C^N^C is 2,6-di(*p*-tolyl)pyridine, with a) as a monocyclometallated species with respect to the C^N^C ligand, and b) as the bis-cyclometallated equivalent after exchange of a chloride ligand; c) model structure reported by Giménez *et al.*,[42] with a cyclometallated benzoquinolinyl ligand, where the C^N ligand is equivalent to six different heterocycles, including 2-(2,4-difluorophenyl)pyridine (dfppy), 2-phenylbenzothiazole (pbt), 2-(4-bromophenyl)benzothiazole (Br-pbt), 2-phenylquinoline (pq), 2-(2-thienyl)pyridine (thpy), 1-(2-pyridyl)pyrene (pypy)

These recent reports are an interesting gateway into further structure/property relationships, and indicate that with further modification both the cyclometallating and ancillary ligands involved, predictable, tuneable emission is within reach.

2.1.3 Liquid-Crystalline Complexes of Platinum(IV)

There are very few examples in the literature of platinum(IV) complexes with true mesomorphic behaviour, as the 3D octahedral geometry at the metal centre makes the induction of molecular anisotropy more challenging than in a square-planar complex. Liquid-crystalline complexes of platinum(II) are, by comparison, far more common, due to the obvious anisotropy afforded to the molecules by the square-planar nature of the metal centre and the ability to include co-planar ligands; a brief overview of square-planar metallomesogens is given in Chapter 1, Section 1.1.2, and is discussed in more detail in Chapter 3, Section 3.1.1.

The few reported instances of liquid-crystalline platinum(IV) complexes all utilise one of the strategies outlined in Chapter 1 for inducing mesophases in octahedral species: including one highly anisotropic, rod-like ligand to shield the metal core, combined with small ancillary ligands. Complexes of this nature display phases typical of calamitic mesogens, such as smectic and nematic phases.

Examples of complexes of this type are reported in two related papers by Ghedini *et al*.[43, 44] The complexes have azobenzene cyclometallating ligands and β-diketonate chelating ligands, and are formed through the oxidative addition of I_2 or MeI to a platinum(II) precursor (Figure 2-9). As may be expected due to the reduced ability of the complexes to form lateral interactions due to the nature of the supporting ligands, the liquid-crystalline behaviour of these systems are dominated by nematic phases with often elevated transition temperatures.

There is also a report of liquid-crystalline complexes of platinum(IV) by Allenbaugh *et al.*, based on 4,4'-disubstituted bipyridines, as well as mixtures of platinum(II) and platinum(IV) species, although the phases reported were poorly characterised. The SAXS patterns reported also show more order than would typically be expected of a mesophase.[45]

With reference to the iridium(III) complexes reported by Santoto *et al.* (Section 2.1.1.2), it is clear that the induction of liquid-crystallinity in octahedral species cannot be easily predicted purely by chain number, but rather the interplay between the number of terminal alkoxy chains and their positioning in the complex strikes a fine balance that required thorough investigation.

a

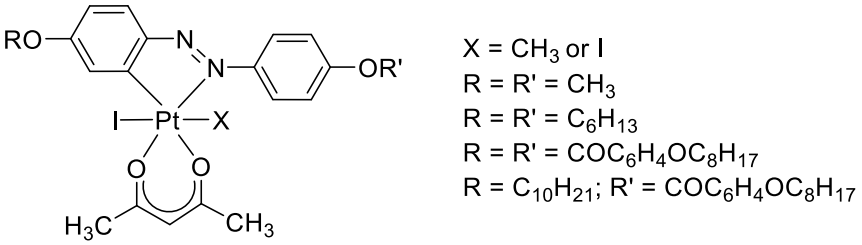

b

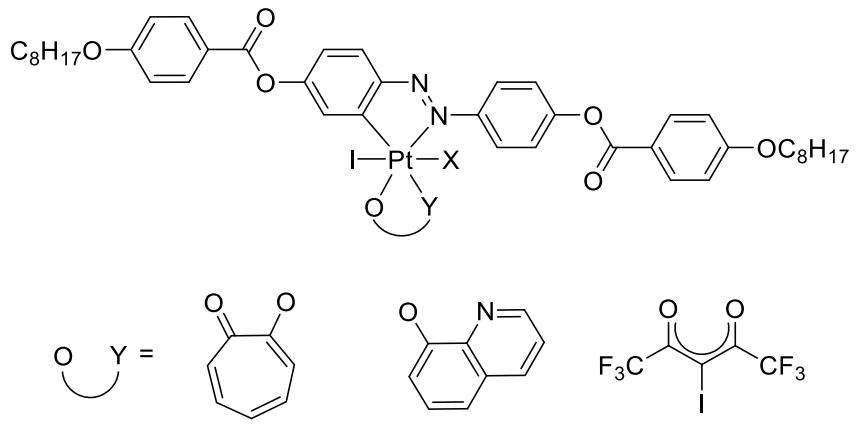

Figure 2-9: Structures of liquid-crystalline platinum(IV) complexes reported by Ghedini *et al*. formed by the oxidative addition of I_2 or MeI to the corresponding platinum(II) species. a) calamitic metallomesogens with cyclometalling azobenzene ligands and chelating β-diketonate ligands[44] b) calamitic metallomesogens with extended ester-linked azobenzene cyclometallating ligands and a selection of O^Y ancillary chelating ligands, where Y = O or N.[43]

2.2 Aims of Chapter

Based on the iridium(III) complexes outlined above, as well as the rising interest in the emissive behaviour of bis-cyclometallated platinum(IV) complexes and the relative dearth of reports of platinum(IV) metallomesogens, there is an obvious area of investigation in the combination of these characteristics.

Utilising the ligands used by Santoro *et al.* in their iridium(III) work, the synthesis and characterisation of analogous platinum(IV) complexes was investigated. Both the phase behaviour and emissive properties of the synthesised complexes were fully analysed, complemented by computational calculations of the frontier molecular orbitals and predicted transitions involved in the photophysical behaviour.

2.3 Synthesis of Platinum(IV) Complexes

2.3.1 Synthesis of [Pt(p-tolpy)$_2$Cl$_2$], (Pt-1)

Subsequent to the initial observation of [Pt(*p*-tolpy)$_2$Cl$_2$], **Pt-1**, effort was undertaken to optimise the reaction in which it was first observed, and if necessary develop a new synthetic route, in order to synthesise **Pt-1** as the majority product.

2.3.1.1 Targeted Synthesis of [Pt(*p*-tolpy)$_2$Cl$_2$], (Pt-1)

An oxidation has taken place to form **Pt-1**; the reaction takes place under an atmosphere of dinitrogen, in 2-ethoxyethanol, in the presence of DMSO, with the intention of forming **Pt-IIa**. Complex **Pt-IIb** is also formed as a minor side product; the structures of all three platinum complexes formed are shown as the products in Scheme 2-1.

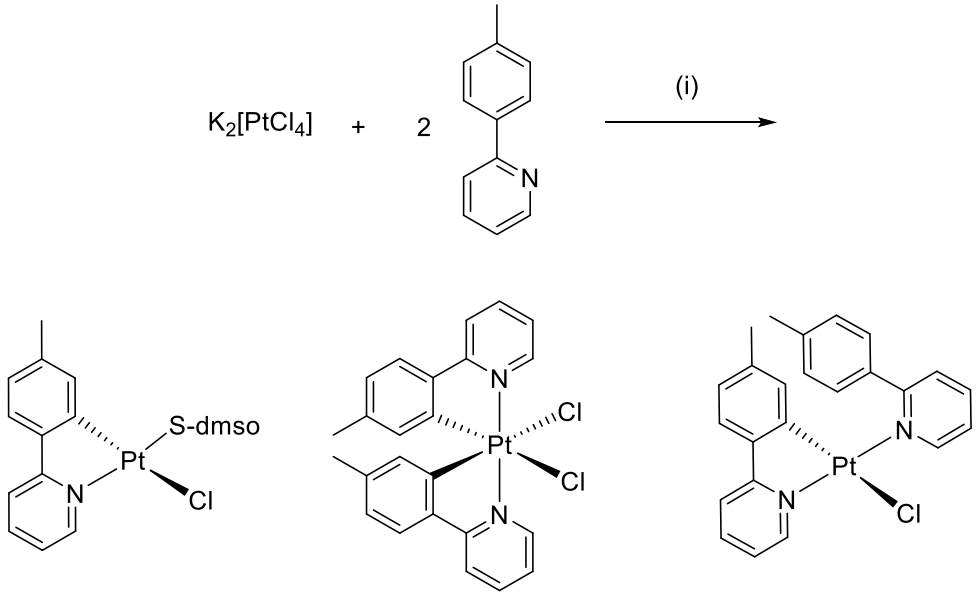

Scheme 2-1: Reaction to form **Pt-IIa**, with **Pt-IIb** and **Pt-1** as recorded side-products. i) DMSO (1 eqv.), 3:1 2-ethoxyethanol:H_2O, 24 h, 80 °C, N_2.

By integration of the ^{1}H NMR spectrum, **Pt-1** is formed as 4% of the crude reaction product. This indicates that is it an extremely minor side product. Given the insoluble nature of this complex, this value is subject to error, as not all of the formed complex may have dissolved in the NMR solvent. It is clear that an alteration of reaction conditions is needed to produce **Pt-1** as the major reaction product. The main variable changes to reaction conditions are outlined in Table 2-1, along with the resulting percentage of **Pt-1** formed as estimated by ^{1}H NMR spectroscopy (as well as

species **Pt-IIa** and **Pt-IIb**). The percentage is given as a proportion of the three main platinum species formed and should not be considered a yield.

Table 2-1: Variable reaction conditions for the formation of **Pt-1** as the primary reaction product; deviations from original reaction conditions are listed in bolded italics.

Reaction	2-*p*-tolylpyridine (eqv.)	DMSO (eqv.)	Temperature (°C)	Atmosphere	Reaction Time (hours)	Percentage of Pt complexes formed (%)		
						Pt-1	Pt-IIa	Pt-IIb
1	1	1	80	N_2	24	4	89	7
2	1	1	80	N_2	***48***	22	12	66
3	1	1	***100***	N_2	24	9	25	66
4	***2***	1	80	N_2	24	15	2	83
5	***2***	1	80	***Air***	24	3	32	65
6	***2***	1	***100***	N_2	24	13	4	83
7	***2***	1	***100***	N_2	***48***	14	38	48
8	***2***	***Excess***	***100***	N_2	***48***	14	20	66
9	***2***	-	***100***	N_2	24	9	-	91
10	***2***	-	***100***	***Air***	24	5	-	95

In reaction 1, the reaction conditions under which **Pt-1** was first observed, the majority species formed is **Pt-IIa**, a mono-cyclometallated platinum(II) species. When the reaction time is increased (reaction 2) this product is disfavoured, and instead the majority complex observed is [Pt(N^C-ppy)Cl(N-ppyH)], **Pt-IIb** (66 %), with a significant increase in the target **Pt-1** (22 %). This is also true of increasing the reaction temperature (reaction 3), although the increase in the percentage of **Pt-1** is smaller (9 %).

When matching the stoichiometry of the 2-*p*-tolylpyridine ligand added to that in the target complex, *i.e.* increasing the equivalents of tolpy ligands to 2, it is always **Pt-IIb** that is the preferred product (reactions 4-10) and **Pt-1** is never formed in more than 15 %. Formation of **Pt-IIa** is also comparatively suppressed.

Given that this reaction proceeds under an atmosphere of dinitrogen, it was assumed that DMSO might act as an oxidant.[46] However, when DMSO was excluded from the reaction, both under dinitrogen and air (reactions 9 and 10), **Pt-1** was still observed. In all previous reports of complexes of this nature, this platinum(IV) target was prepared by chemical oxidation of the corresponding platinum(II) precursor (equivalent to **PtII-b**).[12, 36] As this reaction proceeds without oxygen, it is reasonable to assume that oxidative addition from **Pt-IIb** (with concomitant production of HCl) is the most likely origin of the oxidation.

In addition to the traditional thermal reactions outlined in Table 2-1, the reaction was investigated under conditions of microwave irradiation. The advantages of microwave heating in synthesis are numerous: the ability to superheat a reaction mixture, typically 20-30 °C above the boiling point of

the solvent, results in faster reaction rates, leading to shorter reaction times and higher yields. There are also examples of syntheses in which products are accessible *only* through microwave-assisted synthesis.[47]

Although solvent super-heating is beneficial in microwave-assisted synthesis, in this case, the high boiling point of 2-ethoxyethanol means that, if it were to be heated to 20-30 °C above the boiling point of 136 °C, we would expect to see high levels of platinum decomposition, resulting in platinum black.

Due to the insolubility of **Pt-1** in both the reaction mixture and most common organic laboratory solvents, success of the microwave-assisted reactions was judged by the yield of **Pt-1** isolated at the end of the reaction.

The initial reaction investigated was directly analogous to the thermal conditions discussed above; $K_2[PtCl_4]$ was dissolved in a minimum amount of warm water (approximately 0.1 cm^3 for 10 mg) and added to a solution of 2-*p*-tolylpyridine (2 equivalents) and DMSO (1 equivalent) in 2-ethoxyethanol. The reaction mixture was heated using microwave irradiation at 80 °C for 6 hours. On cooling to room temperature, a colourless precipitate was formed, isolated by filtration, and washed with water and cold methanol to give a pure sample of **Pt-1**.

For this initial reaction, a yield of 86% was recorded, but was never superseded with any further modifications to reagent equivalents or reaction conditions. However, upon modest scale-up (10 mg of $K_2[PtCl_4]$ to 27 mg) at a constant concentration, this yield dropped to 45 %, and the previously excellent recorded yield could not be repeated.

Also to the detriment of this reaction, upon use of a new and pure batch of reaction solvent 2-ethoxyethanol, the reaction appeared to stop working; when previous reactions were repeated with meticulous care, no precipitate was observed, or only a very small amount which proved too fine to be isolated by sinters of even the smallest porosity. When the reaction was repeated with the small remaining volume from the original solvent source, a yield of 66 % was recorded. It was suggested that an impurity in the original bottle was contributing to the reaction, although no clear species was identified by LC-MS. The level of water saturation in an aged solvent bottle may also be a factor.

With systematic alteration of the reagents used, it was found that, with the new solvent and 3 equivalents of DMSO, the reaction would proceed, albeit with much poorer yields; under these conditions, the microwave-irradiated sample produced **Pt-1** in 34% yield. However, this method was found to be reliable and reproducible. Due to the ease of preparation and work-up, this method was deemed to be superior in the synthesis of **Pt-1** and was chosen as the primary synthetic method (Scheme 2-2).

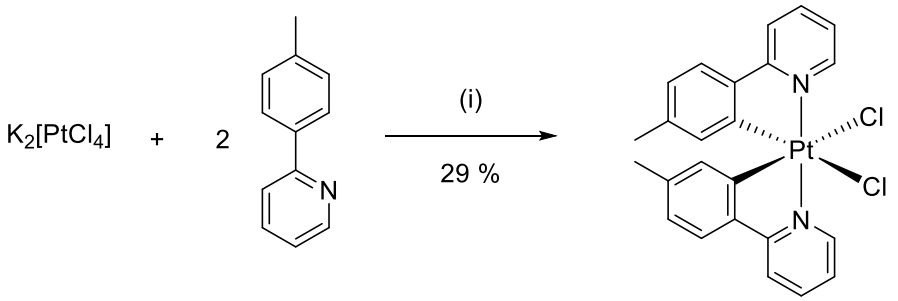

Scheme 2-2: Final synthetic procedure to **Pt-1** *via* microwave-assisted method. i) DMSO (3 eqv.), 2-ethoxyethanol, microwave, 6h, 80 °C ($K_2[PtCl_4]$ dissolved in minimum warm water).

2.3.2 Synthesis of Extended Platinum(IV) Complex $[Pt(L)_2Cl_2]$, (Pt-4)

2.3.2.1 Initial Investigations into Microwave-Assisted Synthesis

As outlined in Chapter 1, Section 1.1, in order for a species to possess liquid-crystallinity, a high degree of molecular anisotropy is required. In order to design molecules of this nature, particularly in the field of metallomesogens, ligands with long, terminal alkoxy chains are often utilised, as in the case of the platinum(II) and iridium(III) complexes reported by Santoro *et. al* described in Section 2.1.1.2 and in the introduction to Chapter 3 (Section 3.1.1).[14, 34]

To investigate the liquid-crystalline potential of complexes of platinum(IV), the same ligands were investigated here. Initially, the chain length was constrained to a length of C12 ($-OC_{12}H_{25}$), with a single chain in the 4-position of each phenyl ring. For reasons outlined later in Section 2.5, this ligand was the only ligand fully investigated, and shall herein be designated **HL1**. This ligand is a natural extension to 2-*p*-tolylpyridine, extending the conjugated system with the inclusion of a second phenyl ring in place of the methyl group. Also advantageous is the established synthetic knowledge of this system within the group, as synthesis of this ligand has been reported previously (Scheme 2-3).[34]

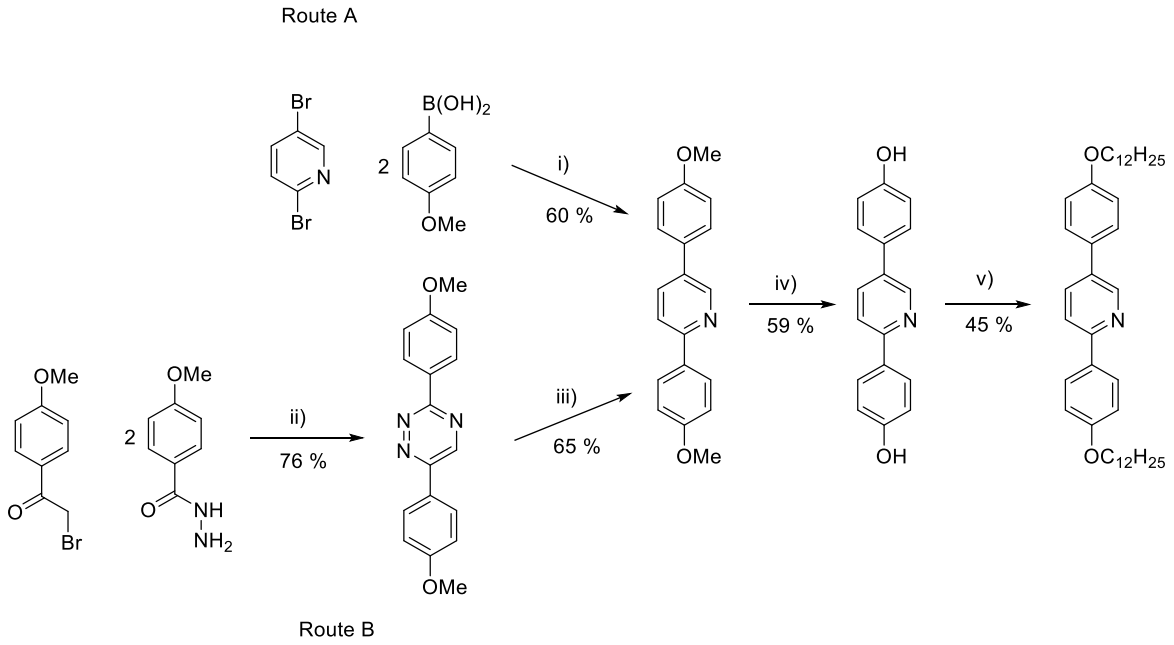

Scheme 2-3: Two possible synthetic routes to **HL1,** 2,5-di(4-dodecyoxyphenyl)pyridine as reported by Santoro *et al.* i) 10% Pd/C, Na_2CO_3, PPh_3, DME, reflux, 50 h (example conditions[13, 48, 49]); ii) NaOAc, EtOH/AcOH, reflux, 12 h; iii) norbornadiene (excess), o-$C_6H_4Cl_2$, reflux, 20 h; iv) pyH^+Cl^-, 200 °C, 12 h; v) $C_nH_{2n+1}Br$, K_2CO_3, DMF, 90 °C, 12 h.[34]

HL1 can be synthesised *via* multiple synthetic routes. The most obvious pathway, perhaps, is that shown as Route A in Scheme 2-3, in which 4-methoxyboronic acid and 2,5-dibromopyridine are coupled under Suzuki-Miyaura conditions to form 2,5-di(4-methoxyphenyl)pyridine. This is then demethylated using pyridinium chloride (pyH^+Cl^-) to form 2,5-di(4-hydroxyphenyl)pyridine, followed by an *O*-alkylation with 1-bromododecane using a Williamson ether synthesis, and for purely diphenylpyridine ligands, this would be the pathway of choice.

However, the method reported by Santoro *et al.* is a four-step reaction, beginning with the synthesis of 3,6-di(4-methoxyphenyl)-1,2,4-triazide, first reported by Saraswathi and Srinivasan,[50] and subsequently progressing through an inverse electron demand Diels-Alder reaction with norbornadiene (first described by Carboni and Lindsey,[51] variation reported by Boger *et al.*[52, 53] and developed for relevant systems by Kozhevnikov *et al.*[54, 55]) to form the 2,5-di(4-methoxyphenyl)pyridine intermediate (Route B, Scheme 2-3). The demethylation and *O*-alkylation remain consistent between the two synthetic routes. This pathway is less known, with an extra step, but allows for the incorporation of further substituents on the pyridine ring, such as a cyclopentane group.[34] This further functionalisation is outwith the scope of this research.

A large quantity of 2,5-di(4-methoxyphenyl)pyridine, synthesised for previous research,[13, 14, 34] was stored in our lab and, with grateful permission, this was used to synthesise the final ligand **HL1**,

reducing the synthesis required to two steps rather than the lengthier Route B outlined in Scheme 2-3.

It is obvious, then, to apply the optimised microwave-assisted synthesis of **Pt-1** to this extended system, **HL1**, to produce the target complex **Pt-4** (Figure 2-10) *via* a one-pot procedure. The most noticeable issue with this replacement was one of solubility; 2-*p*-tolylpyridine is a liquid reagent at room temperature, as it miscible with/soluble in the reaction solvent 2-ethoxyethanol. **HL1** is, as expected, a solid at room temperature, and is not soluble in 2-ethoxyethanol; this is a highly polar alcoholic solvent, generally incompatible with compounds consisting of an extended aromatic core and non-polar hydrocarbon chains.

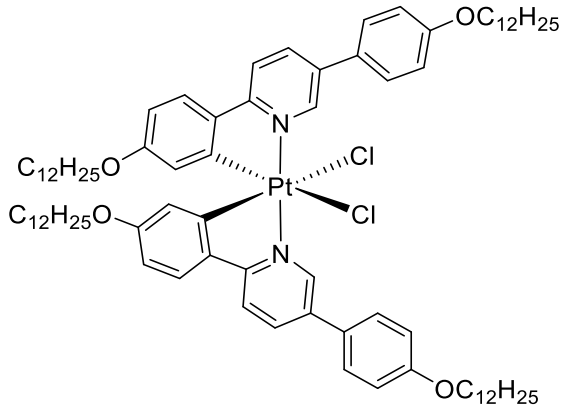

Figure 2-10: Structure of target platinum(IV) complex, **Pt-4**.

The ligand **HL1** proved to be insoluble in 2-ethoxyethanol even at high temperatures. A small amount of product formation was observed by ^{1}H NMR spectroscopy, but this was negligible when compared to the proportion of unreacted ligand; the distinctive resonance of the hydrogen atom *ortho* to the nitrogen of the pyridine ring in **Pt-4** can be seen at 10.18 ppm, with the clear resonance of the unreacted ligand at 8.85 ppm. Based on integration of the signals, unreacted ligand **HL1** constituted 96% of the sample. Also observed is a very minor amount of the platinum(II) DMSO complex (Figure 2-11, analogous to **Pt-IIa** from Section 2.3.1.1).

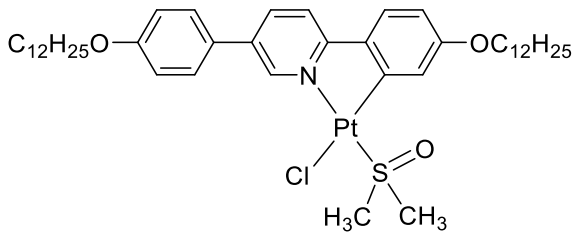

Figure 2-11: Structure of [Pt(L)(S-DMSO)Cl] formed in the attempted microwave-assisted synthesis attempts. This complex is analogous to complex **Pt-IIa** in Section 2.3.1.1.

When the filtrate (*i.e.* everything soluble in the reaction mixture) was evaporated to dryness, a multitude of signals were observed in the range 10.4 to 8.4 ppm, but the two main identifiable species were **Pt-4** and the platinum(II) DMSO complex in a ratio approximately 1:3.

Thus, it is possible to produce **Pt-4** *via* the established microwave-assisted synthetic route, however this is not a clean synthesis due to the presence of many other species, and the crude estimated yield of 8 % (assuming the unidentified resonances in the 10.4 to 9.0 ppm region are also platinum species) is far from ideal.

Thus, investigations using a traditional thermal synthetic procedure were launched.

2.3.2.2 Optimised Thermal Synthetic Procedure to Pt-4

Due to the low yields and difficulty in isolating **Pt-4** in the one-pot, microwave-assisted synthesis, an alternate procedure was investigated. In the literature regarding emissive, cyclometallated platinum(IV) species, the primary synthetic method is a two-step procedure, outlined in Scheme 2-4.

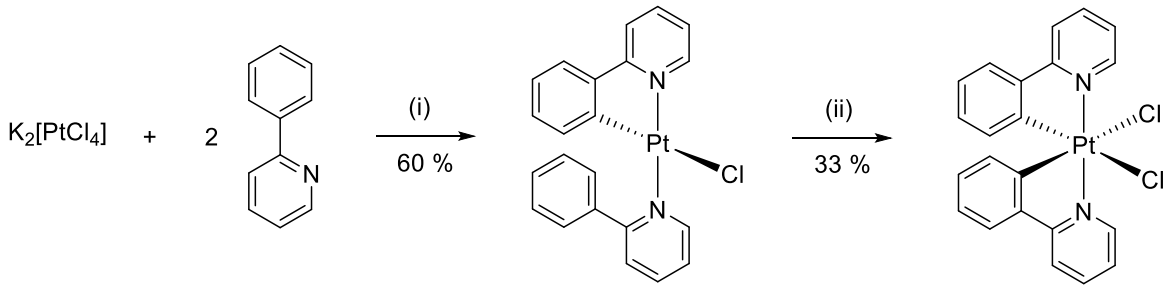

Scheme 2-4: Procedure to bis-cyclometallated platinum(IV) complexes as reported in the literature, with phenylpyridine as an exemplar C^N ligand.[36] i) 3:1 tert-butanol:H_2O, 80 °C, 12 h; ii) CH_2Cl_2, $PhICl_2$, r.t., 24 h.

Taking 2-phenylpyridine as an example ligand for ease of reference, firstly, a mono-cyclometallated platinum(II) species is synthesised, with the two other ligand sites occupied by a chloride ligand and a second 2-phenylpyridine ligand coordinated κ^1 through the nitrogen of the pyridine ring.[36] This species is equivalent to **Pt-IIb**, as observed in Section 2.3.1.1. The second step is an oxidation utilising a hypervalent iodine(III) species, in this case iodobenzene dichloride, to form the targeted platinum(IV) bis-cyclometallated species.

The use of hypervalent iodine reagents is pervasive in platinum chemistry of this nature, as well as in the oxidation of alcohols[56-58] and as selective chlorinating agents.[59-61] In their relevance to oxidation of platinum(II) to platinum(IV), $PhICl_2$ is the common reagent of choice, and is proposed to work through a $PhICl_2$-promoted, two-electron oxidation of the platinum(II) complex to give a pentacoordinated cationic platinum intermediate. It is suggested that this species is stabilised

through an agostic C–H interaction with the κ^1-phenylpyridine (or derivative) ligand, followed by a fast proton transfer to a proximal Cl^-, producing HCl as a by-product to give the *bis*-cyclometallated species.[42, 62]

It has also been shown that the same products can be formed through the use of hydrogen peroxide as an oxidising agent but as this is a much stronger oxidant, as well as more dangerous to handle and store, it is not the preferred route.[12, 63]

In order to attempt this synthetic procedure with the extended ligand **HL1**, it is first necessary to devise a route to the κ^1,κ^2 platinum(II) complex. It is known that the dimeric platinum(II) species **Pt-2** can be synthesised by heating **HL1** and $K_2[PtCl_4]$ to reflux in acetic acid (Scheme 2-5).

This chloride bridged dimer, **Pt-2**, $[Pt(L)(\mu\text{-}Cl)]_2$, is known and is insoluble in the majority of common organic laboratory solvents.[34] It is isolated by filtration from the reaction mixture upon cooling to room temperature, and washed with water, ethanol and diethyl ether to remove any soluble impurities and residual acetic acid. It would be expected that this platinum(II) species would be a characteristic yellow but often appears green due to the presence of platinum black, a decomposition product formed due to the high reaction temperature. This would normally be removed by filtration through a pad of Celite®, but this proved to be difficult due to the insolubility of **Pt-2** and so was removed at a later stage.

Despite its characteristic insolubility, **Pt-2** is partially soluble in boiling chloroform. When in the presence of two equivalents of **HL1**, **Pt-2**, heated to reflux in boiling chloroform is cleaved to form the κ^1,κ^2 platinum(II) complex **Pt-3**, $[Pt(\kappa^2\text{-}L)(\kappa^1\text{-}HL)Cl]$. The reaction mixture is then passed through a pad of Celite® upon cooling to room temperature, removing any platinum black and unreacted **Pt-2**. Upon crystallisation from $CHCl_3$/acetone, **Pt-3** is isolated as a bright yellow powder.

The chosen oxidant in this synthesis, iodobenzene dichloride, is freshly prepared *via* the reaction of (diacetoxyiodo)benzene with concentrated hydrochloric acid, according to the literature procedure outlined by Jenkins and Bernhard.[36] Reaction of $PhICl_2$ with **Pt-3** at room temperature in CH_2Cl_2 for 24 hours results in the oxidation to target platinum(IV) species, **Pt-4**.

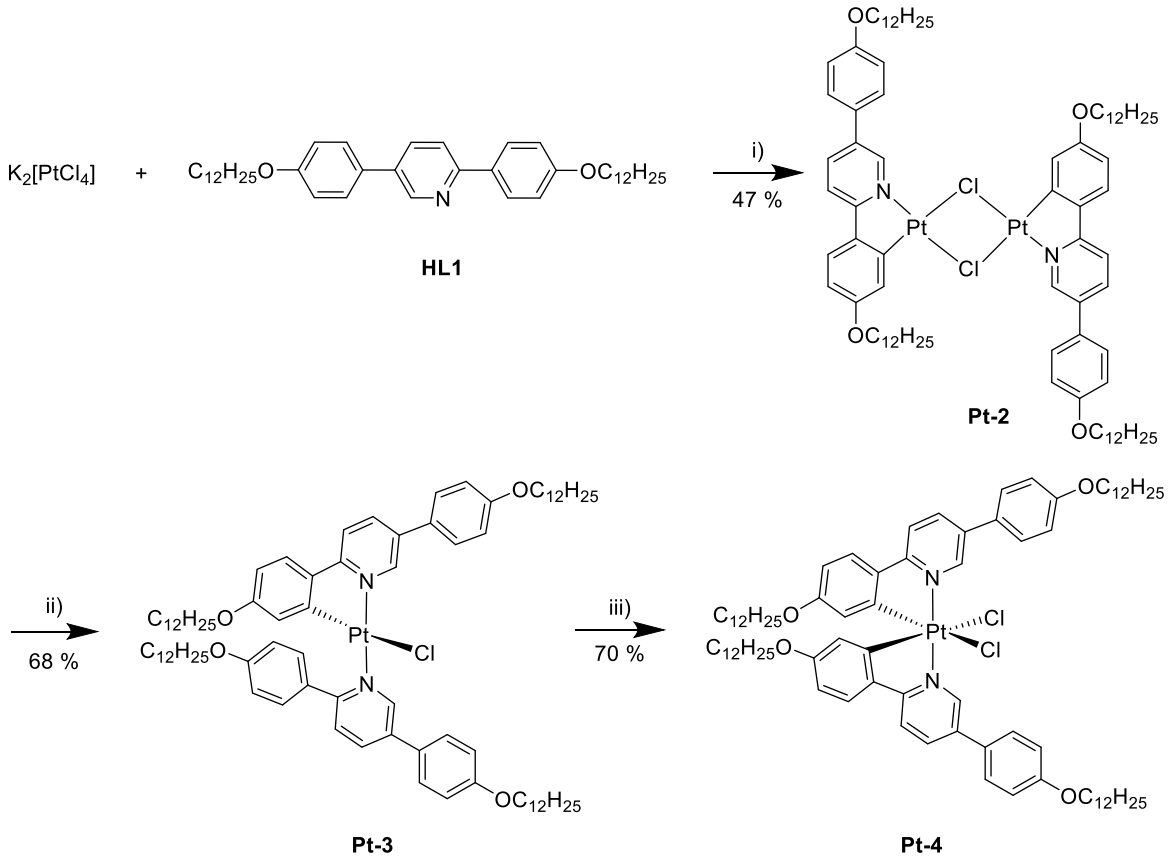

Scheme 2-5: Three-step synthetic procedure to **Pt-4**, through the synthesis of μ-chloro bridged dimer **Pt-2**, cleavage to form κ^1,κ^2 platinum(II) complex **Pt-3**, followed by an oxidation with $PhICl_2$ to give the final species **Pt-4**. i) acetic acid, reflux, 16 h; ii) 2 eq. HL, $CHCl_3$, reflux, 24 h; iii) $PhICl_2$, CH_2Cl_2, r.t., 24 h.

Although this procedure requires three synthetic steps, the comparatively high yields for the synthesis of **Pt-3** (68%) and **Pt-4** (70%), and ease of isolation render it clearly superior to the microwave-assisted synthesis, and was therefore chosen as the optimised route.

2.3.3 Synthesis of Dibromo Analogues Pt-5, [Pt(*p*-tolpy)$_2$Br$_2$], and Pt-6, [Pt(L)$_2$Br$_2$]

Based on the observations of Juliá *et al.* (Section 2.1.2) of the change in the emissive character of platinum(IV) complexes upon exchange of the halogen ancillary ligands,[38] the di-bromo analogues of **Pt-1** and **Pt-4** were prepared. These analogues, **Pt-5** and **Pt-6,** respectively, were synthesised *via* the method reported by Juliá *et al*.[38] Thus, **Pt-1** or **Pt-4** was treated with silver triflate, in the dark in acetone for 5 hours at reflux to form intermediate bis-triflato complexes, which were isolated, but not purified, and then reacted further with excess sodium bromide to form the di-bromo complexes (Scheme 2-6).

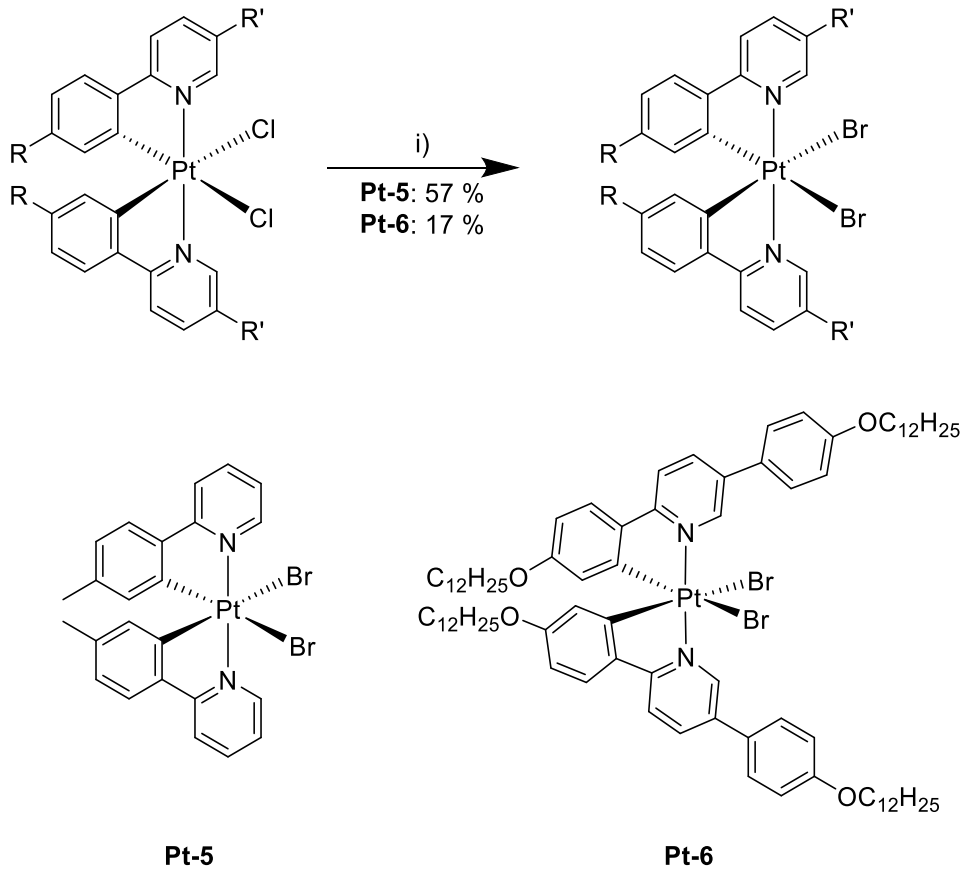

Pt-5 **Pt-6**

Scheme 2-6: Synthetic procedure[38] for the formation of **Pt-5** and **Pt-6**. i) a) AgOTf (2.5 equiv.), acetone, reflux, 5 h, dark, b) excess NaBr, acetone, 50 °C, 1.5 h. **Pt-1**/**Pt-5** R = Me, R' = H; **Pt-4**/**Pt-6** R = $OC_{12}H_{25}$, R' = C_6H_4-*p*-$OC_{12}H_{25}$.

2.4 Single Crystal Structures of Pt-1, Pt-3^{Me} and Pt-5

Although the flexible nature of the long alkoxy chains resulted in a poor level of crystallinity of the products, analogous complexes of **Pt-3** and **Pt-4** were synthesised in which terminal methoxy groups were employed, **Pt-3^{Me}** and **Pt-4^{Me}**, which led to single crystals in both cases. A data set was collected for **Pt-4^{Me}**, but the quality was poor and, as of writing, no satisfactory model has been completed. However, the crystals of **Pt-3^{Me}** were of a higher quality (grown through vapour diffusion of acetone into CH_2Cl_2), and a structure solution was found easily (Figure 2-12).

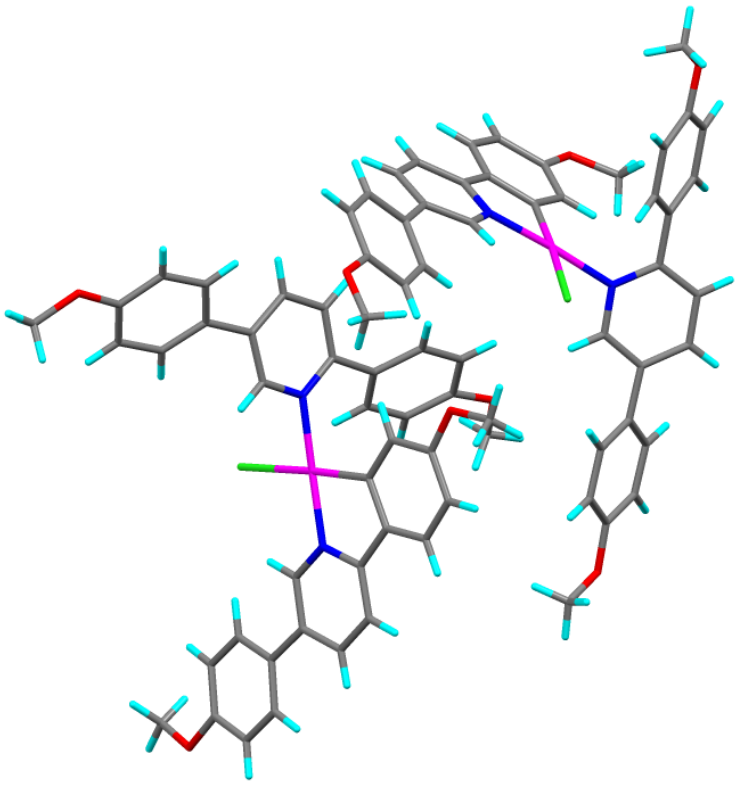

Figure 2-12: Single crystal structure of **Pt-3^{Me}**, showing both molecules in the asymmetric unit. Carbon atoms are shown in grey, hydrogen in cyan, chlorine in green, nitrogen in dark blue, oxygen in red and platinum in magenta.

Complex **Pt-3^{Me}** crystallised with two molecules in the asymmetric unit. They differed in the conformation of the terminal methoxy group such that in one molecule, they were arranged *anti* to each other, whereas in the other they are *syn*. There was also disordered solvent in this structure. One molecule of CH_2Cl_2 was modelled in two positions, while another was situated in a large solvent void with too many positions to model accurately, and so a solvent mask was used. As in the structure of **Pt-1**, **Pt-3^{Me}** showed the expected *trans* geometry of *N*-donors, with the lone chloride ligand *trans* to the platinated carbon. There was a slight decrease in Pt-N bond length upon cyclometallation (2.046(4) Å for the non-cyclometallated ligand compared to 2.014(4) Å for the cyclometallated).

Pt-1 crystallised in the *P*–1 space group with one molecule of $CHCl_3$ per molecule of complex. The hydrogen atom of the solvent molecule forms an asymmetric, bifurcated hydrogen bond with the two ligated chloride ligands of the complex with H···Cl distances of 2.7202(6) and 2.8023(7) Å.

Single crystals of **Pt-5** were grown from slow evaporation of dichloromethane; the structure is shown in Figure 2-13.

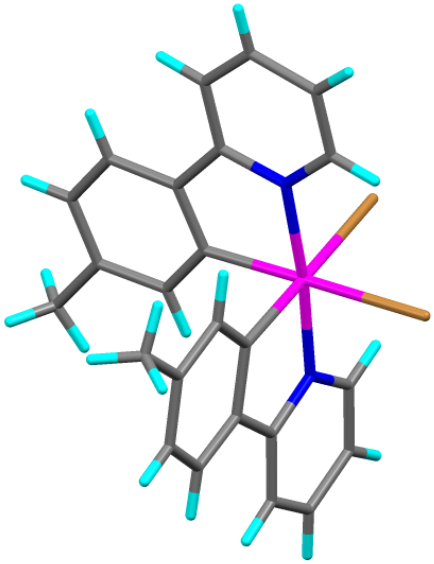

Figure 2-13: Single crystal structure of **Pt-5**. Carbon atoms are shown in grey, hydrogen in cyan, bromine in brown, nitrogen in dark blue, and platinum in magenta.

Complex **Pt-5** crystallised in the *P*–1 space group with half a molecule of CH_2Cl_2 of crystallisation; the crystal was a non-merohedral twin and was modelled with two twin components in the refined ratio 0.543:0.457. The structure is very similar to the chloro analogue **Pt-1** (Figure 2-2), with identical 2-*p*-tolylpyridine ligands in the same configuration around the platinum centre and equivalent Pt-Br bond lengths of 2.5659(8) and 2.5643(8) Å. As with **Pt-1**, the *p*-tolylpyridine ligands are identical, with the same Pt–N and Pt–C bond lengths 2.027(5) and 2.035(5) Å for Pt–N and 2.033(8) and 2.030(7) Å for Pt–C and N–Pt–C bond angles 81.6(3) and 81.31(3)°. It should be noted that the Pt-C bond is significantly longer in **Pt-5** than in **Pt-1**, which is expected when altering the ligand *trans* to the Pt–C bond from a chloride to a bromide, with bromide exerting a stronger *trans* influence than chloride.

2.5 A Short Comment on Ligand Variation

For all the complexes outlined above with 2,5-di(4-alkoxyphenyl)pyridine ligands, the same ligand, **HL1** is utilised. There is no variation in the chain length, as well as no variation in the number of chains or substitution pattern of the phenyl rings. Given the inspiration for this work, the iridium(III) research conducted by Santoro *et. al*, reports a large variation in phase behaviour when increasing the number of alkoxy chains on the cyclometallating ligands,[14] and the well-established changes in phase behaviour observed upon variation of the length of these chains, as reported for a large family of platinum(II) species and others,[34] this may seem surprising.

Ligands with a higher number of chains were investigated for a short time during the phase of the project in which microwave-assisted synthesis was being investigated. Perhaps obviously, as the number of chains increased, the solubility of the ligands in the polar reaction solvent (2-ethoxyethanol) significantly decreased, resulting in no observed complex formation at all.

It was decided, upon consolidation of an optimised synthetic route to **Pt-4**, that synthesising a larger family of complexes with significant variation of the cyclometallating ligand would be a significant time investment. The decision was taken to not pursue this family of complexes further, and rather spend the time on projects outlined later in this thesis (Chapters 3 and 4).

The large variation in phase behaviour observed by Santoro *et al.* when changing both the ancillary ligands (*i.e.* one chloride and one DMSO for an acac ligand) and the number and substitution pattern of the alkoxy chains involved indicates that the induction of liquid-crystallinity into octahedral systems of this nature is not guaranteed and not easily predictable.[14] And, as is shown in the subsequent section, phase behaviour between these iridium(III) complexes and the platinum(IV) species of this chapter are not directly analogous.

It is the opinion of the author that further functionalisation of the ligands involved, as well as significant alteration of the ancillary ligands would produce novel and interesting emissive metallomesogens, and would be worthy of investigation by a successive researcher.

2.6 Liquid-Crystalline Properties of Pt-4 and Pt-6

Complexes **Pt-4** and **Pt-6** display a lamellar liquid crystal phase over a broad temperature range. The thermal behaviour of complexes **Pt-4** and **Pt-6** is outlined in Table 2-2.

Table 2-2: Thermal behaviour of complexes **Pt-4** and **Pt-6**.

Complex	Transition	*T* / °C
Pt-4	Cr-Lam	66.2
	Lam-Iso	254.6
Pt-6	Cr-Lam	77.6
	Lam-Iso	265.0

The temperature range for both of the lamellar phases of **Pt-4** and **Pt-6** are practically identical; there is approximately a 12 °C increase in the melting point when moving to the larger bromide ancillary ligands, and approximately a 10 °C increase in the clearing point. Upon clearing into the isotropic liquid for both complexes, there appeared to be significant degradation or decomposition

of the material, potentially due to the elevated clearing temperature. These melting points are similar to the analogous iridium(III) complexes with a chloride and DMSO ligand, although this cleared at a much lower temperature (122 °C) and showed a Col_r phase in addition to the lamellar phase.[14]

Initial observations of **Pt-4**, using polarising optical microscopy (POM), showed a phase transition from the amorphous solid into a featureless, slightly birefringent phase at 66 °C on first heating, which appeared to be fluid upon shearing. The fluidity increased as the temperature was increased. This transition was difficult to observe by microscopy, for reasons outlined below. The phase was assigned as a lamellar phase after small-angle X-ray scattering (SAXS) experiments showed four orders of lamellar reflection (Figure 2-14a), with a calculated *d*-spacing of 35.3 Å.

There is a further reflection at 7.3 Å that could possibly be indexed as *d*(005) as the spacing is approximately correct. However, due to the broad peak shape and high intensity, this is suggested to be a short range Pt···Pt correlation. A clear lamellar phase is also observed in the SAXS pattern on heating for **Pt-6** (Figure 2-14b), which also shows four orders of lamellar reflections with a periodicity of 34.9 Å, slightly smaller than for **Pt-4** (35.3 Å), but not a large enough difference to be considered greatly significant. Again, a fifth reflection with a broad shape and inconsistent intensity is assigned as a Pt···Pt correlation. A summary of the parameters extracted from the SAXS data for **Pt-4** and **Pt-6** is shown in Table 2-3.

Table 2-3: X-ray diffraction data of complexes **Pt-4** and **Pt-6** on heating, presenting the measured and calculated spacing, and the Miller indices.

Complex	**Phase**	**2θ (°)**	**d_{obs}/ Å**	**d_{calc}/ Å**	***hkl***
Pt-4	Lam *T* = 189 °C	2.50	35.3	35.3	001
		5.05	17.5	17.6	002
		7.55	11.7	11.7	003
		10.05	8.8	8.8	004
		12.03	7.3		
Pt-6	Lam *T* = 178 °C	2.53	34.9	34.9	001
		5.09	17.3	17.4	002
		7.62	11.6	11.6	003
		10.03	8.8	8.7	004
		12.09	7.3		

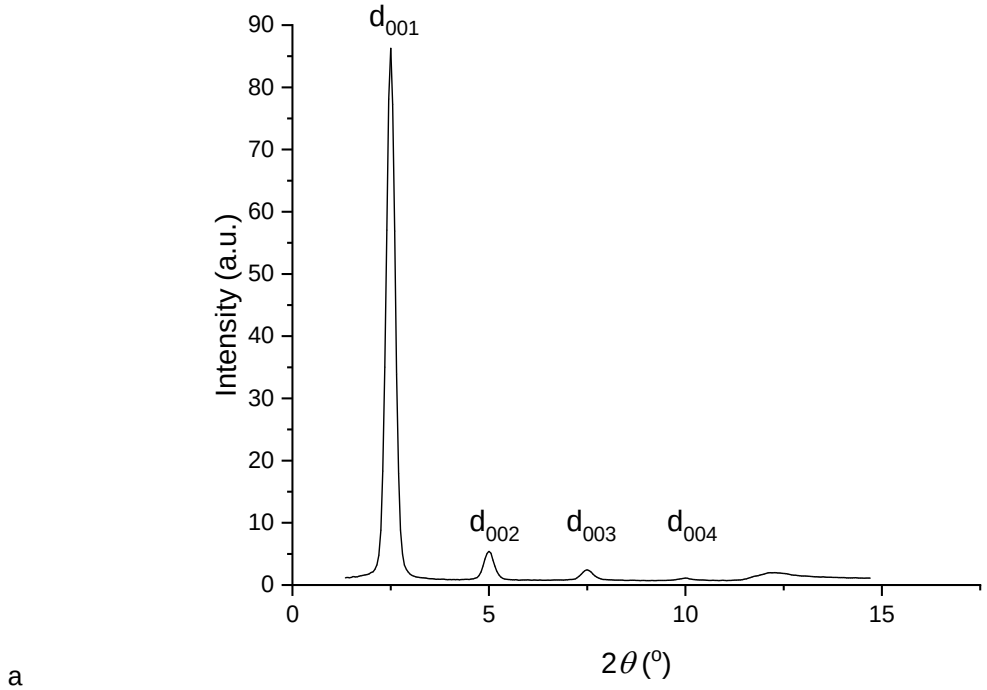

a

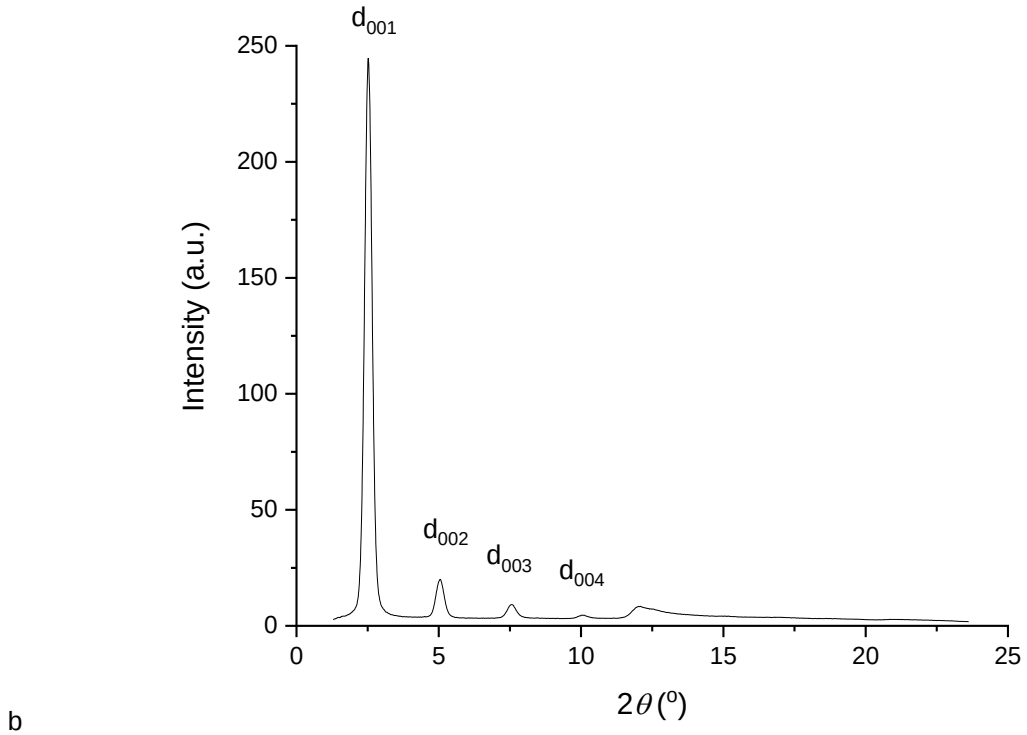

b

Figure 2-14: Small angle X-ray scattering (SAXS) pattern of a) **Pt-4** at 189 °C on heating and b) **Pt-6** at 178 °C on heating

The *d*-spacing for both **Pt-4** and **Pt-6** is shorter than the length of the free ligand, which can be calculated to be approximately 45 Å, and is likely the largest dimension in the individual complexes. Given the unusual shape of these molecules, and their deviation from tradition liquid-crystalline architectures, it is not clear how the molecules will pack in the lamellar mesophase, or what the most favourable space-filling arrangement will be, but due to the flexible nature of the alkoxy chains, some degree of interdigitation and/or chain folding can be expected.

The optical change between the crystalline phase and the lamellar phase for **Pt-4** as observed by microscopy did not appear as sharp transition and any increase in birefringence was only noticeable upon shearing. Afterwards, there was a clear increase in fluidity whilst in the lamellar phase, but upon transition into the phase, there was no obvious 'flow out' to indicate this. In order to create a thin sample where optical differences of phase transitions would be more noticeable, a sample of **Pt-4** dissolved in chloroform or dichloromethane was loaded on the glass slide and the solvent slowly evaporated, leaving behind a thin film. For this sample, it was easier to observe the melting point of **Pt-4**.

Typically, optical microscopy textures are recorded on cooling slowly from the isotropic liquid in order to observe the natural textures, as on cooling, the molecules are free to self-organise in the phase from an absence of positional order (isotropic liquid). Due to the decomposition of **Pt-4**, this technique was unsuitable in this case, although a sample was heated to just above the clearing point of 255 °C and then cooled quickly to avoid much decomposition. The textures observed (for multiple microscopy samples from the same batch of **Pt-4**) showed no identifiable defects that would typically be observed for a lamellar mesophase, such as focal conic and fan-like defects. An example of the textures observed is shown in Figure 2-15.

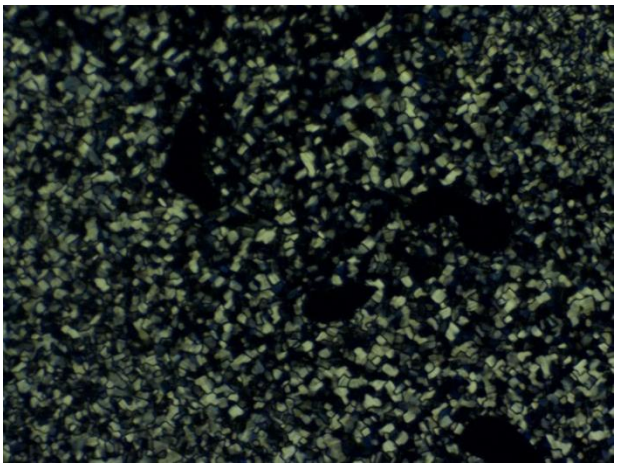

Figure 2-15: Photomicrograph of **Pt-4** on cooling from the isotropic liquid to room temperature, where is remains in the lamellar phase.

It was also observed on cooling to room temperature that the sample did not crystallise, but rather remains in the lamellar phase. Fluidity is lost and there is no alteration in birefringence upon shearing, suggesting that the sample has formed a glass.

The use of coated cells to alter the alignment of a mesophase is a useful technique to capture optical textures for difficult samples; cells are designed to force either homeotropic (perpendicular) or planar (parallel) alignment of the phase to the surface. When **Pt-4** was inserted into these cells, the textures observed did not display any identifiable defects (Figure 2-16).

a 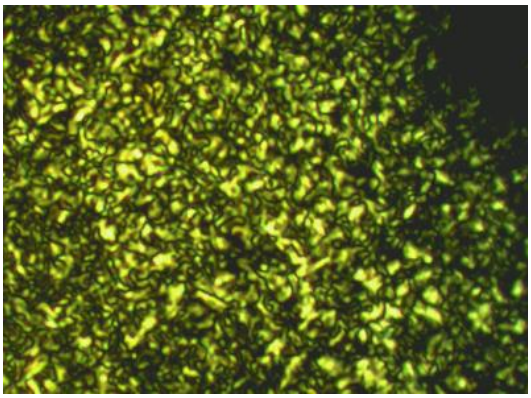 b 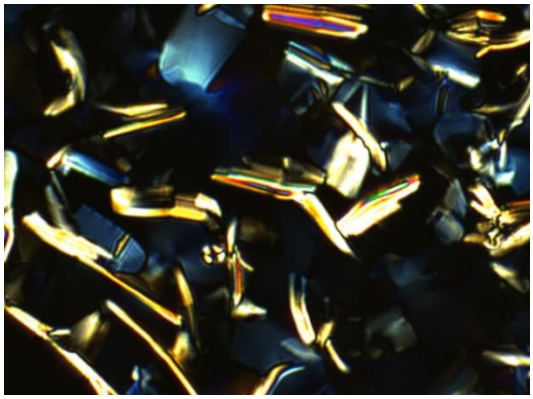

Figure 2-16: Photomicrograph of **Pt-4** on cooling from the isotropic liquid in a a) homeotropic cell at 240 °C and b) planar cell at 185 °C

It is known that deposition of a material on a microscope slide in a solution of a high-boiling solvent, such as DMF, DMSO or diglyme, followed by slow evaporation of the solvent at a temperature at which the material is in the liquid crystalline phase, can lead to textures which are otherwise difficult to obtain. This technique was attempted, and a selection of the textures produced are shown in Figure 2-17a and b. Similar difficulties were encountered with complex **Pt-6** (Figure 2-16c).

a 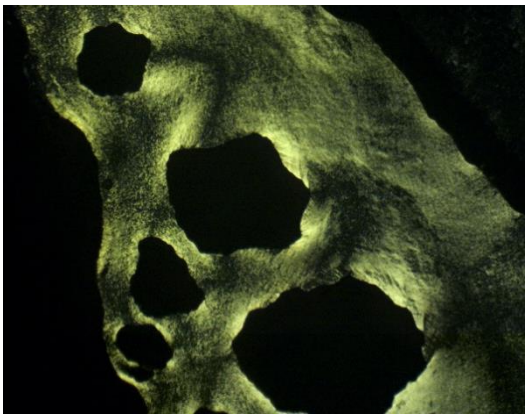 b 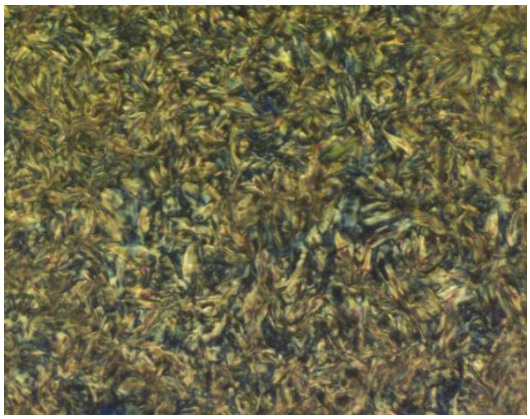

c 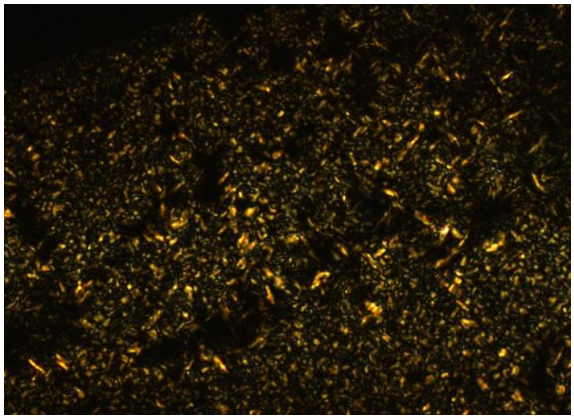

Figure 2-17: Textures obtains from slow evaporation of a solution of **Pt-4** in a) DMF at 152 °C and b) diglyme at 152 °C and of c) **Pt-6** at 214 °C on cooling from the isotropic liquid

To record the thermodynamic parameters of liquid-crystal phase transitions, differential scanning calorimetry (DSC) is used. The DSC traces recorded for **Pt-4** give a slight insight into transitions, but

due to the unstable nature of the complex, only data collected on the first heating cycle can be used. An example DSC trace for **Pt-4** is shown in Figure 2-18.

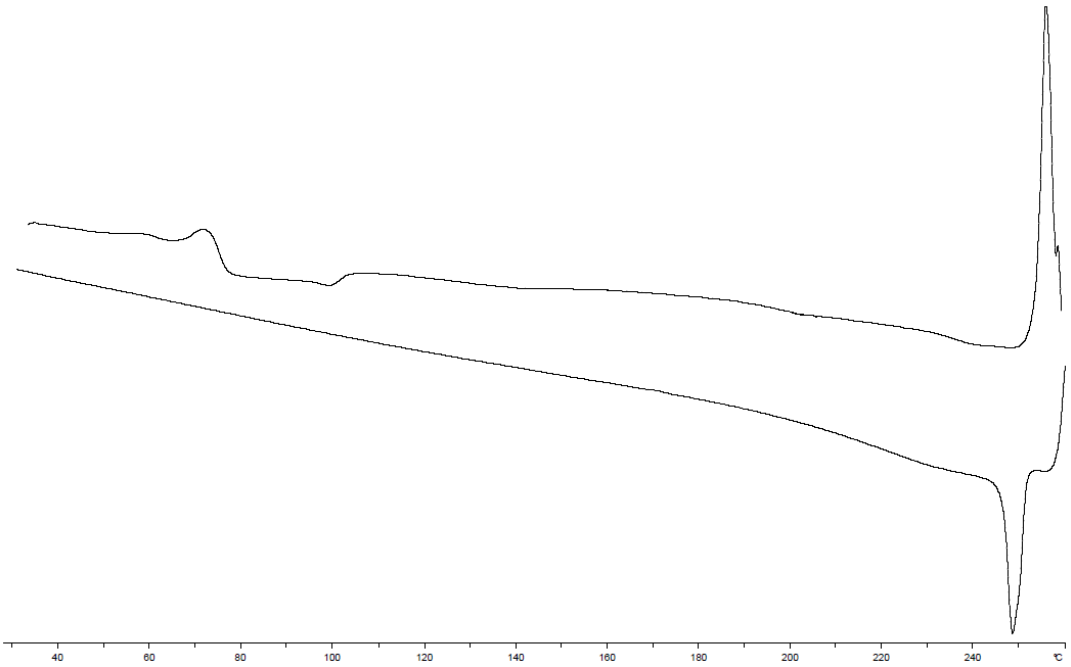

Figure 2-18: DSC trace of **Pt-4** showing the first heating (top) and cooling (bottom) cycles.

It can be seen that, even on the first heating cycle, the trace is poor, and it would be unwise to rely on the parameters derived. However, the enthalpy of the melting point can be calculated as approximately 7.0 kJ mol^{-1}, and of the clearing point as 20.2 kJ mol^{-1}. In the broadest terms, in comparison to the large clearing point enthalpy, the melting point enthalpy is small. This indicates that the lamellar phase has a significant amount of order; this is in corroboration to the patterns observed by SAXS, in which four orders of reflection are observed. When the same sample is subjected to successive heating/cooling cycles, only the clearing point is observed, the enthalpy of which becomes increasingly smaller as the sample decomposes.

2.7 Thermal Oxidation and Ortho-metallation of Pt-3

Complex **Pt-3** has no obvious anisotropy, and has low levels of rigidity due to the flexibility of the κ^1-**HL1** ligand, which is coordinated only through the nitrogen atom. It would be unexpected, then, for **Pt-3** to display any liquid-crystalline behaviour. However, for the sake of completeness, **Pt-3** was investigated by polarising optical microscopy.

On the first heating cycle, there appeared to be only a crystal-to-crystal transition at 152 °C, followed by a melting point into the isotropic liquid at 201 °C. However, on cooling, the texture

formed showed fan-like features, typical of a liquid-crystalline phase (photomicrograph shown in Figure 2-19); the phase also had flow and was brightly birefringent.

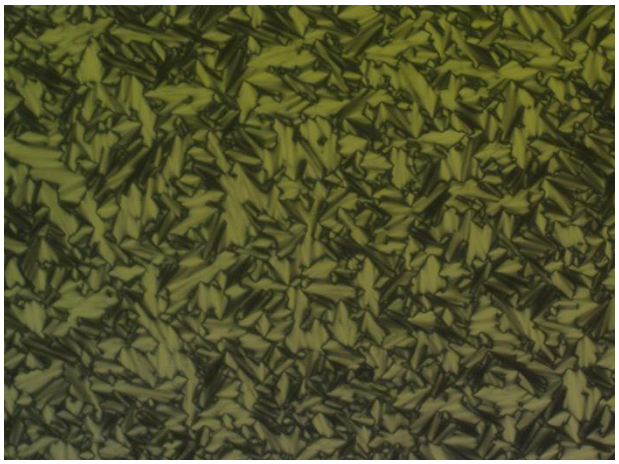

Figure 2-19: Photomicrograph of **Pt-3**, taken at 165 °C upon cooling from the isotropic liquid.

When the same sample was subjected to a second heating cycle, the observations were markedly different; there is a clear phase transition at 111 °C, which is perhaps best illustrated through the use of differential scanning calorimetry (DSC). The annotated DSC trace of three successive heating and cooling cycles is shown in Figure 2-20.

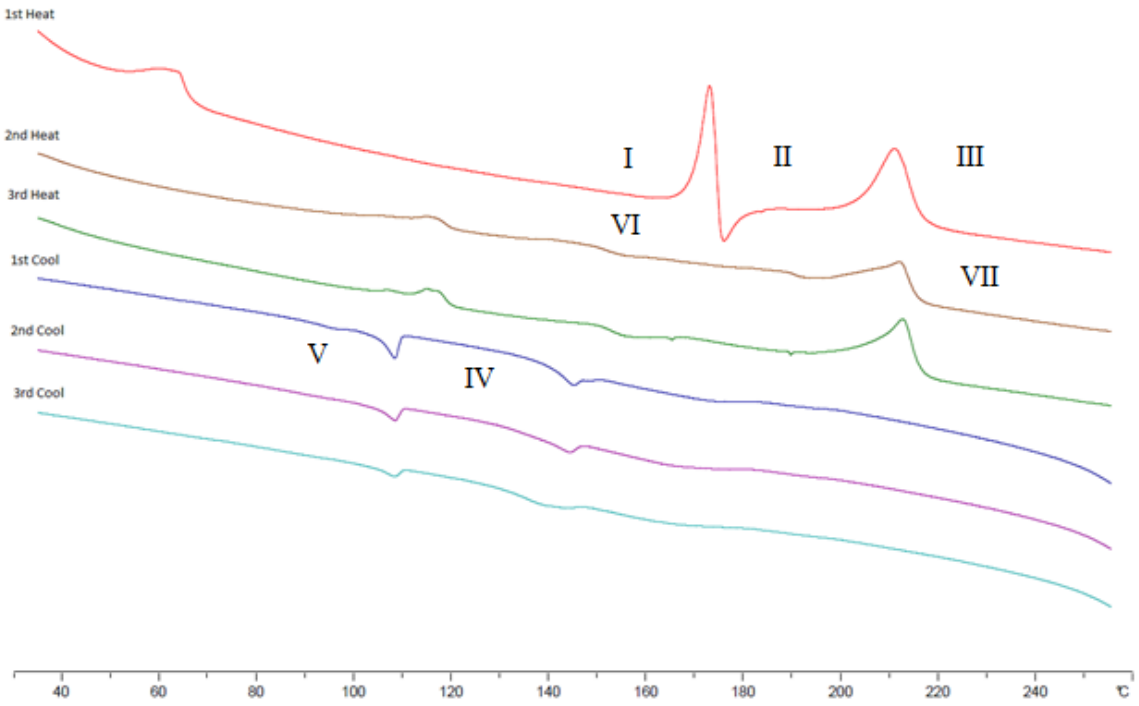

Figure 2-20: Annotated DSC trace of **Pt-3**, showing 3 successive heating and cooling cycles, with heating cycle one in red, two in brown and three in green, and cooling cycle one in blue, two in purple, and three in cyan. Specific points of reference are labelled as points **I-VII**.

By following the successive heating and cooling cycles, it can be seen that there are two endothermic transitions at approximately 30 °C (not shown) and 54 °C which were not observed by microscopy. Following this, a coupled endothermic/exothermic event was observed with an onset temperature of 152 °C, as observed by microscopy (transition from point **I** to **II**). A further transition is then observed (**II** to **III**) into the isotropic liquid (clearing point).

On cooling, there is a small transition at 146 °C (**III** to **IV**), and a further transition of a similar magnitude at 111 °C (**IV** to **V**). On the second heating cycle, we do not observe the first two endothermic transitions, but rather a new transition at 110 °C (**V** to **VI**). The coupled endothermic/exothermic transition that was observed on the first heating cycle is not observed on the second, but the clearing point at 201 °C remains unchanged (**VI** to **VII**). The second and third cooling cycles remain the same as the first.

Given the lack of anisotropy in **Pt-3**, these observations were deemed suspicious, as was the disappearance of three transitions on heating, and it was decided to investigate this further. Using DSC, a sample was subjected to 4 heating/cooling cycles, with the maximum temperature increased for the third and fourth heating cycles so that, each time, a further phase transition is added to the cycle. The traces are shown in Figure 2-21, with only the curve shown for clarity.

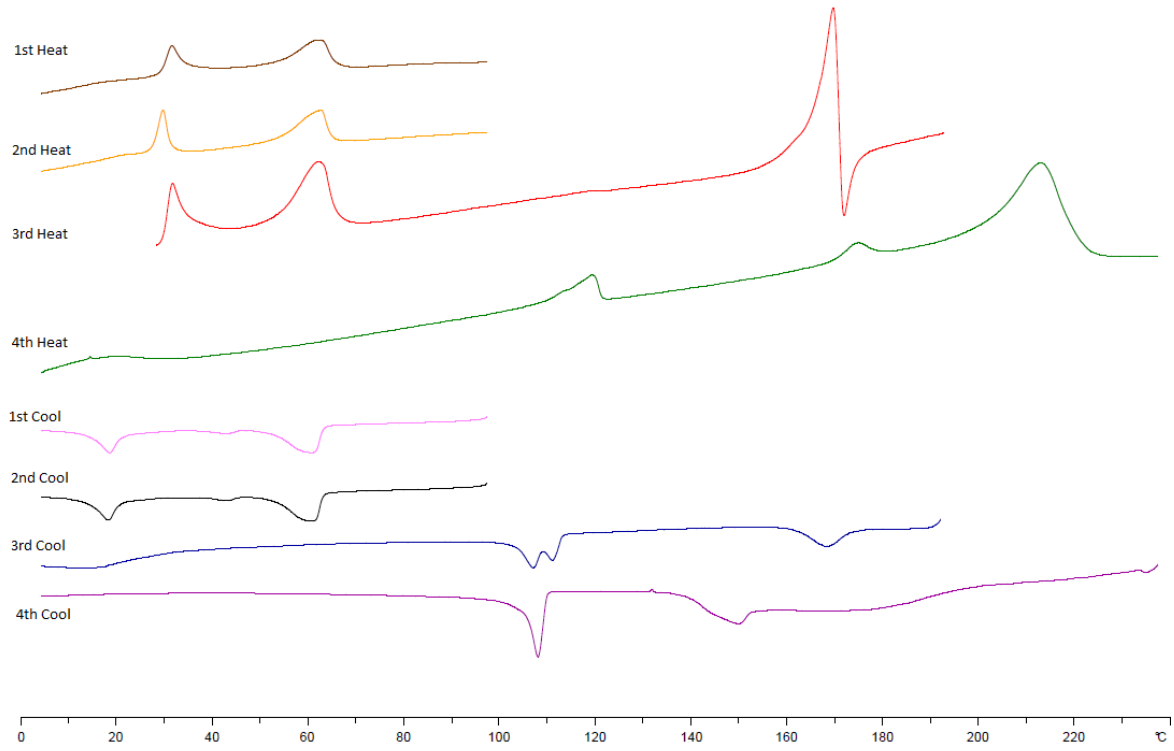

Figure 2-21: DSC traces of **Pt-3**, showing four successive heating and cooling cycles with different maximum temperatures. 1st and 2nd cycle: 0 to 100 °C; 3rd cycle: 0 to 185 °C; 4th cycle: 0 to 240 °C.

The first two heating cycles range from 0 to 100 °C; it can be seen that the first two observed endothermic transitions at *ca*. 30 and 54 °C are reproducible when the temperature does not exceed 100 °c, *i.e.* when there is no further phase transition at 152 °C. On the third heating cycle, the maximum temperature was increased to 185 °C; here we see the transitions at 30 and 54 °C, but also the previously observed coupled endothermic/exothermic event at 152 °C. On cooling (3rd cool, blue trace), there is a small transition with an onset of 173 °C; this transition is not observed when heating above the transition at 201 °C. Following this, there are two small transitions close together at 113 and 109 °C; again, these are not observed when the sample has been heated into the isotropic liquid. On the fourth and final heating cycle, there is a transition at 111 °C, as observed in the initial trace shown in Figure 2-20, as well as a before-unseen small transition at 170 °C, followed by the transition into the isotropic liquid at 201 °C.

It is very clear, then, that the changes observed arise not from phase transitions, but rather a *chemical* change in the sample when it is heated over 180 °C and a further change when it is in the isotropic liquid.

Temperature-dependent, small-angle X-ray scattering (SAXS) was very useful in investigating this change; it is possible to mimic the heating/cooling cycles from the DSC investigations.

On the first SAXS heating cycle, only crystalline phases are observed for the transitions at 30 and 54 °C, after which the transition at 152 °C results in the formation of a lamellar phase, with clear *d*(001), *d*(002) and *d*(003) reflections and a *d*-spacing of 35.2 Å (Figure 2-22). This phase is retained on cooling to room temperature, with a reduction in the lamellar periodicity to 33.8 Å at 39 °C.

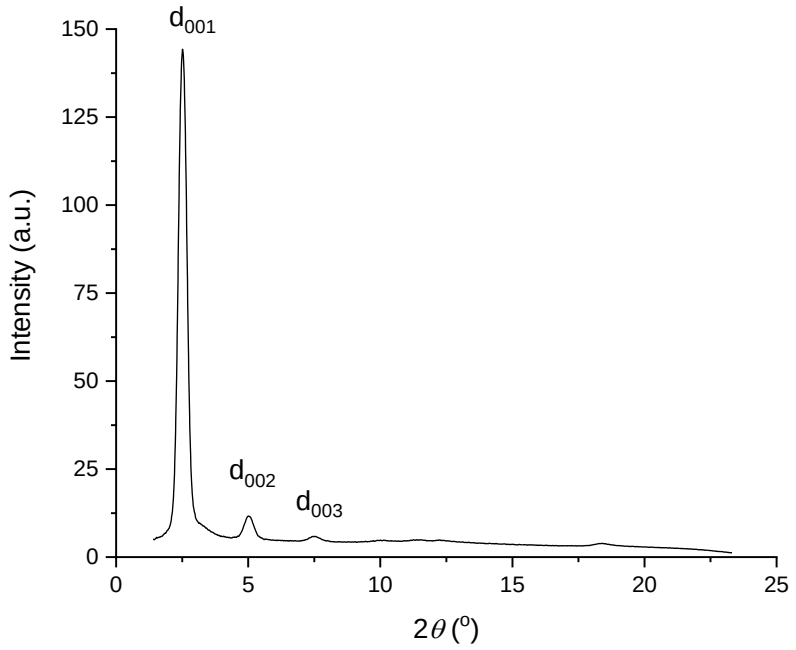

Figure 2-22: Diffraction pattern of **Pt-3**, taken at 174 °C on the first cooling cycle after heating to 191 °C, showing the clear *d*(001), *d*(002) and *d*(003) of a lamellar phase.

On the second heating cycle, this lamellar phase remains until the clearing point at 201 °C, where the isotropic liquid is observed. The SAXS pattern of a sample of **Pt-3** taken at 178 °C after cooling from the isotropic liquid (equivalent to the fourth heating cycle) shows another lamellar arrangement (Figure 2-23), with clear reflections corresponding to the *d*(001), *d*(002) and *d*(003) with a lamellar periodicity of 36.3 Å, a slightly larger spacing than observed in Figure 2-22, but not different enough to be considered especially significant. These data are very similar to those of **Pt-4** (Table 2-4), and led to the hypothesis that the κ^1-ligand in **Pt-3** has undergone an oxidative addition to form either **Pt-4** or a very similar complex. It should be noted that the sample was not purified/isolated, and all measurements have been carried out on the crude product formed after heating. In purification attempts, the majority of the free ligand (**HL1**) was removed from the sample by crystallisation, but no further efforts were successful in isolating any of the metal complexes present in the mixture.

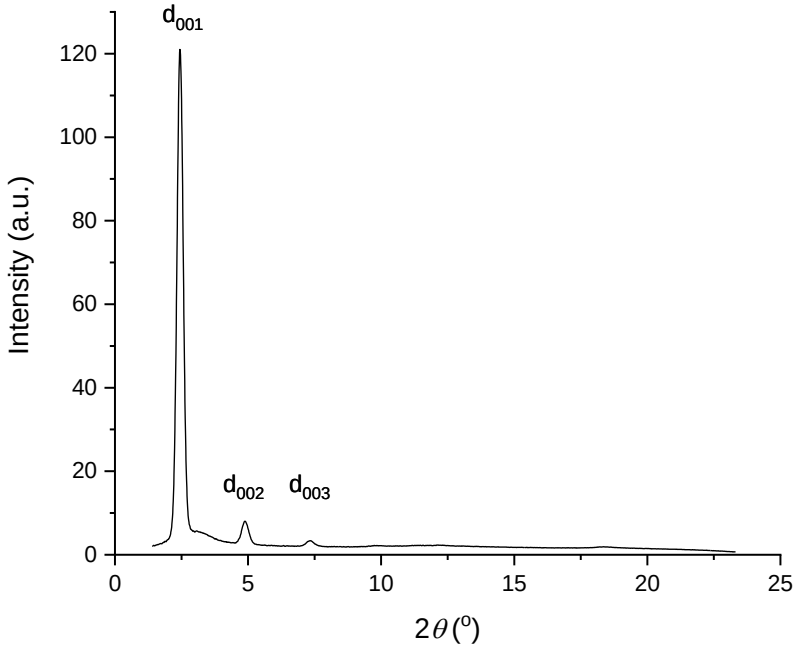

Figure 2-23: Diffraction pattern of **Pt-3**, taken at 178 °C on the second cooling cycle after heating to 220 °C, showing the clear *d*(001), *d*(002) and *d*(003) of a lamellar phase.

Table 2-4: X-ray diffraction data of **Pt-4** and the mixture formed upon cooling **Pt-3** from the isotropic liquid, presenting the measured and calculated spacing, and the Miller indices.

Complex	**Phase**	**2θ(°)**	**d_{obs}/ Å**	***hkl***
Mixture from **Pt-3**	Lamellar *T* = 174 °C on cooling from 190 °C	2.51	35.2	001
Mixture from **Pt-3**	Lamellar *T* = 178 °C on cooling from 220 °C	2.43	36.3	001
Pt-4	Lamellar *T* = 189 °C	2.50	35.3	001

To aid in the investigation of the nature of this chemical change, ^{1}H and ^{195}Pt NMR spectroscopy were employed. A pure sample of **Pt-3**, in which the ^{1}H NMR spectrum showed no impurities and which gave satisfactory elemental analysis, was taken as the starting point for all experiments.

After heating to 100 °C, the ^{1}H NMR spectrum of the sample showed only pristine **Pt-3**; no chemical change had taken place and no other species were observed. This was expected, due to the reproducibility of the transitions in the DSC trace. The ^{1}H NMR spectrum of the mixture obtained after heating **Pt-3** to 180 °C showed a complex mixture of which the major components were **Pt-3** (resonances at 9.48 and 9.88 ppm), **Pt-4** (10.2 ppm) and free ligand, **HL** (8.87 ppm) (Figure 2-24); a distinctive chemical change has taken place. There are also a number of previously unobserved and unidentified resonances in the region between 10.8 and 8.8 ppm, labelled **a-f**. Due to the characteristic downfield shift for protons *ortho* to the nitrogen atom of the cyclomatalling ligand to 8.8 ppm and higher chemical shifts in these platinum complexes, it is this region of the spectrum that is expanded below and utilised for the analysis of a multi-component system, as in the remainder of the aromatic region of the spectrum no specific signals can be isolated due to intense overlap.

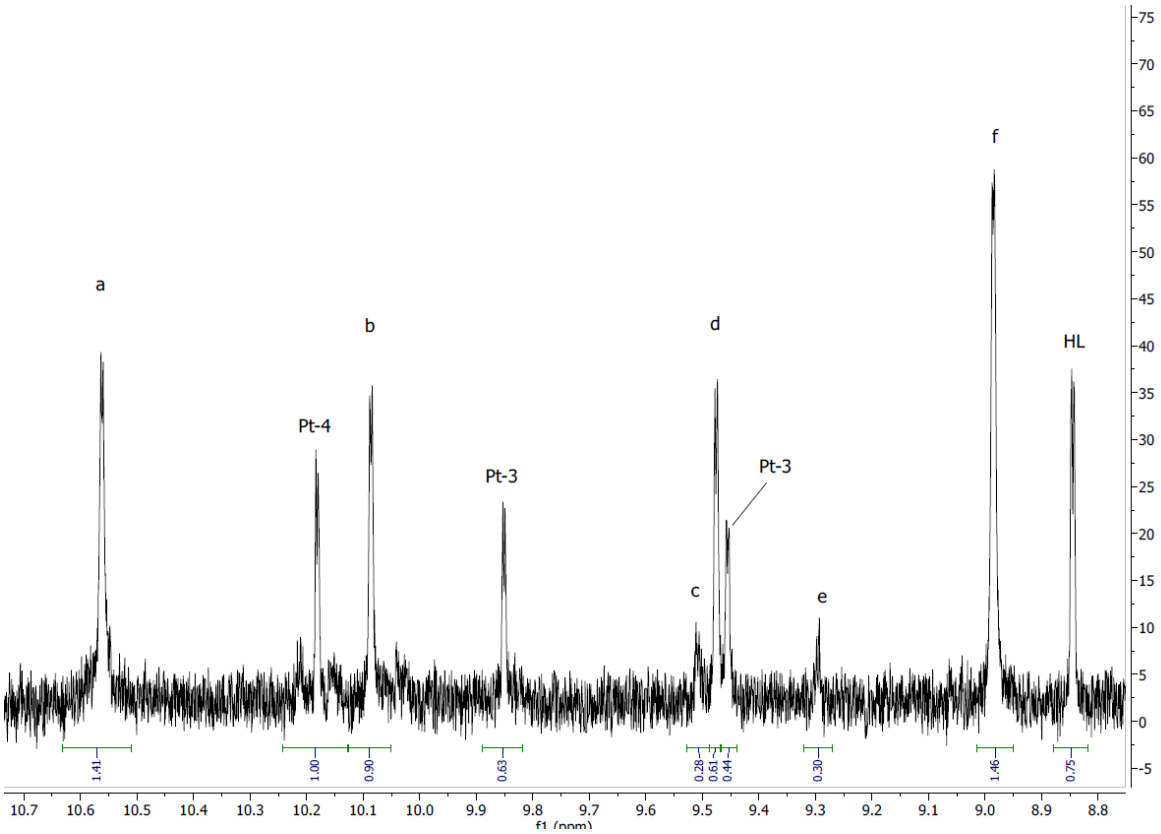

Figure 2-24: ^{1}H NMR spectrum in the 10.8 to 8.8 ppm region of **Pt-3** after heating to 190 °C. The main species observed are **Pt-4**, **Pt-3** and unreacted ligand **HL**. Other unidentified species present are labelled **a-f**. Resonances are arbitrarily integrated against the **Pt-4** signal, assigned a value of one. It should be noted that for **Pt-4**, this resonance is indicative of two protons due to the symmetric nature of the cyclometallating ligands, whereas the two resonances for **Pt-3** each arise from one proton.

The presence of a significant amount of **Pt-3** indicates that whatever change has taken place has not gone to completion, despite the sample being held at 190 °C for 2 hours. The presence of **Pt-4** corroborates the observations in the SAXS pattern that an oxidation to **Pt-4** or a similar species has taken place.

The mixture was then subjected to further heating to 230 °C. The ^{1}H NMR spectrum shows distinctive changes (Figure 2-25). Now, the dominant species is **Pt-4**. There is still a significant contribution from **Pt-3** and **HL**. Most noticeable is the (almost) complete disappearance of resonance **a** and the reduction in the intensity of **f**. Generally, the other unidentified resonances remain of a similar intensity.

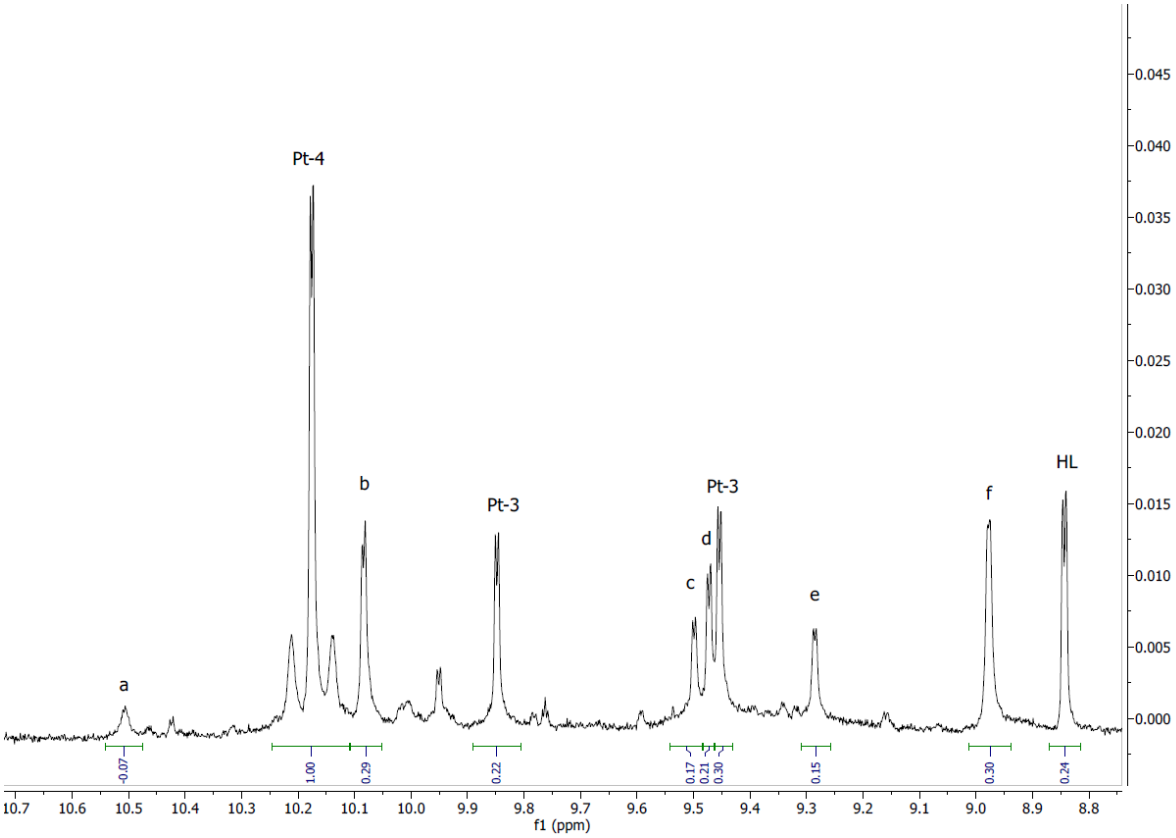

Figure 2-25: ^{1}H NMR spectrum in the 10.8 to 8.8 ppm region of **Pt-3** after heating to 230 °C (isotropic liquid). The main species observed are **Pt-4**, **Pt-3** and unreacted ligand HL. Other unidentified species present are labelled **a-f**. Resonances are arbitrarily integrated against the **Pt-4** signal, which has a value of one. It should be noted that for **Pt-4**, this resonance is indicative of two protons due to the symmetric nature of the cyclometallating ligands, whereas the two resonances for **Pt-3** each arise from one proton.

It should be noted that a variation in the species present in the ^{1}H NMR spectrum was observed when individual samples from the same batch of **Pt-3** were heated to 230 °C in individual, seperate heating events. An example of this is shown in Figure 2-26. Here, the reaction involved seems to progress with significantly fewer side products, as the only resonances recorded in any appreciable quality correspond to **Pt-4**, **Pt-3**, **HL** and the unidentified species **b**.

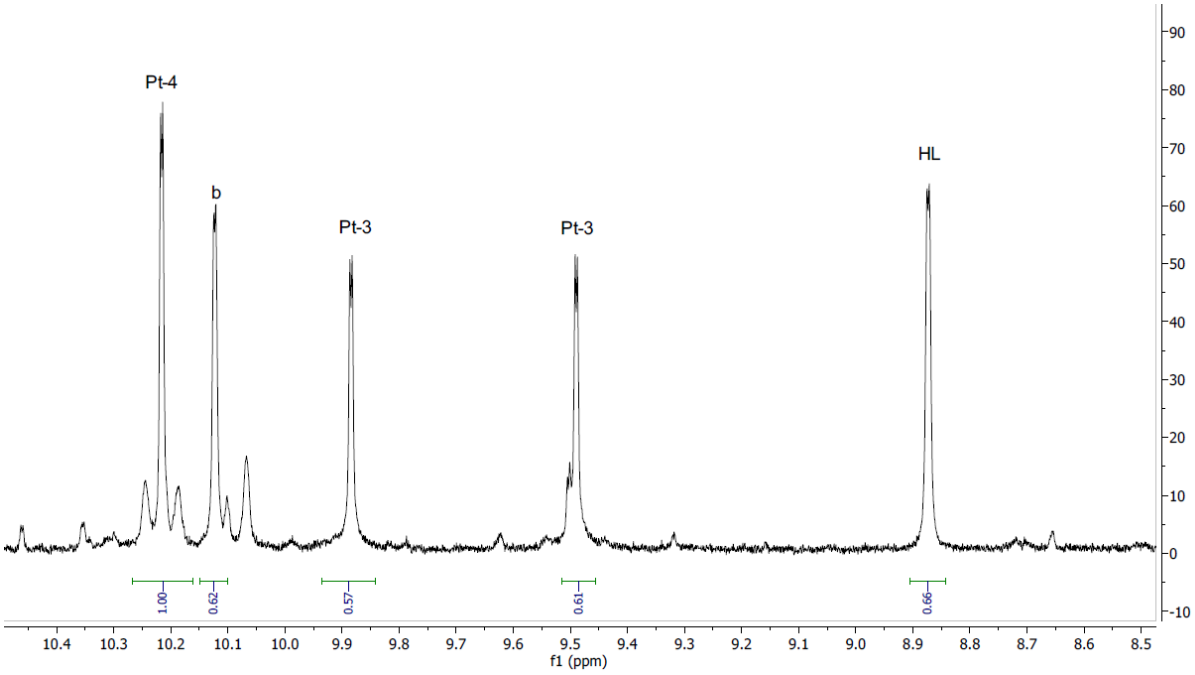

Figure 2-26: ^{1}H NMR spectrum in the 10.8 to 8.8 ppm region of **Pt-3** after heating to 230 °C (isotropic liquid) of a new sample. The main species observed are **Pt-4**, **Pt-3** and unreacted ligand HL, as well as unidentified species **b**. Resonances are arbitrarily integrated against the **Pt-4** signal, which has a value of one. It should be noted that for **Pt-4**, this resonance is indicative of two protons due to the symmetric nature of the cyclometallating ligands, whereas the two resonances for **Pt-3** each arise from one proton.

Utilising this less complicated sample, the ^{195}Pt NMR spectrum of the material was collected in order to glean further insight into speciation, and showed resonances at -1734, -1738 and -3169 ppm, and a less intense signal at -1303 ppm. The signal at -3169 ppm corresponds to **Pt-3**. The signal for a pure sample of **Pt-4** in ^{195}Pt NMR spectrum occurs at -1740 ppm, and the resonance recorded at -1738 ppm is assigned as the same; the two signals at -1734 and -1738 ppm did not vary when the spectrum was recorded at different field strengths, demonstrating that they were separate resonances and not a doublet.

Chemical shifts in ^{195}Pt NMR spectroscopy are extraordinarily sensitive to a number of factors, including oxidation state and solvent. Therefore, it is proposed that the species that gives rise to the resonance at -1734 ppm was very similar to **Pt-4**. This is supported by the observation that the mixture gives only a single texture when viewed by microscopy- *i.e.* the constituent components are co-miscible and behave homogenously. Clearly then, the chemical change observed when **Pt-3** is heated into the isotropic liquid is an oxidative *ortho*-metallation.

Ortho-metallation is an active research area, not least because of its relevance to C–H bond activation/functionalisation.[64-67] With respect to platinum(II) chemistry, reactions reported in the literature have been shown to proceed both with retention of the platinum(II) oxidation state, as well as oxidative reactions to form platinum(IV) species.[64, 68]

A study by Newman *et al.*[63] in 2007 based on platinum chemistry with functionalised phenylpyridine (ppy) ligands identified five possible isomers (**A** – **E**) that could arise from the oxidation of [Pt(κ^2-ppy')(Cl)(κ^1-ppy'H)], where ppy'H is 2-(4-fluorophenyl)pyridine) (Figure 2-27).[63] Through utilisation of ^{19}F and ^{19}F–^{195}Pt correlation NMR spectroscopy, they concluded that the ultimate isomer formed was **D**, but that isomer **E** was also formed before isomerising to **D**.

A subsequent study by Whitfield and Sandford[62] using unsubstituted 2-phenylpyridine itself (Figure 2-27, X = H) reported that the oxidation of the platinum(II) species *cis*-[Pt(ppy)$_2$] with the hypervalent iodine species PhICl$_2$, as utilised in this work, led to two observable products, the major isomer **E** (64 %), and a symmetric species (29 %) that they hypothesise is one of species **A**-**D**.

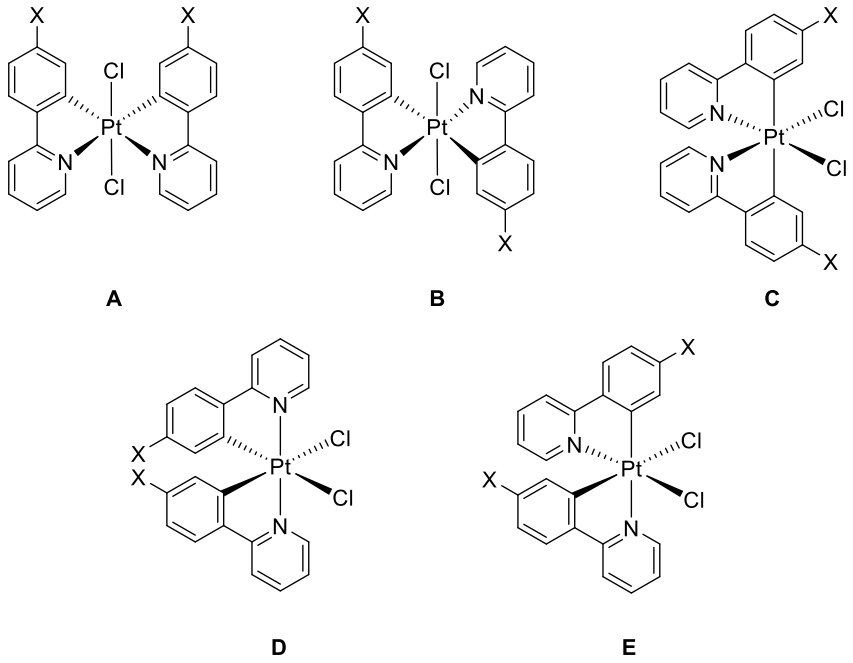

Figure 2-27: Different isomers of [Pt(ppy)$_2$Cl$_2$] and proposed by Newman *et al.* (X = F)[63], Whitfield and Sandford,[62] and Juliá *et al*.[38] (both X = H)

Due to the mutually *trans ortho*metallated carbon atoms in **B** and **C**, these species were ruled out as unlikely possibilities due to the strongly σ-donating nature of the anionic carbon atoms. Data from ^{1}H NMR spectroscopy led them to suggest isomer **A** as the minor product, corresponding to a resonance in the ^{195}Pt NMR spectrum of -1725 ppm in DMF. Later work by Juliá *et al.* investigated the same oxidation, with the conclusion that **E** is the main product observed, however they do not mention the possible isolation of isomer **A**.[38]

However, using PhICl$_2$, the oxidation of [Pt(κ^2-ppy)(Cl)(κ^1-ppyH)], a species analogous to **Pt-3**, and with a single *ortho*metallated phenylpyridine ligand (κ^2-ppy) and a neutral (κ^1-ppyH) coordinated only through the nitrogen donor, led to isomer **D**. From these studies, it can be concluded that both the symmetric isomer **D** and the asymmetric isomer **E** are both readily accessible with small changes in reaction conditions.

Given that **Pt-4** has been identified as the major product of this thermal reaction, that the SAXS data for the thermally treated **Pt-3** are almost exactly the same as that measured for **Pt-4** and that the two major species observed are co-miscible, it is proposed that the isomers present are **D** (= **Pt-4**) and the asymmetric isomer **E**. The assignment of isomer **A** as the second platinum(IV) species present was thought to be less likely on the grounds that **A** and **D** were unlikely to be miscible.

What, then, can be gleaned about the mechanism of the oxidation? The study outlined above by Newman *et al.* started from [Pt(κ^2-ppy')(Cl)(κ^1-ppy'H)] (the platinum(II) species analogous to **Pt-3**) and, based on the conditions required for accessing [Pt(κ^2-ppy)$_2$], concluded that this *bis*-chelated platinum(II) species was not an intermediate. It was proposed that the oxidation of platinum(IV) is the first step of the mechanism, followed by an *ortho*-metallation with retention of the +4 oxidation state (Figure 2-28).[63]

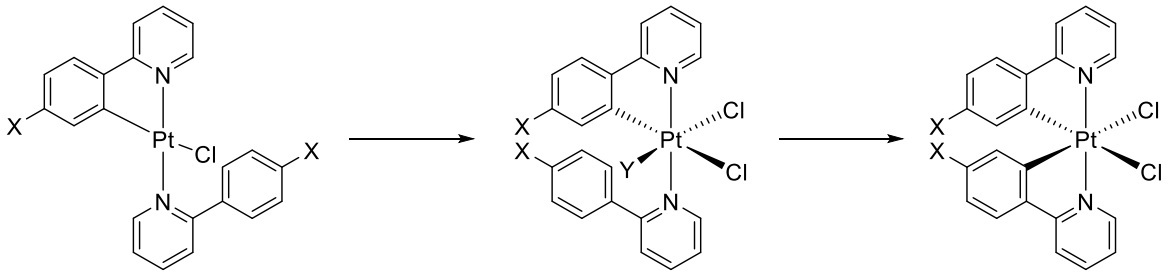

Figure 2-28: Mechanistic pathway proposed by Newman *et al.* for the oxidation of [Pt(κ^2-ppy)(Cl)(κ^1-ppyH)] to *cis*-[Pt(κ^2-ppy')$_2$Cl$_2$].[63]

However, it should be noted that they had accounted for stoichiometry of the platinum(IV) product through addition of chloride (in the form of KCl) as well as an oxidant (hydrogen peroxide). The reaction is also carried out in the solution-phase. This is in contrast to the case of **Pt-3**, where the reaction is occurring in the solid state/melt without the addition of any further chloride or oxidative species. The reaction also proceeds consistently under atmospheres of both air and argon.

It is obvious, then, that without any further added species, it requires two molar equivalents of **Pt-3** to generate one molar equivalent of **Pt-4** (the same applies to the proposed isomer) to satisfy stoichiometry. Accordingly, the generation of **Pt-4** must therefore be bimolecular, so it is unsurprising that both free ligand and further unidentified species are observed by NMR spectroscopy subsequent to heating.

It can be rationalised that under these solvent-free, inert atmosphere conditions that this oxidation occurs through either an intra- or inter-molecular cyclometallation or disproportionation. No platinum black was observed in the mixture, the observation of which disfavours disproportionation. Therefore, an initial oxidation and *ortho*-metallation of **Pt-3** could lead to a

five-coordinate platinum(IV) species, which then scavenges a second chloride ligand from a further molecule of **Pt-3** to form **Pt-4**, resulting in decomposition or degradation of the second molecule, which would be coordinatively unsaturated. Free rotation about the Pt–N bond in the κ^1-ppy'H ligand could possibly account for the observation of the different isomers, or, as proposed by Newman *et al.*[63] it could be that the asymmetric isomer **E** is formed and gradually isomerises to **Pt-4**. Full elucidation of the mechanism is outwith the scope of this project.

It should also be noted that observation of this phenomenon is exclusively observed for **Pt-3**; no chemical change is observed for the analogous species with 2-*p*-tolylpyridine ligands (named as **Pt-IIb** in Section 2.3.1.1) nor the same complex with methoxy (OCH_3) chains in place of the dodecyloxy ($OC_{12}H_{25}$), **Pt-3^{Me}**, indicating that the extension of the conjugation and inclusion of the flexible alkoxy chains is somehow necessary for this process.

2.8 Photophysical Properties of Platinum(IV) Complexes

The emissive behaviour of the four platinum(IV) complexes formed is of great interest; as mentioned in the introductory section to this chapter (Section 2.1.2), alteration of both the cyclometallating ligand and ancillary ligands of bis-cyclometallated platinum(IV) complexes has a significant impact on the emissive character.[36-42] The photophysical behaviour of platinum(IV) complexes **Pt-1**, **Pt-4**, **Pt-5** and **Pt-6** were fully characterised, as well as platinum(II) complex **Pt-3**, as it is novel, and for the sake of completeness.

2.8.1 Absorption Spectra

The UV-Visible absorption spectra of **Pt-1**, **Pt-3**, **Pt-4**, **Pt-5** and **Pt-6** were recorded in CH_2Cl_2 solution at room temperature (~1 x10^{-5} M). The spectrum of **Pt-3** is shown in Figure 2-29, while the spectra for **Pt-1** and **Pt-5** are in Figure 2-30 and those for **Pt-4** and **Pt-6** are found in Figure 2-31.

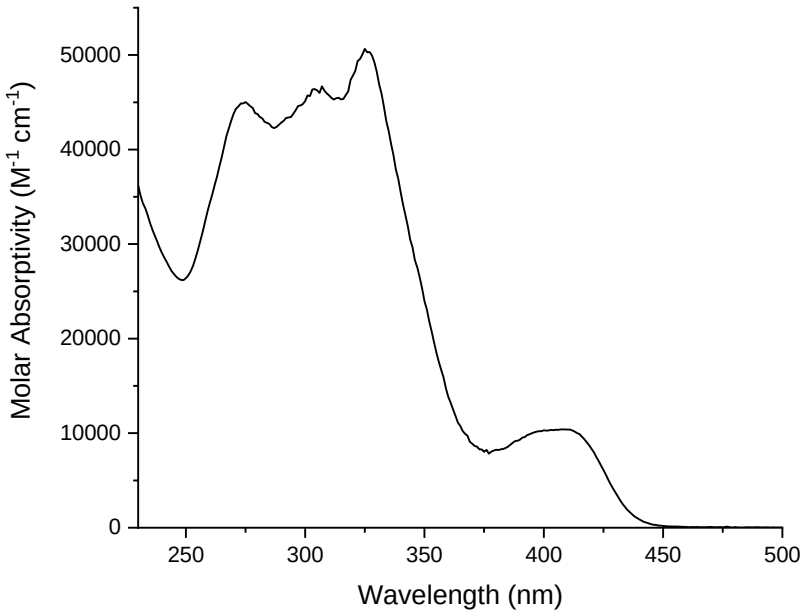

Figure 2-29: UV-Vis absorption spectrum of **Pt-3** recorded in CH_2Cl_2 at room temperature.

For the only platinum(II) complex in the series, the yellow **Pt-3** (Figure 2-29), the lowest-energy absorption band is centred at 408 nm (ε = 10400 M^{-1} cm^{-1}), with a series of more intense bands in the UV region, at 274 (ε = 48900 M^{-1} cm^{-1}), 306 (ε = 49600 M^{-1} cm^{-1}) and 326 (ε = 52700 M^{-1} cm^{-1}) nm. The low-energy band at 408 nm is quite typical of cyclometallated platinum(II) complexes, and is attributed to $d_{Pt}/\pi_{N^C} \rightarrow \pi^*_{py}$ charge-transfer transitions.[22, 69-80]

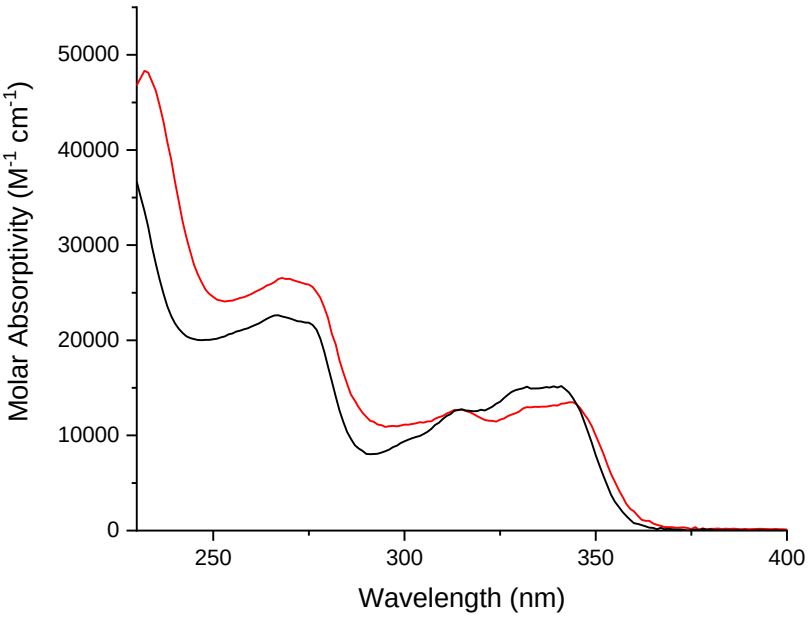

Figure 2-30: UV-Vis absorption spectra of **Pt-1** (black) and **Pt-5** (red) recorded in CH_2Cl_2 at room temperature.

In contrast to this, the lowest energy absorption band for the platinum(IV) species **Pt-1** and **Pt-5** with 2-*p*-tolylpyridine ligands is significantly blue-shifted into the UV region, found at 335 nm (ε = 14900 M^{-1} cm^{-1}) for **Pt-1** and 344 nm (ε = 13500 M^{-1} cm^{-1}) for **Pt-5**. It is consistent that in the more

oxidised platinum(IV) species, the metal-based *d*-orbitals are stabilised, resulting in a shift to a more ligand-based $\pi \rightarrow \pi^*$ excited state. This $\pi \rightarrow \pi^*$ transition is also observed in many of the literature platinum(IV) species with C^N cyclometallating ligands.[36-38, 40]

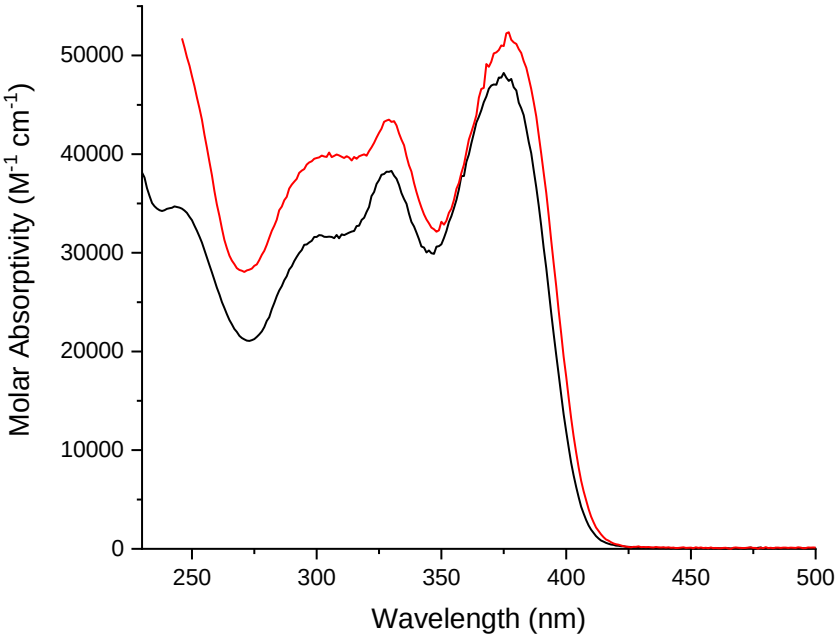

Figure 2-31: UV-Vis absorption spectra of **Pt-4** (black) and **Pt-6** (red) recorded in CH_2Cl_2 at room temperature.

The UV-Vis spectra of **Pt-4** and **Pt-6** show the same shift blue-shift of the spectrum as the other two platinum(IV) species compared to the platinum(II) species **Pt-3**, however, it should be noted that there is a significant red-shift on incorporation of the 2,5-di(4-dodecyoxyphenyl)pyridine ligands (**HL1**) compared to the analogous complexes with 2-*p*-tolylpyridine; there is a decrease in the absorption energy of 3200 cm^{-1} for the bis-chloride complexes (335 nm for **Pt-1** to 375 nm for **Pt-4**) and 2500 cm^{-1} for the bis-bromide complexes (344 nm for **Pt-5** to 377 nm for **Pt-6**). It is proposed that this trend arises from the destabilisation of the π–orbitals of the C^N ligands upon extension of the conjugated systems and the addition of electron-donating alkoxy substituents on the phenyl rings.

2.8.2 Luminescence of Platinum(II) and Platinum(IV) Species

Solution-state emission spectra for complexes **Pt-1**, **Pt-3**, **Pt-4**, **Pt-5** and **Pt-6** were recorded in degassed CH_2Cl_2 at room temperature, and in a diethyl ether – isopentane – ethanol (EPA) (2:2:1 v/v) mixture at 77 K. The photophysical behaviour data for the above complexes is given in Table 2-5, including calculated photoluminescence quantum yields (PLQY), emission lifetimes (τ) and calculated radiative (k_r) and non-radiative (k_{nr}) rate constants.

Table 2-5: Photophysical data for complexes **Pt-1**, **Pt-3**, **Pt-4**, **Pt-5** and **Pt-6** [a]

Complex	Absorption	Emission	$10^2\,\Phi_{lum}$ [b]	τ / ns	$10^3\,k_r$ / s^{-1} [c]	$10^3\,\Sigma k_{nr}$ / s^{-1} [c]	$10^7\,k_Q$ (O_2)	Emission 77 K [e]	
	λ_{max} / nm (ε / $M^{-1}\,cm^{-1}$)	λ_{max} / nm		degassed [aerated]			$M^{-1}s^{-1}$ [d]	λ_{max} / nm	τ / ns
Pt-1	266 (29700), 274 (28800), 315 (13200), 335 (14900)	457, 489, 518, 562sh	7.0	72,000 [5,000][f]	0.97	13	8.5	452, 486, 519, 555, 613	318,000
Pt-3	274 (48900), 306 (49600), 326 (52700), 408 (10400)	541, 581, 631sh, 706sh	22[g]	28,000 [510]	7.9	28	88	537, 583, 626, 697	38,000
Pt-4	244 (41000), 302 (42000), 329 (43200), 375 (48200)	532, 571, 621sh	9.0	230,000 [1,100]	0.39	4.0	41	528, 574, 616, 684	336,000
Pt-5	268 (26500), 315 (12700), 333 (12900), 344 (13500)	457, 490, 518, 562	0.6	--[h]	--	--	--[i]	452, 470, 477, 486, 515, 525,	
Pt-6	306 (54400), 313 (49000), 361 (52400)	532, 572, 618sh	11	230,000 [1,500]	0.48	3.9	30	528, 574, 615, 678	360,000

(a) In degassed CH_2Cl_2 at 295 ± 3 K, except where indicated otherwise. (b) Quantum yields measured relative to aqueous $[Ru(bpy)_3]Cl_2$. (c) Radiative k_r and non-radiative Σk_{nr} rate constants estimated from quantum yield and lifetime: $k_r = \Phi/\tau$, $k_{nr} = (1-\Phi)/\tau$. (d) Bimolecular Stern-Volmer constant for quenching by molecular oxygen. (e) In diethyl ether – isopentane – ethanol (2:2:1 v/v). (f) This aerated value of 5 µs is subject to considerable uncertainty (and consequently also the $k_Q(O_2)$ value), as it is recorded using a microsecond flashlamp source to access the necessary short wavelength of excitation. (g) PLQY in solid state was also measured for this sample, Φ = 0.02. For the platinum(IV) complexes, only very weak emission was observable in the solid state. (h) The lifetime of this complex could not be recorded due to the very low absorption at wavelengths available for TCSPC measurements. (i) The intensity of emission decreases by a factor of approximately 2.5 for an air-equilibrated as compared to a deoxygenated solution

Emission of Pt-3

The collected photophysical spectra for the platinum(II) complex **Pt-3**, including UV-Vis absorption, excitation and emission spectra (at 298 and 77 K), are shown in Figure 2-30a. The solid-state emission spectrum of a powdered sample is shown in Figure 2-32b.

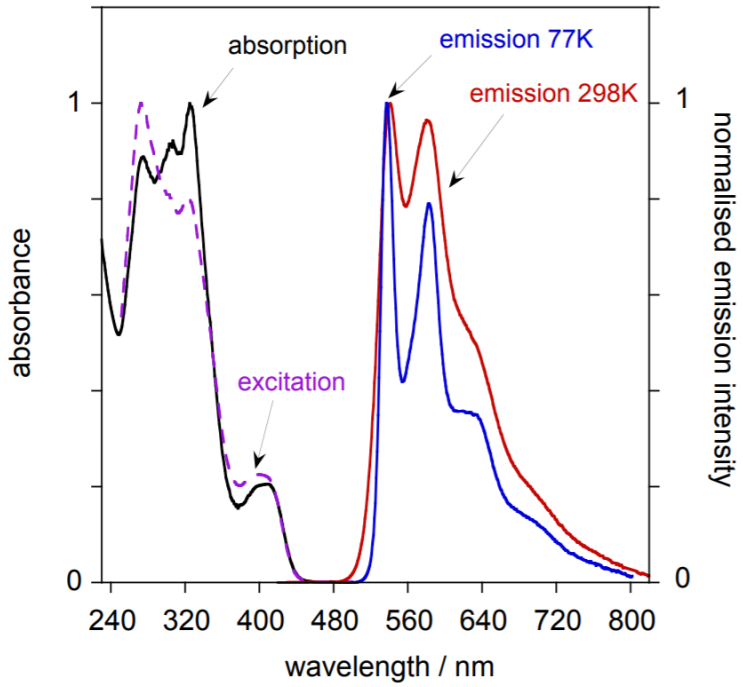

a

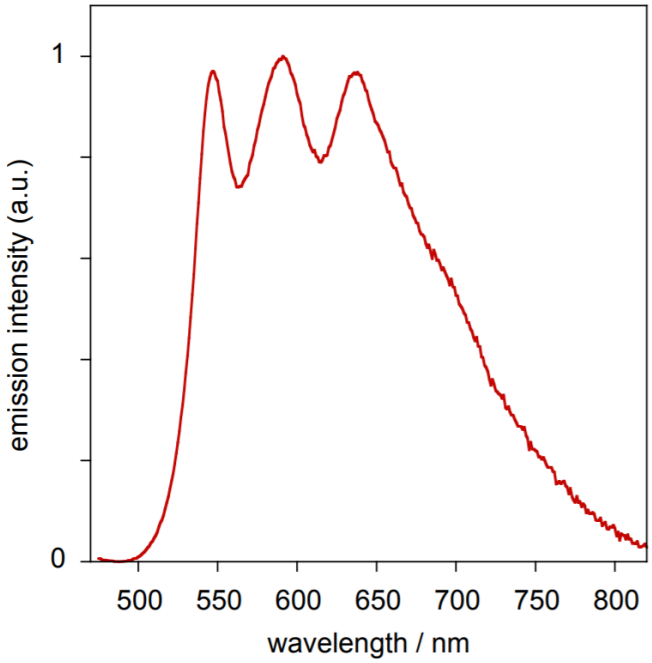

b

Figure 2-32: *(a)* Absorption (black line), excitation (dashed purple) and emission (red) spectra of complex **Pt-3** in degassed CH_2Cl_2 at 298 K and the emission spectrum in EPA at 77 K (blue). *(b)* The emission spectrum of powdered **Pt-3** at 298 K.

Complex **Pt-3** is strongly luminescent in degassed CH_2Cl_2 solution in the green-yellow region of the spectrum, with λ_{max} = 541 nm. The emission band is vibrationally structured, indicating a ligand-

centred transition, with a second emission peak at 581 nm and two lower-energy shoulders at 631 and 706 nm. Vibronic coupling, leading to vibrationally structured bands, arises from the interaction of vibrational and electronic motion, (hence, 'vibronic'). Here, the spacing of approximately 1300 cm^{-1} between the (0,1) and (0,2) bands corresponds well to the C=N and C=C stretching frequencies of the C^N^C backbone. The emission is bright, with a quantum yield of luminescence, ϕ, of 0.22, or 22%, and long-lived, with a lifetime, τ, of 28 μs at room temperature.

As outlined in the introductory section to this chapter (Section 2.1.2), the photophysics of platinum(II) complexes of this nature, [Pt(C^N)(X)(L)], and the comparable [Pt(C^N)(L^X)], where C^N is a phenylpyridine-based cyclometallating ligand and X and L represent a variety of other heteroatom-based mono- or bi-dentate ligands, has been very well established over the past 20 years.[22, 69-80] However, the emission of reported complexes of this nature have much shorter lifetimes and poorer quantum yields than those displayed by **Pt-3**. By comparison to the well-known complex [Pt(ppy)Cl(Hppy)], first reported by Ford and co-workers in 1995,[81] where ppy is phenylpyridine, this significant difference is apparent; the emission of [Pt(ppy)Cl(Hppy)] is blue shifted compared to **Pt-3**, with a λ_{max} of 489 nm, a shift to higher energy of 2000 cm^{-1}, and is much shorter lived, with a lifetime of emission of 641 ns.

The rationalisation for this change is mirrored in the shift to lower energy absorption upon the extension of the conjugation and inclusion of electron-donating substituents in the form of the dodecyloxyphenyl groups. It is well established in the literature that upon increasing the conjugation, brighter and longer-lived emission is observed; for example, work by Kozhevnikov *et al.* established that complexes utilising thienylpyridine ligands showed higher PLQYs and lifetimes than the analogous complexes with phenylpyridine ligands.[33] This observation probably arises from an increase in the energy gap between the emissive state and higher-energy deactivating states, such as metal based *d-d* states, which may lead to non-radiative decay, due to the decrease in energy of the excited state.

Complex **Pt-3** is also luminescent in the solid state (Figure 2-32b) and the emission from the powdered form of the complex shows a broad, vibrationally structured emission band in the orange-red region of the spectrum. Due to the square-planar nature of **Pt-3**, it is very likely that there are face-to-face intermolecular interactions in the axial position of the sample, resulting in aggregates in the powdered form, which contribute broad, red-shifted bands to the spectrum, superimposed on the emission bands of the monomeric species.[82, 83] Compared to the solution state, the quantum yield of emission in the solid state is low, with ϕ = 0.02.

Emission of Pt-1 and Pt-5

The luminescence of the platinum(IV) 2-*p*-tolylpyridine complex **Pt-1** has been briefly reported previously, although spectra were not provided, nor a quantum yield.[12] Here, we report the full characterisation of the photophysicial properties of **Pt-1**. Compiled photophysical spectra for **Pt-1** are given in Figure 2-33.

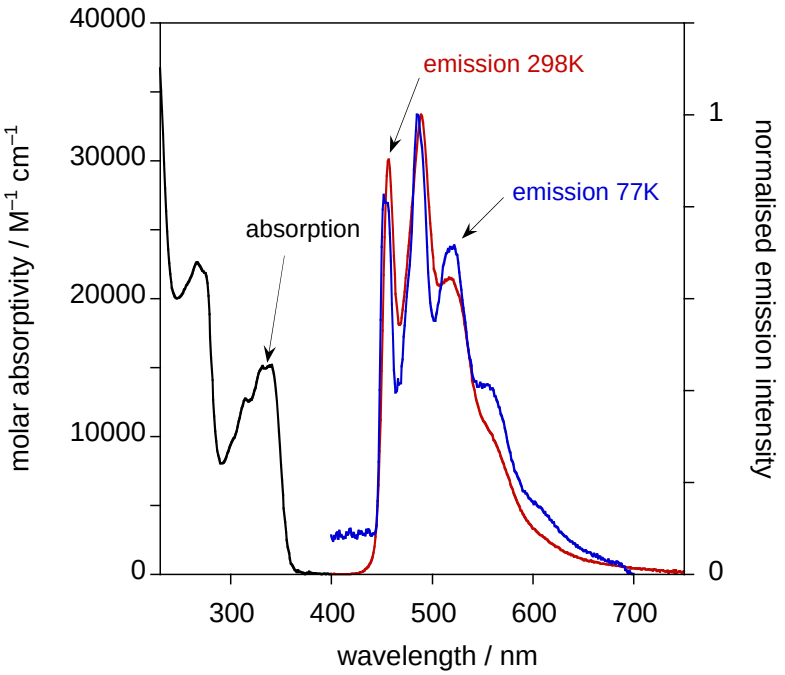

Figure 2-33: Absorption (black line) and emission (red) spectra of complex **Pt-1** in CH_2Cl_2 at 298 K and its emission spectrum in EPA at 77 K (blue).

The emission of **Pt-1** is highly structured and at room temperature there are two distinct bands arising from vibronic coupling, the (0,0) at 457 nm and the (0,1) at 489 nm; the (0,1) band is the most intense band for this complex. There is also a less well-defined peak at 518 nm, and a shoulder at 562 nm. The quantum yield was determined to be 0.07 and the lifetime of emission 72 µs. At 77 K, the vibronically coupled bands are more defined, as would be expected for a more rigid system with less thermal energy, and the lifetime of emission increases to 318 µs.

The room-temperature spectra and excited state properties at 77 K of **Pt-5**, the dibromo-analogue of **Pt-1** are essentially identical (Figure 2-34). Although, at room temperature, the quantum yield is calculated to be 0.006, an order of magnitude lower than that observed for **Pt-1**. This is broadly in agreement with the findings of Julià *et al.*, where on changing the ancillary halide ligand, there was a significant decrease in the efficiency of emission when substituting a chloride by a bromide.[38] This loss of efficiency can be rationalised by an (estimated, due to lack of lifetime measurement) 60-fold increase in the non-radiative rate constant, k_{nr}, attributed to higher-lying $p_{hal} \rightarrow \pi^*_{ppy}$

and/or $p_{hal} \rightarrow d\sigma^*_{Pt}$ states becoming thermally accessible when the halogen ligands are bromides and serving as a pathway of non-radiative decay.

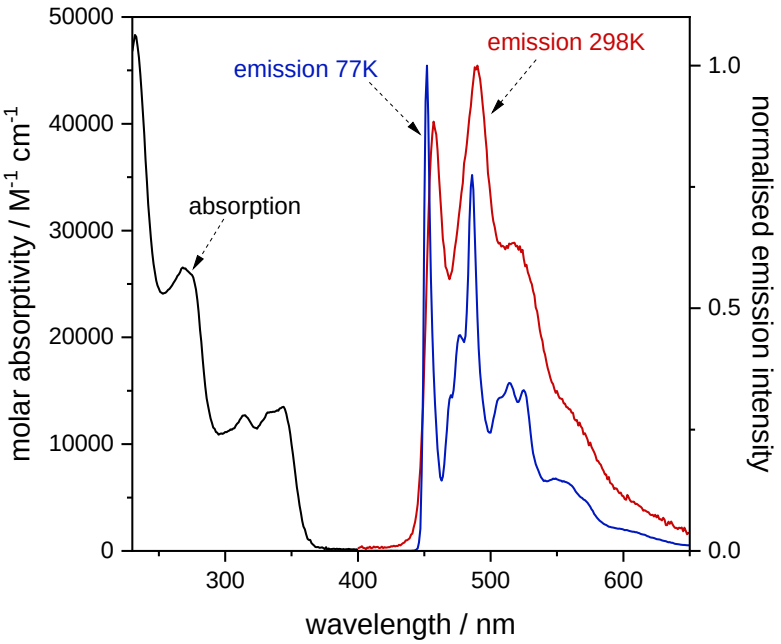

Figure 2-34: Absorption (black line), and emission spectra of complex **Pt-5** in CH_2Cl_2 at 298 K (red) and its emission spectrum in EPA at 77 K (blue)

Due to the very low absorption of **Pt-5** at wavelengths suitable to carry out time-correlated single-photon counting (TCSPC) measurements, the lifetime of the observed emission was could not be measured. Subsequently, calculated parameters that depend on the lifetime, such as radiative and non-radiative rate constants, also could not be derived.

Emission of Pt-4 and Pt-6

Strong luminescence is also observed for the extended platinum(IV) systems **Pt-4** and **Pt-6** and the spectra of these complexes are very similar, as shown in Figure 2-35 (**Pt-4**) and Figure 2-36 **(Pt-6**).

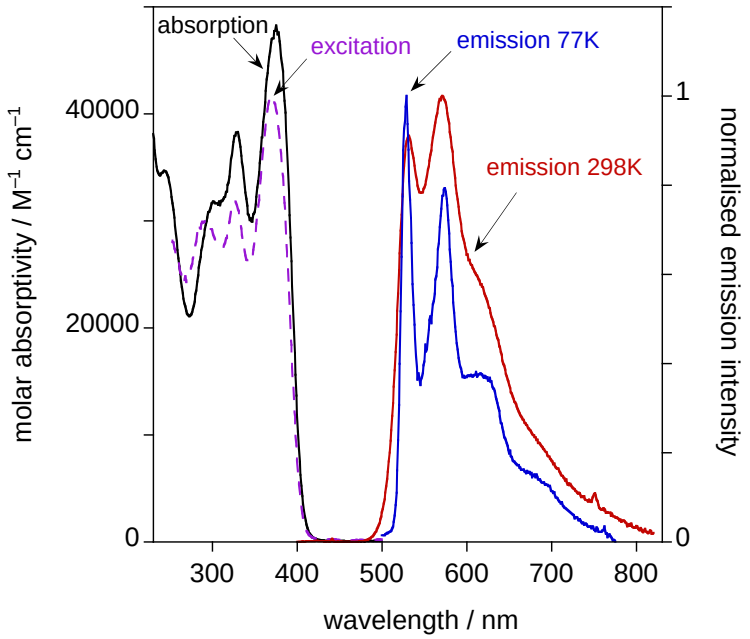

Figure 2-35: Absorption (black line), excitation (dashed purple) and emission spectra of complex **Pt-4** in CH_2Cl_2 at 298 K (red) and its emission spectrum in EPA at 77 K (blue)

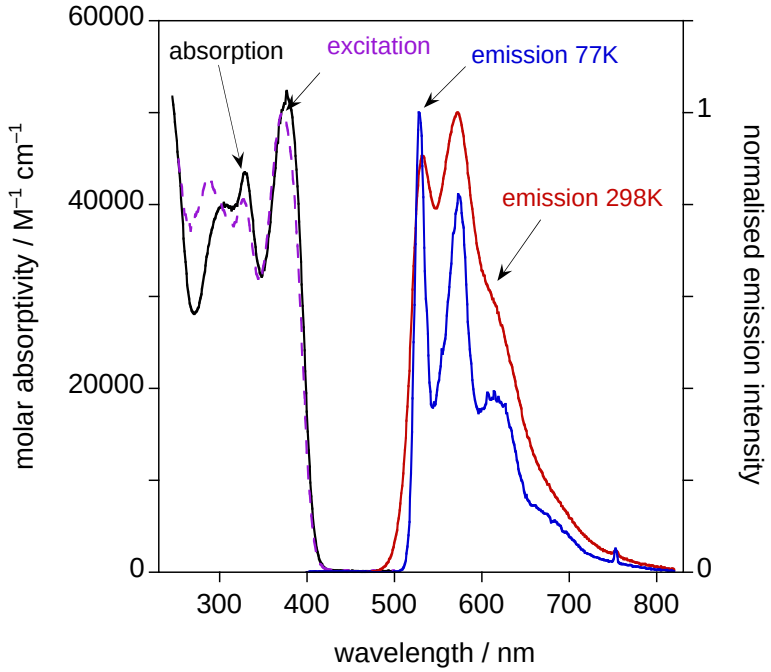

Figure 2-36: Absorption (black line), excitation (dashed purple) and emission spectra of complex **Pt-6** in CH_2Cl_2 at 298 K (red) and its emission spectrum in EPA at 77 K (blue).

As with the previously discussed platinum(IV) complexes, the emission bands show strong vibronic coupling and for both **Pt-4** and **Pt-6**, the emission maximum is the (0,0) band at 532 nm with the (0,1) band lying at 571 nm and a shoulder at 621 nm. This is significantly red-shifted in comparison to the 2-*p*-tolylpyridine analogues (**Pt-1** and **Pt-5**), indicating an energy gap between the ground and excited states that is lower in energy by approximately 3100 cm^{-1}. As noted above, a similar red-shift is observed in the lowest-energy band in the absorption spectra.

The quantum yields for both complexes can be considered to be the same within error; 0.09 for **Pt-4** and 0.11 for **Pt-6**, and are only slightly higher than that of **Pt-1** (ϕ = 0.07). The measured lifetimes of emission in degassed CH_2Cl_2 for both is 230 μs, around three times longer than for **Pt-1** (76 μs) which is indicative of a lower radiative rate constant, k_r.

It is suggested that the emission is primarily based on ligand-localised triplet states with relatively little metal orbital participation, consistent with other reports of luminescent platinum(IV) systems.[37-39] With respect to **Pt-4** and **Pt-6**, the appendage of dodecyloxyphenyl substituents further extends this conjugation and increases the energy difference between the ligand-based π-orbitals and the metal *d*-orbitals. The result of this mismatch is an excited state with less metal character, leading to a decrease in the efficiency of spin-orbit coupling required for intersystem-crossing, and subsequently, lower radiative rate constants, k_r, and longer lifetimes. As the quantum yields for **Pt-4** and **Pt-6** are very similar to those of **Pt-1**, there must be a concomitant decrease in the non-radiative rate constant for these systems, or a significant reduction of the PLQY would be observed; the calculated k_{nr} for **Pt-1** is $13x10^3$ s^{-1}, significantly higher than the values of $4 x 10^3$ and $3.9x10^3$ s^{-1} for **Pt-4** and **Pt-6**, respectively. The opposite is observed for k_r, with a calculated k_r for **Pt-1** of 970 s^{-1}, much higher than the values of 390 and 480 s^{-1} for **Pt-4** and **Pt-6**, respectively.

It is proposed that the complexes have a high level of structural rigidity and show minimal levels of distortion upon excitation between the singlet ground state, S_0 and the triplet excited state, T_1; this rigidity often favours low values for the non-radiative rate constants due to a minimisation of non-radiative pathways often invoked through flexibility or distortion in the excited state. This is supported by the very small blue shift of as little as 4 nm observed for all four platinum(IV) complexes when in the rigid glass at 77 K (diethyl ether – isopentane – ethanol (2:2:1 v/v)).

The consistency in the quantum yield and the lifetime of emission for **Pt-4** and **Pt-6** is remarkable. This is in stark contrast to the observations when changing the halogen ligand for the complexes with 2-*p*-tolylpyridine ligands (**Pt-1** and **Pt-5**), as well as the literature systems with 2-phenylpyridine,[38] in which both the quantum yields and lifetimes are greatly decreased in the bromo complex. For **Pt-4** and **Pt-6**, it is clear that the nature of the halogen-ligand has little or no influence on the nature of the emissive excited state. As outlined above, the halogen dependent change was attributed to high-lying, deactivating $p_{hal} \rightarrow \pi^*_{ppy}$ and/or $p_{hal} \rightarrow d\sigma^*_{Pt}$ states which were readily accessible when the ancillary halogen ligands were bromide (**Pt-5** and literature $[Pt(ppy)_2Br_2]$ derivatives), but less-so in the dichloro complexes (**Pt-1** and literature $[Pt(ppy)_2Cl_2]$ derivatives).[36-38, 40] By comparison of the (0,0) bands of the emission spectra of **Pt-5** and **Pt-6**, is can be shown that the emissive excited state of **Pt-6** is significantly lower in energy than that of **Pt-5**, 18800 and 22200 cm^{-1}, respectively. It is suggested that, from this lower energy excited state, the

higher-lying deactivating states in **Pt-6** may remain thermally inaccessible, rendering the emissive characteristics of **Pt-6** more like those of **Pt-4** than **Pt-5**.

It should be noted that all platinum(IV) complexes showed only very weak emission in the solid state, which was not strong enough to be characterised.

2.9 Computational Chemistry

In order to rationalise and understand the absorption spectra of complexes **Pt-1**, **Pt-4** and **Pt-6**, TD-DFT calculations were performed. Single-point and TD-DFT calculations were performed using a hybrid PBE0 functional and a TZVPP basis set with a 60-electron effective core potential. All calculations were performed by Dr Jason Lynam. Due to the emissive properties of **Pt-1** and **Pt-5** agreeing with the reported literature systems in which there is an extensive computational study, **Pt-5** was not modelled, and any insight necessary was gleaned from literature data.[38] As only electronic properties of the complexes were investigated, to aid computational efficiency and lower computational costs, the dodecyloxy chains ($OC_{12}H_{25}$) of **Pt-4** and **Pt-6** were substituted with methoxy groups (OMe), herein referred to as **Pt-4^{Me}** and **Pt-6^{Me}**.

The calculations reproduced the key experimental data to a reasonable degree, and predicted differences between the complexes reliably; for example, the experimentally observed red-shift observed in the absorption spectra between **Pt-1** and **Pt-4** is also observed when comparing **Pt-1** and **Pt-4^{Me}**. A summary of the computationally predicted transitions, including the occupied and virtual orbitals involved and their designation (*i.e.* HOMO/LUMO), are shown in Table 2-6.

For **Pt-1**, the lowest-energy band consists of transitions between the HOMO (115) and HOMO-1 (114) to the LUMO+1 (117) and LUMO (116), with the numbers of the virtual orbitals shown in brackets. The filled orbitals HOMO and HOMO-1 are based on the non-bonded lone pairs on the two chloride ligands, with a small contribution from the conjugated π-system of the 2-*p*-tolylpyridine ligand; the unoccupied LUMO and LUMO+1 are best viewed as ligand-based π*-orbitals. The HOMO-1 (114) orbital has a contribution from metal-based *d*-orbitals. These orbitals are visualised and presented in Figure 2-37 (Kohn-Sham orbitals). The next series of transitions also involve transfer to the LUMO (116) and LUMO+1 (117), from the HOMO-2 (113) and HOMO-3 (112), which have a similar composition to the HOMO (114) and HOMO-1 (115).

Table 2-6: Summary of experimental and DFT-predicted transitions for complexes **Pt-1**, **Pt-4** and **Pt-4^{Me}**, and **Pt-6** and **Pt-6^{Me}**. Only transitions with an oscillator strength >0.01 and orbital contributions >10% are listed.

Complex	Calculated Energy (Experimental Energy) / nm	Oscillator strength	Occupied orbital(s)	Virtual orbital(s)	Coefficient / %	Transition	
						From	To
Pt-1	342 (335)	0.0233	114	117	53.6	HOMO-1	LUMO
			115	116	34.0	HOMO	LUMO +1
	341	0.0552	115	117	66.2	HOMO	LUMO
			114	116	19.8	HOMO-1	LUMO+1
Pt-4/Pt-4^{Me}†	368 (375)	0.766	179	180	63.0	HOMO	LUMO
			178	181	26.8	HOMO-1	LUMO+1
	367	0.396	179	181	48.9	HOMO	LUMO+1
			178	180	41.0	HOMO-1	LUMO
	357	0.0236	178	181	57.0	HOMO-1	LUMO+1
			179	180	27.2	HOMO	LUMO
Pt-6/Pt-6^{Me}†	380 (376)	0.0455	197	199	61.1	HOMO	LUMO+1
			195	199	30.5	HOMO-2	LUMO+1
	377	0.131	197	199	62.0	HOMO	LUMO+1
			195	199	26.2	HOMO-2	LUMO+1
	370	0.459	196	198	67.9	HOMO-1	LUMO
			194	198	12.6	HOMO-3	LUMO
	368	0.244	196	199	65.7	HOMO-1	LUMO+1
			195	198	12.0	HOMO-2	LUMO
	355	0.0484	195	198	52.3	HOMO-2	LUMO
			197	198	22.8	HOMO	LUMO
			196	199	13.7	HOMO-1	LUMO+1
	354	0.0435	195	199	41.9	HOMO-2	LUMO+1
			197	199	28.3	HOMO	LUMO+1
			196	198	18.2	HOMO-1	LUMO
	352	0.0136	194	199	70.2	HOMO-3	LUMO+1
			196	199	11.7	HOMO-1	LUMO+1
	351	0.151	194	198	69.4	HOMO-3	LUMO
			195	199	17.9	HOMO-2	LUMO+1
	348	0.225	193	198	78.7	HOMO-4	LUMO
			192	199	10.6	HOMO-5	LUMO+1

†Data for **Pt-4** and **Pt-6** are experimental, while those for **Pt-4^{Me}** and **Pt-6^{Me}** arise from calculation.

Complex **Pt-4^{Me}** involved similar transitions, with the lowest-energy band consisting of transfers between HOMO (179) and HOMO-1 (178), to LUMO (180) and LUMO+1 (181). The HOMO (179) and HOMO-1 (178) of **Pt-4^{Me}** do not contain any chloride lone-pair character, but are based solely on the 2,5-diphenylpyridine π-orbitals. Again, the unoccupied orbitals, LUMO (180) and LUMO+1 (181), are based on the π*-orbitals of the cyclometallating ligands. The subsequent series of transitions, including the HOMO-2 (177), HOMO-3 (176) and HOMO-4 (175) orbitals, are those with significant chloride non-bonded pair character and very little contribution from 2,5-diphenylpyridine.

Comparison between **Pt-1** and **Pt-4^{Me}** indicated that the addition of the second alkoxyphenyl ring to the cyclometallating ligand in **Pt-4^{Me}** extends the conjugated system, and so increases the energy of the π-based HOMO orbital so that there is little mixing with the chloride non-bonded orbitals. By comparison, and with reference to Table 2-6, the individual transitions in both species are essentially identical. This observation is consistent with the observed photophysical data; it was posited above that increasing the conjugation of the π-system lowered the metal character of the excited state. This can be seen visually in Figure 2-37.

In the analogous bromo-containing complex **Pt-6**, modelled as **Pt-6^{Me}**, the calculated transitions are similar to **Pt-4^{Me}**, which is also observed in the spectra collected experimentally. In contrast, however, the occupied orbital contributions to the lowest-energy band are more diverse; the transition originates from a combination of the HOMO (197), HOMO-1 (194), HOMO-2 (195) and HOMO-3 (194) orbitals. Of these, 197, 195 and 194 all have bromide non-bonded lone pair character, with the HOMO (197) also based on the π-system of the cyclometallating ligands. Once again, the unoccupied orbitals involved are the LUMO (198) and LUMO+1 (199), which are π* in nature.

The observed photophysical behaviour of **Pt-4** and **Pt-6** is identical with respect to emission wavelength, quantum yield and lifetime of emission, both at 298 and 77 K. This implies that it is only the nature of the excited state that is relevant to these properties; in **Pt-4^{Me}** and **Pt-6^{Me}** both the LUMO and LUMO+1 are π*-based orbitals with a very small amount of metal *d*-character, but the occupied orbitals involved are significantly different.

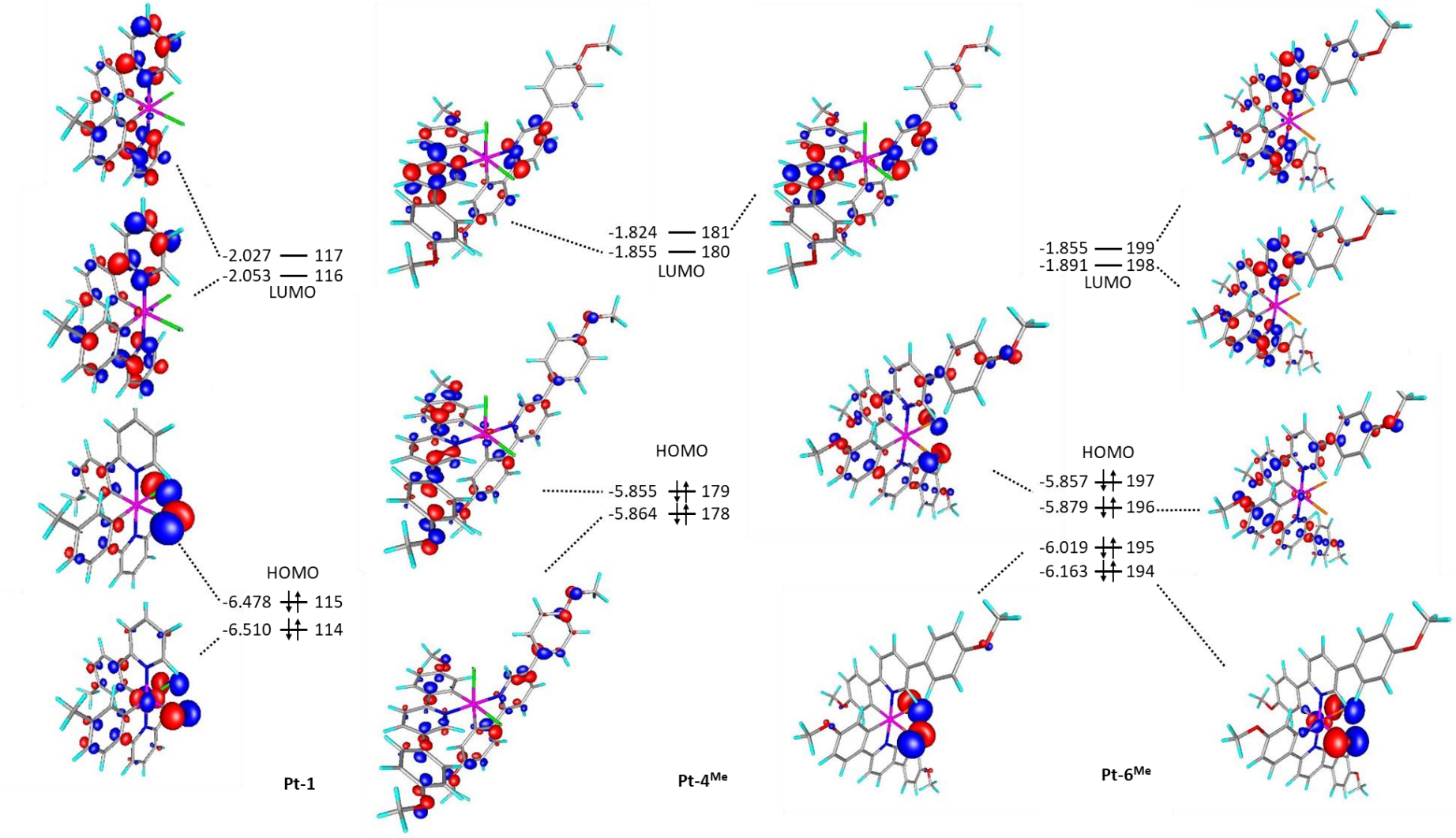

Figure 2-37: Frontier orbitals for complexes **Pt-1**, **Pt-4^{Me}** and **Pt-6^{Me}**.

2.10 Conclusions

A new, one-pot, microwave-assisted synthesis to the known[12] species $[Pt(tolpy)_2(Cl)_2]$, **Pt-1,** has been developed, giving the product in moderate yield. The *bis*-bromide equivalent $[Pt(tolpy)_2(Br)_2]$, **Pt-5**, was synthesised through the substitution of the ancillary halide ligand to form the *bis*-triflato complexes which proved to be good leaving groups when reacted with excess NaBr to form **Pt-5**. Anisotropy was introduced through the inclusion of dodecyloxyphenyl substituents on the cyclometallating ligand to produce two novel platinum(IV) species, synthesised through a three-step process adapted from literature sources[34, 36] in which a di-chloro-bridged platinum(II) dimer, $[Pt(L)(\mu\text{-}Cl)]_2$ (**Pt-2**) is formed through the reaction of the free ligand **HL** with $K_2[PtCl_4]$. Complex **Pt-2** may subsequently be cleaved with a two further equivalents of **HL** to form **Pt-3** and then oxidised with the hypervalent iodine reagent $PhICl_2$ to form **Pt-4**; the ancillary halide ligands were altered as previously outlined to form the *bis*-bromide analogous species, **Pt-6**.

It is proposed that the microwave-assisted synthetic procedure developed for **Pt-1** could be applied to further functionalised derivatives of phenylpyridine (ppy), such as those reported by Jenkins and Bernhard or Julia *et al.* The obvious limiting factor for this procedure is the one encountered for the 2,5-di(4-dodecyloxy)pyridine ligands in this work, namely solubility. Small variations in structure and inclusion of comparatively small functional groups in a ppy-based ligand are likely to result in free ligands which are either soluble in the polar solvents necessary for both microwave polarisation (due to the necessity for a dipole in the solvent) and solubility of $K_2[PtCl_4]$, or ligands which are liquid reagents at room temperature and soluble or miscible in the same. This may lead to easy, one-pot syntheses of novel platinum(IV) complexes with interesting emissive behaviour, but would preclude the synthesis of larger derivatives needed to impart specific properties such as liquid-crystallinity.

The observation of a thermal *ortho*-metallation/oxidation process for complex **Pt-3** to form **Pt-4** and its structural isomer has potential for further investigation. This phenomenon was only observed for the species with dodecyloxy chains when heated into the isotropic liquid; the methoxy-substituted analogue, **Pt-3^{Me}**, showed no chemical change upon the same treatment, indicating that the orientation of the extended alkoxy chains may force the molecule into a favourable confirmation in the melt to undergo the initial oxidation and *ortho*-metallation steps. As this transformation occurs when the chains are dodecyloxy and does not when they are methoxy, it would be interesting to investigate the chain length at which the oxidation becomes feasible, whether it also occurs at chain lengths greater than dodecyloxy, and whether the chain length has any impact on speciation of the resulting complexes. C–H activation is extraordinarily important, particularly in the field of catalysis,[65-67] and the observation that inclusion of bulky

hydrocarbon chains can direct favourably direct molecular orientation to this end is worthy of further research.

Complexes **Pt-4** and **Pt-6** are the first reported platinum(IV) *bis*-cyclometallated complexes with two modestly functionalised, rod-like 2,5-diphenylpyridine ligands to show liquid crystallinity, and suggest that the observations of liquid-crystallinity in similar systems of iridium(III) by Santoro *et al*. are not an isolated report.[14] They present the potential for an expansive new class of octahedral emissive materials, particularly *ordered* emissive materials. The near-identical nature of the lamellar mesophases observed for **Pt-4** and **Pt-6** with the same cyclometallating ligands indicates that to tune the phase behaviour, more significant changes to the ancillary ligand may be required; this is in contrast to the extreme alteration of the phase behaviour when changing the ancillary ligand in the iridium(III) work. It is hypothesised that a change in the cyclometallating ligands with respect to chain length and number may also induce drastic changes in the mesosphases; it is difficult to predict what these changes may be due to the unclear orientation of the molecules in the observed lamellar phases, but such changes could increase the stability of the complexes and induce a wider range of observed liquid-crystalline phases, such as columnar phases.[13, 14]

All five of the final platinum complexes show phosphorescent emission at room temperature. Complex **Pt-3** shows emission consistent with mono-cyclometallated platinum(II) complexes from the literature, although the lifetime of emission is longer and the quantum yield significantly higher than similar reported [Pt(ppy)Cl(Hppy)] systems as a result of the extended conjugation upon appendage of the second phenyl ring.[81] For the platinum(IV) complexes **Pt-1** and **Pt-5**, a blue emission is observed for both and the loss of emission intensity when the halogen ligand is changed to a bromide in **Pt-5** is an accordance with previous literature reports due to the accessibility of deactivating states.[38]

The noteworthy differences in emission when the conjugation is extended also has an impact in the platinum(IV) complexes; for complexes **Pt-4** and **Pt-6** the emission is significantly red-shifted in comparison to the 2-*p*-tolylpyridine analogues, into the green region of the spectrum, and is almost identical between the two species, with no loss of emission efficiency for **Pt-6**, which has bromide ancillary ligands. The lowering in energy of the excited state for **Pt-6** in comparison to **Pt-5** renders the deactivating states thermally inaccessible, and results in an emission which is independent of the halide ligand. This observation is remarkable and unreported in the literature, and suggests that emission from complexes such as these can be tuned *via* the functional group of the cyclometallating ligands, a useful behaviour in the search for stable blue emitters. As the emission for all of the platinum(IV) complexes is ligand-based (^{3}LC), the inclusion of further chains on the

cyclometallating ligands, and therefore electron-donating substituents, may change not only the liquid-crystalline behaviour of the systems, but also the emission character and properties.

Although the instability and high temperature liquid-crystalline regime preclude the use of **Pt-4** and **Pt-6** in traditional OLED architectures, it has been shown in the literature by Santoro *et al.*[14] that small functional alterations can make a significant change to the stability of complexes such as these. The development of a robust three-step synthetic procedure to **Pt-4** with readily available reagents and without the use of more intensive techniques such as inert atmosphere manipulations, and the presence of easily exchanged ancillary ligands to form further species such as **Pt-6**, also suggests that the procedure is easily transferable to more functionalised ligands, in this case pertinent to more or longer/shorter hydrocarbon chains. This can have a profound impact on the stability of any mesophases formed, and a drastic reduction in the transition temperatures, which, with fine tuning, could result in bright, stable, liquid-crystalline complexes of platinum(IV) which are emissive and device compatible. [21]

2.11 References

1. S. R. Forrest, *Nature*, 2004, **428**, 911.
2. S. Laschat, A. Baro, N. Steinke, F. Giesselmann, C. Hägele, G. Scalia, R. Judele, E. Kapatsina, S. Sauer, A. Schreivogel and M. Tosoni, *Angew. Chem. Int. Ed.*, 2007, **46**, 4832-4887.
3. S. Xiao, M. Myers, Q. Miao, S. Sanaur, K. Pang, M. L. Steigerwald and C. Nuckolls, *Angew. Chem. Int. Ed.*, 2005, **44**, 7390-7394.
4. J. Nelson, *Science*, 2001, **293**, 1059-1060.
5. L. Schmidt-Mende, A. Fechtenkötter, K. Müllen, E. Moons, R. H. Friend and J. D. MacKenzie, *Science*, 2001, **293**, 1119-1122.
6. B. J. Coe, M. Helliwell, S. Sanchez, M. K. Peers and N. S. Scrutton, *Dalton Trans.*, 2015, **44**, 15420-15423.
7. R. E. Daniels, S. Culham, M. Hunter, M. C. Durrant, M. R. Probert, W. Clegg, J. A. G. Williams and V. N. Kozhevnikov, *Dalton Trans.*, 2016, **45**, 6949-6962.
8. M. S. Lowry and S. Bernhard, *Chem. Eur. J.*, 2006, **12**, 7970-7977.
9. Y. You and S. Y. Park, *Dalton Trans.*, 2009, 1267-1282.
10. J. Sarju, PhD Thesis, University of York, 2016.
11. B. M. Still, P. G. A. Kumar, J. R. Aldrich-Wright and W. S. Price, *Chem. Soc. Rev.*, 2007, **36**, 665-686.
12. E. A. Katlenok and K. P. Balashev, *Russ. J. Gen. Chem.*, 2013, **83**, 2113-2114.
13. A. Santoro, PhD Thesis, University of York, 2010.
14. A. Santoro, A. M. Prokhorov, V. N. Kozhevnikov, A. C. Whitwood, B. Donnio, J. A. G. Williams and D. W. Bruce, *J. Am. Chem. Soc.*, 2011, **133**, 5248-5251.
15. J. A. G. Williams, in *Photochemistry and Photophysics of Coordination Compounds II*, eds. V. Balzani and S. Campagna, Springer Berlin Heidelberg, Berlin, Heidelberg, 2007, pp. 205-268.
16. M.-C. Tang, A. K.-W. Chan, M.-Y. Chan and V. W.-W. Yam, *Top. Curr. Chem.*, 2016, **374**, 46.
17. V. W.-W. Yam, V. K.-M. Au and S. Y.-L. Leung, *Chem. Rev.*, 2015, **115**, 7589-7728.
18. K. M.-C. Wong and V. W.-W. Yam, *Coord. Chem. Rev.*, 2007, **251**, 2477-2488.
19. T. Fleetham, G. Li and J. Li, *Adv. Mater.*, 2017, **29**, 1601861.
20. R. Ballardini, G. Varani, M. T. Indelli and F. Scandola, *Inorg. Chem.*, 1986, **25**, 3858-3865.
21. D. Sandrini, M. Maestri, V. Balzani, L. Chassot and A. Von Zelewsky, *J. Am. Chem. Soc.*, 1987, **109**, 7720-7724.
22. J. Brooks, Y. Babayan, S. Lamansky, P. I. Djurovich, I. Tsyba, R. Bau and M. E. Thompson, *Inorg. Chem.*, 2002, **41**, 3055-3066.
23. V. N. Kozhevnikov, B. Donnio and D. W. Bruce, *Angew. Chem. Int. Ed.*, 2008, **47**, 6286-6289.
24. V. N. Kozhevnikov, B. Donnio, B. Heinrich, J. A. G. Williams and D. W. Bruce, *J. Mat. Chem. C*, 2015, **3**, 10177-10187.
25. J. Moussa, T. Cheminel, G. R. Freeman, L.-M. Chamoreau, J. A. G. Williams and H. Amouri, *Dalton Trans.*, 2014, **43**, 8162-8165.
26. A. M. Prokhorov, T. Hofbeck, R. Czerwieniec, A. F. Suleymanova, D. N. Kozhevnikov and H. Yersin, *J. Am. Chem. Soc.*, 2014, **136**, 9637-9642.
27. W. A. Tarran, G. R. Freeman, L. Murphy, A. M. Benham, R. Kataky and J. A. G. Williams, *Inorg. Chem.*, 2014, **53**, 5738-5749.
28. J. A. G. Williams, A. Beeby, E. S. Davies, J. A. Weinstein and C. Wilson, *Inorg. Chem.*, 2003, **42**, 8609-8611.
29. W. Lu, B.-X. Mi, M. C. W. Chan, Z. Hui, C.-M. Che, N. Zhu and S.-T. Lee, *J. Am. Chem. Soc.*, 2004, **126**, 4958-4971.
30. Z. He, W.-Y. Wong, X. Yu, H.-S. Kwok and Z. Lin, *Inorg. Chem.*, 2006, **45**, 10922-10937.
31. Y. Wang, J. Luo, Y. Liu, Z. Zhang, H. Tan, J. Yu, G. Lei, M. Zhu and W. Zhu, *Org. Electron.*, 2012, **13**, 1646-1653.
32. L. Zhou, C.-C. Kwok, G. Cheng, H. Zhang and C.-M. Che, *Opt. Lett.*, 2013, **38**, 2373-2375.

33. D. N. Kozhevnikov, V. N. Kozhevnikov, M. Z. Shafikov, A. M. Prokhorov, D. W. Bruce and J. A. Gareth Williams, *Inorg. Chem.*, 2011, **50**, 3804-3815.
34. A. Santoro, A. C. Whitwood, J. A. G. Williams, V. N. Kozhevnikov and D. W. Bruce, *Chem. Mater.*, 2009, **21**, 3871-3882.
35. L. Chassot, A. Von Zelewsky, D. Sandrini, M. Maestri and V. Balzani, *J. Am. Chem. Soc.*, 1986, **108**, 6084-6085.
36. D. M. Jenkins and S. Bernhard, *Inorg. Chem.*, 2010, **49**, 11297-11308.
37. F. Juliá, D. Bautista and P. Gonzalez-Herrero, *Chem. Commun.*, 2016, **52**, 1657-1660.
38. F. Juliá, M.-D. García-Legaz, D. Bautista and P. González-Herrero, *Inorg. Chem.*, 2016, **55**, 7647-7660.
39. F. Julia, D. Bautista, J. M. Fernandez-Hernandez and P. Gonzalez-Herrero, *Chem. Sci.*, 2014, **5**, 1875-1880.
40. F. Juliá and P. González-Herrero, *Dalton Trans.*, 2016, **45**, 10599-10608.
41. Á. Vivancos, D. Bautista and P. González-Herrero, *Chem. Eur. J.*, 2019, **25**, 6014-6025.
42. N. Giménez, E. Lalinde, R. Lara and M. T. Moreno, *Chem. Eur. J.*, 2019, **25**, 5514-5526.
43. M. Ghedini, D. Pucci and G. Barberio, *Liq. Cryst.*, 2000, **27**, 1277-1283.
44. M. Ghedini, D. Pucci, A. Crispini and G. Barberio, *Organometallics*, 1999, **18**, 2116-2124.
45. R. J. Allenbaugh, C. K. Schauer, A. Josey, J. D. Martin, D. V. Anokhin and D. A. Ivanov, *Chem. Mater.*, 2012, **24**, 4517-4530.
46. A. Santoro, M. Wegrzyn, A. C. Whitwood, B. Donnio and D. W. Bruce, *J. Am. Chem. Soc.*, 2010, **132**, 10689-10691.
47. A. de la Hoz, Á. Díaz-Ortiz and A. Moreno, *Chem. Soc. Rev.*, 2005, **34**, 164-178.
48. N. Miyaura and A. Suzuki, *Chem. Rev.*, 1995, **95**, 2457-2483.
49. T. Tagata and M. Nishida, *J. Org. Chem.*, 2003, **68**, 9412-9415.
50. T. V. Saraswathi and V. R. Srinivasan, *Tetrahedron Lett.*, 1971, **12**, 2315-2316.
51. R. A. Carboni and R. V. Lindsey, *J. Am. Chem. Soc.*, 1959, **81**, 4342-4346.
52. D. L. Boger and J. S. Panek, *J. Org. Chem.*, 1981, **46**, 2179-2182.
53. D. L. Boger, J. S. Panek and M. M. Meier, *J. Org. Chem.*, 1982, **47**, 895-897.
54. V. N. Kozhevnikov, D. N. Kozhevnikov, O. V. Shabunina, V. L. Rusinov and O. N. Chupakhin, *Tetrahedron Lett.*, 2005, **46**, 1521-1523.
55. V. N. Kozhevnikov, D. N. Kozhevnikov, O. V. Shabunina, V. L. Rusinov and O. N. Chupakhin, *Tetrahedron Lett.*, 2005, **46**, 1791-1793.
56. X.-F. Zhao and C. Zhang, *Synthesis*, 2007, **2007**, 551-557.
57. X.-Q. Li and C. Zhang, *Synthesis*, 2009, **2009**, 1163-1169.
58. W. Qian, E. Jin, W. Bao and Y. Zhang, 2005, **44**, 952-955.
59. J. Tao, R. Tran and G. K. Murphy, *J. Am. Chem. Soc.*, 2013, **135**, 16312-16315.
60. K. E. Coffey and G. K. Murphy, *Synlett*, 2015, **26**, 1003-1007.
61. L. Liu, D. Zhang-Negrerie, Y. Du and K. Zhao, *Org. Lett.*, 2014, **16**, 436-439.
62. S. R. Whitfield and M. S. Sanford, *Organometallics*, 2008, **27**, 1683-1689.
63. C. P. Newman, K. Casey-Green, G. J. Clarkson, G. W. V. Cave, W. Errington and J. P. Rourke, *Dalton Trans.*, 2007, 3170-3182.
64. J. A. Labinger, *Chem. Rev.*, 2017, **117**, 8483-8496.
65. P. J. Pérez, *Alkane C-H Activation by Single-Site Metal Catalysis*, Springer Netherlands, 2012.
66. R. H. Crabtree, *J. Organomet. Chem.*, 2004, **689**, 4083-4091.
67. J. Q. Yu and Z. Shi, *C-H Activation*, Springer Berlin Heidelberg, 2010.
68. D. D. Wick and K. I. Goldberg, *J. Am. Chem. Soc.*, 1997, **119**, 10235-10236.
69. J. R. Berenguer, Á. Díez, A. García, E. Lalinde, M. T. Moreno, S. Sánchez and J. Torroba, *Organometallics*, 2011, **30**, 1646-1657.
70. A. Colombo, C. Dragonetti, D. Marinotto, S. Righetto, D. Roberto, S. Tavazzi, M. Escadeillas, V. Guerchais, H. Le Bozec, A. Boucekkine and C. Latouche, *Organometallics*, 2013, **32**, 3890-3894.
71. P. I. Djurovich, D. Murphy, M. E. Thompson, B. Hernandez, R. Gao, P. L. Hunt and M. Selke, *Dalton Trans.*, 2007, 3763-3770.

72. S. Fernández, J. Forniés, B. Gil, J. Gómez and E. Lalinde, *Dalton Trans.*, 2003, 822-830.
73. J. Forniés, S. Fuertes, A. Martín, V. Sicilia, B. Gil and E. Lalinde, *Dalton Trans.*, 2009, 2224-2234.
74. P.-H. Lanoë, J.-L. Fillaut, L. Toupet, J. A. G. Williams, H. L. Bozec and V. Guerchais, *Chem. Commun.*, 2008, 4333-4335.
75. J. Moussa, G. R. Freeman, J. A. G. Williams, L.-M. Chamoreau, P. Herson and H. Amouri, *Eur. J. Inorg. Chem.*, 2016, **2016**, 761-767.
76. F. Niedermair, O. Kwon, K. Zojer, S. Kappaun, G. Trimmel, K. Mereiter and C. Slugovc, *Dalton Trans.*, 2008, 4006-4014.
77. D. L. Rochester, S. Develay, S. Záliš and J. A. G. Williams, *Dalton Trans.*, 2009, 1728-1741.
78. N. M. Shavaleev, H. Adams, J. Best, R. Edge, S. Navaratnam and J. A. Weinstein, *Inorg. Chem.*, 2006, **45**, 9410-9415.
79. H. Uesugi, T. Tsukuda, K. Takao and T. Tsubomura, *Dalton Trans.*, 2013, **42**, 7396-7403.
80. T. Zou, C.-N. Lok, Y. M. E. Fung and C.-M. Che, *Chem. Commun.*, 2013, **49**, 5423-5425.
81. M. M. Mdleleni, J. S. Bridgewater, R. J. Watts and P. C. Ford, *Inorg. Chem.*, 1995, **34**, 2334-2342.
82. M. Cocchi, J. Kalinowski, V. Fattori, J. A. G. Williams and L. Murphy, *Appl. Phys. Lett.*, 2009, **94**, 073309.
83. J. Kalinowski, M. Cocchi, L. Murphy, J. A. G. Williams and V. Fattori, *Chem. Phys.*, 2010, **378**, 47-57.

Chapter 3: Synthesis, Mesomorphism and Self-Assembly of Cyclometallated Complexes of Gold(III) with Functionalised Alkynyl Ligands

3.1 Introduction

It has been well-established that square-planar heavy metal complexes can combine liquid-crystalline properties,[1] through functionalisation with extended alkyl or alkoxy chains on the periphery of the ligands, with phosphorescent emission due to the inclusion of the heavy metal, which introduces spin-orbit coupling into the system and facilitates intersystem-crossing to the triplet excited state.[2-6] While such complexes based on platinum(II) are well known, until now, there were no reports of cyclometallated gold(III) complexes showing both of these desirable properties, as the bulk of the literature regarding stable gold(III) emitters is comparatively recent. This is outlined in Chapter 4. These emissive systems are highly reliant on bis-cyclometalling ligands, typically derivatives of 2,6-diphenylpyridine, with a strongly σ-donating ligand in the fourth coordination position, with the most commonly used being an alkynyl group, usually as phenylacetylene derivatives (Figure 3-1).[7-15] This core molecular configuration contains much scope for functionalisation with the aforementioned alkoxy chains, both on the cyclometallating unit and the phenylacetylene ring.

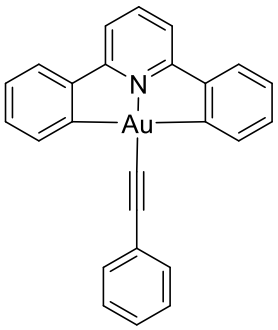

Figure 3-1: Core structure of [Au(C^N^C)(C≡CR)] complexes under investigation.

3.1.1 Square-Planar Metallomesogens

In contrast to the comparatively rare octahedral metallomesogens introduced in Chapter 2, square-planar, liquid-crystalline metal complexes are well established; the planar metal centre and lack of axial ligands lend themselves to the design of mesomorphic complexes through the inclusion of co-planar ligands.

Complexes of platinum(II) and palladium(II) with monodentate ligands are well known in the literature, with ligands such as mono-alkoxy functionalised stilbazoles providing the molecular anisotropy necessary to form smectogenic materials (Figure 3-2a) and tri-alkoxy functionalised stilbazoles showing columnar phases, properties of which which are tuneable *via* the number and length of the appended chains, as well as the other coordinated ligands[16-20] Similar complexes are also known with 3,4,5-alkoxysubstituted benzonitriles and equivalent isonitriles coordinated in the same fashion to form disc-like materials which show columnar phases (Figure 3-2b and c).[21-23] With a single 4-alkoxystilbazole ligand (L), square-planar complexes of rhodium(I) and iridium(I) of the general structure *cis*-[MCl(CO)$_2$(L)] show nematic phases at short chain lengths and smectic A phases at longer chain lengths (Figure 3-2d).[24]

Similar coordination modes were examined in work by Chico *et al.*, in which the functionalised coordinating ligands were pentasubstituted triphenylenes, connected *via* an hexyloxy linkage to an 4-isocyanophenoxy group. Two of these isonitriles were coordinated to a platinum(II) or palladium(II) metal centre in either a *cis* or *trans* fashion with ancillary halogen or cyano ligands (Figure 3-2e).[25] The resulting *cis* species show columnar rectangular phases with transition temperatures dependent on the ancillary ligand, while the *trans* species do not show any liquid-crystallinity, rationalised by the net dipole for the *cis* species with dipole-dipole interactions having a stabilisation effect in anti-parallel stacking within the column which are not present in the non-polar *trans* complexes. The same work also reported liquid-crystalline linear gold(I) and tetrahedral copper(II) species with the same ligand.

Reports of metallomesogens with chelating ligands are far more common than for monodentate species due to the increased stability and favourable molecular geometries for co-planar ligands.[26, 27] Liao *et al.* reported a series of luminescent chelated complexes of platinum(II) with tris(alkoxy)phenyl-functionalised pyridylpyrazolate ligands which form a pseudo-tetradentate complex through hydrogen-bonding interactions between the two ligands.[28] The complexes show columnar phases which change from rectangular symmetry to hexagonal symmetry as the chain length is increased. Very similar systems were recently reported by Cuerva *et al.* in which the two chelating ligands were different (one pyridylpyrazolate and the other isoquinolinylpyrazolate), resulting in unsymmetric species, all of which showed columnar hexagonal phases and also displayed aggregation-enhanced emission (Figure 3-3).[29]

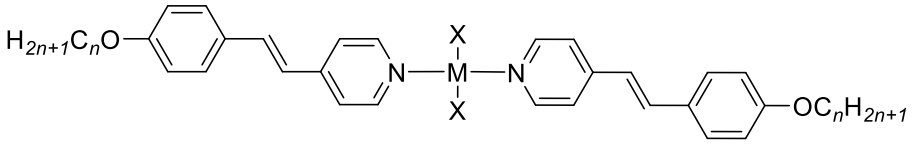

a

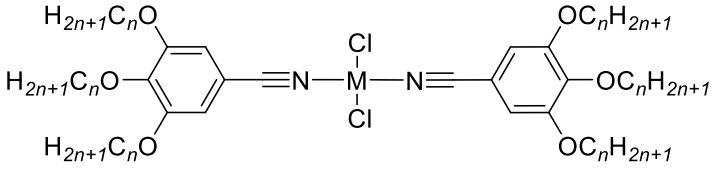

b

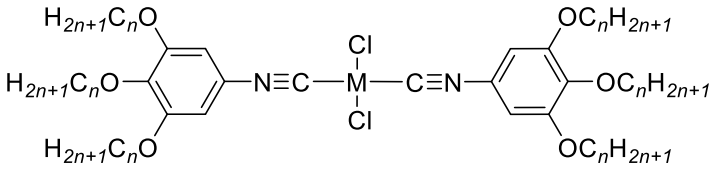

c

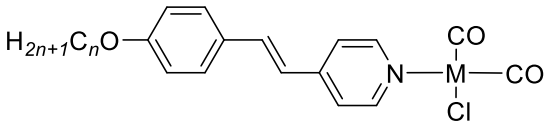

d

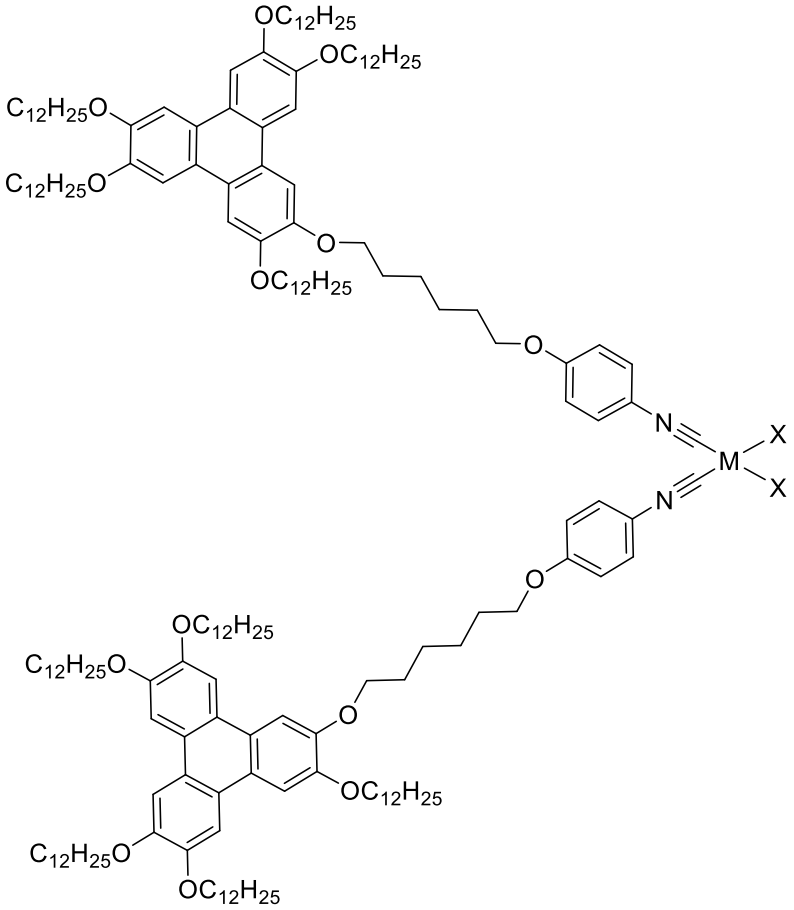

e

Figure 3-2: Structure of square-planar metallomesogens (M = Pd, Pt for a, b, c, e); Rh or Ir for d) with functionalised a) stilbazole ligands X = Cl or alkanoate b) benzonitrile ligands; c) equivalent isonitrile ligands; also shown are d) complexes of Rh(I) and Ir(I) with a 4-alkoxystilbazole ligand of the general formula *cis*-[MCl(CO)$_2$(L)]; e) triphenylene ligands X = Cl, Br, CN

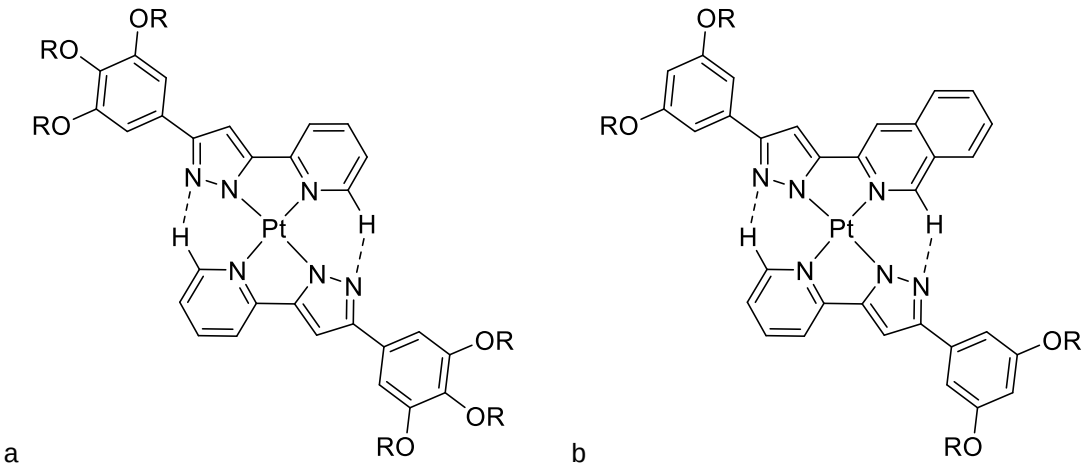

Figure 3-3: Structure of pseudo-tetradentate species formed by hydrogen bonding interaction between two chelating ligands reported by a) Liao *et al.*[28], where R = even integers 4-12 and b) Cuerva *et al.*,[29] where R = even integers 4-18 , both of which show columnar phases.

The nitrogen-based chelating motif has also been expanded to include complexes with terpyridine pincer ligands. Camerel *et al.* reported a charged terpyridine-based platinum(II) complex with an alkynyl-based ligand which showed a columnar hexagonal phase when the six chains appended to the alkynyl ligand were phytol-like; no liquid-crystalline behaviour was observed for the methyl or dodecyloxy equivalents (Figure 3-4).[30] These species also show metallogelation behaviour; both supramolecular assemblies are driven through Pt···Pt interactions, as well as π-π* interactions.

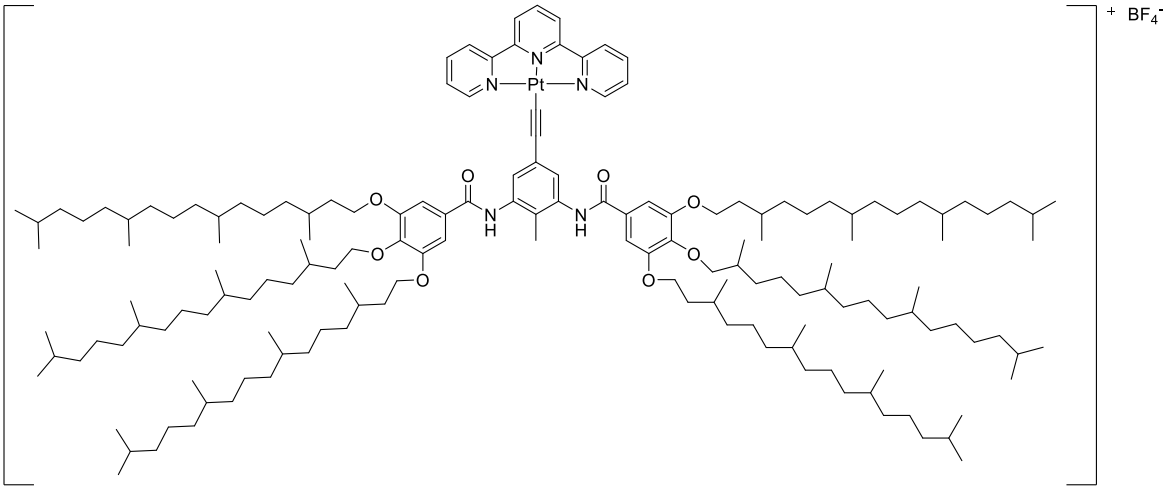

Figure 3-4: Structure of liquid-crystalline platinum(II) complex reported by Camerel *et al.* with terpyridine and functionalised alkynyl ligands.[30]

Metallomesogens based on salicylaldimine chelating ligands are very well known, particularly coordination complexes of nickel, copper, vanadium and iron,[31] as well as a range of lanthanide elements,[32-34] none of which typically adopt a square-planar geometry. However, palladium(II)

complexes of the same ligands are known, such as those reported by Date *et al.* with extensively alkoxy-functionalised salicylaldimine ligands which show columnar hexagonal phases when the alkoxy chains are all decyloxy or hexadecyloxy (*m* = *n* = 10 or 16) (Figure 3-5); the mesophase was stabilised through increasing the chain length, and the phase range was widened through the concurrent depression of the melting point.[35, 36]

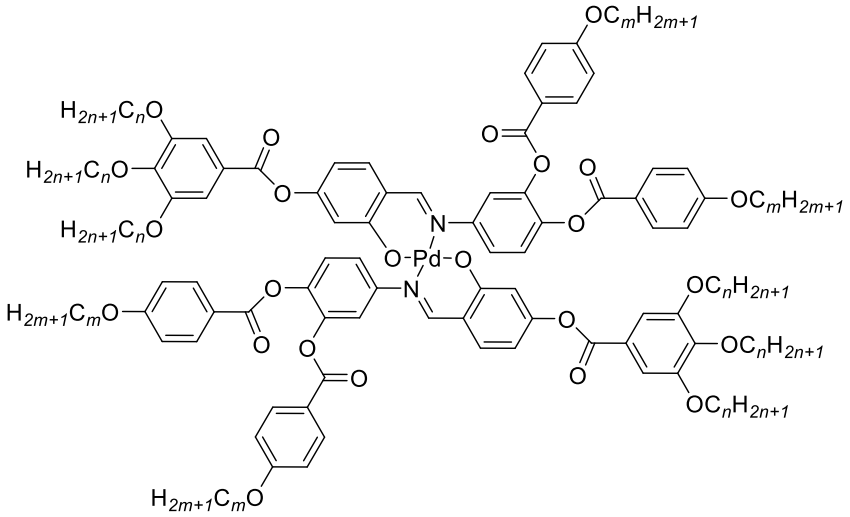

Figure 3-5: Salicylaldimine palladium(II) complex reported by Date *et al.* which shows Col_h phases when *n* = *m* = 10 or 16[35, 36]

Mono-cyclometallated complexes of palladium(II) and platinum(II) with rod-like cyclometallating ligands showing smectic and nematic phases are well known in the literature. The majority of these systems are based on one or more phenylpyridine ligands. The inclusion of organometallic ligands such as these are well-known to improve the emissive properties of metal complexes by increasing the radiative rate constant, k_r, due to the greater covalency in the metal-carbon bond, which raises the energy of the metal-based *d*-orbitals and increases the proportion of metal character in the emissive excited state.

Mocanu *et al.* investigated systems of platinum(II) and palladium(II) based on extended, rod-like Schiff base ligands with *N*-benzoyl thiourea co-ligands which show smectic A and nematic mesophases (Figure 3-6a). The phases formed are dependent on the metal, especially in determination of whether the observed phases are monotropic or enantiotropic, as well as on the nature of the thiourea ligand, which has an alkyl chain of variable length.[37]

Rod-like, alkoxy-functionalised phenylpyridine ligands have been employed by Geng *et al.* with picolinic acid co-ligands to induce liquid-crystalline behaviour in platinum complexes, resulting in a monotropic smectic A phase when the lateral phenylpyridine substituents are both hexadecyloxy chains (Figure 3-6b).[38] Subsequent reports by the same authors utilised the same substituted phenylpyridine ligand in complexes of platinum(II) and investigated the effectiveness of a tetrazole

co-ligand substituted in the 5-position with phenylpyridine (a C^N chelating ligand).[39] Liquid-crystalline behaviour was only observed for complexes in which there were three alkoxy chains per complex, in which a smectic phase was observed (Figure 3-6c). It should be noted that these complexes showed polarised emission in aligned thin films.

Geng *et al.* also reported a series of platinum(II) complexes with unsubstituted phenylpyridine cyclometallating ligands and alkoxy-phenyl substituted pyridyltriazole co-ligands which show columnar hexagonal mesophases only when long chains are absent (Figure 3-6d).[40] Similar observations were reported by Krikorian *et al.* in an investigation into the effect of counterion on phenylpyridine substituted pyridyltriazole platinum systems; complexes with a hexyloxy chain show columnar hexagonal mesophases, but the dodecyloxy equivalent is not liquid-crystalline (Figure 3-6e).[41] The loss of mesophase behaviour as the chain length is increased in both of these systems can be attributed to a deviation in the molecular geometry from truly disc shaped compared to the short chain equivalents and the resulting destruction the columnar phase. The particular threshold for the change in behaviour has not been investigated further and, as these complexes are charged, interactions with the anion may also play an important role.

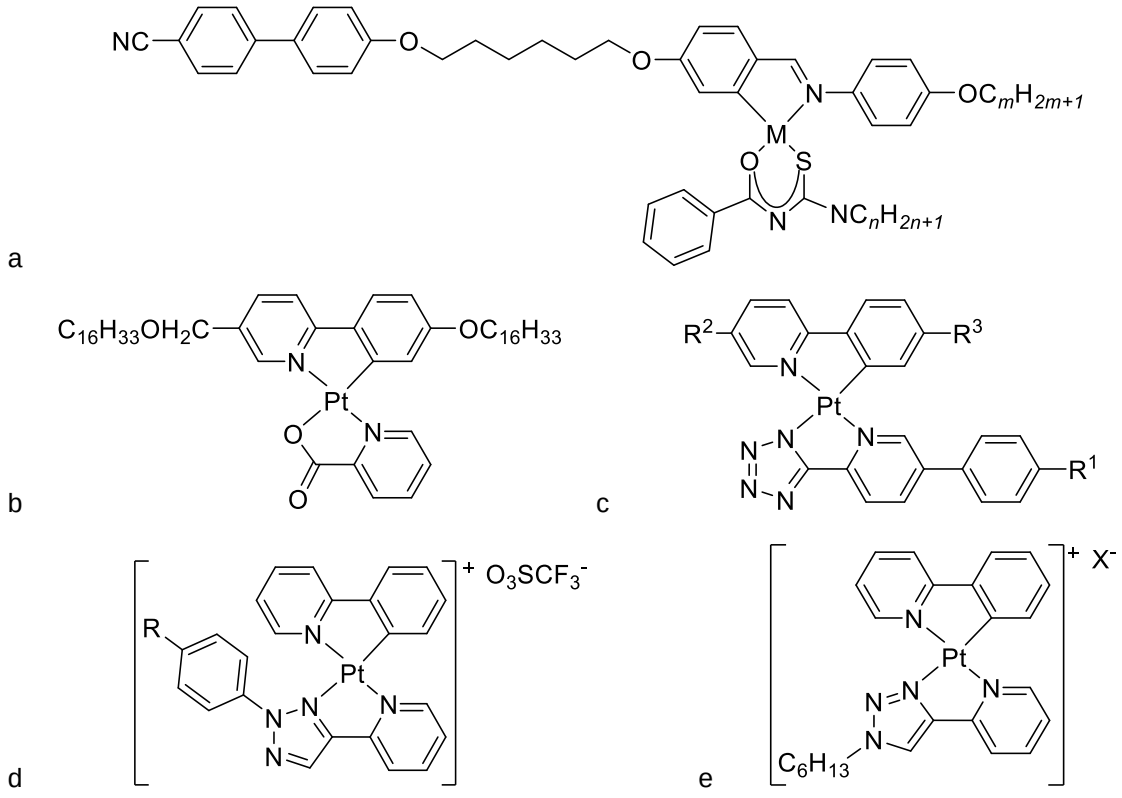

Figure 3-6: a) Platinum(II) and palladium(II) complexes of Schiff bases where *n* = 2-4, 6, 8 and *m* = 1, 10, M = Pd, Pt;[37] b) Platinum(II) complexes with phenylpyridine and picolinic acid ligands;[38] c) Platinum(II) complexes with phenylpyridine and pyridyltetrazole ligands, where $R^1 = OC_{12}H_{25}$ or $OC_{16}H_{33}$, $R^2 = CH_2OC_{16}H_{33}$, $R^3 = OC_{16}H_{33}$. [39] c) Platinum(II) complexes with unsubstituted phenylpyridine cyclometallating ligands and alkoxy-phenyl substituted pyridyltriazole co-ligands, where R = H or OCH_3;[40] d) Phenylpyridine/substituted pyridyltriazole platinum(II) complexes where X = SbF_6, PF_6, BF_4 or OTf.[41]

A large number of *ortho*-metallated palladium(II) systems have been reported based on cyclometallating azobenzenes with both monomeric and dimeric complexes showing nematic and smectic phases (Figure 3-7a).[42-44] Modification of the azobenzene ligand to the morphologically similar imine, and the cleavage of the dimeric complex with a β-diketonate co-ligand leads to complexes which show a chiral SmC* phase due to the chiral centres of the cyclometallated ligand (Figure 3-7b).[45-47] The design of complexes with a hydrolytically labile imine ligand does not lead to any significant instability or ligand exchange in the complexes, which appear to be robust and stable to cycling of the temperature and the resulting phase changes. However, this complex may not be stable to excessive moisture or when stored under standard atmospheric conditions for extended periods of time. This is not commented on in the original literature.

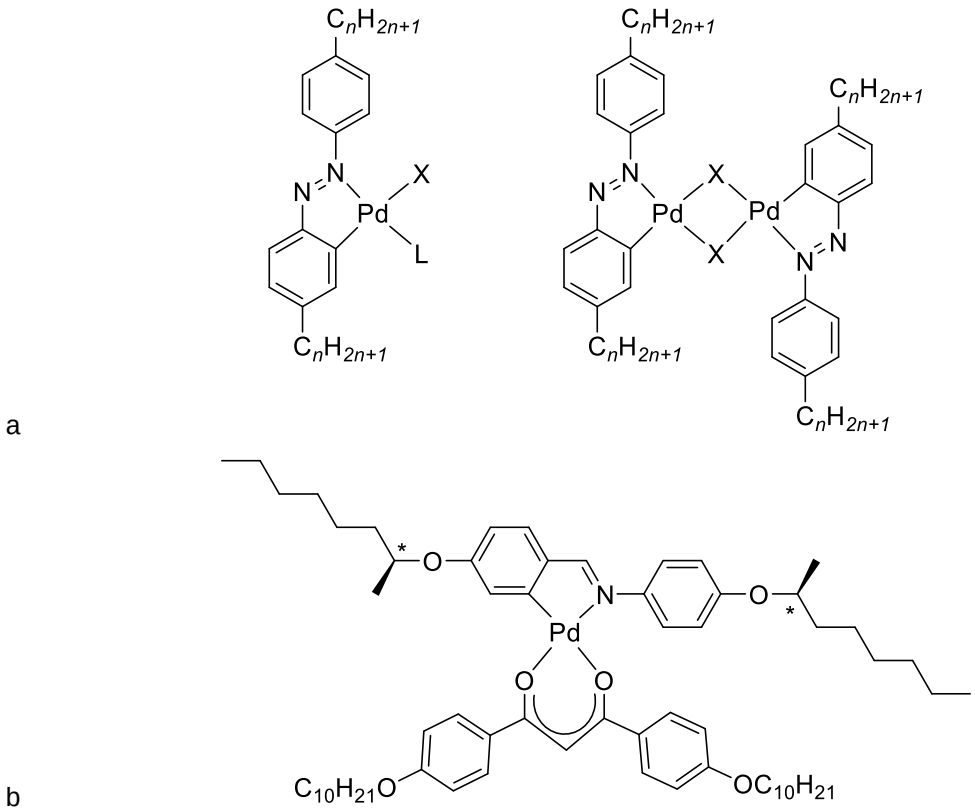

Figure 3-7: Structure of palladium(II) complexes with a) azobenzene ligands, monomeric and dimeric species, where *n* = 1-11, X = Cl, Br, I, L = PPh_3, pyridine, quinoline, aniline;[42-44] b) imine and alkoxyphenyl-functionalised β-diketonate ligands.[45-47]

An extremely thorough and extensive investigation of calamitic platinum(II) complexes with mono-cyclometallated, alkoxy-functionalised 2,5-diphenylpyridine ligands was carried out by Santoro *et al.* and reported in 2009.[5] These complexes, shown in Figure 3-8, showed smectic A and nematic phases. The complexes with 2,5-diphenylpyridine ligands showed only a smectic A phase while for those complexes in which a cyclopentane ring was fused to the backbone of the pyridine ring, a monotropic nematic phase was induced for shorter chain lengths (*n* = 6 and 8) due to the reduced ability for the molecules to arrange side-by-side, whilst the SmA phase, also monotropic, appeared

at longer chain lengths. This difference is accounted for by a significant increase in the stability of the crystalline phase.

The ancillary ligand also played a vital role so that when the ligands were chloride and *S*-DSMO (Figure 3-8a), the SmA phase was only observed for chain lengths with *n* = 6 and 10 (without cyclopentane ring) and a monotropic nematic phase was only observed for a chain length of 10 (with fused cyclopentane ring), whereas the analogous complexes with a β-diketonate co-ligand (Figure 3-8b), with chain lengths of 6 to 12, were all liquid-crystalline. All complexes were emissive in solution at room temperature, and the emission of selected complexes in neat films and as dopants in polycarbonate (PC) films was also investigated, with the emission dependent on the doping percentage, as well as the temperature.

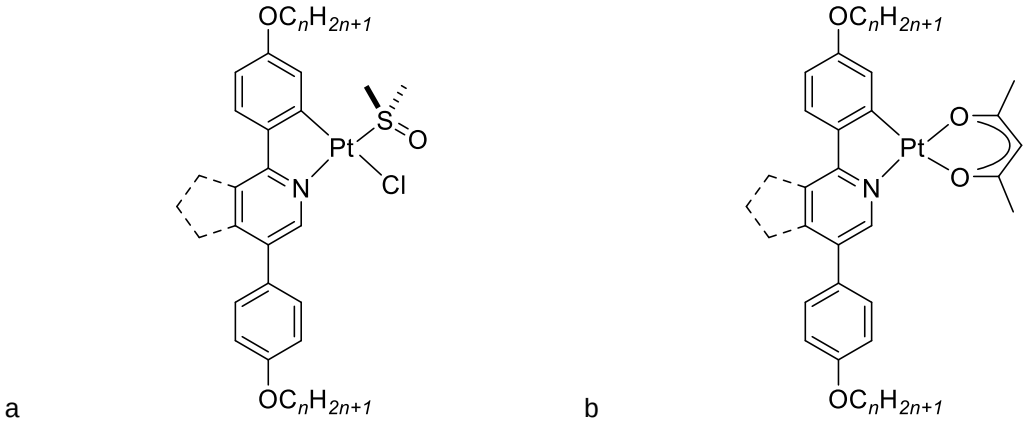

Figure 3-8: Complexes reported by Santoro *et al.* with 2,5-di(4-alkoxyphenyl)pyridine and 2,5-di(4-alkoxyphenyl)cyclopentenopyridine cyclometallating ligands and a) Cl/S-DMSO or b) acac co-ligands ligands, where n = 6, 8, 10, 12.[5]

The utilisation of β-diketonate ligands in metallomesogens is ubiquitous.[48-53] An extensive investigation by Tschierske and co-workers reported many series of platinum(II) and palladium(II) *ortho*-metallated complexes based on phenylpyridine and phenylpyrimidine with substantially functionalised β-diketonate ligands in order to probe the cross-over point between a calamitic and a discotic regime as the number of chains on the diketonate ligand is increased from two to six (Figure 3-9).[54, 55] Phases such as SmC and SmA are observed for β-diketonate ligands with two and three chains, as well four chains in a symmetric arrangement, *i.e.* 2 chains per ring. Columnar hexagonal and nematic columnar (N_{col}) phases were observed when there were five or six chains, as well as four chains in an unsymmetric arrangement (three chains on one ring, one on the other). All chains on the β-diketonate ligand were decyloxy, however the chain length of the substituted phenylpyridine/phenylpyrimidine was also altered, and while the complexes with different chain lengths were compared, this was not done systematically and there is scope for further investigation here.

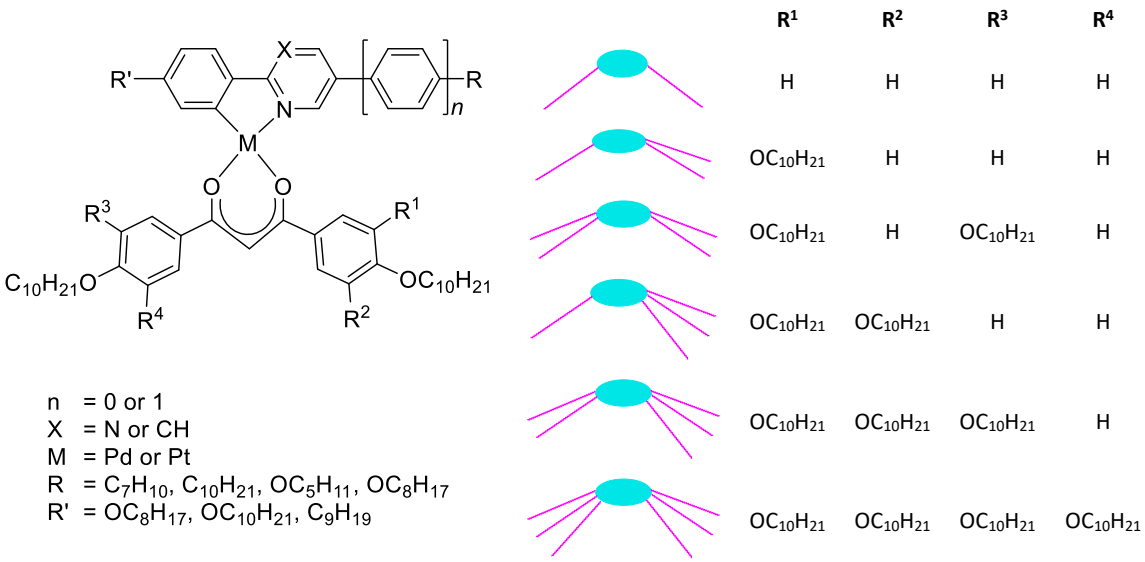

Figure 3-9: *Ortho*-metallated palladium and platinum complexes reported by Hegmann *et al.*, which show a cross-over between a calamitic to a discotic regime with increasing chain volume.[54] Blue ellipses represent phenyl diketonate core, purple lines represent the alkyl/alkoxy chains on the diketonate ligand, showing the progression from di- to hexa-substituted.

Similar observations were reported in a subsequent paper by Venkatesan *et al.* in which, as the alkoxy functionalisation of the β-diketonate ligand was increased, the mesomorphism changed from SmA to Col_h phases for platinum(II) complexes of phenylpyridine and thienylpyridine (Figure 3-10a).[56] The observation of columnar mesophases for heavily functionalised β-diketonate ligands is consistent even with comparatively small cyclometallating ligands; a columnar phase was observed for a platinum(II) complex reported by Ghedini *et al.* with the red Nile chromophore acting as the C^N ligand, which shows strong red emission (Figure 3-10b).[57] Many of these complexes have a 'half-disc' molecular geometry, resulting in an anti-parallel packing arrangement to form the full disc required for the assembly into columns.

Shi *et al.* reported the induction of columnar hexagonal phases in platinum(II) complexes through the inclusion of an alkoxy-functionalised triphenylene moiety on the *ortho*-metallating phenylpyridine unit (Figure 3-11a). Functionalisation of the β-diketonate co-ligand with 4-dodecyloxyphenyl substituents was required for the formation of the Col_h phase; complexes with unfunctionalized acetylacetone were not mesomorphic.[58] Subsequent introduction of an alkyl spacer (hexyl) between the triphenylene unit and the phenylpyridine coordinating moiety resulted in a deactivation of the liquid-crystalline behaviour due to the disruption of the favourable disc-like molecular geometry (Figure 3-11). The only mesomorphic complex in the series (Figure 3-11b) showed promising polarised emission when incorporated as the aligned, emissive layer in a white OLED.[59]

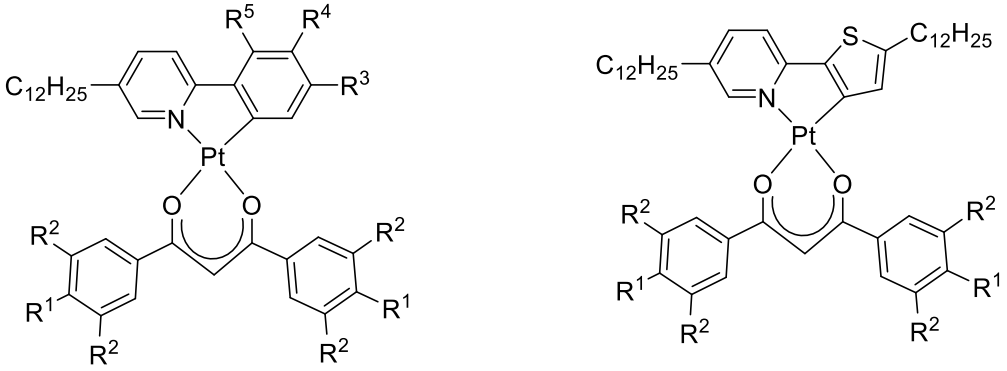

β-Diketonate:
$R^1 = OC_{10}H_{21}$, R^2 = H,
or $R^1 = R^2 = OC_{12}H_{12}$,

Phenylpyridine:
$R^3 = C_{12}H_{25}$, $OC_{12}H_{25}$, $R^4 = R^5$ = H,
or R^3 = H, $R^4 = OC_{12}H_{25}$, $R^5 = OC_{12}H_{25}$,
or $R^3 = OC_{12}H_{25}$, $R^4 = OC_{12}H_{25}$, R^5 = H

a

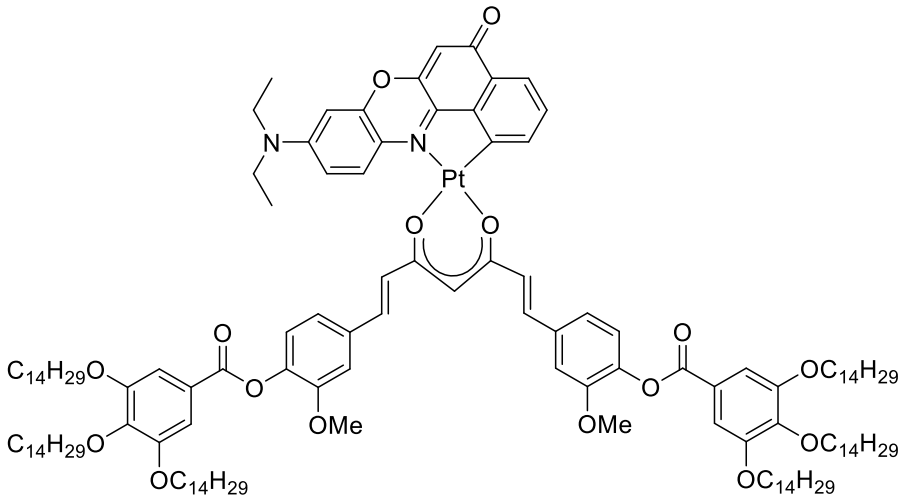

b

Figure 3-10: Structure of platinum(II) complexes reported by a) Venkatesan *et al.* with phenylpyridine or thienylpyridine cyclometallating ligands;[56] b) Ghedini *et al*. with the red Nile chromophore as cyclometallating ligand and functionalised β-diketonate ligand.[57]

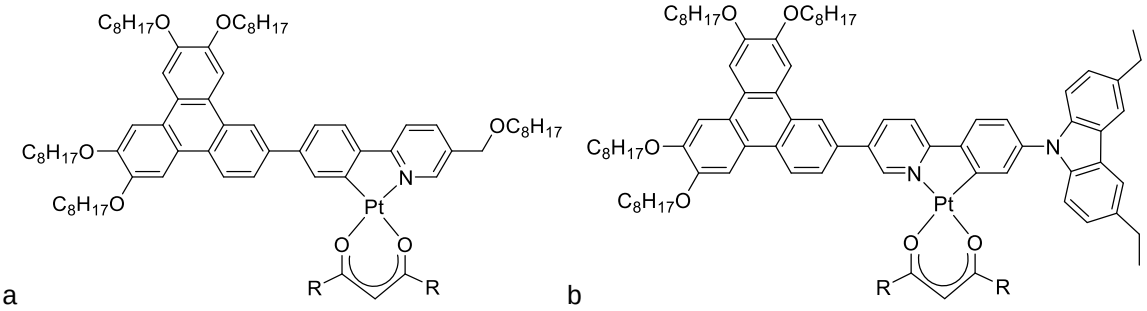

a b

Figure 3-11: Structure of triphenylene-incorporating platinum(II) complexes by a) Shi *et al.* which shows a Col_h phase compared to the non-mesomorphic parent complex, R = CH_3 or $OC_{12}H_{25}$;[58] b) Wang *et al.* showing the liquid-crystalline molecule which shows a Col_h phase and polarised emission in a white OLED.[59]

In keeping with the multitude of half-disc complexes, but moving away from the preponderance of reports of β-diketonate ligands, Zhao *et al.* reported a tetradentate platinum(II) system based on a biphenylpyridine with an ether linked phenyl ring (6,6'-bis((3',4',5'-tris(alkyloxy)[1,1'-biphenyl]-4-yl)oxy)-2,2'-bipyridine), resulting in C^N^N^C coordination mode with lateral alkoxyphenyl substituents (Figure 3-12).[60] These half-disc molecules are reported to stack in an anti-parallel arrangement to form a columnar hexagonal phase when the six terminal chains are C12; the shorter chain homologues were non-mesomorphic, as the chains may not be long enough to prevent crystallisation forces and stabilise the periphery of the columns of the mesophase.

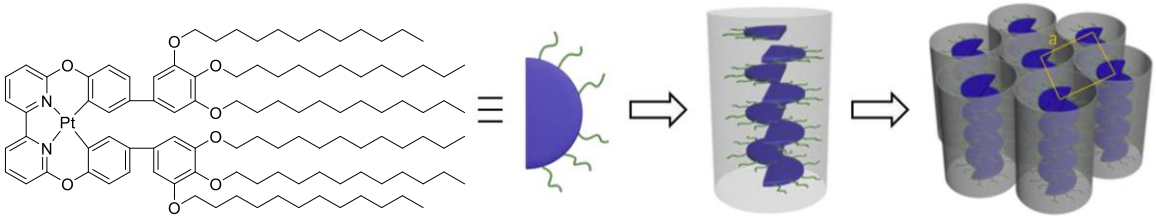

Figure 3-12: Structure of tetradentate platinum(II) complex showing Col_h when the chains are C12 and the proposed packing arrangements in the mesophase as reported by Zhao *et al.* (picture reproduced from reference and altered for clarity).[60]

Most relevant to the work on gold(III) metallomesogens that are the subject of this chapter are metallomesogens with bis-cyclometallating ligands. For the liquid-crystalline platinum(II) complexes reported in the literature, these take the form of alkoxy-functionalised 1,3-dipyridylbenzene ligands with monoanionic ancillary ligands in order to retain charge neutrality.

First reports of such systems came in 2008 from Kozhevnikov *et al.* who synthesised phosphorescent, tridentate platinum(II) complexes with 1,3-dipyridylbenzene N^C^N pincer ligands where the phenyl rings are each decorated with three alkoxy chains of increasing chain length.[2] Two series of complexes are reported, those with the ligands as described, and another where the pyridine rings have a fused cyclopentane ring in the backbone; both have a chloride ancillary ligand (Figure 3-13). The complexes without the cyclopentane ring show columnar rectangular phases, the stability of which decreases as the chain length in increased from C6 to C12, as observed in the decrease in the clearing point from 187 to 151 °C. When the two cyclopentane rings are present, the phase observed has hexagonal symmetry, but only for complexes where the chain length is C10 and C12. There is also a large destabilisation in the crystal lattice, resulting in room temperature liquid-crystals. All of the complexes are luminescent at room temperature in solution, and show stimulus-responsive behaviour in neat films, with the source of

the emission varying between monomeric and excimeric depending on the stimulus applied to the film.

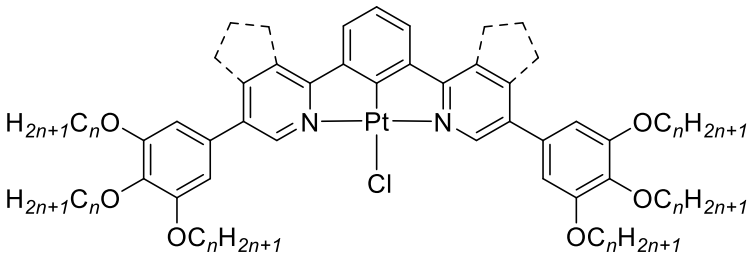

Figure 3-13: Structure of the bis-cyclometallated platinum(II) complexes reported by Kozhevnikov *et al.* showing Col_r (no cyclopentane ring, *n* = 6, 8, 10, 12) and Col_h (cyclopentane ring, *n* = 10, 12) phases.[2]

Research by the same authors in 2014 probed platinum complexes with two alkyl chains appended directly in the 5-position of the pyridyl rings of the N^C^N ligand (Figure 3-14a).[3] Complexes of this nature with chain lengths of C12 and C15 both showed monotropic lamellar phases, the formation of which was accompanied by a distinctive colour change from yellow to red. The phase did not crystallise upon cooling, but rather stayed in the red mesophase and formed a glass which crystallised slowly over time. The photophysical properties of the complexes were fully dependent on the phase they were in; the emission changed from orange for the crystalline state (a mixture of monomer and excimer) to near-IR in the lamellar mesophase (MMLCT). A very similar complex was reported in a subsequent paper by the same authors in which the dodecyl or pentadecyl chains were replaced with hexadecyloxy chains (Figure 3-14b).[4] This resulted in a noteworthy change in mesophase behaviour, with the new complex showing two different enantiotropic mesophases. A second complex was reported in this article which was heavily functionalised and reminiscent of those shown in Figure 3-13, however the terminal phenyl rings were appended *via* ester linkage and the fluorine substituents in the 3- and 5-positions of the cyclometallated phenyl ring are still present (Figure 3-14c). This complex also displayed a mesophase, which is indexed as having rhombohedral $R\bar{3}m$ symmetry. All mesophases for these two complexes were assigned as 3D phases and columnar phases, with 2D hexagonal symmetry extended into the third dimension; the authors are clear to point out that the phases are true mesophases, but the complexes are not liquid-crystalline due to the high level of positional order.[4]

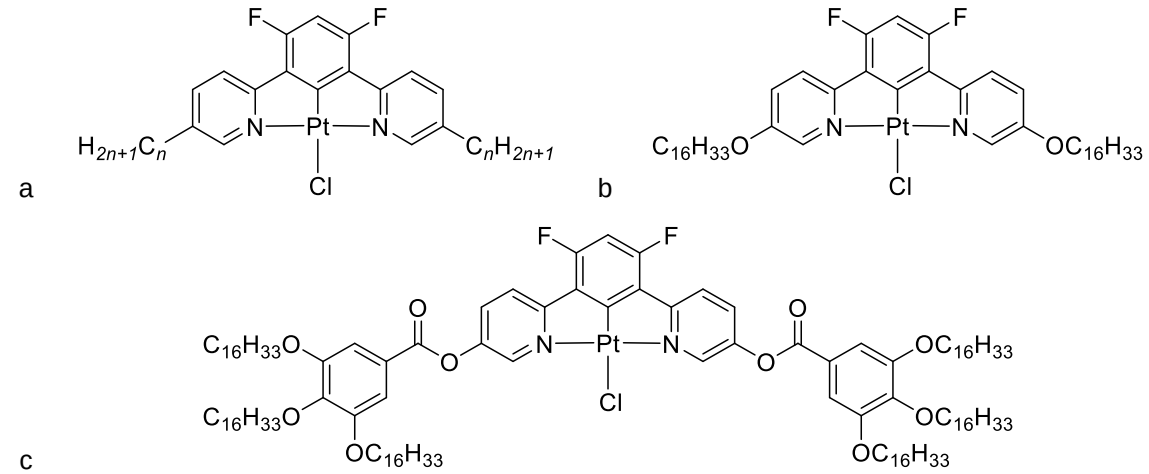

Figure 3-14: Structure of N^C^N cyclometallated platinum(II) complexes reported by Kozhevnikov *et al.* (*n* = 12 or 15).[3, 4]

These three communications are the only ones in the metallomesogen body of literature to concern bis-cyclometallated complexes; there is obviously a large degree of unexplored space for square-planar complexes of this nature, which would be expected to display a wide range of both liquid-crystalline and emissive behaviours given the promising observations reported in these works.

It should be stated that, although emissive observations have been given for a select number of compounds where it was pertinent to do so, the majority of these platinum(II) systems, particularly those which are cyclometallated, show phosphorescent emission due to the inclusion of the heavy metal centre, and show promise as potential OLED emitters, both in their efficiency, and the ability to show polarised emission. Further discussion of the luminescence of these systems is outwith the scope of this chapter, however relevant device performance is outlined in Chapter 4.

It is clear that the formation of mesophases in metal complexes is dependent on a number of factors, including effective space-filling to form truly rod- or disc-like molecules, intermolecular interactions, such as π-π stacking, metal-metal interactions and metal-ligand interactions. For discotic molecules, in the vast majority of cases, peripheral alkyl functionalisation must also be sufficient enough to prevent crystallisation forces between neighbouring columns to stabilise the mesophase, as well as acting as space-filling groups to, essentially, fill out the disc. These associations determine the supramolecular relationship between the individual molecules and therefore their organisation within the liquid-crystalline phase.

3.1.2 The Fluorophobic Effect and Fluorine in Liquid-Crystals

The fluorophobic effect is a term used to describe the incompatibility of perfluoroalkyl chains with aliphatic hydrocarbon chains. The immiscibility is driven by the fact that, in comparison to hydrogen, fluorine is larger, with a van der Waals radius of 1.46 Å, in comparison to 1.20 Å,[61] and the C–F bond is significantly longer than the C–H bond, with an average bond length of 1.35 Å compared to 1.09 Å.[62] The C–F bond is also not polarisable, with a value of $\Delta_\chi = 1.43$ on the Pauling scale,[63] whereas the C–H bond is, with a value of $\Delta_\chi = 0.35$. The result of this is that, when a perfluorinated chain is compared to a hydrocarbon chain, it is approximately 1.5 times larger in terms of volume, requiring a larger amount of space with respect to neighbouring moieties. This leads to reduced intermolecular interactions and lipophobicity; the perfluorinated chains can be considered *more* non-polar than hydrocarbon chains and have an increased rigidity.[64]

Fluorine is most often found in liquid-crystalline materials as a polarising substituent in the core in order to modify transition temperatures and dielectric properties. However, an expanding body of research (outlined and highlighted in the subsequent section) concerns the introduction of fluorine in the form of (semi)perfluorinated chains in place of or in accompaniment to the alkyl or alkoxy chains traditionally found in liquid-crystalline compounds in order to exploit the fluorophobic effect, thereby altering and expanding the mesophase behaviour observed.

3.1.3 Perfluorination in Liquid-Crystalline Materials

The introduction of perfluorinated chains is known to greatly affect the mesophase properties and behaviour of liquid-crystalline materials. The fluorophobic effect, as outlined in the previous section, can result in segregation between the perfluorinated and hydrocarbon chains, leading to the formation of primarily lamellar, columnar or cubic phases.

Perfluorination in liquid crystals spans a variety of molecular geometries and orientations, including calamitic,[65-68] swallowtail,[69, 70] amphiphilic,[71-75] discotic,[76] dendrimeric,[77-82] and hydrogen-[83-85] and halogen-bonded[86] mesogens, as well as a few reports of fluorinated metallomesogens,[87-95] and has recently been reported to induce lamellar assembly in donor-acceptor dye systems.[96] As such, a comprehensive review of individual systems and series of compounds would be too extensive for this short introductory section, however examples from many of these categories will be presented and the effect of perfluorination in these compounds discussed. For a thorough analysis of the liquid-crystalline behaviour of fluorine containing mesogenic compounds, many book chapters[64] and reviews[97-100] can be consulted.

Percec *et al.* reported the self-assembly of tapered materials formed through the esterification of 3,4,5-(semi-perfluorinated)alkoxy- and [3,4,5-(semi-perfluorinated)alkoxybenzyloxy]-benzoic acids with alcohol-substituted 15-crown-5 (Figure 3-15).[101] Upon complexation with lithium, sodium or potassium triflates, multiple molecules arrange themselves with the 15-crown-5 moieties in the centre of a column and the fluorinated chains on the periphery which pack in a hexagonal lattice to form Col_h phases. The uncomplexed molecules only show lamellar crystalline phases, indicating that the complexation is necessary for the mesophase formation.

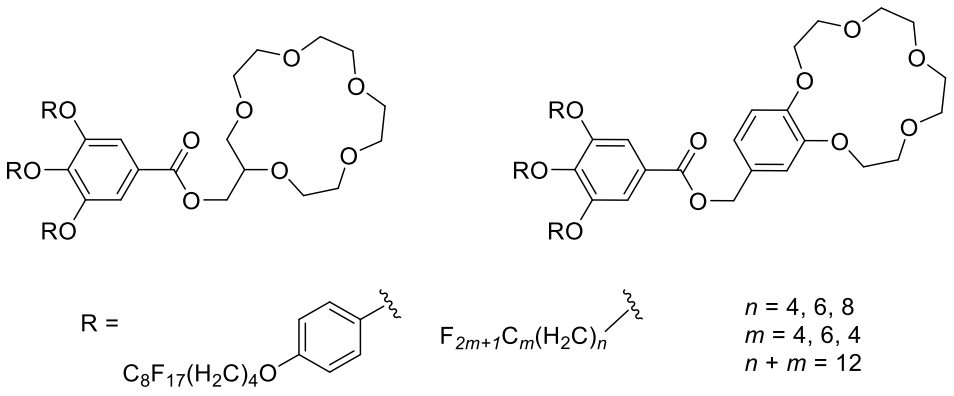

Figure 3-15: Structure of semi-perfluorinated complexes as synthesised by Percec *et al.* which form a microsegregated Col_h phase upon complexation with Li, Na or KOTf (not shown). [101]

Amphiphiles are known to segregate with respect to their polar and non-polar regions, and the inclusion of fluorinated chains can exaggerate this polarity difference as the perfluorinated chain is less polar than the hydrocarbon equivalent. Cheng *et al.* synthesised a series of amphiphilic polyols with increasing number and type of semi-perfluorinated alkoxy chains which show cubic phases when there are two or more chains on the phenyl ring.[102] The corresponding benzoic acids were also reported, which showed Col_h phases regardless of the level of perfluorination (Figure 3-16). When the polyols were compared to the analogous fully hydrocarbon analogues all mesophases types were significantly more stable, and the level of functionalisation necessary to induce cubic mesophases reduced from three chains (hydrocarbon species) to two chains (perfluorinated chains).

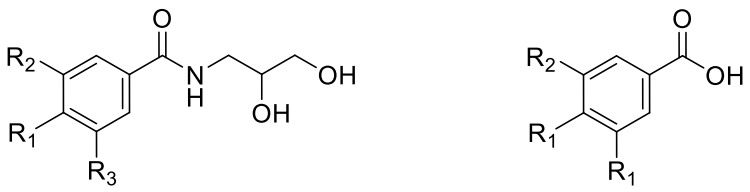

Polyols: R = H, $O(CH_2)_4C_6F_{13}$, $O(CH_2)_6C_4F_9$, $O(CH_2)_4(CF_2)_4CF(CF_3)_2$

Benzoic acids: R = $O(CH_2)_4C_6F_{13}$, $O(CH_2)_4C_4F_9$, $O(CH_2)_6C_4F_9$, $O(CH_2)_4(CF_2)_4CF(CF_3)_2$.

Figure 3-16: Structure of amphiphilic polyols and benzoic acids as reported by Cheng *et al.*[102]

Tschierske and colleagues synthesised a series of semi-perfluorinated tetrahedral pentaerythritol tetrabenzoates, investigating the level of perfluorination in the decyloxy chains, the effect of having one perfluorinated and one fully hydrocarbon chain per phenyl ring, as well as the effect of having one, two or three semi-perfluorinated chains per ring (Figure 3-17a).[103, 104] For those complexes with two chains all complexes show Col_h phases, including those with one hydrocarbon and one perfluorinated chain *ortho* to one another, and the fully hydrocarbon species. However, as the ratio of fluorination was increased (from fully hydrocarbon, to one chain on each ring (six fluorinated carbons), to two perfluorinated chains with four fluorinated carbons, to two perfluorinated chains with six fluorinated carbons), the stability of the columnar phase increased significantly, with the clearing point increasing from 47 to 131 °C. Whilst segregation between the different chain types plays a part in the formation and stability of phase, it is proposed that the most important factor is the incompatibility between the polar core and the chains, which is enhanced as the level of fluorination increases.

As the number of perfluorinated chains per phenyl ring is increased from one to three, the phases formed progress from a smectic A phase, through a Col_h phase for the two-chained compound, to a cubic mesophase (inverted micellar cubic); this is in contrast to the hydrocarbon equivalents, for which the pattern is non-LC (one chain) to a monotropic Col_h (two and three chains). This change is rationalised through increase in interfacial curvature between the polar core region and the chains upon fluorination, leading to a larger cross-section and the formation of a cubic phase.

Similar systems have been reported by Dahn *et al.* in which the tetrahedral polar core from above has been replaced by a planar triphenylene moiety (Figure 3-17b) and each outer ring was decorated with alkoxy chains in which the ring was bonded through the traditional ether linkage to a methylene spacer, followed by an ester linkage to the remaining portion of the chain, which was a 1*H*,1*H*,2*H*,2*H*-semi-perfluoroalkane.[105] Complexes with six, eight and ten perfluorinated carbon atoms in the chain (post-ester total chain length of eight, ten and twelve) show wide ranging columnar phases with good stability in comparison to unfunctionalised equivalents, however the compounds decomposed upon clearing into the isotropic liquid.

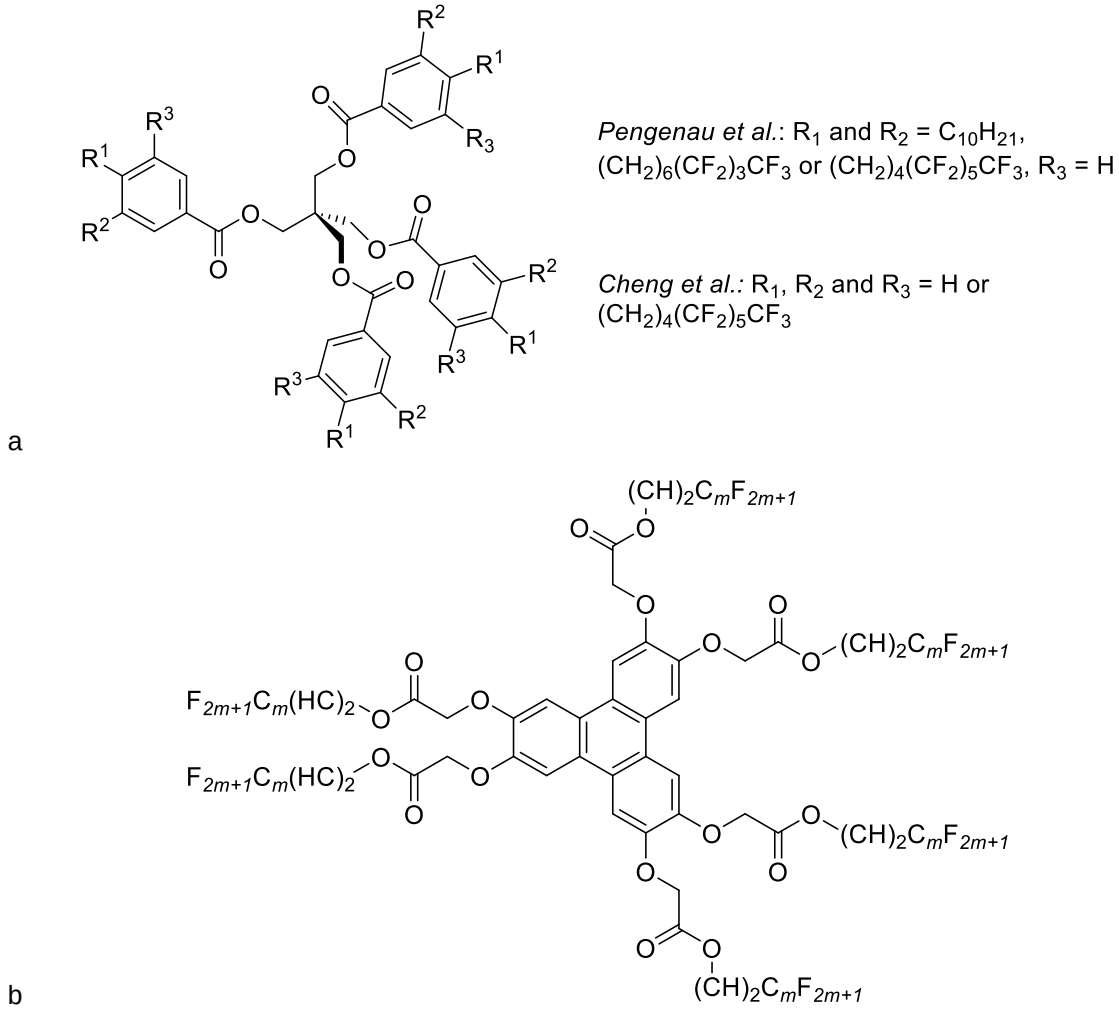

Figure 3-17: a) tetrahedral pentaerythritol tetrabenzoates, as reported by Pengenau *et al.* and Cheng *et al.*;[103, 104] b) triphenylene-based compounds reported by Dahn *et al.*, *m* = 6, 8, 10

Polycatenar liquid crystals are rod-like materials with four or more aromatic rings in the central core, decorated by two (dicatenar) to six (hexacatenar) alkyl/alkoxy chains. The phases they display are highly dependent on the ratio of core-volume to chain volume, with a low number of chains or a short chain length leading to calamitic phases (traditionally SmC, but SmA phases have recently been reported[106]), which changes to a columnar or cubic regime as the chain volume increases, due to a mismatch in chain and core cross-sectional area which can no longer support the lamellar phase structure. An excellent study into the phase behaviour of polycatenar liquid crystals with both hydrocarbon and perfluorinated chains was presented by Gainar *et al.* in 2017, in which the chains of tricatenar and tetracatenar mesogens were systematically altered to include increasing levels of fluorination; both the structure of the polycatenar materials studied and the liquid-crystalline behaviour is shown in Figure 3-18; all hydrocarbon chains are $OC_{12}H_{25}$ (except where the compound is denoted with '-b', which indicates $OC_{14}H_{29}$) and fluorinated chains are $O(CH_2)_4C_8F_{19}$ (except where the compound is denoted with '-b', which indicates $O(CH_2)_4C_{10}F_{21}$).[107]

Complexes without any fluorination were the only ones shown to exhibit nematic phases; this is not unexpected due to the incompatibility of fluorinated and hydrocarbon chains which would be forced interact if there was no positional order to the phase. Complete fluorination of one end of the structure (as for **HH/F(-b)** and **HH/FF**) resulted in lamellar phases consisting of a bilayer structure in which the fluorinated and hydrocarbon chains are segregated; this was determined through measurement of the layer spacing by SAXS. **HH/FF** also showed a Col_r phase with very large lattice parameters, indicating organisation of the columns that results in a structure with segregated regions of hydrocarbon and fluorocarbon chains.

For those compounds in which a fluorinated and hydrocarbon chain were located *ortho* to one another (**HH/HF** and **HF/HF**) on the same ring, no segregation is observed, indicating that there is level of tolerance for association of the chains of different types, although the clearing point for these complexes were lower than for both the purely hydrocarbon species and the chain-segregated compounds, showing that the mixing of the incompatible chains destabilised the mesophase formed.

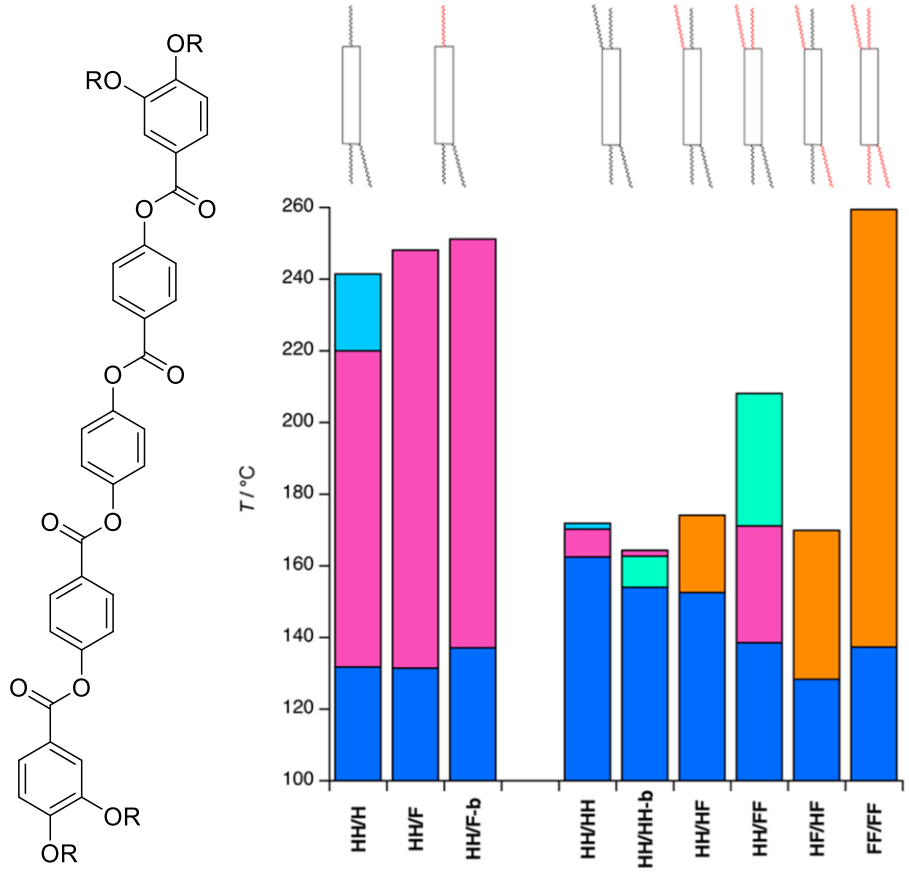

Figure 3-18: Structure of polycatenar materials as reported by Gainer *et al.* and their liquid-crystalline behaviour as the level of fluorination increases; crystalline phases are shown in dark blue, N in light blue, SmC in pink, Col_r in teal, Col_h in orange. Representative hydrocarbon chains are shown in black, fluorocarbon chains in red, and the core volume is represented by the black rectangle, as per polycatenar research convention. Graph of phase transitions from reference.[107]

With regards to metallomesogens, investigations into the effect of inclusion of perfluorinated chains are uncommon, especially in comparison to the purely organic systems outlined above. The first reports of such systems were by Guillevic *et al.* in 2000, based on rhenium(I) complexes with extended imine *ortho*-metallated ligands, which are nematogenic when the chains are hydrocarbon based. In contrast, the semi-perfluorinated free ligands show only lamellar phases and the resulting rhenium(I) complexes (Figure 3-19a) all show SmA phases due to microphase segregation effects, and decompose upon clearing.[91, 92] Interestingly, the fully fluorinated free ligand, *i.e.* with no hydrocarbon spacer, shows a cubic phase, the origin of which the authors describe as a 'mystery' due to the relative rarity of cubic-forming calamitics.

Reports by Dembinski *et al.* into isocyanide complexes of groups 10 and 11 show that inclusion of eight perfluorinated carbon atoms in the dodecyloxy chain of 4-dodecyloxyphenylisocycanide of the free ligand induces liquid-crystallinity where the hydrocarbon equivalents are not mesomorphic.[90] Upon complexation, the molecular anisotropy that predominantly controls liquid-crystallinity is obvious; a tetrahedral copper complex is non-LC, as is the trigonal bipyramidal iron complex, whereas smectic A phases are observed for all the linear (copper, gold and silver) and square-planar (palladium and platinum) complexes. As previously observed the phases are significantly stabilised upon the inclusion of the fluorous chains with clearing points of up to 240 °C.

Enaminoketone ligands have also been utilised in fluorinated metallomesogens, with both rod- and disc-like complexes synthesised and investigated. Reports by Martin *et al.* of bis-chelated palladium(II) complexes change from a nematic mesophase regime for the hydrocarbon parent compounds to a SmA regime for the fluorinated complexes, as would be expected when the phase formation is driven by segregation effects (Figure 3-19b).[93]

a

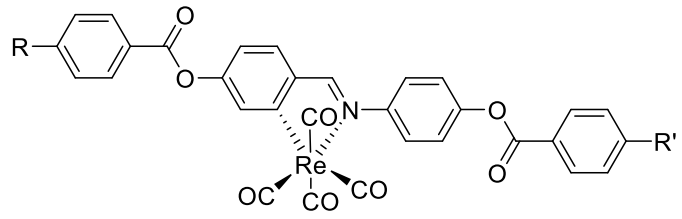

b

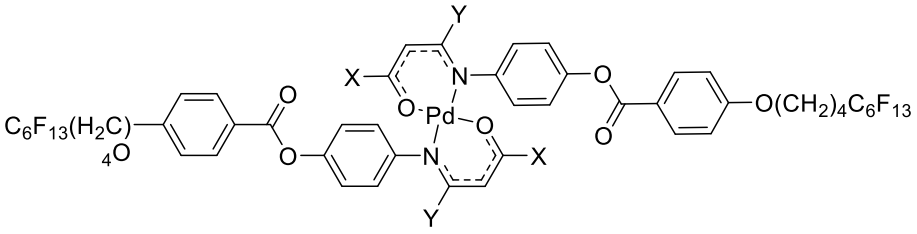

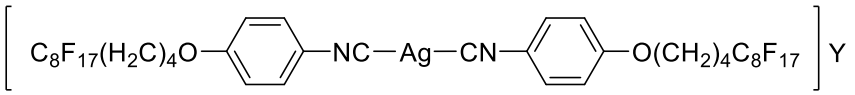

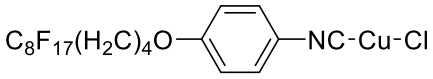

c

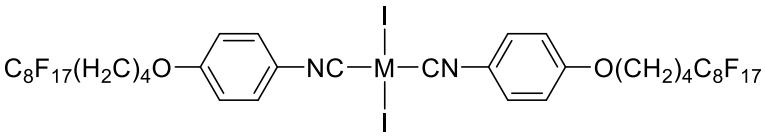

Figure 3-19: Structure of metallomesogens reported by a) Guillevic *et al.* of Re(I), R = C_6H_{13} and R' = C_6F_{13} and vice versa, and R = R' = C_mF_{2m+1}, *m* = 6, 7, 8, 10;[91, 92] b) Martin *et al.*, X = CF_3 and Y = H, and when X = Y = CH_3[93]; c) Dembinski *et al.* based on fluorinated isocyanide ligands

Szydłowska *et al.* synthesised complexes of nickel, copper and vanadium with a tetradentate enaminoketone ligand (two enaminoketone moieties per ligand) in which, if the hydrocarbon parent compound showed a lamellar mesophase, the inclusion of perfluorinated chains destroyed the mesophase, and if the parent compound was discotic in nature, the inclusion of perfluorinated chains induced a columnar hexagonal phase which was not present in the non-liquid-crystalline parent complex (Figure 3-20a).[95]

In an effort impart chirality into segregated, fluorinated complexes, Ocak *et al.* utilised a chiral imine ligand with the chiral centre located on a short chain on one end of the molecule, and a decyloxy perfluorinated chain on the other (Figure 3-20b).[94] In the free ligands, the expected lamellar structure is formed, with the observation of chiral smectic C (SmC*) phases which are also present in the hydrocarbon equivalent but significantly less stable. These ligands were coordinated to a copper(II) centre and the resulting complexes showed smectic A phases which were highly stable, with an increase in the clearing point of over 100 °C in comparison to the parent hydrocarbon complex. It should be noted that the phases formed for the copper complexes did not show any chirality.

Imine ligands, although without chiral functionality, have also been used for a number of complexes reported in a series of papers by Bilgin-Eran and co-workers. The formation of copper and palladium salicylaldimine complexes showed highly stable smectic phases, both smectic A and an unidentified smectic phase for both metals.[89] Also synthesised were chloride bridged dimeric species, primarily of palladium,[88] with reports of the analogous platinum species communicated six years later (Figure 3-20c).[87] The palladium species with 4 fluorinated chains show lamellar phases, with an enantiotropic SmA phase and a monotropic SmC phase, the latter of which is not observed as the level of fluorination within the chain is increased. For those dimers with six fluorinated chains, the appendage of two lateral chains disrupts the rod-like anisotropy by forming a more disc-like geometry, resulting in the observation of Col_h phases; this is the result of an increase in order of the phases with the larger chain volume as the hydrocarbon parent complexes show only monotropic discotic nematic phases (N_D). The story is very similar for the platinum analogues, however the monotropic SmC phase is no longer observed, the cause of which is rationalised as a reduction in the ability of the liquid phase to be sufficiently supercooled.

It is clear then that great differences in phase behaviour can be brought about through the inclusion of perfluorinated chains in both rod-like and disc-like molecules. The number and length of fluorinated chains, as well as the ratio between fluorination and purely hydrocarbon chains plays a vital role in the induction and stabilisation of lamellar, columnar and cubic phases through the fluorophobic effect, resulting in chain segregation between fluorous and hydrocarbon regions, as well as increasing polarity differences between polar cores and the peripheral chains and an increase in volume mismatches between cores and chains in rod-like systems. There were limited reports[87, 88] found of (half)-disc-like compounds, especially metallomesogens, with hydrocarbon/fluorocarbon incompatibilities in close relation, and it so it is of great interest to discover how such materials would behave with respect to their liquid-crystalline and self-assembly behaviour.

With the knowledge that square-planar bis-cyclometallated complexes such as the platinum(II) complexes described above[2-4] can show a wide variety of liquid-crystalline phases, a family of novel gold(III) complexes with morphologically similar cyclometallating ligands were prepared, utilising functionalised 2,6-diphenylpyridine C^N^C ligands. In the fourth coordination position, a functionalised alkynyl ligand provided the σ-donating, anionic ligand necessary for emissive, charge-neutral complexes of the general formula [Au(C^N^C)(C≡C-R)], with the number and length of the appended alkoxy chains imparting the ability to tune the mesomorphism of the complexes.

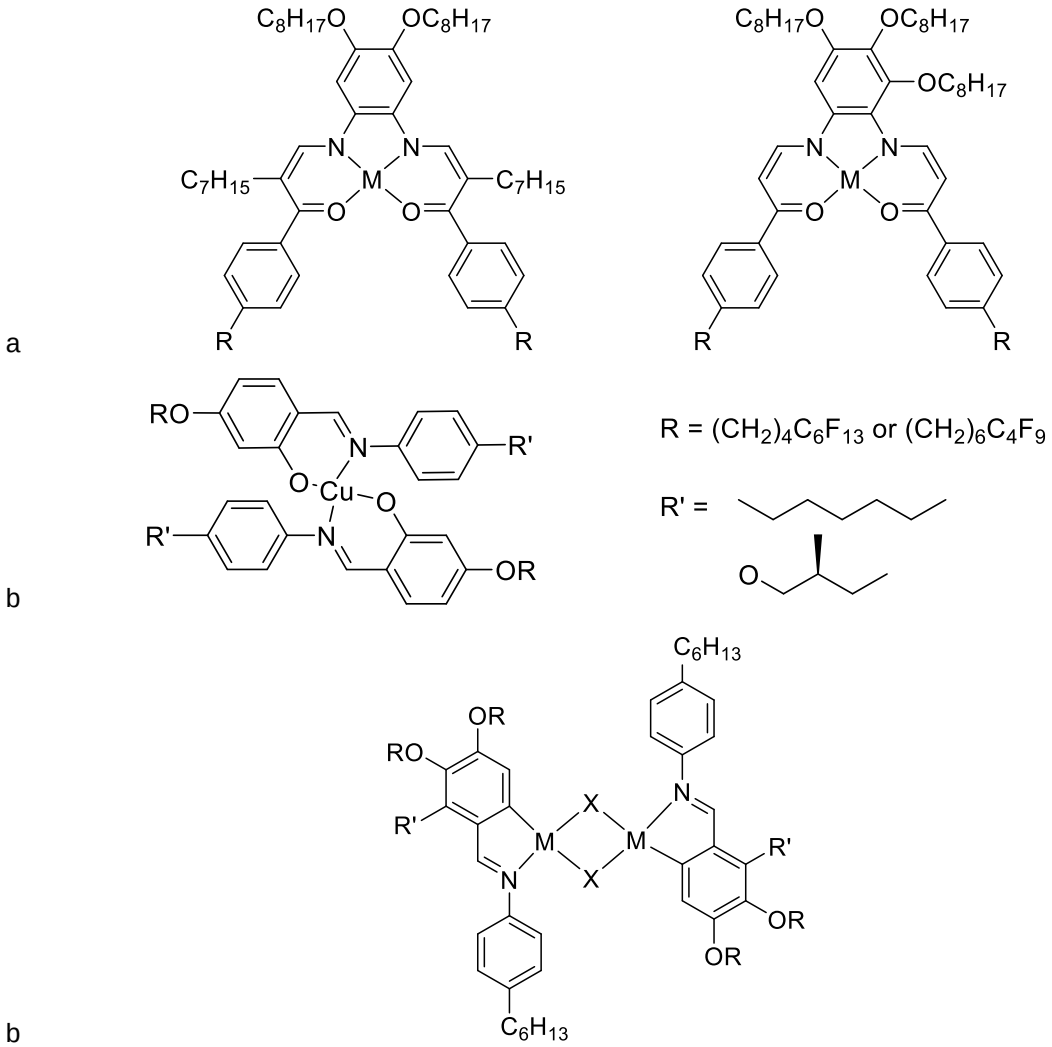

Figure 3-20: Complexes reported by a) Szydłowska *et al.* which show Col_h phases when R = C_8H_{17} (all) and M = Ni, Cu (left), M = Ni, Cu, VO (right);[95] b) Ocak *et al.* with chiral imine ligands and a single fluorinated chain; c) Bilgin-Eran *et al*. of palladium and platinum, M = Pd, Pt, X = Cl, Br, I, R' = H or OR, R = $(CH_2)_4C_6F_{13}$ or $(CH_2)_6C_4F_{13}$.[87, 88]

3.2 Synthesis

3.2.1 Synthesis of Cyclometallating Ligands

In order to provide the rigid core-structure necessary for a charge-neutral gold(III) complex, as well as a suitable substrate on which to append the flexible alkoxy chains as discussed previously, ligands with a coordination pattern of C^N^C were chosen, where both carbon atoms are anionic 1^- donor ligands, and the nitrogen is a neutrally coordinated ligand. In this case, a C^N^C ligand was designed around the 2,6-diphenylpyridine core structure which has been shown to be effective in the development of luminescent gold(III) complexes as introduced above, the scope of which will be fully outlined in Chapter 4.[7-9, 12, 14, 108-111]

There were two related cyclometallating ligands utilised in the target gold(III) complexes; 2,6-di(4-dodecyloxyphenyl)pyridine and 2,6-(3,4-bis(dodecyloxy)phenyl)pyridine. The mono-substituted bis-cyclometallating ligand is a structural isomer analogous to the mono-cyclometallating ligands used in Chapter 2. Synthesis of these ligands can be readily achieved by the modification of established literature procedures (Scheme 3-1), and they are herein named **H_2L1** and **H_2L2** for the two- and four-chain ligands, respectively.[112]

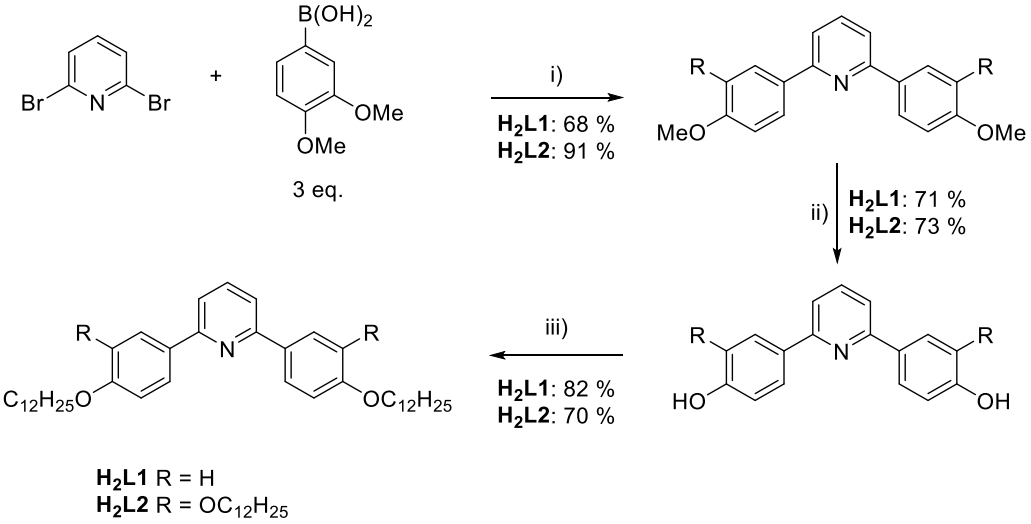

Scheme 3-1: Synthetic procedure to the functionalised 2,6-diphenylpyridine ligands **H_2L1** and **H_2L2**. i) $[Pd_3(OAc)_6]$ (0.5 mol%), K_3PO_4 (3 eq.), ethylene glycol, 1.5 h, 80 °C; ii) pyH^+Cl^- (excess), 16 h, 200 °C; iii) 1-bromododecane, K_2CO_3 (3 eq.), DMF, 16 h, 90 °C.

The methoxy-substituted 2,6-diphenylpyridine ligands were synthesised through a Suzuki-Miyaura cross-coupling reaction with 2,6-dibromopyridine and the appropriately substituted phenylboronic acid. This reaction is a modification of a literature procedure,[112] reaches completion quickly and under moderate conditions, and is also both water and oxygen tolerant. No homocoupling was observed for either reaction. Demethylation of this intermediate was achieved through the use of pyridinium chloride in a melt synthesis at elevated temperatures (200 °C). Finally, the long-chain substituents are appended through a Williamson ether synthesis in DMF with 1-bromododecane.[5]

All reactions progress in good yield (70-90%) with straightforward work-up procedures. The final dodecyloxy-substituted products give satisfactory elemental analysis after removal of impurities by washing with water and acetone alone, without the need for column chromatography or crystallisation.

3.2.2 Synthesis of the Alkynyl Ligands

In the field of liquid-crystalline materials, it has been well established that tuning of the mesophase behaviour is possible through the alteration of the length of the alkoxy chains on the periphery of the molecules, as well as the substitution pattern of the chains, often on terminal phenyl rings. This is apparent in a variety of liquid-crystalline materials,[113-117] including metallomesogens.[2-5, 23]

In order to tune the liquid-crystalline behaviour in this series of gold(III) metallomesogens, a variety of alkynyl ligands were synthesised, with increasing substitution from one alkyl or alkoxy chain to three, varying in chain length from C8 to C14 for alkoxy chains and C5 and C8 for alkyl chains. These different ligands do indeed have an impact on the liquid-crystalline behaviour of the systems (Section 3.4), as well as the photophysical characteristics of the systems as outlined in Chapter 4. The structure of the synthesised ligands are shown in Figure 3-21.

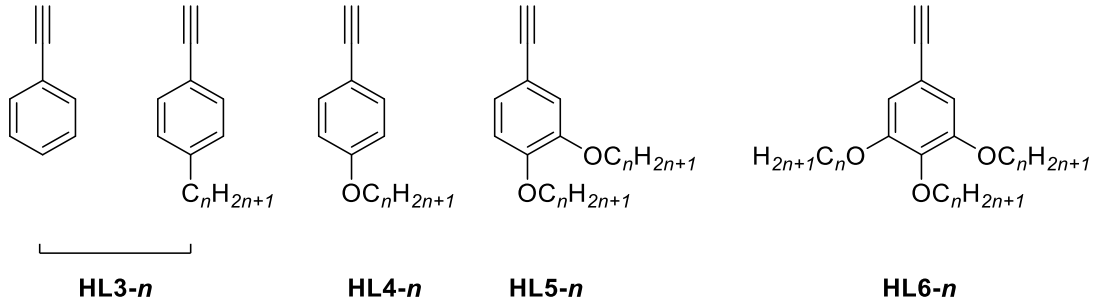

Figure 3-21: Structure of the alkynyl ligands utilised in this chapter, *n* = length of carbon chain; where *n* = H, the ligand is phenylacetylene. Phenylacetylene, 1-ethynyl-4-pentylbenzene and 1-ethynyl-4-octylbenzene were purchased from common suppliers and used without further purification.

Cardinaels *et al.* reported the synthesis of terminal phenylalkynes *via* the equivalent benzaldehyde, and it was this reaction pathway that was used to synthesise the target alkynyl ligands, herein named **HL3-*n***, **HL4-*n***, **HL5-*n*** and **HL6-*n***, where *n* = the number of carbon atoms in the chain (and is denoted as 'H' when the ligand is phenylacetylene) (Scheme 3-2).[113]

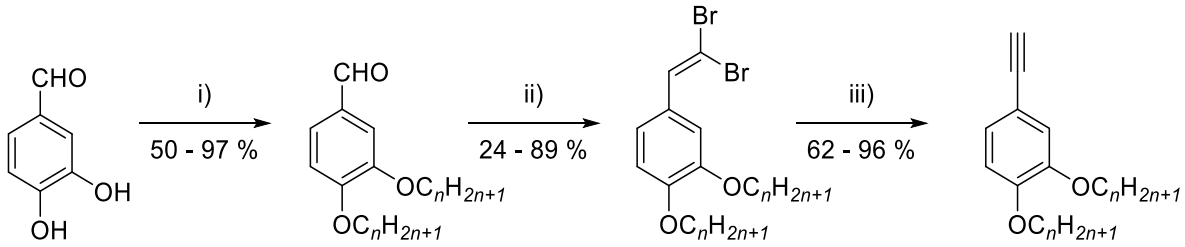

Scheme 3-2: Synthetic route to alkynyl ligands as reported by Cardinaels *et al.*,[113] progressing through the alkylation of 3,4-hydroxybenzaldyhyde, followed by a two-step Corey-Fuchs reaction to form 4-ethynyl-1,2-di(alkyloxy)benzene, showing **HL5-*n*** is shown as a representative example. i) BrC_nH_{2n+1}, K_2CO_3, KI (cat.), DMF, 3 h, reflux, N_2; ii) CBr_4, PPh_3, NEt_3, CH_2Cl_2, 30 mins, 0 °C, N_2; iii) EtMgBr, THF, 1 h, r.t., N_2.

The alkylation of 3,4-hydroxybenzaldehyde proceeds under similar conditions to the alkylation reactions outlined previously. The aldehyde is then subjected to a Corey-Fuchs reaction which, over two steps, converts the aldehyde into the target terminal alkyne. The reaction progresses in good yield (typically in excess of 80% in each step), with a simple purification *via* column chromatography for both the dibromovinyl intermediate and terminal alkyne target species.

This approach proved successful for the mono- and di-substituted ligands **HL4-*n*** and **HL5-*n***, but the comparatively high cost of 3,4,5-trihydroxybenzaldehyde and the large scale of the reactions meant that additional synthetic steps were required to synthesise this from cheaper commercially available starting materials (Scheme 3-3).

1-Bromo-3,4,5-trimethoxybenzene was demethylated using boron tribromide (BBr_3) to form the related trihydroxybenzene. This reaction required temperatures of -78 °C; when the reaction was carried out at 0 °C, only two of the available three methoxy groups were substituted.

1-Bromo-3,4,5-trihydroxybenzene was then alkylated with the appropriate 1-bromoalkane, *via* a Williamson ether synthesis. The final step to the 3,4,5-trialkoxybenzaldehyde intermediate involved the implementation of the Bouveault aldehyde synthesis, a specific formylation reaction in which the aryl halide is replaced by a formyl group from DMF *via* a hemiaminal intermediate. This procedure is designated 'Route A'.

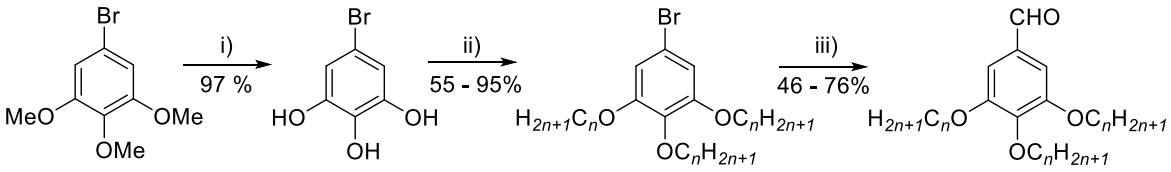

Scheme 3-3: Synthetic route to 3,4,5-trialkoxybenzaldehyde (Route A), including the demethylation of 1-bromo-3,4,5-trimethoxybenzene to form the hydroxy-substituted equivalent, subsequent alkylation with 1-bromoalkane, and finally conversion to 3,4,5-trialkoxybenzaldehyde utilising BuLi and DMF in the Bouveault aldyehyde synthesis, a specific formylation reaction. : i) BBr_3 (3.3 eq.), CH_2Cl_2, 1 h, N_2, -78 °C ii) 1-bromoalkane (5 eq.), K_2CO_3 (9 eq.), DMF, 16 h, N_2, 90 °C; iii) BuLi, DMF (2 eq.), diethyl ether, 1 h, N_2, -25 °C.

This reaction gave poor yields as the chain length increased and it is proposed that the reason for this is poor solubility of the starting material in the reaction solvent, THF, or any other BuLi compatible solvent, such as diethyl ether or hexane, at the low temperatures required for the reaction. For this reason, an alternate method was sought. Literature precedent established by the Bruce group reports that 3,4,5-trialkoxybenzaldehyde species can be synthesised starting from the equivalent hydroxy ester (Scheme 3-4).[16]

Methyl 3,4,5-hydroxybenzoate was first alkylated with the appropriate 1-bromoalkane as before, followed by the reduction of this species to the corresponding benzyl alcohol with $LiAlH_4$. This

species is then re-oxidised to the aldehyde through the use of manganese dioxide (MnO_2). This procedure (Route B) proved to be more reliable, higher yielding and, therefore, preferable.

After synthesis of the 3,4,5-trialkoxybenzaldehyde intermediate, the synthesised compound was treated to the previously established Corey-Fuchs method to form the terminal alkyne ligand, **HL6-*n***.

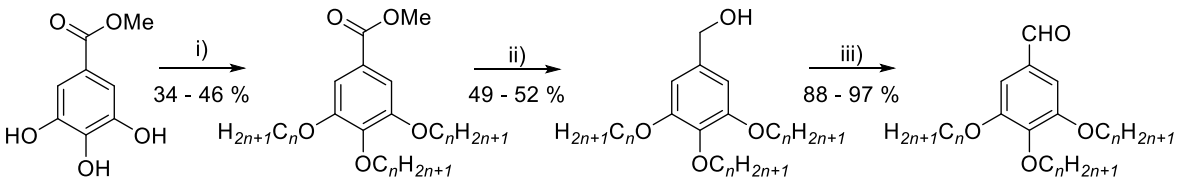

Scheme 3-4: Synthetic route to 3,4,5-trialkoxybenzaldehyde (Route B), including the alkylation of methyl 3,4,5-hydroxybenzoate, the reduction of methyl 3,4,5-alkoxybenzoate with $LiAlH_4$ to form the equivalent benzyl alcohol, which is then selectively oxidised to 3,4,5-trialkoxybenzaldehyde. i) 1-bromoalkane (3.3 eq.), K_2CO_3 (6 eq.), 2-pentanone, 24 h, reflux; ii) $LiAlH_4$, THF, 16 h, N_2, 0 °C; iii) MnO_2 (excess), CH_2Cl_2, 16 h, r.t.

In addition to ligands functionalised with alkoxy chains, 4-ethynylpyridine was also synthesised as an alkynyl ligand. Using a literature procedure, beginning with 4-bromopyridine hydrochloride, using a niche variation on a Sonogashira cross-coupling reaction with trimethylsilylacetylene where ZnBr is used in place of the traditional CuI, the protected species 4-(trimethylsilylethynyl)pyridine was synthesised and purified *via* vacuum distillation. This species was then de-protected with potassium hydroxide under mild conditions to form the terminal alkyne (Scheme 3-5).

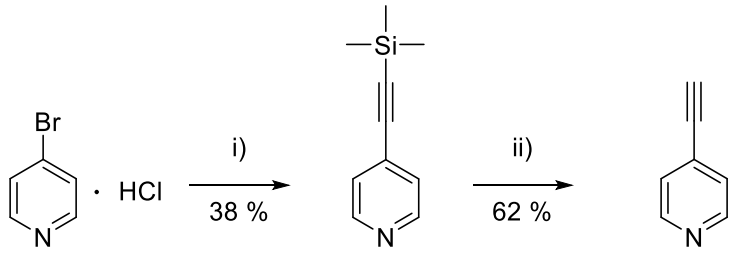

Scheme 3-5: Procedure to form 4-ethynylpyridine through Sonogashira coupling reaction with trimethylsilylacetylene and subsequent deprotection. i) trimethylsilylacetylene, $ZnBr_2$ (2 eq.), PPh_3 (0.2 eq), $PdCl_2$ (0.05 mol%), NEt_3, THF, 0 °C to 60 °C, 4.5 h, N_2; ii) KOH, 2:1 MeOH:CH_2Cl_2, 2 h, r.t., N_2.

All of the ligands synthesised proved to be light and air stable and were stored without issue. The final synthetic routes were robust and reliable and could be applied to substrates with different functional groups, as outlined in the subsequent section.

3.2.3 Synthesis of Semi-Perfluorinated Alkynyl Ligands

In all cases, the perfluorinated chains utilised in this work were of the structure 1H,1H,2H,2H-perfluoroalkoxy (-$O(CH_2)_2(CF_2)_mCF_3$, where m = 5, 7 or 9), meaning that the first two carbons of every chain were not perfluorinated. These were chosen due to the commercial availability of starting materials, as well as comparative ease of synthesis in comparison to fully perfluorinated analogues. The target ligands are shown in Figure 3-22.

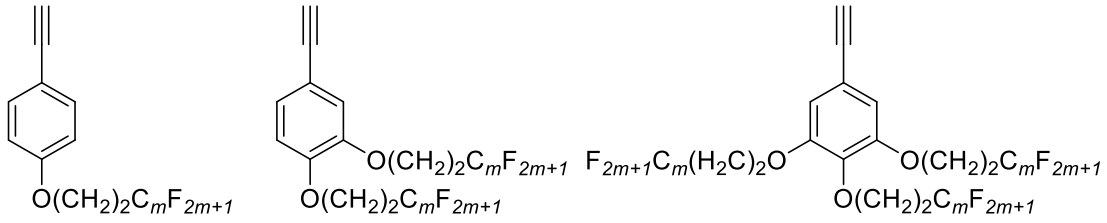

HL7-*n* **HL8-*n*** **HL9-*n***

Figure 3-22: Structure of the semi-perfluorinated alkynyl ligands utilised in this chapter, n = length of carbon chain; the first two carbon atoms in the chain are always CH_2 groups, resulting in a chain of length n, where the number of fluorinated carbon atoms is equal to n-2 or m.

Due to the success of the synthesis of alkynyl ligands *via* the Corey-Fuchs method described extensively in Section 3.2.2, this method was chosen again, although due to availability of starting materials and extreme differences in solubility of compounds with perfluorinated chains in comparison to their hydrocarbon analogues, many modifications were made as outlined below.

1-Iodo(1H,1H,2H,2H-perfluoroalkane)s are available commercially, but have a tendency to undergo elimination side-reactions under Williamson-ether alkylation reaction conditions to form alkenes, leading to poor yields of the desired alkylated product. The alcoholic equivalents, 1H,1H,2H,2H-perfluoroalkan-1-ols, are also available commercially, and while they are themselves unsuitable in alkylation reactions, the can easily be transformed into the related triflates, 1H,1H,2H,2H-perfluoroalkyltrifluoro-methanesulfonate, through reaction with triflic anhydride (Scheme 3-6). The alcohol is deprotonated by the base, in this case pyridine, in a mixture of CH_2Cl_2 and 1,4-dioxane, and added to triflic anhydride at reduced temperature in CH_2Cl_2. Due to the poor solubility of 1H,1H,2H,2H-perfluorododecan-1-ol in CH_2Cl_2, a mixture of 1,4-dioxane and trifluoromethylbenzene was used to solubilise the alcohol.

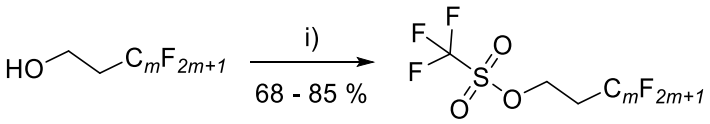

Scheme 3-6: Synthetic procedure to form 1H,1H,2H,2H-perfluoroalkyltrifluoromethanesulfonate starting materials, where *m* = 6, 8 or 10 i) Triflic anhydride, pyridine (in CH_2Cl_2:dioxane), 0 °C, 1 h, N_2.

The triflate moiety is a good leaving group and well-known halogen analogue, and is therefore useful in alkylation reactions. When reaction conditions used previously for this alkylation were implemented (DMF, 90 °C, 16 hours), no alkylated product was formed, but rather an unquantifiable black tar was recovered, and this was also true of high temperature reactions in both acetone and acetonitrile. Evidently, at high temperatures there is some decomposition and so milder conditions were sought. Thus, at room-temperature in acetonitrile, alkylation of 4-hydroxybenzaldehyde and 3,4-dihydroxybenzaldye were successful with all three chain lengths of 1H,1H,2H,2H-perfluoro-octyl, -decyl and -dodecyl. The products proved to be insoluble in acetonitrile and could easily be isolated *via* filtration and washed with water and a further portion of acetonitrile to give the pure products in good yields (70-85%).

The alkylated benzaldehyde was then converted to an acetylene in a two-step Corey-Fuchs reaction. The reactions progressed cleanly and the products were easily isolated and purified by column chromatography. The full three-step synthetic procedure is shown in Scheme 3-7.

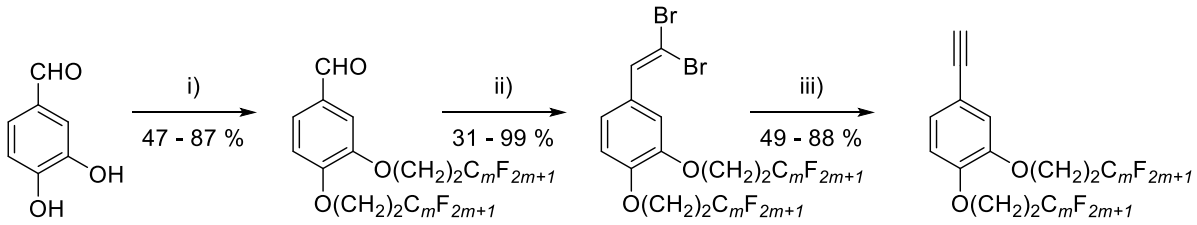

Scheme 3-7: Multistep synthetic procedure to form 4-(1H,1H,2H,2H-perfluoroalkoxy)ethynylbenzene and 3,4-bis(1H,1H,2H,2H-perfluoroalkoxy)ethynylbenzene *via* Williamson-ether and Corey-Fuchs reactions; *m* = 6, 8, 10. i) $TfO(CH_2)_2C_nF_{2n+1}$, K_2CO_3, acetonitrile, 16 h, r.t.; ii) CBr_4, PPh_3, NEt_3, CH_2Cl_2, 30 mins, 0 °C, N_2; iii) EtMgBr, THF, 1 h, r.t., N_2.

As outlined previously, the synthesis of 3,4,5-alkoxysubstituted alkynes requires the addition of two steps to the beginning of the synthetic procedure due the high cost of 3,4,5-trihydroxybenzaldehyde. Utilising the alkylation reaction conditions outlined above, methyl 3,4,5-tri(1H,1H,2H,2H-perfluorooctyloxy)benzoate was successfully synthesised from methyl 3,4,5-trihydroxybenzoate (methyl gallate).

However, for the decyl and dodecyl equivalents, there was no evidence for the triply alkylated product by ^{1}H or ^{19}F NMR spectrometry. Instead, what is observed is the di-substituted product,

suggesting that the insolubility of the di-substituted species in acetonitrile, which was beneficial in isolation of targeted mono- and di-substituted species, resulted in the reaction failing to reach completion. This problem was resolved in the synthesis of methyl 3,4,5-tri(1H,1H,2H,2H-perfluorodecyloxy)benzoate by the alteration of the reaction solvent from acetonitrile to acetone in which the di-substituted species is more soluble, however the reaction to form the dodecyl equivalent was still unsuccessful.

It was observed in the PhD studies of Pamela Martin at the University of York[119] that the addition of benzene to the alkylation reaction of pentabromophenol increased the reaction yield from *ca* 20% to in excess of 75%. It was proposed that this occurred due to the complementary quadrupoles of these species. Using hexafluorobenzene as an idealised complement to benzene (due to the similar nature of the quadrupole to pentabromophenol), the opposing quadrupoles are shown in Figure 3-23. It was observed in 1960 that bringing these two liquid molecules together in the absence of a solvent formed a solid due to the electrostatic effects for the quadrupolar interactions.[120] Benzene was unreactive under the alkylation reaction conditions used by Martin, and it was proposed that the interactions between the complementary rings helped to solubilise the insoluble species through the formation of a complex.

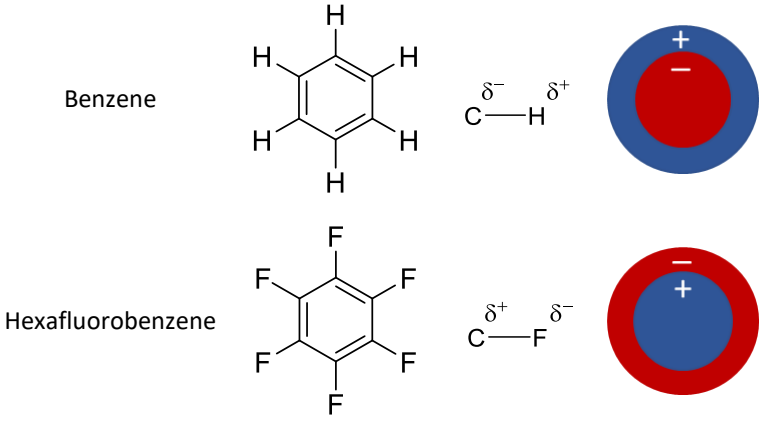

Figure 3-23: Complementary quadrupoles of benzene and hexafluorobenzene

It was suspected that the same effects may be observed with the addition of hexafluorobenzene in this case, that it would be able to solubilise the partially substituted 3,4,5-trihydroxybenzoate due to the formation of a complex between the opposing quadrupoles, allowing the reaction to proceed to completion. The hypothesis appeared well founded, and methyl 3,4,5-tri(1H,1H,2H,2H-perfluorododecyloxy)benzoate was formed in 26% yield when hexafluorobenzene was added as a co-solvent to acetonitrile (Scheme 3-8).

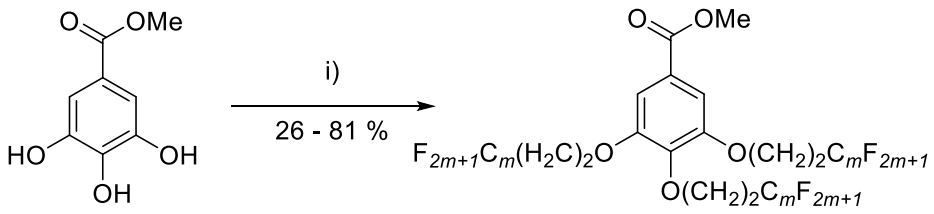

Scheme 3-8: Reaction conditions for the alkylation of methyl 3,4,5-trihydroxybenzoate to form methyl 3,4,5-tri(1H,1H,2H,2H-perfluoroalkyloxy)benzoate. i) $OTf(CH_2)_2C_mF_{2m+1}$, K_2CO_3, *x*, *y* hours, room temperature; where *x* = acetonitrile and *y* = 24 for C8, x = acetone and *y* = 72 for C10 and *x* = 2:1 acetonitrile:hexafluorobenzene and *y* = 72 for C12.

Methyl 3,4,5-tri(1H,1H,2H,2H-perfluoro(alkyloxy)benzoate (where alkoxy is octyloxy and decyloxy) was then reacted with $LiAlH_4$ in CH_2Cl_2, resulting in the complete reduction of the ester group to the benzyl alcohol. Contrary to the reduced temperatures utilised for the hydrocarbon equivalents, the reaction was carried out at room temperature due to the observed precipitation of the esters upon cooling to 0 °C. Poor solubility in THF even at room temperature of methyl 3,4,5-tri(1H,1H,2H,2H-perfluorododecyloxy)benzoate meant the reaction did not progress, with only starting material observed upon work-up. The C12 ester was also not soluble in trifluoromethylbenzene, the common solvent used to solubilise highly fluorinated species,[107] and the addition of hexafluorobenzene was again required for the reaction to progress.

The resulting benzyl alcohol was then re-oxidised with MnO_2 to form the substituted benzaldehyde, which progressed easily in CH_2Cl_2 for the C8 compound. However, for the C10 equivalent, the addition of trifluoromethylbenzene (in a 1:1 ratio with CH_2Cl_2) and heating to reflux was required to solubilise the ester, and even then the yield of the reaction was moderate (51%). (Scheme 3-9). Even with the inclusion of hexafluorobenzene, the replacement of CH_2Cl_2 with the higher boiling $CHCl_3$, and a reaction time of a week under reflux conditions, there was little to no conversion to the benzaldehyde for the dodecyloxy functionalised complexes, and any converted product was exceptionally hard to characterise due to very poor solubility. It was decided not to continue with the synthesis of this ligand and subsequent complexes due to time constraints.

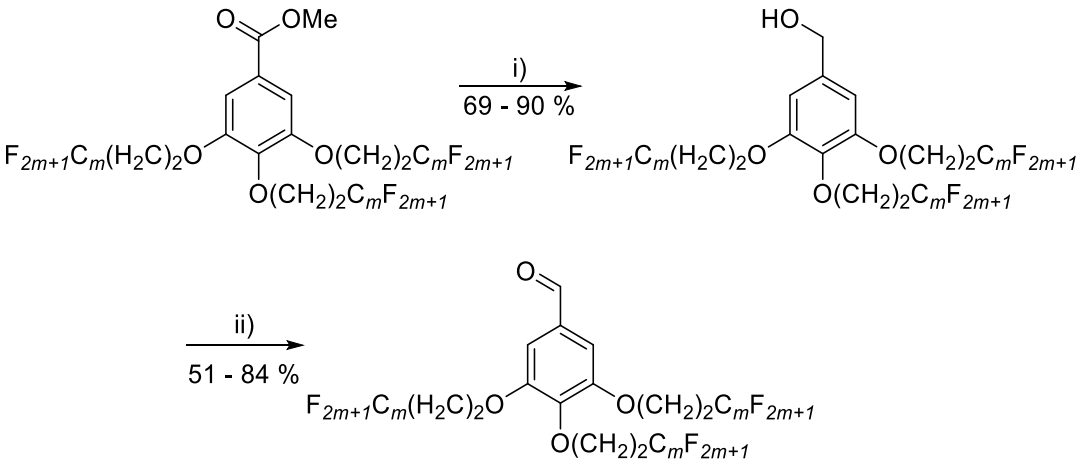

Scheme 3-9: Reaction conditions for the synthesis of 3,4,5-tri(1H,1H,2H,2H-perfluoroalkoxy)benzaldehyde from methyl 3,4,5-tri(1H,1H,2H,2H-perfluoroalkyloxy)benzoate *via* the corresponding benzyl alcohol. i) $LiAlH_4$, *x*, 16 hours, room temperature; ii) MnO_2 (excess), *y*, *a* days, *z*: where *x* = THF for C8 and C10 and 2:1 THF:hexafluorobenzene for C12, *y* = CH_2Cl_2 for C8 and 5:2 CH_2Cl_2:trifluoromethylbenzene for C10, *z* = 1.5 for C8 and 5 for C10, *a* = room temperature for C8 and reflux for C10.

The C8 and C10 substituted benzaldehydes proved to be substantially more soluble in the reaction solvents of CH_2Cl_2 and THF required for subsequent transformations, and the two-step Corey-Fuchs procedure progressed without incident, requiring only the addition of a small amount of benzotrifluoride for the synthesis of the C10 dibromovinyl species.

3.2.4 Synthesis of Gold(III) Chloride Intermediates

The synthesis of gold(III) chloride species with 2,6-diphenylpyridide ligands was reported by Wong *et al.* in 1998.[121] The formation of this complex had previously proven to be elusive, with the difficulty arising from the nature of the two anionic carbon donors on the C^N^C ligand, as these carbanions are strongly σ-donating and do not naturally coordinate in a *trans* confirmation.

To form the desired *trans* confirmation, a two-step metallation process is required. Firstly, the free ligand, **H_2L1** or **H_2L2**, is metallated with mercury acetate, followed by a ligand metathesis with lithium chloride, to form mono-cyclometallated chlorormercury(II) complexes, **Hg-Cl-1** and **Hg-Cl-2** (Scheme 3-10). This mercury complex is then treated with $K[AuCl_4]$ in a trans-metallation reaction, resulting in the *bis*-cyclometallated gold(III) chloride complexes, **Au-Cl-1** and **Au-Cl-2**.

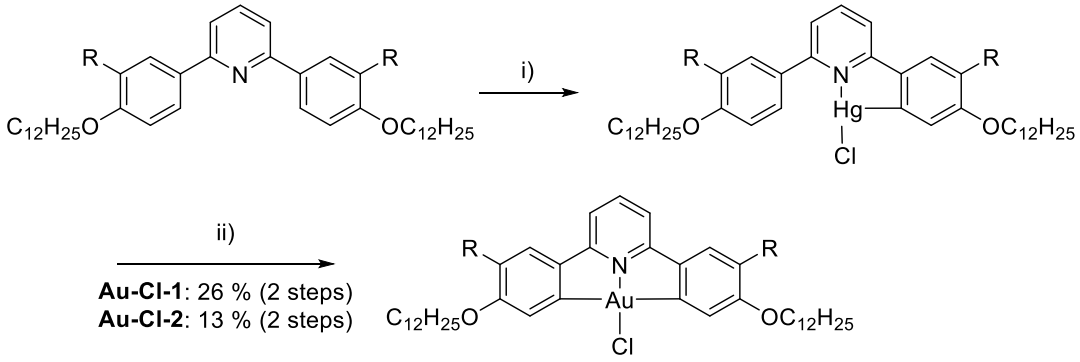

Scheme 3-10: Metallation of **H_2L1** and **H_2L2** with mercury acetate, followed by auration with K[$AuCl_4$] and concomitant C-H activation. R = H for **Au-Cl-1** or $OC_{12}H_{25}$ for **Au-Cl-2** i) $Hg(OAc)_2$, EtOH, 24 h, reflux; LiCl in CH_3OH, heat, 15 mins; ii) K[$AuCl_4$], 1:1 CH_3CN:$CHCl_3$, 24 h, reflux.

In the formation of both species, there was poor conversion to the mercury complex, which has a literature yield limited to 23% (with 2,6-bis(4-tertbutylphenyl)pyridine ligands).[7] For the two-chain species, the unreacted ligand (**H_2L1**) and the mercury complex (**Hg-Cl-1**) had very similar solubilities and R_f values in all chromatographic solvent systems tested. As such, the purification of the mercury complexes proved problematic. From the mixture of **H_2L1** and **Hg-Cl-1**, a large amount of **H_2L1** could be crystallised from the mixture using $CHCl_3$/acetone, but even with multiple crystallisations, there was still always **H_2L1** present. As such, the impure product was taken forward on the rationalisation that the bis-cyclometallated gold complex **Au-Cl-1** would be less soluble due to the increase in rigidity of the planar aromatic core. This proved to be correct, and the **Au-Cl-1** could be isolated from **H_2L1** as a yellow solid after a hot filtration in boiling hexane and was purified subsequently by column chromatography on silica gel with chloroform; crystallisation from CH_2Cl_2/ethyl acetate gave the pure gold(III) complex.

The case was similar for the synthesis of **Au-Cl-2**, however attempts to separate **H_2L2** and **Hg-Cl-2** were wholly unsuccessful. Accordingly, a mixed product of **H_2L2** and **Hg-Cl-2** was taken forward; proportions of each component varied between repeats of this reaction. **Au-Cl-2** proved to be insoluble at room temperature in the vast majority of laboratory solvents excepting chloroform; the purification of **Au-Cl-2** was achieved through recrystallisation from CH_2Cl_2 to give the pure product.

3.2.5 Synthesis of Gold(III) Alkynyl Complexes

3.2.5.1 Gold(III) Alkynyl Complexes with Hydrocarbon Chains

The functionalised alkynyl ligands described in Section 3.2.2, as well as the commercially available phenylacetylene, 1-ethynyl-4-pentylbenzene and 1-ethynyl-4-octylbenzene, were coupled to the

gold(III) chloride intermediates **Au-Cl-1** and **Au-Cl-2** using a literature-based, copper-catalysed coupling reaction (Scheme 3-11).[7, 8] This reaction is well established in the literature, and progresses here without any substantial modifications; the reaction time was increased from three hours[7, 8] to five to ensure complete conversion to the alkynyl complex. The complexes were filtered through Celite, purified by column chromatography on silica gel and were subsequently recrystallised from either acetone or chloroform/acetonitrile to give the pure products in good yields (58-97%).

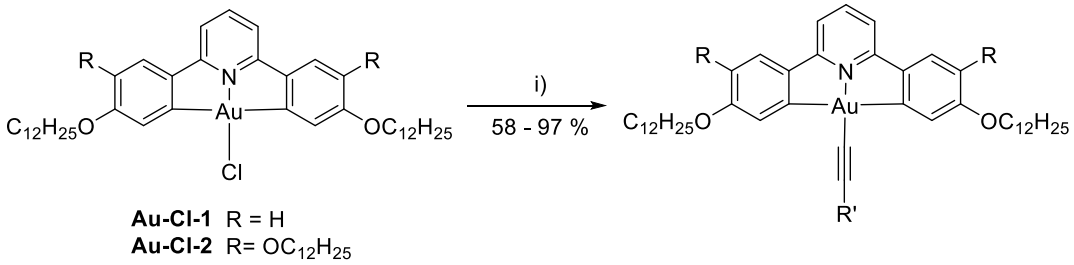

Scheme 3-11: General procedure for the synthesis of final gold(III) alkynyl complexes. i) HC≡C-R' (1.5 equiv), CuI (9 mg), NEt_3 (2 cm^3), CH_2Cl_2, N_2, 5 h, r.t.

The copper-catalysed reaction progresses through the catalytic cycle shown in Figure 3-24, which is not dissimilar to the copper cycle of a Sonogashira reaction. The base in the reaction, in this case triethylamine, reacts with the terminal acetylene ligand in the presence of copper iodide, CuI, to form a copper-acetylide, which then undergoes a trans-metallation reaction with the [Au(C^N^C)Cl] intermediate to form the target complex and regenerate the catalytic species.

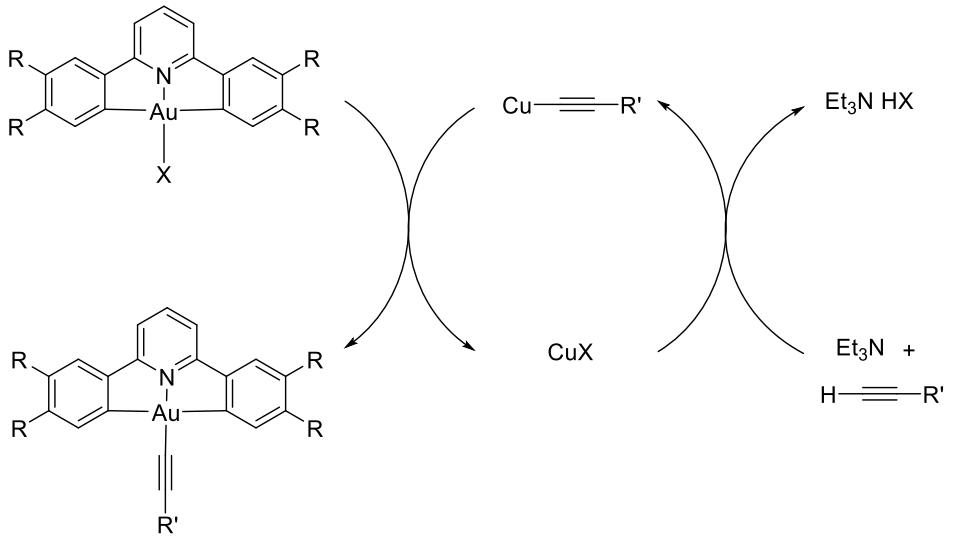

Figure 3-24: Catalytic cycle for the formation of the final gold(III) alkynyl complexes from gold(III) chloride intermediates, where X = Cl or I.

Utilising the alkynyl ligands synthesised above, eight series of complexes have been synthesised, **1-*n*** to **8-*n***, where *n* is the length of the carbon chain on the alkynyl ligand, which can be categorised into two main families based on the C^N^C ligand (Figure 3-25).

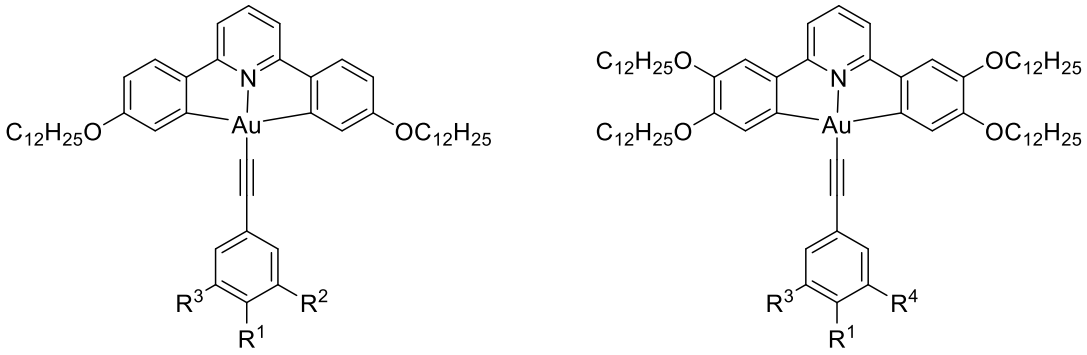

1-*n* R^1 = H, C_5H_{11}, C_8H_{17}; $R^2 = R^3$ = H
2-*n* $R^1 = OC_nH_{2n+1}$; $R^2 = R^3$ = H
3-*n* $R^1 = R^2 = OC_nH_{2n+1}$; R^3 = H
4-*n* $R^1 = R^2 = R^3 = OC_nH_{2n+1}$

5-*n* R^1 = H, C_5H_{11}, C_8H_{17}; $R^2 = R^3$ = H
6-*n* $R^1 = OC_nH_{2n+1}$; $R^2 = R^3$ = H
7-*n* $R^1 = R^2 = OC_nH_{2n+1}$; R^3 = H
8-*n* $R^1 = R^2 = R^3 = OC_nH_{2n+1}$

Figure 3-25: Structure of the gold(III) alkynyl complexes formed. *n* = 8, 10, 12, 14.

All species were isolated as pure materials as evidenced by both ^{1}H NMR spectroscopy (example annotated spectrum of **2-10** shown in Figure 3-27) and CHN analysis (see Chapter 6 for details), with the exception of **3-10**, for which a satisfactory ^{1}NMR spectrum was observed but the elemental analysis showed a 0.9% difference in the calculated and observed values for carbon, which could not be improved upon through multiple purification cycles and even persisted when the complex was re-synthesised. The origin of this impurity is unknown but it was the only formally impure material for a series of 30 complexes. While the impurity may affect the (photo)physical properties, the working hypothesis is that any deviations will be minor and this will be taken into account as required in subsequent discussion.

Complexes utilising the 4-ethynylpyridine ligand, **9-N** and **10-N** (Figure 3-26) were synthesised *via* the same procedure, although it should be noted that for **10-N**, the complex with four chains on the cyclometallating ligand, elevated temperatures were required for the reaction to progress. The reasons for this are unclear, as the synthesis of **9-N** carried out at room temperature shows the reaction is possible with this ligand under standard conditions.

Initially, these complexes were synthesised with the intention of coordinating the nitrogen atom of the pyridine ring to a further metal centre to form multi-metallic systems. However, initial attempts did not result in air or temperature stable complexes, thus these efforts were not pursued and so shall not be discussed further; **9-N** and **10-N** therefore stand alone and shall be compared to the phenylacetylene analogues **1-H** and **5-H** in thermal behaviour.

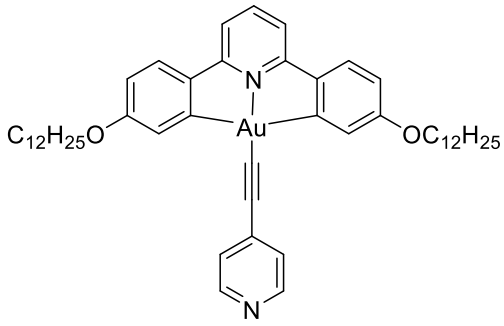

9-N

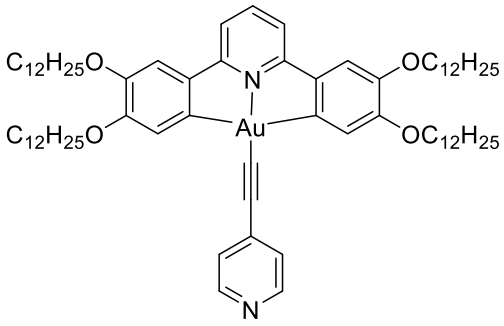

10-N

Figure 3-26: Structure of gold(III) alkynyl complexes with 4-ethynylpyridine

Both **9-N** and **10-N** appeared highly pure by ^{1}H NMR spectroscopy, and **9-N** formed a highly crystalline solid after recrystallisation however both complexes performed poorly when subjected to CHN elemental analysis, with a 1.0% and 1.5% difference between the calculated and observed values of carbon, respectively. It was suspected that an impurity has coordinated to the free nitrogen of the 4-ethynylpyridine ligand which has distorted the elemental analysis, such as water, trace amounts of metal ions from contaminated reagents or perhaps it has been protonated, although there is no evidence of this in the ^{1}H NMR spectrum or crystal structure.

All of the gold(III) alkynyl complexes were novel and investigated for their liquid-crystalline and emissive properties, as presented in Section 3.4.1 and Chapter 4.

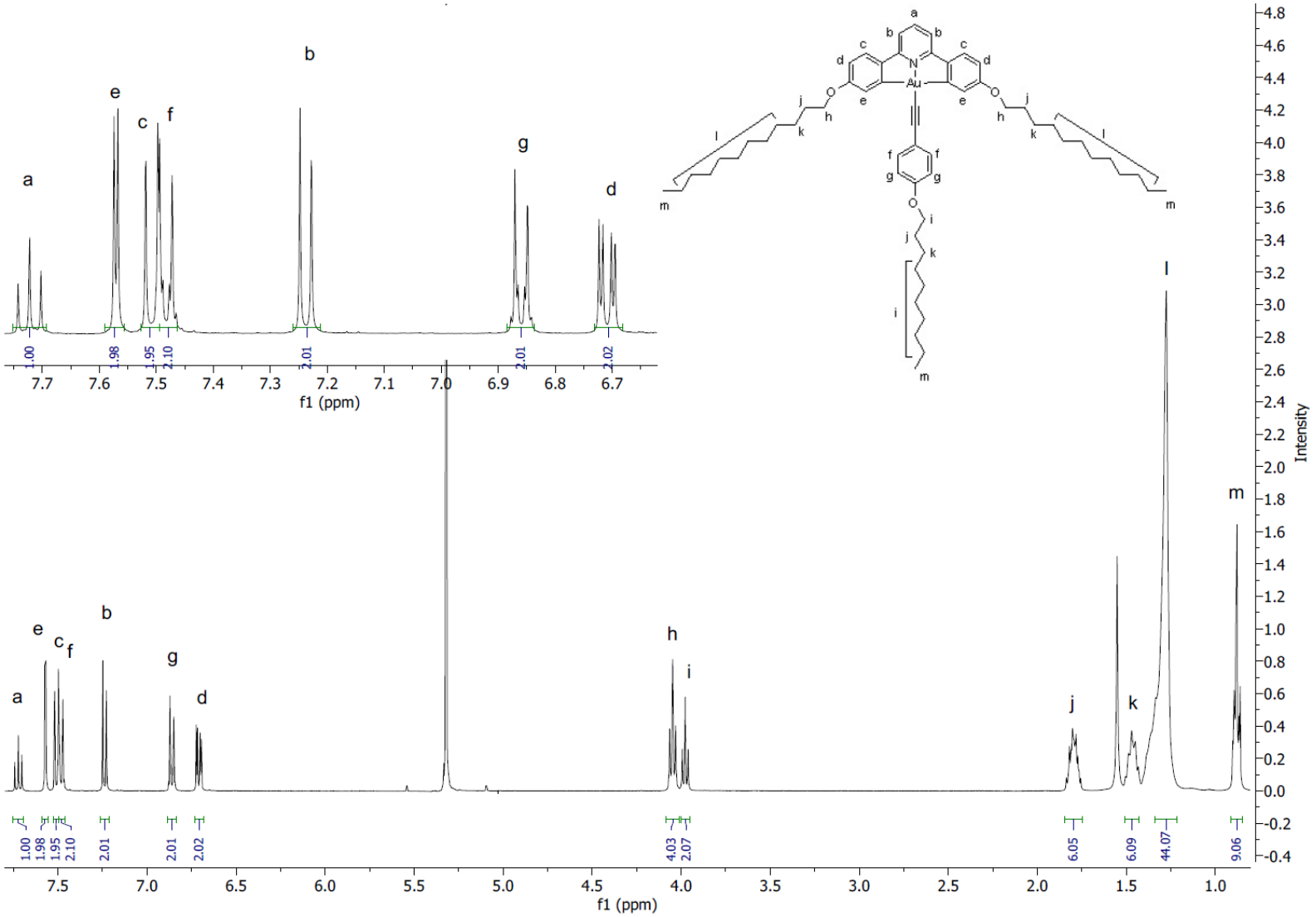

Figure 3-27: Annotated ^{1}H NMR spectrum of **2-10**, with inset structure and aromatic region

3.2.5.2 Gold(III) Alkynyl Complexes with Semi-Perfluorinated Chains

Synthesis of the target semi-perfluorinated gold(III) alkynyl complexes was achieved through the copper-catalysed coupling of the terminal perfluorinated alkyne, as synthesised above, and the corresponding gold-chloride intermediate, **Au-Cl-1** or **Au-Cl-2**, in the presence of NEt_3 in CH_2Cl_2, as described in Section 3.2.5.1. The only required modification of this procedure was to increase the reaction temperature from room temperature to 40 °C to accommodate the reduced solubility of the perfluorinated ligands.

The structure and naming system of the final target complexes are outlined in Figure 3-28. In contrast to the free ligands, complexes **11-*n*** to **16-*n*** show good solubility in $CHCl_3$ and CH_2Cl_2, and are formed in good yield. All complexes were purified by column chromatography on silica gel and crystallised from hexane.

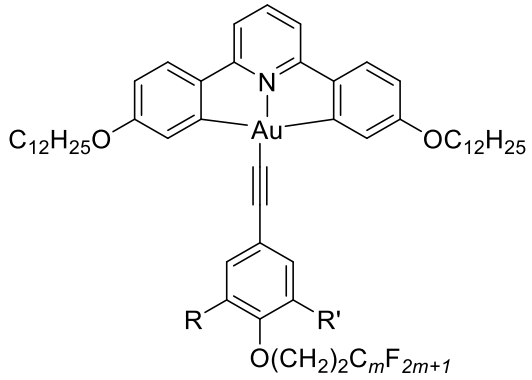

11-*n*: R = R' =H
12-*n*: R = H, R' = $O(CH_2)_2C_mF_{2m+1}$
13-*n*: R = R' = $O(CH_2)_2C_mF_{2m+1}$

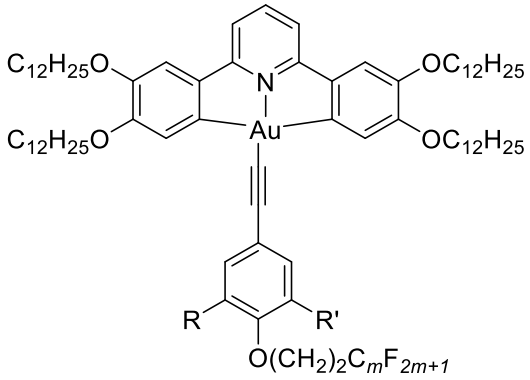

14-*n*: R = R' =H
15-*n*: R = H, R' = $O(CH_2)_2C_mF_{2m+1}$
16-*n*: R = R' = $O(CH_2)_2C_mF_{2m+1}$

Figure 3-28: Structure of final semi-perfluorinated gold(III) alkynyl complexes.

Satisfactory elemental analyses for these species was harder to achieve than for the hydrocarbon analogues; many species gave good data, however there was a 0.7% difference for **12-10** and **12-12** with respect to carbon content, a 0.9% difference for **14-8** and **15-12,** and **11-12** and **14-12** proved even worse with differences of 1.5%. The materials were pure as observed by ^{1}H and ^{19}F NMR spectra, and complexes were recrystallised multiple times and filtered through low porosity filters and Celite to remove any solid contamination. It is known that highly fluorinated species are often difficult to combust fully and can give erroneous elemental analysis results and it was observed that for some of these species that the data from individual analyses (to give a final averaged value) were often quite different. Thus, the high level of fluorination in these species may be the origin of the poor data.

Conspicuously, the majority of the failed samples are for complexes with 1*H*,1*H*,2*H*,2*H*-perfluorododecyloxy chains, which is consistent with increasing difficulty in accurate elemental analyses result as the levels of fluorination increases. However, it was observed that for complexes synthesised with a specific batch of 1*H*,1*H*,2*H*,2*H*-perfluorododecan-1-ol, integration of the resonances in the ^{19}F NMR spectra tended to be slightly low (compared to the integration of the resonance for the terminal CF_3 group of the chain).

Subsequent mass spectrometry experiments also indicated the presence of further species, with a peak spacing of 100 m/z, which corresponds to two CF_2 groups. This spacing was observed for complexes with one perfluorinated chain (**11-12** and **14-12**). For those complexes for two perfluorinated chains (**12-12** and **15-12**), three signals were observed, each at a spacing of 100 m/z. It is therefore proposed that an impure batch of 1*H*,1*H*,2*H*,2*H*-perfluorododean-1-ol was provided, containing a small amount of the C10 equivalent which has skewed the elemental analyses; this would also account for both the inaccurate resonance integration, as well as the mass spectrometry spacings. For **11-12** and **14-12**, with a single perfluorinated chain, there is the presence of **11-10** and **14-10**, respectively, within the sample (spectrum of **11-12** shown in Figure 3-29). For **12-12** and **15-12**, which have two perfluorinated chains per complex, there is the presence of **12-10** and **15-10**, respectively, which arise 200 m/z lighter than **12-12** and **15-12**, respectively, as well as the equivalent complexes with one C12 and one C10 chain each, detected at 100 m/z lighter than **12-12** and **15-12**. This problem was discovered at too late a stage to correct the issue through re-synthesis with a pure batch of starting material.

Full characterisation data, including elemental analyses, for all complexes is given in Chapter 6.

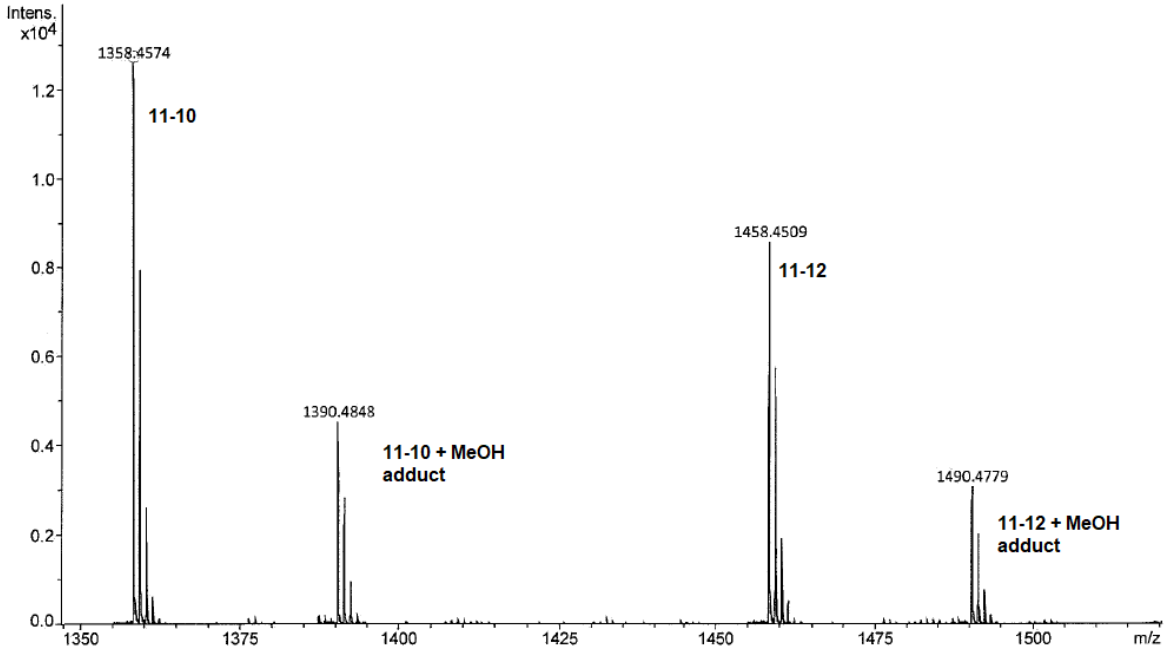

Figure 3-29: Mass spectrum of **11-12** showing the presence of **11-10**.

3.3 Single Crystal Structures of Au-Cl-1, 1-H, 1-5 and 9-N

Single crystals suitable for X-ray diffraction were grown of **Au-Cl-1**, **1-H**, **1-5** and **9-N** through vapour diffusion techniques. A summary of the X-ray diffraction data is shown in Table 3-2.

Crystals of **Au-Cl-1** were grown through vapour diffusion of ethyl acetate into a solution of **Au-Cl-1** in CH_2Cl_2; the resulting crystal structure is shown in Figure 3-30. **Au-Cl-1** crystallised in the *P-1* space group with three molecules in the asymmetric unit. The structure is highly symmetric, with both Au-C bonds equal within 3 standard errors (2.033(9) and 2.072(9) Å) and the same orientation of the oxygen atoms around the C-O-C alkoxy linkage. The Au-N and Au-Cl bond lengths are not abnormal when compared to known values for similar systems[7] with values of 2.008(8) and 2.286(3) Å, respectively. The square-planar geometry is distorted from the ideal 90° and 180° due to the pre-arranged bite angle of the diphenylpyridine ligand, with N^Au^C angles of 82.7(4)° and 81.4(4)°, which, again, are the same within standard error and a C^Au^C angle of 164.2(4)°. There are no significant differences between the three molecules in the asymmetric unit.

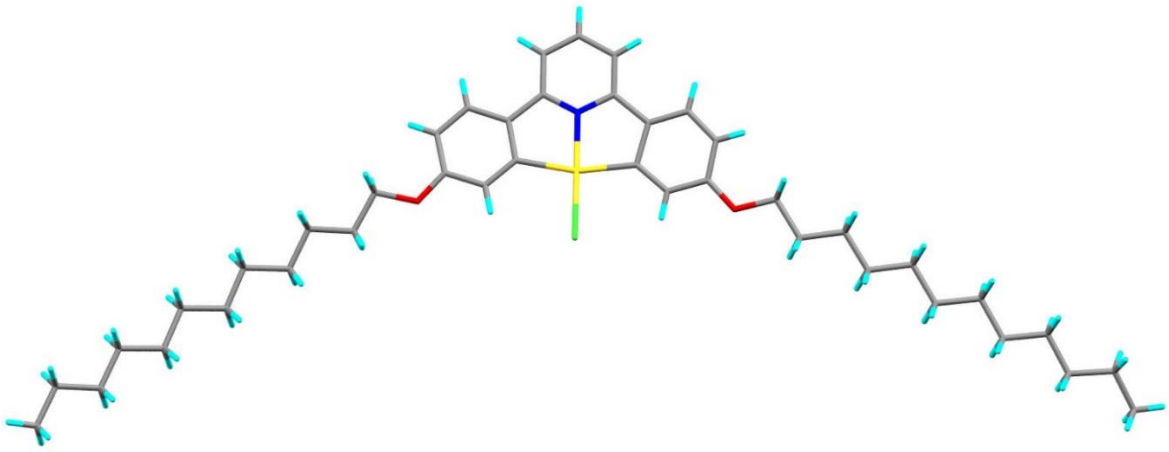

Figure 3-30: Single crystal structure of **Au-Cl-1**. Carbon atoms are shown in grey, hydrogen in cyan, gold in yellow, chlorine in green, nitrogen in blue and oxygen in red. A single molecule of the asymmetric unit is shown.

When the packing of the structure is viewed, the molecules arrange in anti-parallel layers with full interdigitation of the alkoxy chains, resulting in a 2D layered structure (Figure 3-31a). This arrangement is the most favourable with respect to space filling packing forces for the appended alkoxy chains, which possess a large amount of flexibility and many degrees of freedom. When the structure is viewed after a 90° rotation about the *x*-axis, it can be seen that the molecules are arranged in a discrete layered structure, with an undulation throughout the layers (Figure 3-31b). Intermolecular π-π interactions are present between the complexes in the interdigitated 2D layers; the cores of molecules in adjacent layers are arranged anti-parallel to one another, with an

inter-core distance of 3.87 Å for the two rings of the C^N^C ligand which overlap (between centroids 1 and 4, and 2 and 3 on neighbouring molecules, Figure 3-31c).

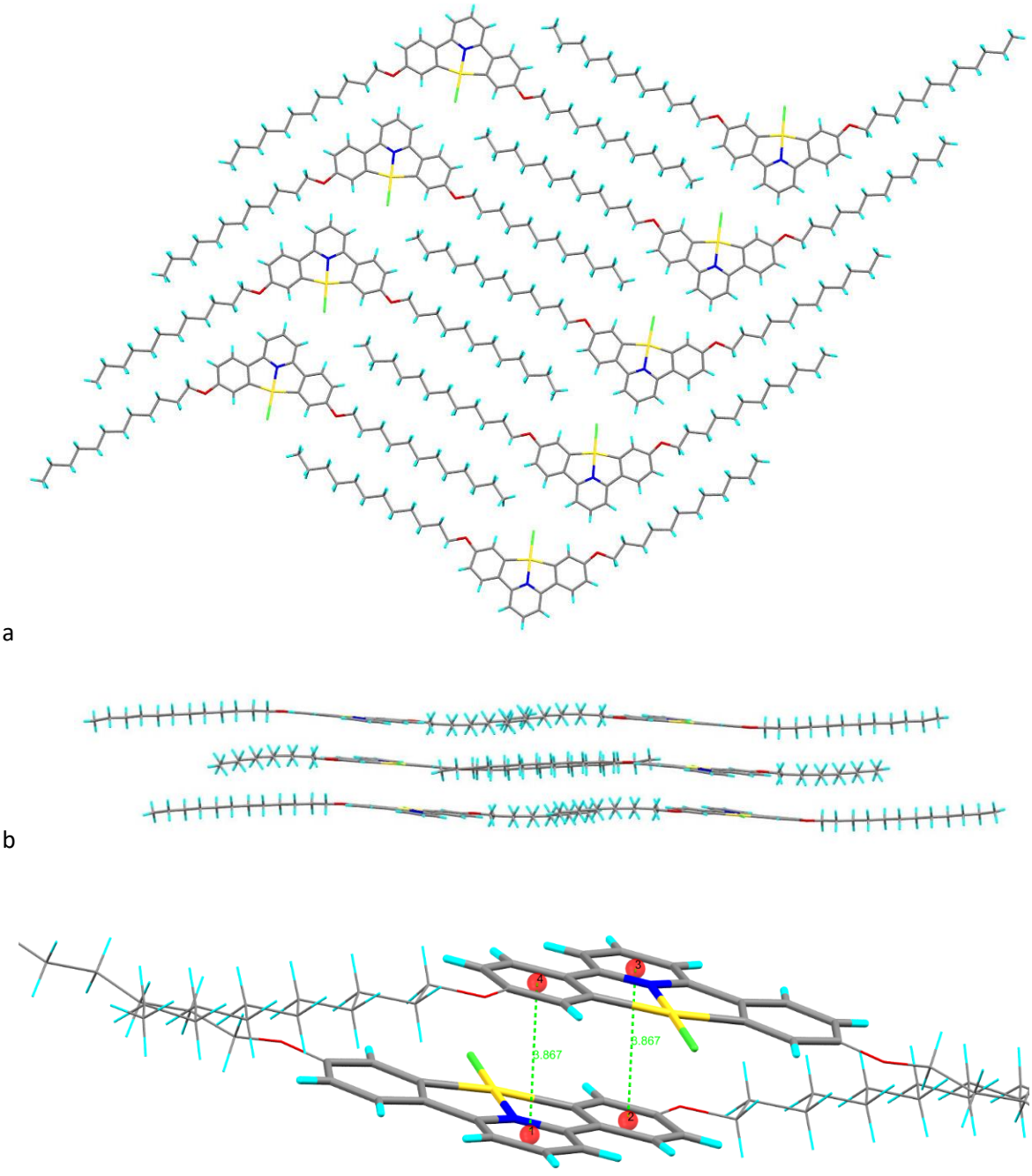

Figure 3-31: Single crystal structure of **Au-Cl-1** showing a) interdigitation of the alkoxy chains to form an anti-parallel lamellar structure; b) the undulating waved structure of the molecules; c) distance between anti-parallel molecules in adjacent layers showing π-π stacking (chains reduced to wireframe and partially cropped for clarity). Carbon atoms are shown in grey, hydrogen in cyan, gold in yellow, chlorine in green, nitrogen in blue and oxygen in red. A single molecule of the asymmetric unit is shown.

Crystals of **1-H** and **1-5** were both grown from vapour diffusion of acetone into CH_2Cl_2 and their structures are remarkably similar in terms of both packing and arrangement. Both crystallise in *P-1*

with two molecules in the asymmetric unit (Figure 3-32 and Figure 3-33), but unlike in **Au-Cl-1**, the orientation of the peripheral chains are unsymmetric with respect to the C-O-C linkage between the ring and the chain, resulting in a distorted structure from the symmetric ideal. For **1-H**, there is no difference between the two Au-C bond lengths of 2.083(9) and 2.097(9) Å when three standard deviations are taken into account, and the Au-N bond length of 2.002(6) is again within the expected range. The deviation from ideal square-planar geometry is retained as the C^N^C ligand is unaltered, with N^Au^C angles of 81.5(3)° and 81.2(3)° and C^Au^C angle of 162.8(4)°. The Au-C bond length of the alkynyl ligand is significantly shorter than that of the Au-C bonds lengths on the C^N^C ligand (1.966(7) Å), and is similar to bond lengths for known gold(III) alkynyl systems.[7, 9-11, 13, 15, 110, 122, 123] The C≡C bond length of 1.177(11) Å is similar to that of other transition metal alkynyl complexes. [124-134]

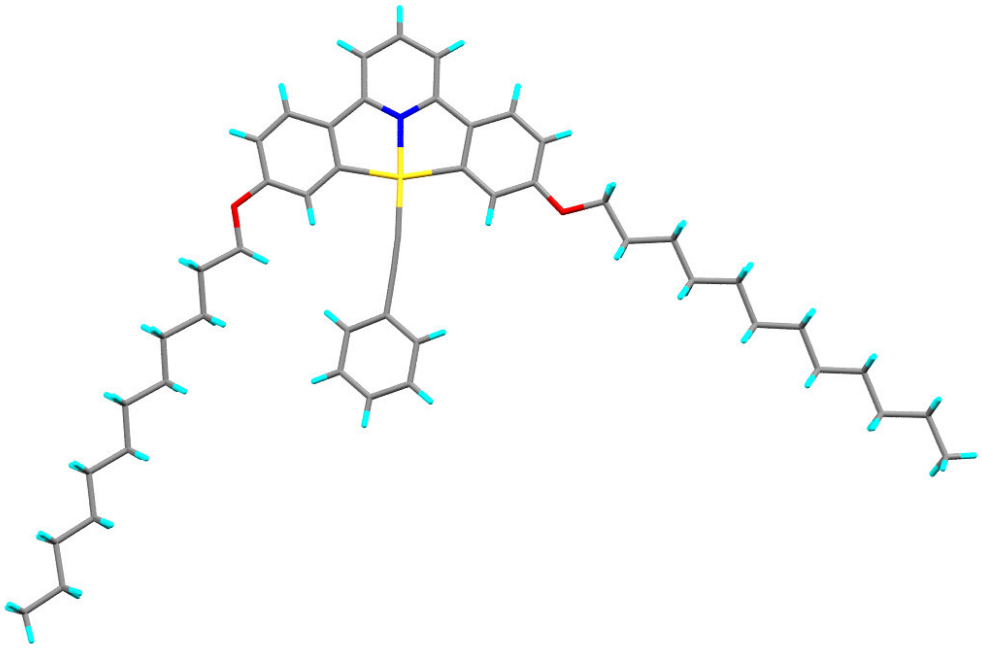

Figure 3-32: Single crystal structure of **1-H**. Carbon atoms are shown in grey, hydrogen in cyan, gold in yellow, nitrogen in blue and oxygen in red. A single molecule of the asymmetric unit is shown.

The structural parameters for **1-5** are not dissimilar to those for **1-H**, with Au-$C_{(py)}$ bond lengths of 2.050(6) and 2.056(6) Å for the C^N^C ligand, a N-Au bond length of 2.008(5) Å, a Au-$C_{(C\equiv C)}$ bond length of 1.973(6) Å and a C≡C bond length of 1.170(9) Å for the alkynyl ligand, and a deviation from 90° of the N^Au^C angles (81.3(2)° and 81.6(2)°), and from 180° for C^Au^C (162.9(3)°).

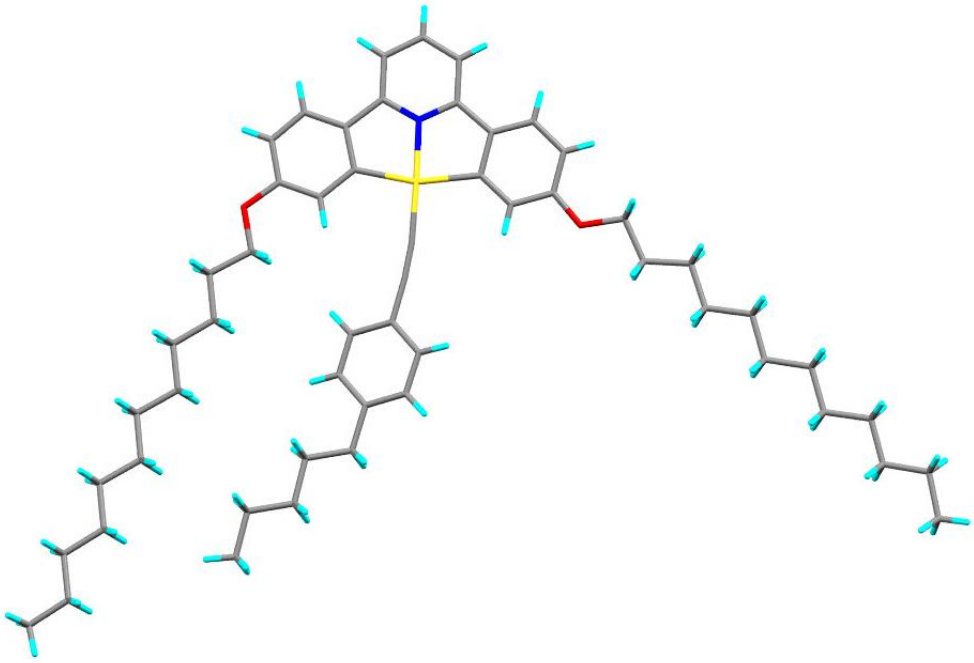

Figure 3-33: Single crystal structure of **1-5**. Carbon atoms are shown in grey, hydrogen in cyan, gold in yellow, nitrogen in blue and oxygen in red. A single molecule of the asymmetric unit is shown.

For both **1-H** and **1-5**, there is a distinctive bend in the geometry of the alkynyl ligand; idealised alkynyl structures usually depict this as linear, with bond angles of 180° from the metal centre to the beginning of the alkynyl R group, in this case the phenyl ring. In reality, this bond has a good degree of flexibility in transition metal complexes.[7, 9-11, 13, 15, 110, 122-134] In the case of **1-H** and **1-5**, the Au-C≡C bond angle is given as 173.2(7)° and 173.4(5)°, respectively. Within the asymmetric unit, the molecules are arranged anti-parallel to one another, in the same way that was observed for **Au-Cl-1**. It is in this arrangement that the origin of the alkynyl bend is realised; the C12 alkoxy chain of the neighbouring complex molecule lies parallel to that of the primary molecule, filling the space in which the alkynyl ligand would occupy if the bond angle was 180°. As the packing of the molecules is driven by the interdigitation of the chains, it is more favourable for the alkynyl ligand to adopt this confirmation. This is shown in Figure 3-34a, using **1-5** as an exemplar structure.

In contrast to **Au-Cl-1**, when the 2D layers of **1-H** and **1-5** stack, the molecular associations lead to a parallel arrangement, with the neighbouring molecules in the 2D sheets above and below all orientated in the same direction. The core-to-core contacts between these molecules are also further apart; the distance between centroids in the case of **1-H** and **1-5** are too far removed to be considered π-π stacking, with a distance of over 5 Å (Figure 3-34b). The packing of these structures is considered to be fully driven by space-filling forces.

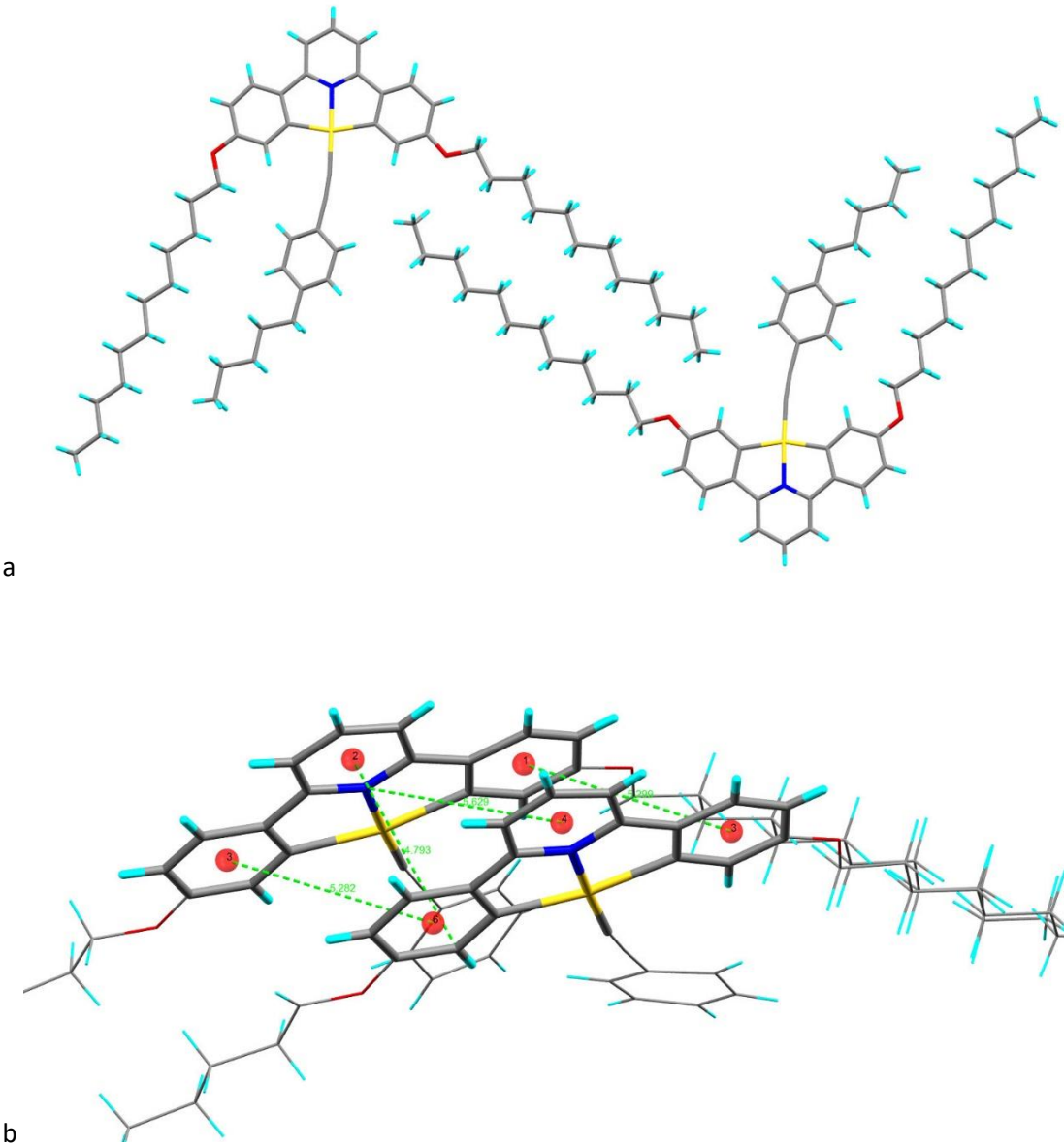

Figure 3-34: Single crystal structure of **1-5**, showing a) two neighbouring molecules and the how the space filling results in a bend from the linear plane of the alkynyl ligand; b) distances between molecules in neighbouring layers which are outwith the distances for π-π stacking. Carbon atoms are shown in grey, hydrogen in cyan, gold in yellow, nitrogen in blue and oxygen in red. A single molecule of the asymmetric unit is shown.

In contrast to the structures of the other gold(III) complexes discussed above, **9-N** crystallised in a monoclinic space group, $P2_1/n$, with one molecule in the asymmetric unit, although the key bond lengths and angles remain unchanged with the inclusion of a pyridine ring over a phenyl ring; the Au-C bond lengths for the coordinated C^N^C ligand are 2.038(6) and 2.067(6) Å, with a Au-N bond length of 2.005(5), a Au-C alkynyl bond length of 1.957(6) and a C≡C bond length of 1.192(9) Å, and N^Au^C angles of 81.1(2)° and 81.8(2)°. As with **1-H** and **1-5**, the alkynyl ligand is bent from the plane of the molecule, with a Au-C≡C bond angle of 174.7(5)° arising from the packing of the alkoxy chain from an adjacent molecule.

Complex **9-N** shows a comparitively exaggerated packing motif, with a significant 'zig-zag' arising from interactions between the free nitrogen group of the 4-ethynylpyridine ligand and the hydrogen atom in the 4-position of the C^N^C pyridine ring. (Figure 3-35).

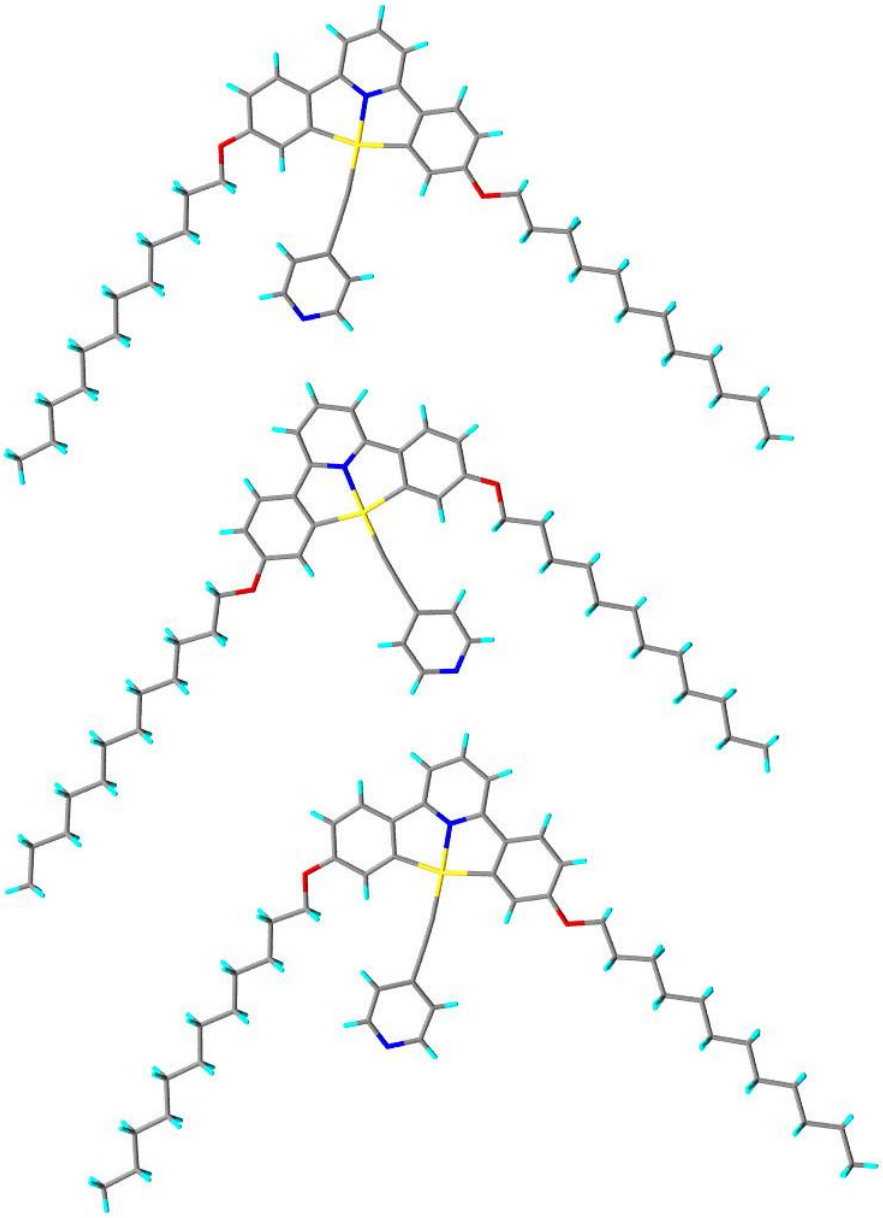

Figure 3-35: Single crystal structure of **9-N**, showing three neighbouring molecules packing in a 'zig-zag' due to interaction between the free nitrogen group of the 4-ethynylpyridine group and the hydrogen atom in the 4-position of the C^N^C pyridine ring. Carbon atoms are shown in grey, hydrogen in cyan, gold in yellow, nitrogen in blue and oxygen in red.

The 'zig-zag' organisation of single molecules pack together with full interdigitation of the alkoxy chains, as before, to form a 2D, planar layer (Figure 3-36). As with **1-H** and **1-5**, the layers stack with individual molecules in the neighbouring layers parallel at a distance that suggests no π-π stacking.

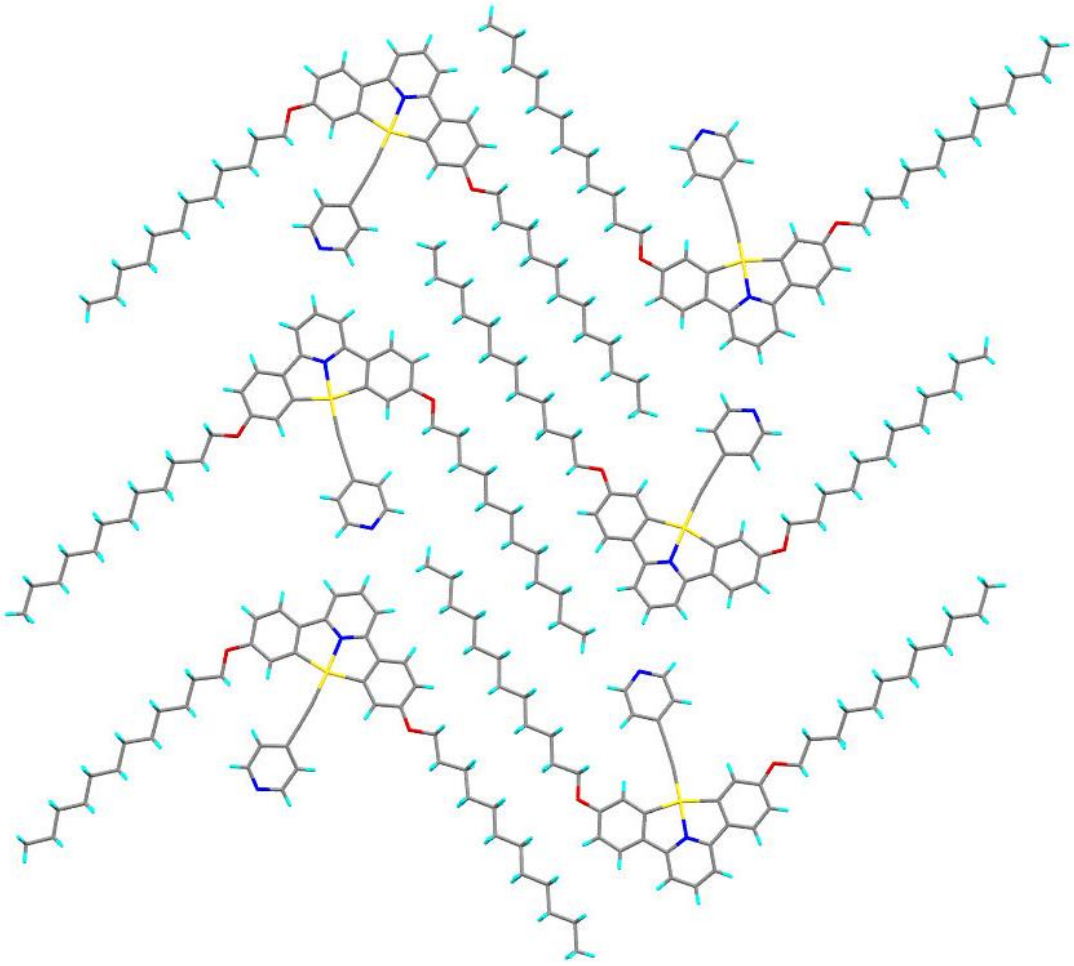

Figure 3-36: Single crystal structure of **9-N**, showing three neighbouring molecules in the 'zig-zag' arrangement packing with the neighbouring molecular chain to form a 2D layer. Carbon atoms are shown in grey, hydrogen in cyan, gold in yellow, nitrogen in blue and oxygen in red.

Unfortunately, all complexes with longer chains and a greater number of chains were highly amorphous, and no single crystals could be grown; this applied to all complexes which had four dodecyloxy chains on the cyclometallating ligand. However, in the research of Olga Vodianova, a visiting researcher, single crystals of a complex with four chains on the cyclometallating ligand (**Au4-BODIPY**) were grown, and proved suitable for X-ray diffraction. This complex was based on the same core moiety as those discussed in this chapter, [Au(C^N^C)(C≡CR)], however the phenylethynyl ligand was functionalised with a boron-dipyrromethane (BODIPY) group. The structure is shown in Figure 3-37 and for relevance and clarity, the BODPY group, single disordered dodecyloxy chain and solvents of crystallisation have been removed.

Due to the presence of the large BODIPY group, packing arrangements and interactions are irrelevant to this work and will not be discussed. This extends to the orientation of the alkynyl ligand, the phenyl ring of which is rotated out of the plane of the molecule, in contrast to the complexes shown above. However, the behaviour of the aromatic core and peripheral chains can be considered.

The core parameters do not deviate from those observed for the two-chain complexes above, with N-Au-C bond angles of 81.15(9) and 80.96(9), Au-N distance of 1.9925(19), and Au-$C_{(py)}$ distances of 2.072(2) and 2.059(2). What is most relevant to analyse in this structure is the orientation of the dodecyloxy chains. With respect to the C-O-C bonds, neighbouring chains are orientated in an *anti* arrangement so that the chains are directed away from one another. This is thought to be the least sterically hindered organisation. It is noticeable that only one of the four chains is fully extended, in the broadest sense, as observed for all chains in the complexes above, while the others show a very minor degree of folding. This observation, coupled with the fact that one of the chains showed a high level of disorder, is indicative of the flexibility and free rotation of the chains prior to crystallisation. Essential bond angles are tabulated in Table 3-1 for all five structures, showing that the core moiety is invariant to the nature of the alkynyl ligand.

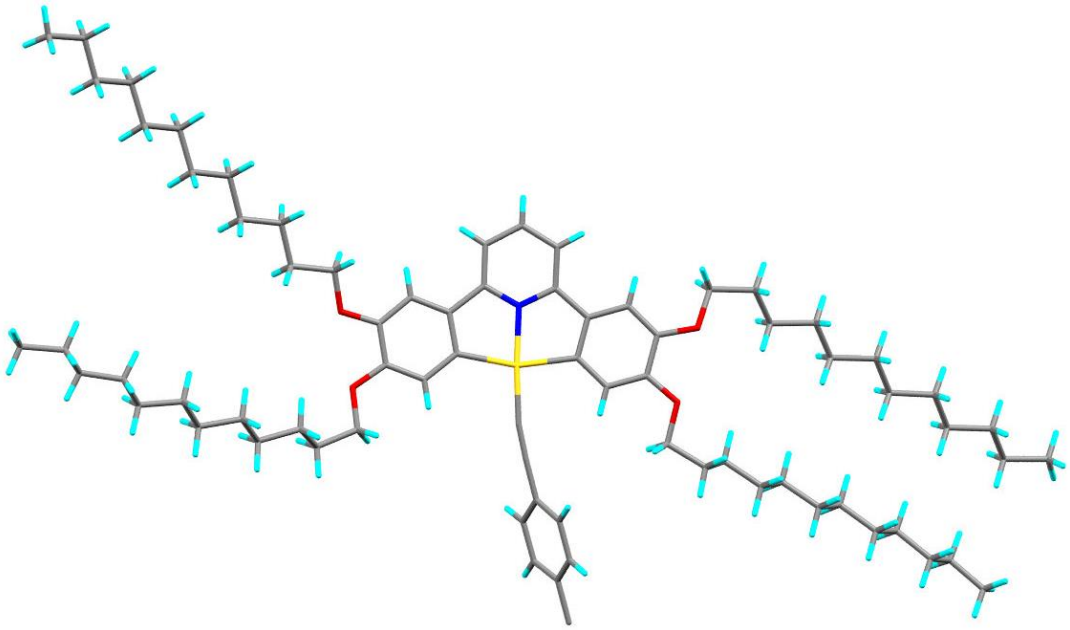

Figure 3-37: Single crystal structure of a related four-chain complex **Au4-BODIPY**. Solvent of crystallisation, disorder of a single alkoxy chain and BODIPY moiety are omitted for clarity. Carbon atoms are shown in grey, hydrogen in cyan, gold in yellow, nitrogen in blue and oxygen in red.

Table 3-1: Bond angles and distances for the central gold(III) moiety for **Au-Cl-1**, **1-H**, **1-5**, **9-N and Au4-BODIPY.**

Complex	N-Au-C bond angle (°)		Au-$C_{(py)}$ bond length (Å)		Au-N bond length (Å)	Au-$C_{(C\equiv C)}$ bond length (Å)
Au-Cl-1	82.7(4)	81.4(4)	2.033(9)	2.072(9)	2.008(8)	-
1-H	81.5(3)	81.2(3)	2.083(9)	2.097(9)	2.002(6)	1.996(7)
1-5	81.3(2)	81.6(2)	2.050(6)	2.056(6)	2.008(5)	1.973(6)
9-N	81.1(2)	81.8(2)	2.038(6)	2.067(6)	2.005(5)	1.957(6)
Au4-BODIPY	81.15(9)	80.96(9)	2.072(2)	2.059(2)	1.9925(19)	1.967(3)

It should be noted that for structures of **1-H**, **1-5** and **9-N** there are large areas of residual electron density (Q peaks) approximately 1.95 Å from the carbon atom *ortho* to one of the cyclometallated carbanions (Figure 3-38). An attempt was made to model this as disorder and, given the distance from the nearest carbon atom, it was suspected that this may have been a small, minor structure where there was a carbon-chlorine bond, or, given the proximity to the alkynyl triple bond, that a copper atom, added as CuI in the coupling reaction to form the gold(III) alkynyl, may have coordinated to the alkynyl. Attempts to model this as disorder were unsuccessful, resulting in an unstable structural refinement, and the R value was higher for the disordered structure than that where the free electron density was untreated.

It was also observed that there was a distortion in the ADP of carbon atoms C1 and C4 in these structures (not apparent in Figure 3-38 due to restraint commands applied in the refinement to deal with this issue). It is proposed that this distortion is a direct result of the large area of electron density, and that all three points (C1, C4 and Q1) arise from a minor twin present in the structures. This twin was could not be modelled and is thought to be correlated to suspected slippage throughout the crystal.

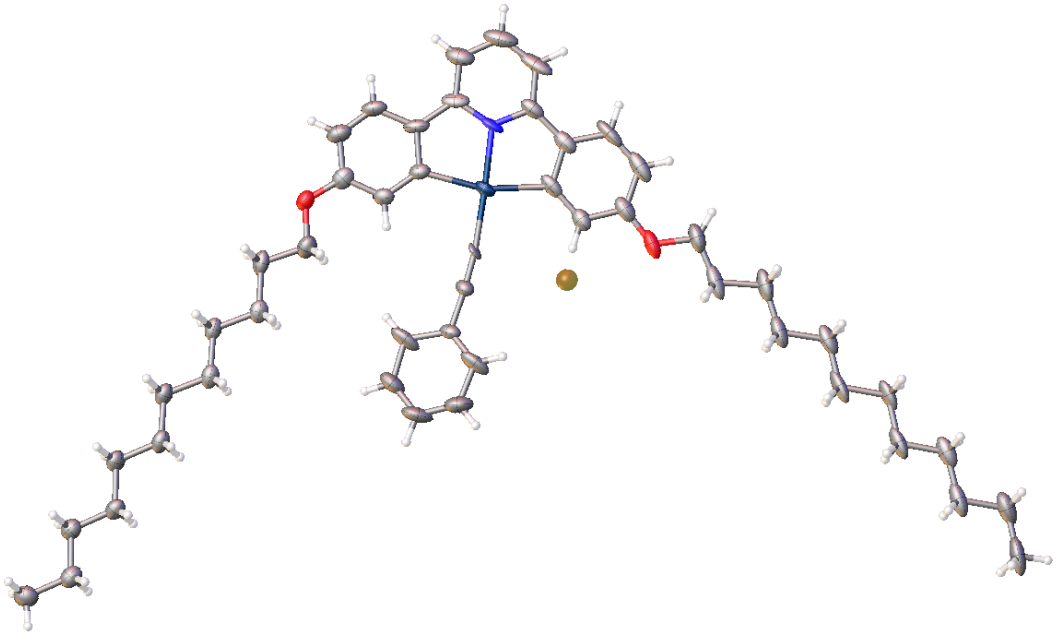

Figure 3-38: Single crystal structure of **1-H**, showing large area of residual electron density (large Q peak) in light brown. Carbon atoms are shown in grey, hydrogen in white, gold in dark blue, nitrogen in light blue and oxygen in red.

Table 3-2: Summary of X-ray diffraction data for **Au-Cl-1, 1-H**, **1-5** and **9-N**.

Complex	**Au-Cl-1**	**1-H**	**1-5**	**9-N**
Empirical formula	$C_{41}H_{59}AuClNO_2$	$C_{49}H_{63}AuNO_2$	$C_{54}H_{74}AuNO_2$	$C_{48}H_{63}AuN_2O_2$
Formula weight	830.30	894.97	966.10	896.97
Temperature/K	110.05(10)	110.05(10)	109.95(10)	110.05(10)
Crystal system	triclinic	triclinic	triclinic	monoclinic
Space group	*P*-1	*P*-1	*P*-1	$P2_1/n$
a/Å	10.0951(4)	12.7876(5)	13.7316(4)	5.96170(10)
b/Å	19.5688(6)	14.4385(7)	13.9293(4)	29.5987(3)
c/Å	29.1623(8)	23.1895(10)	26.4188(6)	23.6907(3)
α/°	97.315(2)	87.661(4)	86.646(2)	90
β/°	95.911(3)	77.162(4)	86.841(2)	95.2020(10)
γ/°	99.572(3)	86.370(4)	66.516(3)	90
Volume/Å^3	5589.0(3)	4164.6(3)	4623.9(2)	4163.21(10)
Z	6	4	4	4
ρ_{calc}g/cm^3	1.480	1.427	1.388	1.431
μ/mm^{-1}	8.336	6.928	6.279	6.938
F(000)	2544.0	1836.0	2000.0	1840.0
Crystal size/mm^3	0.467 × 0.059 × 0.053	0.288 × 0.062 × 0.045	0.214 × 0.079 × 0.058	0.233 × 0.142 × 0.078
Radiation	CuKα (λ = 1.54184)	CuKα (λ = 1.54184)	CuKα (λ = 1.54184)	CuKα (λ = 1.54184)
2θ range for data collection/°	7.142 to 134.154	7.1 to 134.16	6.924 to 134.136	7.05 to 134.158
Index ranges	-11 ≤ *h* ≤ 11, -23 ≤ *k* ≤ 23, -23 ≤ *l* ≤ 34	-15 ≤ *h* ≤ 15, -17 ≤ *k* ≤ 17, -19 ≤ *l* ≤ 27	-16 ≤ *h* ≤ 16, -16 ≤ *k* ≤ 16, -24 ≤ *l* ≤ 31	-7 ≤ *h* ≤ 6, -35 ≤ *k* ≤ 24, -28 ≤ *l* ≤ 28
Reflections collected	20716	29085	48560	27899
Independent reflections	15577 [R_{int} = 0.0523, R_{sigma} = 0.0939]	14876 [R_{int} = 0.0451, R_{sigma} = 0.0595]	16525 [R_{int} = 0.0402, R_{sigma} = 0.0427]	7417 [R_{int} = 0.0413, R_{sigma} = 0.0363]
Data/ restraints/ parameters	15577/0/1231	14876/0/953	16525/0/1051	7417/0/480
Goodness-of-fit on F^2	1.050	1.032	1.044	1.038
Final R indexes [I>=2σ (I)]	R_1 = 0.0606, wR_2 = 0.1413	R_1 = 0.0599, wR_2 = 0.1516	R_1 = 0.0492, wR_2 = 0.1159	R_1 = 0.0438, wR_2 = 0.1036
Final R indexes [all data]	R_1 = 0.0831, wR_2 = 0.1598	R_1 = 0.0805, wR_2 = 0.1740	R_1 = 0.0663, wR_2 = 0.1301	R_1 = 0.0537, wR_2 = 0.1112
Largest diff. peak/hole / e Å^{-3}	4.70/-1.87	8.73/-2.46	4.98/-2.33	5.05/-0.99

The data gleaned from these crystal structures are very useful in probing the molecular interactions in the solid state. Although it is unwise to equate solid-state configurations to other states of matter, these data can be used to estimate parameters such as molecular lengths which may aid with insight into the liquid-crystalline properties of these systems.

3.4 Liquid-crystalline Properties of Gold(III) Complexes

3.4.1 Gold(III) Alkynyl Complexes with Hydrocarbon Chains

3.4.1.1 Complexes with Two Chains, *1-n* to *4-n*

Complex **Au-Cl-1** shows an ordered lamellar phase between 91.9 and 159.8 °C. When observed by polarising optical microscopy (POM), the texture formed shows no identifiable defects, but is birefringent and quite fluid (Figure 3-39a). The small-angle X-ray scattering (SAXS) pattern of the phase shows three orders of lamellar spacing with a *d*-spacing of 30.7 Å. There is also a weak reflection at 8.9 Å which is tentatively assigned as a gold-gold contact. Upon closer inspection, in the wide-angle region of the pattern, there appear to be a large number of weak reflections, indicating a phase with a high degree of order. This is consistent with the large clearing enthalpy of 26.8 kJ mol^{-1} which is an order of magnitude larger than that typically observed for a mesophase to isotropic transition. Given the fluidity observed in microscopy, as well as the reproducibility of the phase transitions when subjected to multiple heating and cooling cycles by differential scanning calorimetry, it is proposed that it is a true mesophase, but not a true liquid-crystal due to the high degree of order.

The transition temperatures and enthalpies for complexes **Au-Cl-1**, **1-*n*** and **2-*n***, are shown in Table 3-3, and the structural parameters from SAXS measurements are shown in Table 3-4.

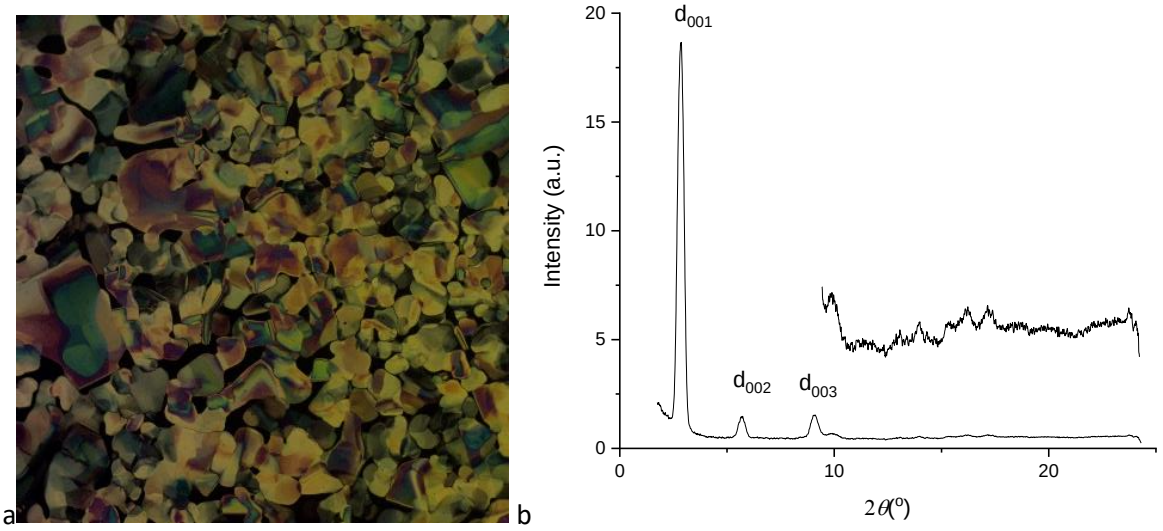

Figure 3-39: a) texture of **Au-Cl-1** at 158.2 °C on cooling from the isotropic liquid and b) corresponding SAXS pattern at 155.0 °C on cooling from the isotropic liquid.

Table 3-3: Transition temperatures and enthalpies of **Au-Cl-1**, **1-*n*** and **2-*n***

Complex	Transition	*T* (°C)	Δ*H* (kJ mol^{-1})
Au-Cl-1	Cr-Lam	91.9	37.4
	Lam-Iso	159.8	28.6
1-H	Cr-Iso	71.2	57.2
1-5	Cr-Cr	45.3	1.9
	Cr-Cr	53.3	12.0
	Cr-Iso	68.2	8.2
1-8	Cr-Col$_h$	57.0	16.3
	Col$_h$-Iso	69.0	1.7
2-8	Cr-Iso	101.8	38.2
	(Iso-Col$_h$)	(90.6)	(3.6)
2-10	Cr-Iso	102.5	32.2
2-12	Cr-Iso	95.9	34.8
2-14	Cr-Iso	101.8	34.4

Table 3-4: X-ray diffraction data **Au-Cl-1**, **1-*n*** and **2-*n***, presenting the measured and calculated spacing, Miller indices and calculated parameters (where applicable).

Complex	Phase	2θ/ °	d_{obs} /Å	d_{calc}/ Å	*hkl*	*a*/ Å
Au-Cl-1	Lam *T* = 155.0 °C cooling	2.87	30.7	30.7	001	-
		5.73	15.4	15.4	002	
		9.14	9.7	10.2	003	
		9.92	8.9			
		13.95	6.3			
		16.13	5.5			
		17.26	5.1			
1-8	Col$_h$ *T* = 60.4 °C cooling	3.04	29.0	29.0	10	33.5
2-8	Col$_h$ *T* = 80.0 °C cooling	3.01	29.3	29.3	10	33.8

Complexes **1-H** and **1-5** are not liquid-crystalline, showing only a simple melting point into the isotropic liquid, whereas **1-8** shows a liquid-crystalline phase between 56.7 and 68.2 °C which has a featureless texture by microscopy (Figure 3-40a) and only a single reflection in the SAXS pattern, with a *d*-spacing of 29.0 Å (Figure 3-40b). This is the only sharp reflection observed even with a

very slow heating rate and extended irradiation times, however there is a broad reflection at approximately 9.5 Å which could be due to gold-gold spacing. No identifiable defects were observed when **1-8** was aligned in homeotropic and planar cells that could further assist in phase identification. However, the mesophase of **1-8** proved to be miscible with **3-10**, which has a columnar hexagonal phase, and thus is assigned as the same.

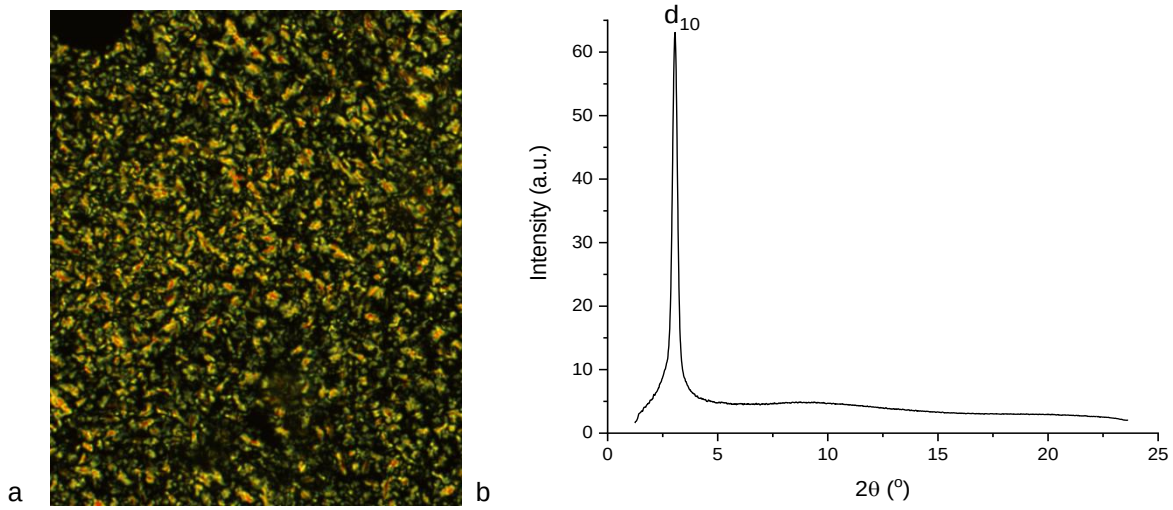

Figure 3-40 a) photomicrograph of Col_h phase of **1-8** at 70.7 °C on cooling from the isotropic liquid and b) corresponding SAXS pattern at 66.0 °C on cooling from the isotropic liquid.

In the **2-*n*** series, complex **2-8** shows a monotropic columnar hexagonal phase between 90.6 and 76.3 °C. As with **1-8**, only a single reflection is observed in the SAXS pattern and the microscopy texture shows no identifiable defects, but the complex is miscible with **3-10**, confirming its identity. However, none of complexes **2-10**, **2-12** and **2-14** are liquid-crystalline, which is surprising. For example, the only difference between **1-8** and **2-10** is an oxygen and two methylene groups yet mesomorphism is suppressed. Interestingly, the Col_h phase of **2-8** is more stable than that of **1-8**, with a clearing temperature of 69.0 °C for **1-8** and 90.6 °C for **2-8**, yet the crystal phase stability shows the inverse relationship, with a melting point of 57.0 °C for **1-8** and 101.8 °C for **2-8**.

Complexes of **3-*n***, which have a 3,4-dialkoxyphenylethynyl co-ligand, show columnar hexagonal phases for all complexes (Table 3-5, Table 3-6). When observed by POM, **3-10**, **3-12** and **3-14** show a phase that is strongly birefringent, has a high level of fluidity and has a texture that contains small, straight-line defects (Figure 3-41a); this is contrast to that of **3-8**, in which the texture is poorly birefringent. However, the DSC trace of **3-8** shows clear and repeatable phase transitions with a clearing point of 103.8 °C. For all four complexes, the assignment as a columnar hexagonal phase is done so through the SAXS pattern, which shows the d_{01}, d_{11} and d_{20} reflections at a spacing of 1:√3:√4 (Figure 3-41b), although the d_{20} reflection is not observed for **3-8** and **3-10**. As the chain length increases, the melting point increases from 75.7 to 82.8 °C and the clearing point decreases

from 103.8 to 100.1 °C, although there is a slight increase for complex **3-10** to 104.9 °C, indicating a relative insensitivity to the chain length.

On cooling **3-10** shows a monotropic columnar hexagonal phase with an onset temperature of 43.3 °C which has a larger *d*-spacing to the enantiotropic Col_h phase (31.3 to 33.3 Å). On the second heating cycle, a further Col_h phase is observed, with a *d*-spacing of 37.2 Å. These transitions are also observed by DSC, showing small transition enthalpies of 1.5 and 1.2 kJ mol^{-1}, respectively.

Table 3-5: Transition temperatures and enthalpies of **3-*n***

Complex	Transition	*T* (°C)	Δ*H* (kJ mol^{-1})
3-8	Cr-Cr	67.2	12.3
	Cr-Col_h	75.7	45.3
	Col_h-I	103.8	5.3
3-10	Cr-Cr	71.8	7.9
	Cr-Col_h^1	77.9	39.1
	Col_h^1 -Iso	104.9	5.8
	(Col_h^1 – Col_h^2)	(43.3)	(1.5)
	Col_h^2-$Col_h^{3\dagger}$	50.6	1.2
3-12	Cr-$Col_h^{\ddagger}$	77.5	40.0
	Col_h -Iso	101.8	3.9
3-14	Cr-Cr	74.9	21.3
	Cr-Col_h	82.8	7.2
	Col_h-I	100.1	3.9

†observed on second heating cycle; ‡overlapping Cr-Cr and Cr-Col_h peaks

a 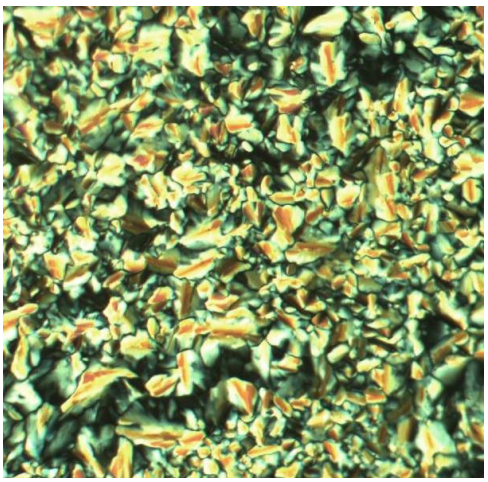 b 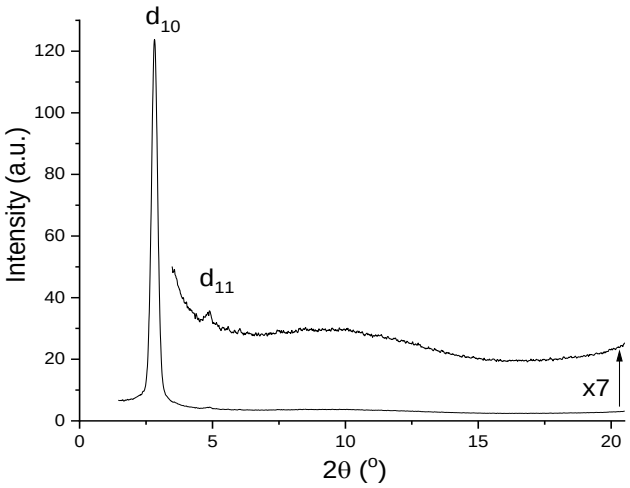

Figure 3-41 a) photomicrograph of Colh phase of **3-10** at 106.7 °C on cooling from the isotropic liquid and b) corresponding SAXS pattern at 80.0 °C on cooling from the isotropic liquid.

Table 3-6: X-ray diffraction data **3-*n***, presenting the measured and calculated spacing, Miller indices and calculated parameters (where applicable).

Complex	Phase	2θ/ °	d_{obs} /Å	d_{calc}/ Å	*hk*	*a*/ Å
3-8	Col_h *T* = 51.1 °C cooling	2.83	31.2	31.2	10	36.0
		4.90	18.0	18.0	11	
3-10	Col_h[1] *T* = 80 °C cooling	2.82	31.3	31.3	10	36.1
		4.88	18.1	18.1	11	
	Col_h[2] *T* = 30 °C cooling	2.65	33.3	33.3	10	38.5
		4.62	19.1	19.2	11	
	Col_h[3] *T* = 60 °C 2nd heating	2.74	32.2	32.2	10	37.2
		4.78	18.5	18.6	11	
3-12	Col_h *T* = 80.0 °C cooling	2.64	33.4	33.4	10	38.6
		4.57	19.3	19.3	11	
		5.24	16.8	16.7	20	
3-14	Col_h *T* = 95 °C heating	2.68	32.9	32.9	10	38.0
		4.61	19.1	19.0	11	

For the trialkoxyphenylethynyl-substituted complexes, **4-*n***, all four homologues for *n* = 8, 10, 12, 14 show columnar phases (Table 3-7, Table 3-8). For **4-8**, this is identified as a columnar rectangular phase, with a texture that is markedly different to those observed for any of the Col_h phases seen in other materials (Figure 3-42a). Both the d_{11} and d_{20} reflections are observed in the SAXS pattern, as well as a few less-intense reflections which are indexed as d_{31}, d_{33} and d_{53} (Figure 3-42b). Due to the lack of reflections in the pattern, the symmetry of the Col_r phase could not be assigned, but the lattice parameters can be determined, with *a* = 59.8 Å and *b* = 44.9 Å, significantly larger than for any of the Col_h phases.

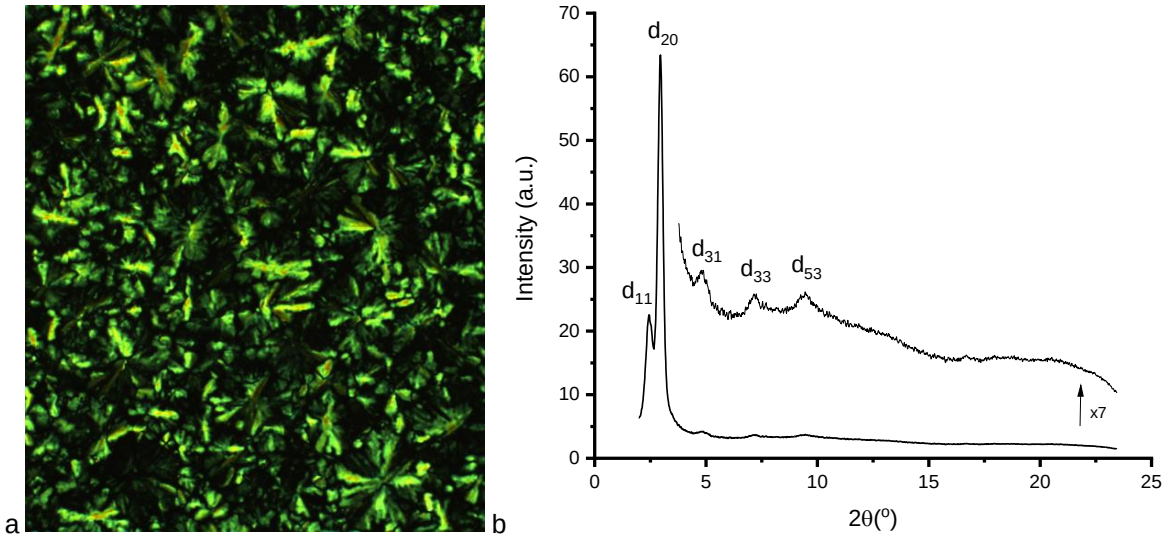

Figure 3-42: a) photomicrograph of Colr phase of **4-8** at 82.7 °C on cooling from the isotropic liquid and b) corresponding SAXS pattern at 60.4 °C on cooling from the isotropic liquid.

Table 3-7: Transition temperatures and enthalpies of **4-*n***

Complex	Transition	*T* (°C)	Δ*H* (kJ mol^{-1})
4-8	Cr-Col$_r$	55.0	3.9
	Col$_r$-I	80.7	22.9
4-10	Cr-Cr	64.6	1.3
	Cr-Col$_r$	79.8	13.9
	Col$_r$-Col$_h$	88.3†	5.7†
	Col$_h$-I	96.7†	2.9†
4-12	Cr-Cr	57.8	0.8
	Cr-Col$_r$	78.1	16.9
	Col$_r$-Col$_h$	95.7	32.7
	Col$_h$ -Iso	102.1	-
4-14	Cr-Cr	52.7	2.2
	Cr-Col$_h$	77.9	53.4
	Col$_h$ -Iso	88.0	3.0
	(Col$_h$ – Col$_r$)	(77.8)	(2.9)

†observed on second heating cycle; ‡ not observed by DSC

Complex **4-10** shows both rectangular and hexagonal columnar phases, with the Col$_r$ phase occurring at lower temperatures. On heating, the Col$_r$ phase is observed between 79.8 and 88.3 °C, with the clearing point observed at 96.7 °C, although the Col$_r$-Col$_h$ transition and clearing point were indistinguishable on the first heating cycle; these values were determined on the second heating cycle. On cooling, both phases are well defined and easily characterised by SAXS; the Col$_r$ phase shows a pattern very similar to that of **4-8**, but with slightly larger lattice parameters (*a* = 62.3 Å and *b* = 48.3 Å) which may be accounted for by the increased chain length.

Complex **4-12** is very similar to **4-10**, showing both a rectangular and hexagonal columnar phase on both heating and cooling. The Col$_r$ phase is observed over a larger temperature range (78.1 to 95.7 °C) with an increased clearing point of 102.1 °C. Again, there is a small increase in both lattice parameters (*a* = 65.6 Å and *b* = 51.1 Å), with the incremental difference approximately consistent as previously observed which can be attributed to the lengthening of the alkyl chains. The transition between the Col$_r$ and Col$_h$ at 102.1 °C has a large enthalpy of 32.7 kJ mol^{-1}, indicating a significant change in molecular organisation between the two phases, and the clearing point is not observed by DSC, which could suggest that the Col$_h$ phase is relatively disordered.

Table 3-8: X-ray diffraction data **4-*n***, presenting the measured and calculated spacing, Miller indices and calculated parameters (where applicable).

Complex	Phase	2θ/ °	d_{obs} /Å	d_{calc}/ Å	*hk*	*a*, *b*/ Å
4-8	Col_r	2.46	35.9	35.9	11	*a* = 59.8
	T = 60.4 °C	2.95	29.9	29.9	20	*b* = 44.9
	cooling	4.82	18.3	18.2	31	
		7.27	12.1	11.9	33	
		9.45	9.3	9.3	53	
4-10	Col_h	2.84	31.1	31.1	10	*a* = 35.9
	T = 75 °C	4.91	18.0	18.0	11	
	cooling					
	Col_r	2.30	38.4	38.4	11	*a* = 63.2
	T = 50 °C	2.79	31.6	31.6	20	*b* = 48.3
	cooling	4.54	19.4	19.3	31	
		6.78	13.0	12.8	33	
		8.97	9.8	9.7	05	
		12.55	7.0	7.1	65	
		11.2	7.9	7.8	55	
		12.6	7.0	7.0	46	
4-12	Col_r	2.19	40.3	40.3	11	*a* = 65.6
	T = 83.8 °C	2.69	32.8	32.8	20	*b* = 51.1
	cooling	3.46	25.4	25.5	02	
		4.34	20.3	20.1	31	
		6.48	13.6	13.8	42	
		7.50	11.8	11.8	43	
		8.67	10.2	10.2	05	
		9.59	9.2	9.2	63	
		10.64	8.3	8.2	26	
	Col_h	2.78	31.7	31.7	10	*a* = 36.6
	T = 86.1 °C	4.81	18.3	18.3	11	
	cooling	5.67	15.6	15.8	20	
4-14	Col_h	2.65	33.3	33.3	10	*a* = 38.5
	T = 79.0 °C	4.58	19.3	19.2	11	
	cooling	5.28	16.7	16.7	20	
	Col_r	2.12	41.6	41.6	11	*a* = 67.2
	T = 60 °C	2.63	33.6	33.6	20	*b* = 53.0
	cooling	4.56	19.4			
		5.27	16.7	16.8	40	
		6.29	14.0	13.9	33	
		8.33	10.6	10.7	53	
		10.32	8.6	8.6	46	

Complex **4-14** shows only a columnar hexagonal phase on heating, with a melting point the same as that of **4-12**, and a Col_h phase that clears at 88.0 °C, showing it to be much less stable than that of **4-10** and **4-12**. Complex **4-14** also displays a monotropic columnar rectangular phase below the Col_h phase on cooling with an onset temperature of 77.8 °C.

The transition temperatures for series **1-*n*** to **4-*n*** are also shown graphically in Figure 3-43. It should be noted that for complex **2-8**, the melting point is shown as a horizontal bar, and the monotropic Col_h phase in blue. The onset temperature on cooling of the Col_h is plotted, but as the crystallisation of this complex is not a thermodynamic transition, but rather under kinetic control, the crystallisation is omitted. Consequently, the crystalline phase is not shown and neither is the true phase range of the monotropic phase; crystallisation occurs at 77.3 °C.

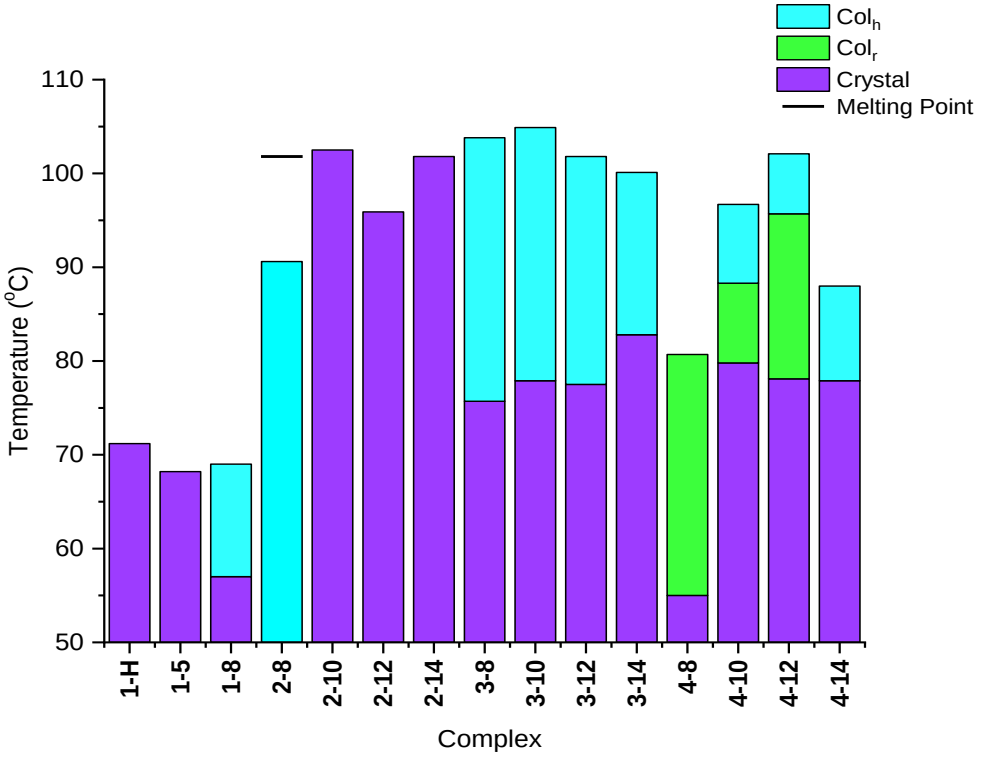

Figure 3-43: Transition temperatures and phases for **1-*n*** to **4-*n*** on heating, with crystal phases shown in purple, Col_r in green and Col_h in blue. The melting point of **2-8** is shown as a black bar.

From this representation, it is clear that the addition of individual alkoxy chains, *i.e.* moving from **2-*n*** to **4-*n*** has a significant impact on both the stability of the phases formed and the symmetry of the columnar phases that are observed. It is obvious that a certain level of functionalisation of the alkynyl ligand has to be achieved to stabilise the formation of any mesophase, but given that **2-8** shows a monotropic Col_h phase, although metastable, and the longer chain lengths of the same series are not liquid-crystalline, it is not a clear chain-functionalised threshold that must be exceeded, but rather a delicate balance between number and length of chains. This is also apparent in the observation of Col_r phases only for the most functionalised series of the family, **4-*n***, which,

when considered as a homologous series, as the chain length increases, the formation of a Col_r phase is disfavoured and the Col_h phase is dominant; **4-8** shows only a wide ranging Col_r phase, whilst in **4-14**, the Col_r is only metastable and the observation of the Col_h is dominant. It is proposed that the destabilisation of the Col_r arises from the successively larger space occupied by the extending fluid alkoxy chains and their locational removal from the stacked cores of the molecule, resulting in a larger columnar cross-section and a higher level of fluidity, which gives way to a more favourable disordered Col_h phase.

3.4.1.2 Complexes with Four Chains, 5-*n* to 8-*n*

In contrast to these complexes, the phase behaviour of the complexes with four chains on the cyclometallating ligand is rather uniform, in as much as all complexes in the **5-*n*** to **8-*n*** series show a columnar hexagonal phase.

It is worth noting that the gold(III) chloride intermediate in this family, **Au-Cl-2**, does not show any liquid crystalline behaviour. This is surprising, given that that the less functionalised gold(III) chloride species **Au-Cl-1** with two chains shows the aforementioned lamellar mesophase, and that all other species with four-chains show a columnar hexagonal phase; a possible reason for this lack of phase behaviour is described below within the discursive element of this section.

For the **5-*n*** series (transitions temperatures and enthalpies shown in Table 3-9, structural parameters from X-ray shown in Table 3-10), when increasing the length of the alkyl chain from **5-H** to **5-8**, there is a destabilisation in the crystal lattice, as noted by the decrease in the melting point, and a significant increase in the stability of the Col_h phase, shown by an increase in the clearing point from 105.9 to 185.0 °C. All three complexes in this series show straight-line defects in the POM textures, which are characteristic of a Col_h phase (Figure 3-44), and clearly show d_{10}, d_{11} and d_{20} reflections in the SAXS pattern. There is also an increase in the lattice parameter, a, when increasing the chain length from 25.7 to 27.6 Å, which is most likely a result of the space required to accommodate the longer alkoxy chains, although the a values for **5-5** and **5-8** are similar (27.3 and 27.6 Å), indicating that that inter-columnar distance for these materials is the same at these chain lengths.

Table 3-9: Transition temperatures and enthalpies of **5-*n***

Complex	Transition	*T* (°C)	ΔH (kJ mol^{-1})
5-H	Cr-Col$_h$	87.7	57.7
	Col$_h$-I†	105.9	-
5-5	Cr-Col$_h$	74.0	28.8
	Col$_h$-I†	179.8	-
5-8	Cr-Col$_h$	71.4	62.8
	Col$_h$-I†	185.0	-

†not observed by DSC

a 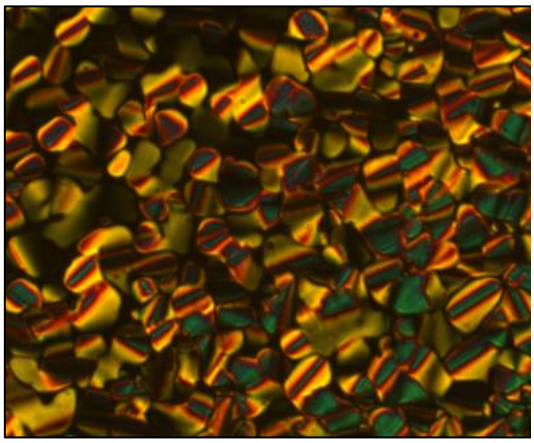 b 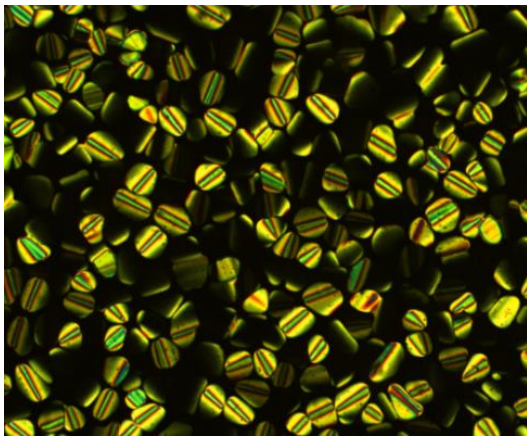

c 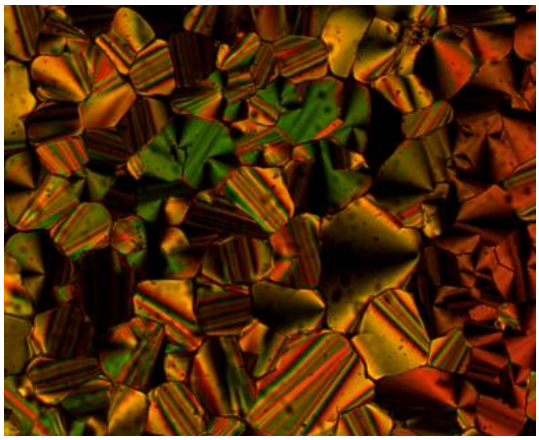

Figure 3-44: Photomicrographs of textures of a) **5-H** at 92 °C on heating; b) **5-5** at 140 °C on cooling; c) **5-8** at 132 °C on cooling.

Table 3-10: X-ray diffraction data **5-*n***, presenting the measured and calculated spacing, Miller indices and calculated parameters (where applicable).

Complex	Phase	2θ/ °	d_{obs} /Å	d_{calc}/ Å	*hk*	*a*/ Å
5-H	Col_h *T* = 105.0 °C cooling	3.95	22.3	22.3	10	25.7
		6.88	12.8	12.9	11	
		7.88	11.2	11.2	20	
5-5	Col_h *T* = 110 °C cooling	3.74	23.6	23.6	10	27.3
		6.44	13.7	13.6	11	
		7.46	11.8	11.8	20	
5-8	Col_h *T* = 82.7 °C heating	3.69	23.9	23.9	10	27.6
		6.38	13.8	13.8	11	
		7.39	11.9	12.0	20	

For the **6-*n*** series (Table 3-11, Table 3-12), there is also a destabilisation of the columnar phase on increasing chain length from *n* = 8 to 12, with a decreasing in the clearing point from 172.1 to 147.8 °C, followed by a dramatic stabilisation of the Col_h phase for **6-14** as indicated by the clearing point of 189.4 °C. The POM textures for this series show a mixture of fan-like and straight-line defects, indicating the columnar nature of the phase, and once again the SAXS pattern shows the d_{10}, d_{11} and d_{20} reflections characteristic of hexagonal order. There is also a modest increase in the lattice parameter *a*, from 28.1 to 29.4 Å, to incorporate the larger chain volume as the series progresses.

Table 3-11: Transition temperatures and enthalpies of **6-*n***

Complex	Transition	T (°C)	ΔH (kJ mol^{-1})
6-8	Cr-Col_h	83.9	58.7
	Col_h-I†	172.1	-
6-10	Cr-Col_h	77.4	75.6
	Col_h-I†	163.2	-
6-12	Cr-Col_h	77.3	91.2
	Col_h-I†	147.8	-
6-14	Cr-Col_h	72.2	68.0
	Col_h-I†	189.4	-

†not observed by DSC

Table 3-12: X-ray diffraction data **6-*n***, presenting the measured and calculated spacing, Miller indices and calculated parameters (where applicable).

Complex	Phase	2θ/ °	d_{obs} /Å	d_{calc}/ Å	*hk*	*a*/ Å
6-8	Col_h *T* = 107.3 °C heating	3.63	24.3	24.3	10	28.1
		6.29	14.0	14.0	11	
		7.21	12.2	12.2	20	
6-10	Col_h *T* = 90.5 °C heating	3.55	24.9	24.9	10	28.8
		6.16	14.3	14.3	11	
		7.12	12.4	12.5	20	
6-12	Col_h *T* = 97.2 °C heating	3.49	25.3	25.3	10	29.2
		6.10	14.5	14.6	11	
		6.92	12.8	12.7	20	
6-14	Col_h *T* = 110.0 °C cooling	3.46	25.5	25.5	10	29.4
		6.02	14.7	14.7	11	
		6.97	12.7	12.8	20	

The same is true for the complexes with the 3,4-disubstituted phenylalkynyl ligands, **7-*n*,** which show a significant decrease in the clearing point from 191.2 to 154.5 °C when the chain length is increased from *n* = 8 to 14 (Table 3-13, Table 3-14). Again, a small increase in *a* is observed when *n* is increased, from 29.4 to 31.6 Å, which is larger than the increase in **6-*n*** due to the lengthening of two alkoxy chains (rather than one) and the proportionally larger increase in volume.

The trend is slightly different for **8-*n***, where the most stable phase is observed for **8-10**, with a clearing point of 195.1 °C, increasing from 187.2 °C for **8-8** and higher than 183.9 and 166.0 °C for **8-12** and **8-14**, respectively (Table 3-15, Table 3-16). Complex **8-12** also forms a monotropic lamellar phase, rather than undergoing crystallisation, when cooled, with a lamellar layer spacing of 36.6 Å.

Table 3-13: Transition temperatures and enthalpies of **7-*n***

Complex	Transition	T (°C)	ΔH (kJ mol^{-1})
7-8	Cr-Col_h	83.0	85.3
	Col_h-I†	191.2	-
7-10	Cr-Col_h	81.0	82.1
	Col_h-I†	179.3	-
7-12	Cr-Col_h	77.0	73.3
	Col_h-I†	170.7	-
7-14	Cr-Col_h	80.0	103.2
	Col_h-I†	154.5	-

†not observed by DSC

Table 3-14: X-ray diffraction data **7-*n***, presenting the measured and calculated spacing, Miller indices and calculated parameters (where applicable).

Complex	Phase	2θ/ °	d_{obs} /Å	d_{calc}/ Å	*hk*	*a*/ Å
7-8	Col_h	3.46	25.5	25.5	10	29.4
	T = 160.9 °C	5.97	14.8	14.7	11	
	heating	6.96	12.7	12.8	20	
7-10	Col_h	3.35	26.3	26.3	10	30.4
	T = 120.7 °C	5.82	15.2	15.2	11	
	cooling	6.75	13.1	13.2	20	
		8.95	9.9	9.9	21	
7-12	Col_h	3.24	27.2	27.2	10	31.4
	T = 109.5 °C	5.66	15.6	15.7	11	
	cooling	6.52	13.5	13.6	20	
		8.65	10.2	10.3	21	
7-14	Col_h	3.22	27.4	27.4	10	31.6
	T = 109.5 °C	5.56	15.9	15.8	11	
	cooling	6.43	13.7	13.7	20	

Table 3-15: Transition temperatures and enthalpies of **8-*n***

Complex	Transition	T (°C)	ΔH (kJ mol^{-1})
8-8	Cr-Cr	44.2	50.8
	Cr-Col_h	53.4	97.8
	Col_h-I†	187.2	-
8-10	Cr-Col_h	58.9	62.1
	Col_h-I	195.1	4.3
8-12	Cr-Col_h	71.2	75.1
	Col_h-I	183.9	5.9
	(Col_h-Lam)	(39.4)	(101.2)
8-14	Cr-Col_h	89.0	118.9
	Col_h-I	166.0	2.8

†not observed by DSC

Table 3-16: X-ray diffraction data **8-*n***, presenting the measured and calculated spacing, Miller indices and calculated parameters (where applicable).

Complex	Phase	2θ/ °	d_{obs} /Å	d_{calc}/ Å	*hkl*	*a*/ Å
8-8	Col_h *T* = 80.5 °C heating	3.31	26.7	26.7	10	30.8
		5.77	15.3	15.3	11	
		6.64	13.3	13.3	20	
		8.72	10.1	10.1	21	
8-10	Col_h *T* = 100.6 °C heat	3.25	27.2	27.2	10	31.4
		5.64	15.7	15.7	11	
		6.54	13.5	13.6	20	
		8.65	10.2	10.2	21	
8-12	Col_h *T* = 160.9 °C cool	3.22	27.4	27.4	10	31.6
		5.58	15.8	15.8	11	
		6.44	13.7	13.7	20	
		8.52	10.4	10.3	21	
	Lam *T* = 26.9 °C cool	2.41	36.6	36.6	001	-
		4.88	18.1	18.3	002	
		5.39	16.4			
		7.27	12.1	12.2	003	
		20.86	4.3		broad	
8-14	Col_h *T* = 100.6 °C heat	3.08	28.7	28.7	10	33.1
		5.34	16.5	16.5	11	
		6.14	14.4	14.4	20	
		8.14	10.8	10.8	21	

A selection of textures from these three series are shown in Figure 3-45, showing example textures with straight line defects, as well as fan-like defects, also common to columnar phases.

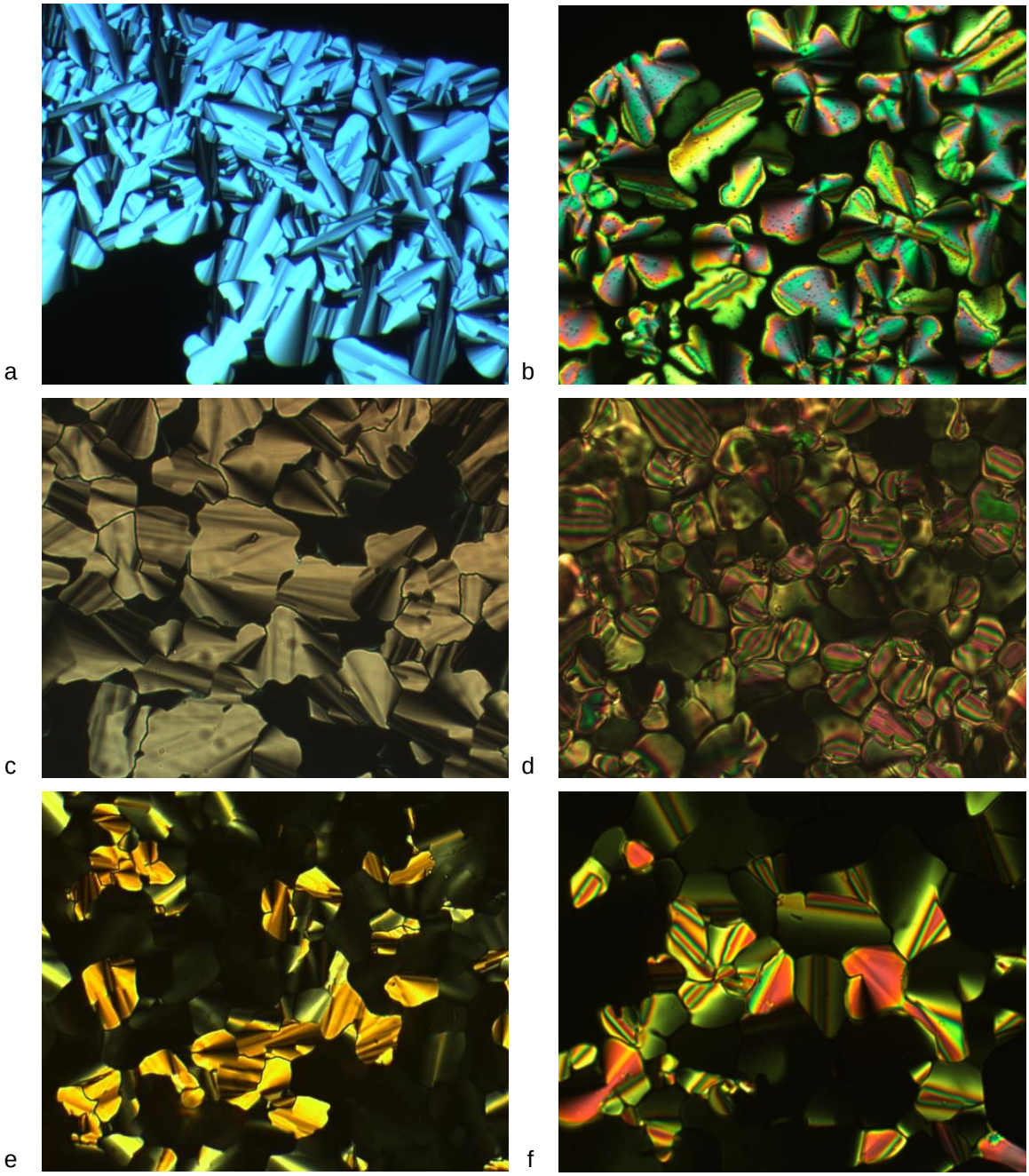

Figure 3-45: Photomicrographs of textures, all on cooling, of the Col_h phase of a) **6-8** at 167.7 °C; b) **6-12** at 132.9 °C; c) **7-12** at 145.2 °C; d) **7-14** at 163.3 °C; e) **8-12** at 142.2 °C; f) **8-14** at 163.3 °C.

Complex **10-N** also shows a columnar hexagonal phase (Table 3-17, Table 3-18); the texture is highly birefringent and contains no identifiable defects, it is reminiscent of the textures observed for **3-10** to **3-12**, and the SAXS pattern is characteristic of the Col_h phase. The lattice parameter, *a*, for this complex is 26.1 Å, which is slightly higher than for the very similar complex **5-H** for which *a* = 25.7, indicating that the columns are contracted, with more favourable interactions between the molecules when the ring is pyridine.

Table 3-17: Transition temperatures and enthalpies of **10-N**

Complex	Transition	T (°C)	ΔH (kJ mol^{-1})
10-N	Cr-Cr	14.5	18.4
	Cr-Col$_h$	95.4	42.1
	Col$_h$-I†	101.8	-

†not observed by DSC

Table 3-18: X-ray diffraction data **10-N**, presenting the measured and calculated spacing, Miller indices and calculated parameters (where applicable).

Complex	Phase	2θ/ °	d_{obs} /Å	d_{calc}/ Å	*hk*	*a*/ Å
10-N	Col$_h$	3.90	22.6	22.6	10	26.1
	T = 99.5 °C	6.80	13.0	13.0	11	
	heating	7.77	11.4	11.3	20	

With the exception of **8-10, 8-12** and **8-14**, none of the complexes in these 4 families show a clearing point when measured by differential scanning calorimetry (DSC), although when observed by microscopy it is sharp and easily observable. This suggests that there is a very small enthalpy change between the Col$_h$ phase and the isotropic liquid, indicating that the columnar phase is highly disordered. This is supported by the comparatively small clearing enthalpies for the three complexes where this transition is observed of 4.3, 5.9 and 2.8 kJ mol^{-1} for **8-10, 8-12** and **8-14**, respectively, and similar to the Col$_h$ clearing points observed for complexes with two-chains on the cyclometallating ligand in the range of 3.9 to 5.8 kJ mol^{-1}. It may also be considered that the clearing point in these complexes corresponds to the destruction of the two-dimensional hexagonal lattice, but that weak associations remain between individual molecules within the column, which then disassociate at a higher temperature, which could be thought of as a second clearing point. This hypothesis is corroborated by the observation of a broad reflection in the small angle region of the X-ray pattern for these complexes when irradiated in the isotropic liquid (Figure 3-46). The conclusive reason of why this transition is unobserved in DSC measurements remains unknown, although it has also been observed previously[135] that metallomesogens often behave unexpectedly under DSC conditions and it may be that this peculiarity is of a similar nature, which remains unexplained.

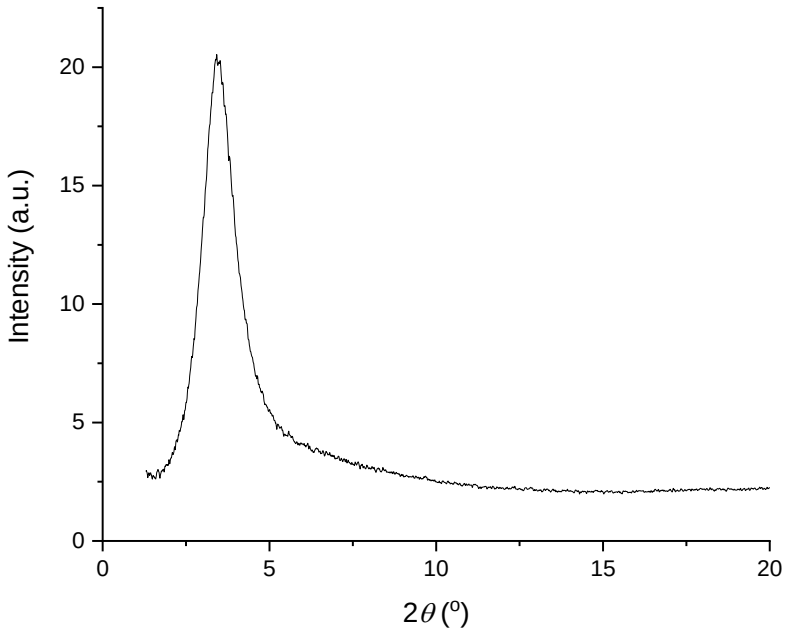

Figure 3-46: SAXS pattern of **7-10** in the isotropic liquid showing a broad reflection in the small-angle region.

Transition temperatures for the **5-*n*** to **8-*n*** series are displayed graphically in Figure 3-47, showing the comparative transition temperatures of all four-chain complexes.

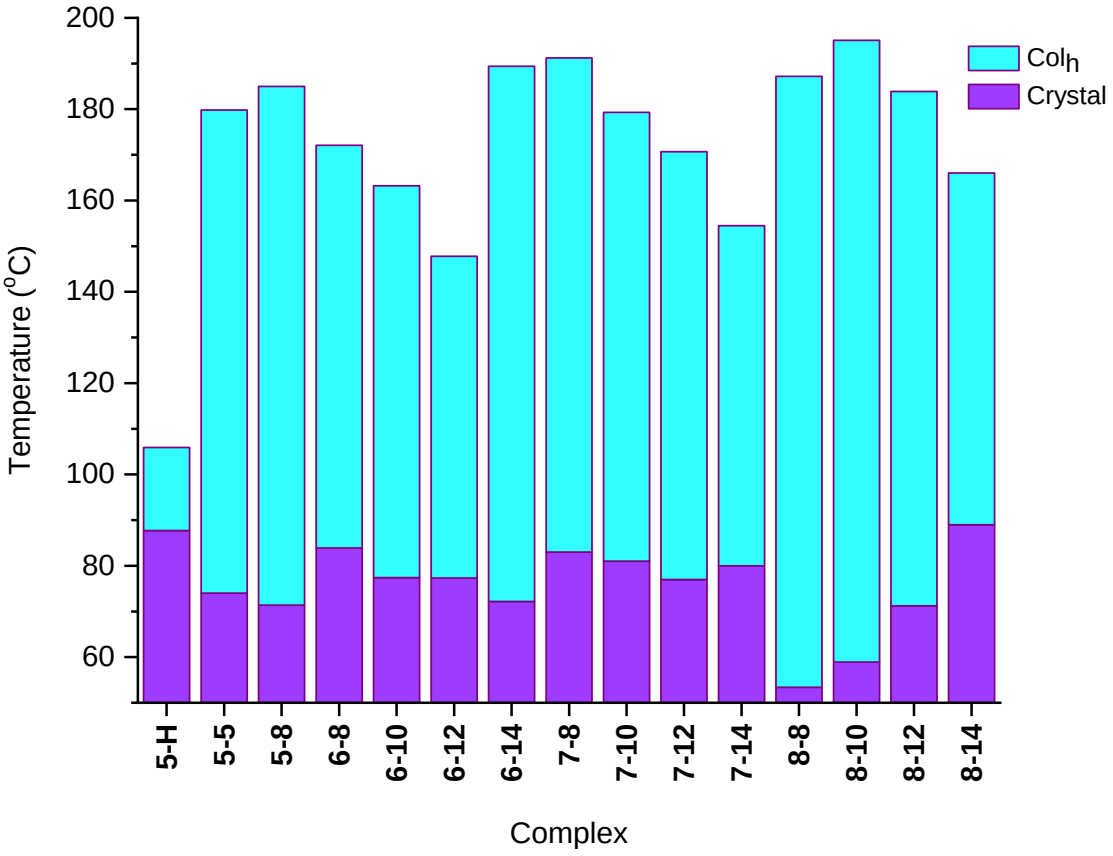

Figure 3-47: Transition temperatures and phases for **5-*n*** to **8-*n***, with crystal phases shown in purple and Col_h in blue.

Complexes **5-H** and **10-N**, those with phenylacetylene and 4-ethynylpyridine ligands, respectively, show the least stabilised columnar phases as illustrated by the drastic reduction in clearing point in comparison to those species with alkyl or alkyoxy chains, regardless of chain number or length. This indicates that a certain volume of ligand in the fourth coordination position is required to form a stable mesophase. As the chloride ligand in **Au-Cl-2** fills significantly less space than either phenylacetylene or 4-ethynylpyridine, is it suggested that the intermolecular interactions, such as π-π stacking, and chain interdigitation are insufficient to stabilise the formation of a columnar phase.

It is obvious that the formation of the Col_h phase for the four-chain complexes has a threshold for the volume of the ligand in the fourth coordination position that must be met or exceeded. This indicates that the barrier to Col_h phase induction is a co-planar ligand of magnitude between that of the chloride of **Au-Cl-2**, which is not liquid-crystalline, and the phenylacetylene of **5-H**, in which a Col_h phase is present for almost 20 °C. The phase behaviour of all complexes is collected in Figure 3-48, with a comparison between related complexes shown in Figure 3-49.

As the volume of the alkynyl ligand is increased *via* the inclusion of alkyl or alkoxy chains, the space-filling becomes exceedingly favourable for the formation of a Col_h mesophase. It is proposed that the change in clearing point within and between all four series arises purely from how well each alkynyl ligand contributes to the formation of an effective disc for each individual molecule, with the suggestion being that the closer the molecule to the optimal disc shape, the more stable the phase formed.

In series **6-*n***, **7-*n*** and **8-*n***, there is a general trend of mesophase destabilisation as the alkoxyphenylalkynyl chain length increases. It is hypothesised that, as the most stable molecular conformation is that which forms the most effective disc, that as the chain length is increases, specifically to C12 and C14, these chains extend past the hypothetical disc boundary, resulting in a deformation from the ideal disc-shape, and therefore a less stable columnar phase.

By estimation of the molecular size, and subsequent comparison to the lattice parameter, *a*, information on the organisation of the molecules in the mesophase can be gleaned, which leads to insight into the stability of the phase. Utilising **8-12** as an example, an idealised molecular size can be estimated based on experimental measurements from similar complexes, *i.e.* the dimensions of the aromatic core can be measured from the single crystal structure of complexes **1-H** and **1-5**, as well as the length of a fully extended dodecyloxy chain. From these individual measurements, molecular confirmations of more functionalised molecules can be probed; this is shown schematically in Figure 3-50.

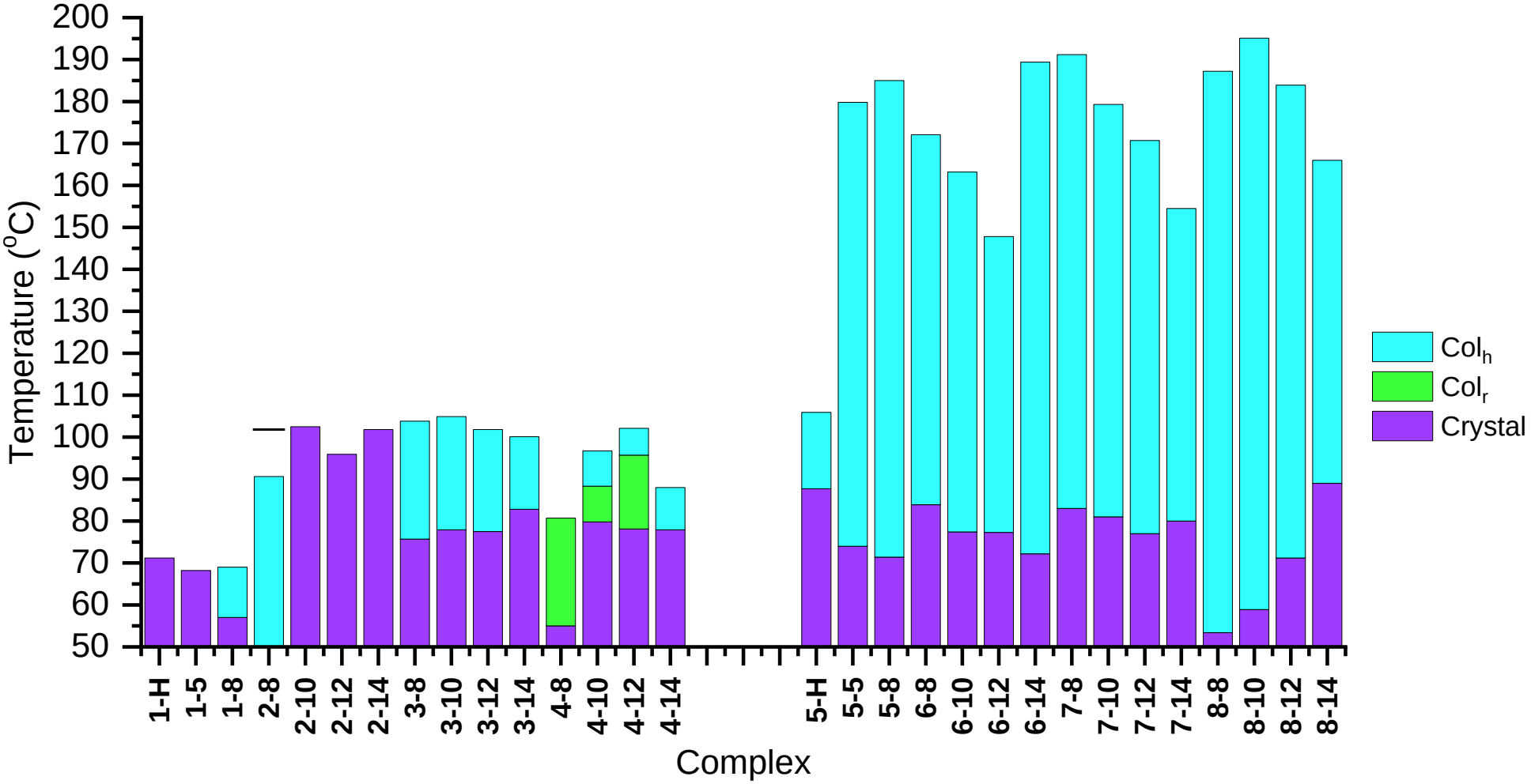

Figure 3-48: Transition temperatures and phases for **1-*n*** to **8-*n*** on heating. The melting point of **2-8** is shown as a black bar.

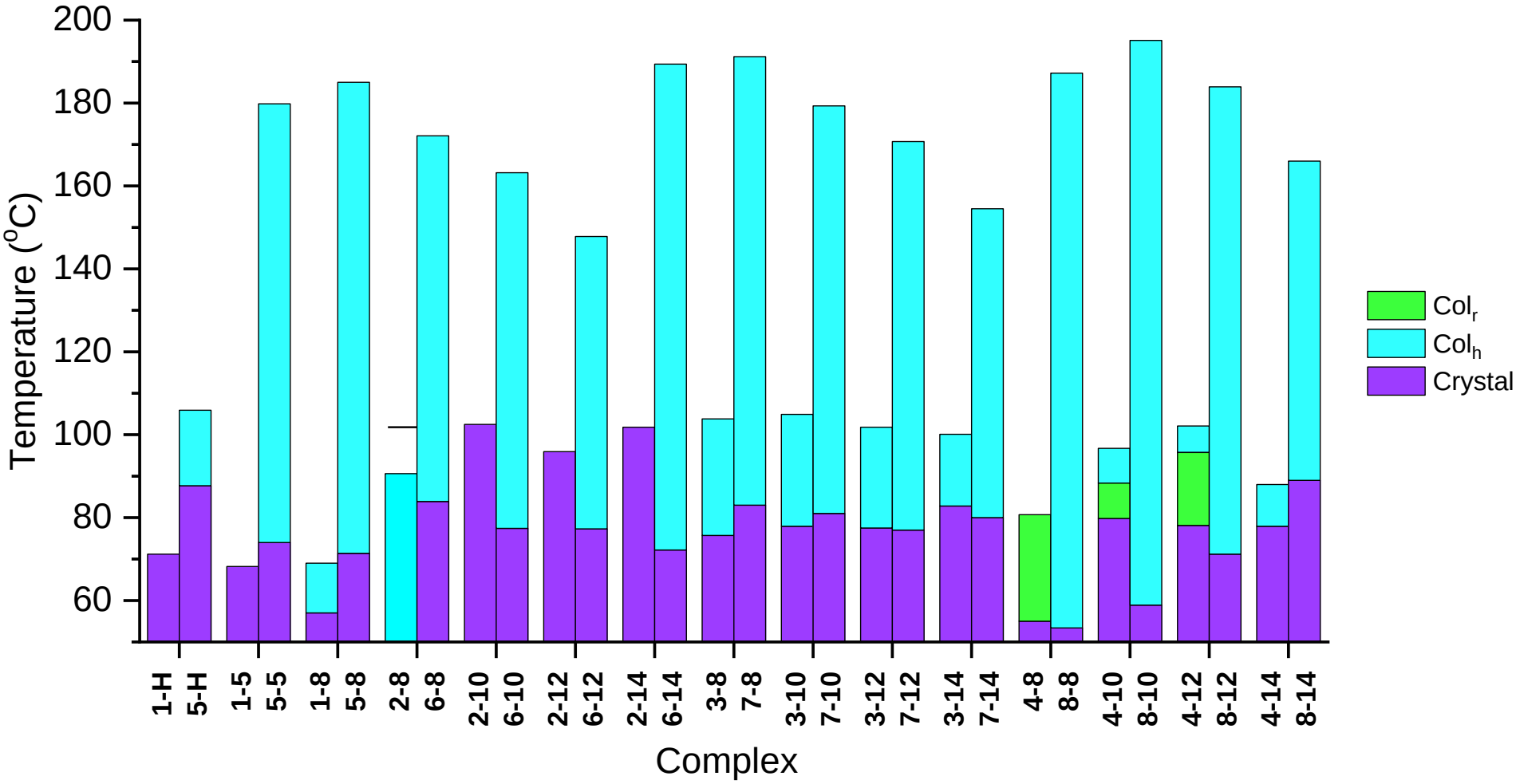

Figure 3-49: Transition temperatures and phases for **1-*n*** to **8-*n*** on heating comparing two-chain and four-chain complexes with the same alkynyl ligand. The melting point of **2-8** is shown as a black bar.

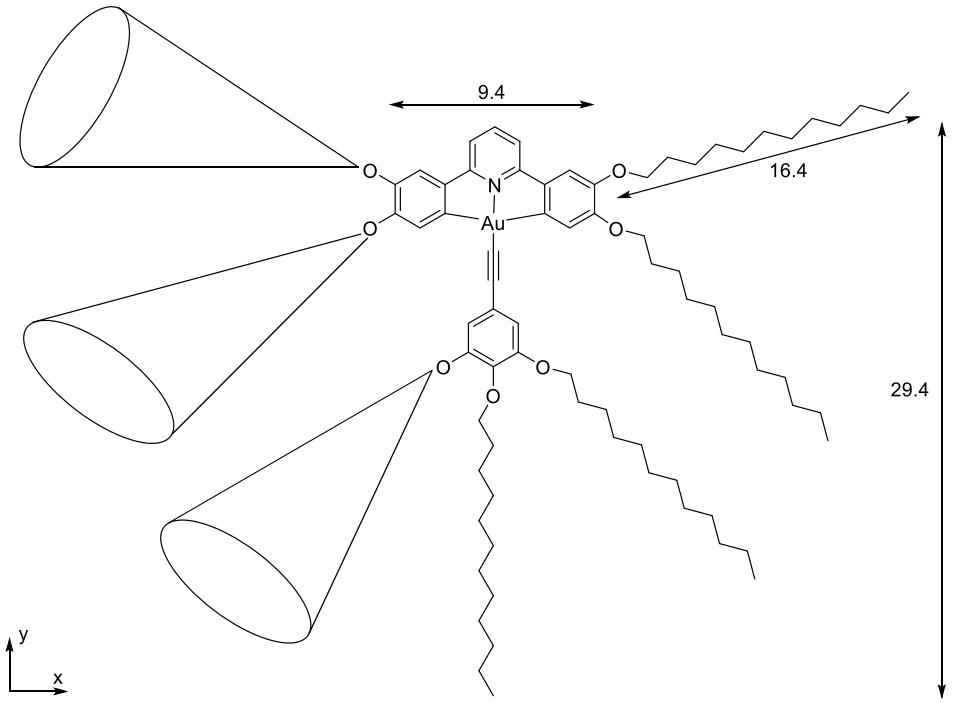

Figure 3-50: Structure of **8-12** with experimentally measured distances and positional estimation. All lengths are in Å, conical ellipses represent the flexibility and rotation of the alkoxy chains.

From this diagram, it can be calculated that the molecular length in the *x* direction, as defined in Figure 3-50, is approximately 37.4 Å and in the y direction is approximately 29.4 Å. The lattice parameter, *a*, for **8-12** is 31.6 Å, which suggests that in the cross section of the column, there is a single molecule, assuming a molecular length of 37.4 Å, and allowing for some measure of interdigitation and chain folding. This model is obviously simplistic, and it is proposed that there is a free rotation around the column axis, *i.e.* the orientation of the molecules along the 1D column axis is not fixed, but there is an averaging of the molecular dimensions.

This model corresponds with the increase in the lattice parameters when the chain length is increased within each series; although the alkyl chains are not at full extension, the diameter of the disc is still increasing, and therefore a larger inter-columnar distance is observed (correlation shown in Figure 3-51). For **6-*n*** the increase in *a* steadily decreases as the chain length is increased as observed by a slight plateauing of the trendline, while for **7-*n*** the increase is constant and directly proportional to the chain length for *n* = 8, 10 and 12, while there is very little difference between **7-12** (31.4 Å) and **7-14** (31.6 Å). There is no obvious pattern for complexes **8-*n***, with a small increase in *a* for *n* = 8, 10 and 12, followed by a significant increase for **8-14**; this trend is in opposition to **7-*n***.

These estimations can also be made for the Col_h formed by complexes with two-chains on the cyclometallating ligand, in which the lattice parameter, *a*, can be compared within and between series, and also to the molecular diameter.

It is clear from the substitution pattern in **1-8** and **2-8** that they are not functionalised enough to support a full disc-like structure, but rather are half-discs which may stack in an anti-parallel fashion. Support for this hypothesis is given by calculation of the columnar lattice parameter, *a*, which is a measure of inter-columnar distance, and for **1-8** is 33.5 Å and 33.8 Å for **2-8**, which is larger than the estimated molecular length of 29.5 Å for both **1-8** and **2-8**, indicating that the formation of the column is unlikely to be due to the stacking of single molecules.

This rationale applies to all of the Col_h phases observed in two-chain complexes, in which the lattice parameter is always larger than the molecular cross-section and increases with the increase in chain length and appendage of further chains. This hypothesis is supported further by the observation that the lattice parameters for the equivalent four-chain species, which are larger molecules due to the additional two dodecyloxy chains on the C^N^C ligand, are always significantly smaller than the analogous two-chain complex; this is shown graphically in Figure 3-51.

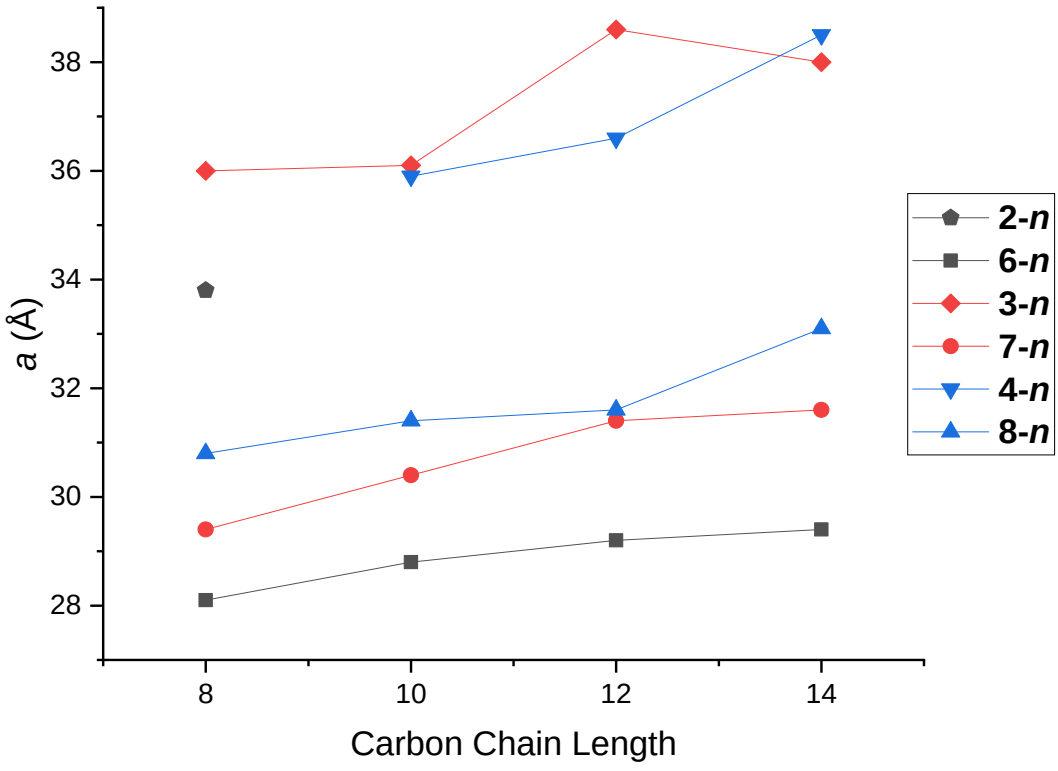

Figure 3-51: Correlation between Col_h lattice parameter, *a*, and chain length of the alkoxy chains on the alkynyl ligand as a comparison between two-chain and four-chain equivalents; those series with the same alkynyl ligand are shown in the same colour.

It seems clear that in the larger four-chain species, the functionalisation of the cyclometallating ligand is sufficient to form a traditional disc-like molecule, while the two-chain species cannot form this full disc and the phase formation may well rely on the back-to-back arrangement of two molecules.

3.4.2 Gold(III) Alkynyl Complexes with Semi-Perfluorinated Chains

3.4.2.1 Complexes with Two Chains, *11-n* to *13-n*

The liquid-crystalline behaviour of the complexes with semi-perfluorinated chains, **11-*n*** to **13-*n***, is significantly different from their purely hydrocarbon analogues, although still dominated by columnar phases. Approximately half of the synthesised complexes with two chains on the cyclometallating ligand do not show any liquid-crystalline properties. An overview of the transition temperatures and enthalpies of those that do (as well as the melting points of those that do not) are shown in Table 3-19, with the associated SAXS parameters collected in Table 3-20.

Table 3-19: Transition temperatures and enthalpies of **11-*n*** to **13-*n***

Complex	Transition	T (°C)	ΔH (kJ mol^{-1})
11-8	Cr-Col$_h$	117.2	25.3
	Col$_h$-Iso	128.4	4.0
11-10	Cr-I	116.4	21.4
11-12	Cr-I	113.9	30.1
12-8	Cr-Col$_h$	99.4	33.4
	Col$_h$-Iso	174.9	20.6
12-10	Cr-Col$_r$	94.9	22.6
	Col$_r$-Iso	179.6	15.8
12-12	Cr-Col$_r$	89.4	12.1
	Col$_r$-Iso†	149.7	-
13-8	Cr-I	161.2	26.0
13-10	Cr-Cr	100.4	22.5
	Cr-I	166.0	23.8

† not observed by DSC

Of the **11-*n*** series, only **11-8** displayed any liquid-crystalline behaviour, with a columnar hexagonal phase found between 117.2 and 128.4 °C. Both **11-10** and **11-12** proved to be unstable to heat and decomposed when heated into the isotropic liquid at 116.4 and 113.9 °C, respectively.

All three complexes in the **12-*n*** series show columnar phases; **12-8** has a Col_h phase between 99.4 and 174.9 °C, and as the perfluorinated chain length is increased, the dominant phase becomes rectangular, with a Col_r phase between 94.9 and 179.6 °C for **12-10** and between 89.4 and 149 °C for **12-12**. The melting points for all three complexes are approximately consistent, however the Col_r phase is destabilised between **12-10** and **12-12** as the chain length, and therefore the level of fluorination, is increased. These transitions are depicted graphically in Figure 3-52.

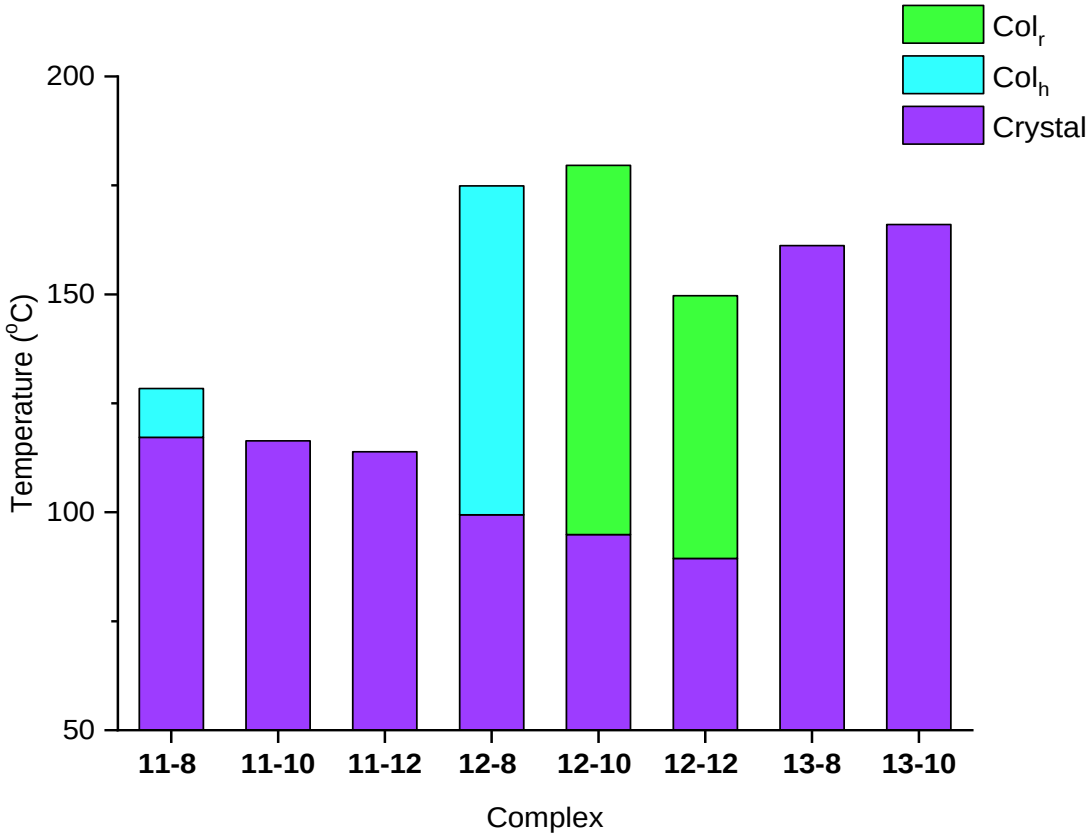

Figure 3-52: Transition temperatures and phases for **11-*n*** and **12-*n***, with crystal phases shown in purple, Col_h in blue and Col_r in green.

Neither **13-8** nor **13-10** showed any liquid-crystalline phases, melting into the isotropic liquid at 161.2 and 166.0 °C, respectively. This is in stark contrast to the analogous fully hydrocarbon species **4-*n***, in which the phase behaviour is rich. This difference will be discussed fully in Section 3.4.3.

Table 3-20: X-ray diffraction data **11-*n*** to **12-*n***, presenting the measured and calculated spacing, Miller indices and calculated parameters (where applicable).

Complex	Phase	2θ/ °	d_{obs} /Å	d_{calc}/ Å	*hk*	*a*, *b*/ Å
11-8	Col_h	3.07	28.7	28.7	10	*a* = 33.1
	T = 122.9 °C	5.33	16.6	16.6	11	
	cooling	6.11	14.4	14.4	20	
12-8	Col_h	2.92	30.2	30.2	10	*a* = 34.9
	T = 130.0 °C	5.03	17.5	17.4	11	
	cooling	5.84	15.1	15.1	20	
		8.76	10.1			
		10.52	8.4			
		11.66	7.6			
12-10	Col_r	2.74	32.2	32.2	11	*a* = 48.8
	T = 140.0 °C	3.62	24.4	24.4	20	*b* = 42.6
	cooling	4.61	19.3	19.5	12	
		5.39	16.4	16.2	30	
		6.15	14.4	14.2	03	
		9.61	9.2	9.5		
		11.99	7.4	7.2		
12-12	Col_r	2.79	31.6	31.6	11	*a* = 48.0
	T = 100 °C	3.67	24.0	24.0	20	*b* = 42.0
	heating	4.52	19.5	19.3	12	

The lattice parameters for the Col_r phase of **12-10** and **12-12** are remarkably similar, with an *a* parameter of 48.8 and 48.0 Å, respectively, and a *b* parameter of 42.6 and 42.0 Å, respectively. It is surprising that the lattice of the larger complex, **12-12**, appears to be smaller than that of **12-10**, indicating that the columns are situated closer to each other. Also of interest is by the fact that the enthalpy for the clearing transition of **12-10** is 15.8 kJ mol^{-1}, whereas the same transition for **12-12** is not observed by DSC, indicating a small organisational change between the Col_r phase and the isotropic liquid. This could be an indication that the Col_r phase of **12-10** has a higher level of correlation between the columns, and the phase of **12-12** has a higher level of disorder.

In addition to the sharp reflections in the small angle region of the diffraction pattern of **12-10**, there are also two broad reflections at 9.5 and 7.2 Å (shown in Figure 3-53, along with the corresponding POM texture). The origin of these reflections are unknown, but they could originate from an Au···Au correlation.

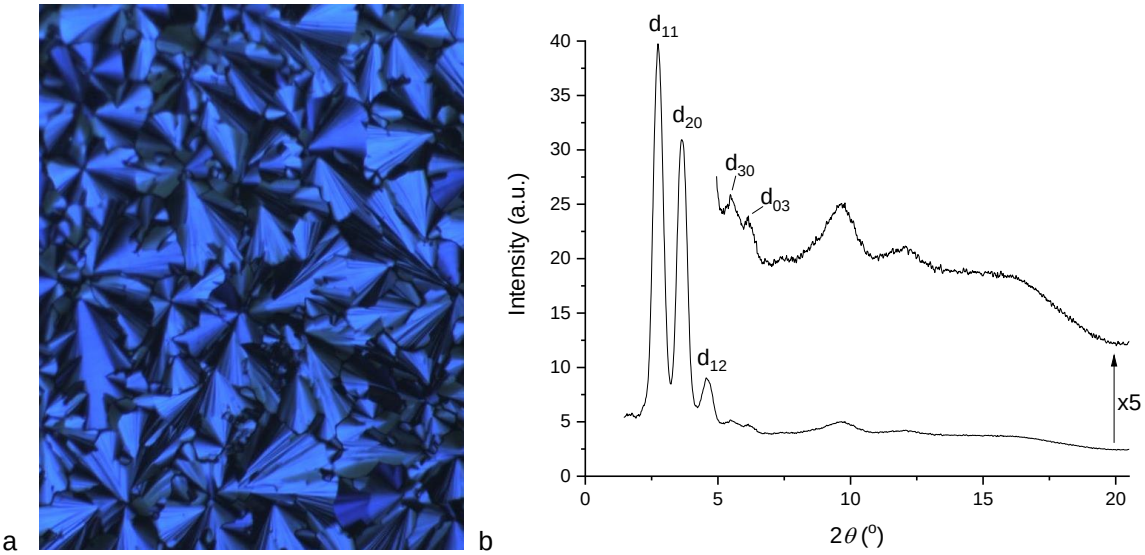

Figure 3-53: a) photomicrograph of Col_r phase of **12-10** at 134.4 °C on cooling from the isotropic liquid and b) corresponding SAXS pattern at 140.0 °C on cooling from the isotropic liquid.

3.4.2.2 Complexes with Four Chains, *14-n* to *16-n*

As with the hydrocarbon analogues, all of the perfluorinated complexes with four chains on the cyclometallating ligand (**14-*n*** to **16-*n***) show liquid-crystalline behaviour, with the observation of both hexagonal and rectangular columnar phases (transition data shown in Table 3-21, with associated SAXS data and parameters shown in Table 3-22). Once more, for the majority of species the clearing point is not observed by DSC.

Complexes of the **14-*n*** series all show columnar hexagonal phases. **14-8** shows a broad phase, with a melting point of 92.7 °C and a clearing point of 186.3 °C. The stability of the Col_h phase is severely reduced for **14-10** and **14-12**, with clearing points of 96.7 and 96.5 °C, respectively, and comparatively little change in the melting point indicating only a small decrease in the stability of the crystalline phase. From the SAXS data, the *a* value for **14-8** is 29.7 Å, significantly smaller than those for **14-10** and **14-12**, in which the lattice parameters are a very similar 34.5 and 34.3 Å, respectively, suggesting that the molecular organisation within the Col_h phase is significantly different between **14-8** and **14-10**, which is then very similar to **14-12**. The optical texture of **14-8** is similar to those previously observed, with fan-like and focal conic defects dominating (Figure 3-54a), however both **14-10** and **14-12** show a mosaic texture (Figure 3-54b).

Table 3-21: Transition temperatures and enthalpies of **14-*n*** to **16-*n***

Complex	Transition	T (°C)	ΔH (kJ mol^{-1})
14-8	Cr-Col_h	92.7	56.9
	Col_h-Iso†	186.3	-
14-10	Cr-Col_h	94.0	60.2
	Col_h-Iso†	96.7	-
14-12	Cr-Col_h	89.7	52.0
	Col_h-Iso†	96.5	-
15-8	Cr-Col_r	89.2	52.3
	Col_r-Col_h	92.5	6.1
	Col_h-Iso†	238.8	-
15-10	Cr-Col_r	87.6	46.9
	Col_r-Col_h	92.8	2.3
	Col_h-Iso†	199.9	-
15-12	Cr-Col_r^1	88.4	46.4
	Col_r^1 – Col_r^2	93.5	1.5
	Col_r^2 – N	139.4	2.7
	N-Col_h†	156.1	-
	Col_h-I†	201.3	-
	(Col_r^1 – Col_r^3)	76.4	1.1
16-8	Cr-Col_h	114.1	35.4
	Col_h-Iso	232.3	3.0
16-10	Cr-Col_h	135.1	40.5
	Col_h-Iso	229.7	2.9

† not observed by DSC

a 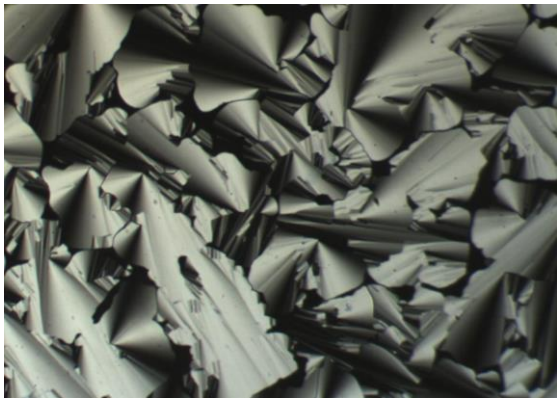 b 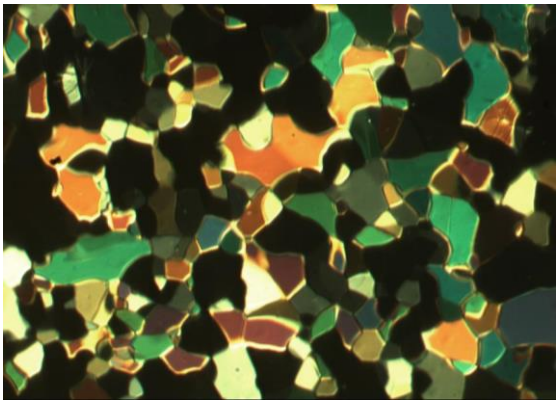

Figure 3-54: Photomicrographs on cooling from the isotropic liquid of a) **14-8** at 177.5 °C showing focal conics and b) **14-10** at 81.6 °C showing a mosaic texture

Table 3-22: X-ray diffraction data **14-*n***, presenting the measured and calculated spacing, Miller indices and calculated parameters (where applicable).

Complex	Phase	2θ/ °	d_{obs} /Å	d_{calc}/ Å	*hk*	*a*/ Å
14-8	Col_h	3.44	25.7	25.7	10	29.7
	T = 177.5	5.95	14.8	14.8	11	
	cooling	6.87	12.9	12.9	20	
14-10	Col_h	2.95	29.9	29.9	10	34.5
	T = 81.6	5.34	16.5	17.2	11	
	cooling	6.02	14.7	15	20	
14-12	Col_h	2.97	29.7	29.7	10	34.3
	T = 89.7	5.37	16.4	17.1	11	
	cooling	5.97	14.8	14.9	20	

Complexes **15-*n*** show similar melting points both within the series and in comparison to **14-*n***, showing that addition of the second semi-perfluoroalkyl chain has little effect on the crystal phase stability, however the clearing points for all three **15-*n*** complexes are elevated to 200 °C and above. Complex **15-8** shows a wide-range Col_h phase on heating between 92.5 and 238.8 °C, as well as a lower-temperature columnar rectangular phase between 89.2 and 92.5 °C. Similarly, **15-10**, shows a Col_h phase between 92.8 and 199.9 °C and a Col_r phase between 87.6 and 92.8 °C; the Col_r phase clears at approximately the same temperature as the Col_r phase of **15-8**, indicating a similar level of stability (X-ray data are shown in Table 3-23). The depression of the clearing point for **15-10**, although not of the same magnitude of that observed previously, mirrors that of **14-*n*** on the increase of the fluorinated chain length to eight or more. The lower clearing point is also seen in **15-12**, for which a temperature of 201.3 °C is recorded.

Complex **15-12** melts at 88.4 °C to form a columnar rectangular phase, designated Col_r^1, which undergoes a phase transition at 93.5 °C to form a second rectangular phase, Col_r^2, with a contraction of both lattice parameters. Then at 139.4 °C, a nematic (N) phase is formed, which is

highly birefringent and fluid; this subsequently transitions into a Col_h phase at 156.1 °C which clears into the isotropic liquid at 201.3 °C. On cooling, a further monotropic rectangular phase is observed at 76.4 °C which crystallises at 70.5 °C. The textures of these five phases on cooling from the isotropic liquid are shown in Figure 3-55, and the corresponding SAXS patterns are found in Figure 3-56 to Figure 3-60. Neither the transition from the N phase into the Col_h phase nor the clearing point into the isotropic liquid are observed by DSC. The observation of a nematic mesophase between the Col_r and the Col_h is remarkable, and is discussed in more detail in Section 3.4.2.3.

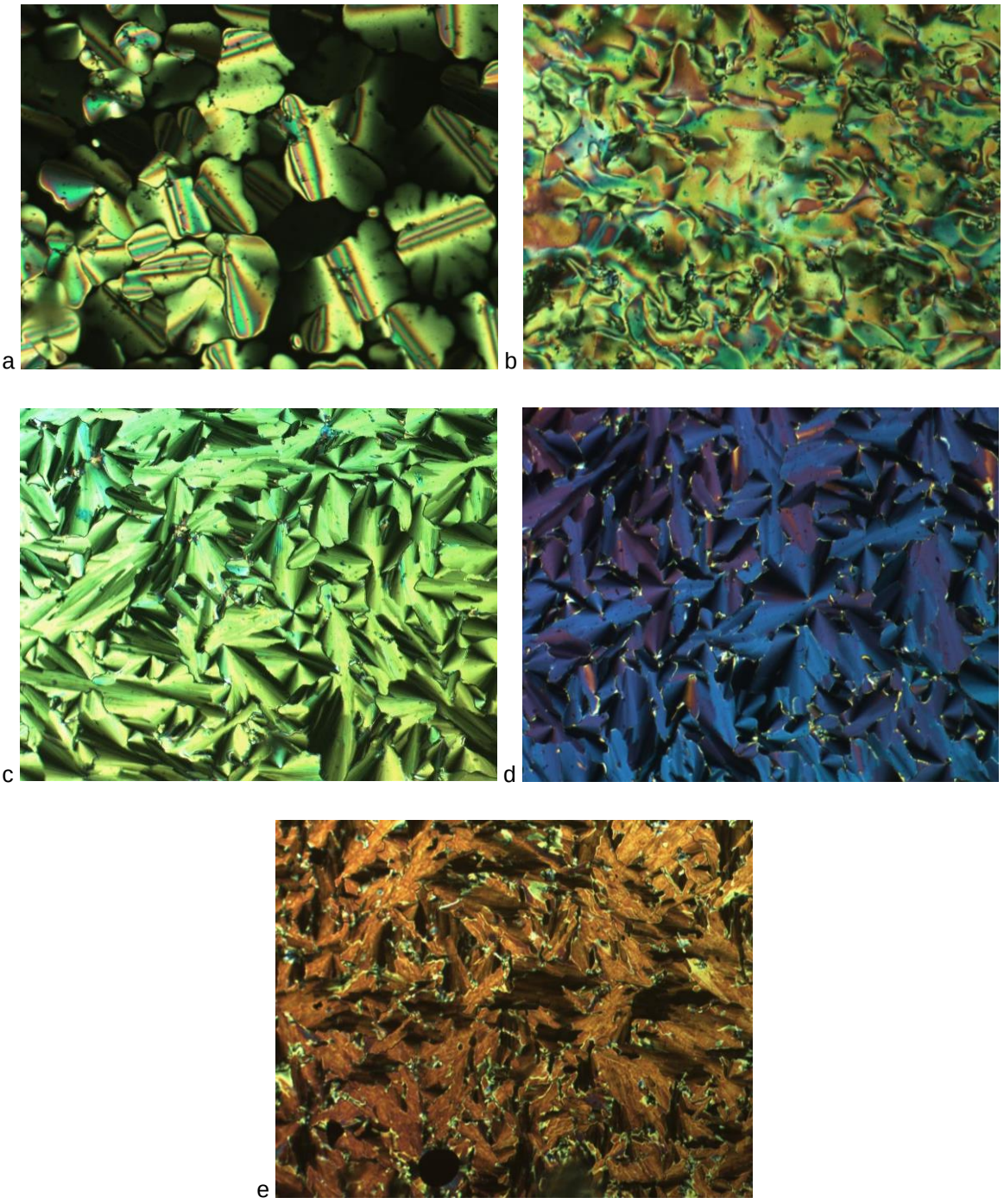

Figure 3-55: Photomicrographs of **15-12** on cooling from the isotropic liquid, showing a) Col_h at 188.3 °C; b) M at 156.4 °C; c) Col_r^2 142.0 °C; d) Col_r^1 at 90.9 °C; e) Col_r^3 at 70.9 °C

Table 3-23: X-ray diffraction data **15-*n***, presenting the measured and calculated spacing, Miller indices and calculated parameters (where applicable).

Complex	Phase	2θ/ °	d_{obs} /Å	d_{calc}/ Å	*hk*	*a*, *b*/ Å
15-8	Col_h *T* = 140 °C cooling	3.30	26.7	26.7	10	*a* = 30.8
		5.69	15.5	15.4	11	
		6.61	13.4	13.4	20	
		8.70	10.2	10.1	21	
	Col_r *T* = 83.0 °C cooling	2.75	32.1	32.1	11	*a* = 55.6
		3.17	27.8	27.8	20	*b* = 39.3
		4.43	19.9			
		5.27	16.7	16.8	31	
		6.34	13.9	13.9	40	
		8.19	10.8	10.7	33	
15-10	Col_h *T* = 130 °C cooling	3.13	28.2	28.2	10	*a* = 32.6
		5.39	16.4	16.3	11	
		6.21	14.2	14.1	20	
	Col_r *T* = 80 °C cooling	2.07	42.6	42.6	11	*a* = 59.8
		2.95	29.9	29.9	20	*b* = 60.7
		4.44	19.9	19.9	30	
		5.52	16.0			
		5.90	14.9	14.9	40	
15-12	Col_h *T* = 150 °C heating	3.14	28.1	28.1	10	*a* = 32.4
		5.43	16.3	16.2	11	
		6.18	14.3	14.1	20	
	N *T* = 145 °C heating	3.24 (br)	27.2 (br)	-	-	-
	Col_r^2 *T* = 120 °C cooling	1.54	57.3			
		1.80	49.0			
		2.12	41.6			
		3.05	28.9			
		3.72	23.7			
		3.93	22.5			
		4.24	20.8			
		4.64	19.0			
		5.84	15.1			
		6.05	14.6			
		16.0(br)	5.5(br)		<h_f>	
	Col_r^1 *T* = 80 °C cooling	1.45	60.9			
		1.66	53.2			
		2.00	44.1			
		2.87	30.7			
		3.49	25.3			
		4.02	22.0			
		4.33	20.4			
		4.51	19.6			
		4.87	18.1			
		5.42	16.3			
		5.75	15.4			
		16.0(br)	5.5(br)		<h_f>	
	Col_r^3 *T* = 71 °C cooling	1.99	44.3	44.3	11	*a* = 62.0
		2.85	31.0	31.0	20	*b* = 63.3
		4.46	19.8	19.6	31	
		7.59	11.6	11.5	52	
		16.2(br)	5.5(br)		<h_f>	
		18.4(br)	4.8(br)		<h_h>	

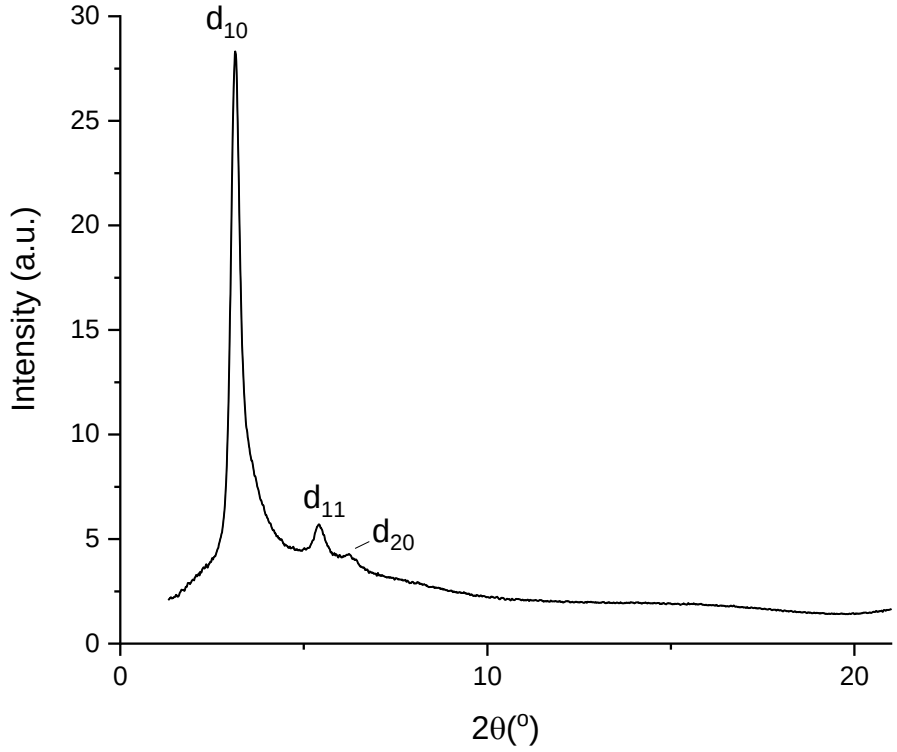

Figure 3-56: Indexed SAXS pattern of **15-12** showing Col_h at 170.0 °C on heating corresponding to the texture shown in Figure 3-55a

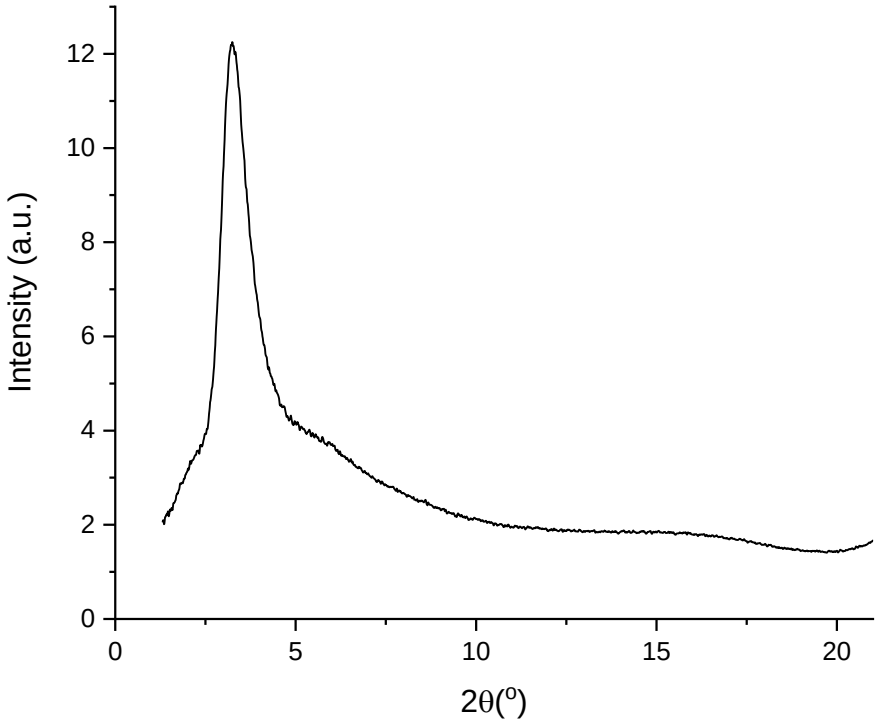

Figure 3-57: Indexed SAXS pattern of **15-12** showing N at 145 °C on heating corresponding to the texture shown in Figure 3-55b

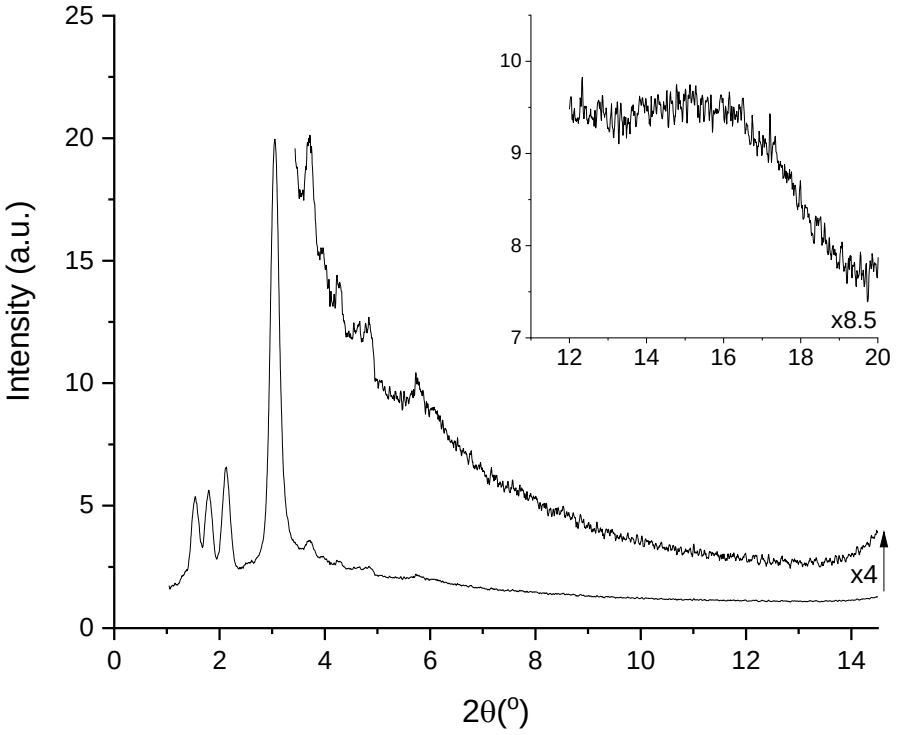

Figure 3-58: Indexed SAXS pattern of **15-12** showing Col_r^2 at 120.0 °C on cooling corresponding to the texture shown in Figure 3-55c

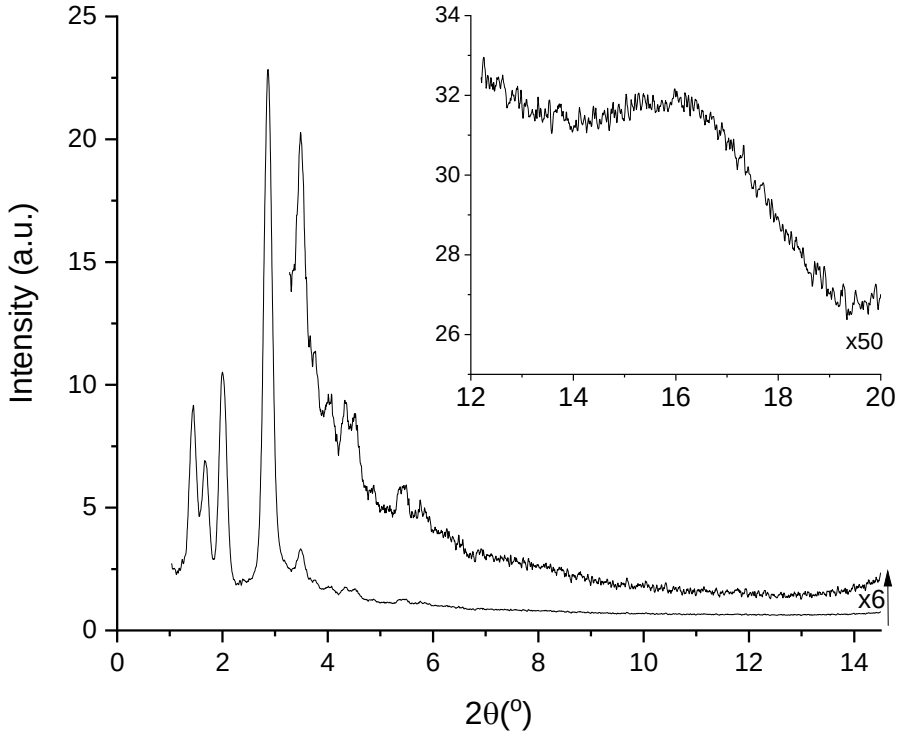

Figure 3-59: Indexed SAXS pattern of **15-12** showing Col_r^1 78.0 °C on cooling corresponding to the texture shown in Figure 3-55d

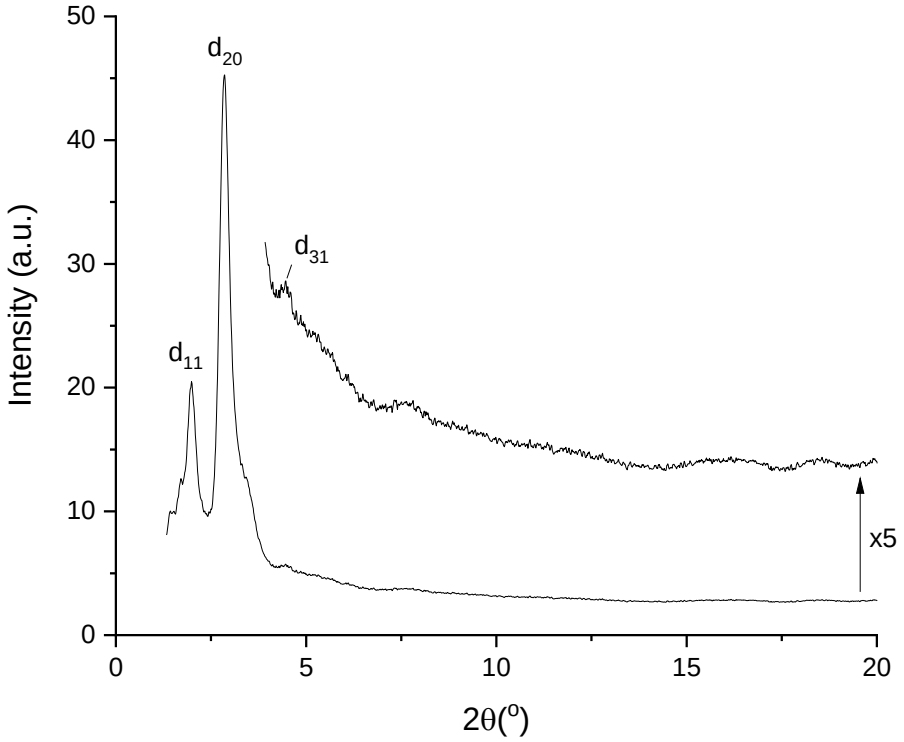

Figure 3-60: Indexed SAXS pattern of **15-12** showing Col_r^3 at 71.0 °C on cooling corresponding to the texture shown in Figure 3-55d

The SAXS measurements of Col_r^1 and Col_r^2 show a diffraction pattern previously unobserved and requires further comment. In the small-angle region, both phases show three strong reflections, followed by a significantly more intense reflection and then a number of weaker reflections as 2θ increases. In a Col_r phase, the d_{11} and d_{20} must be known in order to calculate the lattice parameters a and b. The observation of four intense reflections in the small angle region of the pattern for Col_r^1 and Col_r^2 makes indexation of the d_{11} and d_{20} ambiguous, and thus, the columnar rectangular phases of **15-12** are presented unindexed to avoid the presentation of inaccurate data.

These extra peaks are not observed in the SAXS pattern of the monotropic Col_r^3 phase, or least they have not been detected, and so this phase has been indexed assuming the two most intense small-angle peaks are the d_{11} and d_{20}, giving lattice parameters of a = 62.0 and b = 63.3 Å. The patterns of Col_r^1, Col_r^2 and Col_r^3 all show a broad reflection at 5.5 Å which is assigned as originating from the molten semi-perfluorinated chains.[107] A broad reflection is also observed at 4.8 Å for Col_r^3 which is indexed as originating from the molten hydrocarbon chains.

The d_{11} and d_{20} reflections for the Col_r^3 mesophase occur in approximately the same place as the third and fourth reflections (counting from the largest d-spacing to smallest) for Col_r^1, the diffraction pattern for which, in turn, greatly resembles that for Col_r^2. Therefore, it is suspected that, for the Col_r^1 and Col_r^2 phases, the reflections observed at 44.0 and 41.4 Å, respectively, are the d_{11} and the reflections at 30.8 and 28.9 Å, respectively, are the d_{20}. It is suspected that the two

reflections with the largest *d*-spacing for Col_r^1 and Col_r^2 arise from extra symmetry in the phase due to isolated regions of fluorocarbon carbon chains at a distance greater than that which defines the lattice parameters. This hypothesis requires further substantiating evidence; investigation into these data and the organisation of the molecules and columns within the phase is ongoing.

Both **16-8** and **16-10** show columnar hexagonal phases that show the same level of stability, with a small stabilisation of the melting point as the chain length increased (114.1 to 232.3 °C for **16-8** and 135.1 to 229.9 °C for **16-10**), and an increase in the lattice parameter, with a = 32.1 Å for **16-8** to 33.4 Å for **16-10** (Table 3-24). These two complexes are the only ones for **14-*n*** to **16-*n*** to show observable clearing points by DSC, showing clearing enthalpies of 3.0 and 2.9 kJ mol^{-1} for **16-8** and **16-10**, respectively.

The mesophases and transition temperatures of complexes **14-*n*** to **16-*n*** on heating are shown graphically in Figure 3-61. The Col_r phases of **15-*n*** are coloured differently as to not conflate phase structures which may arise from different molecular orientations.

Table 3-24: X-ray diffraction data **16-*n***, presenting the measured and calculated spacing, Miller indices and calculated parameters (where applicable).

Complex	Phase	2θ/ °	d_{obs} /Å	d_{calc}/ Å	*hk*	*a*/ Å
16-8	Col_h *T* = 180.0 °C cooling	3.18	27.8	27.8	10	32.1
		5.50	16.0	16.0	11	
		6.41	13.8	13.9	20	
		8.42	10.5	10.5	21	
16-10	Col_h *T* = 180.0 °C cooling	3.05	28.9	28.9	10	33.4
		5.26	16.8	16.7	11	
		6.12	14.4	14.4	20	
		8.05	11.0	10.9	21	

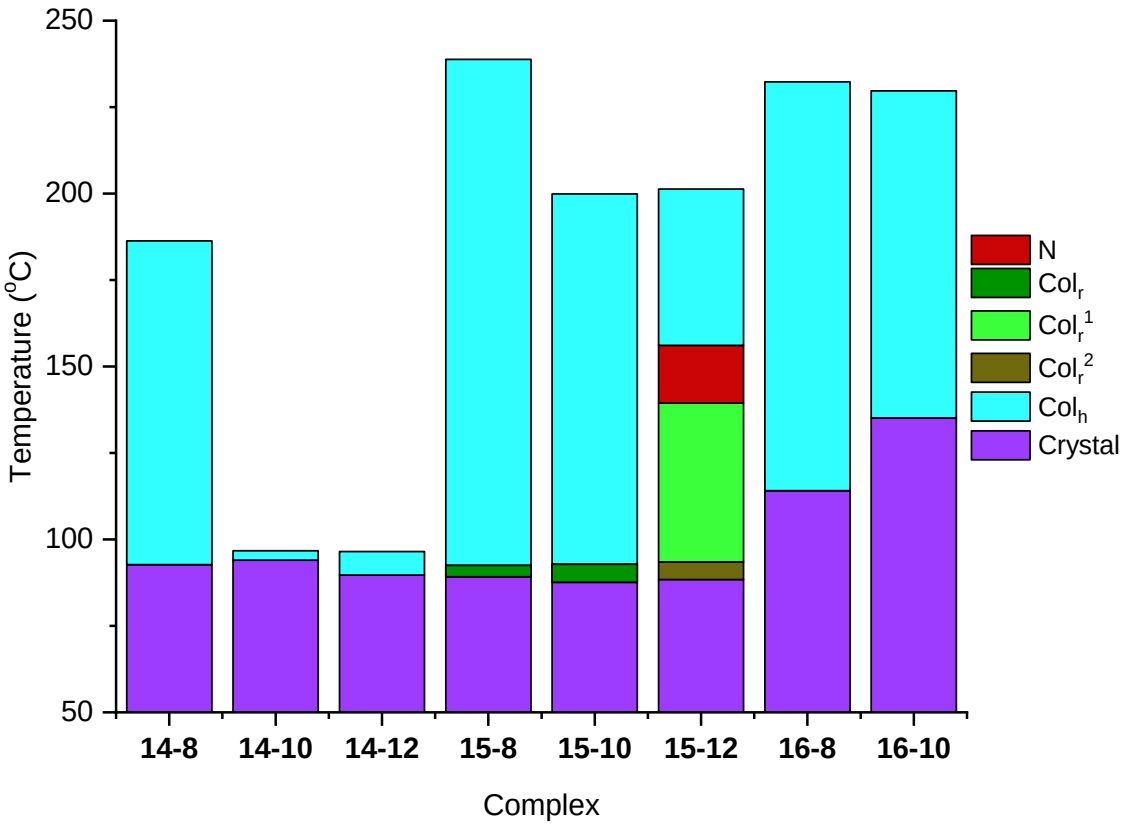

Figure 3-61: Transition temperatures and phases for **14-*n*** to **16-*n*** on heating, with crystal phases shown in purple, N in red, Col_h in blue and Col_r in shades of green. The monotropic Col_r^3 phase is not shown.

The destabilisation of the Col_h phase in **14-*n*** is drastic when the number of fluorinated carbons is equal to or in excess of eight. It is proposed that for the complexes with a C8 chain, in which there are six fluorinated carbon atoms, the level of fluorination is insufficient to require microsegregration between the fluorinated and hydrocarbon chains to form a stable conformer, however when the chain length is increased, the different chains become immiscible as dictated by the fluorophobic effect. For these complexes, this would result in the loss of ability of the molecules to freely rotate around the axis of the column in order to accommodate the incompatibility of fluorinated and hydrocarbon chains, which proves to be a less stable molecular conformation. This effect appears to be a transition point rather than a continuum, as the clearing points of **14-10** and **14-12** are approximately the same.

The depression of the clearing point for **15-10** and **15-12** compared to **15-8** is proposed to be a function of the same immiscibility-driven phase organisation and hindrance of free rotation. However, with two perfluorinated chains the instability is mitigated and the proportional difference in clearing points significantly less. This is proposed to be due to the increased volume occupied by fluorinated chains, meaning that a small amount of rotation is possible without significant interaction with the hydrocarbon regions of the neighbouring molecules in the column, resulting in a stabilisation of the phase.

There is no significant reduction in clearing point as the level of fluorination is increased between **16-8** and **16-10** in contrast to the phase destabilisation observed for both **14-*n*** and **15-*n***, which may indicate that, with three semi-perfluorinated chains on the alknynyl ligand, the volume occupied by fluorinated chains is large enough that the molecular confirmation which is adopted due to the fluorophobic effect is sufficiently flexible to sustain and stabilise the formation of the Col_h phase; with four dodecyloxy chains and 3 semi-perfluorinated dodecyloxy chains, the ratio of hydcarbon:fluorocarbon with respect to volume is approximately the same (1 : 0.84 when considering the number of individual carbon atoms and assuming the volume of perfluorinated carbons is 1.5x that of hydrocarbons).

In the comparison between **11-*n*** and **14-*n***, and **13-*n*** and **16-*n***, the two-chain equivalent shows a higher melting point, indicating that the crystalline phase is more stable. For **12-*n*** and **15-*n***, the melting point between series is very similar, indicating a similar level of stability of the crystalline lattice. Conversely, with the exception of **14-10** and **14-12**, the clearing points for the four-chain complexes are higher, indicating that the phases formed are more stable. It is proposed that the origin in this stability is the increased ability of the four-chain complexes to form a full disc compared to the half-disc two-chain complexes. This is the same rationale as presented for the hydrocarbon equivalents. A comparison of the transition temperatures of the two- and four-chain species is shown in Figure 3-62 and Figure 3-63.

The lattice parameter, *a*, for all Col_h phases in the **14-*n*** to **16-*n*** series is consistent with one molecule in the cross section of the column, as has been previously observed for the hydrocarbon equivalents. For all Col_r phases where the lattice parameters have been determined, both *a* and *b* are approximately double that observed for the *a* value in the Col_h equivalents. It is believed that this large lattice arises from the reorganisation required to accommodate spatial accommodation of the different regions (hydrocarbon and fluorocarbon) of the complex, which appears more prevalent at lower temperatures. This is consistent with behaviour observed in amphiphilic polycatenar compounds discussed earlier.[107]

In contrast to the fully hydrocarbon species, for this family of complexes both the mesophases observed and the transition temperatures are highly dependent on the level of substitution and chain length of the alkynyl ligand. It is clear that the inclusion of semi-perfluorinated chains into these gold(III) alkynyl complexes has a significant impact on the liquid crystallinity of the species, as is observed from the vast differences between the fluorinated species and the hydrocarbon parent complexes. The phase behaviour of these two families of compounds with respect to each other is discussed in the Section 3.4.3.

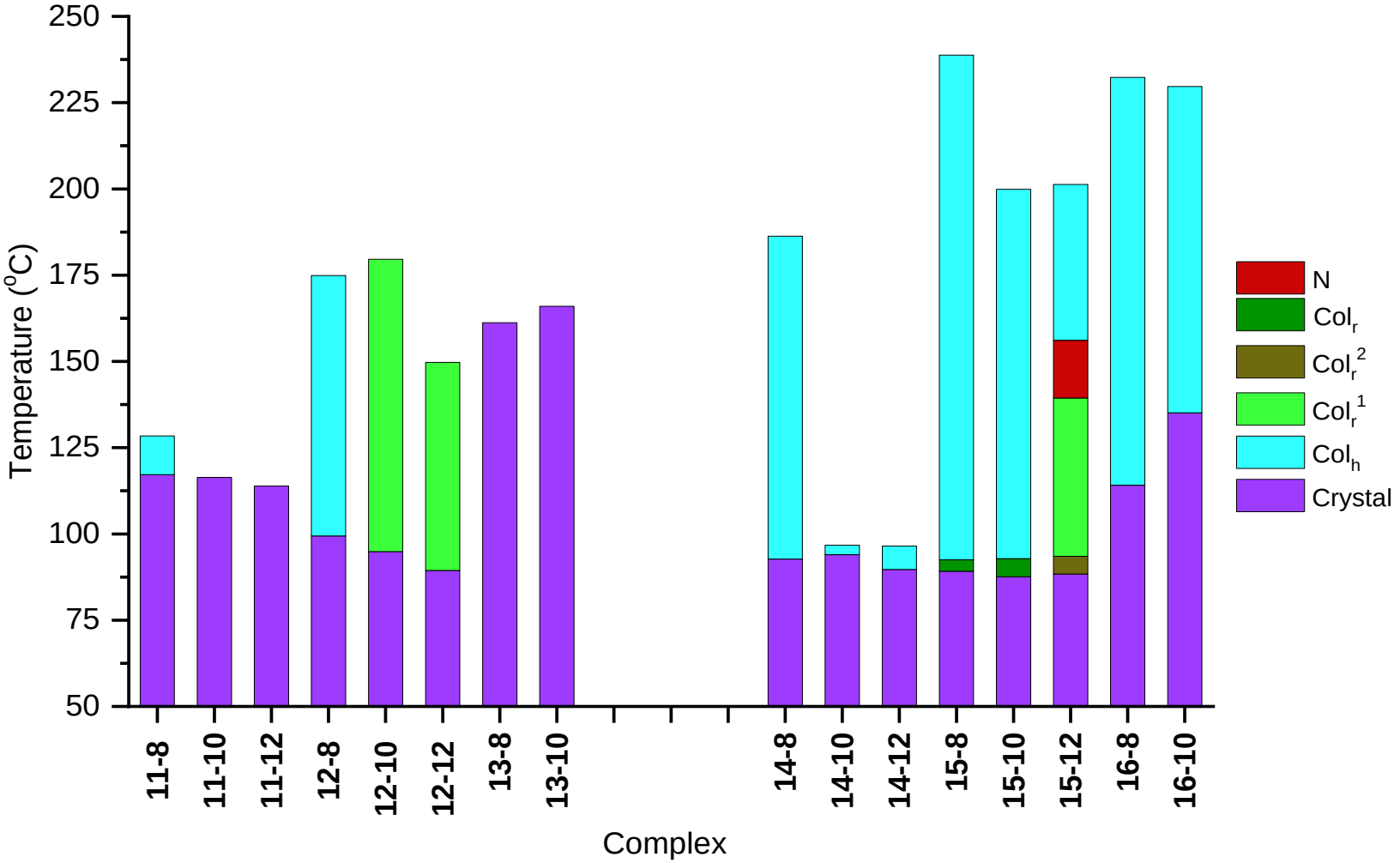

Figure 3-62: Transition temperatures and phases for **11-*n*** to **13-*n*** and **14-*n*** to **16-*n*** on heating, with crystal phases shown in purple, N in red, Col_h in blue and Col_r in shades of green. The monotropic Col_r^3 phase is not shown.

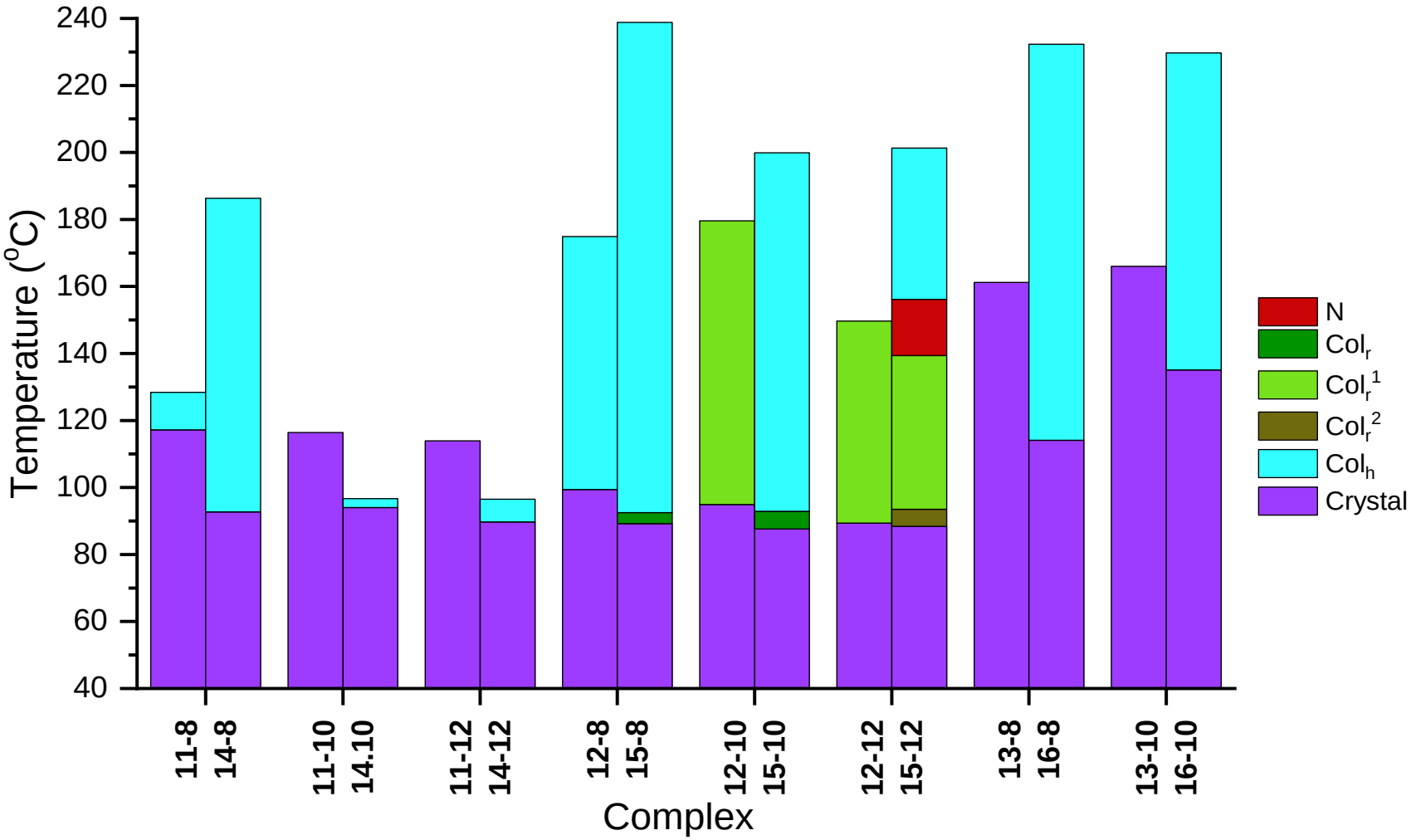

Figure 3-63: Transition temperatures and phases for **11-*n*** ***n*** to **16-*n*** on heating shown as a comparison of complexes with the same alkynyl ligand, with crystal phases shown in purple, N in red, Col_h in blue and Col_r in shades of green. The monotropic Col_r^3 phase is not shown.

3.4.2.3 The Observation of a Nematic Phase for Complex *15-12*

The nematic phase is the most disordered of all mesophases, showing no positional order and only orientational order with respect to the director, **n**, as introduced in Section 1.1.1. Unsurprisingly, the observation of a nematic phase between two columnar phases is exceedingly rare for thermotropic liquid crystals and, given the very disordered nature of the nematic phase compared to a columnar phase, is also rather unexpected. In general terms, there is an expected thermodynamic ordering of mesophases with decreasing temperature that sees increasing degrees of order/correlation introduced. For example, in calamitic materials, the hexagonal order of a SmB phase would be expected at lower temperature than the disordered layer structure of a SmA phase, which in turn would be expected to be below a nematic phase with no positional order. Occasionally, however, phases can appear out of such a sequence and there are examples, particularly with cyanobiphenyl liquid crystals, where the following phase sequence is observed with decreasingly temperature:

$$\text{Iso} - \text{N} - \text{SmA} - \text{N}_{re}$$

where N_{re} is the so-called re-entrant nematic phase, so named to account for it being out of normal sequence. The N_{re} phase was investigated particularly by Cladis[136] and the behaviour is understood by the observation that the extent of the anti-parallel correlation between the cyanobiphenyls is different in the different nematic phases.

Such behaviour in columnar phases is much rarer and there are reports of a re-entrant nematic phase for functionalised truxenes,[137-139] in addition to a reports of a nematic phase between a crystalline and columnar phase[140] in the same general class of materials; these were reported in the early 1980s.

Complexes **15-12** shows an enantiotropic nematic phase between 139.4 and 156.1 °C; these transition temperatures are reproducible and the phase is stable when held within the phase for multiple hours. The nematic phase does not reappear at a higher temperature, but due to its presence below a lower symmetry and less fluid Col_h phase, out of thermodynamic order, it is tempting to consider it as formally re-entrant. The SAXS pattern (Fig. 3-56b) shows, as expected for a nematic phase, a broad reflection at smaller angle which should correspond approximately to the molecular size and a wider-angle reflection that appears to correspond to the separation of perfluorinated chains. While the data obtained at even wider angles are less reliable, there does not appear to be a shorter correlation that might correspond to a separation between cores that would provide direct evidence for columnar organisation. Using confocal microscopy, the birefringence ($\Delta n = n_e - n_o$) of the nematic phase was determined to be negative. This would be expected for an N_D phase and it is probably also the case for an N_{col} phase, too, as the polarisability

perpendicular to the molecular plane is likely so small that even aggregated into a column it would not change the sign of Δn. As such, it is not possible to be definitive about the nature of the nematic phase.

That **15-12** forms a Col_h phase on cooling is unsurprising when comparing with the behaviour of both **15-8** and **15-10**, both of which also show a Col_r phase, although this is not seen for **16-8** or **16-10** (which contain three perfluoroalkyl chains). Evidence from the structural parameters provided by SAXS and consistent with solution NMR measurements (see below) suggests that the complexes with four chains on the C^N^C ligand are able to self-organise in such a way that the complexes sit one upon the other with no significant rotational displacement. This is clearly favourable from the point of view of molecular amphiphilicity as it allows the fluorocarbon moieties and the hydrocarbon moieties each to self-associate. As the temperature drops, so the mobility of the hydrocarbon chains will gradually reduce and the overall shape of the complex will also slowly change to reflect this. A consequence is that a phase transition can ensue, but is self-evident here is that this transition is frustrated *either* because the change in overall shape prevents the complexes from easily self-organising into columns (which would need to be of a tilted nature to accommodate the reduced rectangular symmetry) *or* because columns do indeed form but cannot themselves self-organise into a phase of lower symmetry. The compromise is to form an alternative structure and one might conclude that if there is difficulty forming columns then a conventional N_D phase might results, while if the difficulty is in the self-organisation of the columns, then a N_{col} phase would be seen. The fact that the enthalpy change in and out of the nematic phase is either small or not seen suggests that the extent of reorganisation at the transition is small and so this may support the assertion that it is a N_{col} phase that forms and the absence of a wide-angle reflection may simply reflect significant disorder in along the columnar axis. What is clear is that the frustration is moving from the Col_h to the Col_r phase is significant as the nematic phase exists over almost 17 °C and is enantiotropic.

Considering then complexes **16-8** and **16-10**, the fluorocarbon chains occupy a significantly greater area of the complex and so the nature of the potential shape change driven by the reduced mobility of the hydrocarbon chains is quite different and so there is no change in phase type on cooling. However, why this phenomenon is observed for **15-12** and not **15-10** or **15-8** is at this stage unclear.

3.4.3 Comparison between Hydrocarbon and Semi-Perfluorinated Complexes

A greater number of liquid-crystalline materials were observed for those species with purely hydrocarbon chains than their fluorinated analogues when there were two chains on the cyclometallating ligand.

For those complexes with one chain on the alkynyl ligand the observations are consistent, with both **2-8** and **11-8** being the only complexes in their respective series to show any liquid-crystallinity. However, the phase behaviour observed for both is vastly different, with **2-8** showing only a monotropic Col_h phase and **11-8** showing an enantiotropic Col_h phase. The clearing points of **11-8** is significantly higher than for **2-8**, as is common with the addition of fluorinated chains due to higher level of chain rigidity. This comparison, along with at the other complexes in the two families, is shown graphically in Figure 3-64.

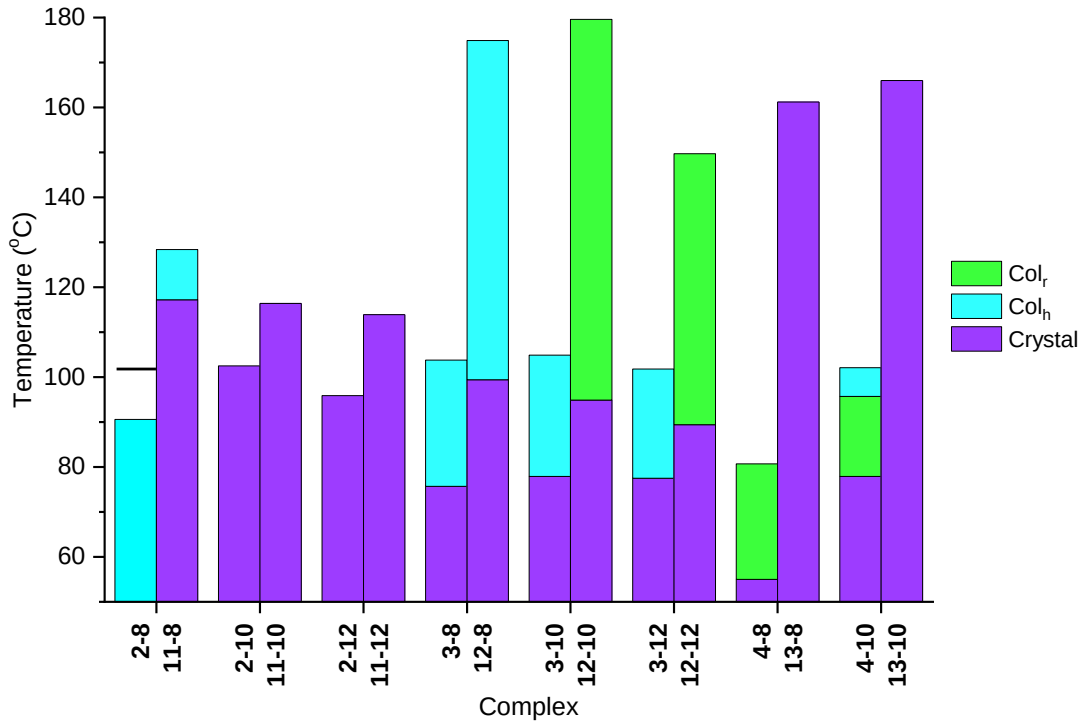

Figure 3-64: Graphical comparison of the liquid-crystalline behaviour of analysis of perfluorinated (**11-8** and **12-*n***) and hydrocarbon species (**2-8** and **3-*n***), with crystalline phases shown in purple, Col_h in blue and Col_r in green.

Comparing **3-*n*** and **12-*n***, the observed differences are approximately consistent across the series with respect to the melting and clearing points; there is an increase of 71 °C in the melting point between **3-8** and **12-8** which decreases as the chains become longer. The observation of an increase in the clearing point when moving from C8 to C10, followed by a reduction in the increase to C12, is the same for both series, although there is an alteration in the phases observed; for **12-10** and **12-12**, the columnar phase is rectangular in nature, compared to the Col_h observed for the other four complexes. It is proposed that this change in organisation is prompted by a more favourable segregation of the perfluorinated chains in the Col_r phase compared to the Col_h, as discussed above.

Those complexes with three alkoxy chains on the alkynyl ligand show Col_h and Col_r phases for the hydrocarbon species (**4-*n***), however no liquid-crystalline behaviour was observed for the

analogous perfluorinated complexes (**13-*n***). It is proposed that a phase conformation where the three perfluorinated chains were segregated from the two hydrocarbon chains with sufficient stabilisation was not present. From analysis of the lattice parameters of the complexes with perfluorinated chains which do show liquid-crystallinity, it can be proposed that the disc is formed through the association of two molecules in an anti-parallel arrangement. Thus, when the complex contains three perfluorinated chains and two hydrocarbon chains, the ratio of fluorinated to hydrocarbon is too great for the anti-parallel confirmation where the hydrocarbon chains can segregate to be stable. For this reason, it is suspected that the missing member of the series **13-12** would also not be liquid-crystalline.

The case is somewhat different for the series of complexes with four chains on the cyclometallating ligand, with all hydrocarbon and fluorocarbon complexes showing liquid-crystallinity. (Figure 3-65).

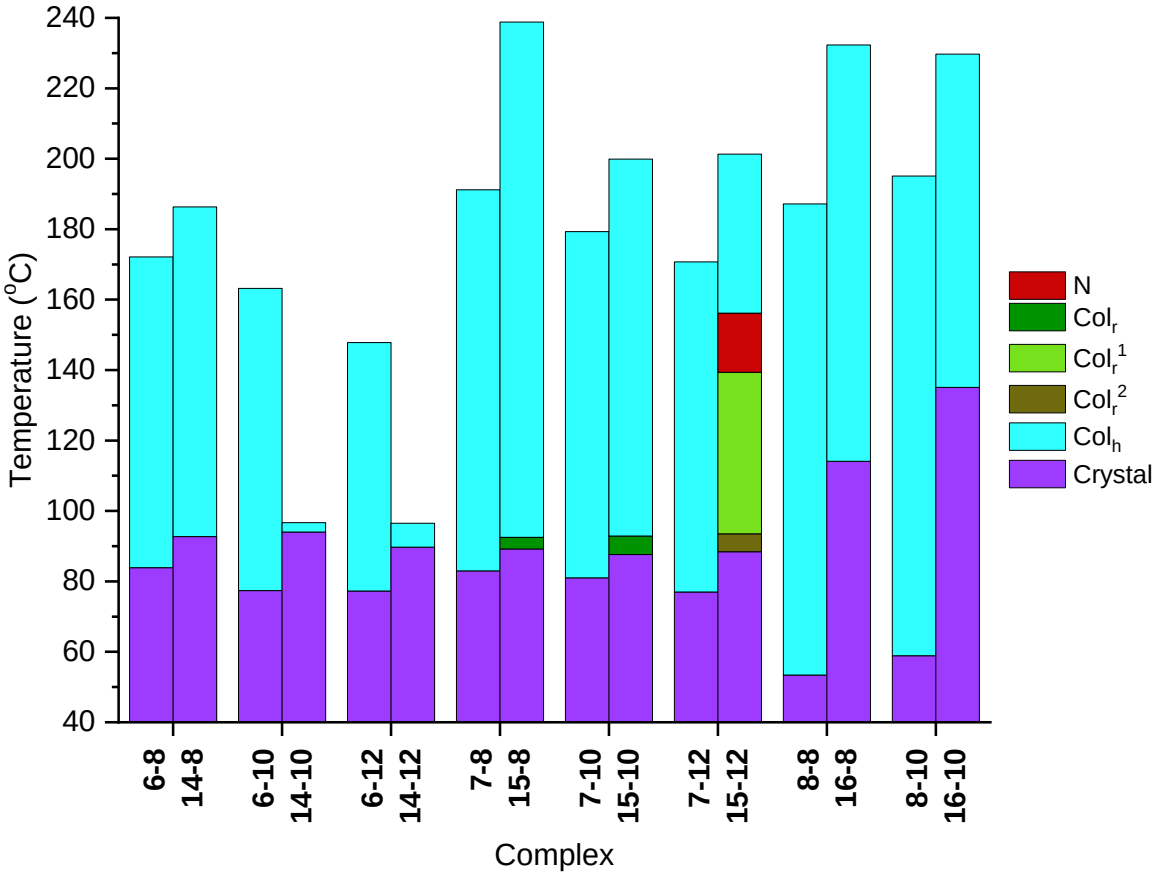

Figure 3-65: Graphical comparison of the liquid-crystalline behaviour of analysis of perfluorinated (**14-*n***, **15-*n*** and **16-*n***) and hydrocarbon species (**6-*n***, **7-*n*** and **8-*n***), with crystalline phases shown in purple, Col_h in dark blue, Col_r in shades of green and N in red. The monotropic Col_r^3 phase is not shown.

When comparing **6-*n*** and **14-*n***, the impact of fluorination on the Col_h phase is drastic; **6-8** and **14-8** show similar transition temperatures, with a 14 °C increase in the clearing point due to the stabilising effect of the inclusion of perfluorinated chains. However, when the number of fluorinated carbons is greater or equal to eight, as is the case for **14-10** and **14-12**, the Col_h phase

is significantly destabilised, as seen in the significantly reduced clearing points in comparison to the hydrocarbon parent complexes **6-10** and **6-12**, with a difference of 66.5 °C and 51.3 °C, respectively. This loss of stability within **14-*n*** is attributed to molecular incompatibility between the fluorinated and hydrocarbon chains as the level of fluorination increases, as outlined in Section 3.4.2, and results in a substantial instability in comparison to the hydrocarbon equivalents, in which rotation around the columnar axis is not hindered.

A comparison of the lattice parameters for these series is also telling; comparing **6-*n*** and **14-*n***, there is a slight increase between **6-8** and **14-8** of 1.6 Å which can be accounted for by the larger volume occupied by the fluorinated chains (Figure 3-66, black squares and green inverted tringles, respectively). For **14-10** and **14-12**, this difference is much greater (5.7 and 5.1 Å, respectively), which suggests that the organisation of the columns is quite different to the organisation observed in **6-*n*** and **14-8**, which is consistent with the hypothesis of segregated phase organisation.

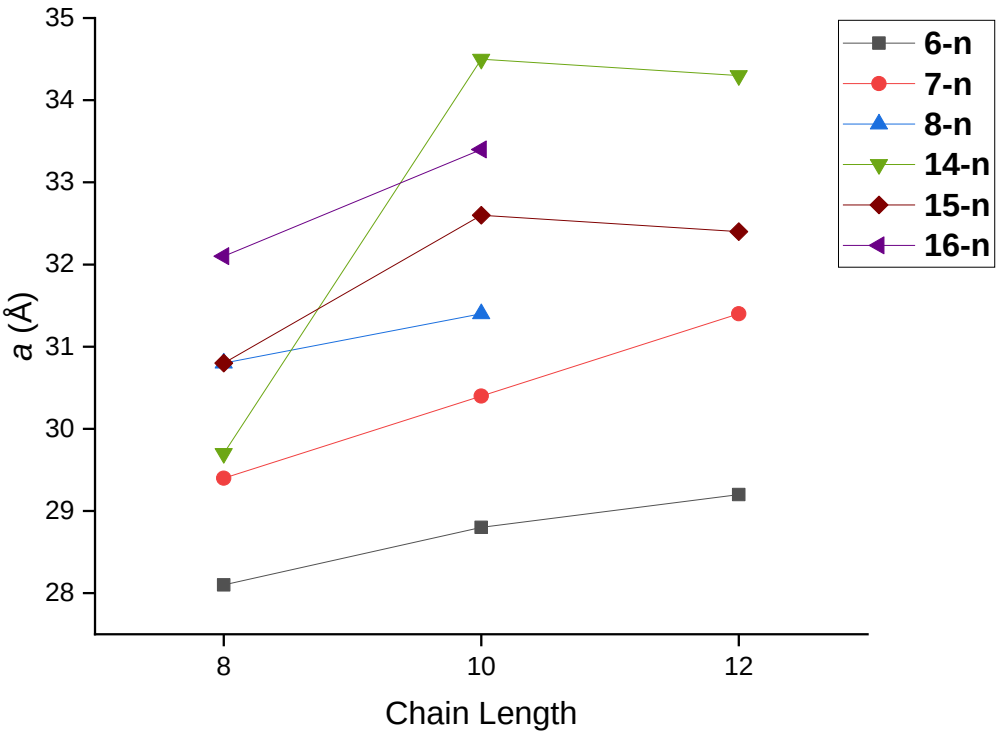

Figure 3-66: Correlation between Col_h lattice parameter, *a*, and chain length of the alkoxy chains on the alkynyl ligand as a comparison between hydrocarbon and fluorocarbon equivalents for the series with four-chains on the cyclometallating ligand.

For **7-*n***, only columnar hexagonal phases are observed, in contrast to **15-*n***, where Col_h and (multiple) Col_r phases are observed, as well as the nematic of **15-12**. For **15-8** and **15-10**, the Col_r phase has a short temperature range, and the phase behaviour is dominated by the Col_h phase which for **15-8** clears at a much higher temperature than **7-8** due to the reduced flexibility of the fluorinated chains as previously observed. The difference in clearing point between **15-10** and **7-10**

is reduced due to the lower clearing point of **15-10** (also observed in **15-12**), which is again attributed to destabilisation of the phase due to enhanced microsegregation effects when the fluorination is increased, although the clearing points for the fluorinated analogues are still approximately 20 °C higher.

The phase behaviour between **8-*n*** and **16-*n*** is not significantly different; there is an increase in crystalline lattice stability as observed from the melting points, and the clearing points of the fluorinated species are significantly higher, however this is not unexpected given the trend of increased stability in perfluorinated analogues. Through comparison of the lattice parameter, *a*, (Figure 3-66), it can be seen that the absolute values for **16-8** and **16-10** are not significantly larger than for **8-8** and **8-10** and can be accounted for by the larger fluorinated chain volume.

From these comparisons, it can be concluded that the inclusion of perfluorinated chains has a substantial effect of the phase behaviour of the gold(III) alkynyl complexes, including phase stabilisation as observed by the general trend of increased clearing points (not including **14-10** and **14-12**) and the induction of different phases, such as Col_r and N in the **15-*n*** series, compared to the parent hydrocarbon complexes, and that any differences observed are mainly driven by the fluorophobic effect and microsegregation of the perfluorinated and hydrocarbon regions of the complexes.

3.5 Self-assembly in Solution: Concentration Dependent ^{1}H, ^{19}F NMR and Electronic Spectroscopy Studies

It was observed that, particularly for those complexes with four chains on the cyclometallating ligand, **Au-Cl-2** and **5-*n*** to **8-*n***, there was an inconsistency in the chemical shifts of certain resonances in the ^{1}H NMR spectra. It was suspected that there was a concentration dependence in the ^{1}H NMR spectra, which could result from the formation of aggregates in solution. Aggregation has often been observed for square-planar complexes due to the available axial positions and interactions between dz^2 orbitals on neighbouring molecules. These interactions have been recently probed by Suleymanova *et al.* for a cyclometallated platinum(II) complex by both ^{1}H and ^{195}Pt NMR spectroscopy, in which the authors managed to determine association constants and concluded that the aggregates formed an anti-parallel association.[141] To investigate this aggregation, solutions of precise concentration were studied by ^{1}H NMR and electronic spectroscopy. Samples were prepared by serial dilution in CD_2Cl_2; the errors associated with the concentration values are provided in Section 6.4. Complex **8-8** was selected as an exemplar molecule; the naming structure used in the following figures is shown in Figure 3-67.

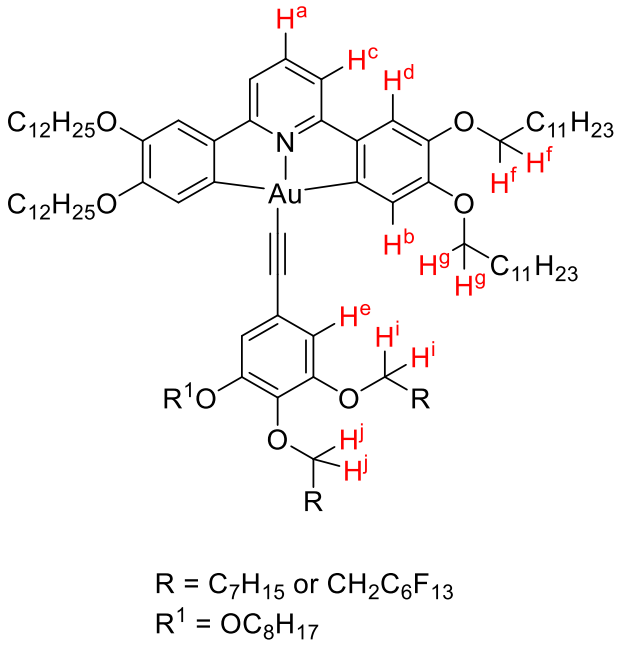

$R = C_7H_{15}$ or $CH_2C_6F_{13}$
$R^1 = OC_8H_{17}$

Figure 3-67: Structure of **8-8**, showing the hydrogen naming system herein used. The same naming system was applied to spectra of **16-8** and **16-10**.

In the ^{1}H NMR spectra, it was observed by that there was a downfield shift for aromatic protons on the cyclometallating rings (**H^a**, **H^b**, **H^c** and **H^d**) upon decreasing the concentration, while the chemical shift of the single resonance for the aromatic protons of the alkynyl ligand, **H^e**, was concentration independent (Figure 3-69). The change in the chemical shift was small, approximately 0.07-0.06 ppm on increasing the concentration from 5.0 x10^{-5} mmol to 1.4 x10^{-2} mmol, but the trend over the concentration range was clear.

This trend was also observed in the resonances for the O-CH_2 protons of the alkyl chains on the cyclometallating ring, **H^f** and **H^g** (in the 4 ppm region, Figure 3-70). The shift here was smaller, with a downfield shift of 0.02-0.04 ppm, and, again, little change was observed for protons **H^i** and **H^j** of the alkynyl ligand. It should be noted that 2,6-di(3,4-dodexyloxy)phenylpyridine, the free ligand, does not show aggregation in solution in this concentration range.

These data are consistent with a 'back-to-back' self-assembly in solution where there is overlap of the rigid aromatic cores of the complex, resulting in a shielding of the protons of the C^N^C ligand, and where the alkynyl ligand is free of any associations (Figure 3-68). This molecular arrangement has been reported for other square-planar species, particularly of the platinum(II) discussed above.[141]

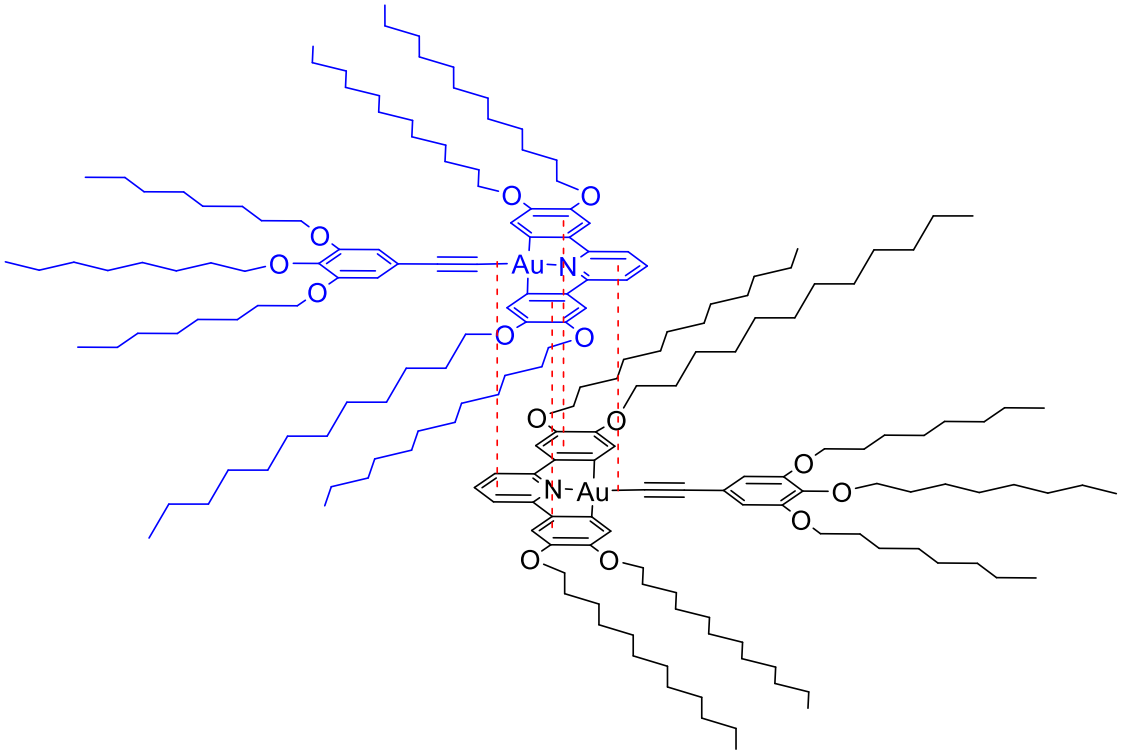

Figure 3-68: Proposed aggregate of **8-8** in concentrated solution showing a 'back-to-back' dimer. Distances are exaggerated for clarity.

It can be seen that the change in chemical shift reaches a plateau as the concentration decreases to approximately 1 x10^{-4} mM. UV-Visible spectroscopy in this concentration region and weaker shows no change in the absorption wavelength or molar extinction coefficient for any of the observed transitions, nor the appearance of any new absorption bands, which would be expected if there were aggregates present in solution; this is consistent with the ^{1}H NMR spectra. In the more concentrated solutions used for electronic spectroscopy, no changes in absorption wavelength or appearance of new peaks were observed.

Concentration-dependent ^{1}H and ^{19}F NMR spectroscopy were also carried out on semi-perfluorinated analogues **16-8** and **16-10** to investigate the effect of fluorination. Both complexes were investigated due to noted observations that oftentimes any effect of fluorination is only apparent when the number of fluorinated carbons exceeds eight, as has been discussed in Section 3.4.2.

The aromatic region of the ^{1}H NMR spectrum of **16-8** is shown in Figure 3-71, and as with **8-8**, there is a noticeable and very much larger downfield shift of all four hydrogens on the cyclometallating rings when the concentration is decreased. Additionally, in contrast to what is observed for the fully hydrocarbon species, there is also a downfield shift of the resonance arising from the alkynyl ligand (**H^{e}**) of 0.04 ppm, although this change is smaller in magnitude than that of the other aromatic signals, **H^{a}** to **H^{d}** which range from 0.12 to 0.07 ppm.

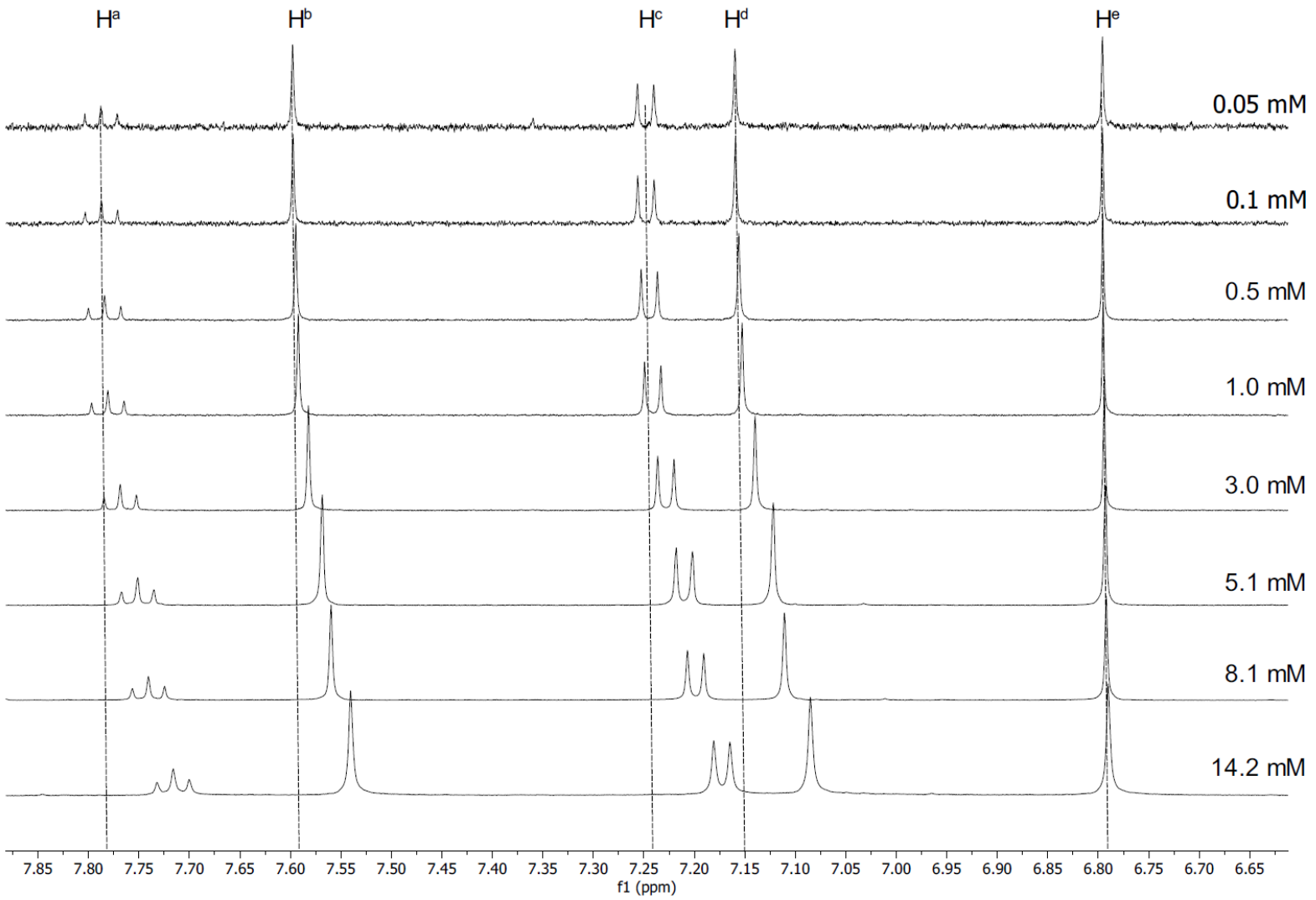

Figure 3-69: ^{1}H NMR spectra at decreasing concentration showing the downfield shift of the aromatic protons on the C^N^C ligand of **8-8**.

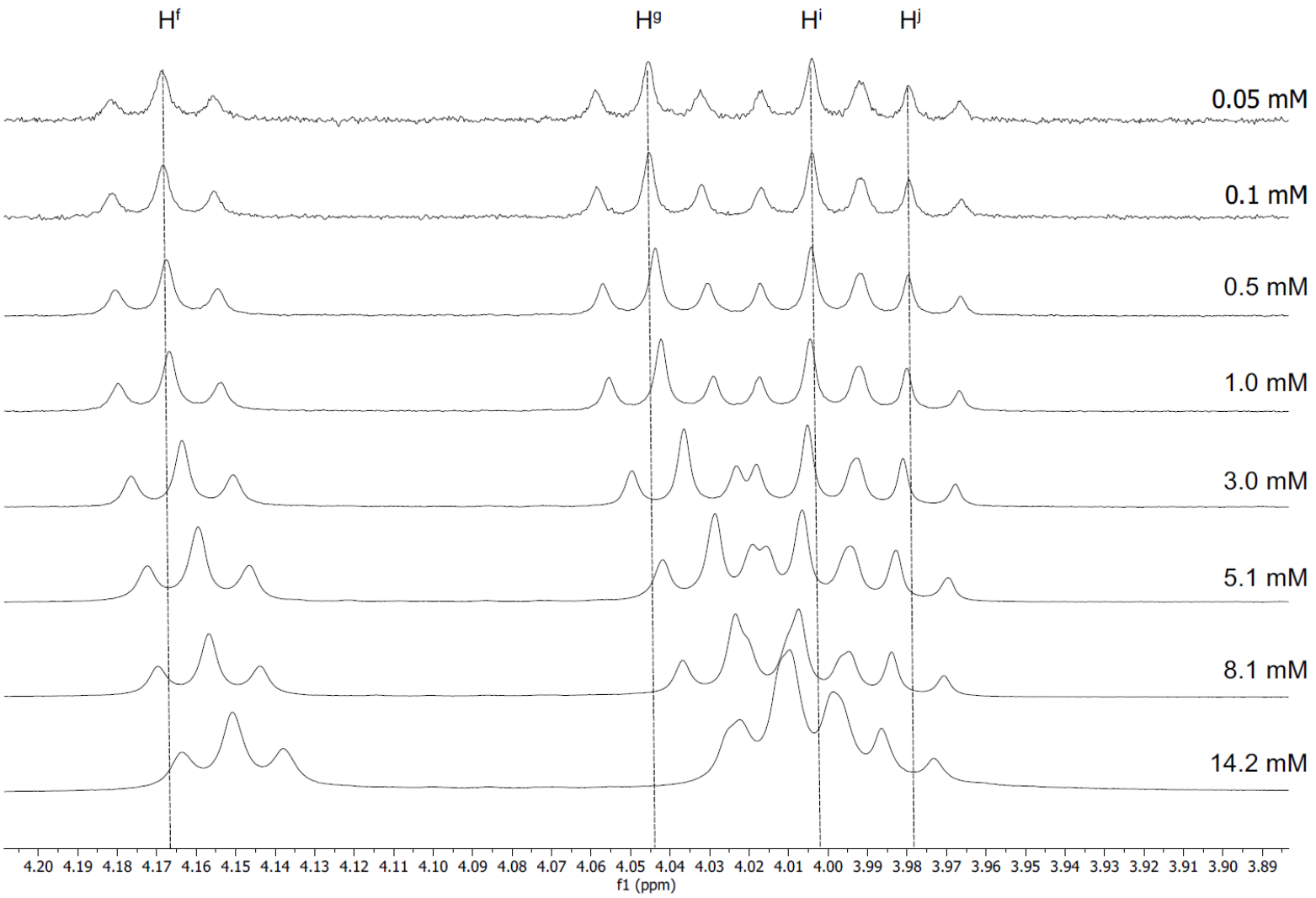

Figure 3-70: ^{1}H NMR spectra at decreasing concentration showing the change in the chemical shift of the O-CH_2 protons of the alkyl chains on the cyclometallating ring of **8-8**.

As with **8-8** there were also changes in the chemical shifts for the O-CH_2 of both of the hydrocarbon chains on the cyclometallating ligand and the semi-perfluorinated chains. For protons $\mathbf{H^f}$ and $\mathbf{H^g}$ on the cyclometallating ligand, $\Delta\delta$= 0.04 and 0.05 ppm, respectively, very similar to that observed for $\mathbf{H^i}$ from the equivalent semi-perfluorinated chains in the 3 and 5 (*meta*) positions of the alkynyl ring (0.03 ppm). The only relevant resonance of **16-8** that does not show a concentration-dependent shift is $\mathbf{H^j}$, from the alkoxy chain in the 4 (*para*) position of the alkynyl ring. This is in stark contrast to **8-8**, where both protons $\mathbf{H^i}$ nor $\mathbf{H^j}$ show only minimal concentration dependence, indicating that for **16-8**, the aggregation contains interactions in the alkynyl region of the molecule.

For **16-10** the observed changes in chemical shift appear to be similar to those observed for **16-8**, however the magnitude of the changes were significantly greater; in the aromatic region they range from 0.15 to 0.10 ppm for the cyclometallating protons $\mathbf{H^a}$ to $\mathbf{H^d}$, and there was also a modest increase in the change of the aromatic proton on the alkynyl ligand, $\mathbf{H^e}$, which was shifted downfield by 0.06 ppm (Figure 3-73).

The same can also be said for the relevant protons on the alkoxy chains; there was a slight increase for $\mathbf{H^f}$ and $\mathbf{H^g}$ with a shift of 0.06 ppm for both, as well as a doubling of the change of $\mathbf{H^i}$, also to 0.06 ppm and $\mathbf{H^j}$ to 0.01 ppm, although the change in the latter is still negligibly small (Figure 3-74).

Complexes **16-8** and **16-10** were also both investigated by ^{19}F NMR. A slight shift was observed for the terminal CF_3 groups of all three chains (Figure 3-75) for both **16-8** and **16-10**. For the fluorine atoms of **16-8** this shift is equivalent to 0.06-0.07 ppm, but is significantly larger for **16-10** with a change of 0.12-0.13 ppm; the difference in magnitude of these changes between the two species is similar to that observed in the ^{1}H NMR spectra.

Differences are also observed between **16-8** and **16-10** when observing the fluorine atoms on the internal –CF_2– groups of the semi-perfluorinated chains. For **16-8**, the chemical shift of the fluorine atoms are invariant with concentration (Figure 3-76), however in **16-10**, there is a downfield shift for all resonances. This shift is small, ranging from 0.04 to 0.1 ppm across the five measured resonances.

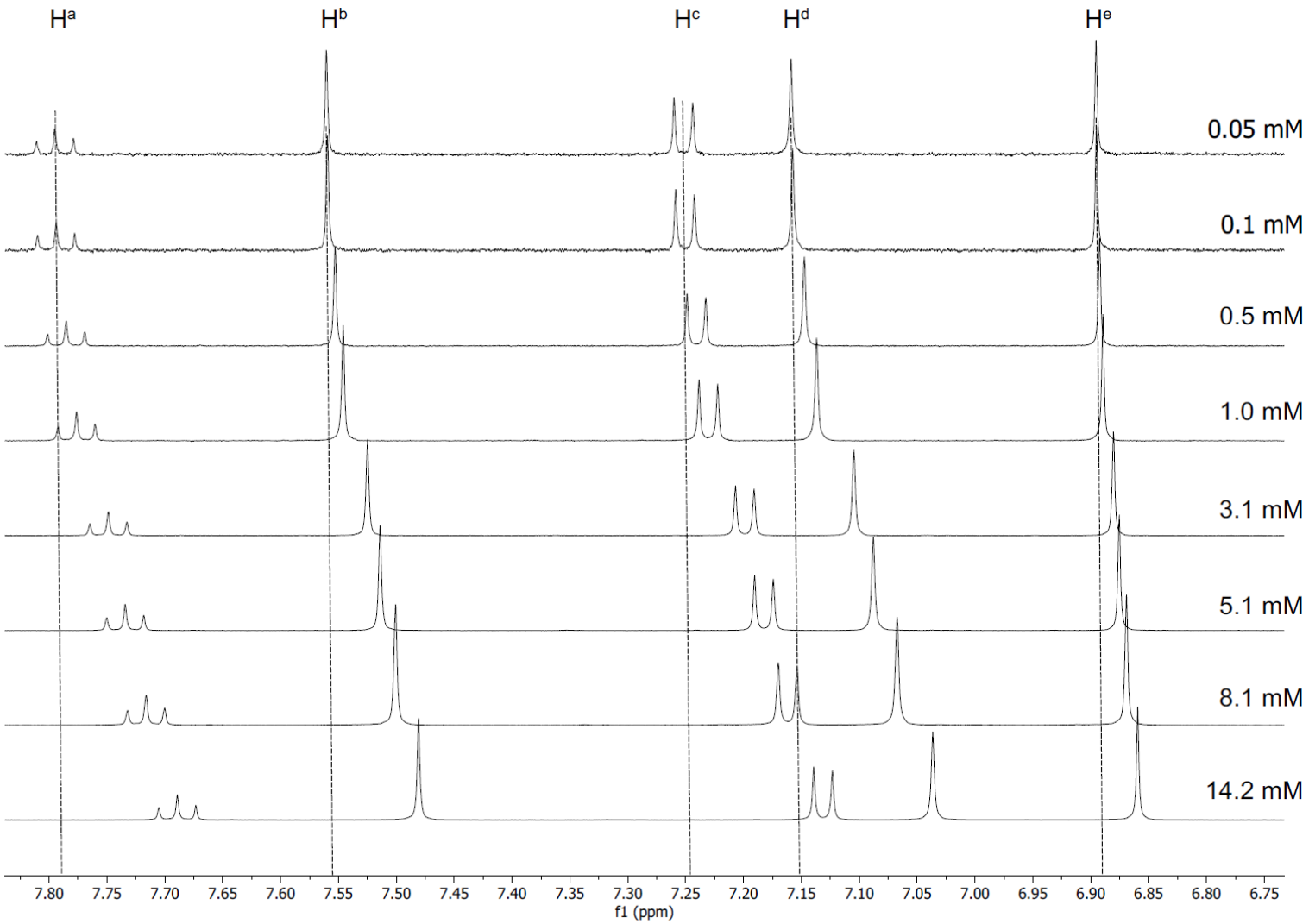

Figure 3-71: ^{1}H NMR spectra at decreasing concentration showing the downfield shift of the aromatic protons on the C^N^C ligand and of the perfluorinated alkynyl ligand of **16-8**.

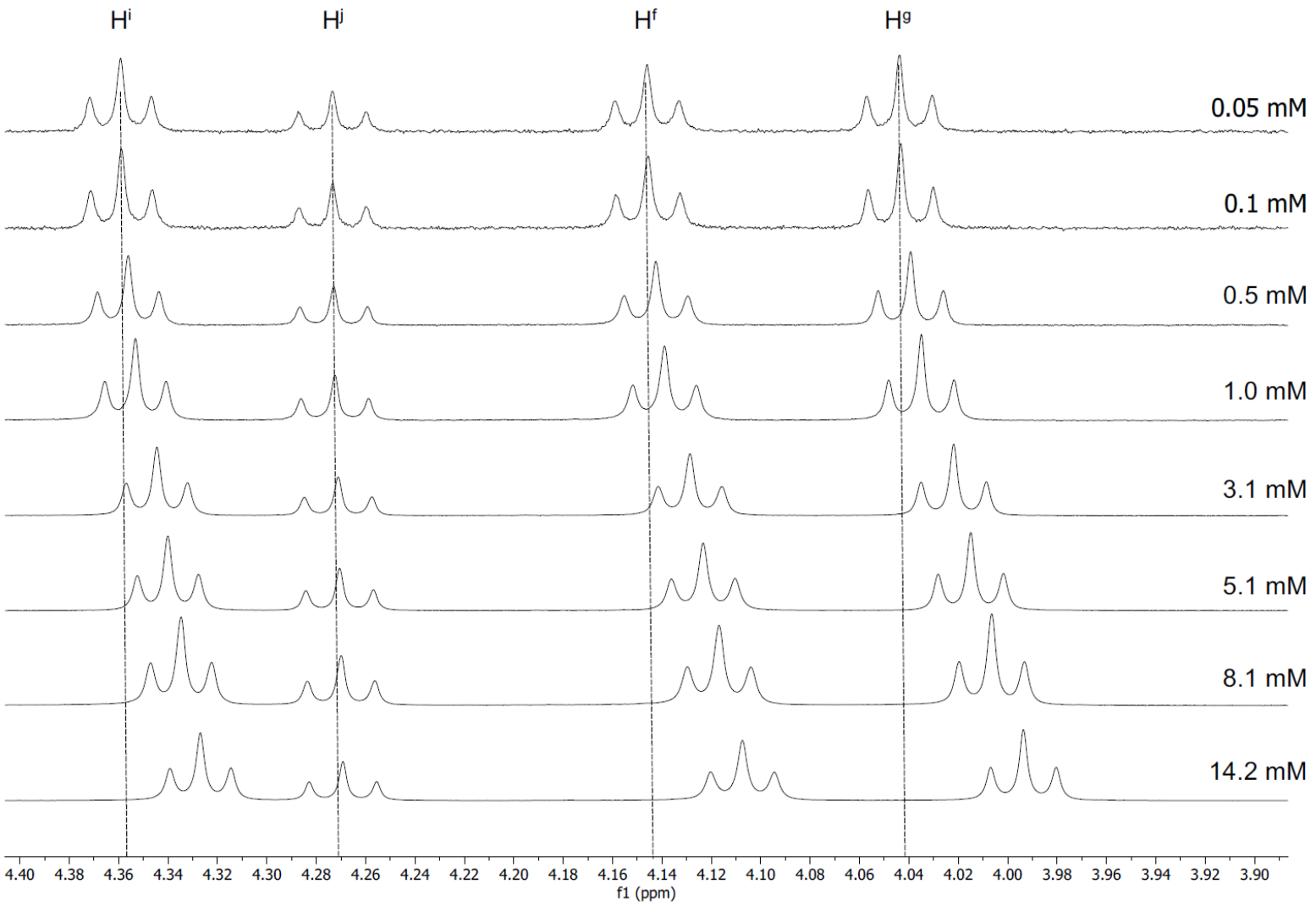

Figure 3-72: ^{1}H NMR spectra at decreasing concentration showing the downfield shift of the O-CH_2 protons of the alkyl chains of **16-8**.

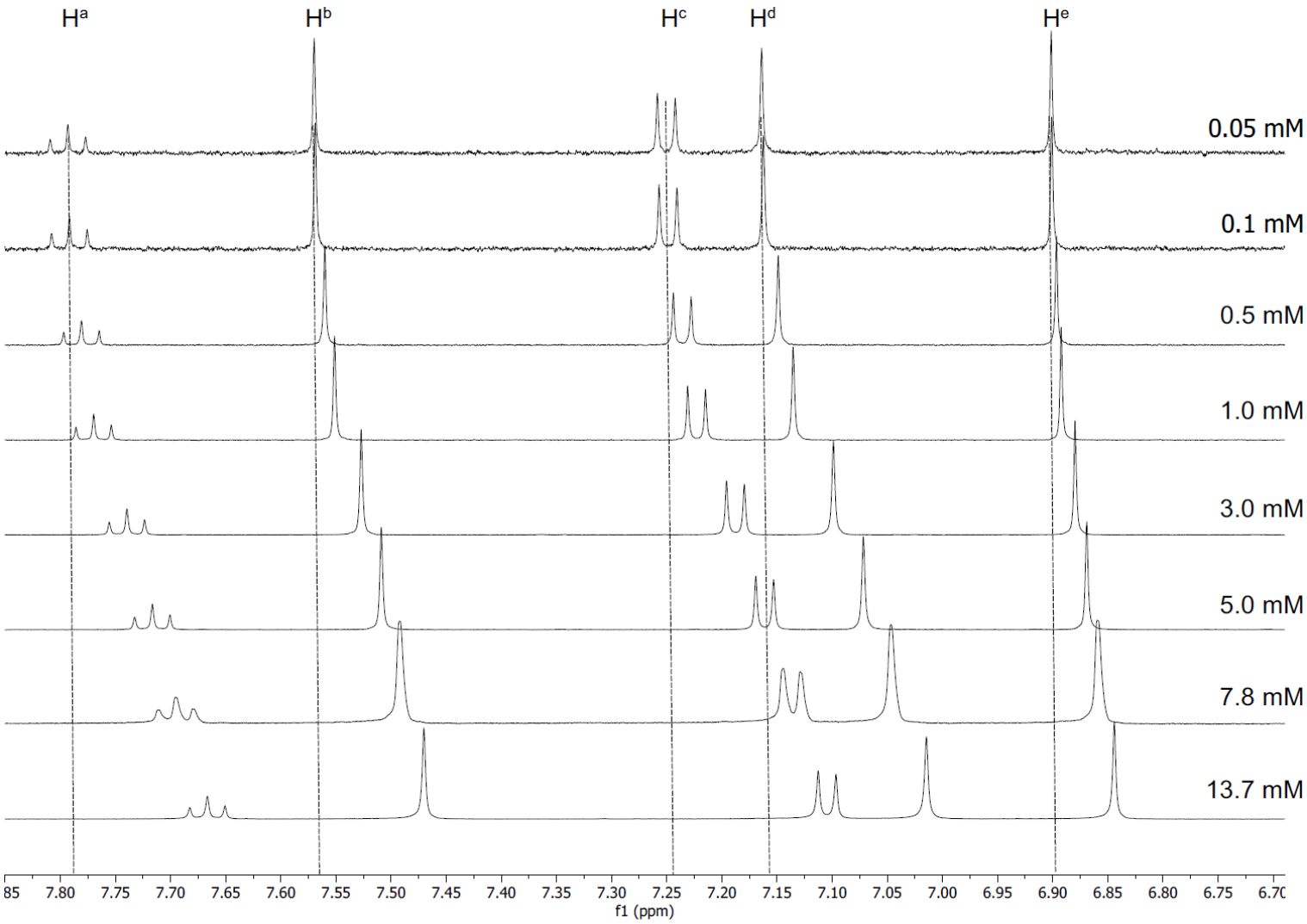

Figure 3-73: ^{1}H NMR spectra at decreasing concentration showing the downfield shift of the aromatic protons on the C^N^C ligand and of the perfluorinated alkynyl ligand of **16-10**.

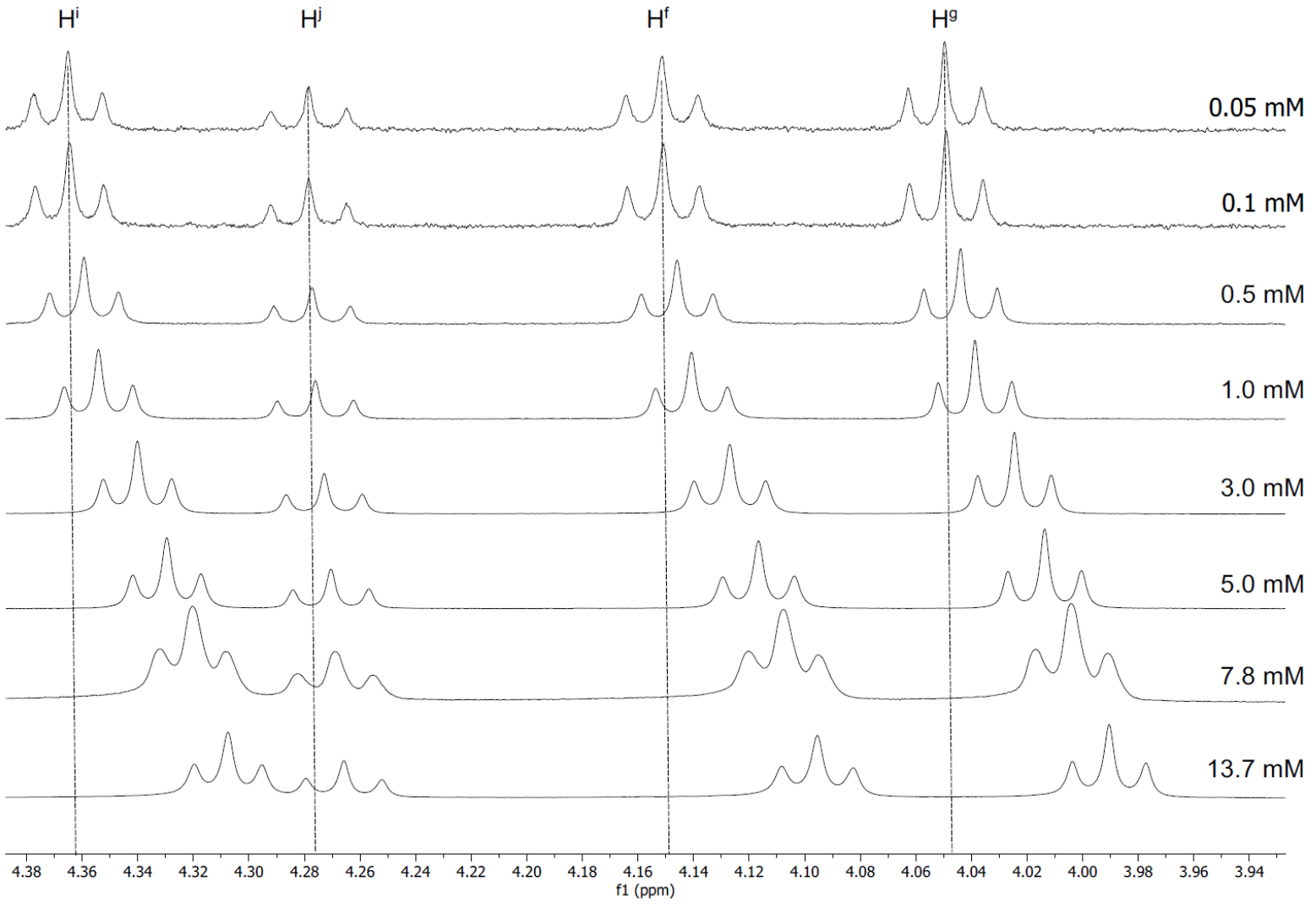

Figure 3-74: ^{1}H NMR spectra at decreasing concentration showing the downfield shift of the O-CH_2 protons of the alkyl chains of **16-10.**

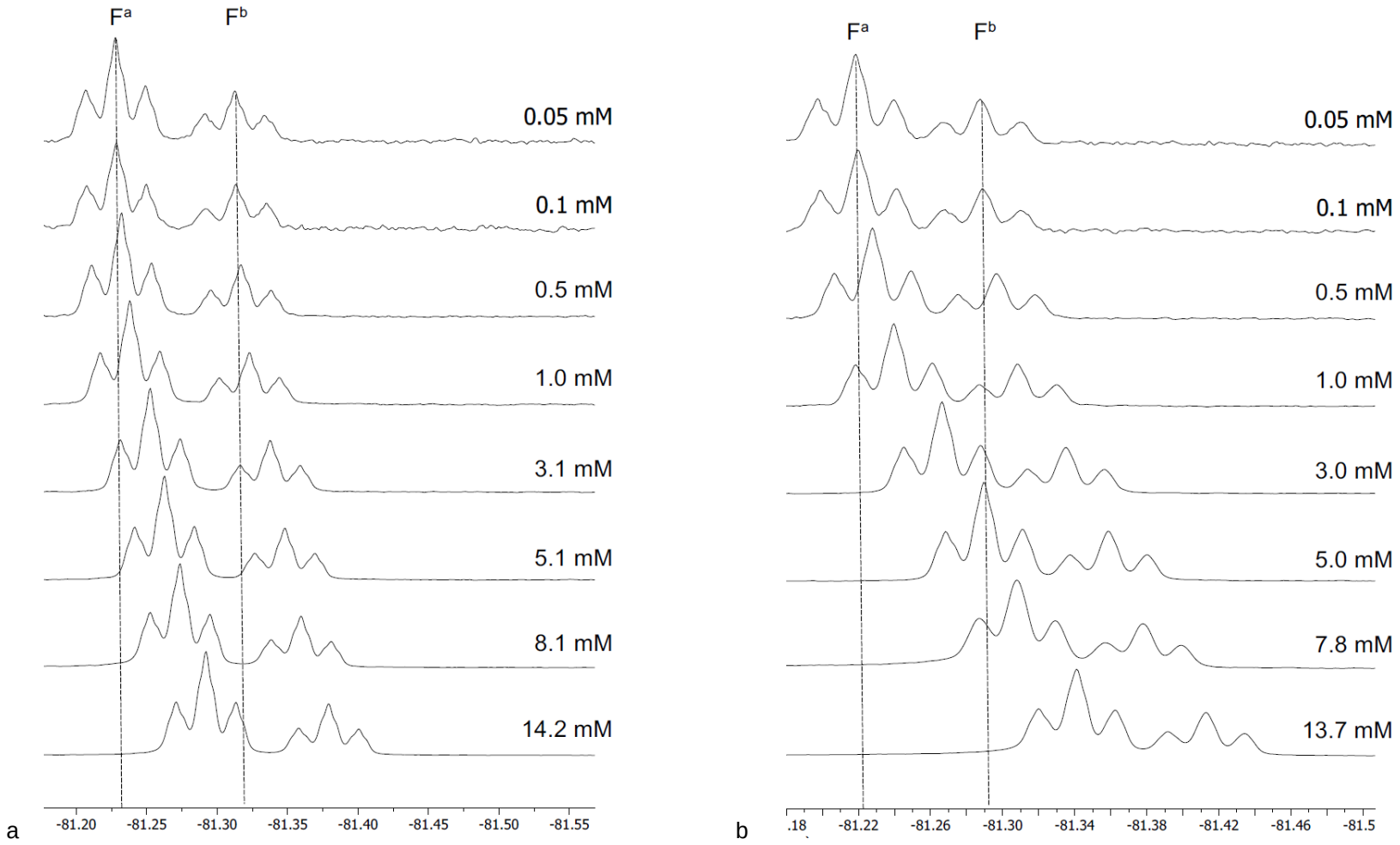

Figure 3-75: ^{19}F NMR spectra at decreasing concentration showing the downfield shift of the $-CF_3$ atoms of the perfluoroalkyl chains of a) **16-8** and b) **16-10**.

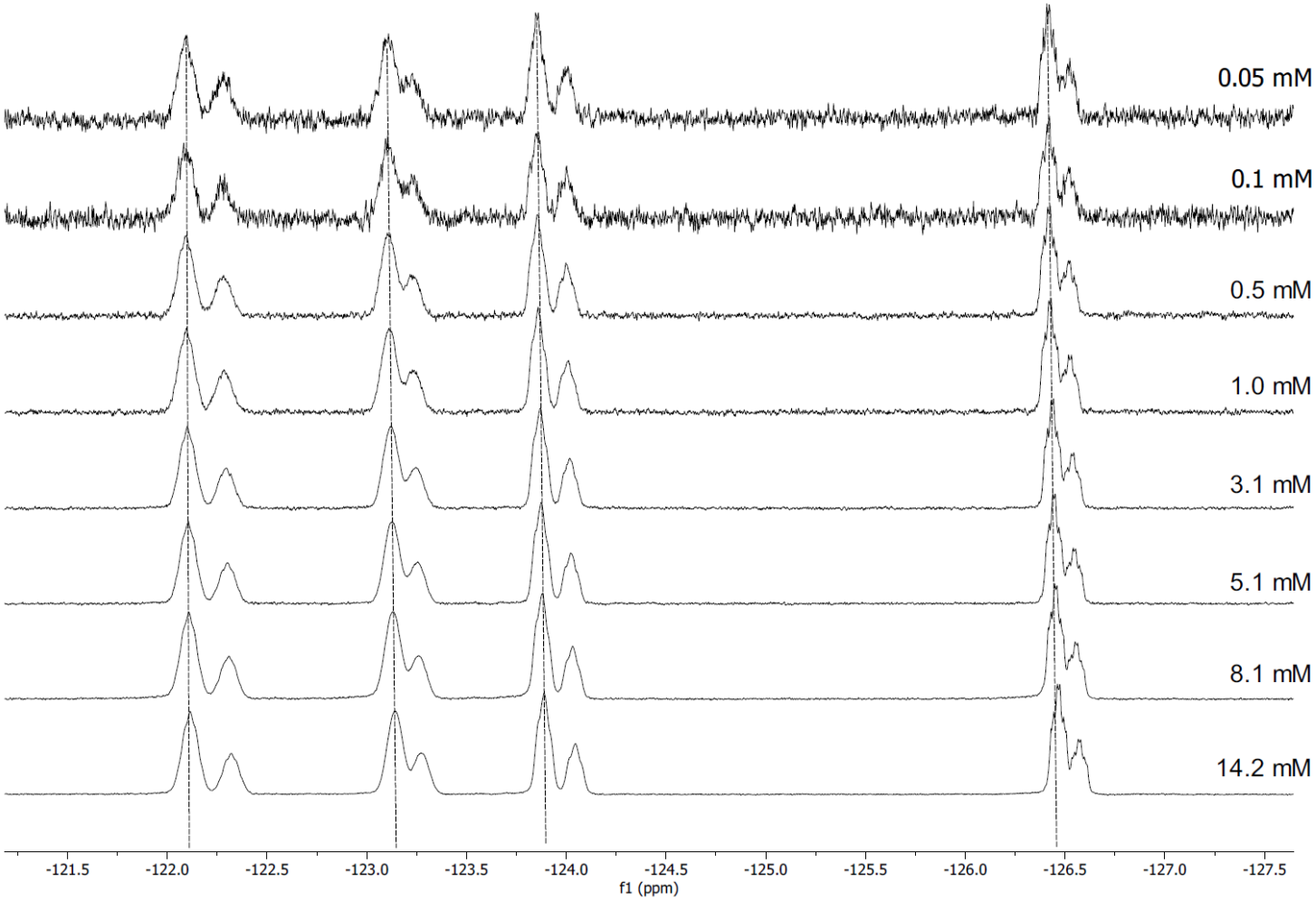

Figure 3-76: ^{19}F NMR spectra at decreasing concentration showing the consistency of chemical shift of the $–CF_2–$ atoms of the perfluoroalkyl chains of **16-8**

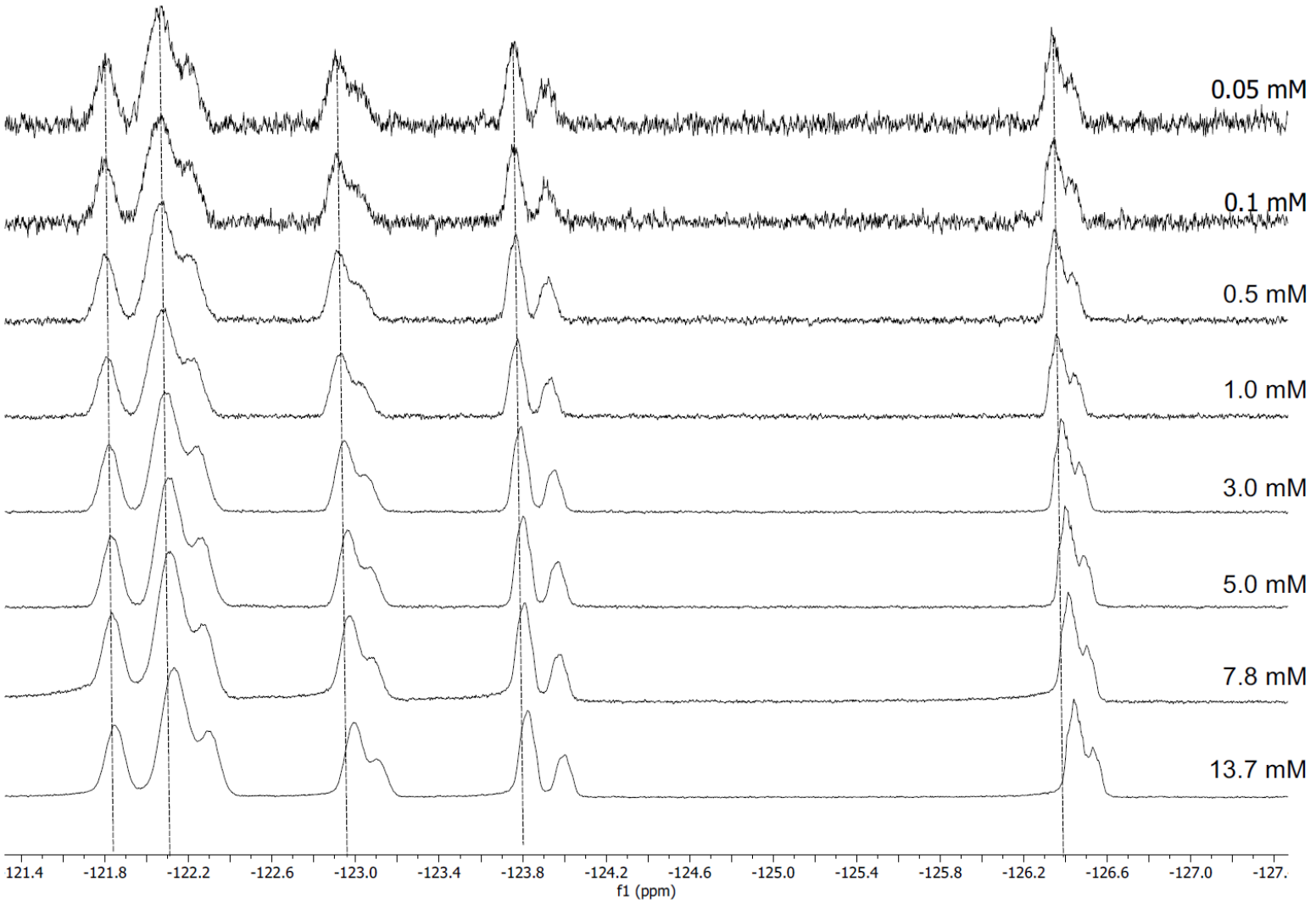

Figure 3-77: ^{19}F NMR spectra at decreasing concentration showing the small downfield shift of the $–CF_2–$ atoms of the perfluoroalkyl chains of **16-10**

A summary of the concentration dependency of all the relevant proton and fluorine resonances for species **8-8**, **16-8** and **16-10** is given in Table 3-25, with this shown graphically for proton $\mathbf{H^d}$ in Figure 3-78; $\mathbf{H^d}$ was chosen as it was this resonance which showed the largest change in chemical shift for all species. It can be seen in both plots that the change in chemical shift for the fluorinated species is significantly larger than for **8-8**, and that the shift for **16-10** is larger than that of **16-8**; the origin of this is discussed below**.**

Table 3-25: Change in chemical shift of significant proton resonances between the most and least concentrated samples in concentration dependent ^{1}H and ^{19}F NMR spectroscopy investigation for complexes **8-8**, **16-8** and **16-10**

	Change in Chemical Shift (ppm)										
Complex	$\mathbf{H^a}$	$\mathbf{H^b}$	$\mathbf{H^c}$	$\mathbf{H^d}$	$\mathbf{H^e}$	$\mathbf{H^f}$	$\mathbf{H^g}$	$\mathbf{H^i}$	$\mathbf{H^j}$	$\mathbf{F^a}$	$\mathbf{F^b}$
8-8	0.07	0.06	0.06	0.06	0.005	0.02	0.02	0.004	0.004	-	-
16-8	0.07	0.08	0.12	0.12	0.04	0.04	0.05	0.03	0.004	0.06	0.07
16-10	0.13	0.1	0.15	0.15	0.06	0.06	0.06	0.06	0.01	0.12	0.13

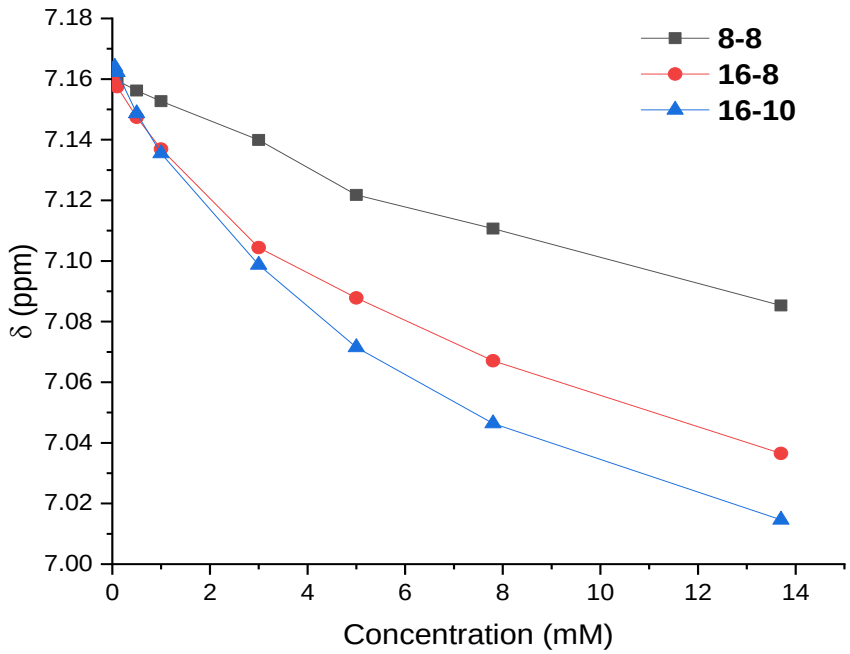

Figure 3-78: Concentration-dependent chemical shift of proton $\mathbf{H^d}$ for complexes **8-8**, **16-8** and **16-10**.

Given the changes that are observed for all three complexes as the concentration is decreased, it is clear that the model proposed for the dimerisation of **8-8** in is unsuitable for the fluorinated species **16-8** and **16-10**, especially given the downfield shift of protons $\mathbf{H^e}$, $\mathbf{H^i}$ and $\mathbf{H^j}$. For **16-8** and **16-10**, it is proposed that, in contrast to the back-to-back arrangement suggested for **8-8**, the aggregation is driven by segregation of the hydrocarbon and perfluorinated chains, resulting in dimers or oligomers in which the molecules are orientated in the same direction to one another as they aggregate, *i.e.* they are directly superimposed on one another (Figure 3-79).

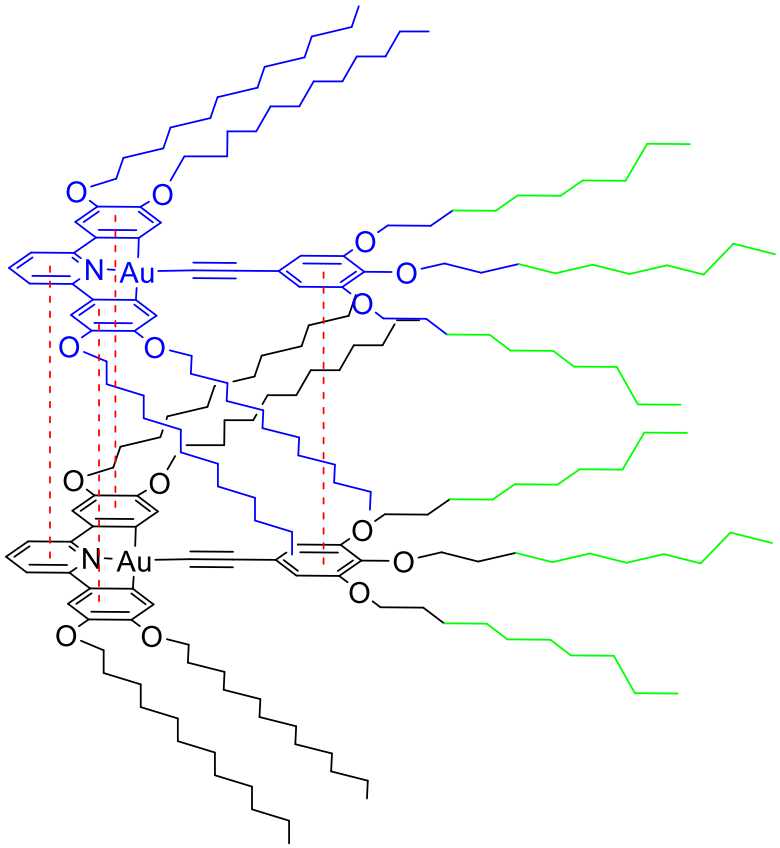

Figure 3-79: Proposed aggregate of **16-10** in concentrated solution showing a superimposed dimer. Distances exaggerated for clarity. Fluorinated chains shown in green.

The change in all chemical shifts between the two fluorinated species can also be explained by the incompatibility of the chains; it has been observed that segregation occurs when there are eight or more perfluorinated carbon atoms in the chain in the liquid-crystalline state of **14-*n*** to **16-*n*** (Section 3.4.2). Given the freedom of movement of the molecules in solution, it is not surprising that in a transient aggregate of **16-8**, in which there are six fluorinated carbons in the chains, the most favourable confirmation would associate the fluorinated portion of the molecule, even with a reduced level of fluorination. However, the change in chemical shift of proton $\mathbf{H^e}$ is substantially less than that observed for the other aromatic protons, indicating that this confirmation may not be exclusive and the level of interaction between the two molecules of the aggregate (assuming the aggregate is dimeric in nature) could be flexible.

For complex **16-10**, in which each semi-perfluorinated chain has eight perfluorinated carbon atoms, it would be expected that the molecules would aggregate in a superimposed fashion due to the incompatibility of the fluorinated chains with the hydrocarbon-dominated core of the molecule. The changes in chemical shift for **16-10** are larger than for **16-8**, and there is an increase in the proportion by which $\mathbf{H^e}$ is shifted, indicating that the association between the alkynyl ligands is stronger than for **16-8**, which in consistent with an increased fluorophobic effect. This is supported by the fact that the internal $–CF_2–$ atoms of the perfluoroalkyl chains are invariant with

concentration for **16-8**, but show a downfield shift for **16-10**, indicating that the fluorinated chains on neighbouring molecules of the aggregate have a small degree of association that is absent in **16-8**. The downfield shift of the CF_3 fluorine atoms in **16-8** can be attributed to interaction of the ends of the chains with neighbouring molecules which are not officially aggregating.

It is clear that the inclusion of fluorinated chains, and indeed the level of fluorination, has an impact of the molecular associations of these complexes, which has a substantial effect on the material and supramolecular properties.

3.6 Gelation Properties of Gold(III) Complexes

It was observed during purification that complexes **3-*n*** had the ability to form metallogels. These were first formed during the chromatographic purification of **3-10**, where the most concentrated individual fractions collected formed gels that were stable to inversion upon standing at room temperature (Figure 3-80). The gels were only observed when the eluent used was petroleum ether (40-60), containing a small percentage of ethyl acetate (95:5).

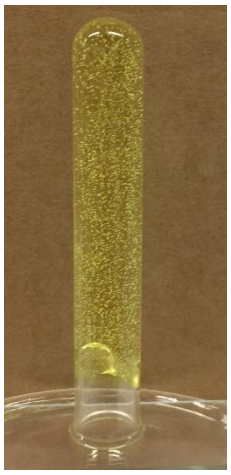

Figure 3-80: Photograph of an inverted column fraction of **3-10** in 95% petroleum ether (40-60)/5% ethyl acetate, which has formed a stable metallogel.

For complexes **2-*n***, weak gels were also observed when using chloroform/acetonitrile as a solvent system for crystallisation, although these gels were not stable to inversion, and the supramolecular network could be disrupted upon agitation. When attempting recrystallisation of **3-*n*** systems in CH_2Cl_2/acetone, similar metastable gels were observed.

It should be noted that under both the aforementioned conditions, no gels were observed for complexes with four chains on the cyclometallating ligand (**5-*n*** to **8-*n***).

It was also observed that complexes with two semi-perfluorinated chains on the cyclometallating ligand, **11-*n*** to **13-*n***, formed weak gels upon cooling during crystallisation from hexane, similar to those observed for the **2-*n*** species. Similarly, gels were also observed for many of the intermediate products during the synthesis of the semi-perfluorinated ligands, but these were not characterised.

Metallogels for gold(III) alkynyl complexes with functionalised ligands are not unknown, and literature systems show examples from gold(III) alkynyls modified by L-valine alkynyls,[110] which are driven by π–π stacking, hydrogen bonding and hydrophobic–hydrophobic interactions in DMSO (Figure 3-82a). Other systems containing three alkoxy chains on the phenylethynyl ligand form luminescent metallogels in hexane and cyclohexane which are luminescent (Figure 3-82b).[108] Other gold(III) gelators include a complex with 2,6-bis(benzimidazol-2'-yl)pyridine cyclometallating ligands and an alkynyl ligand as used in this study (**HL6-12**), which forms a stable-to-inversion gel in chloroform (Figure 3-82c).[142]

Also relevant are the observations by Kato of gelators which interact with liquid-crystalline molecules, to form 'liquid-crystalline physical gels'.[143] Traditional physical gels are formed through the encapsulation of solvent molecules in a network of gelator molecules to form a supramolecular network, whereas in a liquid-crystalline physical gel, the mesogen molecules essentially act as an ordered solvent, which forms a supramolecular network with a gelator, such as oligomeric amides or alkyl functionalised anthracene (Figure 3-81). Liquid-crystalline physical gels have many appealing properties, such as enhanced light-scattering and switching in electro-optical devices, and, specifically with reference to mesogenic compounds which form columnar phases, higher hole-transport mobilities than the free liquid-crystalline material.[143, 144]

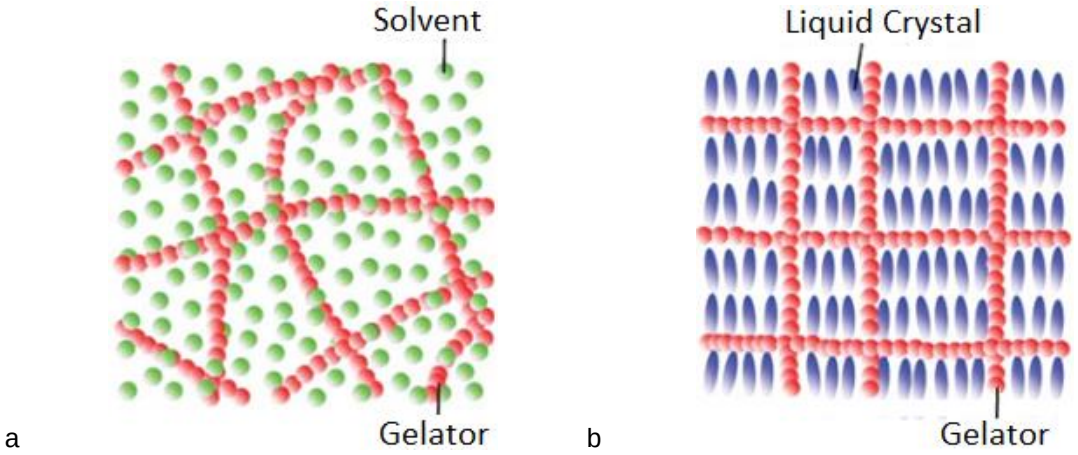

Figure 3-81: Schematic representation of the structure of a a) traditional physical gel and b) a liquid-crystalline physical gel. Adapted from reference.[143]

Although the observations of gels in the case of the [Au(C^N^C)(C≡CR)] complexes here are most likely standard physical gels due to the interactions between the gold(III) complexes and organic

solvents, the observation that they can form gels at all invites further investigation into whether these molecules are suitable for applications as liquid-crystalline physical gels.

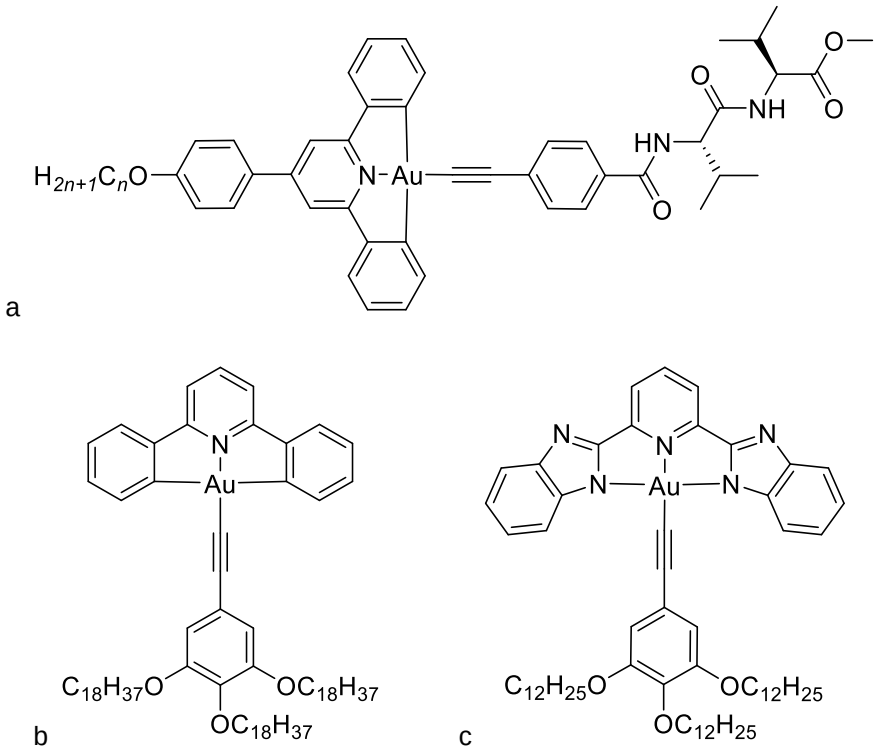

Figure 3-82: Structure of gold(III) complexes which form metallogels reported by a) Siu *et al.* which show gels in DMSO when *n* = 6, 12, 18;[110] b) Au *et al.* which shows gels in hexane and cyclohexane;[108] c) Yim *et al.* which forms a gel in chloroform.[142]

Morphologically, the complexes shown in Figure 3-82b are most similar to **2-*n*** and **3-*n***; given that these complexes retain their emission whilst in the gel, it would be prudent to investigate the gelation properties of the novel complexes reported here, both in structural characterisation of the supramolecular network, as well as the emissive properties of the gel. Due to the time-constraints of this project, this may be considered an attractive avenue for future work.

3.7 Conclusions

Multiple series of liquid-crystalline gold(III) alkynyl complexes of the general formula [Au(C^N^C)(C≡CR)] with varying alkyl and alkoxy substitution levels on both the cyclometallating and alkynyl ligands have been synthesised successfully, and their liquid-crystalline and self-assembly properties fully characterised. Directly analogous amphiphilic semi-perfluorinated complexes where the alkoxy chains on the alkynyl ligand were exchanged for the 1*H*,1*H*,2*H*,2*H*-perfluoroalkoxy moiety were also prepared and investigated, showing significantly different phase behaviour to the parent hydrocarbon complexes.

The liquid-crystallinity of the complexes **1-*n*** to **8-*n*** appears to be driven purely by effective space-filling and formation of disc-like molecular geometries. Accordingly, the less functionalised species with two-chains on the cyclometallating ligand (**1-8** to **4-*n***), show columnar phases in which a back-to-back confirmation is adopted by two effectively half-disc molecules. Those complexes with four-chains on the cyclometallating ligand (**5-*n*** to **8-*n***) appear to have sufficient surface coverage by the terminal chains to be considered as discs in their own right, resulting in a dominance of columnar hexagonal phases with one molecule in the columnar cross section. This molecular organisation results in a more stable mesophase than the intermolecular associations formed for the equivalent two-chain complexes, as observed in the increase of up to 115 °C in the clearing points.

These materials are the first of bis-cyclometallated complexes gold(III) to be investigated with respect to liquid crystallinity. Bis-cyclometallated metallomesogens with pincer ligands such as these are rare, with only a few reports of platinum(II) complexes with N^C^N ligands reported by Kozhevnikov *et al.*[2-4] and no reports of cyclometallated gold(III) metallomesogens. In these literature systems, the majority of functionalisation introduced to induce liquid-crystallinity arises through modification of the cyclometallating ligand, with an unchanged chloride ancillary ligand utilised in all cases. For the systems reported in this chapter, the main structural variation occurs from the alkynyl ligand and different columnar phases are formed with different levels of stability by varying the chain number and length. This opens the door to investigation of similar complexes of other metal centres, such as platinum(II), which may impart similar liquid-crystalline behaviour to strongly emissive materials. The same reasoning can be applied to changing the ancillary ligand from alkynyl to other σ-donating ligands that can promote luminescence to the Au(C^N^C) chromophore and can be functionalised by addition of alkoxy chains, such as aryl ligands.[145]

In addition to the interesting phase behaviour observed for the fully hydrocarbon species, the amphiphilic complexes **11-*n*** to **16-*n*** showed significant differences to their parent hydrocarbon complexes due to required segregation between the perfluorinated chains and the hydrocarbon chains. This resulted in a rich phase behaviour, including the appearance of rectangular phases

more frequency than in the parent complexes, as well as the observation of a variety of phases for complexes with four alkoxy chains on the cyclometallating ligand, including Col_h, Col_r and N phases, where the parent complexes show only Col_h. Also worthy of note is the loss of liquid crystallinity in a selection of complexes (specifically **13-*n***) in which the hydrocarbon equivalents (**4-*n***) show stable Col_r and Col_h phases, resulting from an instability of the necessarily anti-parallel conformation required to form the mesophase due to the high volume of fluorocarbon chains in comparison to hydrocarbon chains.

The orientation of the fluorinated molecules in the mesophase is highly dependent on the fluorocarbon chain-length, with complexes with short perfluorinated chains more likely to resemble the hydrocarbon analogues than the longer chain lengths, for which there is a higher requirement for segregation due to the fluorophobic effect. To gain further understanding on the systematic effect of fluorination, it may be of interest to increase the levels of fluorination further (*i.e.* longer chain lengths), or perhaps the *proportion* of fluorine in the chain, utilising the same chain lengths (or longer) but increasing the length of what is currently a -$(CH_2)_2$- spacer; spacers of C4 and C6 are often utilised in the literature,[101-104] with the ratio of hydrocarbon to fluorocarbon having an effect on the phase behaviour.

Most interesting amongst the phase behaviours for the fluorinated complexes is the remarkable observation of a re-entrant nematic phase sandwiched between a Col_r and Col_h phase in complex **15-12**. This is the first example of a N believed to be driven by amphiphilicity-induced frustration due to the immiscibility of fluorinated and hydrocarbon chains, although amphiphilicty has been known to alter phase organisation but not to the extent of inducing a phase out of thermodynamic order.[146-148] All other observations of re-entrant nematic phases for discotic systems[138-140] are from over 30 years ago, with no further research into their formation published. Thus, the observation of this phenomenon for **15-12** is exciting and warrants further investigation with the targeted synthesis of similar molecules which may show the same phase, as well as mixture studies, perhaps with **15-10** or **15-8** to investigate whether this phase could be induced.

A subset of the gold(III) complexes also have the ability to self-assemble in solution, as observed through concentration dependent ^1H and ^{19}F NMR spectroscopy measurements. The changes in chemical shift for species **8-8**, **16-8** and **16-10** indicated that for the fully hydrocarbon species **8-8**, an anti-parallel association was formed as all aromatic resonances apart from that of the alkynyl ligand experienced an upfield shift as the concentration was increased, in contrast to both fluorinated species, in which all relevant resonances, including that of the alkynyl ligand, experienced a upfield shift, indication a parallel arrangement, with the fluorinated and hydrocarbon regions experiencing an association due to the fluorophobic effect. With further

experimental investigation over wider concentration ranges, association constants for these aggregates may be able to be calculated.

The affinity for these complexes to form supramolecular assemblies is also apparent in the observation of metallogel formation in a select number of complexes, particularly those hydrocarbon species with two chains on the cyclometallating ligand, such as **2-*n*** and **3-*n***, and most of the perfluorinated complexes; it is a phenomenon also observed for the majority of the perfluorinated ligands and intermediates due to the amphiphilicity of the molecules. As the gels form with the addition of common organic solvent such as hexane, they can be classified as classical physical gels, rather than liquid-crystalline physical gels as described by Kato,[143] and are added to the canon of metallogels observed for similar cyclometallated gold(III) systems. The interaction of these mesogens with common gelators, as described by Kato, may result in the formation of liquid-crystalline physical gels, and is worthy of further investigation.

The nature of the gels were not fully characterised by common techniques in the field, such as SEM and TEM, nor the critical concentrations for gelation and stability testing due to time constraints, but this may be an exciting avenue of future investigation, especially probing the emissive properties of the gold(III) chromophore whilst in the gel, as has been investigated by Au *et al*.[108]

In combination with the emissive properties of the complexes, to be described in the following chapter, the [Au(C^N^C)(C≡CR)] reported in this thesis represent a class of multi-functional materials with behaviours, in particular their extensive liquid-crystalline properties, that show promise in both commercial application (expanded in Chapter 4) and in the fundamental understanding of metallomesogens.

3.8 References

1. X. Wu, M. Zhu, D. W. Bruce, W. Zhu and Y. Wang, *J. Mat. Chem. C*, 2018, **6**, 9848-9860.
2. V. N. Kozhevnikov, B. Donnio and D. W. Bruce, *Angew. Chem. Int. Ed.*, 2008, **47**, 6286-6289.
3. V. N. Kozhevnikov, B. Donnio, B. Heinrich and D. W. Bruce, *Chem. Commun.*, 2014, **50**, 14191-14193.
4. V. N. Kozhevnikov, B. Donnio, B. Heinrich, J. A. G. Williams and D. W. Bruce, *J. Mat. Chem. C*, 2015, **3**, 10177-10187.
5. A. Santoro, A. C. Whitwood, J. A. G. Williams, V. N. Kozhevnikov and D. W. Bruce, *Chem. Mater.*, 2009, **21**, 3871-3882.
6. A. Santoro, A. M. Prokhorov, V. N. Kozhevnikov, A. C. Whitwood, B. Donnio, J. A. G. Williams and D. W. Bruce, *J. Am. Chem. Soc.*, 2011, **133**, 5248-5251.
7. K. M.-C. Wong, L.-L. Hung, W. H. Lam, N. Zhu and V. W.-W. Yam, *J. Am. Chem. Soc.*, 2007, **129**, 4350-4365.
8. K. M.-C. Wong, X. Zhu, L.-L. Hung, N. Zhu, V. W.-W. Yam and H.-S. Kwok, *Chem. Commun.*, 2005, **1**, 2906-2908.
9. V. W.-W. Yam, K. M.-C. Wong, L.-L. Hung and N. Zhu, *Angew. Chem. Int. Ed.*, 2005, **44**, 3107-3110.
10. V. K.-M. Au, W. H. Lam, W.-T. Wong and V. W.-W. Yam, *Inorg. Chem.*, 2012, **51**, 7537-7545.
11. V. K.-M. Au, D. P.-K. Tsang, K. M.-C. Wong, M.-Y. Chan, N. Zhu and V. W.-W. Yam, *Inorg. Chem.*, 2013, **52**, 12713-12725.
12. V. K.-M. Au, D. P.-K. Tsang, Y.-C. Wong, M.-Y. Chan and V. W.-W. Yam, *J. Organomet. Chem.*, 2015, **792**, 109-116.
13. V. K.-M. Au, K. M.-C. Wong, D. P.-K. Tsang, M.-Y. Chan, N. Zhu and V. W.-W. Yam, *J. Am. Chem. Soc.*, 2010, **132**, 14273-14278.
14. V. K.-M. Au, K. M.-C. Wong, N. Zhu and V. W.-W. Yam, *J. Am. Chem. Soc.*, 2009, **131**, 9076-9085.
15. V. K.-M. Au, K. M.-C. Wong, N. Zhu and V. W.-W. Yam, *Chem. Eur. J.*, 2011, **17**, 130-142.
16. B. Donnio and D. W. Bruce, *J. Chem. Soc., Dalton Trans.*, 1997, 2745-2756.
17. C. P. Roll, B. Donnio, W. Weigand and D. W. Bruce, *Chem. Commun.*, 2000, 709-710.
18. C. Mongin, B. Donnio and D. W. Bruce, *J. Am. Chem. Soc.*, 2001, **123**, 8426-8427.
19. J. P. Rourke, F. P. Fanizzi, N. J. S. Salt, D. W. Bruce, D. A. Dunmur and P. M. Maitlis, *J. Chem. Soc., Chem. Commun.*, 1990, 229-231.
20. J. P. Rourke, F. P. Fanizzi, D. W. Bruce, D. A. Dunmur and P. M. Maitlis, *J. Chem. Soc., Dalton Trans.*, 1992, 3009-3014.
21. Y.-S. Y. Myongsoo Lee, Moon-Gun Choi, *Bull. Korean Chem. Soc.*, 1997, **18**, 1067 - 1070.
22. S. Coco, F. Díez-Expósito, P. Espinet, C. Fernández-Mayordomo, J. M. Martín-Álvarez and A. M. Levelut, *Chem. Mater.*, 1998, **10**, 3666-3671.
23. L. Plasseraud, L. G. Cuervo, D. Guillon, G. Süss-Fink, R. Deschenaux, D. W. Bruce and B. Donnio, *J. Mater. Chem.*, 2002, **12**, 2653-2658.
24. D. W. Bruce, D. A. Dunmur, M. A. Esteruelas, S. E. Hunt, R. L. Lagadec, P. M. Maitlis, J. R. Marsden, E. Sola and J. M. Stacey, *J. Mater. Chem.*, 1991, **1**, 251-254.
25. R. Chico, E. de Domingo, C. Domínguez, B. Donnio, B. Heinrich, R. Termine, A. Golemme, S. Coco and P. Espinet, *Chem. Mater.*, 2017, **29**, 7587-7595.
26. Y. Li, A. Y. Y. Tam, K. M. C. Wong, W. Li, L. Wu and V. W. W. Yam, *Chem. Eur. J.*, 2011, **17**, 8048-8059.
27. H.-C. Chang, T. Shiozaki, A. Kamata, K. Kishida, T. Ohmori, D. Kiriya, T. Yamauchi, H. Furukawa and S. Kitagawa, *J. Mater. Chem.*, 2007, **17**, 4136-4138.
28. C. T. Liao, H. H. Chen, H. F. Hsu, A. Poloek, H. H. Yeh, Y. Chi, K. W. Wang, C. H. Lai, G. H. Lee, C. W. Shih and P. T. Chou, *Chem. Eur. J.*, 2011, **17**, 546-556.
29. C. Cuerva, J. A. Campo, M. Cano and C. Lodeiro, *Chem. Eur. J.*, 2019, **0**.
30. F. Camerel, R. Ziessel, B. Donnio, C. Bourgogne, D. Guillon, M. Schmutz, C. Iacovita and J.-P. Bucher, *Angew. Chem. Int. Ed.*, 2007, **46**, 2659-2662.

31. N. Hoshino, *Coord. Chem. Rev.*, 1998, **174**, 77-108.
32. K. Binnemans and C. Görller-Walrand, *Chem. Rev.*, 2002, **102**, 2303-2346.
33. F. Martin, S. R. Collinson and D. W. Bruce, *Liq. Cryst.*, 2000, **27**, 859-863.
34. Y. G. Galyametdinov, G. I. Ivanova and I. V. Ovchinnikov, *Bull. Acad. Sci. USSR, Div. Chem. Sci*, 1991, **40**, 1109-1109.
35. R. W. Date, E. F. Iglesias, K. E. Rowe, J. M. Elliott and D. W. Bruce, *Dalton Trans.*, 2003, 1914-1931.
36. R. Date and D. Bruce, *Liq. Cryst.*, 2004, **31**, 1435-1444.
37. A. S. Mocanu, M. Iliş, F. Dumitraşcu, M. Ilie and V. Cîrcu, *Inorg. Chim. Acta*, 2010, **363**, 729-736.
38. H. Geng, K. Luo, G. Zou, H. Wang, H. Ni, W. Yu, Q. Li and Y. Wang, *New J. Chem.*, 2016, **40**, 10371-10377.
39. H. Geng, K. Luo, G. Zou, L. Zhao, H. Wang, Q. Li and H. Ni, *Dyes Pigments*, 2018, **149**, 82-91.
40. H. Geng, K. Luo, H. Cheng, S. Zhang, H. Ni, H. Wang, W. Yu and Q. Li, *RSC Adv.*, 2017, **7**, 11389-11393.
41. M. Krikorian, S. Liu and T. M. Swager, *J. Am. Chem. Soc.*, 2014, **136**, 2952-2955.
42. M. Ghedini, M. Longeri and R. Bartolino, *Mol. Cryst. Liq. Cryst.*, 1982, **84**, 207-211.
43. M. Ghedini, S. Armentano and F. Neve, *Inorg. Chim. Acta*, 1987, **134**, 23-24.
44. M. Ghedini, S. Licoccia, S. Armentano and R. Bartolino, *Mol. Cryst. Liq. Cryst.*, 1984, **108**, 269-275.
45. M. J. Baena, P. Espinet, M. B. Ros, J. L. Serrano and A. Ezcurra, *Angew. Chem. Int. Ed.*, 1993, **32**, 1203-1205.
46. M. J. Baena, J. Barbera, P. Espinet, A. Ezcurra, M. B. Ros and J. L. Serrano, *J. Am. Chem. Soc.*, 1994, **116**, 1899-1906.
47. M. J. Baena, J. Buey, P. Espinet, H.-S. Kitzerow and G. Heppke, *Angew. Chem. Int. Ed.*, 1993, **32**, 1201-1203.
48. M. Spencer, A. Santoro, G. R. Freeman, Á. Díez, P. R. Murray, J. Torroba, A. C. Whitwood, L. J. Yellowlees, J. A. G. Williams and D. W. Bruce, *Dalton Trans.*, 2012, **41**, 14244-14256.
49. Á. Díez, S. J. Cowling and D. W. Bruce, *Chem. Commun.*, 2012, **48**, 10298-10300.
50. Y. Wang, Y. Liu, J. Luo, H. Qi, X. Li, M. Nin, M. Liu, D. Shi, W. Zhu and Y. Cao, *Dalton Trans.*, 2011, **40**, 5046-5051.
51. Y. Wang, J. Fan, T. Li, Q. Wang, J. Shi, Z. Qu, H. Tan, Y. Liu and W. Zhu, *RSC Adv.*, 2016, **6**, 45864-45872.
52. Y. Wang, Q. Chen, Y. Li, Y. Liu, H. Tan, J. Yu, M. Zhu, H. Wu, W. Zhu and Y. Cao, *J. Phys. Chem. C*, 2012, **116**, 5908-5914.
53. X. Yang, X. Wu, D. Zhou, J. Yu, G. Xie, D. W. Bruce and Y. Wang, *Dalton Trans.*, 2018, **47**, 13368-13377.
54. T. Hegmann, J. Kain, S. Diele, B. Schubert, H. Bögel and C. Tschierske, *J. Mater. Chem.*, 2003, **13**, 991-1003.
55. C. Damm, G. Israel, T. Hegmann and C. Tschierske, *J. Mater. Chem.*, 2006, **16**, 1808-1816.
56. K. Venkatesan, P. H. J. Kouwer, S. Yagi, P. Müller and T. M. Swager, *J. Mater. Chem.*, 2008, **18**, 400-407.
57. M. Ghedini, D. Pucci, A. Crispini, A. Bellusci, M. L. Deda, I. Aiello and T. Pugliese, *Inorg. Chem. Commun.*, 2007, **10**, 243-246.
58. J. Shi, Y. Wang, M. Xiao, P. Zhong, Y. Liu, H. Tan, M. Zhu and W. Zhu, *Tetrahedron*, 2015, **71**, 463-469.
59. Y. Wang, J. Fan, J. Shi, H. Qi, E. Baranoff, G. Xie, Q. Li, H. Tan, Y. Liu and W. Zhu, *Dyes Pigments*, 2016, **133**, 238-247.
60. L. Zhao, B. Yang, L. Zeng, K. Luo, H. Wang, H. Ni, C. Yang and Q. Li, *Dyes Pigments*, 2019, **164**, 398-406.
61. A. Bondi, *J. Phys. Chem.*, 1964, **68**, 441-451.
62. D. O'Hagan, *Chem. Soc. Rev.*, 2008, **37**, 308-319.
63. L. Pauling, *The Nature of the Chemical Bond, and the Structure of Molecules and Crystals: An Introduction to Modern Structural Chemistry*, Cornell University Press, Ithica, NY, 1940.

64. C. Tschierske, in *Liquid Crystals: Materials Design and Self-assembly*, ed. C. Tschierske, Springer Berlin Heidelberg, Berlin, Heidelberg, 2012, pp. 1-108.
65. J. Hopken and M. Moller, *Macromolecules*, 1992, **25**, 2482-2489.
66. C. Viney, T. P. Russell, L. E. Depero and R. J. Twieg, *Mol. Cryst. Liq. Cryst. inc. Nonlinear Opt.*, 1989, **168**, 63-82.
67. C. Viney, R. J. Twieg, T. P. Russell and L. E. Depero, *Liq. Cryst.*, 1989, **5**, 1783-1788.
68. C. Viney, R. J. Twieg, B. R. Gordon and J. F. Rabolt, *Mol. Cryst. Liq. Cryst.*, 1991, **198**, 285-289.
69. D. Lose, S. Diele, G. Pelzl, E. Dietzmann and W. Weissflog, *Liq. Cryst.*, 1998, **24**, 707-717.
70. G. Pelzl, S. Diele, D. Lose, B. I. Ostrovski and W. Weissflog, *Cryst. Res. Technol.*, 1997, **32**, 99-109.
71. O. M. Martin, L. Yu and S. Mecozzi, *Chem. Commun.*, 2005, 4964-4966.
72. C. de Gracia Lux, B. Donnio, B. Heinrich and M. P. Krafft, *Langmuir*, 2013, **29**, 5325-5336.
73. G. Johansson, V. Percec, G. Ungar and J. P. Zhou, *Macromolecules*, 1996, **29**, 646-660.
74. V. Percec, D. Schlueter, Y. K. Kwon, J. Blackwell, M. Moeller and P. J. Slangen, *Macromolecules*, 1995, **28**, 8807-8818.
75. G. Johansson, V. Percec, G. Ungar and K. Smith, *Chem. Mater.*, 1997, **9**, 164-175.
76. G. Yang, K. Zhao, W. Yu, P. Hu and B. Wang, *Sci. China. Ser. B.*, 2009, **52**, 1244-1252.
77. V. Percec, M. Glodde, G. Johansson, V. S. K. Balagurusamy and P. A. Heiney, *Angew. Chem. Int. Ed.*, 2003, **42**, 4338-4342.
78. V. Percec, M. R. Imam, T. K. Bera, V. S. K. Balagurusamy, M. Peterca and P. A. Heiney, *Angew. Chem. Int. Ed.*, 2005, **44**, 4739-4745.
79. V. Percec, M. Glodde, M. Peterca, A. Rapp, I. Schnell, H. W. Spiess, T. K. Bera, Y. Miura, V. S. K. Balagurusamy, E. Aqad and P. A. Heiney, *Chem. Eur. J.*, 2006, **12**, 6298-6314.
80. Y. H. Kim, D. K. Yoon, E. H. Lee, Y. K. Ko and H.-T. Jung, *J. Phys. Chem. B.*, 2006, **110**, 20836-20842.
81. V. Percec, E. Aqad, M. Peterca, M. R. Imam, M. Glodde, T. K. Bera, Y. Miura, V. S. K. Balagurusamy, P. C. Ewbank, F. Würthner and P. A. Heiney, *Chem. Eur. J.*, 2007, **13**, 3330-3345.
82. I. Bury, B. Heinrich, C. Bourgogne, G. H. Mehl, D. Guillon and B. Donnio, *New J. Chem.*, 2012, **36**, 452-468.
83. A. Kohlmeier and D. Janietz, *Liq. Cryst.*, 2007, **34**, 65-71.
84. E. Nishikawa, J. Yamamoto and H. Yokoyama, *Liq. Cryst.*, 2003, **30**, 785-798.
85. D. Janietz and A. Kohlmeier, *Liq. Cryst.*, 2009, **36**, 685-703.
86. P. Metrangolo, C. Präsang, G. Resnati, R. Liantonio, A. C. Whitwood and D. W. Bruce, *Chem. Commun.*, 2006, 3290-3292.
87. B. Bilgin-Eran, H. Ocak, C. Tschierske and U. Baumeister, *Liq. Cryst.*, 2012, **39**, 467-476.
88. B. Bilgin-Eran, C. Tschierske, S. Diele and U. Baumeister, *J. Mater. Chem.*, 2006, **16**, 1136-1144.
89. B. Bilgin-Eran, Ç. Yörür, C. Tschierske, M. Prehm and U. Baumeister, *J. Mater. Chem.*, 2007, **17**, 2319-2328.
90. R. Dembinski, P. Espinet, S. Lentijo, M. W. Markowicz, J. M. Martín-Alvarez, A. L. Rheingold, D. J. Schmidt and A. Sniady, *Eur. J. Inorg. Chem.*, 2008, **2008**, 1565-1572.
91. M.-A. Guillevic and D. W. Bruce, *Liq. Cryst.*, 2000, **27**, 153-156.
92. M.-A. Guillevic, T. Gelbrich, M. B. Hursthouse and D. W. Bruce, *Mol. Cryst. Liq. Crys. A.*, 2001, **362**, 147-170.
93. A. Martin, C. Mügge, D. L. Gin, B. Donnio and W. Weigand, *Eur. J. Inorg. Chem.*, 2014, **2014**, 5609-5617.
94. H. Ocak, B. Bilgin-Eran, C. Tschierske, U. Baumeister and G. Pelzl, *J. Mater. Chem.*, 2009, **19**, 6995-7001.
95. J. Szydłowska, A. Krówczyński, U. Pietrasik and A. Rogowska, *Liq. Cryst.*, 2005, **32**, 651-658.
96. J. C. Haenle, Y. Stöckl, R. Forschner, E. Haenle and S. Laschat, *ChemPhysChem*, 2018, **19**, 2758-2767.

97. M. Bremer, P. Kirsch, M. Klasen-Memmer and K. Tarumi, *Angew. Chem. Int. Ed.*, 2013, **52**, 8880-8896.
98. M. P. Krafft and J. G. Riess, *Chem. Rev.*, 2009, **109**, 1714-1792.
99. M. Hird, *Chem. Soc. Rev.*, 2007, **36**, 2070-2095.
100. F. Guittard, E. Taffin de Givenchy, S. Geribaldi and A. Cambon, *J. Fluorine Chem.*, 1999, **100**, 85-96.
101. V. Percec, G. Johansson, G. Ungar and J. Zhou, *J. Am. Chem. Soc.*, 1996, **118**, 9855-9866.
102. X. Cheng, M. K. Das, S. Diele and C. Tschierske, *Langmuir*, 2002, **18**, 6521-6529.
103. A. Pegenau, X. Hong Cheng, C. Tschierske, P. Göring and S. Diele, *New J. Chem.*, 1999, **23**, 465-467.
104. X. H. Cheng, S. Diele and C. Tschierske, *Angew. Chem. Int. Ed.*, 2000, **39**, 592-595.
105. U. Dahn, C. Erdelen, H. Ringsdorf, R. Festag, J. H. Wendorff, P. A. Heiney and N. C. Maliszewskyj, *Liq. Cryst.*, 1995, **19**, 759-764.
106. J. D. Herod, M. A. Bates, A. C. Whitwood and D. W. Bruce, *Soft Matter*, 2019, **15**, 4432-4436.
107. A. Gainar, M.-C. Tzeng, B. Heinrich, B. Donnio and D. W. Bruce, *J. Phys. Chem. B.*, 2017, **121**, 8817-8828.
108. V. K.-M. Au, N. Zhu and V. W.-W. Yam, *Inorg. Chem.*, 2013, **52**, 558-567.
109. C.-H. Lee, M.-C. Tang, Y.-C. Wong, M.-Y. Chan and V. W.-W. Yam, *J. Am. Chem. Soc.*, 2017, **139**, 10539-10550.
110. S. K.-L. Siu, C. Po, K.-C. Yim, V. K.-M. Au and V. W.-W. Yam, *CrystEngComm*, 2015, **17**, 8153-8162.
111. K.-C. Yim, V. K.-M. Au, L.-L. Hung, K. M.-C. Wong and V. W.-W. Yam, *Chem. Eur. J.*, 2016, **22**, 16258-16270.
112. C. Liu, N. Han, X. Song and J. Qiu, *Eur. J. Org. Chem.*, 2010, **2010**, 5548-5551.
113. T. Cardinaels, J. Ramaekers, P. Nockemann, K. Driesen, K. Van Hecke, L. Van Meervelt, G. Wang, S. De Feyter, E. F. Iglesias, D. Guillon, B. Donnio, K. Binnemans and D. W. Bruce, *Soft Matter*, 2008, **4**, 2172-2185.
114. B. Donnio, B. Heinrich, H. Allouchi, J. Kain, S. Diele, D. Guillon and D. W. Bruce, *J. Am. Chem. Soc.*, 2004, **126**, 15258-15268.
115. A. I. Smirnova, D. Fazio, E. F. Iglesias, C. G. Hall, D. Guillon, B. Donnio and D. W. Bruce, *Mol. Cryst. Liq. Cryst.*, 2003, **396**, 227-240.
116. D. Fazio, C. Mongin, B. Donnio, Y. Galerne, D. Guillon and D. W. Bruce, *J. Mater. Chem.*, 2001, **11**, 2852-2863.
117. B. Donnio, B. Heinrich, T. Gulik-Krzywicki, H. Delacroix, D. Guillon and D. W. Bruce, *Chem. Mater.*, 1997, **9**, 2951-2965.
118. B. Sahu, R. Muruganantham and I. N. N. Namboothiri, *Eur. J. Org. Chem.*, 2007, **2007**, 2477-2489.
119. P. J. Martin, PhD Thesis, University of York, 2008.
120. C. R. Patrick and G. S. Prosser, *Nature*, 1960, **187**, 1021-1021.
121. K.-H. Wong, K.-K. Cheung, M. C.-W. Chan and C.-M. Che, *Organometallics*, 1998, **17**, 3505-3511.
122. L. A. Méndez, J. Jiménez, E. Cerrada, F. Mohr and M. Laguna, *J. Am. Chem. Soc.*, 2005, **127**, 852-853.
123. O. Schuster and H. Schmidbaur, *Organometallics*, 2005, **24**, 2289-2296.
124. W. Lu, H.-F. Xiang, N. Zhu and C.-M. Che, *Organometallics*, 2002, **21**, 2343-2346.
125. C.-M. Che, H.-Y. Chao, V. M. Miskowski, Y. Li and K.-K. Cheung, *J. Am. Chem. Soc.*, 2001, **123**, 4985-4991.
126. V. W.-W. Yam and S. W.-K. Choi, *J. Chem. Soc., Dalton Trans.*, 1996, 4227-4232.
127. X.-X. Lu, C.-K. Li, E. C.-C. Cheng, N. Zhu and V. W.-W. Yam, *Inorg. Chem.*, 2004, **43**, 2225-2227.
128. V. W.-W. Yam, S.-K. Yip, L.-H. Yuan, K.-L. Cheung, N. Zhu and K.-K. Cheung, *Organometallics*, 2003, **22**, 2630-2637.

129. S.-K. Yip, E. C.-C. Cheng, L.-H. Yuan, N. Zhu and V. W.-W. Yam, *Angew. Chem. Int. Ed.*, 2004, **43**, 4954-4957.
130. C.-W. Chan, L.-K. Cheng and C.-M. Che, *Coord. Chem. Rev.*, 1994, **132**, 87-97.
131. M. Hissler, W. B. Connick, D. K. Geiger, J. E. McGarrah, D. Lipa, R. J. Lachicotte and R. Eisenberg, *Inorg. Chem.*, 2000, **39**, 447-457.
132. W. Lu, B.-X. Mi, M. C. W. Chan, Z. Hui, C.-M. Che, N. Zhu and S.-T. Lee, *J. Am. Chem. Soc.*, 2004, **126**, 4958-4971.
133. V. W.-W. Yam, K. M.-C. Wong and N. Zhu, *J. Am. Chem. Soc.*, 2002, **124**, 6506-6507.
134. V. W.-W. Yam, K. M.-C. Wong and N. Zhu, *Angew. Chem. Int. Ed.*, 2003, **42**, 1400-1403.
135. N. S. S. Kumar, M. Z. Shafikov, A. C. Whitwood, B. Donnio, P. B. Karadakov, V. N. Kozhevnikov and D. W. Bruce, *Chem. Eur. J.*, 2016, **22**, 8215-8233.
136. P. E. Cladis, R. J. Mandle and J. W. Goodby, in *Handbook of Liquid Crystals*, eds. J. W. Goodby, C. Tschierske, P. Raynes, H. Gleeson, T. Kato and P. J. Collings, Wiley, Weinheim, Germany, 2014, pp. 1-30.
137. N. H. Tinh, J. Malthete and C. Destrade, *Mol. Cryst. Liq. Cryst.*, 1981, **64**, 291-298.
138. N. H. Tinh, P. Foucher, C. Destrade, A. M. Levelut and J. Malthete, *Mol. Cryst. Liq. Cryst.*, 1984, **111**, 277-292.
139. N. H. Tinh, J. Malthête and C. Destrade, *J. Physique Lett.*, 1981, **42**, 417-419.
140. C. Destrade, J. Malthete, N. H. Tinh and H. Gasparoux, *Phys. Lett. A*, 1980, **78**, 82-84.
141. A. F. Suleymanova, O. S. Eltsov, D. N. Kozhevnikov, A. O. Lantushenko, M. P. Evstigneev and V. N. Kozhevnikov, *ChemistrySelect*, 2017, **2**, 3353-3355.
142. K.-C. Yim, E. S.-H. Lam, K. M.-C. Wong, V. K.-M. Au, C.-C. Ko, W. H. Lam and V. W.-W. Yam, *Chem. Eur. J.*, 2014, **20**, 9930-9939.
143. T. Kato, Y. Hirai, S. Nakaso and M. Moriyama, *Chem. Soc. Rev.*, 2007, **36**, 1857-1867.
144. Y. Hirai, H. Monobe, N. Mizoshita, M. Moriyama, K. Hanabusa, Y. Shimizu and T. Kato, *Adv. Funct. Mater.*, 2008, **18**, 1668-1675.
145. W.-P. To, D. Zhou, G. S. M. Tong, G. Cheng, C. Yang and C.-M. Che, *Angew. Chem. Int. Ed.*, 2017, **56**, 14036-14041.
146. A. Zelcer, B. Donnio, C. Bourgogne, F. D. Cukiernik and D. Guillon, *Chem. Mater.*, 2007, **19**, 1992-2006.
147. S. Westphal, S. Diele, A. Mädicke, F. Kuschel, U. Scheim, K. Rühlmann, B. Hisgen and H. Ringsdorf, *Die Makromolekulare Chemie, Rapid Communications*, 1988, **9**, 489-493.
148. S. Diele, S. Oelsner, F. Kuschel, B. Hisgen and H. Ringsdorf, *Mol. Cryst. Liq. Cryst. inc. Nonlinear Opt.*, 1988, **155**, 399-408.

Chapter 4: Photophysical Properties of Cyclometallated Complexes of Gold(III) with Functionalised Alkynyl Ligands and their Application in OLED Devices

4.1 Introduction

In Chapter 2 (and briefly in Chapter 3), the phosphorescence of metal complexes has been addressed, giving an overview of emissive complexes of platinum(IV), reports of which have become increasingly common. In a similar vein, in comparison to the well-known emissive systems of iridium(III) and platinum(II), the study of emissive complexes of gold(III) has only become prominent in the past 20 years.

4.1.1 Emissive Complexes of Gold(III)

4.1.1.1 Gold(III) Complexes with Alkynyl Ligands

Reports of emissive gold complexes, especially emissive species of gold(III), have lagged significantly behind those of the intensely studied platinum(II), ruthenium(II) and iridium(III), although it has been shown that gold(I) complexes can display efficient emission.[1-9] However, until this century, reports of emissive gold(III) species were rare due to the presence of low-lying *d*-*d* states. These states quench the possible emissive excited states and lead to deactivation through thermal equilibration or energy transfer due to their proximity in energy to the emissive state. Furthermore, gold(III) systems show a tendency to undergo reductive elimination to gold(I); this problem is overcome through the use of rigid cyclometallating ligands, resulting in organogold(III) systems.[10]

Investigation into the rich photophysical behaviours of gold(III) complexes is a recent field of study; the first luminescent gold(III) complexes were reported by Che and colleagues and were based on 2,9-diphenyl-1,10-phenanthroline or 4'-(4-methoxyphenyl)-6'-phenyl-2,2'-bipyridine ligands.[11, 12] Room-temperature emission of organogold(III) complexes was first achieved by Yam *et al.* in 1993 through the use of electron-donating mesityl or (trimethylsilyl)methyl ligands to form emissive gold(III) complexes which utilise bipyridine or phenanthroline chelating ligands (Figure 4-1a).[13]

Most relevant to the complexes outlined in this chapter is the first report of a luminescent *bis*-cyclometallating gold(III) complex by Che *et al.* with the structure [Au(C^N^C)Cl], where C^N^C is

2,6-diphenylpyridine (Figure 4-1b), which is only weakly luminescent at 77 K in a glass, due to the aforementioned presence of low-lying, deactivating *d-d* states.[14] In this structure, the anionic carbanion ligands are mutually *trans*, with the chloride ligand in the fourth position of the square-planar geometry, *trans* to the coordinated nitrogen atom of the pyridine ring; this was the first example of a gold(III) complex with the C^N^C moiety.

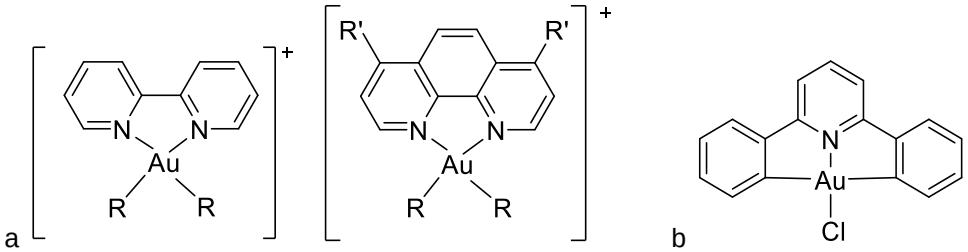

Figure 4-1: a) Structure of first reported emissive organogold(III) complexes as reported by *Yam et al.*in 1993 where R = mesityl or CH_2SiMe_3 and R' = H or Ph;[13] b) Structure of gold(III) complex reported by Che *et al.* which shows weak emissive properties at cryogenic temperatures.[14]

Following this, Yam reported room-temperature luminescence of gold(III) complexes through the incorporation of an alkynyl ligand in the fourth position of the square-planar architecture to give [Au(C^N^C)(C≡C-R)] complexes, where C^N^C is a derivative of 2,6-diphenylpyridine and C≡C-R is an alkynyl ligand (Figure 4-2a).[10, 15] The alkynyl ligand is strongly σ-donating, donating electron density into the gold(III) d-orbitals and rendering the metal centre more electron-rich. Most importantly, the alkynyl ligand also increases the energy of the low-lying, deactivating d-d states, increasing the energy gap between the emissive excited state and the deactivating states, resulting in the effective population of the emissive states and thus giving room-temperature luminescence. Of the nine complexes reported, the emission for all but one is located in the green region of the spectrum and shows strong vibronic coupling, and appears independent of the nature of the alkynyl ligand. It is assigned as occurring from a metal-perturbed $\pi \rightarrow \pi*$ intraligand transition based on the C^N^C cyclometallating ligand. The quantum yields for these complexes are poor, with the most efficient emission a mere 0.6%. For the complex with the strongly electron donating NH_2 group in the *para* position of the phenyl ring of alkynyl ligand, the emission is broad and featureless, and is significantly red-shifted to 610 nm. In this case, the orbitals of the alkynyl ligand are raised in energy due to the electron-donating nature of the NH_2 group, and the transition becomes ^{3}LLCT from the alkynyl ligand to the C^N^C ligand, indicating that the emission has the ability to be tuned (Figure 4-2b).

a

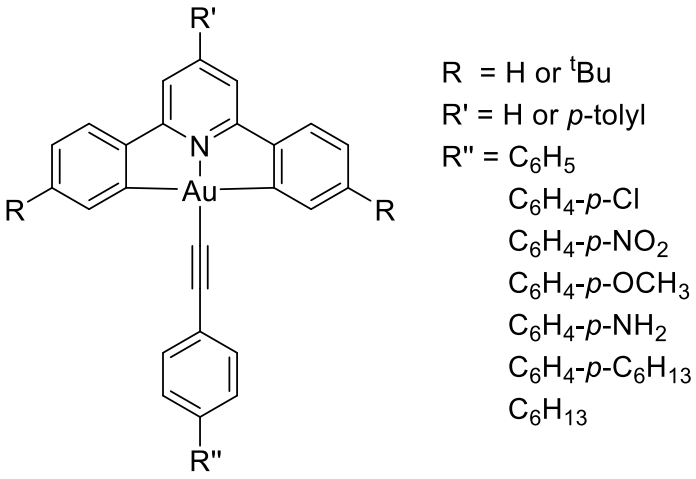

b

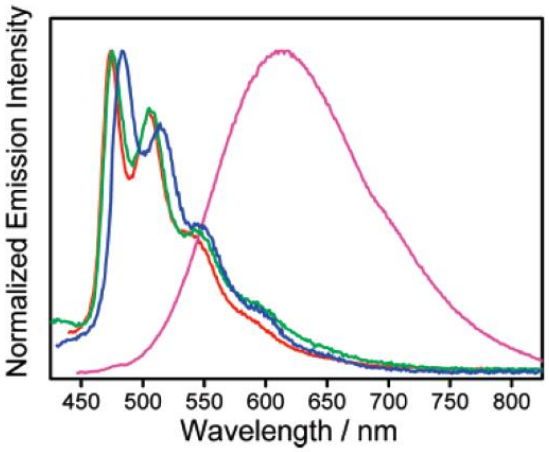

Figure 4-2: a) Structure of the [Au(C^N^C)(C≡C-R)] complexes reported by Wong *et al.*,[10] where C^N^C is a derivative of 2,6-diphenylpyridine and C≡C-R is an alkynyl ligand; b) emission profile of selected complexes, reproduced from source. Red: R = R' = H, R'' = C_6H_5; pink: R = R' = H, R'' = C_6H_4-*p*-NH_2; green: R = ^{t}Bu, R' = H, R'' = C_6H_5; blue: R = H, R' = C_6H_4-*p*-CH_3, R'' = C_6H_4-*p*-C_6H_{13}.

The success of this strategy has resulted in significant modification of the [Au(C^N^C)(C≡C-R)] moiety to tune the emissive properties with respect to emission wavelength and quantum yield, and induce a wide range of further interesting behaviours, such as metallogelation[16] and supramolecular self-assembly,[17] thermally stimulated delayed phosphorescence (TSDP)[18] and thermally activated delayed fluorescence (TADF).[19, 20] A more detailed overview of these complexes and their history is outlined below.

The first modification included the use of a 2,5-difluoro substituted phenyl ring in the 4-position of the pyridine ring of the C^N^C ligand, as well as a 4-diphenylaminophenylacetylene alkynyl ligand (Figure 4-3a). This complex showed a broad emission band in the red-region of the spectrum in solution, albeit with a low quantum yield of 0.85%.[21] The triphenylamine alkynyl ligands can be functionalised further with additional triphenylamine groups to form dendimers, complexes of which show improved quantum yields of 3-7% (albeit with an alternate C^N^C ligand based on fluorine-substituted 1,3-diphenylisoquinoline) (Figure 4-3b).[22]

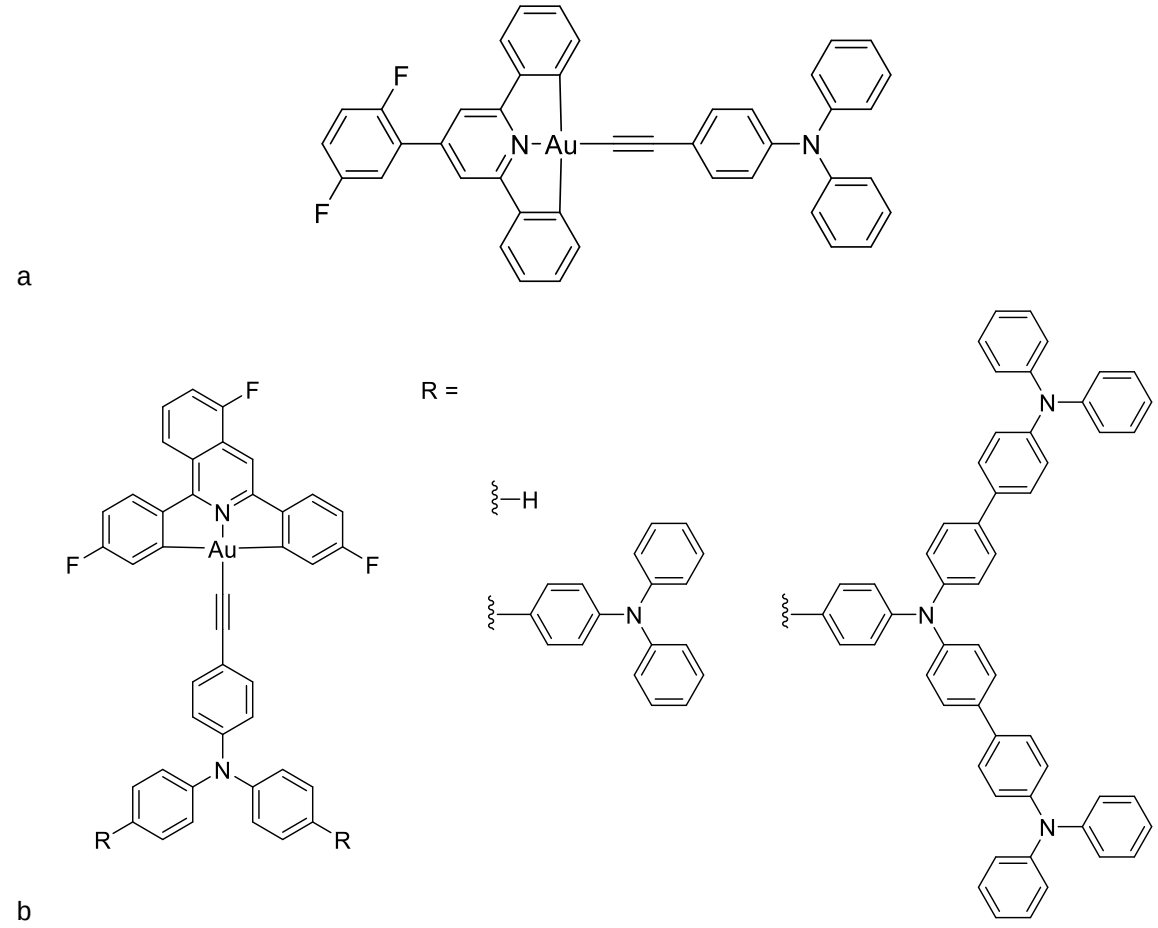

Figure 4-3: Structure of modified gold(III) alkynyl complex reported by a) Au *et al.* with 2,6-diphenyl-4-(2,5-difluorophenyl)pyridine C^N^C ligand and C≡C-C_6H_4-*p*-N(C_6H_5)$_2$ alkynyl ligand;[21] b) Tang *et al.* with extended triphenylamine alkynyl ligands and fluorine-substituted 1,3-diphenylisoquinoline C^N^C ligand.[22]

Subsequently, the same group reported the further functionalisation of the N(Ph)$_2$ alkynyl group with carbazole groups in the *para*-position of the phenyl rings to form dendrimeric species with the previously utilised 2,6-diphenyl-4-(2,5-difluorophenyl)pyridine C^N^C ligand (Figure 4-4a). These complexes showed structureless emission bands in the 620–695 nm region, with a quantum yield of up to 10% and lifetime of > 1 μs.[23] Further carbazole-based dendrimers have been reported in which the quantum yield is greatly improved to as much as 30% through the inclusion of further generations in the dendrons with no effect on the lifetime of emission (Figure 4-4b).[24]

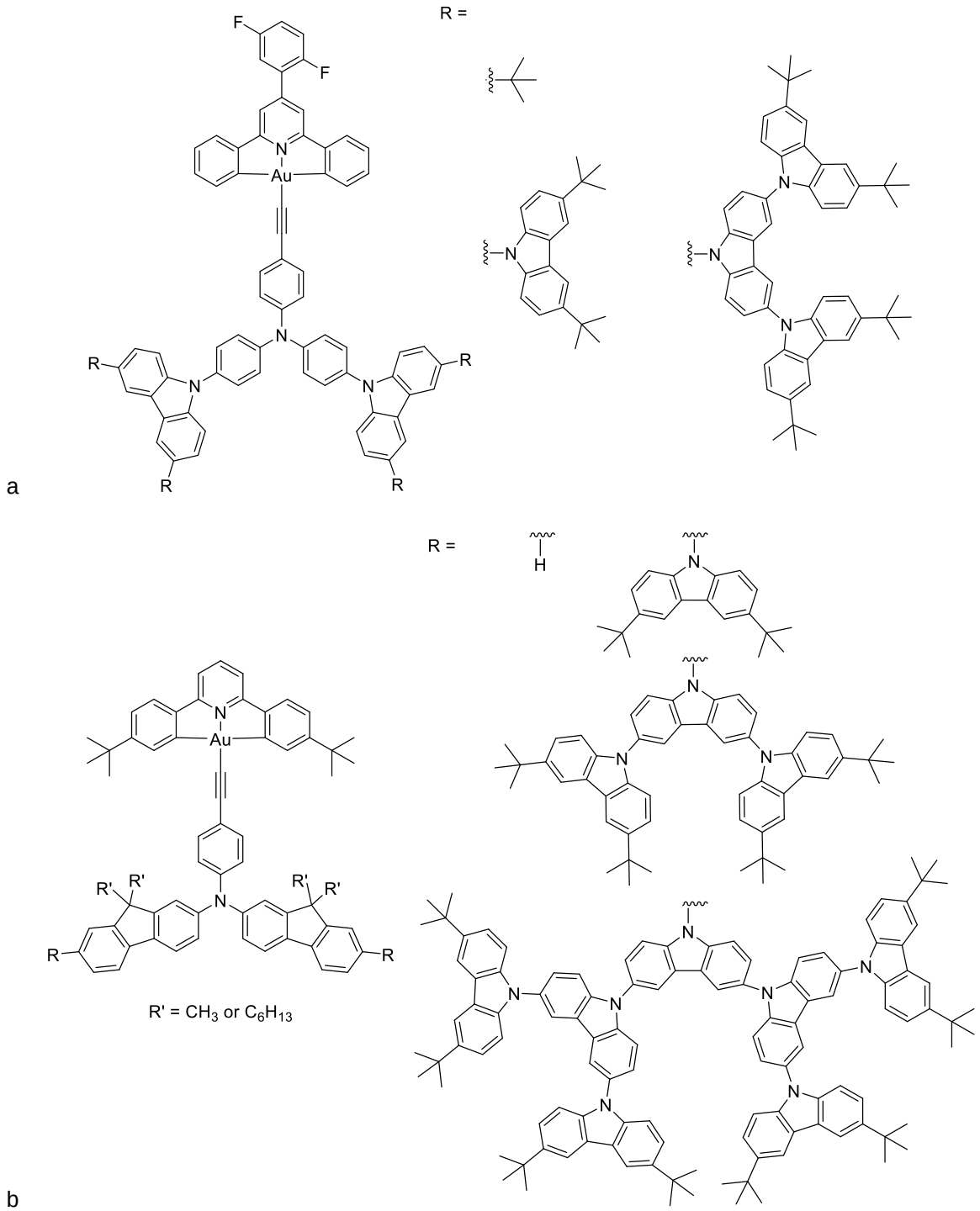

Figure 4-4: Structure of modified gold(III) alkynyl complex reported by a) Tang *et al.* with the same core structure (2,6-diphenyl-4-(2,5-difluorophenyl)pyridine C^N^C ligand) and addition carbazole moieties on the alkynyl ligands to form dendrimers;[23] b) Lee *et al.* with 2,6-bis(4-(^{t}butyl)phenyl)pyridine C^N^C ligand and carbazole-based dendrimer alkynyl ligands.[24]

To tune the wavelength of emission, Au *et al.* reported a comparatively large series of 18 [Au(C^N^C)(C≡C-R)] complexes with modifications to the cyclometallating ligand with the aim of modifying the energies of the frontier molecular orbitals to tune the emission energies (Figure 4-5). These complexes showed a range of emission wavelengths ranging from 451 to 669 nm when

measured in degassed CH_2Cl_2 at room temperature.[25] Two alkynyl ligands were utilised for all complexes, 4-methoxyphenylacetylene and 4-diphenylaminophenylacetylene, with one exception where a 4-ethylphenylacetylene ligand was used. Surprisingly, not all combinations of C^N^C and alkynyl ligands were reported, with no explanation as to why.

The complexes with 4-methoxyphenylacetylene and 4-ethylphenylacetylene ligands show the previously observed vibronic coupling in the emission band, but λ_{max} is altered depending on the nature of the C^N^C ligand. In comparison to the system with an unsubstituted 2,6-diphenylpyridine ligand, the complexes with an appended aryl ring on the central pyridine moiety show a red-shifted emission due to the more efficient delocalisation of electrons in the conjugated system, stabilising the π* based LUMO. A similar red-shift was observed upon the inclusion of one or two napthyl moieties in place of the phenyl rings of the C^N^C ligand due to the stabilisation of the HOMO upon increasing the conjugation of the system, as well as for the 5,6-dihydro-2,4-diphenylbenzo[*h*]quinolone (dhpbzq) based complexes, due to the electron-donating $–CH_2CH_2–$ linkage and increased rigidity, which decreases the HOMO-LUMO gap.

For those complexes with a 4-diphenylaminophenylalkynyl ligand, a broad, featureless emission band was observed in the red region of the spectrum, in accordance with the previously observed changes when including an amino substituent in the *para*-position of the alkynyl ligand.[10, 22-24] All of the reported novel complexes are compared to the literature system with an unsubstituted 2,6-diphenyl pyridine C^N^C ligand and the same alkynyl ligand. When an aryl substituent is included on the central pyridine group, there was a red-shift in the emission, as described above, but the observations of the napthyl and dhpbzq groups are not consistent between alkynyl ligands. The singular dhpbzq complex shows a blue-shift compared to the complex with an unsubstituted C^N^C ligand due to the destabilisation of the LUMO, as do the complexes with napthyl groups on the C^N^C ligand, in contrast to the observations of a red-shift for the 4-methoxyphenylacetylene complexes. This is rationalised through the observations for electrochemical experiments which show that the π* orbital of the LUMO is higher in energy as a result of the increase electron density in this orbital due to the increased conjugation and the more rigid confirmation of the napthyl rings in comparison to the phenyl group.

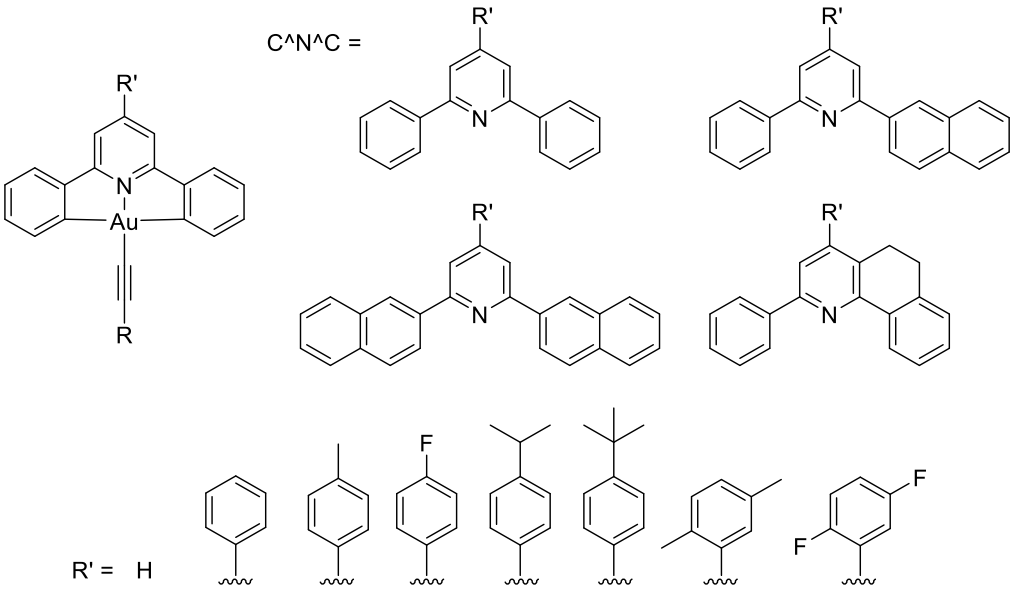

Figure 4-5: Complexes reported by Au *et al.* which show variation of the C^N^C cyclometallating ligand through appendage of a) further aryl groups; b) the change of a phenyl group for a napthyl group; c) the use of 5,6-dihydro-2,4-diphenylbenzo[*h*]quinolone (dhpbzq) as the C^N^C ligand. Alkynyl ligands used are 4-methoxyphenylacetylene and 4-diphenylaminophenylacetylene, with one complex utilising 4-ethylphenylacetylene. Complex numbering systems have been changed from the literature for ease of reference.[25]

Further functionalisation of the C^N^C ligand was reported by Au *et al.* to form ethyl 2,6-diphenylisonicotinate alkynyl gold(III) complexes (Figure 4-6).[26] The structures showed very close gold(III)···gold(III) contacts in the crystalline state which were smaller than the sum of the Van der Waals radii and of the theoretical distance where aurophilic interactions may occur,[27] which can be utilised in supramolecular chemistry as stabilising interactions for the extended structure as they have approximately the same strength as hydrogen bonds.[28] The complexes with a phenyl ring or a fluorine atom in the *para*-position of the phenyl ring of the alkynyl ligand showed the structured emission band previously observed, however, in contrast to all the previous literature for complexes with an amine group in this position, in which its inclusion results in a significant red-shift and a loss of structure in the band, the ethyl 2,6-diphenylisonicotinate alkynyl gold(III) complex with a 4-diphenylaminophenylacetylene shows a blue-shift from both the literature complexes and the other species reported, to 463 nm. This is assigned as an alkynyl-centred intraligand excited state due to the similarity between the emission profile of the complex and free alkynyl ligand, suggesting that, with respect to tuning the emission wavelength, PLQY and excited state origin, modification of both the alkynyl and C^N^C ligand are important.

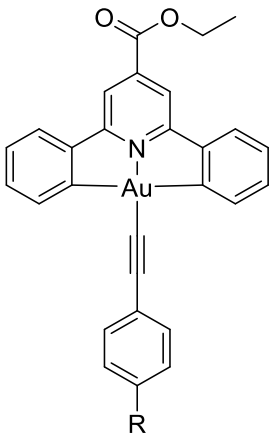

Figure 4-6: Structure of ethyl 2,6-diphenylisonicotinate alkynyl gold(III) complexes reported by Au *et al.*, where R = NPh_2, Ph or F.[26]

Alteration of the cyclometallating ligand was further investigated by Yim *et al.*, in which the phenyl groups were substituted for benzimidazolyl groups to form the 2,6-bis(benzimidazol-2'-yl)pyridine ligand, which is a dianionic N^N^N ligand.[29] The resulting complexes, with alteration of the substituents on the alkynyl ligand, were shown to be non-emissive in solution at both room and cryogenic temperatures due to the presence of low-lying metal-centred anti-bonding orbitals which present efficient pathways for non-radiative decay, indicating that only specific dianionic ligands give rise to rich luminescence properties. Interestingly, one of the complexes reported shows gelation behaviour, indicating the possibility of these structures to form supramolecular networks. The formation of gels for such complexes was discussed previous in Chapter 3, Section 3.6.

The gelation behaviour of [Au(C^N^C)(C≡C-R)] complexes, as well as the ability of the gels to emit, are characterised thoroughly in a report by Au *et al.*, in which 2,6-diphenylpyridine was utilised as the C^N^C ligand and the alkynyl ligand used is 3,4,5-tri(alkyloxy)ethynylbenzene, a phenylacetylene ring heavily functionalised with alkoxy chains; this ligand is not unlike the alkynyl ligands utilised in the research outlined in this thesis (see Chapter 3).[16] When these chains are octadecyloxy (C18), stable gels are observed in non-polar solvents such as hexane and cyclohexane (Figure 4-7a). Gels are also observed when the cyclometallating ligand is 2,6-dinapthylpyridine, although these became unstable after only a few minutes; the same can be said of complexes with shorter chain lengths. The stable gel is emissive in both solvents, showing a structured emission band at 470 to 620 nm, the intensity of which decreases as the temperature is increased (Figure 4-7b) and is assigned as arising from a ^{3}LLCT between the π-orbital on the alkynyl ligand and the π*-orbital based on the C^N^C. For the cyclohexane gel, there are extra vibronically coupled bands observed at higher temperatures in the solution phase, which is assigned as ^{3}IL based on the C^N^C ligand; the observation of both transitions suggests that both excited states are similar in

energy. The emission intensity is significantly reduced when the material transitions from the gel to the solution, indicating that the rigid media is beneficial to the suppression of non-radiative pathways which, when in the solution phase, are very prominent.

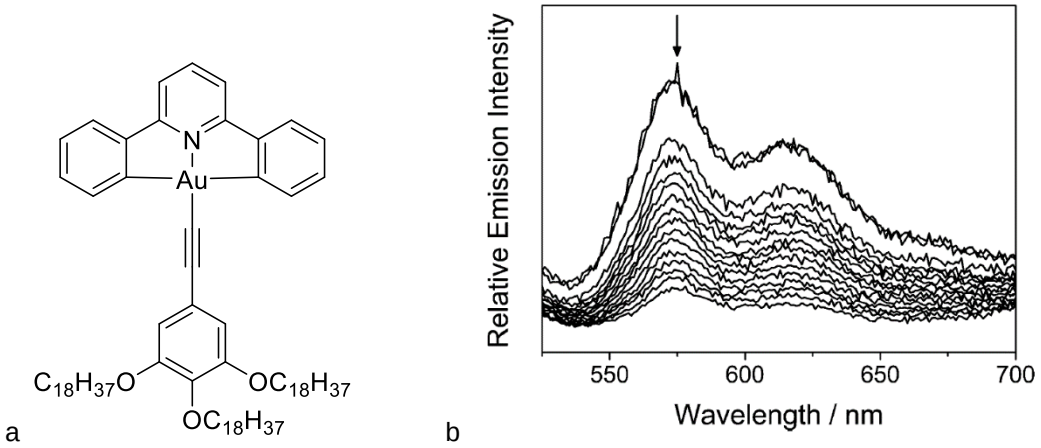

Figure 4-7: a) structure of organogold(III) alkynyl complex with 3,4,5-tri(octadecyloxy)ethynylbenzene ligands which forms a stable metallogel in hexane and cyclohexane; b) emission spectra of this complex in hexane upon increasing the temperature from 10 to 40 °C showing the decrease in luminescence intensity (directly from source).[16]

Metallogels are also observed for [Au(C^N^C)(C≡C-R)] complexes reported by Siu *et al.* with alkynyl ligands functionalised with L-valine and alkoxyphenyl substituents on the C^N^C ligand (Figure 4-8).[30] These complexes are emissive in solution with C^N^C-substituent-dependent, structured bands in the λ_{max} = 438 to 498 nm region, although no quantum yields are reported. In terms of gelation, four of the gold(III) complexes show gelation properties in DMSO (**Siu5**, **Siu7-9**), with the presence of gels heavily reliant on the C^N^C substituents, the number and length of alkoxy chains and the number of L-valine units on the alkynyl ligand, *e.g.* in complexes with one alkoxy chain and 2 L-valine units, the C6 chain (**Siu6**) does not show any gelation behaviour, but the C12 (**Siu7**) does and, as a second example, the complex with ^{t}Bu groups on the C^N^C ligand (**Siu4**) does not form a gel, but the methyl equivalent (**Siu5**) does. As with the luminescent gels described above, the emission profile is structured and C^N^C ^{3}IL-based with a loss of intensity upon increasing temperature.

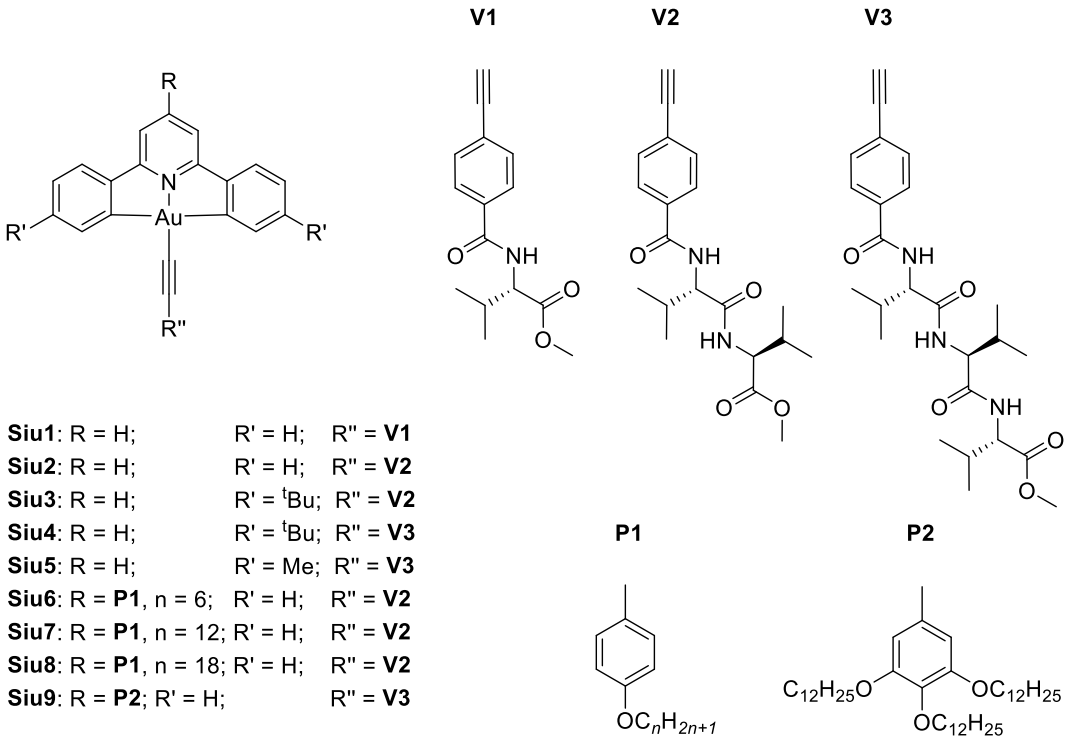

Siu1: R = H; R' = H; R'' = **V1**
Siu2: R = H; R' = H; R'' = **V2**
Siu3: R = H; R' = ^{t}Bu; R'' = **V2**
Siu4: R = H; R' = ^{t}Bu; R'' = **V3**
Siu5: R = H; R' = Me; R'' = **V3**
Siu6: R = **P1**, n = 6; R' = H; R'' = **V2**
Siu7: R = **P1**, n = 12; R' = H; R'' = **V2**
Siu8: R = **P1**, n = 18; R' = H; R'' = **V2**
Siu9: R = **P2**; R' = H; R'' = **V3**

Figure 4-8: Structure of complexes based on L-valine alkynyl ligands. Complexes **Siu5**, **Siu7**, **Siu8** and **Siu9** form metallogels in DMSO. Complexes relabelled from source for clarity.[30]

Chan *et al.* reported a series of complexes in which the alkynyl ligands consisted of heteroaromatic functionalities (Figure 4-9) which showed quantifiable phosphorescence, although with poor quantum yields (0.3-4%).[31] With an unsubstituted 2,6-diphenylpyridine C^N^C ligand, the emissive transitions in these complexes originated from a $\pi \rightarrow \pi^*$ intraligand transition based on the alkynyl ligand. This is in contrast to the majority of previously reported complexes, in which the $\pi \rightarrow \pi^*$ transition is predominantly based on the cyclometallating ligand or is interligand in nature between the alkynyl and the C^N^C. It should be noted that when the heteroaromatic moiety on the alkynyl ligand is BODIPY-based, only fluorescence is observed due to the large gap between the singlet and triplet excited states, resulting in poor spin-orbit coupling between the states and therefore a lack of effective intersystem crossing.

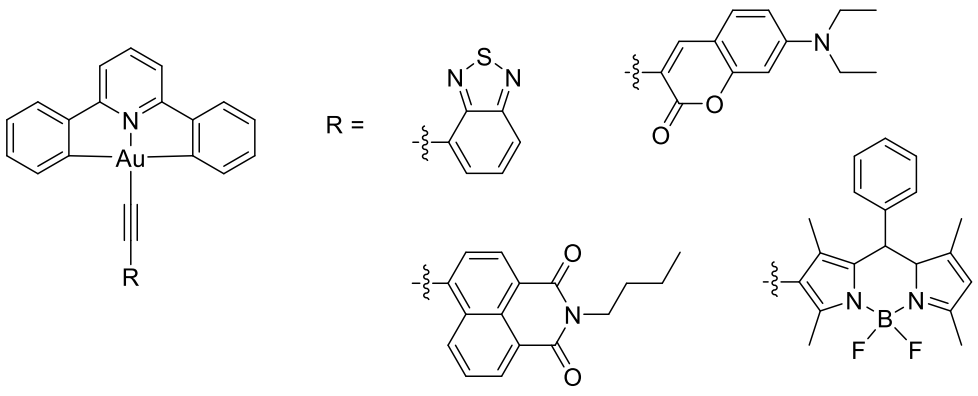

Figure 4-9: Structure of gold(III) alkynyl complexes with heteroaromatic alkynyl ligands as reported by Chan et al.[31]

Inclusion of a fluorene moiety into the structure of the cyclometallating ligand resulted in a series of complexes with intense phosphorescence, with quantum yields of up to 58% and lifetimes of emission of up to 305 µs for complexes with alkynyl ligands (Figure 4-10).[32] This PLQY is the highest reported for a gold(III) alkynyl complex at the time of writing. Complexes with NHC or CN ligands also showed emission with similar PLQYs and lifetimes. It was observed that the emission energies were rather insensitive to the nature of the ligand in the fourth coordination position, but that this could have a significant impact on the quantum yield and lifetime, as could modification of the solvent.

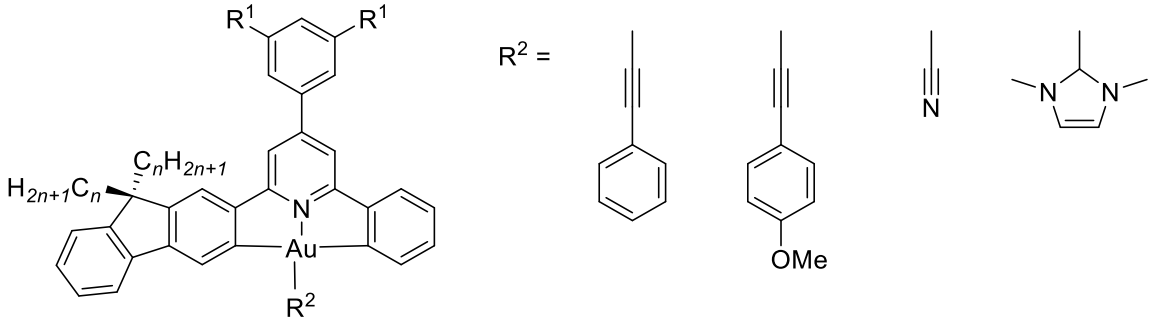

Figure 4-10: Structure of gold(III) complexes with fluorene-containing C^N^C ligands reported by To *et al.* which show excellent quantum yields and long lifetimes of emission, where R^1 = H or ^{t}Bu, *n* = 2, 4, 6, 8.[32]

Tuneable luminescence behaviour and self-assembly are not confined to monomeric species; Yim *et al.* reported a series of dinuclear gold(III) complexes which vary in the length and composition of the alkynyl spacer between the two metal centres (Figure 4-11).[33] Here, the nature of the alkynyl spacer is highly significant, as alteration of the alkynyl substituents or level of conjugation leads to noteworthy changes in the emission energy, although quantum yields are still poor for those complexes with C^N^C ligands without alkoxyphenyl substituents (**Yim1**-**Yim8**). As the level of conjugation in the alkynyl spacer is increased, *i.e.* increasing the number of phenyl rings and alkyne segments (**Yim1** to **Yim3**, **Yim4** to **Yim5**), the emission showed a bathochromic shift due to the increased ease of oxidation of the ligand, as shown by cyclic voltammetry, indicating a HOMO which was lower in energy as the conjugation increased. When alkoxy or triethyleneglycol (OTEG) substituents were appended to the spacer (**Yim6** to **Yim10**), a red-shift was also observed, however assignment of this transition is ambiguous, as the authors suggest a mixing of ^{3}IL [$\pi \rightarrow \pi^*$(C^N^C)] with ^{3}IL [$\pi \rightarrow \pi^*$(C≡C-R)], but also do not exclude the possibility of ^{3}LLCT due to the observed band broadening. The alkoxy an OTEG complexes (**Yim8-Yim10**) also showed concentration-dependent self-assembly behaviour in a variety of solvents to form supramolecular networks with a honeycomb structure.

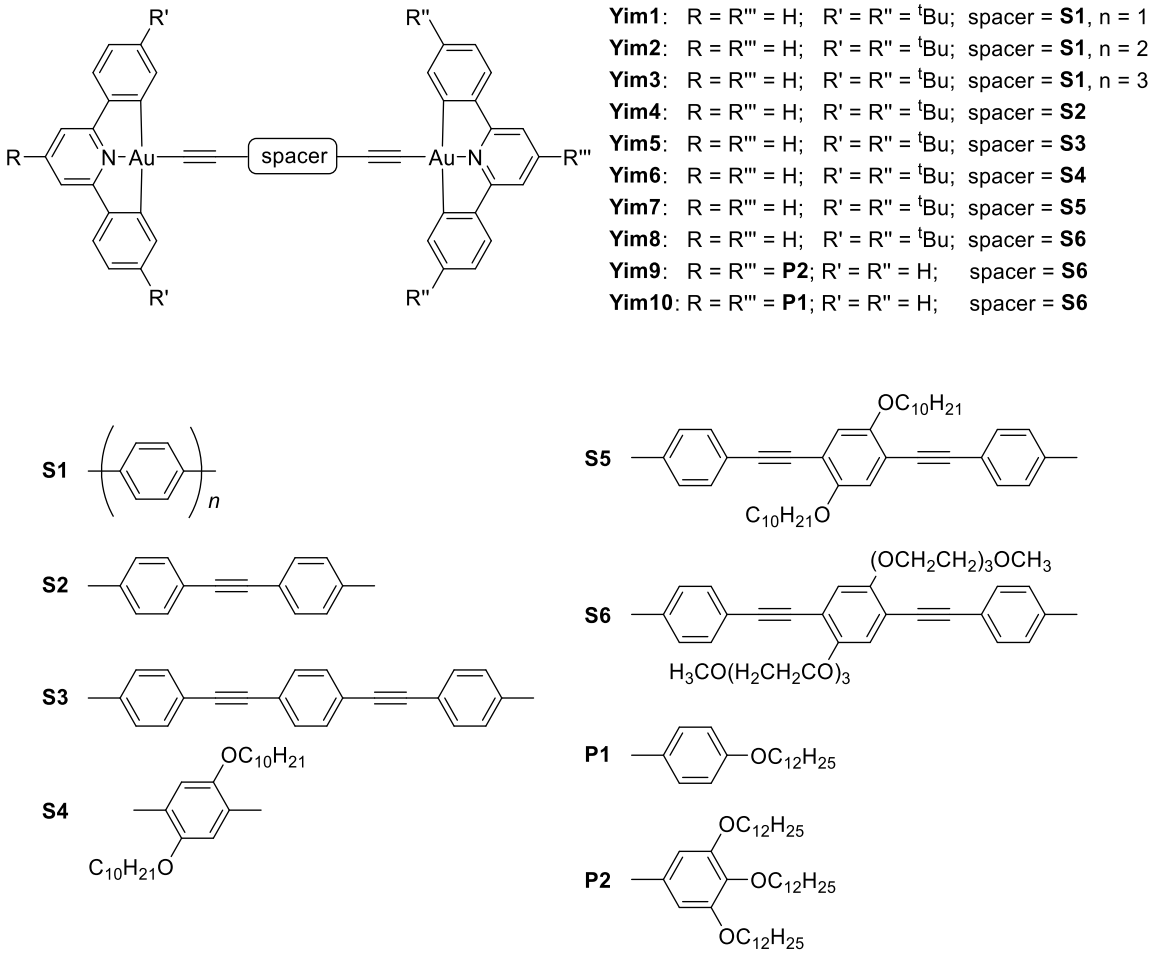

Figure 4-11: Structure of dinuclear gold(III) alkynyl complexes with varying spacers showing emissive and self-assembly behaviour.[33]

Alkynyl derivatives of hexaphenylbenzene and hexabenzocoronene have also been employed as ligands for multinuclear species, the most functionalised of which is a hexameric species with a gold(III) centre coordinated through an alkynyl ligand on every peripheral phenyl ring of hexaphenylbenzene (Figure 4-12).[17] All of the complexes synthesised with these highly conjugated alkynyl ligands showed structured emission bands with very poor quantum yields (0.0072% to 0.62%) but displayed interesting self-assembly behaviour. In scanning electron microscopy (SEM), a 2D layered structure of π-π-stacked aggregates was observed upon solvent evaporation. These appeared as a thin film in comparison to the fibrous networks previously established.

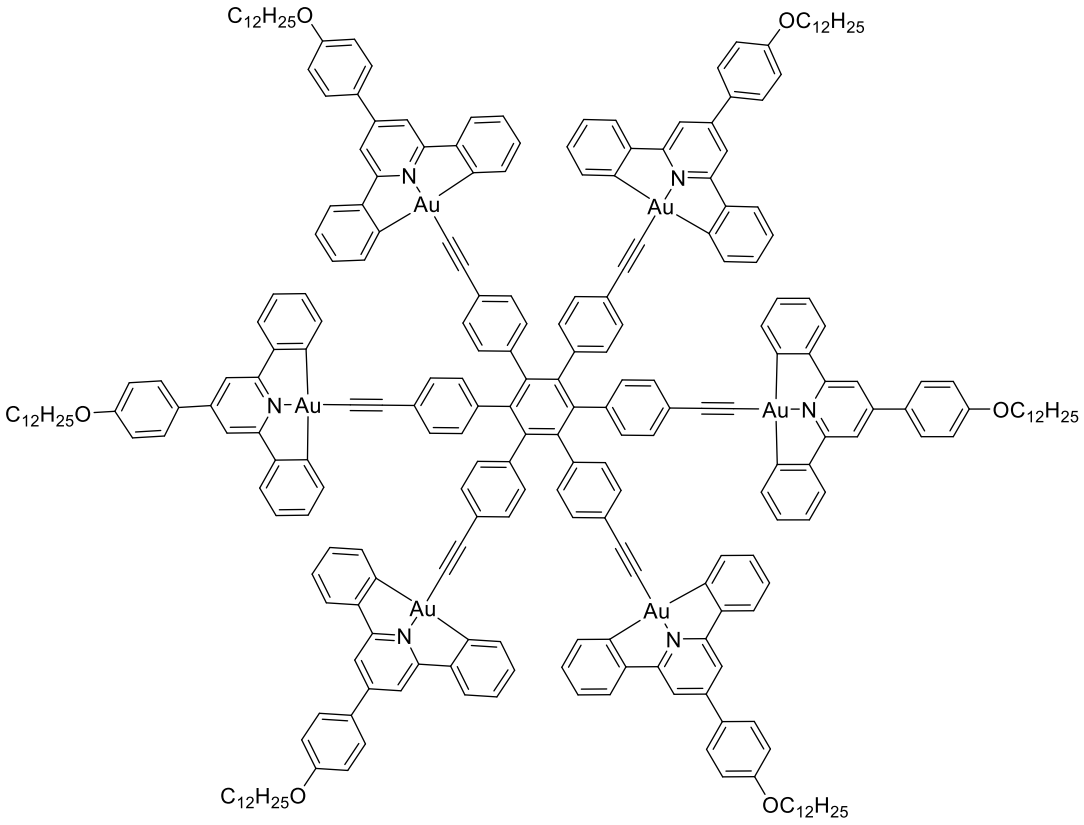

Figure 4-12: Structure of hexameric gold(III) complex with alkynyl functionalised hexaphenylbenzene ligand.[17]

An alkynyl complex with an excellent photoluminescence quantum yield (49%) compared to similar systems was synthesised by Wong *et al*. and based on a tetradentate system, where an extra final step is included in the synthetic procedure to connect the C^N^C and alkynyl ligands to form a C^N^C^C ligand *via* a Buchwald-Hartwig intramolecular cyclisation (Scheme 4-1).[34] The emission band is intense and featureless in the range of 584-615 nm and is triplet in nature, arising from an intraligand charge transfer (^{3}LLCT) from the diphenylamine to the cyclometallating diarylpyridine. The increase in quantum yield when moving to this tetradentate ligand is remarkable and indicates that by increasing ligand rigidity there is a decrease in the non-radiative rate constant, k_{nr}.

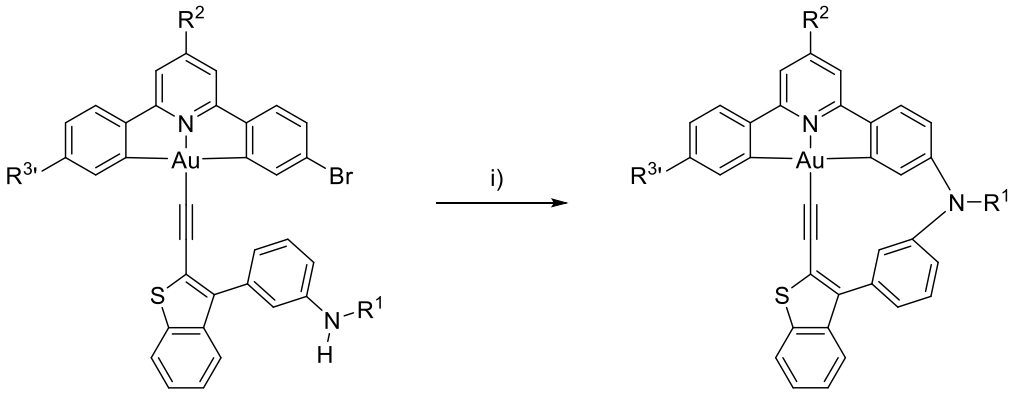

Scheme 4-1: Buchwald-Hartwig intramolecular cyclisation to form tetradentate gold(III) alkynyl complexes which show high PLQY values of up to 49%. i) $^{t}Bu_3P$, $Pd_2(dba)_2$, $NaO^{t}Bu$, toluene, reflux, 24 h, inert atmosphere. R^1 = 4-tolyl or 9,9-dihexyl-fluorene-2-yl; R^2 = H or ^{t}Bu; R^3 = ^{t}Bu or CF_3.[34]

Many of these [Au(C^N^C)(C≡CR)] complexes also behave promisingly when utilised as dopants in the emissive layer of OLED devices, and the majority of reports from the past three years have been focused on OLED performance and efficiency. A full overview of the performance of the above gold(III) complexes in devices (where applicable) and the extensive recent devices studies of specifically designed materials will be given in Section 4.1.2. Other related [Au(C^N^C)(C≡C-R)] complexes have been used in the fabrication of memory devices[35, 36] and have been observed to act as stimuli responsive materials.[37]

Outwith the use of functionalised alkynyl ligands, promising gold(III) C^N^C complexes with N-heterocyclic carbene (NHC) ligands, including multiple dimeric species, have also been reported to show emission in the green region of the spectrum, although quantum yields are poor; of the eleven complexes reported, ten have PLQY values of less than 1%, and the highest reported value is 1.7% for a dimeric complex.[38]

4.1.1.2 Gold(III) Complexes with Other σ-Donating Ligands

In the work of both Bochmann and Che, the [Au(C^N^C)(X)] complexes, where X = NHC, alkynyl, alkyne, alkene, aryl, CO, CO_2, H, isocyanide or olefin, have been used extensively in both detailed structural, theoretical and mechanistic studies,[39-52] in biomedical anti-cancer applications[53-64] and in self-assembly investigations;[65, 66] a full analysis of these applications is beyond the scope of this section, however complexes with emissive behaviour will be outlined in this section.

In 2012, Roşca *et al.* reported the alternate functionalisation of [Au(C^N^C)Cl] to form the equivalent cyclometallated gold(III) hydroxide *via* reaction with caesium hydroxide.[67] This hydroxide complex proved to be a versatile intermediate, providing easy reaction pathways to further gold(III) species, including aryls and N-heterocyclic carbenes, which displayed

phosphorescence with quantum yields of up to 6%, as well as [Au(C^N^C)(C≡C-R)] complexes under much milder reaction conditions than the inert-atmosphere, copper-catalysed conditions reported previously (Scheme 4-2).

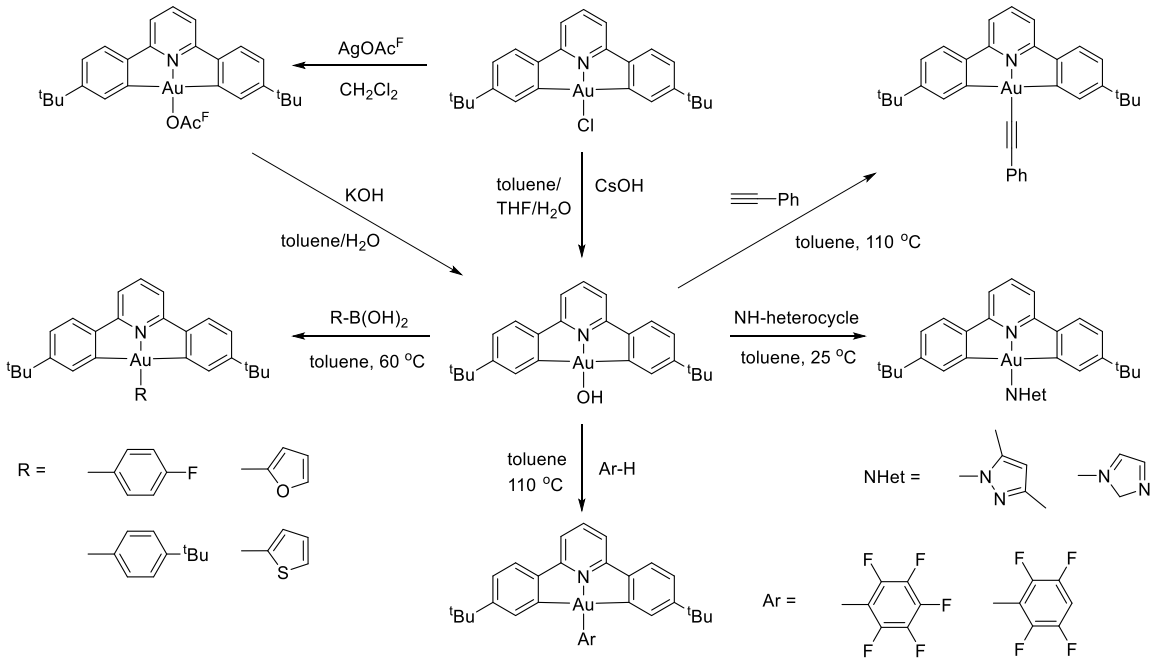

Scheme 4-2: Synthesis of gold(III) hydroxide species and possible subsequent ligand derivations as reported by Roşca *et al.*[67]

Modification of the C^N^C ligand to form complexes with a pyrazine in the central ring (as opposed to the pyridine ring) gave a complex with a second nitrogen atom that is able to undergo further modification, such as N-alkylation, protonation, or further coordination to another metal (Figure 4-13).[68] This modification in turn modified the luminescence behaviour of the complexes, crucially, without having to pre-functionalise the C^N^C ligand and synthesise each complex, *i.e.* it is a post-metallation functionalisation. The authors rationalised the tuneable nature of the system through the coexistence of ^{3}IL (C^N^C) and ^{3}LLCT (X $\rightarrow$ C^N^C) states, as previously described, as well as thermally activated delayed fluorescence (TADF) transitions, as illustrated by the extreme temperature dependence of the emission, ranging from red at cryogenic temperatures to blue at room temperature when the pyrazine ligand was protonated or coordinated to a metal ion (M = Zn, Cd, Hg). Lifetimes of emission were not given. This was the first example of a TADF process in gold(III) systems.

It should also be noted that the gold(III) chloride complex [Au(C^N^C)Cl] with the pyrazine-based ligand (Figure 4-13) is emissive at room-temperature, unlike the pyridine equivalent, which only shows weak emission at 77 K. This trend is observed for other complexes, such as the pyrazolato complex, indicating that alteration of the nitrogen-based ring can lead to many more systems which are emissive at room temperature.

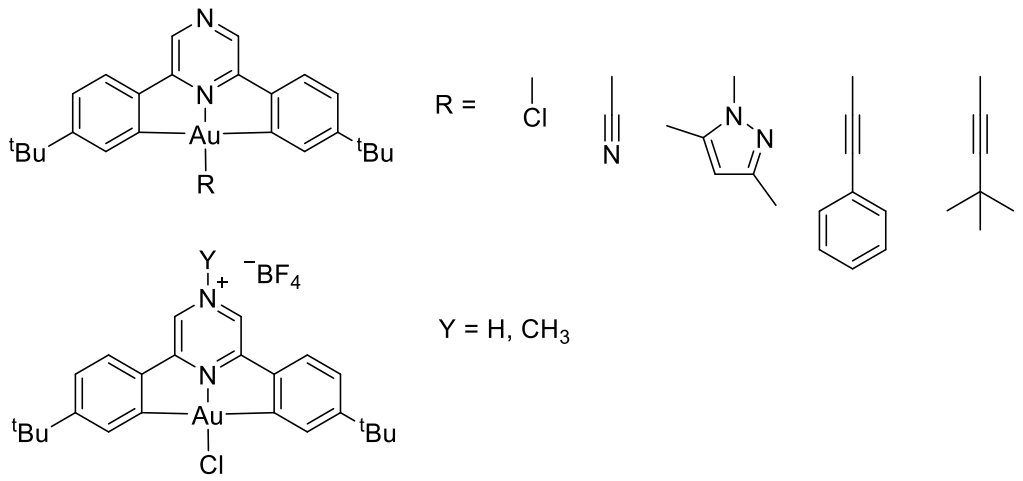

Figure 4-13: Structure of pyrazine-based gold(III) complexes showing tuneable emission through the post-metallation functionalisation of the free nitrogen of the pyrazine ring.[68]

Subsequent investigation into the correlation between emission wavelength and the acidity of the C-H bond of a $H_2CR^1R^2$ ancillary ligand, resulting in [Au(C^N^C)(CHR^1R^2)] complexes, where the C^N^C ligands used were 2,6-di((4-^{t}butyl)phenyl)pyridine and 2,6-di((4-^{t}butyl)phenyl)pyrazine (Figure 4-14), found that the emission could be fine-tuned through the alteration of the pK_a of the alkyl ligand *trans* to the pyridine/pyrazine ring; as the pK_a of the ligand was increased, and therefore the electron-donating capability of the ligand, the energy of the LUMO, which is pyridine/pyrazine based, was also increased, resulting in a higher-energy emission.[59] Again, this emission was assigned as a mixture of ^{3}IL (C^N^C) and ^{3}LLCT (X $\rightarrow$ C^N^C) states and consisted of a band with well-resolved vibronic coupling both in solution and in PMMA films (10 wt%). The pyrazine-based systems generally showed more intense emission than the pyridine analogues, although quantum yields were not reported for solution-phase data.

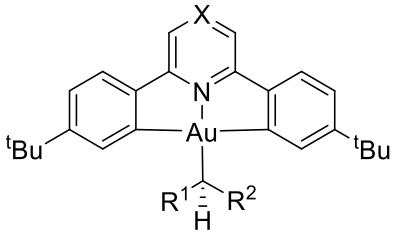

FC1 X = N; $R^1 = R^2$ = CN
FC2 X = CH; $R^1 = R^2$ = CN
FC3 X = N; $R^1 = R^2$ = C(O)Ph
FC4 X = CH; $R^1 = R^2$ = C(O)Ph
FC5 X = N; $R^1 = R^2$ = CO_2Et
FC6 X = N; R^1 = H; R^2 = C(O)Ph
FC7 X = N; R^1 = H; R^2 = C(O)Me
FC8 X = CH; R^1 = H; R^2 = C(O)Me

Figure 4-14: Structure of [Au(C^N^C)(CHR^1R^2)] complexes reported by Fernandez-Cestau *et al.* which show emission varying with the electron-donating potential of the ancillary alkyl ligand.[59]

Che and co-workers have also investigated the effect of utilisation of an alkyl ligand in place of the alkynyl, reporting complexes with methyl ligands with quantum yields in solution of up to 40%, the emission energies of which could be tuned *via* modification of the cyclometallating ligand.[69] Work by the same authors also report phosphorescent complexes with NHC ligands which are

luminescent in their own right, although show very poor PLQYs of <1%, but show enhanced luminescence when they are incorporated into a metal-organic framework (MOF), even showing triplet emission under aerated conditions, which is remarkable due to the quenching of triplet excited states by molecular oxygen.[70]

In addition to the complexes outlined above, there has also been a significant interest in cyclometallating ligands of alternate morphologies, such as aryl-substituted bipyridine and 2,9-diphenyl-1,10-phenanthroline C^N^N ligands, as well as N^C^N and C^C^N ligands, where all 'C' donors are aryl rings, and all 'N' donors arise from a pyridine ring. Related monocyclometallated complexes showing impressive emissive behaviour have also been reported.[71] Full elucidation of these structures and their properties is outwith the scope of this thesis, but a useful and thorough review is given by Kumar and Nevado.[72]

Although many of these compounds in the literature show multifunctional behaviour, as yet, there have been no reports of liquid-crystalline behaviour from [Au(C^N^C)(C≡C-R)] or related complexes; the liquid-crystalline properties of the gold(III) alkynyl complexes presented in this thesis were given in Chapter 3.

4.1.2 Gold(III) Alkynyl Complexes in OLED Devices

The predominant application for the gold(III) complexes outlined above, and those of similar structural design, is as the emitter in an OLED device, the working of which was outlined in Section 1.3 in Chapter 1. To that end, many of the complexes previously discussed have been tested in the fabrication of OLED devices both by solution-processed and vacuum-deposited methodology, the latter of which gives more efficient emission as characterised by the current efficiency (CE), power efficiency (PE) and external quantum efficiency (EQE) due to better film morphology (less defects) and the lack of crystallisation processes that can occur during spin-coating processes.[73] Of these, the EQE value is the most telling as to the efficiency of the device, and it is this measure that shall be judged for the literature systems herein discussed.

Of those complexes shown previously, many have been tested in OLED devices, with performance ranging from poor to excellent. The gold(III) dendrimeric complexes synthesised by Tang *et al.* and shown above in Figure 4-3b were used as the emitter in solution-processed devices which showed EQEs ranging from 0.92 to 3.62% at doping concentrations of 10-20% in host 1,3-bis(carbazole-9-yl)benzene (MCP) for red devices, which are poorly efficient when compared to other devices, but commendable for red-emitting devices at the time.[22] However, the devices showed a notably low turn-on voltage of less than 3V. The ethyl 2,6-diphenylisonicotinate-based gold(III) complex shown

in Figure 4-6 was used as the emitter in a vacuum-deposited OLED device, also doped into MCP, and showed an EQE of 2.8%.[26] Improved performance was observed for devices incorporating the complexes reported by Au *et al.* in 2013 (shown in Figure 4-5) in which complexes with a 4-diphenylaminophenylacetylene alkynyl ligand and 4-(2,5-dimethylphenyl)-2,6-diphenylpyridine (EQE = 4.8%) or 4-(4-(tert-butyl)phenyl)-2,6-diphenylpyridine (EQE = 3.6%) C^N^C ligand were used.[25]

Significant improvements in device efficiency were observed when including fluorine substituents on the cyclometallating ligand for the complex shown in Figure 4-3a, which shows an EQE of 11.5% at a doping concentration of 4% in 4,4'-bis(9-carbazolyl)-1,1'-biphenyl (CBP) for a vacuum deposited device.[21] This improvement was also observed to a lesser extent in the dendrimeric complexes reported by Tang *et al.* (Figure 4-4a) in which a maximum EQE of 7.8% was recorded at 10 wt% in MCP which decreased to 7.0% (10 wt%), then 3.8% (20 wt%) as the generations of dendrons increased. This was expected, due to previously observed reduction in efficiency of both organic[74] and iridium(III)[75] dendrimers as a result of reduced carrier mobility,[76] however the small decrease from 7.8% to 7.0% between the first and second generations, respectively, is surprisingly small given the aforementioned degradation. It should be noted that these devices were solution processed, and so absolute EQE values are not directly applicable for comparison to vacuum-deposited devices. Similar observations were made for the sky-blue emitting complexes reported by Lee *et al.* when incorporated into solution-processed OLED devices (Figure 4-4b), in which the EQE is reduced from 7.1% for the generation 0 complex to 4.3% for the generations 3 and 4 complexes.

In addition to these tridentate systems, the tetradentate complexes shown as the product in

Scheme 4-1 show colour-tuneable emission in devices (yellow to orange-red) when doped at 10-20 wt% in MCP with EQEs in the range of 11.1% to 7.0%, which were excellent efficiencies for solution processed devices based on this gold(III) central moiety, indicating that the improved emission for the tetradentate species formed by 'post-synthetic modification' is retained upon device fabrication and testing.[34]

More recently, many of the reports of gold(III) alkynyl complexes and related structures have been purely focussed on the synthesis of materials for device applications, and thus many structures with specific functional group modifications for efficiency in OLED devices which have not been discussed will be outlined below.

Green-blue emitting solution-processed devices have been reported based on gold(III) complexes with poly(benzyl ether) dendrons. These showed increasing device performance as the dendron generations increased, displaying EQEs from 0.9% to 2.4% at 5 wt% in MCP hosts on increasing

the generations from one to two, contrary to previously established observations as described above (Figure 4-15a).[77] Devices of complexes with alkynyl ligands based on triphenylamine and benzimidzole moieties (Figure 4-15b) have shown EQEs of up to 10% when doped at 10-20 wt% in MCP, an improvement of those reported by Tang *et al.* with carbazole moieties in similar ligands[32] (Figure 4-4a), which also show small efficiency roll-off values of less than 1%;[78] the efficiency roll-off is the tendency of OLED devices to show decreased efficiency at high brightness levels.[79]

Small efficiency roll-off values have also been observed for devices reported by Lee *et al.* utilising complexes with both hole- and electron-transporting moieties in different regions of the complexes; an electron-transporting phosphine oxide was present in the 4-position of the pyridine ring of the cyclometallating ligand, with a hole-transporting triphenylamine group on the alkynyl ligand (Figure 4-16). The device performance is excellent, with an EQE of 15.3% and a CE of 51.6% when the complex was doped at 20 wt% in a 3:1 mixture of MCP:TCTA (4,4'4"-tris(carbazol-9-yl)triphenylamine) in solution-processed devices, which remains the highest reported value at the time of writing. Also included in the same communication from Lee *et al.* are complexes with fluorene or carbazole moieties appended onto the architecture of the alkynyl ligand which showed EQE values of up to 14.3%.[80]

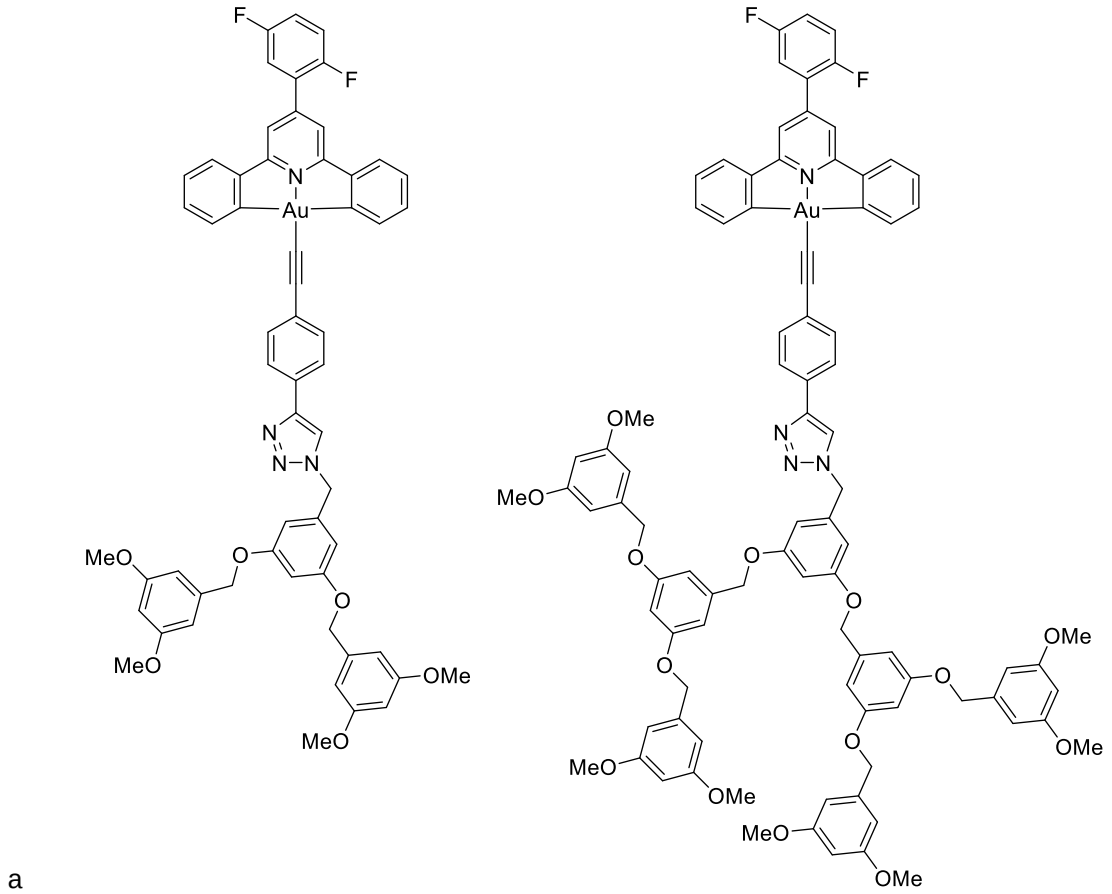

a

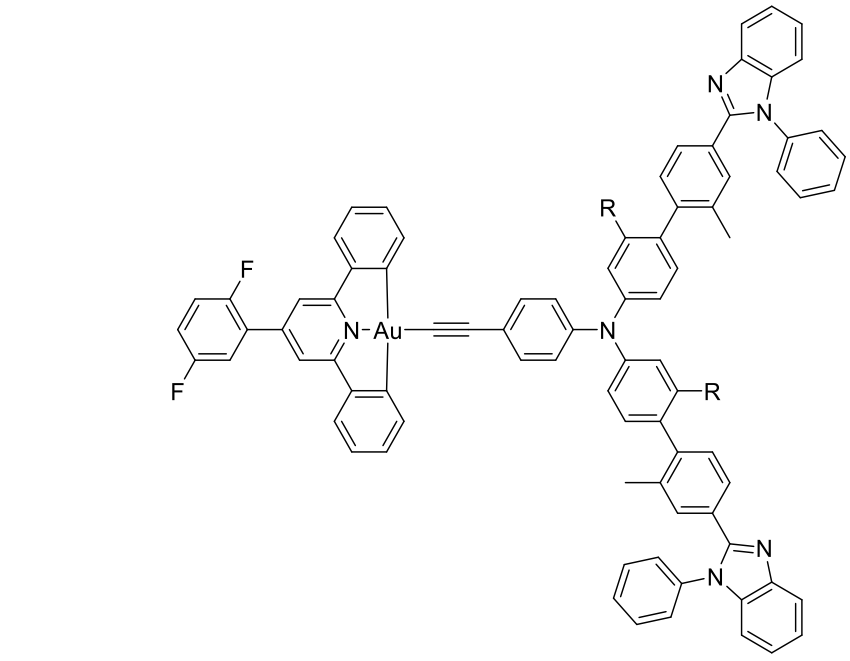

b

Figure 4-15: Structure of gold(III) complexes with a) poly(benzyl ether)-based alkynyl ligands which show improved device performance as the generation of dendrons is increased;[77] b) benzimidizole-based alkynyl ligands which show EQEs of up to 10%.[78]

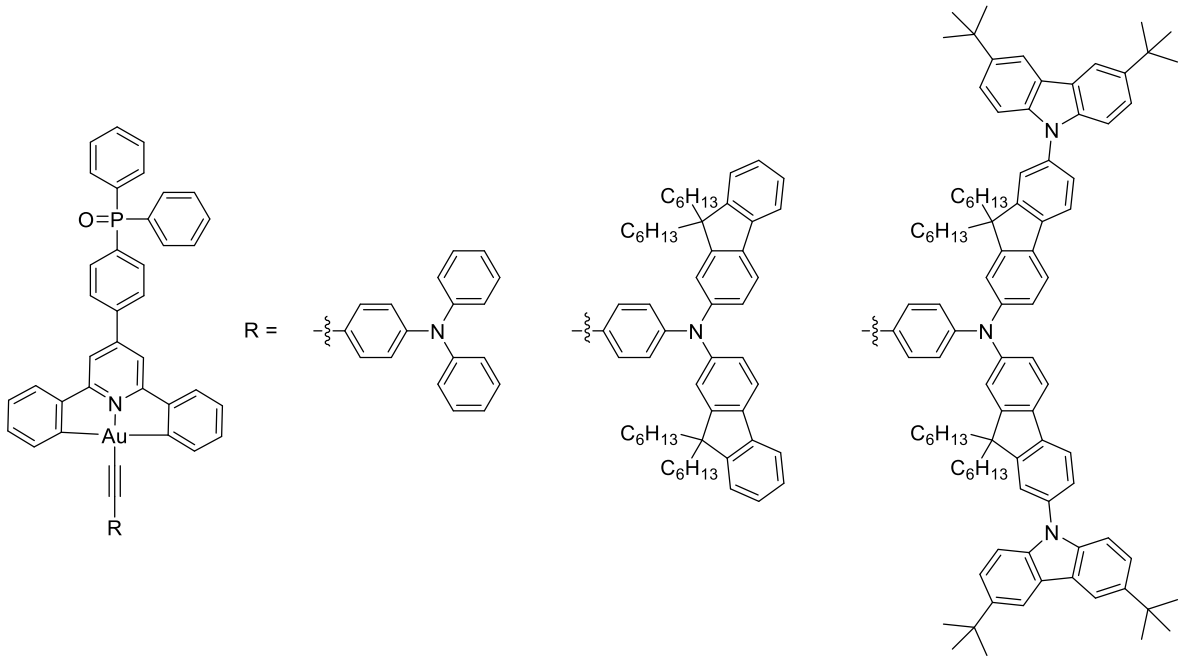

Figure 4-16: Structure of gold(III) complexes with both phosphine oxide and triphenylamine moieties which show excellent EQEs and small roll-off values.[80]

Alkynyl ligands of the same general structure were expanded upon by Tang *et al.*, with the complexes displaying colour-tuneable behaviour from green to red emission when doped at 20 wt% in MCP in solution-processed devices, with a maximum EQE of 13.5% for the yellow device (Figure 4-17a, **Tang3**).[81] Further investigations into the same complex probed its efficiency as an emitter in white OLED (WOLED) devices through combination with the known blue emitter iridium(III)bis(3,5-difluoro-2-(2-pyridyl)phenyl-(2-carboxypyridyl) (FIrpic), resulting in a device with an EQE of 12.9% and exceptionally small roll-off values. Both MCP and TCTA were investigated as potential hosts, with an increase in device performance for the MCP-based devices due to more efficient energy transfer between the host and the emitter.[82] Fluorene moieties have also been utilised in devices fabricated by Cheng *et al.* (Figure 4-17b) which show remarkable EQEs of 22.02% for vacuum-deposited devices and 13.2% for solution-processed devices (with a mixed emissive system of 2% [Au]:10% FIrpic in PVK:OXD-7.[83]

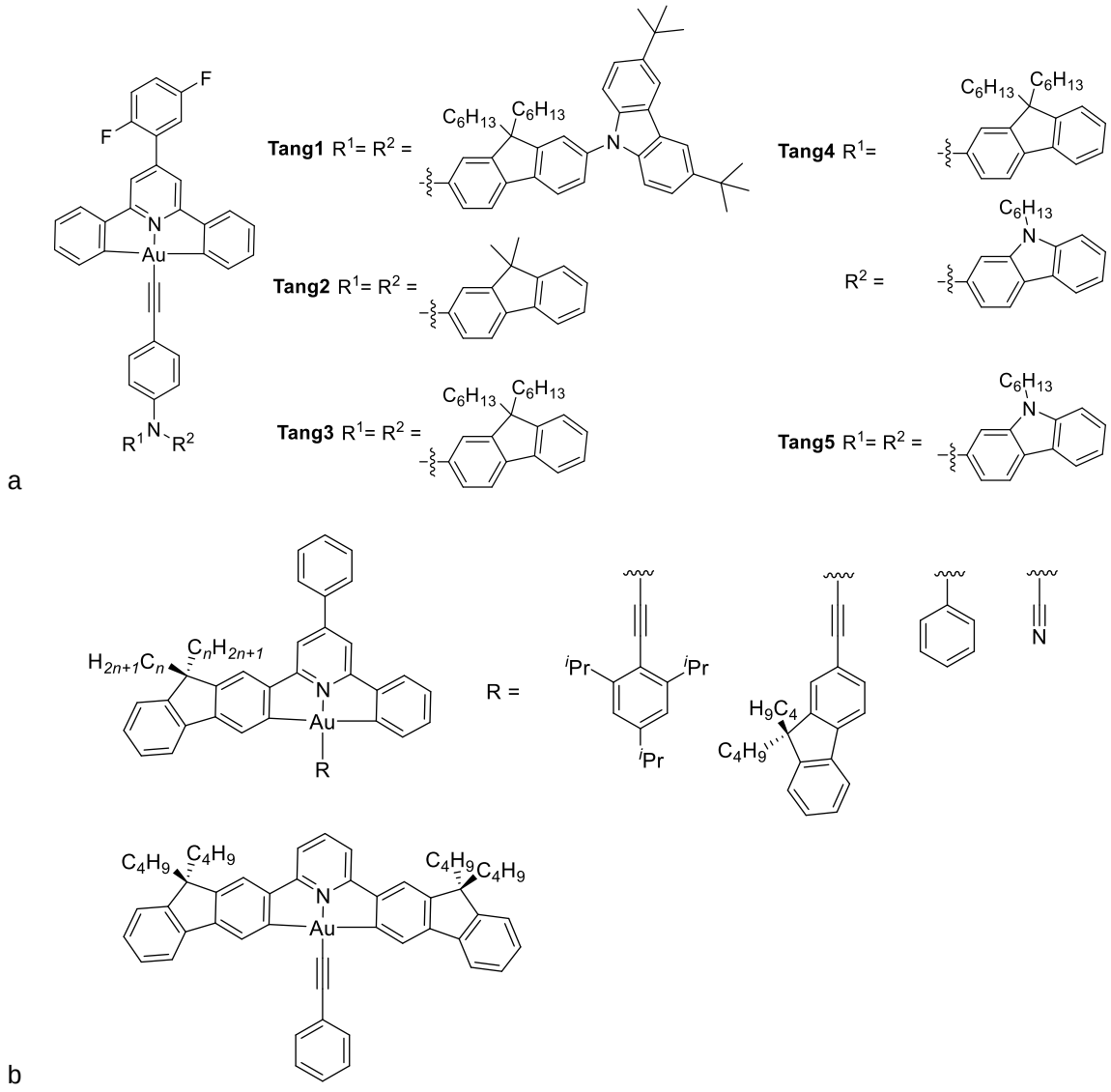

Figure 4-17: Structure of a) fluorene- and carbazole-containing gold(III) complexes reported by Tang *et al.* showing excellent solution-processed device performance;[81, 82] b) fluorene containing complexes reported by Cheng *et al.*[83]

Related complexes with aryl ligands in place of the alkynyl have also been thoroughly investigated for their applications in OLED devices. In recent work by Yam and co-workers,[84] the effect of the substitution pattern of the C^N^C ligand with F, CN, ^{t}Bu, CF_3 and OCF_3 groups was investigated in which both vacuum-deposited and solution-processed devices were fabricated for two of the series of seven complexes due to their comparatively high energy emission (Figure 4-18a); the device behaviour of the other complexes was not investigated, and cannot be predicted, so performance for this series may exceed the reported efficiencies. The solution processed devices showed EQE values of 2.3% when $R_1 = R_3 = R_5 = F$ and $R_2 = R_4 = R_6 = H$, and 4.8% when $R_1 = R_3 = R_4 = R_6 = H$ and $R_2 = R_5 = OCF_3$. These efficiencies were significantly higher, as expected, in the vacuum-deposited devices with EQEs of 10.7 and 11.3%, respectively. The inclusion of further fluorine

substituents on the aryl ligand resulted in an increase of the EQE of solution-processed devices to 7.3% when doped at 15 wt% in MCP (Figure 4-18b).[85]

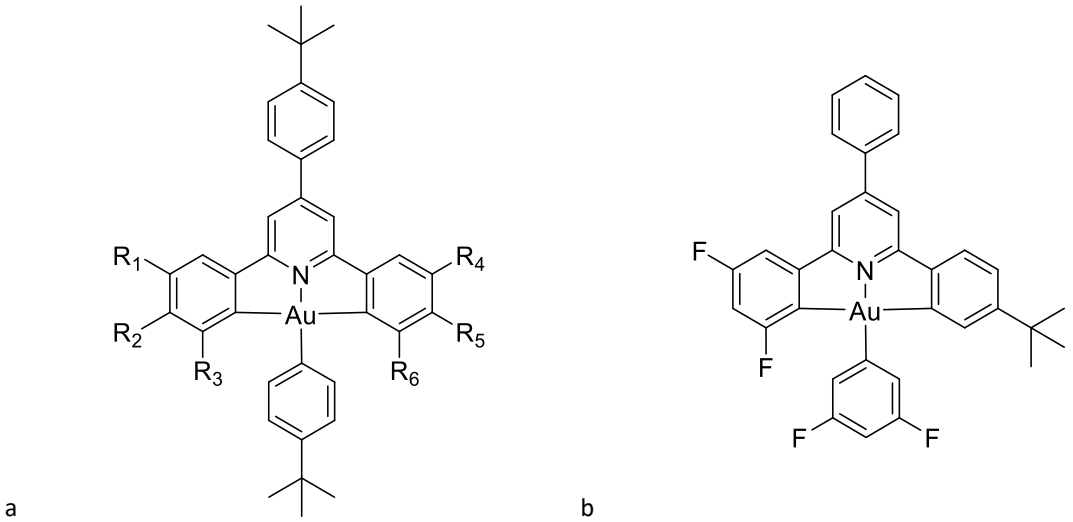

a b

Figure 4-18: Gold(III) complexes reported by Tang *et al.* with aryl ligands: a) varying substitution patterns on the cyclometallating ligand, $R_1 = R_3 = R_5 = F$ and $R_2 = R_4 = R_6 = H$ or $R_1 = R_3 = R_4 = R_6 = H$ and $R_2 = R_5 = OCF_3$;[84] b) with fluorine substitution on the aryl ligand.[85]

Recent reports from Li *et al*. with C^C^N ligands and NHC or thiolate ligands in the fourth coordination position have been shown to be highly efficient in both vacuum-deposited and solution-processed devices, with EQEs of up to 21.6% and 11.9% for each technique, respectively (Figure 4-19). These devices show tuneable emission colours from red to blue based on both the ancillary ligand and the conjugation of the pyridine ring (no second ring, or a second ring in either position as shown in Figure 4-19), and long term stability.[86]

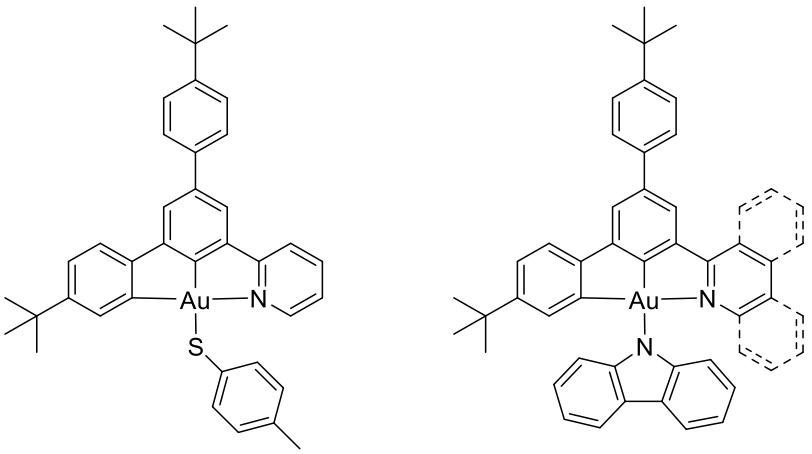

Figure 4-19: Structure of C^C^N gold(III) complexes showing tuneable emission in devices and long-term operational stability.[86]

All of the devices discussed above exhibit pure phosphorescent emission. Recently, gold(III) complexes with alternate modes of emission have been investigated for their OLED device

capabilities. Gold(III) aryl systems have been shown to exhibit thermally stimulated delayed phosphorescence (TSDP) (Figure 4-20a), and inclusion of these complexes in vacuum-deposited OLED devices showed poor performance, with EQEs of up to 7.7%, which is not comparable to the majority of complexes outlined above.[18] There have also recently been multiple reports of gold(III) complexes with C^N^C ligand and both aryl and alkynyl ligands showing thermally activated delayed fluorescence (TADF); this emission pathway has become very popular in state of the art OLED displays.[87, 88] To *et al.* reported TADF emitters which, when included as the emitter in solution-processed OLED devices, show excellent device performance, with EQEs of 14.8% and 23.8% for complexes with triphenylamine aryl ligands (Figure 4-20b).[20] This efficiency is remarkable, and the highest value reported for solution-processed devices of such cyclometallated gold(III) complexes and comparable to that of vacuum-deposited counterparts. Zhou *et al.* have also recently reported TADF emitters with C^N^C ligand where the nitrogen donor originated from either a pyridine or pyrazine ring, with alkynyl ligands of varying substitution (Figure 4-20c).[19] When utilised in vacuum-deposited devices, these complexes show excellent device performance of up to 23.4% EQE values.

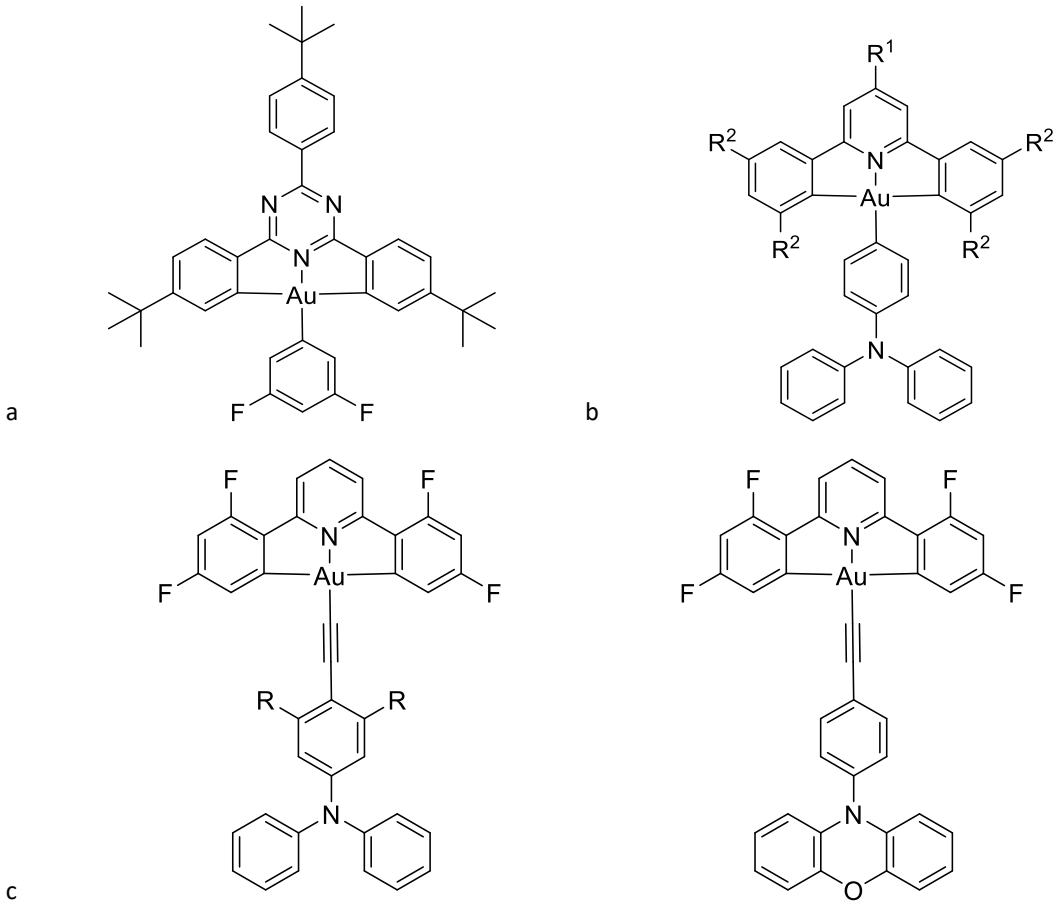

Figure 4-20: Structure of gold(III) complexes with C^N^C ligands showing a) thermally-stimulated delayed phosphorescence and poor device performance;[18] b) TADF and excellent performance for solution-processed devices when R^1 = H or OEt, R^2 = H or F;[20] c) TADF with alkynyl ligand and excellent EQEs for vacuum-deposited devices.[19]

The above complexes all function as dopants in a polymer host-matrix within the emissive layer, which is amorphous. To investigate the ability of the film/device to show polarised emission, further configuration is needed.

The research outlined in this introductory section shows definitively that these gold(III) complexes are a robust framework for strongly emissive and stable materials that are promising for use in commercial OLED architectures. These complexes can be structurally modified to tune the emission parameters and additional material properties, including self-assembly behaviours. While supramolecular structures have been investigated, specifically in terms of gelation, no gold(III) complexes of this nature have been shown to be liquid-crystalline; synthesis of such materials may prove to have additional features in devices, such as polarised emission.

4.1.2.1 Metallomesogens in OLED Devices

In addition to the use of small-molecule emissive complexes as emitters in OLED devices, metallomesogens can also be used, with the aim of utilising the inherent order afforded the system through its liquid-crystallinity to form an ordered or aligned emissive layer to reduce power requirements or display polarised emission, as described fully in Chapter 1. To this end, a brief overview metallomesogens in polarised films and OLED devices will be given below.

The most common way to investigate the ability of a complex to show polarised emission is through application to a polymer film, very commonly polyimide or nylon-6, which has been aligned through uniaxial rubbing. The complex can then be coated on the aligned layer and annealed in the mesophase. This method was used by Zhang *et al.* to investigate the polarised emission of a series of tetradentate platinum(II) complexes[89] (Figure 4-21a) which show a dichroic ratio (R, the ratio of emission intensities in the parallel and perpendicular orientations and the best measure of polarisability) of 5.1 when coated onto rubbed nylon-6. Utilising phenylpyridine cyclometallating ligands and tetrazole ligands substituted in the 5-position with further a phenylpyridine group, a dichroic ratio of 7.1 can be achieved after coating on a polyimide film and annealing in the mesophase (Figure 4-21b).[90] Alteration of the tetrazole ligand for an ancillary acac ligand, as reported by Wang *et al.* resulted in an increase in the dichroic ratio to 10.5 (Figure 4-21c), although the SAXS pattern of the supposed smectic phase shows many ordered reflections and the clearing enthalpies are significantly larger than what would be expected for a smectic to isotropic transition.[91] Given that the POM textures also do not show any defects typical of a smectic phase, such as focal-conic and fan-like defects, the assignment of these complexes as liquid-crystalline is suspected to be incorrect. Further alteration of the co-ligand to picolinic acid

derivatives in this position gave complexes with a dichroic ratio of 24.6, the highest reported value for any metallomesogen (Figure 4-21d).[92]

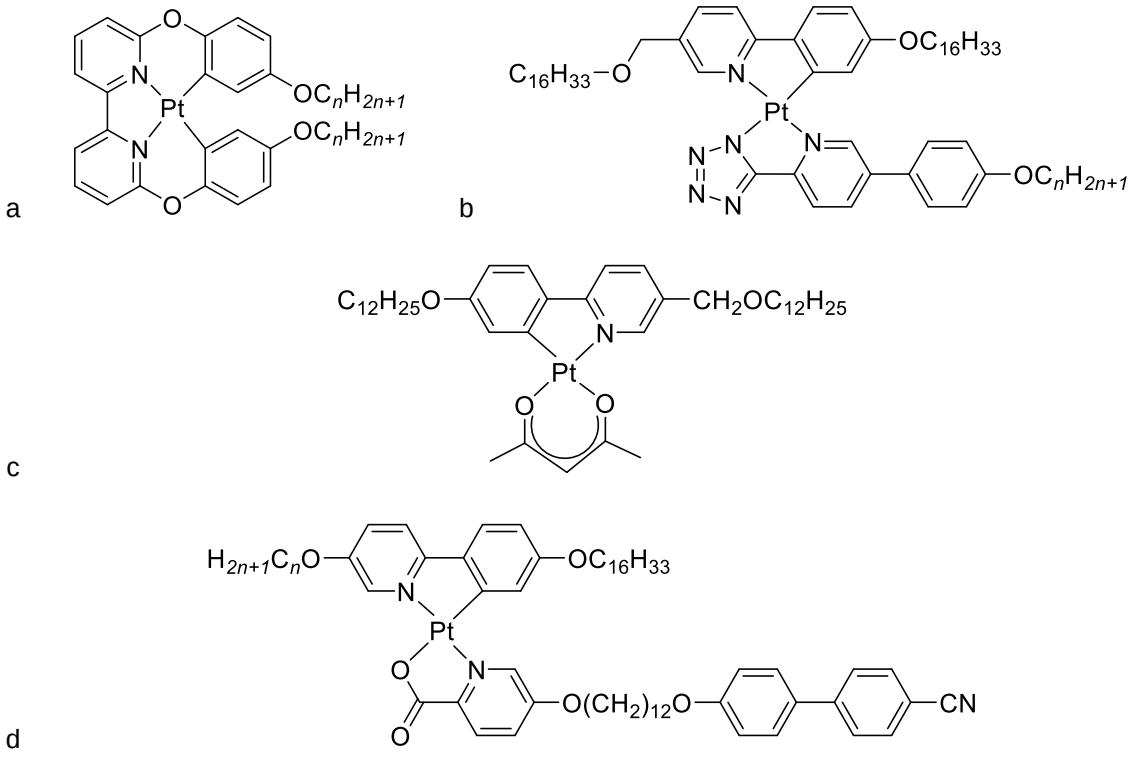

Figure 4-21: Structure of platinum(II) complexes reported by a) Zhang *et al.* showing tetradentate complexes with a dichroic ratio of 5.1 when *n* = 12 or 16;[89] b) Geng *et al.* with phenylpyridine and tetrazole-based ligands which show a dichroic ratio of 7.1, *n* = 12 or 16;[90] c) Wang *et al.* showing dichroic ratio of 10.5;[91] d) Zou *et al*. with a dichroic ratio of up to 24.6 when *n* = 12.[92]

This method has also been utilised for multimetallic emissive species, such as the platinum dimers reported by Jiang *et al.* which show a dichroic ratio of 3.1[93] and the platinum polymeric species reported by Díez *et al.* (commented on in Chapter 3) in which a dichroic ratio of 2.5 was achieved for a film deposited on an aligned layer of nylon-6.[94] Significant improvements in polarisation were achieved by Wang *et al.* for a dimeric platinum(II) species linked by a fluorene moiety which showed a high dichroic ratio of 10.3 (Figure 4-22).[95] The enthalpy of the clearing transition for this complex is also anomalously high, with a featureless POM texture, as mentioned above for complexes by the same authors. As such, the reported liquid-crystalline behaviour of this dimeric complex is thought to be incorrect.

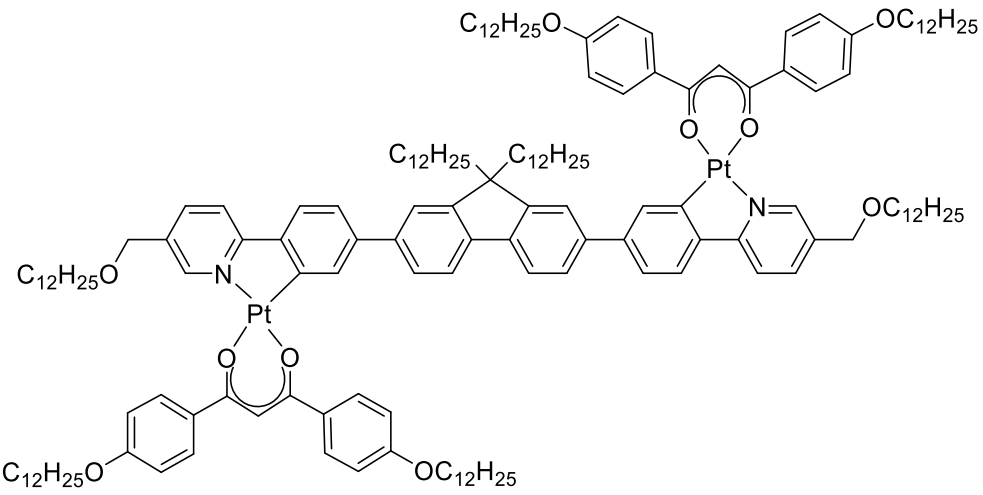

Figure 4-22: Structure of platinum(II) dimeric complex reported by Wang *et al.* showing a high dichroic ratio of 10.3 when coated onto an aligned polyimide film.[95]

It is clear from these reports that an impressive level of polarisation can be achieved in aligned films, however these results are not directly applicable to polarisation in *devices* (electropolarisation), in which polarisation is decidedly poorer.

Wang *et al.* reported a platinum(II) complex with a phenylpyridine ligand functionalised with a triphenylene unit and a carbazole moiety (shown in Figure 3-11 in Chapter 3) which showed a dichroic ratio of 1.4 in a WOLED device structure when doped with the blue emitter poly(9,9'-dioctylfluorene) (PFO) at 20 wt% after direct rubbing of the emissive layer.[96] Subsequent reports by Yang *et al.* of a platinum(II) complex with a 2,4-difluorophenylpyridine cyclometallating ligand and functionalised acac chelating ligand displayed a nematic phase and sky-blue emission in solution (Figure 4-23a).[97] When included as the emitting layer in an OLED device in which the emissive layer was uniaxially rubbed directly and then annealed in the mesophase, the device showed polarised emission with a dichroic ratio of 1.3. Polarised emission was not observed in a similar device configuration for the same complex in which was not rubbed, only annealed. The device showed a poor EQE of 1.1% due to self-quenching in the neat film.

A platinum(II) complex reported by Liu *et al.* which showed a columnar hexagonal phase (Figure 4-23b) was used as the emitter in an aligned OLED device in which it was doped in penta[9,9-bis(2-methylbutyl)fluorene], F(MB)5, a nematic liquid-crystal.[98, 99] The hole-injection layer, PEDOT:PSS, was rubbed to form an aligned substrate onto which the emissive layer was spin-coated, resulting in a device which showed polarised emission with a dichroic ratio of 2.

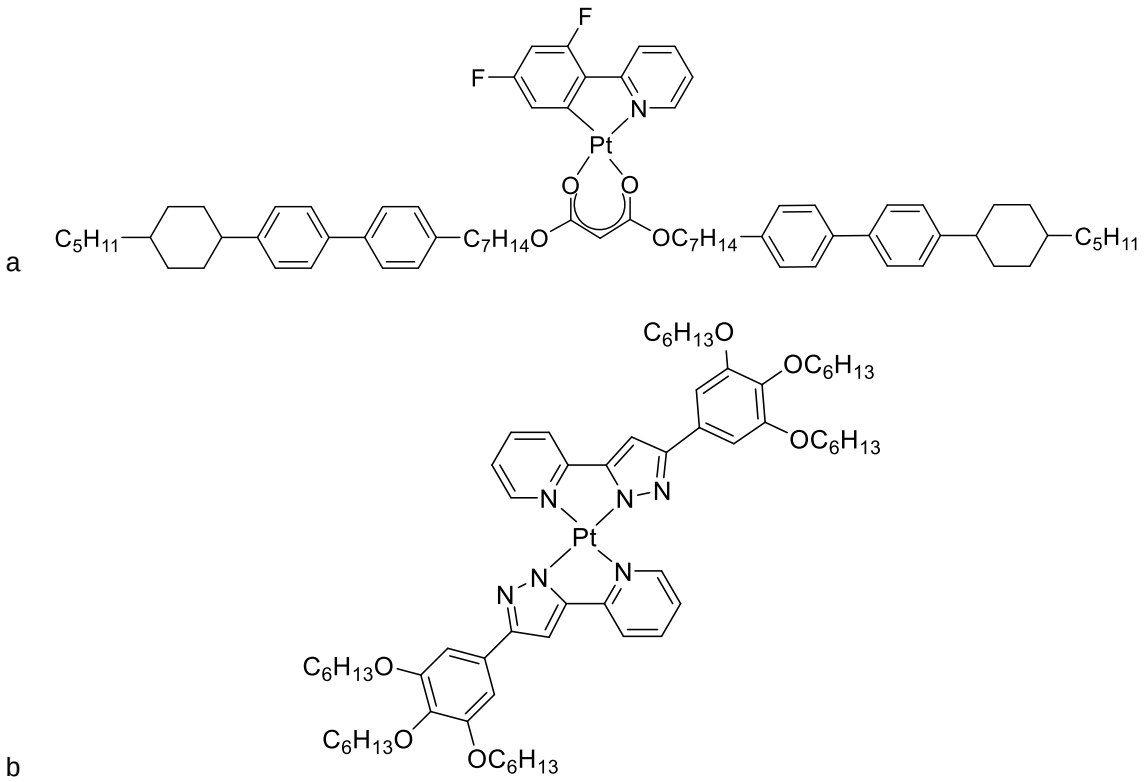

Figure 4-23: Structure of complexes used in polarised OLED devices as reported by a) Yang *et al.* which shows a dichroic ratio of 1.3 and an EQE of 1.1%;[97] b) Liu *et al.* which showed polarised emission with a dichroic ratio of 2 when doped into nematic host F(MB)5.[98, 99]

All previously discussed systems have been based on platinum(II), however several iridium(III) complexes also show polarised emission in fabricated devices. Reports by Wu *et al.* of iridium(III) complexes with two unfunctionalized phenylpyridine ligands and one highly functionalised bipyridine ligand showed enantiotropic SmA phases and solution-phase red emission (Figure 4-24a).[100] A variety of alignment methods were tested including: only thermal annealing in the liquid-crystalline state; rubbing of the layer directly below the emissive layer (PVK), following by annealing in the mesophases; or direct rubbing of the emissive layer and annealing in the mesophase. These different device configurations resulted in varied polarised emissive performances for both of the reported complexes. Only thermal annealing resulted in devices with dichroic ratios of 1.4 and 1.1 for complexes **A** and **B**, respectively, polarisation was destroyed for **B** when the PVK layer was aligned and for **A** R = 1.2, however the greatest polarisation came from direct rubbing of the emissive layer, in which polarisation ratios of 1.1 for **A** and 4.0 for **B** were achieved, the latter of which remains the highest polarisation ratio for a metallomesogen in an OLED device. It should be noted that other device parameters were compromised for the devices in which the emissive layer was directly rubbed due to the partial destruction of the layer, resulting in a drop in EQE from 1.1% to 0.04% for **A** between rubbed and non-rubbed devices.

Also worth note is a report by Wang *et al.* of devices containing phosphorescent iridium(III) complexes in which aligned films showed significantly increased hole mobilities compared to unaligned counterparts (0.004 $cm^2V^{-1}s^{-1}$ compared to 10^{-7} $cm^2V^{-1}s^{-1}$) (Figure 4-24b).[101] The devices were designed as hole-only devices, and as such the emissive properties, including polarised emission, were not investigated.

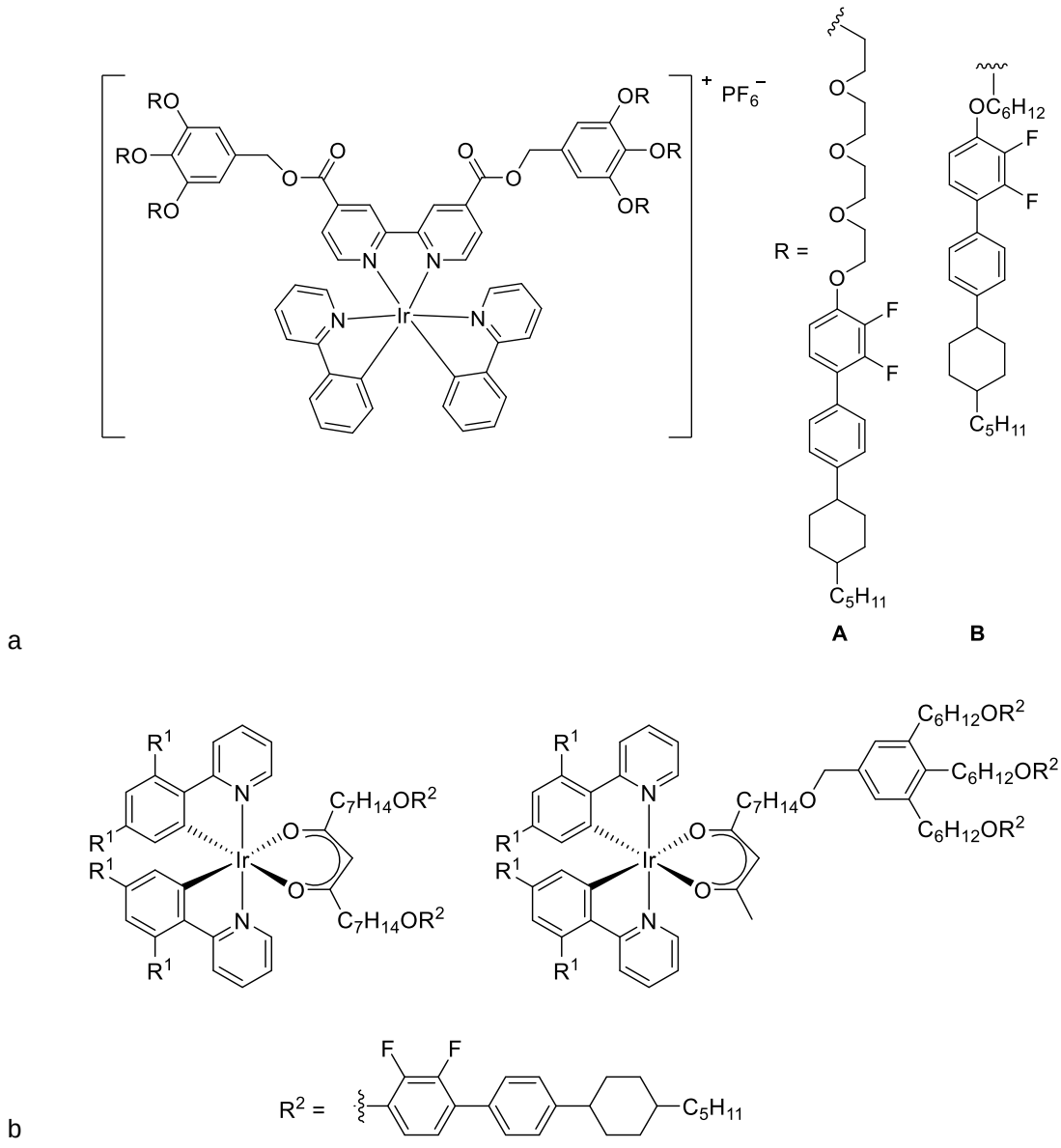

Figure 4-24: Structure of iridium(III) complexes reported by a) Wu *et al.* which show polarised emission in OLED devices with a dichroic ratio of up to 4;[100] b) Wang *et al.* which show increased hole-mobilities when the film is aligned, R^1 = H or F.[101]

Clearly, the study of phosphorescent metallomesogens in polarised OLED devices is still in its infancy, although reports of increasing levels of polarisation show promise. The main issue to overcome is the compromised overall device efficiency when using a neat film of the emitter in place of a doped layer, where emission efficiency is significantly improved due to the spacing of emissive centres and reduction of self-quenching. It has been shown that doped systems can show

polarised emission, but further investigation into a favourable mix of polarizability and efficiency of the emission is required.

4.2 Aims of Chapter

This chapter reports the investigation of the photophysical properties of the gold(III) alkynyl complexes of the general formula [Au(C^N^C)(C≡CR)], the synthesis of which were presented in Chapter 3; both the fully hydrocarbon species **1-*n*** to **8-*n*** and the fluorocarbon analogues **11-*n*** to **16-*n*** have been investigated. It was suspected that the different modes of functionalisation of both the cyclometallating ligand and the alkynyl ligand may have an influence on the photophysical behaviour of the complexes. Time-resolved density functional theory (TD-DFT) calculations also assist in the rationalisation of the emission observed through the visualisation of the orbitals involved in the relevant electronic transitions. A select number of complexes have also been investigated for their performance in OLED devices, both as emissive dopants in a polymeric host and as a neat emissive layer with the aim to align the film through the positional order of the liquid-crystalline phase to achieve polarised emission.

4.3 Photophysical Properties of Gold(III) Complexes

4.3.1 Electronic Spectra of Gold(III) Complexes

The UV-Vis absorption spectra of all the alkynyl complexes (structures shown in Figure 4-25 for ease of reference) were measured in CH_2Cl_2 at room temperature (Figure 4-26, two-chain complexes and Figure 4-26, four-chain complexes). The spectra fall into two categories, those with two chains on the cyclometallating ligand (**1-*n*** to **4-*n***) and those with four (**5-*n*** to **8-*n***). Within these categories, the spectra are identical, *i.e.* the electronic spectra are independent of the nature of the alkynyl ligand and of the length of the alkyl/alkoxy chains, and depend wholly on the substitution pattern of the C^N^C ligand. There are variations in molar extinction coefficients between different complexes in the same families, however, they can be accounted for through the variation in number and position of electron-donating substituents and measurement errors.

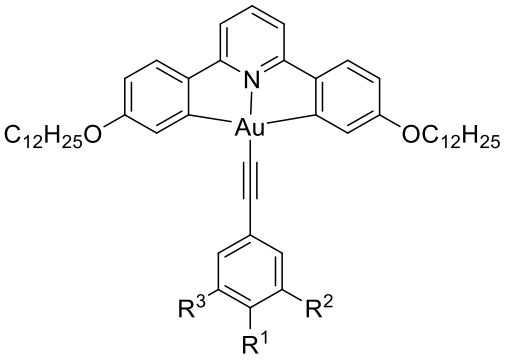

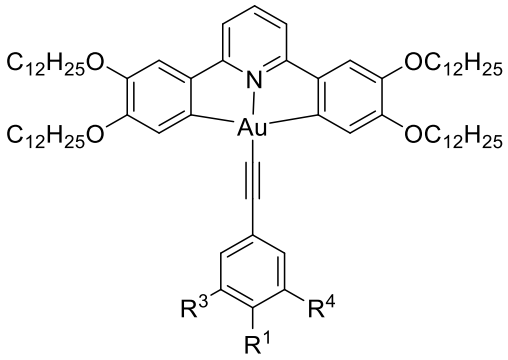

1-*n* R^1 = H, C_5H_{11}, C_8H_{17}; R^2 = R^3 = H
2-*n* R^1 = OC_nH_{2n+1}; R^2 = R^3 = H
3-*n* R^1 = R^2 = OC_nH_{2n+1}; R^3 = H
4-*n* R^1 = R^2 = R^3 = OC_nH_{2n+1}

5-*n* R^1 = H, C_5H_{11}, C_8H_{17}; R^2 = R^3 = H
6-*n* R^1 = OC_nH_{2n+1}; R^2 = R^3 = H
7-*n* R^1 = R^2 = OC_nH_{2n+1}; R^3 = H
8-*n* R^1 = R^2 = R^3 = OC_nH_{2n+1}

Figure 4-25: Structure of the gold(III) alkynyl complexes under investigation. *n* = 8, 10, 12, 14.

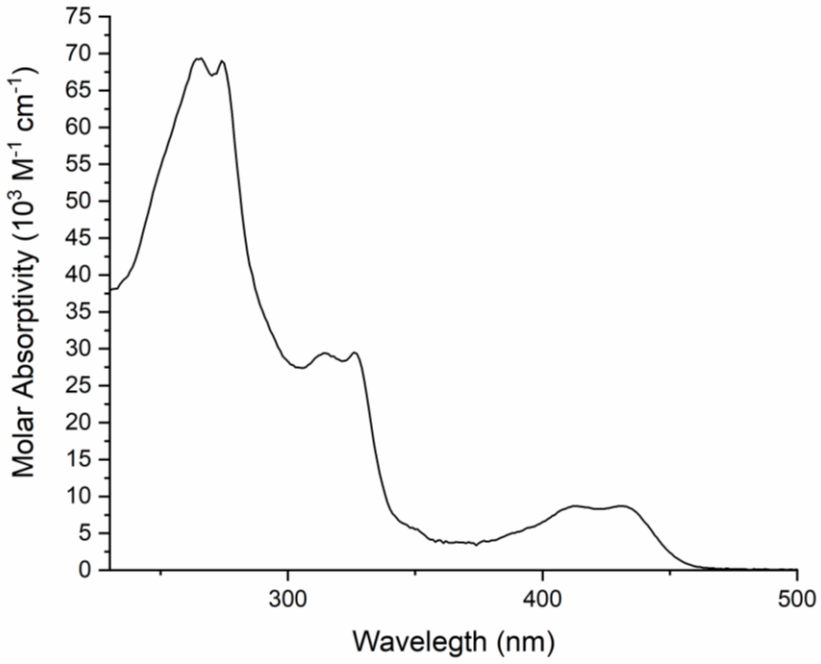

Figure 4-26: UV-Vis absorption spectrum of **1-8** in CH_2Cl_2 at room temperature, taken as an exemplar spectrum for complexes with two-chains on the C^N^C.

Using **1-8** as and exemplar spectrum, the lowest-energy absorption is found at 430 nm (ε = 8870 M^{-1} cm^{-1}) followed by a second transition at 412 nm of a similar intensity, with more intense bands found in the UV region at 324 (ε = 25300 M^{-1} cm^{-1}), 313 (ε = 24600 M^{-1} cm^{-1}), 272 (ε = 59000 M^{-1} cm^{-1}) and 263 (ε = 61900 M^{-1} cm^{-1}) nm. It can be seen that these transitions come in pairs, with an essential doubling of every band, resulting from vibronic coupling; the spacing of approximately 1100-1300 cm^{-1} is consistent with the C=N and C=C stretching frequencies of the C^N^C backbone and is seen in all complexes in the **1-*n*** to **4-*n*** families, as well as in similar literature systems.[10, 14, 15, 21, 38, 102]

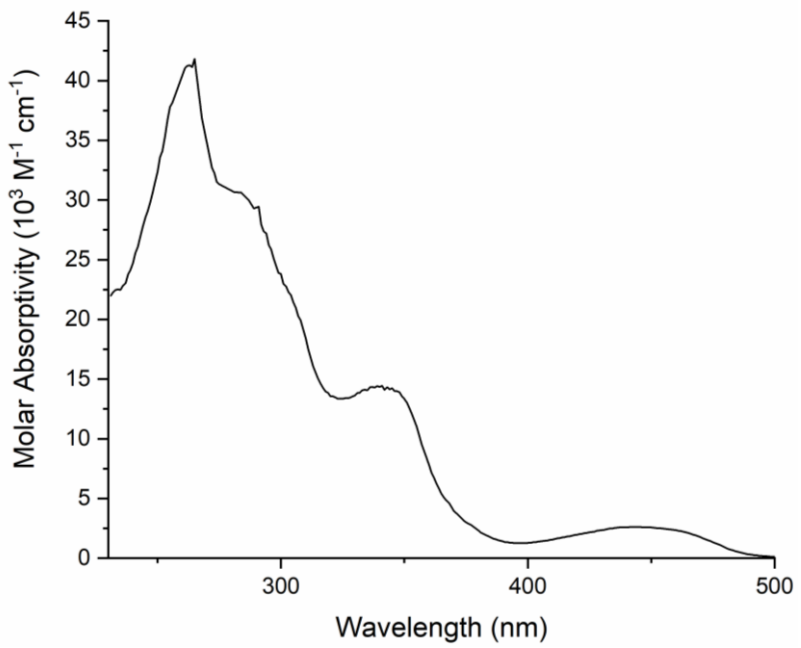

Figure 4-27: UV-Vis absorption spectrum of **5-8** in CH_2Cl_2 at room temperature, taken as an exemplar spectrum for complexes with four-chains on the C^N^C.

Using **5-8** as an exemplar spectrum, the lowest energy band is red-shifted when compared to the two-chain analogue, lying at 440 nm (ε = 2590 M^{-1} cm^{-1}). Again, more intense absorptions can be found in the UV region of the spectrum at 340 (ε = 20000 M^{-1} cm^{-1}), 279sh (ε = 44000 M^{-1} cm^{-1}) and 259 (ε = 62800 M^{-1} cm^{-1}) nm. For **5-*n*** to **8-*n***, there is no observed doubling of the absorption bands, rather the peak at 440 nm is broad and featureless, without the vibronic spacing upon the addition two electron-donating alkoxy groups on the cyclometallating ligand, which may indicate more effective coupling of lower-energy vibrations, resulting in a loss of definition in the vibronically coupled structured bands.

It should be noted that the electronic spectra of the analogous semi-perfluorinated complexes **11-*n*** to **16-*n*** were identical to the hydrocarbon equivalents, and the rationalisation of the absorption bands for the species above is also applicable to them. This was expected, as the fluorinated regions of the chains are electronically isolated from the core of the molecules through the $-(CH_2)_2-$ linkage, and their inclusion would therefore not alter the electronic energies of any of the orbitals involved in absorption transitions.

4.3.2 Emissive Properties of Gold(III) Complexes

4.3.2.1 Gold(III) Complexes with Hydrocarbon Alkynyl Ligands

As would be expected based on literature precedent,[14] **Au-Cl-1** and **Au-Cl-2** were not luminescent at room temperature, either in solution or in the solid state. It is suspected that they may show very weak luminescence in a glass at 77 K, as is the case for the gold(III) chloride species reported by Wong *et al.*,[14] but these measurements were not carried out.

All of the [Au(C^N^C)(C≡C-R)] species show triplet emission both at room-temperature in degassed CH_2Cl_2 solution ($1x10^{-5}$ M) and in diethyl ether – isopentane – ethanol (EPA) (2:2:1 v/v) glasses at 77 K. The emission is assigned as triplet due extreme loss of emission intensity under aerated conditions, as triplet emission is quenched by molecular oxygen. The photophysical behaviour data for the above complexes is given in Table 4-1, including calculated photoluminescence quantum yields (PLQY), emission lifetimes (τ) and calculated radiative (k_r) and non-radiative (k_{nr}) rate constants. As the length of the alkyl/alkoxy chains was deemed inconsequential to the solution state photophysical behaviour, all emissive characterisation was carried out on exemplar systems of n = 8, *i.e.* **2-8**, **7-8** *etc*. The exception to this was the inclusion of **1-H** and **5-H**, resulting in ten species for investigation.

Complexes **1-*n*** to **4-*n***, those with two chains on the cyclometallating ligand, emit at approximately 502 nm, in the green region of the spectrum; all associated spectra, including the absorption, excitation and emission (at 298 and 77 K) spectra are shown in Figure 4-28 and Figure 4-29. The emission wavelength was consistent at room temperature throughout the series.

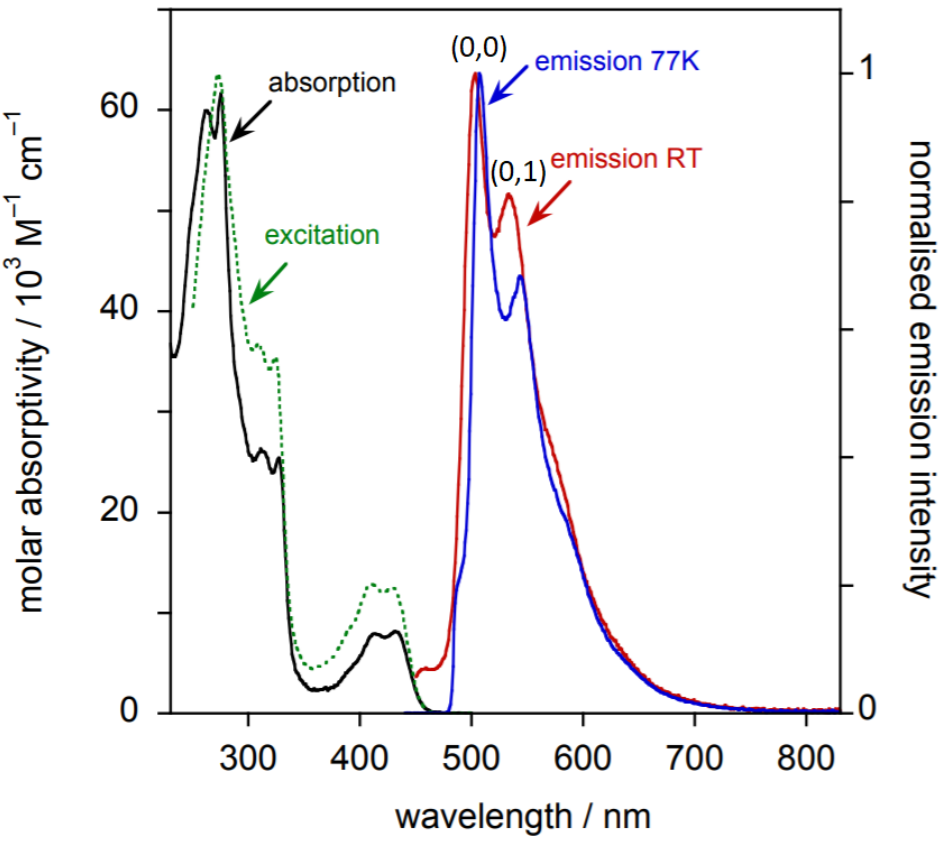

Figure 4-28: Photophysical spectra, including absorption (black), excitation (dashed green), and emission at 298 (red) and 77 K (blue) spectra for **1-H**

Table 4-1: Photophysical data for complexes **1-*n*** to **8-*n***, where *n* = H or 8[a]

Complex	Absorption λ_{max} / nm (ε / M^{-1} cm^{-1})	Emission λ_{max} / nm	ϕ_{lum} x10^2 [b]	τ / ns[c] Degassed [aerated]	k_r / 10^3 s^{-1} [d]	Σk_{nr} / 10^3 s^{-1} [d]	$k_Q(O_2)$ / 10^9 M^{-1} s^{-1} [e]	Emission 77 K[f]	
								λ_{max} / nm	τ / µs
1-H	260 (57600), 272 (55200), 310 (22100), 325 (22800), 411 (8300), 430 (8100)	502, 534	1.1	13,000 [380]	0.85	76	1.2	507, 544	270
1-8	263 (61900), 272 (59000), 313 (24600), 324 (25300), 412 (8720), 430 (8870)	501, 533	2.4	9200 [470]	2.6	110	0.97	515, 548	410/160[g] (2:1)
2-8	264 (69000), 272 (68900), 314 (26000), 326 (27800), 411 (6890), 431 (7120)	501, 532	2.5	7300 [460]	3.4	130	0.93	511, 548, 691sh	290
3-8	266 (67600), 272 (70400), 312 (25700), 325 (27800), 410 (9120), 431 (9040)	501, 533	1.6	7000 [410]	2.3	140	1.0	511, 552, 594sh	430/160[g] (2:1)
4-8	266sh (66400), 272 (69600), 312 (22500), 325 (25500), 410 (6800), 431 (6220)	502, 534	1.9	8,400 [400]	2.3	120	1.1	525, 556	300/120[g] (2:1)
5-H	259 (61700),282 (44900), 300sh (20400), 340 (17600), 445 (4880)	553, 581sh	25	150,000 [350]	1.7	5.0	1.3	565, 611	230
5-8	259 (62800), 279sh (44000), 340 (20000), 440 (2590)	551, 579	13	60,000 [390]	2.2	14.5	1.2	565, 610, 661sh	240
6-8	260 (57200), 282sh (43200), 341 (22000), 444 (3530)	554, 582	24	100,000 [390]	2.4	7.6	1.2	565, 612, 661sh	220
7-8	262 (65100), 297sh (38600), 342 (23100), 448 (5080)	552, 581	24	120,000 [390]	2.0	6.3	1.2	559, 600, 649	260/120[g] (4:1)
8-8	262 (59500), 300sh (36400), 341 (23000), 448 (3560)	552, 579	14	77,000 [390]	1.8	11	1.2	562, 603, 659	200

(a) In degassed CH_2Cl_2 at 295±3 K, except where indicated otherwise. *(b)* In degassed solution; values in air-equilibrated solution are given in parenthesis. *(c)* Quantum yields measured relative to $[Ru(bpy)_3]Cl_2$ (aq). *(d)* Radiative k_r and non-radiative Σk_{nr} rate constants estimated from quantum yield and lifetime: $k_r \sim \phi / \tau$, $k_{nr} \sim (1-\phi) / \tau$. *(e)* Bimolecular Stern-Volmer constant for quenching by molecular oxygen. *(f)* In diethyl ether – isopentane – ethanol (2:2:1 v/v). *(g)* Poor fit to mono-exponential kinetics.

All five complexes show a structured emission band with vibronic coupling. At room temperature, the (0,0) band at 502 nm is the most intense, with the smaller (0,1) lying at approximately 533 nm. There is also the suggestion of a slight shoulder on the low energy side of the emission band, although this is not resolved enough to be characterised. Based on the structure of the band, the fact that the emission seems independent of the level of substitution of the alkynyl ligand, and in tandem with computational studies outlined in Section 4.4, the emission is assigned as arising from a metal-perturbed $\pi \rightarrow \pi^*$ intraligand transition based on the cyclometallating ligand. This is well established for gold(III) alkynyl complexes of the core [Au(C^N^C)(C≡C-R)] structure, and is the dominating transition in the majority of literature complexes.[10, 15, 25, 26, 30, 102]

At 77 K, there is a characteristic bathochromic shift to lower energy, although the magnitude of the shift is not consistent throughout the series; for **1-H** this shift is as little as 196 cm^{-1}, but for **4-8** the red-shift is significant at 873 cm^{-1}. This is an unexpected observation, as the majority of metal complexes tend to exhibit a hypsochromic (blue) shift upon reduction of temperature due to the rigidochromic effect in which, as the solution medium becomes more rigid, the emission shifts to higher energy, although this tends to be observed mainly for MLCT-based emission.[103] The origin of the red-shift for these gold(III) complexes remains unknown.

Although the emission character is almost identical, there is significant variation in both the photoluminescence quantum yields (PLQY), ϕ, and the lifetimes, τ, of emission. Complex **1-H** has a PLQY of 1.1% and a lifetime of emission of 13 µs. Following appendage of an alkyl or alkoxy chain in this *para* position, there is a distinct increase in the PLQY and a decrease in the lifetime, with ϕ = 2.4% and τ = 9.2 µs for **1-8** and ϕ = 2.5% and τ = 7.3 µs for **2-8**. As further alkoxy substituents are added there is a decrease in quantum yield, but the lifetimes remain approximately constant, with ϕ = 1.6% and τ = 7.0 µs for **3-8** and ϕ = 1.9% and τ = 8.4 µs for **4-8**. Although PLQY values of 1-3% are poor, in comparison to the initial [Au(C^N^C)(C≡C-R)] complexes reported by Wong *et al.*, as well as many subsequent reports from the same group, they are an order of magnitude higher than most and are comparable to more recently designed complexes.[10, 15, 17, 18, 21, 77, 78, 80]

These differences cannot be accounted for purely by the number of electron-donating substituents on the alkynyl ligand; if this were the case, it would be rational to assume that the brightest emission would be observed for complex **4-8** in which there is the greatest number of donating substituents, which is not the case. The impact of the number and position of alkoxy substituents on the quantum yield and lifetime of emission will be discussed below.

When measured at 77 K in the glass, as well as the red-shift of the emission for all complexes, there is also a significant increase in the lifetime of emission into the hundreds of µs regime. Samples **1-8**, **3-8** and **4-8** showed a poor fit to mono-exponential kinetics when measuring the lifetime at

77 K, which arises from the presence of excited states which are close-lying in energy which can all be populated at low-temperature, resulting in emission from multiple states.

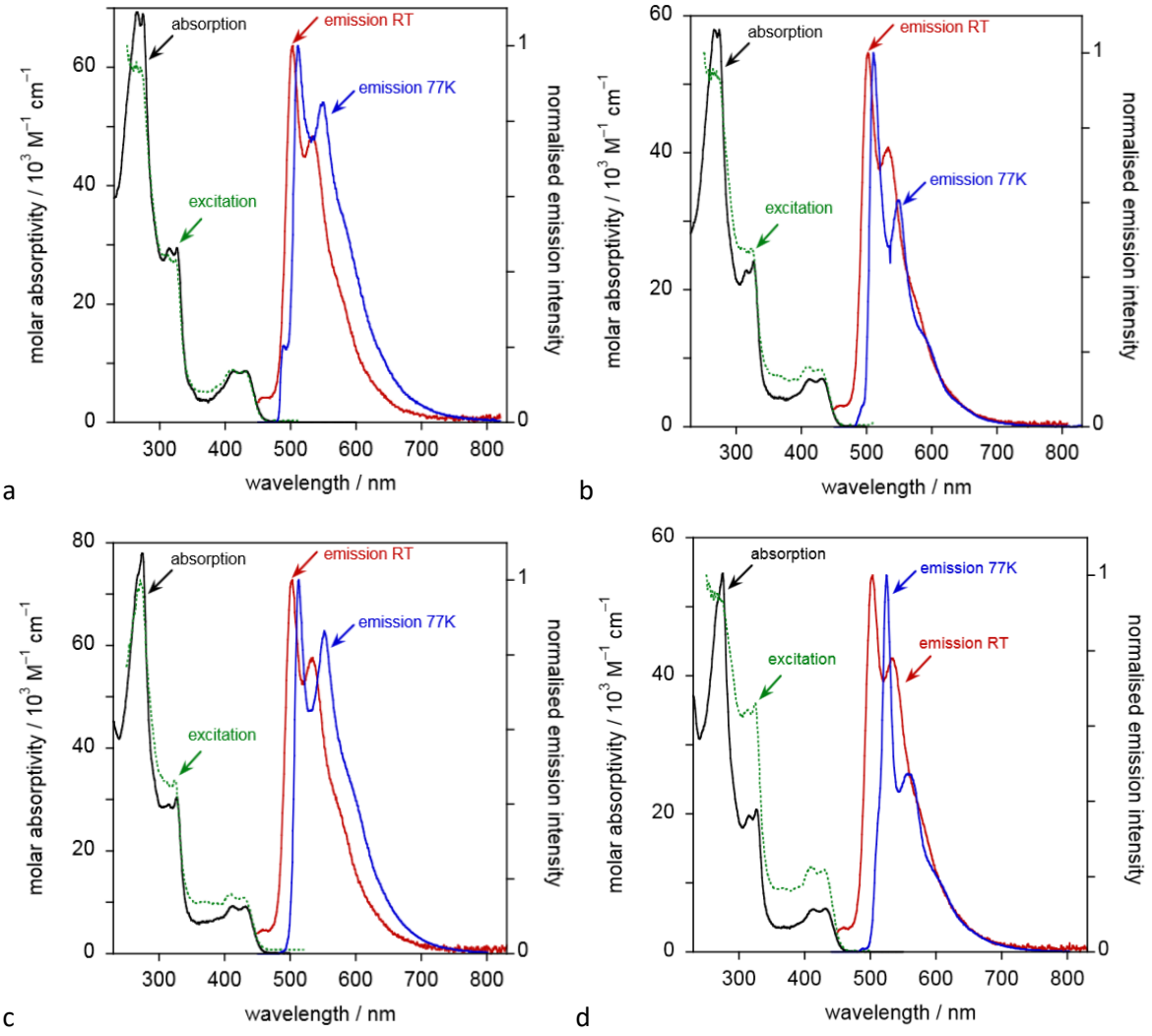

Figure 4-29: Photophysical spectra, including absorption (black), excitation (dashed green), and emission at 298 (red) and 77 K (blue) spectra for a) **1-8**; b) **2-8**; c) **3-8**; d) **4-8**.

A similar pattern is observed for the complexes with four chains on the cyclometallating ligand; all five show consistent, vibronically-coupled, structured emission bands in the yellow region with a λ_{max} of 552 nm for the (0,0) band and the (0,1) band at approximately 580 nm; for **5-H** this appears as a shoulder, while for **5-8**, **6-8**, **7-8** and **8-8** it is a well-defined peak. All associated spectra, including the absorption, excitation and emission (at 298 and 77 K) spectra are shown in Figure 4-30 and Figure 4-31.

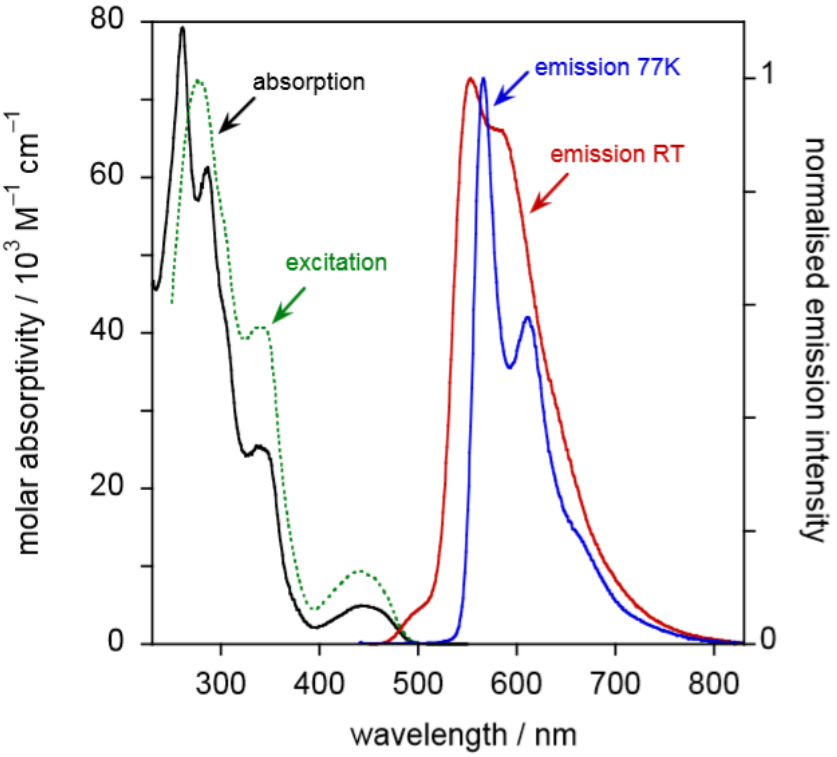

Figure 4-30: Photophysical spectra, including absorption (black), excitation (dashed green), and emission at 298 (red) and 77 K (blue) spectra for **5-H**

At room temperature, the emission bands are less well-defined than they were for the two-chain complexes, which may indicate that there is more effective mixing of the vibrational states. When the samples were measured at 77 K in rigid diethyl ether – isopentane – ethanol (EPA) (2:2:1 v/v) glasses, the vibronic coupling was more apparent, with a narrower emission and more definition in the (0,1) band. As with the two-chain complexes, there is a distinctive red-shift when measuring the emission at 77 K compared to the room-temperature measurements. However, there is no relationship between the shift in the two families; for example, in the two-chain complexes, **4-8** had the largest bathochromic shift and **1-H** the smallest, but in the four-chain complexes, the largest shift is given by **5-8** (450 cm^{-1}) and the smallest by **7-8** (227 cm^{-1}). This indicates that it is not only the nature of the alkynyl ligand that plays a part in this red-shift, but that the entire system must be considered.

When the samples were measured in the glass at 77 K, there was the expected lengthening of the lifetime to emission to approximately 200 – 300 µs. This was also observed in the two-chain complexes, and arises from reduced deactivating collisions and vibrational motion at low-temperature. In this series, **7-8** is the only sample for which the lifetime shows a poor fit of mono-exponential kinetics.

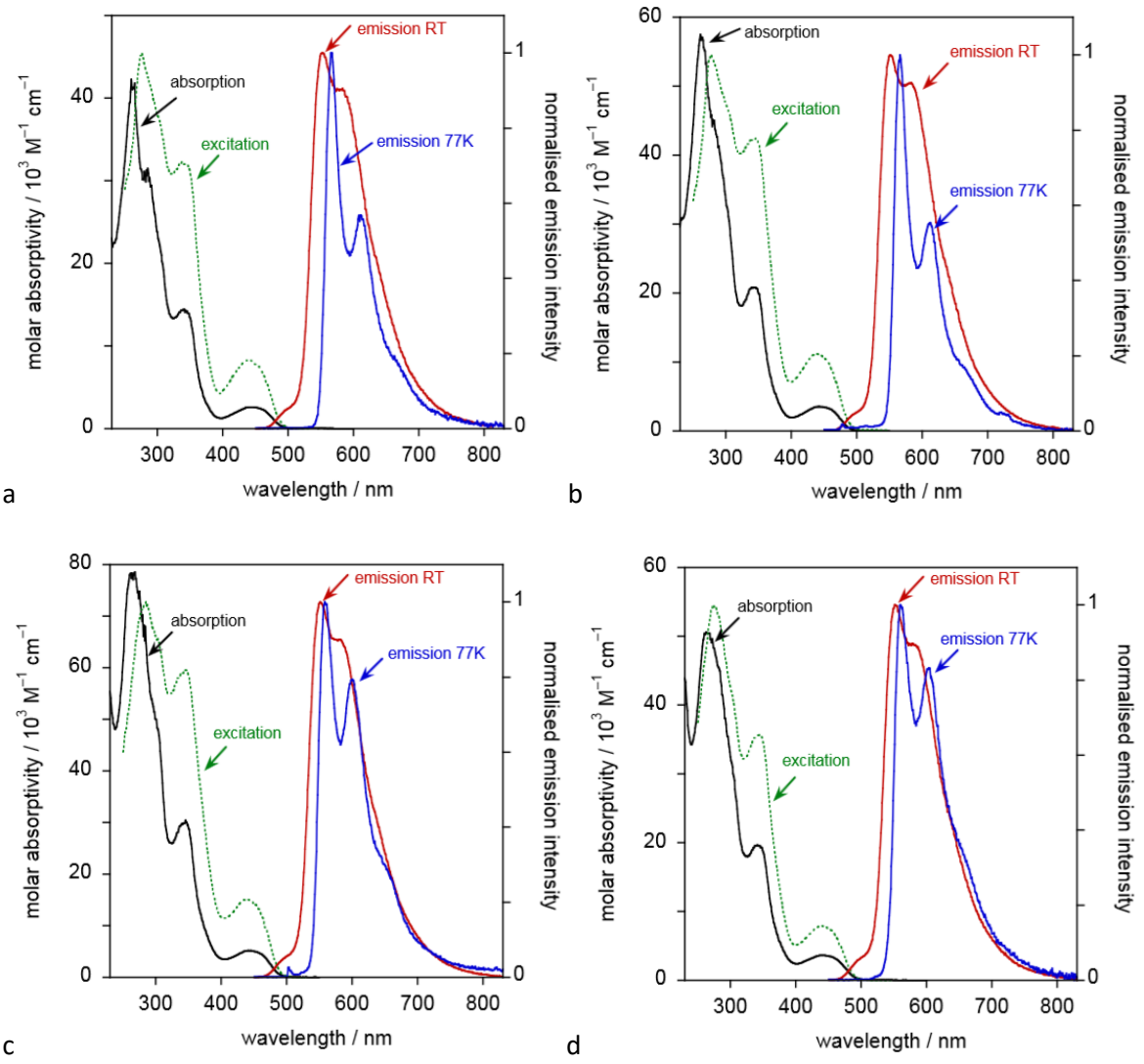

Figure 4-31: Photophysical spectra, including absorption (black), excitation (dashed green), and emission at 298 (red) and 77 K (blue) spectra for a) **5-8**; b) **6-8**; c) **7-8**; d) **8-8**.

As with the two-chain complexes, there is significant variation in the photoluminescence quantum yields and lifetimes of emission between the complexes in this series, however as with the observed red-shift at low-temperature, this does not follow the same pattern based on the alkynyl ligand. The phenylacetylene complex **5-H** had a quantum yield of 25% and a lifetime of 150 µs. When this hydrogen was exchanged for an alkyl chain in **5-8**, the quantum yield was almost halved to 13% and there was a significant reduction in the lifetime to 60 µs. However, when the substituent in this *para* position was an alkoxy chain, as in **6-8**, the quantum yield was restored to that in the region **5-H** with ϕ = 24%, and the lifetime increases to τ = 100 µs. This output is similar in **7-8**, with ϕ = 24% and another slight increase in lifetime to 120 µs. Complex **8-8** performs similarly to **5-8**, with ϕ = 14% and τ = 77 µs.

For all complexes **5-H** to **8-8**, both the PLQY and lifetime are an order of magnitude higher than for the equivalent complexes **1-H** to **4-8**, purely from the inclusion of two further alkoxy chains

on the cyclometallating ligand. This increase is notable, especially when put in the context of literature systems, the most efficient of which show a quantum yield of 58%, but requires intense functionalisation of the C^N^C ligand with bulky dialkylfluorene groups, partly to mitigate self-quenching, to achieve this level of brightness.[32, 83] The high PLQY of 30% reported by Lee *et al.* is for a dendritic system with 4-diphenylaminophenylacetylene ligands (see Figure 4-5), where the emissive transition is ^{3}LLCT [π(C≡C-R) $\rightarrow$ π^*(C^N^C)] based, which differs from the ^{3}IL [$\pi \rightarrow \pi^*$(C^N^C)] transition for complexes **5-*n*** to **8-*n***. These are stand-out examples of the strength of the emission of complexes of this nature specifically designed for efficient emission in devices; the majority of reported complexes show significantly poorer emission, with reported PLQY values of less than 10%[22, 25, 33, 37, 59, 85] and, very often, less than 1%.[10, 15, 17, 18, 21, 77, 78, 80]

The work of Yam demonstrated that the donating ability of the substituent in the *para* position of the phenyl ring of the alkynyl has an influence on the PLQY; the quantum yields of complexes with 4-methoxyphenylacetylene ligands are significantly higher (up to 9%[25]), although this is obviously also dependent on the composition of the C^N^C ligand. There are also examples of systems in which the brightness of the emission is wholly solvent dependent; PLQYs for complexes reported by Hong *et al.* range from 22% in toluene to 0.1% in CH_2Cl_2.[36]

When considering the radiative and non-radiative rate constants, k_r and k_{nr}, respectively, it can be seen that k_r is approximately consistent both within and across families; for the two-chain complexes the values span from 0.85x10^3 s^{-1} for **1-H** to 3.4 x10^3 s^{-1} for **2-8** and for the four-chain complexes they range from 1.7x10^3 s^{-1} for **5-H** to 2.5 x10^3 s^{-1} for **6-8**. Unlike the low-temperature red-shift, here there is a correlation between the two families; it is the species with the phenylacetylene ligand which shows the lowest radiative rate constant in both, and the species with the mono-substituted *para*-alkoxy alkynyl ligand, **HL4-*n***, which shows the highest. In both families, the k_r for the species with ligands **HL5-*n*** and **HL6-*n***, *i.e.* with two and three chains on the alkynyl ligand (complexes **3-8**, **4-8**, **7-8** and **8-8**), show a radiative rate constant towards the low end of the range, and the *para*-alkyl complexes **1-8** and **5-8**, towards the higher end of the range.

In contrast, the non-radiative rate constants are vastly different between the two-chain and four-chain complexes; for the two-chain complexes, values span from 76 x10^3 s^{-1} for **1-H** to 140 x10^3 s^{-1} for **3-8** and for the four-chain complexes they range from 5x10^3 s^{-1} for **5-H** to 14.5 x10^3 s^{-1} for **5-8**.

This order of magnitude difference in the rate constants is the origin of the difference in quantum yields in the two- and four-chains complexes, which itself spans an order of magnitude; the radiative pathways are consistent, but for **5-*n*** to **8-*n***, the deactivating pathways

are far less accessible. It is proposed that with the inclusion of two further electron-donating alkoxy chains on the cyclometallating ligand, the energy of the triplet excited state is substantially reduced, increasing the gap between the emissive states and the deactivating *d-d* states, assuming that the energy of these states are consistent across the whole series. Subsequently, the activation energy required to depopulate *via* pathways including the *d-d* states is significantly larger and is less effective, thereby reducing the non-radiative rate constant, leading to significantly higher quantum yields.

The fact that there is no obvious trend between differences in the quantum yield and lifetimes of emission between the two families suggests that the source of this variation is due to a combination of factors. The electron-donating potential of the alkoxy substituents may account for some of this difference; the higher the number of alkoxy chains, the greater σ-donation of the alkynyl ligand to the metal centre, which may render the deactivating *d-d* states higher in energy, lowering the non-radiative rate constant. However, as there is no consistent ligand-based pattern between the two families of complexes, it is thought that this may only play a small part in the variation of rate constants k_r and k_{nr}, or that any pattern may be perturbed by other factors.

Another, more likely, reason for this variation is due to the interaction of the molecules with both each other and the solvent molecules. It has been shown that, in highly-concentrated solutions, these molecules tend to aggregate (Chapter 3, Section 3.5); the emission of all complexes was analysed at concentrations of approximately 1 $x10^{-5}$ M, where there is no aggregation observed by ^{1}H NMR spectroscopy, however this association exists in equilibrium and collisions between molecules will obviously occur. Interaction of the excited molecules with the solvent is prevalent, and if these interactions lead to deactivation of the excited state and non-radiative emission, it is reasonable to suggest that the number and orientation of the substituents on the alkynyl ligand may have a significant effect on the extent to which this occurs.

In the spectra shown in Figure 4-28 to Figure 4-31, it can be seen that there is a very small peak on the high energy side of the emission band in the room-temperature measurements (marked with an * in Figure 4-28), which is no longer present when the sample is cooled to 77 K. This peak has also been observed in literature systems, although no explanation or investigation into its origin has been provided.[25] It is possible that this small peak may arise from a competing fluorescence process; this will be fully discussed in Section 4.3.2.4.

4.3.2.2 Gold(III) Complexes with Semi-Perfluorinated Alkynyl Ligands

All of the [Au(C^N^C)(C≡C-R)] species show triplet emission both at room-temperature in degassed CH_2Cl_2 solution ($1x10^{-5}$ M) and in diethyl ether – isopentane – ethanol (EPA) (2:2:1 v/v) glasses at 77 K. The photophysical behaviour data for complexes **11-*n*** to **16-*n***, where *n* = 8, are given in Table 4-2, including calculated photoluminescence quantum yields (PLQY), emission lifetimes (τ) and calculated radiative (k_r) and non-radiative (k_{nr}) rate constants. The structures of complexes **11-*n*** to **16-*n*** are shown in Figure 4-32 for ease of reference.

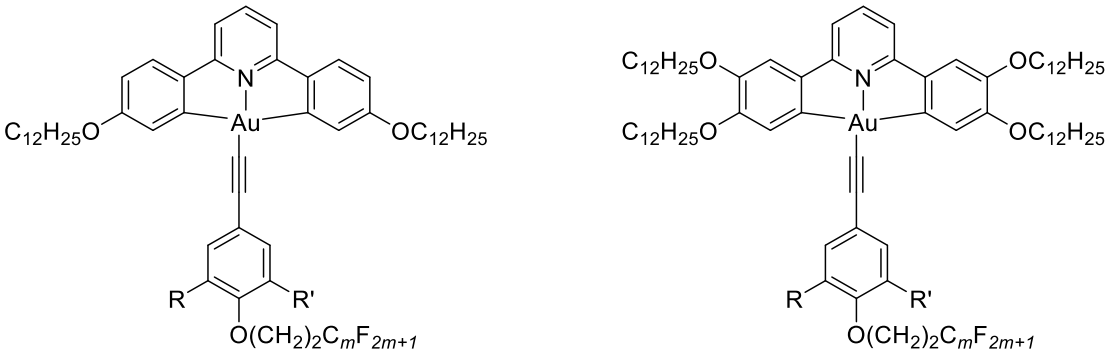

11-*n*: R = R' =H
12-*n*: R = H, R' = $O(CH_2)_2C_mF_{2m+1}$
13-*n*: R = R' = $O(CH_2)_2C_mF_{2m+1}$

14-*n*: R = R' =H
15-*n*: R = H, R' = $O(CH_2)_2C_mF_{2m+1}$
16-*n*: R = R' = $O(CH_2)_2C_mF_{2m+1}$

Figure 4-32: Structure of the gold(III) alkynyl complexes with semi-perfluorinated chains under investigation. *m* = 6, 8, 10.

It was originally thought that the photophysical behaviour of these complexes would not vary from the hydrocarbon analogues presented and discussed in the previous section due to the localisation of the frontier molecular orbitals involved in the emissive transitions on the cyclometallating ligand, both examples of which were consistent between the fluorinated and non-fluorinated series of complexes. However, differences in the photoluminescence quantum yields and lifetimes of emission were observed as the substitution pattern of the alkynyl ligand was altered and so, although the perfluorinated chains were electronically isolated from the core molecular structure through the bridging $–O(CH_2)_2–$ linker, the emissive behaviour of complexes **11-*n*** to **16-*n*** was fully characterised.

Table 4-2: Photophysical data for complexes **11-*n*** to **16-*n***, where n = 8[a]

Complex	Absorption λ_{max} / nm (ε / M^{-1} cm^{-1})	Emission λ_{max} / nm	ϕ_{lum} x10^2 [b]	τ / ns [c] Degassed [aerated]	k_r / 10^3 s^{-1} [d]	Σk_{nr} / 10^3 s^{-1} [d]	$k_Q(O_2)$ / 10^9 M^{-1} s^{-1} [e]	Emission 77 K[f]	
								λ_{max} / nm	τ / µs
11-8	264 (56500), 273 (55800), 314 (21800), 325 (22500), 412 (6590), 431 (6660)	503, 533	1.5	6500 [550]	2.3	150	0.76	488, 517, 555, 605sh	330@488[g] 230@555[h]
12-8	265 (52000), 273 (52000), 314 (20600), 325 (21000), 412 (6490), 431 (6630)	503, 533	1.9	6800 [570]	2.8	140	0.73	487, 512, 549	350@488[g] 210@550[h]
13-8	265 (59200), 273 (61000), 314 (21600), 325 (21800), 412 (7120), 431 (7380)	504, 533	1.9	7000 [560]	2.7	140	0.75	500sh, 510, 545, 587sh	250@545[h]
14-8	261 (59300), 281 (44500), 342 (19300), 444 (3440)	552, 584	20	139,000 [460]	1.4	5.8	0.98	563, 604, 659sh	220
15-8	261 (62100), 283 (46200), 341 (20000), 444 (3440)	553, 584	27	157,000 [550]	1.7	4.6	0.82	557, 599, 648	284
16-8	262 (62100), 283 (46400), 341 (17700), 445 (3220)	555, 583	34	175,000 [520]	1.9	3.7	0.87	554, 600	270

(a) In degassed CH_2Cl_2 at 295±3 K, except where indicated otherwise. *(b)* In degassed solution; values in air-equilibrated solution are given in parenthesis. *(c)* Quantum yields measured relative to $[Ru(bpy)_3]Cl_2$ (aq). *(d)* Radiative k_r and non-radiative Σk_{nr} rate constants estimated from quantum yield and lifetime: $k_r \sim \phi / \tau$, $k_{nr} \sim (1-\phi) / \tau$. *(e)* Bimolecular Stern-Volmer constant for quenching by molecular oxygen. *(f)* In diethyl ether – isopentane – ethanol (2:2:1 v/v). *(g)* The high-energy band at 488 and 487 nm for **11-8** and **12-8** gave a good fit to mono-exponential decay. *(h)* The decay registered around 550 nm gave a rather poor fit to mono-exponential decay with the value indicated. A better fit could be obtained using a bi-exponential model, but with components rather similar to one another, so too much meaning cannot be attached to the precise values that emerge.

The emission profiles for complexes **11-8**, **12-8** and **13-8** are not dissimilar to those observed for the hydrocarbon parent complexes, showing emission bands with vibronic coupling at approximately 503 nm (Figure 4-33 and Figure 4-34). For all three complexes, the excitation spectra show a good correlation to the absorption spectra, where again the doubling of each band is observed due to the vibronic coupling of the C^N^C backbone.

For **11-8** (Figure 4-33) the (0,0) band is the most intense an occurs at 503 nm, followed by the (0,1) at 533 nm. A small shoulder in also observed on the low energy side of the band, although this is not well resolved. As with the fully-hydrocarbon complexes discussed in the previous section, there is a small peak on the high energy side of the emission band very close to the excitation energy. This is present in all of the fluorinated complexes; the origin of this peak will be discussed fully in Section 4.3.2.4 below. When **11-8** is cooled to 77 K in diethyl ether – isopentane – ethanol (EPA) (2:2:1 v/v) to form a glass, the structure in the emission band shows a higher level of resolution, with the (0,0) and (0,1) bands sharp and the aforementioned shoulder well resolved at 605 nm. When the sample is cooled, there is a red shift of approximately 535 cm^{-1}; this is consistent with the observations for the parent hydrocarbon complex. Unexpectedly, at low temperature a higher energy peak is also observed at 488 nm. This peak is also observed for **12-8**, but none of the other complexes, and it thought to be of a different origin to the high energy peak observed at room temperature.

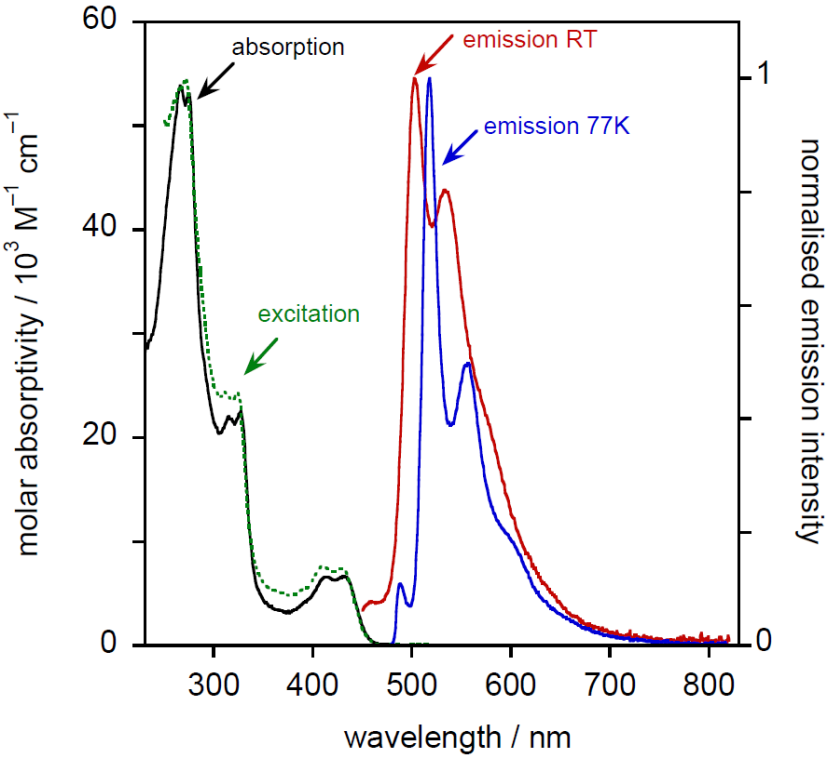

Figure 4-33: Photophysical spectra, including absorption (black), excitation (dashed green), and emission at 298 (red) and 77 K (blue) spectra for **11-8**

The case is similar for **12-8** (Figure 4-34a), however the coupling in the bands is not as well resolved, especially at low temperature, with the (0,0) band at 503 nm and the (0,1) at 533 nm as before. At low temperature, the observed red-shift is smaller (350 cm^{-1}), but, as mentioned above, there is the appearance of a high energy band at 487 nm.

For absolute confirmation of the origin of this emission band, further measurements may be required, but several hypotheses can be made. At 77 K, it is possible to detect emission from possible impurities that are present at a concentration as to not be detected in room temperature emission measurements or in NMR spectroscopy, such as any unreacted free ligand which may be present in trace amounts previously undetectable. If such a species was present, the origin of this signal could be assigned through collection of its low-temperature emission spectrum, but may only prove successful it the impurity was known. Adding doubt to the speculation of a fluorescent impurity is the long lifetime of emission for this band of 330 µs, which is longer than any observed for the triplet emission of the complexes. It may also be that the presence of this band is due to an organic phosphorescent impurity, but the same argument can be made that the lifetime of emission here would be too short for such a species, which may be expected to be on the millisecond scale.[104-106] The third hypothesis considered is that this peak may arise from the presence of another excited state for the complex itself which is not thermally accessible or favoured at higher temperature.

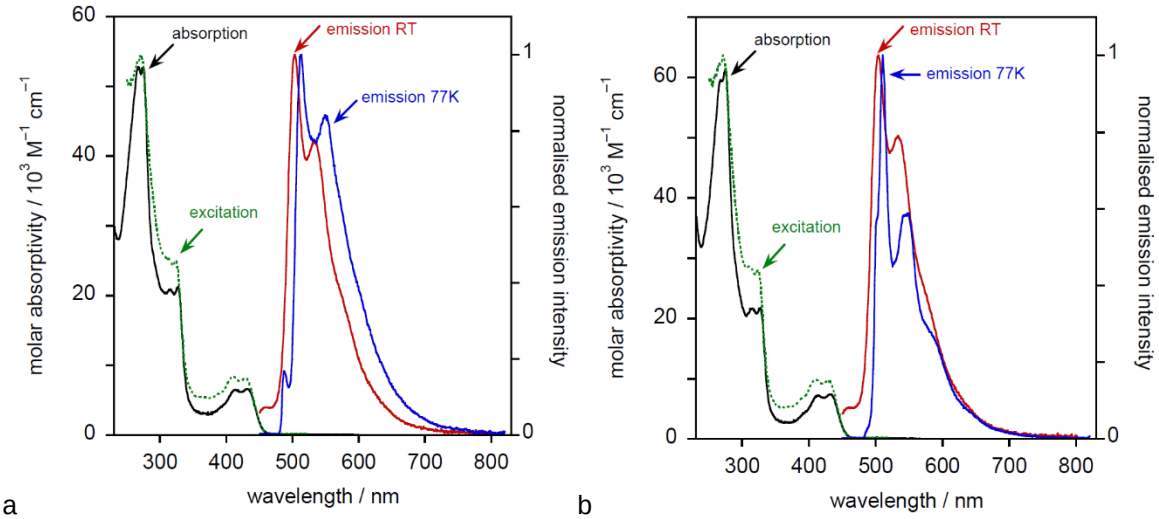

Figure 4-34: Photophysical spectra, including absorption (black), excitation (dashed green), and emission at 298 (red) and 77 K (blue) spectra for a) **12-8** and b) **13-8**.

The room temperature emission of **13-8** (Figure 4-34b) is the same as the less-functionalised analogues, with the (0,0) band at 504 nm and the (0,1) at 533 nm as previously observed. The red-shift on lowering the temperature to 77 K is further reduced to 273 cm^{-1} with a significant increase in the resolution of the vibronic coupling of the bands. There is no peak observed for **13-8** at

approximately 488 nm as for the previous two complexes, however a shoulder is observed at 500 nm that may be of a similar origin.

All three complexes with two chains on the cyclometallating ligand show very similar emission parameters, with both the quantum yield and lifetimes of emission for all species within measurement error; quantum yields for **11-8**, **12-8** and **13-8** were determined to be 1.5, 1.9 and 1.9%, respectively, with lifetimes of 6.5, 6.8 and 7.0 μs. From these parameters, both the radiative and non-radiative rate constants can be calculated and, unsurprisingly, show very little variation. As previously observed, the poor quantum yield values are due to the presence of a high non-radiative rate constant, k_{nr}, the values of which for these three complexes lie between 140 x 10^3 and 150 x 10^3 s^{-1}. These rate constants are significantly higher than the radiative rate constants, which are almost two orders of magnitude smaller.

The lifetime of emission for all three complexes at 77 K was characterised both for the high-energy transition only observed in **11-8** and **12-8**, in which the lifetime was found to be 330 μs (as mentioned above) and 350 μs, respectively, as well as the main emission band for all three complexes, centring on the (0,0) transition. For the main emission, the lifetimes did not fit very well to mono-exponential kinetics, although it should be noted that these values are the ones listed in Table 4-2, but a better fit was achieved when a bi-exponential kinetics model was applied.

As expected, emission from complexes with four chains on the cyclometallating ligand (**14-8**, **15-8** and **16-8**) was significantly red-shifted in comparison to the two-chain species, with the emission maximum for all three complexes at approximately 553 nm (Figure 4-35 and Figure 4-36).

For **14-8**, the (0,0) band occurs at 552 nm and the (0,1) at 584 nm; the previously observed low-intensity, high-energy peak is also observed for this complex. As with the hydrocarbon equivalents, the room temperature emission band is less well resolved, with the vibronically coupled structure smoothed out (Figure 4-35). At 77 K, the emission band is more structured, with clear distinctions between the (0,0) and (0,1) band as well as a well resolved shoulder at 659 nm. A red-shift of 354 cm^{-1} is also observed which is comparable in magnitude to that of the two-chain complexes.

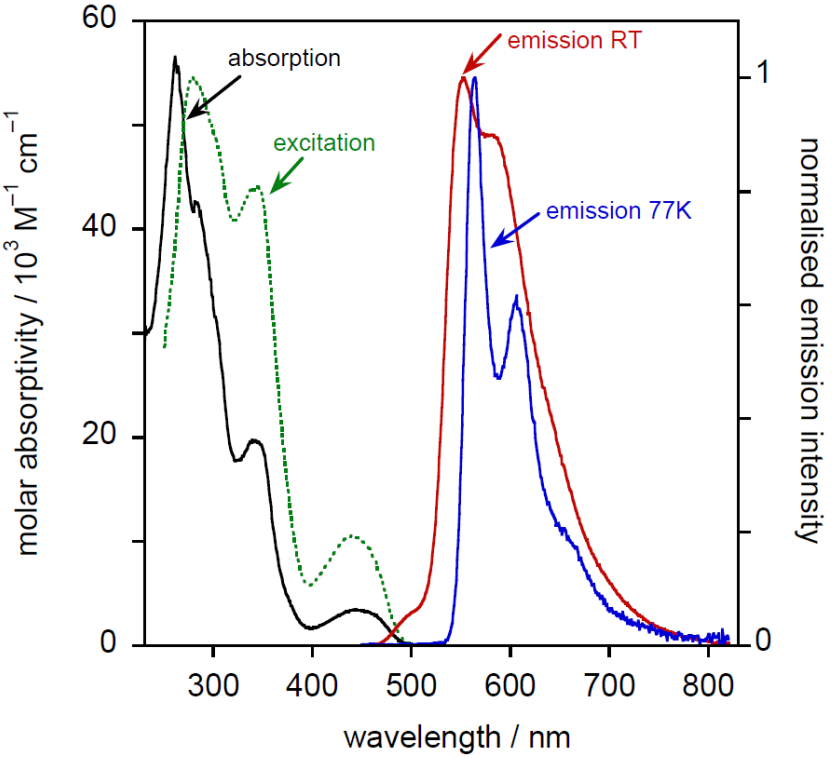

Figure 4-35: Photophysical spectra, including absorption (black), excitation (dashed green), and emission at 298 (red) and 77 K (blue) spectra for **14-8**

At room temperature, the situation is the same for both **15-8** and **16-8**, with a loosely structured emission profile with the (0,0) band the most intense at 553 and 555 nm, respectively, followed by the less intense (0,1) which lies at 584 and 583 nm, respectively. For both of these complexes, the emission profiles are very similar at 77 K, but they appear different to those previously observed due to the increase in intensity of the (0,1) band to approximately equal (**15-8**) or more intense (**16-8**) that the (0,0). Both low-temperature emission profiles show a shoulder, quantifiable in **15-8** at 648 nm, but much broader in **16-8**. Also apparent for these two complexes is the significant reduction in the red shift upon cooling to 77 K. For complex **15-8** this shift is as small as 130 cm^{-1} and is not present at all in **16-8**, in which the (0,0) bands at both room temperature at 77 K occur at the same wavelength.

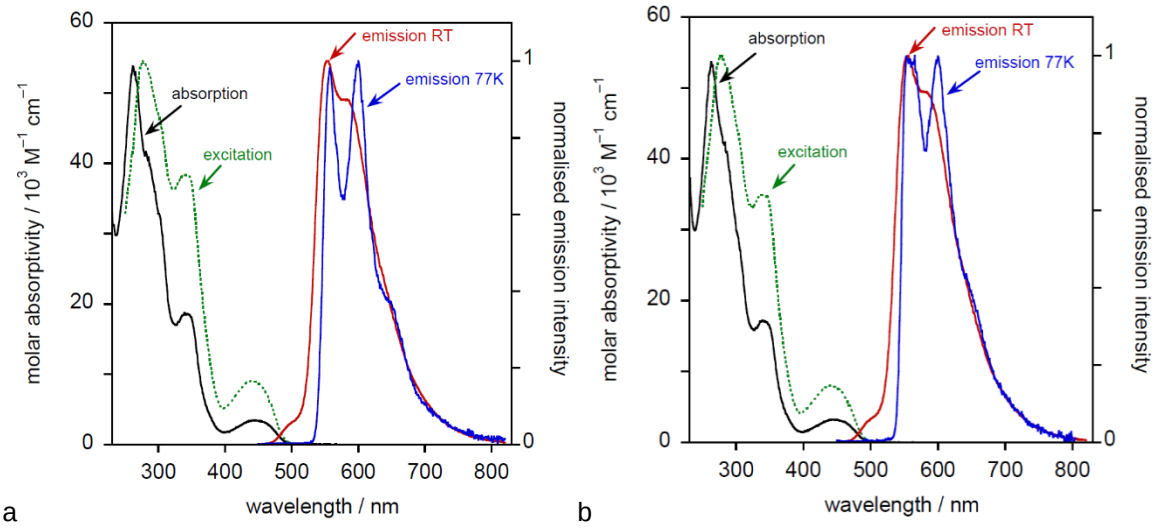

Figure 4-36: Photophysical spectra, including absorption (black), excitation (dashed green), and emission at 298 (red) and 77 K (blue) spectra for a) **15-8** and b) **16-8**.

Contrary to the observations for the two-chain species outlined above, there are significant differences between the photoluminescence quantum yields and lifetimes of emission between these complexes. Both parameters display a significant increase as the number of the chains on the alkynyl ligand increase; **14-8** has a PLQY of 20% which increases to 27% and 34% for **15-8** and **16-8**, respectively, with the same pattern appearing the lifetimes, which increase from 139 µs to 157 µs to 175 µs across the series.

The order of magnitude increase in the quantum yields for the four-chain species in comparison to the two-chain analogues, as was observed for the hydrocarbon complexes, is due to the substantial reduction in the non-radiative rate constants, k_{nr}, by almost two orders of magnitude when two further alkoxy chains are appended on the cyclometallating ligand, *e.g.* from 150 x1 0^3 s^{-1} for **11-8** to 5.8 x 10^3 s^{-1} for **14-8**, both of which are complexes with a single chain on the alkoxy ligand. Similar reductions were observed for **15-8** and **16-8**, in which k_{nr} values were calculated to be 4.6 x 10^3 and 3.7 x 10^3 s^{-1}, respectively. As for the aforementioned hydrocarbon complexes (**5-H** to **8-8**) this reduction is due to the inclusion of two further dodecyloxy chains on the cyclometallating ligand; these substituents result in the lowering of energy of the triplet state by approximately 1700 cm^{-1} between analogous two-chain and four-chain complexes (*e.g.* between **11-8** and **14-8**), resulting in an increase in the gap between the emissive and deactivating states, and as such these deactivation pathways are less favourable.

For all the fluorinated complexes considered in this section, the emission can be assigned to a metal-perturbed $\pi \rightarrow \pi^*$ intraligand transition based on the cyclometallating ligand, as was observed above and in a multitude of literature systems.[10, 15, 25, 26, 30, 102]

4.3.2.3 Comparison between the Photophysics of Hydrocarbon and Semi-Perfluorinated Complexes

It is clear with reference to the previous two sections that the emission profile and energies of the complexes can be segregated into two mains families: those with two chains on the cyclometallating ligand, and those with four; the energy of emission is independent of the alkynyl ligand.

However, for the hydrocarbon species with four chains on the cyclometallating ligand (**5-H** to **8-8**) and the equivalent fluorinated species (**14-8** to **16-8**), there are significant differences in the photoluminescence quantum yields and lifetimes of emission. These are also present within the **1-H** to **4-8** and **11-8** to **13-8** series, although due to the weak nature of the emission, *i.e.* the low quantum yields, the changes are proportionally smaller and harder to recognise. As outlined above, the differences in parameters for **5-H** to **8-8** do not show any reasonable pattern when they are considered as a series, for example, that the quantum yields are higher as more electron donating substituents are appended to the alkynyl ligand.

A further explanation, bolstered by the data for the fluorinated species, it that these differences are due to deactivating interactions between the complexes and the surrounding solvent; such interactions can be dependent on, and altered by, lateral alkyl/alkoxy chains. Such interactions have been described by Coogan *et al.*, in which the emission from a rhenium(I) complex with a single dodecyl chain (Figure 4-37) could be significantly altered in water due to hydrophobic effects between the chain and the solvent, resulting in chain folding in an orientation in which the emissive core was shielded from the solvent.[107] As a consequence, the quantum yield was significantly increased in water compared to acetonitrile. This effect was temperature dependent and did not occur for alternate chains lengths of 6 or 16. Obviously this aqueous system in which the solvation effects are driven by hydrophobicity are not directly applicable to the gold(III) complexes in which the solvent in question is CH_2Cl_2, however as an example of how chain shielding and solvent interactions can affect the quantum yields and lifetimes of emission, it provides a proof of concept.

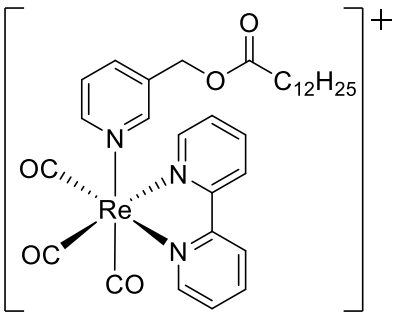

Figure 4-37: Structure of rhenium(i) complex as reported by Coogan *et al.*[107]

In this case, the alkoxy chains may shield the gold(C^N^C) core of the molecule from solvation effects that may lead to non-radiative emission. There is not a clear pattern of an increase in PLQY as the number of chains increases, as many aspects of the molecule have to be considered, including vibrational deactivation, and as the molecule increases in size through the inclusion of chains, there may be more available vibrational deactivation pathways. Thus, there are two non-correlated effects that have an impact on the PLQY as the number of chains increases: the solvation shielding of the core increases PLQY and the increased vibrational deactivation decreases PLQY. The overall observed PLQY is a function of both of these effects, but they are not a direct trade-off and are not related.

For the four chain complexes, comparison between **6-8**, **7-8** and **8-8** and the analogous fluorinated complexes **14-8**, **15-8** and **16-8** is especially telling as these complexes are electronically identical, and thus any differences observed (as displayed in Table 4-3) can be attributed to non-radiative emission.

Table 4-3: Comparison of quantum yield, ϕ_{lum}, and lifetime of emission, τ, for fluorocarbon and hydrocarbon equivalents with four chains on the C^N^C ligand.

	Quantum Yield, ϕ_{lum} x10^2		**Lifetime of Emission, τ / µs**	
Complex	**Hydrocarbon**	**Fluorocarbon**	**Hydrocarbon**	**Fluorocarbon**
6-8/14-8	24	20	100	139
7-8/15-8	24	27	120	157
8-8/16-8	14	34	77	175

From this comparison, it is clear that the hydrocarbon and fluorocarbon species do not follow the same trend, for as the alkoxy functionalisation increases between **6-8** and **8-8**, there is a decrease in both quantum yield (by 10%) and lifetime. For the fluorinated species, there is a consistent increase in both the quantum yield and lifetime as the number of chains, and therefore the level of fluorination increases. This is perhaps most striking in the comparison between **8-8** and **16-8**, in which there is an increase of 20% in the quantum yield and approximately 100 µs in the lifetime of emission. This increase is striking and, although the change is not so large over the possible lifetie range, *i.e.* the measurements are both on a tens or hundreds of microsecond scale, within the series the variation is still significant and is due to a reduction in the non-radiative rate constant for the fluorinated species.

It is proposed that the reduction in k_{nr} arises from increased shielding of the emissive core of the molecule from the increased volume of the fluorinated chains, which are also more rigid than hydrocarbon chains. This rigidity may be beneficial in lowering k_{nr}; the vibrational frequency of the C–F bond (between 1350 and 1100 cm^{-1}) is lower than that of the C–H bond (approximately 2900 cm^{-1}),[108] resulting in a less effective energy transfer through these bonds as a non-radiative decay pathway. This rationalisation applies to all of the complexes and provides a sensible rationale to the substantial differences observed between species which are electronically identical.

4.3.2.4 The Origin of the High-Energy Peak at Room Temperature

For all of the studied complexes, a high-energy peak is observed at room-temperature that disappears on cooling to cryogenic temperatures (marked with an * in Figure 4-28 but observed in all). For the two-chain complexes, this peak appears at 458 nm, and at 495 nm for the four-chain complexes. This peak is in very close relation to the excitation wavelength of 431 and 444 nm for the two- and four-chain species, respectively, resulting in a Stokes Shift for the emission of 1368 cm^{-1} and 2321 cm^{-1}, respectively, smaller than typically observed for phosphorescent processes in these complexes.

Further to this, in comparing air-equilibrated and degassed solutions of **14-8** in CH_2Cl_2 (normalised spectra shown in Figure 4-38), it is observed that in air-equilibrated solution, this peak is substantially more intense than in the degassed solution. It is worth stating that the air-equilibrated spectra are substantially less intense than the degassed spectra, hence the need for normalised spectra for comparison; when non-normalised spectra are compared, the features of the air-equilibrated spectra lost.

With consideration of all these observations, it is proposed that the origin of this peak is emission from the singlet excited state; *i.e.* a competing fluorescence process. This would account for the loss of the peak at low temperature where the structure shows a higher level of rigidity and more effective intersystem crossing, as well as the increased relative intensity in air-equilibrated solution; emission from the triplet excited states which make up the main emission band are quenched by molecular oxygen and therefore are reduced in intensity compared to a fluorescent process.

It was considered that the fluorescence observed may be thermally activated delayed fluorescence (TADF). However, while TADF has been observed for similar gold complexes,[19, 20, 68] it is severely quenched by O_2 due to the deactivation of triplet states from which the singlet excited state is re-populated and therefore was discarded as a possibility here.

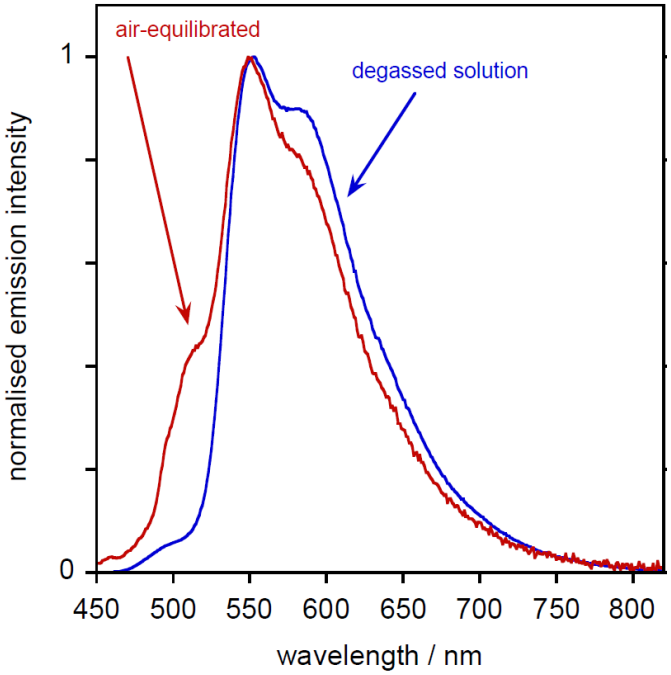

Figure 4-38: Emission spectra of **14-8** in both air-equilibrated (red) and degassed (blue) solutions of CH_2Cl_2

The assignment of this peak as prompt-fluorescence (as opposed to delayed-fluorescence) remains a hypothesis based on the available information. Unfortunately, due to the proximity of the band to the main emission peak, it cannot be resolved to measure a lifetime for only this band, the magnitude of which may yield further information as to the origin of the emission.

In contrast, it remains a possibility that the emission is triplet in origin and arises from a shorter-lived triplet excited state that is not populated at low temperature and, due to the short lifetime, is less effectively quenched by O_2.

The hypotheses presented above may be further substantiated through additional experimental investigation, aided by the use of computational chemistry.

4.4 Computational Calculations

The gold(III) alkynyl species were subjected to time-dependent density functional theory (TD-DFT) calculations for comparison with experimental results and rationalisation of the orbitals involved in any relevant transitions. All calculations were performed by Dr Jason Lynam. To aid in computational efficiency, any alkyl or alkoxy chains were substituted for ethyl or methoxy groups, including those on the cyclometallating ligand. This approach is supported by the apparent lack of any electronic factors from the length of the carbon chains. These simplified complexes will be designated with a prime, *e.g.* **1'-*n***, where *n* is the carbon chain length of the alkynyl ligand, as above, but here shall always be H, 1 or 2, which will be designated as 'Me' or 'Et' for clarity, *e.g.* **6'-Me**. Ethyl groups were only present for the short-chain equivalents of **1-*n*** and **5-*n*** with alkyl

chains; it was rationalised that the electronic effects of a methyl group in this position may be different to that of an alkyl chain of any greater length. A selection of these modified structures (**5'-H**, **5'-Et** and **8'-Me**) are shown in Figure 4-39 for clarity.

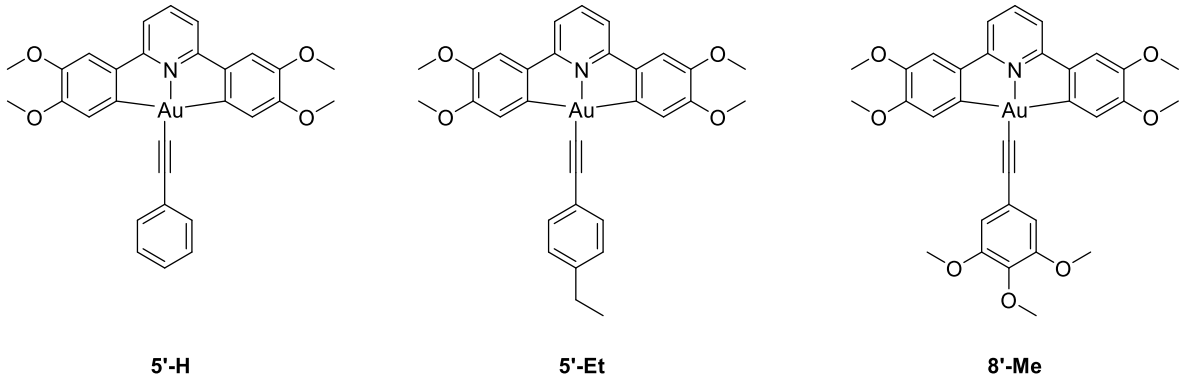

Figure 4-39: Structures of modified complexes **5'-H**, **5'-Et** and **8'-Me** used for calculations.

The electronic transitions for the modified gold(III) alkynyl species were calculated using BP86/SV(P) for geometry optimisation and PBE0/def2-TZVPP for TD-DFT calculations. The composition of the two lowest-energy electronic transitions for each are shown in Table 4-4 for the two-chain complexes and Table 4-5 for the four-chain complexes.

Table 4-4: Summary of DFT-predicted transitions for complexes **1'-H**, **1'-Et**, **2'-Me**, **3'-Me** and **4'-Me**. Only transitions with an oscillator strength >0.001 and orbital contributions >10% are listed.

Complex	Calculated Energy (Experimental energy)/ nm	Oscillator strength	Occupied orbital	Virtual orbital	Coefficient / %	Transition
1'-H	406 (430,	0.036	112a	113a	93.6	HOMO LUMO
	398 411)	0.148	111a	113a	95.5	HOMO-1 LUMO
1'-Et	417 (430,	0.0476	120a	121a	94.8	HOMO LUMO
	398 412)	0.148	119a	121a	95.4	HOMO-1 LUMO
2'-Me	440 (431,	0.057	120a	121a	96.3	HOMO LUMO
	397 411)	0.143	119a	121a	94.6	HOMO-1 LUMO
3'-Me	440 (431,	0.056	128a	129a	96.1	HOMO LUMO
	398 410)	0.142	127a	129a	94.6	HOMO-1 LUMO
4'-Me	444 (431,	0.047	136a	137a	96.0	HOMO LUMO
	398 410)	0.141	134a	137a	94.6	HOMO-2 LUMO

For the two-chain complexes **1'-H** and **1'-Et**, both the HOMO-1 and LUMO are based fully on the C^N^C cyclometallating ligand (shown as Kohn-Sham orbitals for complexes **1'-H** in Figure 4-40). The HOMO is predominantly based on the alkynyl ligand. There is a small amount of metal character in both the HOMO and LUMO. It is these three orbitals that are the most relevant in understanding the excitation process in these complexes, as will be discussed in more detail below.

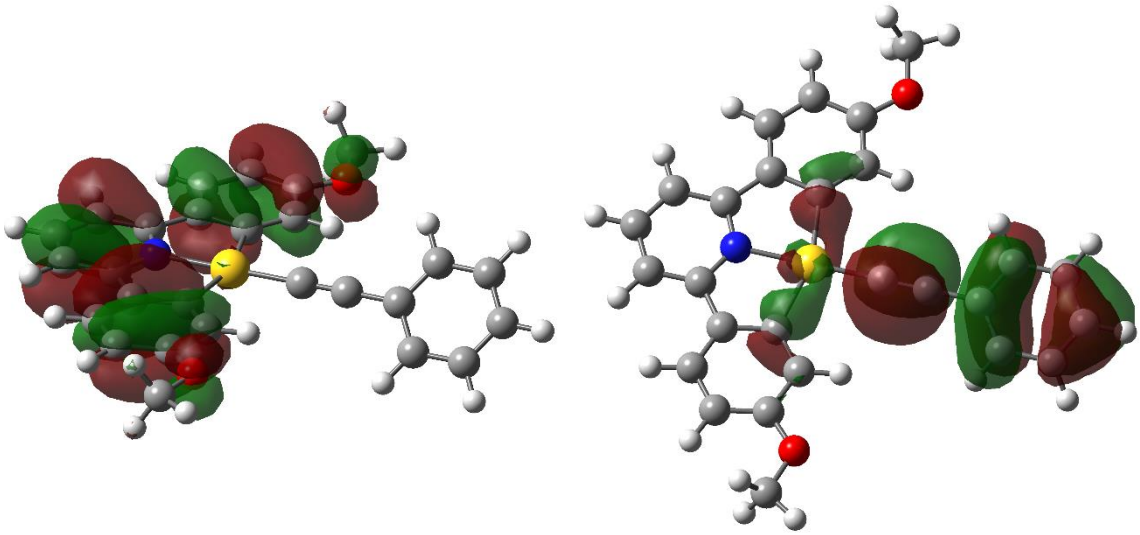

HOMO-1 **HOMO**

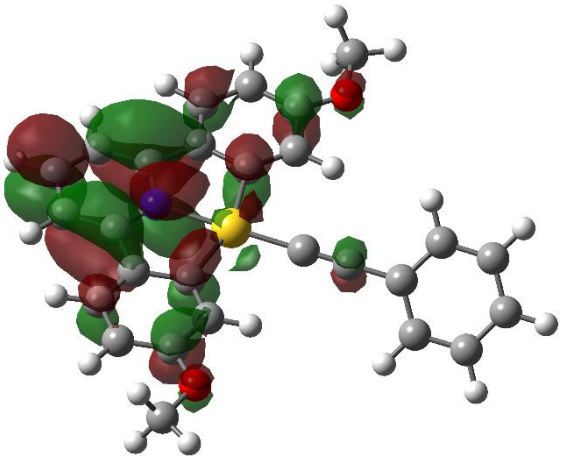

LUMO

Figure 4-40: Kohn-Sham orbitals of **1'-H** showing the orbitals involved in the excitation

The case is slightly different for the species with methoxy groups on the phenylalkynyl ligand, **2'-Me**, **3'-Me** and **4'-Me**. Here, the HOMO-1 is fully based on the organic portion of the C^N^C ligand, with no contribution from the nitrogen or gold atoms. Conversely, the orbitals of the LUMO, which are also majority C^N^C based, have substantial gold character, which is not observed for **1'-H**. The HOMO for these complexes remains largely unchanged and is based on the alkynyl ligand. These orbitals are shown using **2'-Me** as an example in Figure 4-41. It should be noted that the HOMO-2 of **4'-Me**, which is relevant to these transitions, is almost identical to the HOMO-1.

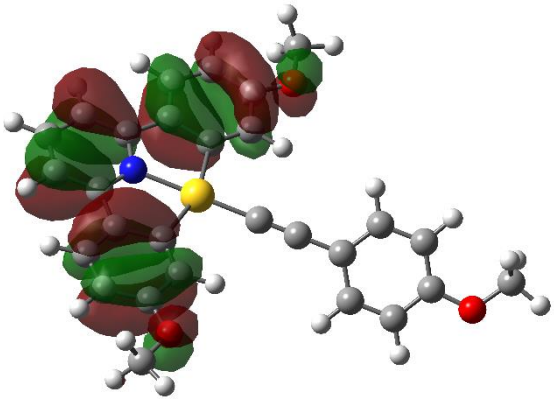

HOMO-1

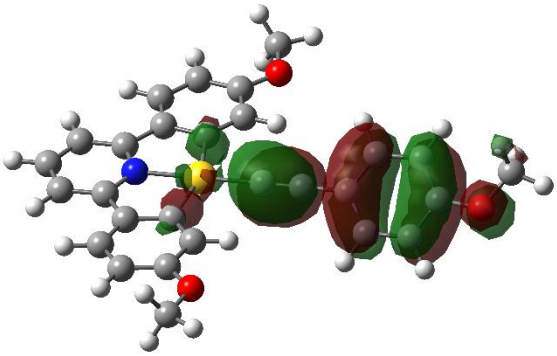

HOMO

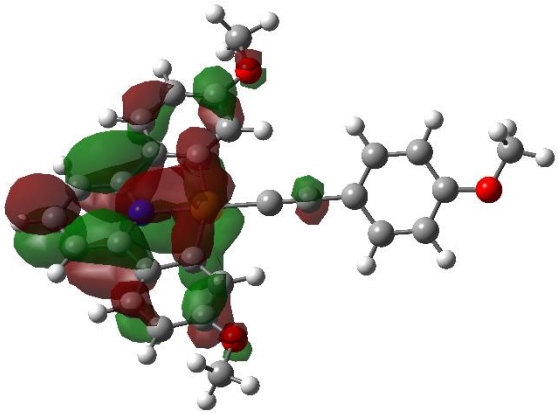

LUMO

Figure 4-41: Kohn-Sham orbitals of **2'-Me** showing the orbitals involved in the excitation

For **1'-H** the lowest energy transition is HOMO to LUMO, with the second lowest energy transition HOMO-1 to LUMO. **1'-Et** shows the same orbital involvement as **1'-H** with successive HOMO to LUMO and HOMO-1 to LUMO transitions, although the first transition occurs at a lower-energy (417 nm compared to 406 nm). For the methoxy-substituted phenylalkynyl complexes **2'-Me**, **3'-Me** and **4'-Me**, the calculated lowest energy transition is again HOMO to LUMO, but occurs at lower energy than the preceding two complexes at 440 nm for **2'-Me** and **3'-Me** and at 444 nm for **4'-Me**. The second calculated transition for **2'-Me** and **3'-Me** occurs at 398 nm and is HOMO-1 to LUMO, and for **4'-Me** occurs at 397 nm and is HOMO-2 to LUMO. The contribution of the HOMO-2 to the excitation transition responsible for the emission for **4'-Me** in contrast to the other species where the HOMO-1 is involved can be rationalised by the similarity in the orbital energies of the HOMO-1 (-6.05 eV) and HOMO-2 (-6.07 eV) for **4'-Me**, which is not the case for the other four species, where there is a larger energy gap (*vide infra*). The HOMO-2 of **4'-Me** is located fully on the C^N^C like the HOMO-1 of the other species, suggesting that this transition has the same origin.

For both complexes, the HOMO-1 to LUMO transition (or HOMO-2 to LUMO for **4'-Me**) contributes more to the excitation than the HOMO to LUMO transition, as quantified by the oscillator strength, and is a $\pi \rightarrow \pi^*$ intraligand transition based on the cyclometallating ligand. There is a small

contribution of a ^{3}LLCT from the HOMO to LUMO transition. This is in corroboration with the assignment of the experimentally observed data (Section 4.3.2.1).

For the methoxy-substituted four-chain complexes outlined below, the situation is very similar; the transitions are mainly HOMO to LUMO for all complexes. Utilising **5'-H** as exemplar species, the Kohn-Sham orbital diagrams of the HOMO-1, HOMO and LUMO are shown in in Figure 4-42. For **5'-H**, both the HOMO and the HOMO-1 are based on both the C^N^C and alkynyl ligands, with an even distribution over the whole molecule. The LUMO is based on the C^N^C ligand and gold(III) metal centre.

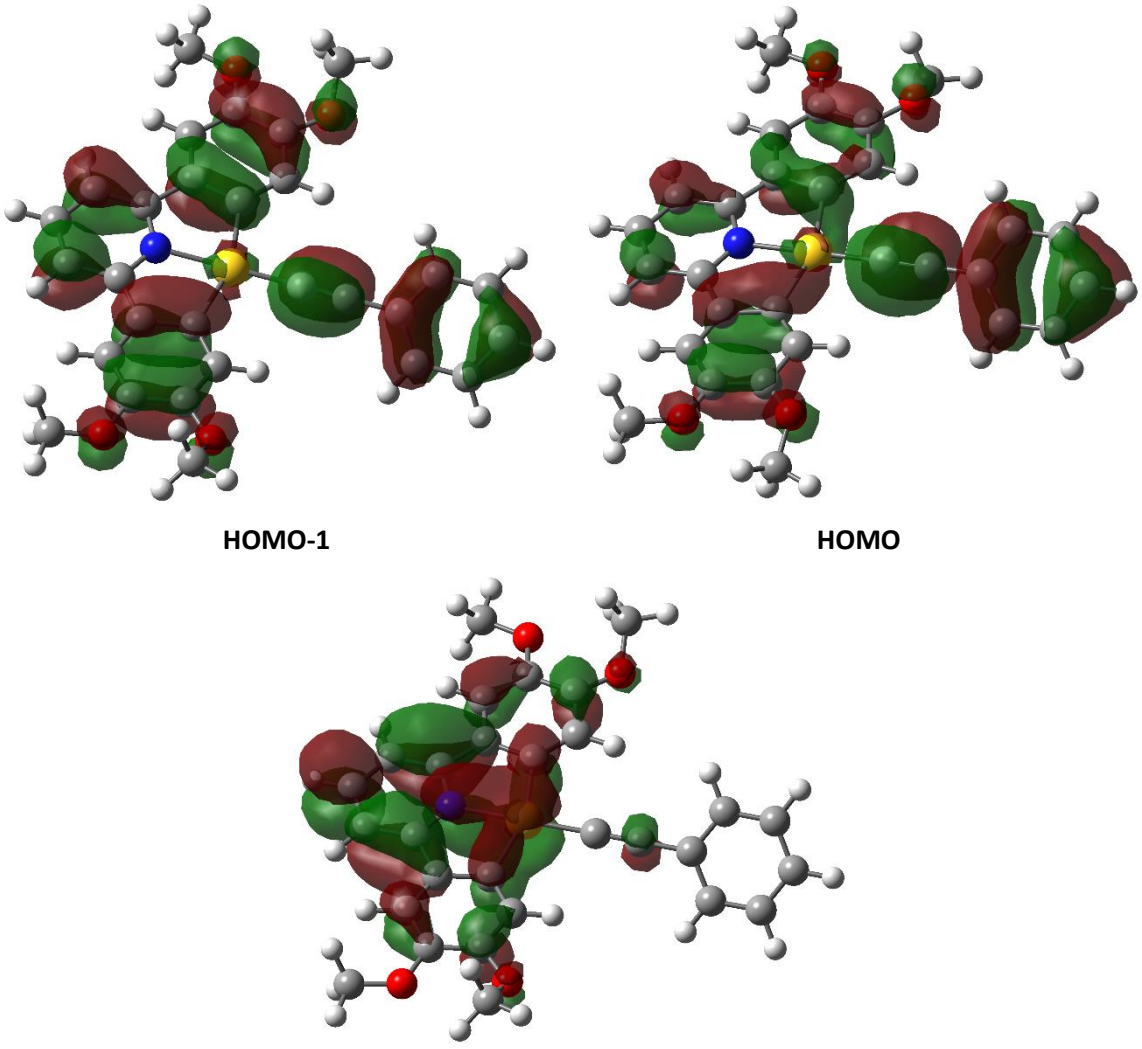

HOMO-1 **HOMO**

LUMO

Figure 4-42: Kohn-Sham orbitals of **5'-H** showing the orbitals involved in excitation

For **5'-Et**, **6'-Me**, **7'-Me** and **8'-Me**, orbital distribution is different; using **6'-Me** as an example, the Kohn-Sham orbitals are shown in Figure 4-43. Here, both the HOMO-1 and the LUMO are C^N^C based. For the HOMO-1, the localisation of the orbital is unsymmetric on the C^N^C ligand, with more contribution from one phenyl ring than the other. This occurs due to the loss of symmetry in the molecule as the orientation of the methoxy group on the phenylalkynyl ligand is fixed and is not subject to rotation. The HOMO for these complexes is based fully on the alkynyl ligand.

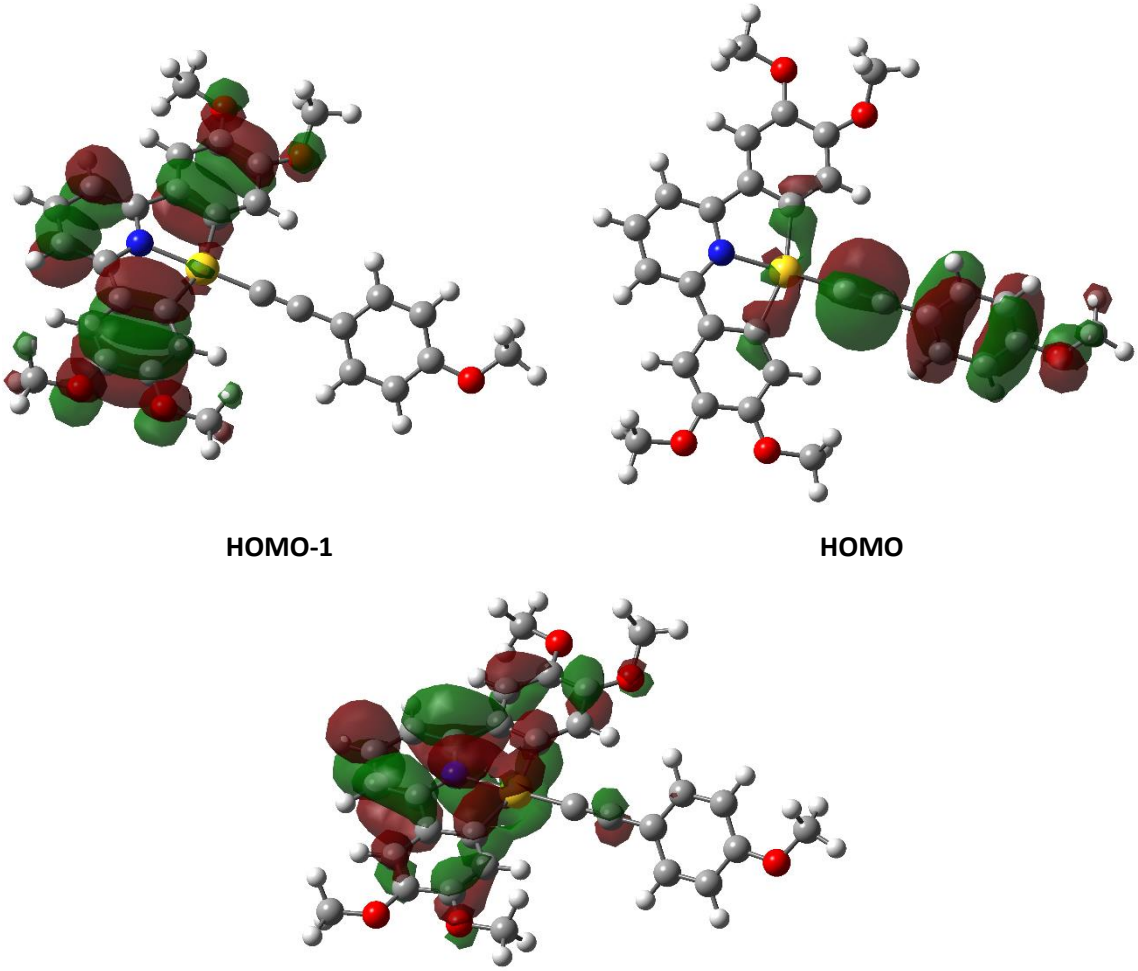

Figure 4-43: Kohn-Sham orbitals of **6'-Me** showing the orbitals involved in excitation

Table 4-5: Summary of DFT-predicted transitions for complexes **5'-H**, **5'-Et**, **6'-Me**, **7'-Me** and **8'-Me**. Only transitions with an oscillator strength >0.001 and orbital contributions >10% are listed.

Complex	Calculated Energy (Experimental energy)/ nm	Oscillator strength	Occupied orbital	Virtual orbital	Coefficient / %	Transition	
5'-H	438 (445)	0.0707	127a	129a	50	HOMO-1	LUMO
			128a	129a	47.5	HOMO	LUMO
	414	0.0352	128a	129a	47.7	HOMO	LUMO
			127a	129a	45.8	HOMO-1	LUMO
5'-Et	445 (440)	0.0545	135a	137a	92.7	HOMO-1	LUMO
	419	0.0404	136a	137a	90	HOMO	LUMO
6'-Me	445 (444)	0.0516	135a	137a	91.9	HOMO-1	LUMO
	439	0.0419	136a	137a	90.5	HOMO	LUMO
7'-Me	445 (448)	0.0520	143a	145a	94.5	HOMO-1	LUMO
	437	0.0548	144a	145a	92.6	HOMO	LUMO
8'-Me	452 (448)	0.00290	152a	153a	92.6	HOMO	LUMO
	444	0.0533	151a	153a	93.8	HOMO-1	LUMO

For the transitions listed in Table 4-4 and Table 4-5 there is good correlation to experimental data for all complexes. An example of this is shown in Figure 4-44 for complex **6-8**/**6'-Me**, in which the calculated and experimental UV-Vis spectra are both shown. There is a slight difference in the absolute λ_{max} values, specifically for the transitions within the UV region, however they can be considered sufficiently accurate as to draw conclusions from the calculated data, especially for the lowest energy transition which is the most relevant to the emission. This example can be considered representative of all complexes.

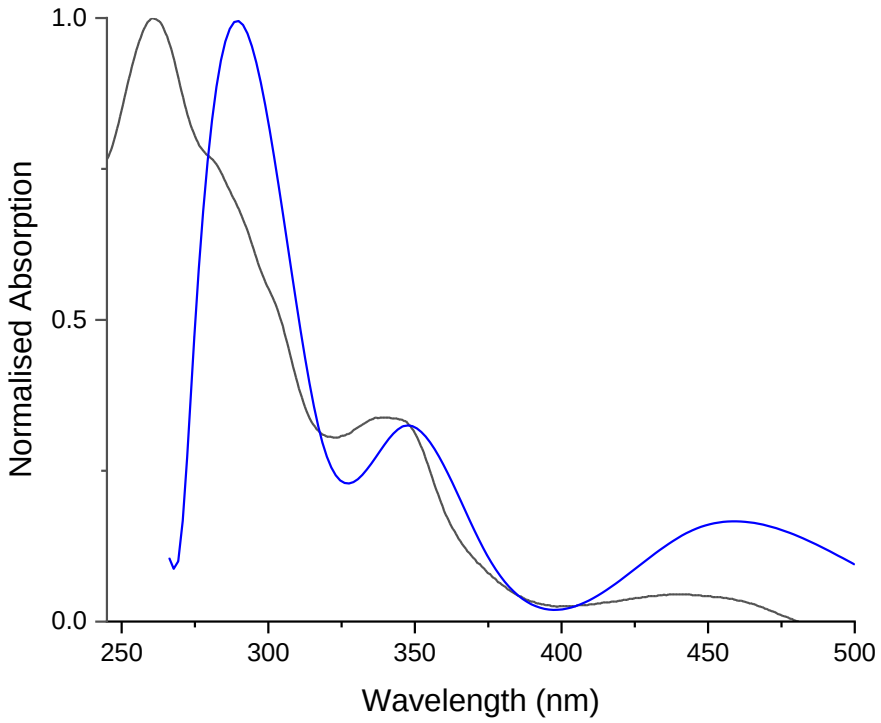

Figure 4-44: Experimental (black) and calculated (blue) UV-Vis spectra for **6-8** (experimental) and **6'-Me** (calculated).

For **5'-H**, the lowest energy transition results from transitions between the HOMO-1 and LUMO and the HOMO and LUMO in approximately equal contribution, with the same transitions involved in the second lowest-energy transition in a similar proportion. For **5'-Et**, **6'-Me**, **7'-Me** and **8'-Me**, the two lowest energy transitions are single component (when orbital contributions of >10% are considered) and arise from a HOMO-1 to LUMO transition at approximately 445 nm. For **5'-Et**, a second transition is observed at 419 nm (HOMO to LUMO). The HOMO to LUMO transition for **6'-Me** and **7'-Me** is calculated to occur at 439 and 437 nm, respectively. For **8'-Me**, the HOMO to LUMO transition occurs at lower energy (452 nm), although this transition is comparatively weaker than both the HOMO to LUMO transition for the other complexes.

The calculation of the dual contributions to both low-energy transitions observed for **5'-H**, in contrast to the four other related species, in which all calculated transitions have a single orbital contribution, is rationalised through the calculation of the orbital energies of the HOMO (-5.77 eV)

and HOMO-1 (-5.81 eV) orbitals, which prove to be much closer in energy than in the other four-chain species (apart from **5'-Et**).

For all five complexes with four methoxy groups on the C^N^C ligand, contributions to the relevant excitation transition occur from mixed origin as both calculated transitions, as shown in Table 4-5, contribute to the experimentally observed transition at approximately 445 nm, with character from both the C^N^C and alkynyl ligands in the ground state. Consequently, the transition can be described as a mixture between $\pi \rightarrow \pi^*$ intraligand transition based on the cyclometallating ligand (^{3}LC) and intraligand charge transfer (^{3}LLCT). Such mixing is not unknown in similar literature systems[33] and may account for decreased vibronic coupling in the experimental emission bands of these complexes in comparison to the two-chain complexes where the emission is predominantly ^{3}IL.

Changes in frontier molecular orbital energies are shown graphically in Figure 4-45. For the two-chain complexes (**1'-H** to **4'-Me**), across the series there is a stabilisation of the HOMO, while the energies of the LUMO and LUMO+1 remain approximately constant. Energies of the HOMO-1 and HOMO-2 also appear invariant to the substitution changes, with the exception of the HOMO-2 of **4'-Me**, which is noticeably higher in energy than the HOMO-2 orbitals of the other species and very similar to the HOMO-1, as discussed above. For the four-chain complexes (**5'-H** to **8'-Me**), stabilisation of the HOMO across the series is observed, and the energy of the LUMO remains approximately constant for all five species. The other relevant orbital to the emissive transitions is the HOMO-1, the energy of which remains approximately consistent across the series.

This indicates that the main difference in changing from an H, to an alkyl, to an alkoxy, is a stabilisation of the HOMO. This makes sense, as for all complexes the HOMO is based on the phenylalkynyl ligand, where this alteration is localised.

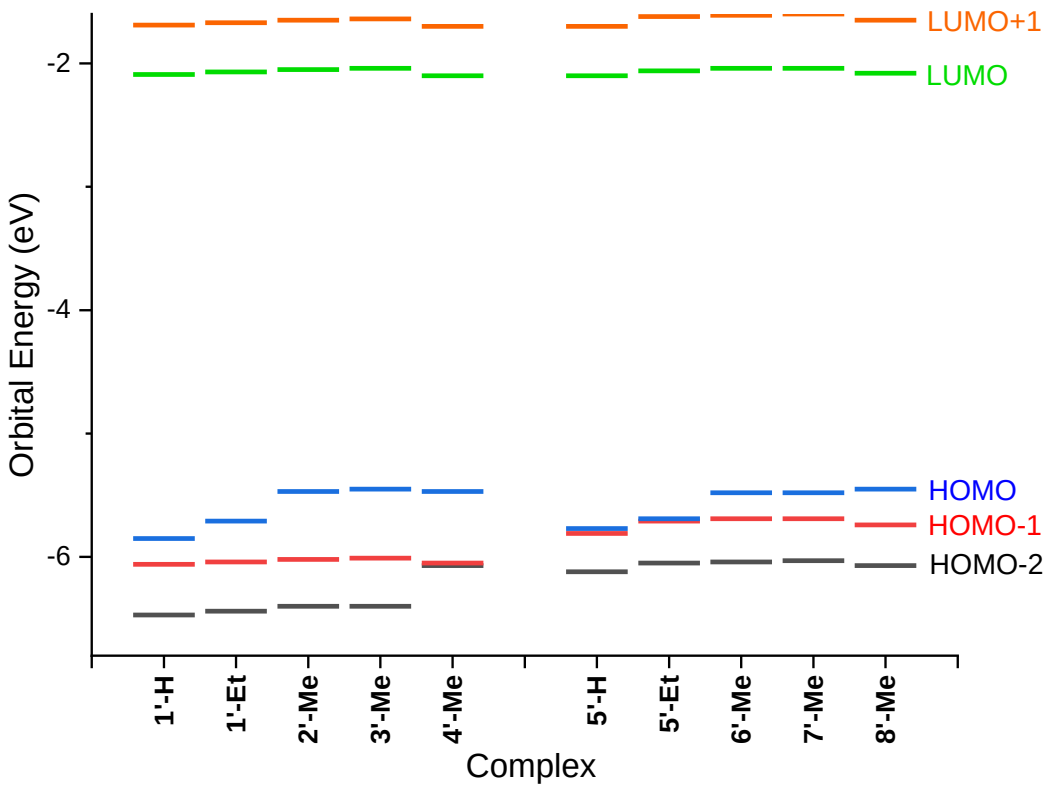

Figure 4-45: Energies of frontier molecular orbitals for all species calculated at PBE0/def2-TZVPP

From singlet calculations, the orbitals involved in the excited state can be calculated. However, this is a calculation of the singlet excited state, and so cannot predict the *emissive* properties of a triplet-emitter. In order to model the triplet excited state and any phosphorescent properties, further calculations must be undertaken in which the energy of the triplet excited state is calculated. As the emissive character (*i.e.* the emission energy and band structure) remains consistent when measured experimentally, complexes **1'-H** and **5'-H** were used as exemplar species to calculate the triplet excited state.

In this method, the ground state geometry of the complex is optimised as before. Subsequently, the spin state of the optimised structure is assigned as triplet, and the structure is re-optimised using the same functional and basis set. What is calculated is the predicted energy of the triplet excited state; the energy of an excitation from the ground state to the singlet excited state is already known. As the triplet state is lower in energy that the singlet, when the difference between the two calculated values is taken, the energy gap between the triplet excited state and singlet ground state can be realised and, therefore, the calculated energy of emission.

For **1'-H**, the calculated energy of emission is 500 nm. This is in excellent agreement with the experimental value of 502 nm. The same can be said for **5'-H**, in which the calculated value of 548 nm is in accordance with the experimental value of 553 nm. This success is an indicator of the validity of these calculations and lends credence to the conclusions drawn from them.

4.5 Applications of Gold(III) Complexes in Solution-Processed OLED Devices

4.5.1 Initial Aims and Choice of Complexes

The performance of a select number of complexes in OLED devices was tested, both doped in a polymer host and as a neat film as the emissive layer. Initially, complexes **1-8**, and **3-14** were investigated in doped devices. In the previous section regarding the photophysical properties of all gold(III) complexes, exemplar complexes were investigated, utilising the chain length of C8 for all systems (with the inclusion of **1-H** and **5-H**), as at 1 x10^{-5} M, it was not thought that the chain length would have an impact on the emissive behaviour. However, solution phase data are not directly applicable to thin-film and device emission data; an increase in chain length can affect the efficiency of the device, as it can alter the spacing between individual molecules within a host, which can have an impact on the rate of self-quenching and therefore device performance.

Although perhaps not the most intuitive choice, complexes **1-8** and **3-14** were chosen due to the range of emissive properties and promising liquid-crystalline properties, as well as the practical availability of starting materials in order to remake these complexes for large scale testing in a short timescale. These complexes were tested both as emissive dopants in polymeric hosts (at a range of doping concentrations), and as neat emissive layers within the device to investigate any polarising ability when annealed in the liquid-crystalline state. Complexes **1-H**, **5-8**, **6-8**, **7-14** and **8-14** were also tested in the final optimised device structure.

Fabrication of the following devices was carried out during a two week research trip to collaborators at Changzhou University, China. Many of the devices were fabricated by, or under the instruction of, Denghui Liu, who was also responsible for the majority of the data collection.

Fabrication of the following devices was carried out during a two week research trip to collaborators at Changzhou University, China. Many of the devices were fabricated by, or under the instruction of, Denghui Liu, who was also responsible for the majority of the data collection.

4.5.2 Cyclic Voltammetry

For the successful fabrication of devices, all components of the device must have compatible energy levels and work functions for transfer of the charge carriers, and as such the device materials chosen are done so through knowledge of the HOMO and LUMO energies of the emitter.

This was achieved through the collection of cyclic voltammograms of complexes **1-H** and **5-H** (Figure 4-46).

It has been well established that the orbitals involved in the emissive transition are predominantly based on the C^N^C ligand for the two-chain complexes and on a mix the C^N^C ligand and alkynyl ligand for the four-chain complexes, both through the insensitivity of the emission energies and profiles when the alkynyl ligand was altered and extensive TD-DFT calculations. For this reason, the HOMO and LUMO energies fully measured and calculated for **1-H** and **5-H** were considered to be approximately correct for all other complexes in the same families, and accurate enough for the other materials within the device to remain constant during fabrication and testing.

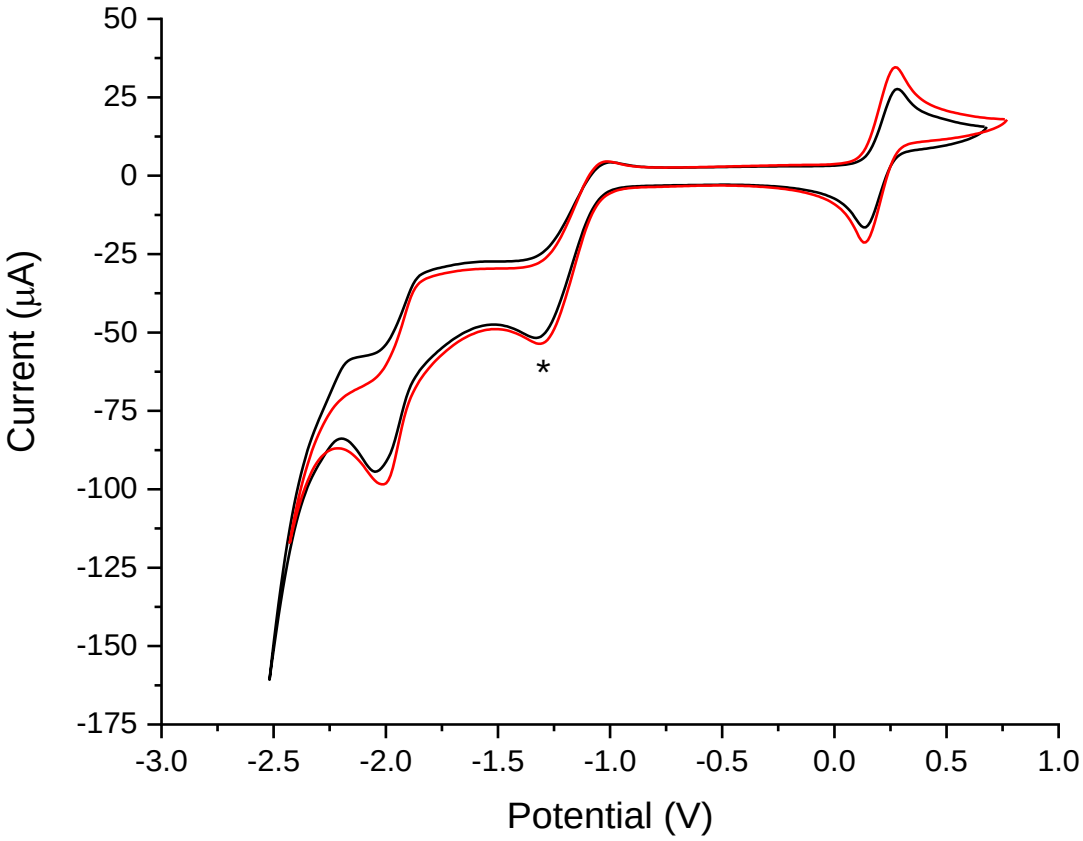

Figure 4-46: Cyclic voltammograms of **1-H** (black) and **5-H** (red), referenced against the ferrocene/ferrocenium couple. The presence of water is marked by an * and should be ignored.

Complex **1-H** showed a partially-reversible reduction wave at -2.02 V, with a partial oxidation at -1.83 V as measured with a glossy carbon electrode *vs* a platinum wire in CH_2Cl_2, utilising the ferrocene/ferrocenium couple as an internal reference. From this value, using the method reported by Pan *et al.*,[109] the optical band gap can be calculated and thus the approximate HOMO and LUMO energies. In the reported procedure, the following equations are given:

$$E_{\mathrm{g}} = \frac{\mathrm{h}c}{\lambda_{\mathrm{onset}}}$$

$$E_{\mathrm{HOMO}} = -(E_{\mathrm{onset}}(OX) + 4.8 - E_{\mathrm{FOC}})$$

$$E_{\mathrm{LUMO}} = -(E_{\mathrm{onset}}(RED) + 4.8 - E_{\mathrm{FOC}})$$

$$E_{\mathrm{LUMO}} = E_{\mathrm{HOMO}} + E_{\mathrm{g}}$$

Where E_g is the optical band gap of the complex, h is the Planck constant (6.63×10^{-34} J s), c is the speed of light (2.99×10^{8} m s^{-1}), λ_{onset} is the onset absorption (taken from the UV-Vis spectra), E_{HOMO} and E_{Lumo} are the energies of the HOMO and LUMO orbitals, respectively, E_{onset}(OX/RED) is the onset of the oxidation or reduction potential, respectively (taken from CV), 4.8 eV is the reference energy level of ferrocene below the vacuum level and E_{FOC} is the potential of the ferrocene/ferrocenium couple, measured in this experiment to be +0.21 V vs a platinum wire.

Complex **1-H** has a reduction onset potential of -1.70 V, and an absorption onset of 461 nm. Application of the above method results in a HOMO energy of -5.60 eV and a LUMO energy of -2.90 eV. These values were in approximate agreement with those calculated by DFT (Section 4.4) in which the HOMO energy was calculated to be -5.85 eV and the LUMO energy -2.09 eV. The LUMO energy calculated by DFT is substantially lower than that calculated by CV measurements; the latter is presumed to be the more accurate value due to the physical measurement of the addition of an electron into the LUMO in the reduction process whereas, in its simplest form, the DFT calculation is a calculation of the location of electrons of which, in the LUMO, there are none, and it known to be more inaccurate.

Complex **5-H** displayed the same semi-reversible reduction peak at -2.07 V with the partial oxidation at -1.9 V. Application of the Pan method,[109] where the reduction onset potential was measured to be -1.94 V and the absorption onset 491 nm, resulted in calculated orbital energies of -5.18 eV for the HOMO and -2.65 eV for the LUMO. From DFT calculations (Section 4.4), these were calculated to be -5.77 eV for the HOMO and -2.10 eV for the LUMO.

From these values, appropriate device fabrication materials were selected for the design of both the doped and non-doped devices.

4.5.3 Device Structure and Choice of Materials

The appropriate choice of materials for each layer of the device is vital to its function; the materials have to have compatible electronic characteristics to the emitter. Due to the range of HOMO energies (-5 to -6 eV) and LUMO energies (-2 to -3 eV), appropriate materials were chosen as follows.

As for all devices of this type, a glass substrate coated with indium tin oxide (ITO) is used as the anode as it is both an electrical conductor and optically transparent, and can be easily deposited as a thin film. PEDOT:PSS, poly(3,4-ethylenedioxythiophene) polystyrene sulfonate, is a polymer mixture and was used as a hole injection layer. Bis[2-(diphenylphosphino)phenyl]ether oxide (DPEPO) was used as hole/exciton blocking layer. 1,3,5-Tris(3-pyridyl-3-phenyl)benzene (TmPyPB) was used as an electron-transport layer. Caesium fluoride was used in the electron-injecting layer and aluminium as the metal cathode. In the initial screening of device materials, tris(2,4,6-trimethyl-3-(pyridin-3-yl)phenyl)borane (3TPYMB) was also investigated as a potential hole/exciton blocking layer.

For the doped devices, three hosts were investigated in optimisation experiments. The first, ubiquitous in the device studies of Yam and co-workers,[21, 22, 26, 34, 77, 78, 80, 81] was 1,3-bis(carbazole-9-yl)benzene (MCP), the second was 10-(4-(4-(9H-carbazol-9-yl)phenylsulfonyl)phenyl)-9,10-dihydro-9,9-dimethylacridine (CzAcSF) which is a host typically used for TADF materials, and the third a mixture of poly(9-vinylcarbazole) (PVK) and 1,3-bis[2-tert-butylphenyl)-1,3,5-oxadiazo-5-yl]benzene (OXD-7), typically in a 7:3 ratio. PVK also functions as a hole-transport layer. The chemical structure of all relevant materials is shown in Figure 4-47.

Full experimental details on the fabrication of all devices are given in Chapter 6, and a brief overview will be given here; the device structure described is that found to be the most successful, for reasons described below.

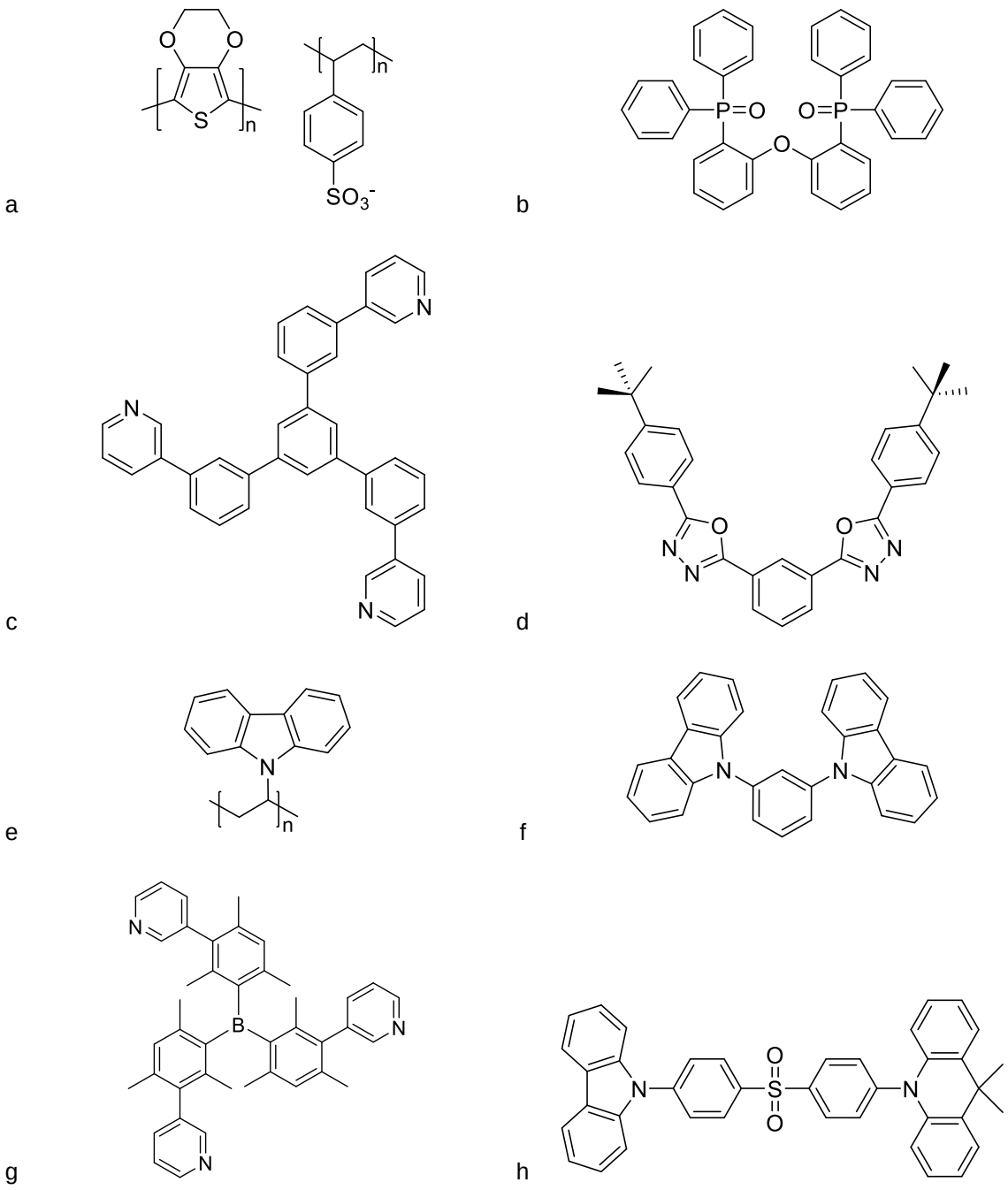

Figure 4-47: Chemical structure of materials used in the OLED devices. a) PEDOT:PSS; b) DPEPO; c) TmPyPB; d) OXD-7; e) PVK; f) MCP; g) 3TPYMB; h) CzAcSF

An ITO-coated glass substrate was cured with ozone at 100 °C for 10 minutes. A layer of PEDOT:PSS (35 nm) was spin-coated onto the glass substrate and annealed at 120 °C for 10 minutes under an inert atmosphere. A prepared solution of the host and emitter of the appropriate weight ratio was added on top of the PEDOT:PSS layer *via* spin-coating (50 nm) and annealed at 120 °C for 10 minutes. Successive layers of DPEPO (9 nm), TmPyPB (40 nm), CsF (1.2 nm) and Al (120 nm) were added to the device by thermal evaporation. The device was encapsulated with a further glass substrate which secured using a UV-curable adhesive (Figure 4-48).

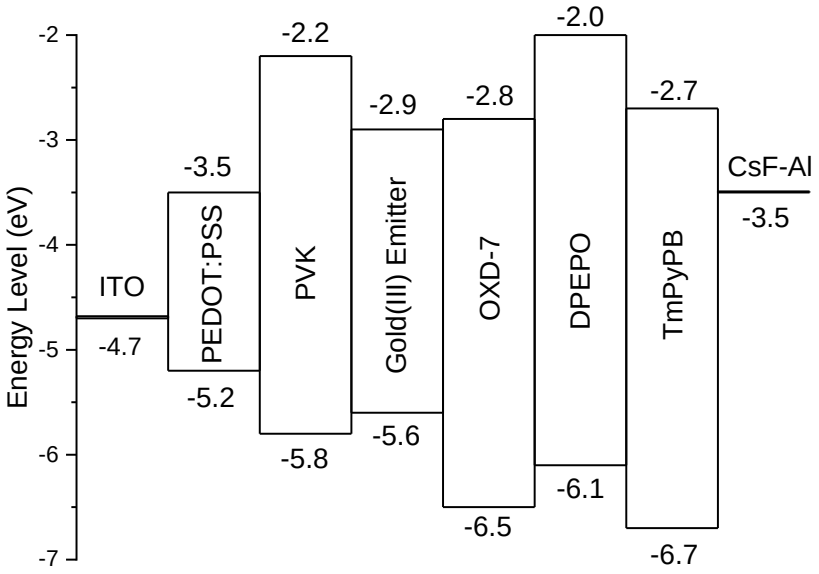

Figure 4-48: General schematic for the structure of doped-devices with gold(III) emitters (emitter energy levels shown are those calculated for **1-H**)

For the devices in which the gold(III) complexes were present as a neat film, the aim was to investigate the ability for the device to show polarised emission due to the supramolecular order given by the liquid-crystalline properties of the gold(III) complexes. To achieve this, the emissive layer must be aligned. Alignment can also be achieved in doped devices by the same techniques.

There are multiple ways to do this, including mechanical stretching, Langmuir-Blodgett techniques (although this deposition method is rare), liquid-crystalline self-assembly or a rubbing and annealing technique.[110] For the devices fabricated in this work, the alignment was achieved by uniaxial rubbing of the hole-injection layer (PEDOT:PSS) with a dust-free cloth, followed by application and annealing of the emissive layer.

4.5.4 Device Performance

The performance of the doped devices was tested through the simultaneous acquisition of current-voltage-luminescence data. The most relevant parameters to the quantification of the effectiveness of the emitter are the current efficiency (CE), power efficiency (PE) and the external quantum efficiency (EQE), as defined in Chapter 1, Section 1.3.1. The last is perhaps the most telling of the parameters, as it is a measure of the overall emission efficiency for the entire device as a percentage of the number of photons emitted compared to the total number of charge-carrier/hole recombinations. Also relevant are the electroluminescence spectra, which are compared as the applied voltage is increased, and the Commission Internationale de l'Elcairage (CIE) coordinates,[111] which are an accurate measure of colour in two dimensions. For the neat-film

devices and a select few doped devices, in addition to the parameters above, the ability of the device to show polarised emission was also tested.

4.5.5 Initial Testing Using 1-8 and 3-14

Full device optimisation testing was carried out for complexes **1-8** and **3-14**. The first devices tested investigated the compatibility of the three hosts outlined above; MCP, CzACSF and PVK:OXD-7 (7:3). From the initial data collection, it was clear that the devices utilising CzAcSF as a host were of lower quality, with poor EQE values and significant broadening of the electroluminescence spectrum as the applied voltage was increased, which may be due to excimer formation. For these reasons, the CsAcSF based devices were not pursued further.

The devices using hosts PVK:OXD-7 and MCP showed more promise. At 10 wt%, PVK:OXD-7 was the more favourable host for **1-8**, showing and EQE of 5.24% compared to 1.57% for the MCP-based devices; CE values were also substantially higher, with **1-8** showing 5.19 cd A^{-1} in MCP and 17.31 cd A^{-1} in PVK:OXD-7 (Figure 4-49). It was this host that was used in the optimised devices and in all of the further testing. Similar differences were observed for the devices with **3-14** as the emitter. The MCP-based device was also tested in which the (3TPYMB) was used as the hole/exciton blocking layer; for both **1-8** and **3-14**, device performance was inferior to that observed for the DPEPO devices.

From these initial screening tests, it was concluded that the device structure of ITO/PEDOT:PSS/[PVK:OXD-7(7:3)]:[Au](5wt%)/DPEPO/TmPyPB/CsF/Al was the best performing, where [Au] represents the relevant gold(III) complex and it was this configuration which was used in the optimised devices.

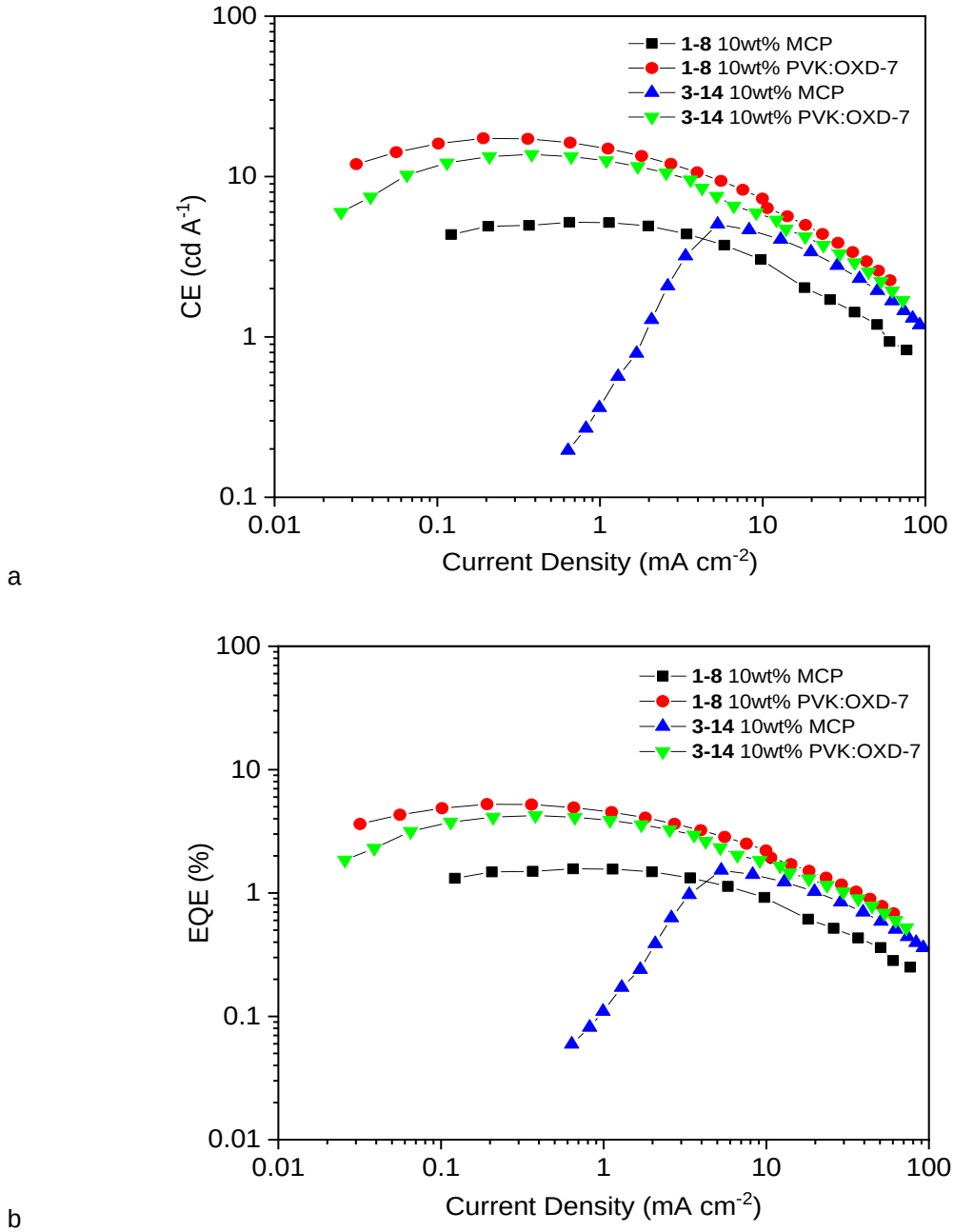

Figure 4-49: Comparison of MCP and PVK:OXD-7 as hosts for doped OLED devices at 10 wt%, showing a) CE and b) EQE

4.5.6 Optimised Devices

Following the initial scope testing outlined in the previous section, the complexes chosen for analysis were fabricated using the same device structure for all. For all complexes, devices with a doping concertation of 5, 10 and 15 wt% were fabricated, and it was found in all cases that the most efficient devices were those doped at 5 wt% (Table 4-6).

Table 4-6: Optimised device data for complexes **1-H**, **1-8**, **3-14**, **5-8**, **6-8**, **7-14**, **8-14** doped at 5, 10 and 15% in a host of PVK:OXD-7 (7:3) showing the turn-on voltage, V_{on}, maximum luminescence, maximum current and power efficiencies, maximum external quantum efficiencies, wavelength of the emission and Commission Internationale de l'Elcairage (CIE) coordinates.

Complex	wt%	V_{on} / V	L_{max} / cd m^{-2}	CE_{max} / cd A^{-1}	PE_{max} / lm W^{-1}	EQE_{max}	Emission Peak / nm	CIE Coordinates
1-H	5	4.0	1243	22.01	12.51	6.72	508	(0.293, 0.577)
	10	4.4	1378	22.32	12.71	6.71	510	(0.308, 0.570)
	15	4.4	1004	15.23	8.37	4.58	510	(0.312, 0.575)
1-8	5	4.4	1259	21.41	12.67	6.58	508	(0.312, 0.570)
	10	4.4	1370	17.31	9.69	5.24	508	(0.310, 0.563)
	15	6.0	734	8.29	3.34	2.57	508	(0.306, 0.569)
3-14	5	4.0	1233	20.14	10.97	6.27	506	(0.315, 0.565)
	10	4.4	1229	13.76	6.97	4.25	508	(0.314, 0.570)
	15	6.8	304	2.38	0.65	0.72	508	(0.295, 0.575)
5-8	5	3.6	1765	22.53	13.41	7.14	554	(0.465, 0.516)
	10	4.0	1441	21.18	11.73	6.94	556	(0.472, 0.506)
	15	4.8	1142	9.71	4.00	3.14	558	(0.477, 0.509)
6-8	5	4.0	1705	21.31	12.45	6.82	554	(0.465, 0.513)
	10	4.4	1768	21.45	11.21	6.74	556	(0.466, 0.510)
	15	4.8	1261	17.59	8.92	5.57	556	(0.470, 0.513)
7-14	5	4.4	1401	17.14	8.94	5.52	554	(0.468, 0.511)
	10	5.2	867	7.62	3.17	2.50	556	(0.472, 0.509)
	15	6.4	494	4.45	1.62	1.46	556	(0.468, 0.508)
8-14	5	4.4	1191	18.04	10.10	5.69	554	(0.461, 0.508)
	10	4.4	1138	13.14	7.28	4.06	554	(0.465, 0.516)
	15	4.4	911	11.75	6.58	3.66	554	(0.461, 0.520)

In order to provide comparison between the different weight concentrations in the optimised OLED device structure, CE, PE, EQE and EL device data for 5, 10 and 15 wt% weight loadings of **1-8** are shown in Figure 4-50, as well as the changes in CE and luminescence as a function of applied voltage, and a photograph of the emission from the device. It can be observed that for all three relevant parameters (CE, PE and EQE), the efficiency of the device decreases as the doping concentration increases. The maximum current efficiency of **1-8** is drastically reduced from 21.41 cd A^{-1} for 5 wt%, to 17.31 cd A^{-1} for 10 wt% and 8.39 cd A^{-1} for 15 wt% in a non-linear drop-off. The

same trend is observed for the maximum power efficiency, which decreases from 12.67 to 9.69, to 3.34 lm W^{-1} for 5, 10 and 15 wt%, respectively. As may be expected from the CE and PE, the trend is mimicked the in the EQE, which decreased from the optimum 6.58% for 5 wt%, to 5.24% for 10 wt% to 2.57% for 15 wt%. For all three parameters, and indeed all three doping concentrations, the examined characteristic increases as the current density increases to approximately 0.2 mA m^{-2}, where the curve peaks and subsequently decreases in efficiency as the current density increases.

The electroluminescence spectrum is unchanged as the concentration is increased. The emission profile resembled that observed in the solution phase measurements, with the (0,0) and (0,1) bands appearing well resolved, as well as a poorly resolved shoulder on the low-energy side of the emission peak. Also present is the high-energy peak that was discussed in Section 4.3.2.4 and assigned as a competing fluorescence process. The relative intensity of this peak is similar to that observed in the degassed solution phase spectra, perhaps due to the fabrication and encapsulation of the device under inert-atmospheric conditions. In examining the change in current density and luminescence as a function of applied voltage, the devices with doping concentrations of 5 and 10 wt% function with a similar effectiveness, however this efficiency is drastically reduced at 15 wt%, especially for the luminescence of the system.

These data are not consistent across all of the two-chain complexes; the case is similar for **3-14**, with a substantial reduction in efficiency for the key parameters as the dopant concentration is increased, however for **1-H**, although the device which was doped at 5 wt% is the most efficient, the data for the 10 wt% device presents only a slight drop in efficiency across the maximum CE, PE and EQE values. For example, for **1-8**, the EQE value decreases by 20% in the increase of concentration from 5 wt% to 10 wt%, and by 61 % from 5 wt% to 15 wt%. For **1-H**, the EQE is decreased by 1% between 5 and 10 wt% and 40% between 5 and 15 wt%.

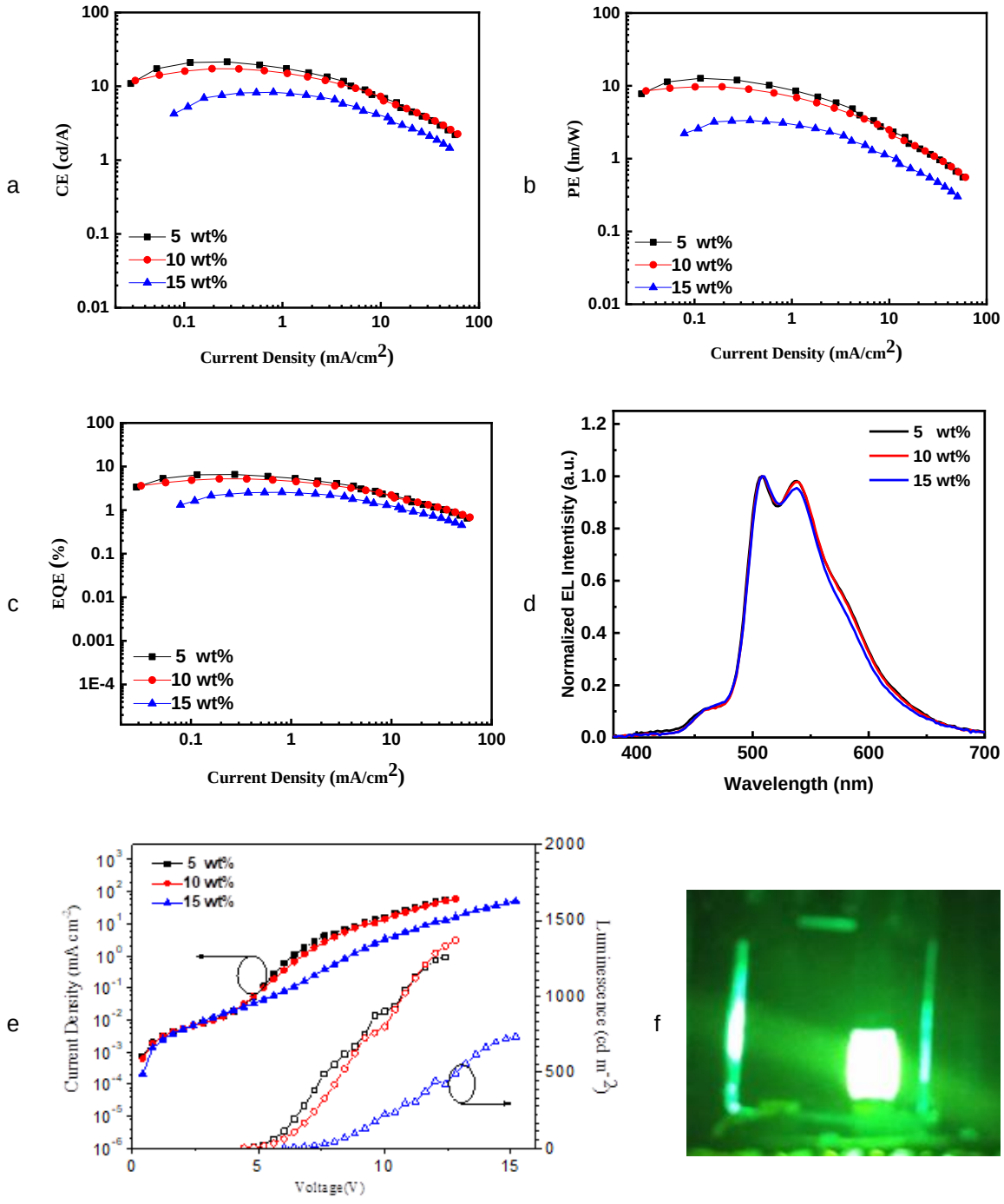

Figure 4-50: Device performance comparison of **1-8** at 5 (black), 10 (red) and 15 (blue) wt% in PVK:OXD-7 (7:3) showing a) current efficiency as a function of current density; b) power efficiency as a function of current density; c) external quantum efficiency as a function of current density; d) electroluminescence emission profile; e) current density (block colour) and luminescence (open colour) as a function of voltage; f) photograph of the green emission of the device

Characterisation of the same parameters for complexes **5-8** are shown in Figure 4-51. In analysis of the current and power efficiencies and EQEs, the findings are changed from that of **1-8** and are more similar to those for **1-H**, in which a dopant concentration of 5 wt% proved to be the most efficient in the device structure, but the devices fabricated at 10 wt% were only slightly less

efficient. This was found to be true for **6-8**, but not **7-14** and **8-14** in which the decline was stark between the 5, 10 and 15 wt% devices.

This is clear from analysis of the plots in Figure 4-51a, b and c in which the 5 wt% and 10 wt% doped devices (black and red lines, respectively) perform to similar standard, with the 15 wt% doped devices showing better performance for CE, PE and EQE at low current densities. However, at the maximum CE, PE and EQE values, the 5 wt% device is superior, with outputs of 22.53 cd A^{-1}, 13.41 lm W^{-1} and 7.14%, respectively. In contrast, the device fabricated at 15 wt% show significantly poorer performance, especially at low current densities as evidenced by the steep gradient of the trend-line for the first few data points.

The electroluminescence spectra for the three dopant concentrations remained fundamentally unchanged as the concentration increased. The measured current density of the devices as the applied voltage increased was not dissimilar across the three devices, with repeated intersections of the trend-lines across the measurement range, but in general terms, the current density was higher as a function of applied voltage for the devices doped at lower concentrations. The luminescence of the device is also improved with a lower density of emitters in the emissive layer, with a poorer increase in luminescence as a function of applied voltage as the doping concentration increased. The turn-on voltage, *i.e.* the minimum applied voltage at which electroluminescence is detectable, is also dopant concentration dependant, especially for the devices based on **5-8**; for the 5 wt% device, the turn-on voltage is 3.6 V, which increases to 4.0 and 4.8 V for the 10 and 15 wt% devices, respectively. This is observed for the majority of complexes; the only complex for which the turn-on voltage is concentration independent is **8-14**.

The emission colour of the devices, observed by the naked eye as green and yellow for the two-chain and four-chain complexes, respectively (as shown in Figure 4-50f and Figure 4-51f) can be quantified through the measured CIE coordinates, which could be plotted in CIE 1931 colour space (Figure 4-52). This resulted in two clusters of data points, those for the two-chained species, at $x \approx 0.3$, and for the four-chained species, $x \approx 0.45$. There is a slight variation between the absolute colour values within these series, as observed through the smaller *x* coordinate of **1-H** compared to the **1-8** and **3-14** although this difference would not be distinguishable to the naked eye or in a traditional emission spectrum. The four-chain species all exist as a tight cluster of points in the yellow region of colour space, with less variation than their two-chain counterparts.

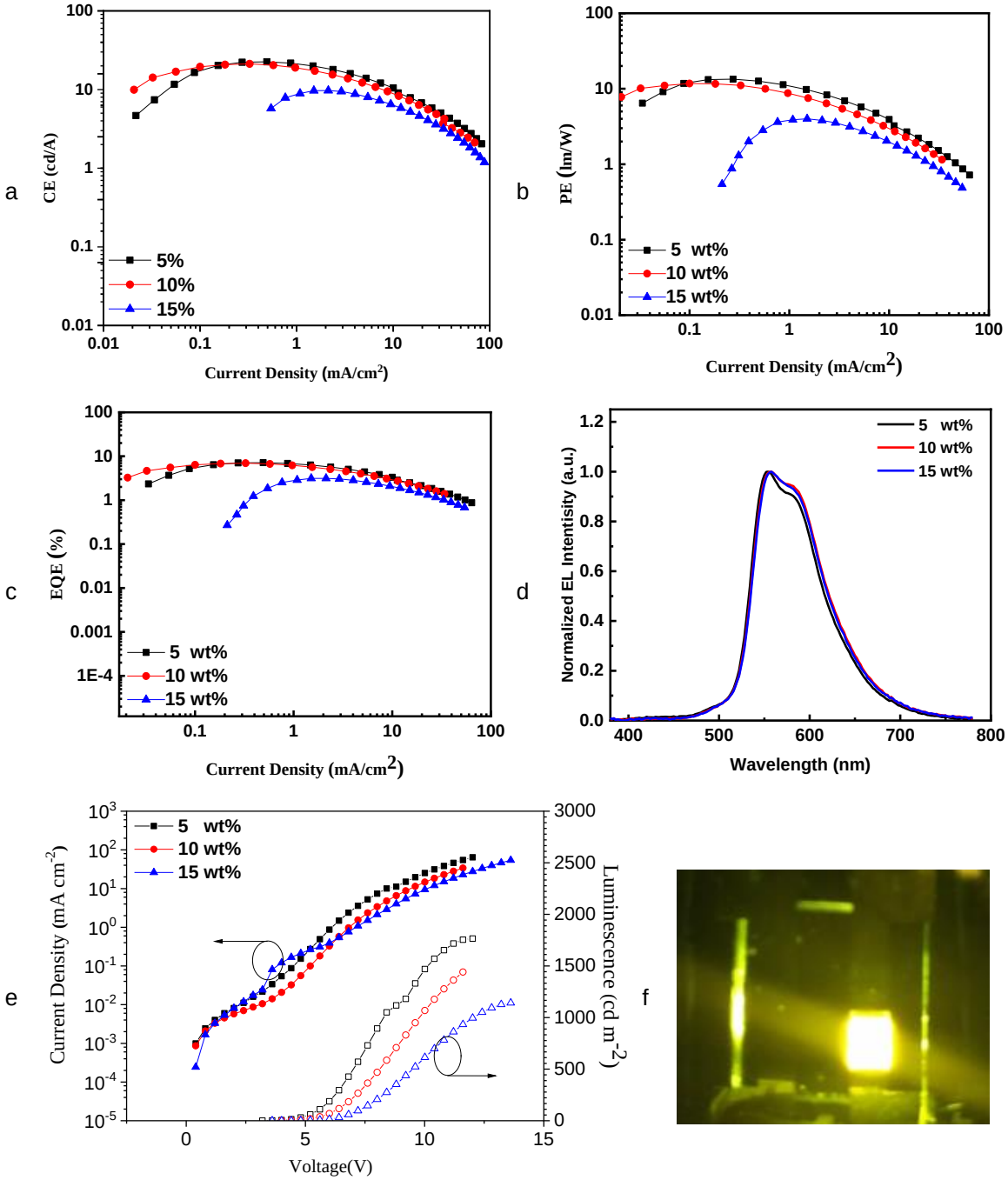

Figure 4-51: Device performance comparison of **5-8** at 5 (black), 10 (red) and 15 (blue) wt% in PVK:OXD-7 (7:3) showing a) current efficiency as a function of current density; b) power efficiency as a function of current density; c) external quantum efficiency as a function of current density; d) electroluminescence emission profile; e) current density and luminescence as a function of voltage; f) photograph of the green emission of the device

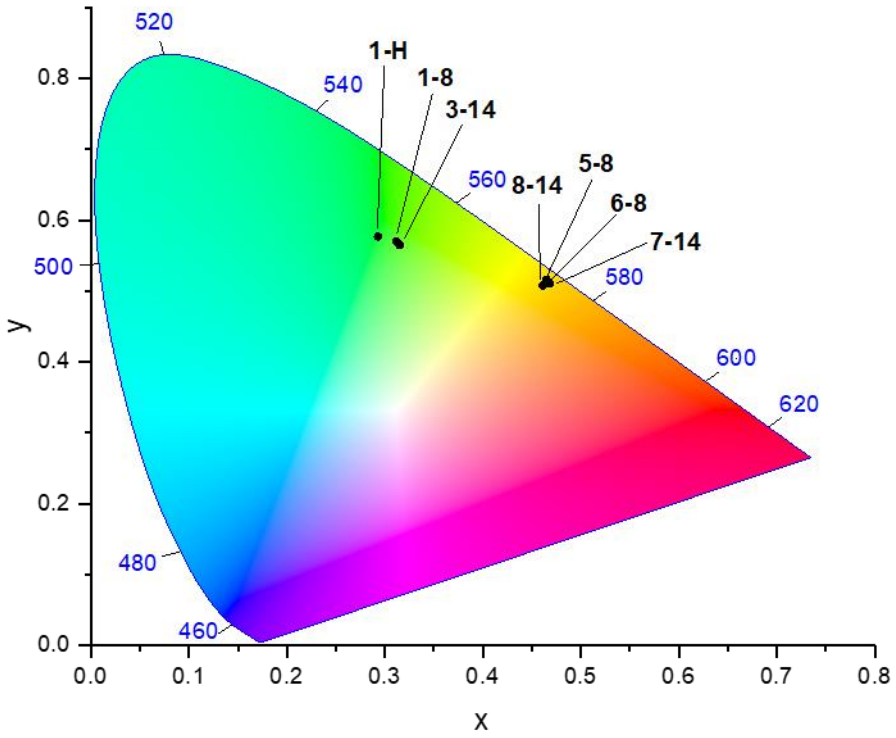

Figure 4-52: Plotted CIE coordinates of **1-H**, **1-8**, **3-14**, **5-8**, **6-8**, **7-14** and **8-14** in CIE 1931 colour space, showing the clusters of two chain complexes $x \approx 0.3$ and the cluster of 4 chain complexes $x \approx 0.45$ (data taken from 5 wt% devices).

It is clear from the comparable CE, PE and EQE values across this series of seven complexes that the trends observed in the solution phase emission are not applicable in understanding the processes in OLED devices. Thus, the device performance of those complexes with two-chains on the cyclometallating ligand is indistinguishable from that of the four-chain equivalents, whereas there is an order of magnitude difference in the solution phase data.

The best performing device is that constructed using **5-8**, with an external quantum efficiency of 7.14% and the worst **7-14** with an EQE of 5.52%. The difference in performance between the best and worst devices is small, and so correlations between chain number and length and device performance are difficult to discuss, compounded by the lack of any discernible patterns in the device efficiency compared to the systematic variation in substitution pattern of the complexes.

It is proposed that the efficiency of the devices is due to the relative spacing of the emissive centres within the dopant in relation to each other. The main form of deactivation within the device is thought to be from self-quenching *via* triplet-triplet annihilation. It then follows that as the dopant concentration within the device is decreased, associations between the individual molecules of the gold(III) complex are reduced, resulting in a reduction of self-quenching processes. As well as the dopant concentration, the number and length of the appended alkoxy chains may affect the

spacing of the molecules within the doped film by spacing the emissive cores of the molecules in such a way to minimise triplet-triplet annihilation.

Clearly, due to the lack of coherent trend across the series, this cannot be the only factor. The additional degrees of freedom and excited state deformation in the system with an increasing number of flexible chains may mitigate this spacing effect, resulting in a trade-off in the device efficiency.

The EQE of all devices, especially that of **5-8** with an EQE of 7.14%, can be considered to be good within the body of literature on similar [Au(C^N^C)(C≡CR)] complexes. As outlined in the introductory section to this chapter, EQEs of similar complexes in solution processed devices range from 0.9%[22, 77] to 15.3%,[80] which is the highest reported for a solution processed device of the same central moiety. Higher EQEs can be achieved through the fabrication of vacuum deposited devices, however given the large molecular weight of the liquid-crystalline gold complexes, due to the inclusion of multiple extended alkoxy chains, this method is not feasible here.

4.5.7 Polarised Emission in Doped and Non-Doped Devices

The ability of complexes **6-8** and **8-14** to show polarised emission whilst in doped devices was investigated by attempting to align the film. The device structure was kept consistent with that described above (ITO/PEDOT:PSS/[PVK:OXD-7(7:3)]:[Au](5wt%)/DPEPO/TmPyPB/CsF/Al), however the hole injection layer (PEDOT:PSS) was rubbed uniaxially with a dust-free cloth after annealing to provide an aligned substrate for the emissive layer, which was subsequently coated on top and annealed at 100 °C, a tempterature at which the complex is in the Col_h phase. The emission of the device was then characterised and the polarisation investigated by measuring the emission in both parallel and perpendicular directions.

Unfortunately, neither complex showed polarised emission in the doped devices, as the brightness observed in both parallel and perpendicular configurations was equal, *i.e.* the devices showed a dichroic ratio of 1, where the dichroic ratio is defined as $E_{\parallel}/E_{\perp}$ and E is electroluminescence intensity (Figure 4-53).

While the lack of polarisation may arise from the intrinsic properties of the complexes, it is also possible that no alignment can be gained at such a low molecular concentration within the emissive layer of the device, hence the fabrication and attempted alignment of devices with higher emitter concentration and non-doped devices, as outlined below.

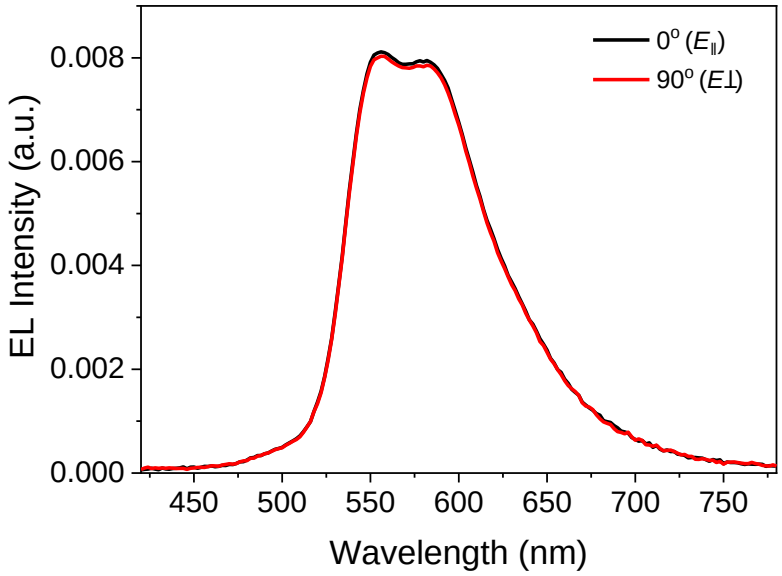

Figure 4-53: Electoluminescence spectra of **6-8** at 0° ($E_{\parallel}$, black) and 90° ($E_{\perp}$, red), showing the same intensity, and thus lack of polarised emission.

When the emitter concentration was increased to 25 wt%, a very slight polarisation was observed, with a polarisation ratio, R, of 1.04 (Figure 4-54), however, the device efficiency was severely compromised, as may be expected given the optimised device function more effectively with a very low concentration of emissive centres (5 wt%) as discussed above, with an EQE of 1.6%.

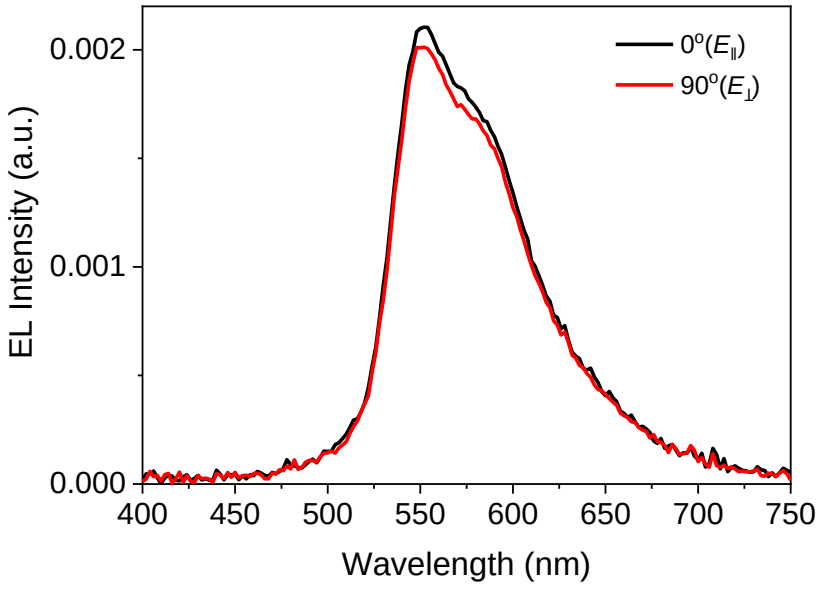

Figure 4-54: Electoluminescence spectra of **6-8** at 0° ($E_{\parallel}$, black) and 90° ($E_{\perp}$, red), showing a slight decrease in emission intensity at 0°, indicating a very small amount of polarisation.

For non-doped devices, *i.e.* those with a neat film of **6-8** as the emissive layer, no emission was detected from the device at all. Film formation of the complex was poor, and aggregation of the molecules was observed through a visible colour change of the layer from green to red upon

standing after a few minutes. The result of this was an increased presence of triplet-triplet annihilation self-quenching processes and a loss of emission.

Aggregation processes can be combatted through the use of bulky substituents to provide steric hindrance, and indeed this technique has been used successfully in similar complexes.[80-86] However, these groups reduce the anisotropy of the complexes, and would almost certainly result in the loss of any liquid-crystalline behaviour.

The observation of no or poor polarisation for these complexes illustrates the difficulty in achieving polarised emission for materials which show columnar mesophases in comparison to calamitic metallomesogens due to the direction of the unique axis of the molecules, which is perpendicular to the substrate.

4.6 Conclusions

A thorough account of the photophysical properties of the series of gold(III) alkynyl complexes introduced in Chapter 3 has been outlined, both those with fully hydrocarbon alkoxy functionalisation and those with semi-perfluorinated chains. The emission energy of the complexes was fully dependent on the substitution pattern of the chains on the cyclometallating ligand and was independent of the number and nature of chains on the alkynyl ligand. Complexes with two-chains on the cyclometallating ligand, **1-H** to **4-8** and **11-8** to **13-8** showed emission in the green region of the spectrum, with quantum yields in the 1-2% range, whilst appendage of two further chains to this ligand to give species **5-H** to **8-8** and **14-8** to **16-8** resulted in a red-shift of approximately 50 nm and an order of magnitude increase in the quantum yield to up to 34%, as the inclusion of two electron-donating substituents reduced the energy of the triplet excited state and increased the gap to potentially deactivating *d-d* states.

Interestingly, other quantifiable characteristics of emission, namely the photoluminescence quantum yield and lifetime of emission, were dependent on these alterations within a series, showing up to a 12% change in quantum yield and 90 μs change in lifetime upon addition of further substituents, and up to a 20% difference in quantum yield and a 98 μs change in lifetime when changing hydrocarbon to fluorocarbon chains. These changes were ascribed to solvation effects and protection of the emissive core of the molecules through extension of the peripheral alkoxy functionalisation, as well as extended shielding of the core and reduction in deactivating vibrational pathways through the introduction of fluorination to the complex.

That the simple molecular alteration of the addition of two alkoxy groups to the C^N^C has such a substantial effect on the quantum yield and lifetime is remarkable and indicates that simple functional group alterations can have significant effects of the photophysical properties of complexes such as these. Previously, large alterations to molecular structure have been required to invoke such a change, for example, through the inclusion of fluorene moieties on the C^N^C to give excellent PLQYs of up to 58%[32] or tuning of the alkynyl ligands with further functionalities such as amines to change the origin of the emission from ^{3}IL [$\pi \rightarrow \pi^*$(C^N^C)] to ^{3}LLCT from the alkynyl ligand to the C^N^C ligand.[10, 19, 21, 22, 26, 80] Although not of the magnitude of the aforementioned 58% PLQY, the observation of quantum yields in the 25-35% range with so few structural changes is impressive, especially considering the many potential deactivation pathways due to the presence of a high number of flexible alkoxy chains.

It is clear that while the emission characteristics for these novel liquid-crystalline gold(III) complexes are competitive, they do not represent the state of the art in terms of the most efficient or impressive phosphorescence. However, taking the lead from the increasing literature library for

related compounds as outlined in Section 4.1.1, it would be possible to modify either the cyclometallating ligand or the alkynyl ligand, or both, to tune the emission of these systems whilst retaining a suitable core molecular geometry on which to append the necessary flexible peripheral substituents for liquid-crystallinity. It may also be possible to do this and invoke TADF as an emission pathway by modelling the core structure on that reported by Zhou *et al.*[19] and To *et al.*,[20] although this would be non-trivial due to the rigidity and spacing typically required for TADF in which bulky functional groups tend to be used, which are difficult to incorporate into liquid-crystalline materials, in which anisotropy is obviously necessary. Additionally, facile modification of the dendrimeric species reported by Yam and colleagues[22-24] may also induce liquid-crystallinity with retention of the emissive properties.

It is important to note that the strong emission displayed by these complexes marks the first liquid-crystalline complexes of phosphorescent gold(III) alkynyl complexes and thus makes them interesting novel multi-functional materials, from both the standpoint of advancing the understanding behind metallomesogens, and applications of multifunctional materials in optoelectronic devices.

The moderate-to-good performance of the complexes in doped OLED devices is promising; the performance does not reach that of the literature complexes showing the highest EQE values of 15.3% for solution-processed device,[80] however devices with this level of performance are outliers, with devices based on gold(III) complexes considered to show 'good' performance when the EQE values are in the region of 5% and above. However, these complexes have been designed specifically to impart liquid-crystallinity, whereas those recently reported in the literature have been specifically designed for use in OLED devices, with many complexes utilising groups which would prevent aggregation and reduce the rate of triplet-triplet annihilation. These groups do not tend to be anisotropic, and are therefore not conducive to forming liquid-crystalline materials. This indicates that the devices synthesised for these gold(III) complexes can be considered well performing.

Worth noting is the low doping concentration for the best performing devices, at 5 wt%; this is in contrast to similar literature systems where it is common for the doping concentration to be in excess of 10%.[21, 22, 34, 78, 85] Given the high molecular weight of the complexes, and the low doping concentration, the number of emissive centres in the emissive layer of the device will be comparatively lower, resulting in a smaller overall cost as the percentage of precious metal in the complex is lower than in devices fabricated at high doping concentrations for low molecular weight complexes. This suggests that the fabrication of devices with high molecular weight complexes which appropriately space emissive centres to minimise triplet-triplet annihilation may be favourable and cost-effective in the long term.

The lack of polarised emission, or observation of very slight levels of polarisation, in the doped devices is disappointing but not surprising; unlike in calamitic compounds, the direction of polarizability in a material displaying a columnar mesophase is small and perpendicular to the axis of the column. It is therefore more difficult to achieve compatible alignment, hence why the majority of reports of polarised emission from metallomesogens arise from calamitic complexes.[89-95, 97, 100] The singular report of a columnar metallomesogens showing polarised emission was doped in a nematic host.[98, 99] Thus it is proposed that the doping of these gold(III) complexes within a nematic host, may induce polarised emission.

These novel gold(III) alkynyl complexes show impressive photophysical properties which can be substantially modulated through the substitution pattern of the alkoxy chains on the alkynyl ligand, and further tuned through the number and nature of substituents on the alkynyl ligand. Their application as emissive dopants in OLED devices is highly promising, demonstrating the promise of potential applications of multifunctional, emissive metallomesogens.

4.7 References

1. D. Li, X. Hong, C.-M. Che, W.-C. Lo and S.-M. Peng, *J. Chem. Soc., Dalton Trans.*, 1993, 2929-2932.
2. T. E. Müller, S. W.-K. Choi, D. M. P. Mingos, D. Murphy, D. J. Williams and V. Wing-Wah Yam, *J. Organomet. Chem.*, 1994, **484**, 209-224.
3. W. Lu, H.-F. Xiang, N. Zhu and C.-M. Che, *Organometallics*, 2002, **21**, 2343-2346.
4. C.-M. Che, H.-Y. Chao, V. M. Miskowski, Y. Li and K.-K. Cheung, *J. Am. Chem. Soc.*, 2001, **123**, 4985-4991.
5. V. W.-W. Yam, S. W.-K. Choi and K.-K. Cheung, *Organometallics*, 1996, **15**, 1734-1739.
6. X.-X. Lu, C.-K. Li, E. C.-C. Cheng, N. Zhu and V. W.-W. Yam, *Inorg. Chem.*, 2004, **43**, 2225-2227.
7. V. W.-W. Yam, S.-K. Yip, L.-H. Yuan, K.-L. Cheung, N. Zhu and K.-K. Cheung, *Organometallics*, 2003, **22**, 2630-2637.
8. S.-K. Yip, E. C.-C. Cheng, L.-H. Yuan, N. Zhu and V. W.-W. Yam, *Angew. Chem. Int. Ed.*, 2004, **43**, 4954-4957.
9. V. W.-W. Yam, K. Kam-Wing Lo and K. Man-Chung Wong, *J. Organomet. Chem.*, 1999, **578**, 3-30.
10. K. M.-C. Wong, L.-L. Hung, W. H. Lam, N. Zhu and V. W.-W. Yam, *J. Am. Chem. Soc.*, 2007, **129**, 4350-4365.
11. C.-W. Chan, W.-T. Wong and C.-M. Che, *Inorg. Chem.*, 1994, **33**, 1266-1272.
12. H.-Q. Liu, T.-C. Cheung, S.-M. Peng and C.-M. Che, *J. Chem. Soc., Chem. Commun.*, 1995, 1787-1788.
13. V. W.-W. Yam, S. W.-K. Choi, T.-F. Lai and W.-K. Lee, *J. Chem. Soc., Dalton Trans.*, 1993, 1001-1002.
14. K.-H. Wong, K.-K. Cheung, M. C.-W. Chan and C.-M. Che, *Organometallics*, 1998, **17**, 3505-3511.
15. V. W.-W. Yam, K. M.-C. Wong, L.-L. Hung and N. Zhu, *Angew. Chem. Int. Ed.*, 2005, **44**, 3107-3110.
16. V. K.-M. Au, N. Zhu and V. W.-W. Yam, *Inorg. Chem.*, 2013, **52**, 558-567.
17. K.-C. Yim, V. K.-M. Au, K. M.-C. Wong and V. W.-W. Yam, *Chem. Eur. J.*, 2017, **23**, 5772-5786.
18. M.-C. Tang, M.-Y. Leung, S.-L. Lai, M. Ng, M.-Y. Chan and V. Wing-Wah Yam, *J. Am. Chem. Soc.*, 2018, **140**, 13115-13124.
19. D. Zhou, W.-P. To, Y. Kwak, Y. Cho, G. Cheng, G. S. M. Tong and C.-M. Che, *Adv. Sci*, 2019, **0**, 1802297.
20. W.-P. To, D. Zhou, G. S. M. Tong, G. Cheng, C. Yang and C.-M. Che, *Angew. Chem. Int. Ed.*, 2017, **56**, 14036-14041.
21. V. K.-M. Au, K. M.-C. Wong, D. P.-K. Tsang, M.-Y. Chan, N. Zhu and V. W.-W. Yam, *J. Am. Chem. Soc.*, 2010, **132**, 14273-14278.
22. M.-C. Tang, C. K.-M. Chan, D. P.-K. Tsang, Y.-C. Wong, M. M.-Y. Chan, K. M.-C. Wong and V. W.-W. Yam, *Chem. Eur. J.*, 2014, **20**, 15233-15241.
23. M.-C. Tang, D. P.-K. Tsang, M. M.-Y. Chan, K. M.-C. Wong and V. W.-W. Yam, *Angew. Chem. Int. Ed.*, 2013, **52**, 446-449.
24. C.-H. Lee, M.-C. Tang, Y.-C. Wong, M.-Y. Chan and V. W.-W. Yam, *J. Am. Chem. Soc.*, 2017, **139**, 10539-10550.
25. V. K.-M. Au, D. P.-K. Tsang, K. M.-C. Wong, M.-Y. Chan, N. Zhu and V. W.-W. Yam, *Inorg. Chem.*, 2013, **52**, 12713-12725.
26. V. K.-M. Au, D. P.-K. Tsang, Y.-C. Wong, M.-Y. Chan and V. W.-W. Yam, *J. Organomet. Chem.*, 2015, **792**, 109-116.
27. F. Mendizabal and P. Pyykkö, *PCCP*, 2004, **6**, 900-905.
28. H. Schmidbaur, *Gold Bulletin*, 2000, **33**, 3-10.

29. K.-C. Yim, E. S.-H. Lam, K. M.-C. Wong, V. K.-M. Au, C.-C. Ko, W. H. Lam and V. W.-W. Yam, *Chem. Eur. J.*, 2014, **20**, 9930-9939.
30. S. K.-L. Siu, C. Po, K.-C. Yim, V. K.-M. Au and V. W.-W. Yam, *CrystEngComm*, 2015, **17**, 8153-8162.
31. K. T. Chan, G. S. M. Tong, W.-P. To, C. Yang, L. Du, D. L. Phillips and C.-M. Che, *Chem. Sci*, 2017, **8**, 2352-2364.
32. W.-P. To, K. T. Chan, G. S. M. Tong, C. Ma, W.-M. Kwok, X. Guan, K.-H. Low and C.-M. Che, *Angew. Chem. Int. Ed.*, 2013, **52**, 6648-6652.
33. K.-C. Yim, V. K.-M. Au, L.-L. Hung, K. M.-C. Wong and V. W.-W. Yam, *Chem. Eur. J.*, 2016, **22**, 16258-16270.
34. B. Y.-W. Wong, H.-L. Wong, Y.-C. Wong, M.-Y. Chan and V. W.-W. Yam, *Angew. Chem. Int. Ed.*, 2017, **56**, 302-305.
35. V. K.-M. Au, D. Wu and V. W.-W. Yam, *J. Am. Chem. Soc.*, 2015, **137**, 4654-4657.
36. E. Y.-H. Hong, C.-T. Poon and V. W.-W. Yam, *J. Am. Chem. Soc.*, 2016, **138**, 6368-6371.
37. S. K.-L. Siu, C. Y.-S. Chung and V. W.-W. Yam, *J. Organomet. Chem.*, 2017, **845**, 177-188.
38. V. K.-M. Au, K. M.-C. Wong, N. Zhu and V. W.-W. Yam, *J. Am. Chem. Soc.*, 2009, **131**, 9076-9085.
39. I. Chambrier, L. Rocchigiani, D. L. Hughes, P. M. H. Budzelaar and M. Bochmann, *Chem. Eur. J.*, 2018, **24**, 11467-11474.
40. A. Pintus and M. Bochmann, *RSC Adv.*, 2018, **8**, 2795-2803.
41. A. Pintus, L. Rocchigiani, J. Fernandez-Cestau, P. H. M. Budzelaar and M. Bochmann, *Angew. Chem. Int. Ed.*, 2016, **128**, 12509-12512.
42. L. Rocchigiani, P. H. M. Budzelaar and M. Bochmann, *Chem. Sci*, 2019, **10**, 2633-2642.
43. L. Rocchigiani, J. Fernandez-Cestau, G. Agonigi, I. Chambrier, P. H. M. Budzelaar and M. Bochmann, *Angew. Chem. Int. Ed.*, 2017, **56**, 13861-13865.
44. L. Rocchigiani, J. Fernandez-Cestau, P. H. M. Budzelaar and M. Bochmann, *Chem. Eur. J.*, 2018, **24**, 8893-8903.
45. L. Rocchigiani, J. Fernandez-Cestau, I. Chambrier, P. Hrobárik and M. Bochmann, *J. Am. Chem. Soc.*, 2018, **140**, 8287-8302.
46. D.-A. Roşca, J. Fernandez-Cestau, J. Morris, J. A. Wright and M. Bochmann, *Sci. Adv.*, 2015, **1**, e1500761.
47. D.-A. Roşca, J. Fernandez-Cestau, A. S. Romanov and M. Bochmann, *J. Organomet. Chem.*, 2015, **792**, 117-122.
48. N. Savjani, D.-A. Roşca, M. Schormann and M. Bochmann, *Angew. Chem. Int. Ed.*, 2013, **52**, 874-877.
49. D. A. Smith, D.-A. Roşca and M. Bochmann, *Organometallics*, 2012, **31**, 5998-6000.
50. W.-P. To, G. S.-M. Tong, W. Lu, C. Ma, J. Liu, A. L.-F. Chow and C.-M. Che, *Angew. Chem. Int. Ed.*, 2012, **51**, 2654-2657.
51. L. Gregori, D. Sorbelli, L. Belpassi, F. Tarantelli and P. Belanzoni, *Inorg. Chem.*, 2019, **58**, 3115-3129.
52. G. S. Ming Tong, K. T. Chan, X. Chang and C.-M. Che, *Chem. Sci*, 2015, **6**, 3026-3037.
53. B. Bertrand, M. R. M. Williams and M. Bochmann, *Chem. Eur. J.*, 2018, **24**, 11840-11851.
54. B. Bertrand, M. A. O'Connell, Z. A. E. Waller and M. Bochmann, *Chem. Eur. J.*, 2018, **24**, 3613-3622.
55. M. R. M. Williams, B. Bertrand, J. Fernandez-Cestau, Z. A. E. Waller, M. A. O'Connell, M. Searcey and M. Bochmann, *Dalton Trans.*, 2018, **47**, 13523-13534.
56. B. Bertrand, J. Fernandez-Cestau, J. Angulo, M. M. D. Cominetti, Z. A. E. Waller, M. Searcey, M. A. O'Connell and M. Bochmann, *Inorg. Chem.*, 2017, **56**, 5728-5740.
57. M. Williams, A. I. Green, J. Fernandez-Cestau, D. L. Hughes, M. A. O'Connell, M. Searcey, B. Bertrand and M. Bochmann, *Dalton Trans.*, 2017, **46**, 13397-13408.
58. F. Wang, M. Lan, W.-P. To, K. Li, C.-N. Lok, P. Wang and C.-M. Che, *Chem. Commun.*, 2016, **52**, 13273-13276.
59. J. Fernandez-Cestau, B. t. Bertrand, A. Pintus and M. Bochmann, *Organometallics*, 2017, **36**, 3304-3312.

60. J. L.-L. Tsai, A. O.-Y. Chan and C.-M. Che, *Chem. Commun.*, 2015, **51**, 8547-8550.
61. T. Zou, C. T. Lum, C.-N. Lok, J.-J. Zhang and C.-M. Che, *Chem. Soc. Rev.*, 2015, **44**, 8786-8801.
62. J. J. Yan, A. L.-F. Chow, C.-H. Leung, R. W.-Y. Sun, D.-L. Ma and C.-M. Che, *Chem. Commun.*, 2010, **46**, 3893-3895.
63. S. Castelli, O. Vassallo, P. Katkar, C.-M. Che, R. W.-Y. Sun and A. Desideri, *Arch. Biochem. Biophys.*, 2011, **516**, 108-112.
64. C. K.-L. Li, R. W.-Y. Sun, S. C.-F. Kui, N. Zhu and C.-M. Che, *Chem. Eur. J.*, 2006, **12**, 5253-5266.
65. Q. Wan, J. Xia, W. Lu, J. Yang and C.-M. Che, *J. Am. Chem. Soc.*, 2019, **141**, 11572-11582.
66. J. Fernandez-Cestau, R. J. Rama, L. Rocchigiani, B. t. Bertrand, E. Lalinde, M. Linnolahti and M. Bochmann, *Inorg. Chem.*, 2019, **58**, 2020-2030.
67. D.-A. Roşca, D. A. Smith and M. Bochmann, *Chem. Commun.*, 2012, **48**, 7247-7249.
68. J. Fernandez-Cestau, B. Bertrand, M. Blaya, G. A. Jones, T. J. Penfold and M. Bochmann, *Chem. Commun.*, 2015, **51**, 16629-16632.
69. W.-P. To, G. S. M. Tong, C.-W. Cheung, C. Yang, D. Zhou and C.-M. Che, *Inorg. Chem.*, 2017, **56**, 5046-5059.
70. C.-Y. Sun, W.-P. To, X.-L. Wang, K.-T. Chan, Z.-M. Su and C.-M. Che, *Chem. Sci*, 2015, **6**, 7105-7111.
71. M. Bachmann, R. Fessler, O. Blacque and K. Venkatesan, *Dalton Trans.*, 2019, **48**, 7320-7330.
72. R. Kumar and C. Nevado, *Angew. Chem. Int. Ed.*, 2017, **56**, 1994-2015.
73. L. Duan, L. Hou, T.-W. Lee, J. Qiao, D. Zhang, G. Dong, L. Wang and Y. Qiu, *J. Mater. Chem.*, 2010, **20**, 6392-6407.
74. J. M. Lupton, I. D. W. Samuel, R. Beavington, M. J. Frampton, P. L. Burn and H. Bässler, *Physical Review B*, 2001, **63**, 155206.
75. J. P. J. Markham, I. D. W. Samuel, S.-C. Lo, P. L. Burn, M. Weiter and H. Bässler, *J. Appl. Phys.*, 2003, **95**, 438-445.
76. J. Li and D. Liu, *J. Mater. Chem.*, 2009, **19**, 7584-7591.
77. M.-C. Tang, D. P.-K. Tsang, M.-Y. Chan, K. M.-C. Wong and V. W.-W. Yam, *Mater. Chem. Front.*, 2017, **1**, 2559-2568.
78. M.-C. Tang, D. P.-K. Tsang, Y.-C. Wong, M.-Y. Chan, K. M.-C. Wong and V. W.-W. Yam, *J. Am. Chem. Soc.*, 2014, **136**, 17861-17868.
79. C. Murawski, K. Leo and M. C. Gather, *Adv. Mater.*, 2013, **25**, 6801-6827.
80. C.-H. Lee, M.-C. Tang, W.-L. Cheung, S.-L. Lai, M.-Y. Chan and V. W.-W. Yam, *Chem. Sci*, 2018, **9**, 6228-6232.
81. M.-C. Tang, C.-H. Lee, M. Ng, Y.-C. Wong, M.-Y. Chan and V. W.-W. Yam, *Angew. Chem. Int. Ed.*, 2018, **57**, 5463-5466.
82. W.-L. Cheung, S.-L. Lai, M.-C. Tang, C.-H. Lee, M.-Y. Chan and V. W.-W. Yam, *J. Mat. Chem. C*, 2019, **7**, 8457-8464.
83. G. Cheng, K. T. Chan, W.-P. To and C.-M. Che, *Adv. Mater.*, 2014, **26**, 2540-2546.
84. M.-C. Tang, W.-K. Kwok, S.-L. Lai, W.-L. Cheung, M.-Y. Chan and V. Wing-Wah Yam, *Chem. Sci*, 2019, **10**, 594-605.
85. M.-C. Tang, C.-H. Lee, S.-L. Lai, M. Ng, M.-Y. Chan and V. W.-W. Yam, *J. Am. Chem. Soc.*, 2017, **139**, 9341-9349.
86. L.-K. Li, M.-C. Tang, S.-L. Lai, M. Ng, W.-K. Kwok, M.-Y. Chan and V. W.-W. Yam, *Nature Photonics*, 2019, **13**, 185-191.
87. M. Godumala, S. Choi, M. J. Cho and D. H. Choi, *J. Mat. Chem. C*, 2019, **7**, 2172-2198.
88. T. Huang, W. Jiang and L. Duan, *J. Mat. Chem. C*, 2018, **6**, 5577-5596.
89. S. Zhang, K. Luo, H. Geng, H. Ni, H. Wang and Q. Li, *Dalton Trans.*, 2017, **46**, 899-906.
90. H. Geng, K. Luo, G. Zou, L. Zhao, H. Wang, Q. Li and H. Ni, *Dyes Pigments*, 2018, **149**, 82-91.
91. Y. Wang, Y. Liu, J. Luo, H. Qi, X. Li, M. Nin, M. Liu, D. Shi, W. Zhu and Y. Cao, *Dalton Trans.*, 2011, **40**, 5046-5051.
92. G. Zou, K. Luo, L. Zhao, H. Ni, H. Wang and Q. Li, *Liq. Cryst.*, 2018, **45**, 593-606.

93. S. P. Jiang, K. J. Luo, Y. H. Wang, X. Wang, Y. Jiang and Y. Y. Wei, *Chin. Chem. Lett.*, 2011, **22**, 1005-1008.
94. Á. Díez, S. J. Cowling and D. W. Bruce, *Chem. Commun.*, 2012, **48**, 10298-10300.
95. Y. Wang, Q. Chen, Y. Li, Y. Liu, H. Tan, J. Yu, M. Zhu, H. Wu, W. Zhu and Y. Cao, *J. Phys. Chem. C*, 2012, **116**, 5908-5914.
96. Y. Wang, J. Fan, J. Shi, H. Qi, E. Baranoff, G. Xie, Q. Li, H. Tan, Y. Liu and W. Zhu, *Dyes Pigments*, 2016, **133**, 238-247.
97. X. Yang, X. Wu, D. Zhou, J. Yu, G. Xie, D. W. Bruce and Y. Wang, *Dalton Trans.*, 2018, **47**, 13368-13377.
98. C.-T. Liao, H.-H. Chen, H.-F. Hsu, A. Poloek, H.-H. Yeh, Y. Chi, K.-W. Wang, C.-H. Lai, G.-H. Lee, C.-W. Shih and P.-T. Chou, *Chemistry – A European Journal*, 2011, **17**, 546-556.
99. S.-H. Liu, M.-S. Lin, L.-Y. Chen, Y.-H. Hong, C.-H. Tsai, C.-C. Wu, A. Poloek, Y. Chi, C.-A. Chen, S. H. Chen and H.-F. Hsu, *Org. Electron.*, 2011, **12**, 15-21.
100. X. Wu, G. Xie, C. P. Cabry, X. Xu, S. J. Cowling, D. W. Bruce, W. Zhu, E. Baranoff and Y. Wang, *J. Mat. Chem. C*, 2018, **6**, 3298-3309.
101. Y. Wang, C. P. Cabry, M. Xiao, L. Male, S. J. Cowling, D. W. Bruce, J. Shi, W. Zhu and E. Baranoff, *Chemistry – A European Journal*, 2016, **22**, 1618-1621.
102. K. M.-C. Wong, X. Zhu, L.-L. Hung, N. Zhu, V. W.-W. Yam and H.-S. Kwok, *Chem. Commun.*, 2005, **1**, 2906-2908.
103. A. J. Lees, *Comments Inorg. Chem.*, 1995, **17**, 319-346.
104. L. Gu, H. Shi, L. Bian, M. Gu, K. Ling, X. Wang, H. Ma, S. Cai, W. Ning, L. Fu, H. Wang, S. Wang, Y. Gao, W. Yao, F. Huo, Y. Tao, Z. An, X. Liu and W. Huang, *Nature Photonics*, 2019, **13**, 406-411.
105. S. Xu, R. Chen, C. Zheng and W. Huang, *Adv. Mater.*, 2016, **28**, 9920-9940.
106. Y. Su, S. Z. F. Phua, Y. Li, X. Zhou, D. Jana, G. Liu, W. Q. Lim, W. K. Ong, C. Yang and Y. Zhao, *Science Advances*, 2018, **4**, eaas9732.
107. M. P. Coogan, V. Fernández-Moreira, J. B. Hess, S. J. A. Pope and C. Williams, *New J. Chem.*, 2009, **33**, 1094-1099.
108. B. Scott, in *Infrared Spectroscopy: Fundamentals and Applications*, ed. D. J. S. Ando, B. H., 2005, pp. 71-93.
109. L. Pan, B. Hu, X. Zhu, X. Chen, J. Shang, H. Tan, W. Xue, Y. Zhu, G. Liu and R.-W. Li, *J. Mat. Chem. C*, 2013, **1**, 4556-4564.
110. Y. Wang, J. Shi, J. Chen, W. Zhu and E. Baranoff, *J. Mat. Chem. C*, 2015, **3**, 7993-8005.
111. T. Smith and J. Guild, *Transactions of the Optical Society*, 1931, **33**, 73-134.

Chapter 5: Summary, Conclusions and Future Work

The research presented in this thesis was the result of thorough investigations into the synthesis and characterisation of liquid-crystalline, emissive complexes of platinum(IV) and gold(III).

The discovery of a novel, one-pot procedure to synthesise **Pt-1** is promising, especially given the recent investigation into similar small, *bis*-cyclometallated platinum(IV) complexes for applications in OLED devices.[1-7] While this procedure proved to be unsuitable in the preparation of complexes where the ligand had extended alkoxy functionality due to issues of solubility, as seen in the synthesis of **Pt-4**, it may prove to be more useful for the synthesis of small phenylpyridine-based complexes as the type reported by Jenkins and Bernhard,[2] and Juliá *et al.*[4-6] which have only been synthesised over two steps at the time of writing (structures of the relevant platinum complexes are shown in Figure 5-1 for ease of reference).

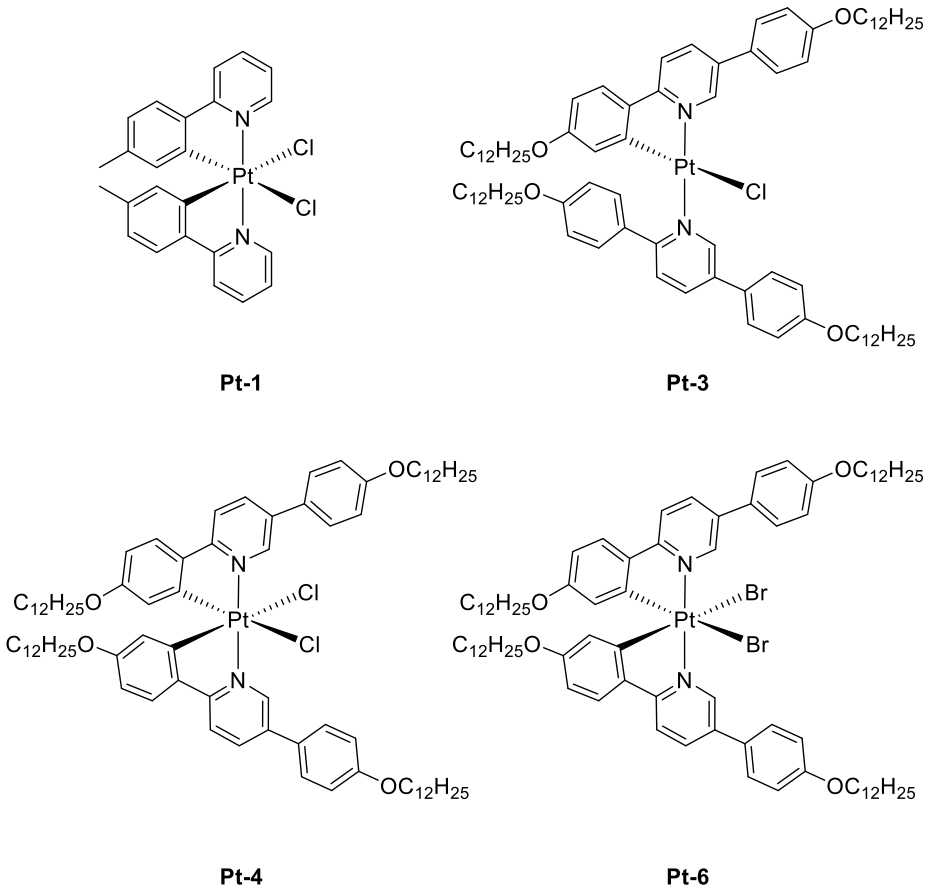

Figure 5-1: Structures of platinum complexes under discussion.

The investigation into the thermal oxidative *ortho*-metallation of **Pt-3** to form **Pt-4** elucidates the mechanism of the oxidation process in those two-step literature systems, indicating that the platinum(II) species is first oxidised to platinum(IV), followed by an *ortho*-metallation to form the

bis-cyclometallated species. This mechanism is proposed to apply to both the purposeful oxidation using hypervalent iodine reagents, such as $PhICl_2$, and the oxidative *ortho*-metallation of **Pt-3** when heated into the isotropic liquid. Also worth noting was the observed formation of multiple isomers of **Pt-4** and the ability of these isomers to undergo a conformational change to preferentially form **Pt-4**. This mechanism was not studied further, but additional research into the conditions required for both the oxidative *ortho*-metallation and isomerisation could prove fruitful.

The lamellar liquid-crystallinity found for the two complexes with alkoxyphenyl functionalised ligands (**Pt-4** and **Pt-6**) is remarkable given the lack of obvious structural anisotropy in the octahedral complexes. The thermal instability of **Pt-4** and **Pt-6** upon transition from the lamellar liquid-crystalline state to the isotropic liquid is disappointing, as it precludes their use in any form of device where the components are required to be stable over long periods of time under a variety of conditions.

However, from an academic standpoint, investigation of the photophysical properties of these complexes proved interesting, with **Pt-1** showing high-energy blue emission and a moderate quantum yield of 7%. The emission was of a lower energy when the cyclometallating ligands were extended in complexes **Pt-4** and **Pt-6**, and there was a slight improvement in the quantum yield. Worth noting is the alteration of the orbitals involved in the emissive processes upon extending the conjugation of the cyclometallating ligands. The change to orbitals that are based purely on the cyclometallating ligands, as opposed to a mixture of the cyclometallating and halogen ligands, indicates that the emissive character can be tuned *via* relatively simple modification of the cyclometallating ligand. The extension of the conjugation also made the emission independent of the nature of the ancillary ligands, with **Pt-4** (*bis*-chloride) and **Pt-6** (*bis*-bromide) showing identical emission, in contrast to literature systems and in **Pt-1** and **Pt-5**, where the halogen ligand has a significant impact of the quantum yield of emission.[5]

The inclusion of further alkoxy chains on the periphery of the cyclometallating ligands would almost certainly alter the character of emission of the complexes, as has been observed for the gold(III) complexes in this thesis (and discussed below). By increasing the level of electron density in the conjugated system through the addition of further electron-donating substituents, the colour of emission can be altered; the extent of this change would be dependent on the effect of the substitution on the energies of the orbitals involved in the emissive process. This energy difference could be calculated through TD-DFT calculations to support experimental data. The effect of such changes on the quantum yield and lifetime of emission cannot be predicted at this time, as the radiative and non-radiative rate constants which govern these properties are dependent on many deactivation pathways that may not be immediately apparent. The emission

could also be altered through the use of non-alkoxy-based electron-donating substituents, such as NR_2 or OH, as well as electron-withdrawing substituents, such as CF_3 or CN, as these would all have an effect on the energy of the orbitals involved in emission.

For the platinum(IV) complexes **Pt-1**, **Pt-4**, **Pt-5** and **Pt-6**, the lifetime of emission is substantially longer than would be ideal for use in OLED devices, in which a shorter lifetime of approximately 1 μs is desired. Therefore, a relatively simple structural modification or ligand substitution as described above which may yield more desirable emission characteristics would be worth pursuing. This would be of heightened interest if the stability of the complexes could be improved through the same modifications.

It has been shown that for complexes of this molecular geometry, *i.e.* octahedral metal complexes with two heavily functionalised cyclometallating ligands,[8] that small changes in functionalisation of the cyclometallating ligand can drastically change the liquid-crystalline properties of the complexes, as well as their thermal stability. This is also true of small changes to ancillary ligands. This suggests that similar structural modifications to complexes **Pt-4** and **Pt-6** may yield increases in stability, which would no longer preclude them from incorporation into OLED architectures, which is the target application for complexes of this nature. The potential alteration of the liquid-crystalline properties of the complexes is also worth investigation, with the potential to display columnar phases (based on the observations for structurally similar iridium(III) complexes) and even room-temperature mesomorphism.

The most obvious and prominent line of enquiry must be the pursuit of ligand modification to simultaneously alter the liquid-crystalline and photophysical properties. The proposed progression of investigation would be to sequentially increase the number of alkoxy chains per ligand from two to six; the syntheses of these ligands are well known through the work of Santoro *et al*.[8-10] The addition to the canon of octahedral metallomesogens that do not conform to the strategies traditionally used to induce liquid-crystallinity (the use of one highly anisotropic ligand with small ancillary ligands or the use of many highly functionalised ligands to shield the metal centre) would be a worthy contribution. Subsequent to this, and dependent upon the outcome and validity of those hypothetical complexes, the ancillary ligands should also be changed to investigate the effects on mesomorphism, photophysics and stability. This experimental work would need to be supported by computational calculations, through which an understanding of the changing orbitals involved in the emissive processes should be probed. The fabrication of a device with a (potentially) stable analogue of these complexes would also be an interesting experiment when considering the potential of these systems to show polarised emission when used as the emitter in an aligned layer in an OLED device.

In addition to these platinum(IV) complexes, an extensive series of gold(III) complexes with C^N^C cyclometallating ligands and a phenylalkynyl ligand, both functionalised by varying levels of extended alkoxy chains, have been synthesised, giving highly stable species which were fully characterised in terms of both analytical and materials properties (structures shown in Figure 5-2 for ease of reference). The self-organisation behaviour of these complexes was rich, with many complexes showing not only well-defined mesomorphism, but also concentration-dependent aggregation and gelation properties.

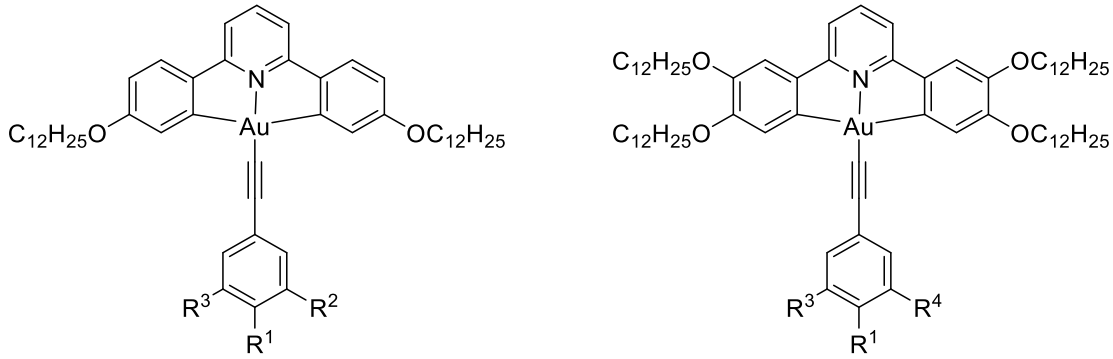

1-*n* R^1 = H, C_5H_{11}, C_8H_{17}; $R^2 = R^3$ = H
2-*n* $R^1 = OC_nH_{2n+1}$; $R^2 = R^3$ = H
3-*n* $R^1 = R^2 = OC_nH_{2n+1}$; R^3 = H
4-*n* $R^1 = R^2 = R^3 = OC_nH_{2n+1}$

5-*n* R^1 = H, C_5H_{11}, C_8H_{17}; $R^2 = R^3$ = H
6-*n* $R^1 = OC_nH_{2n+1}$; $R^2 = R^3$ = H
7-*n* $R^1 = R^2 = OC_nH_{2n+1}$; R^3 = H
8-*n* $R^1 = R^2 = R^3 = OC_nH_{2n+1}$

Figure 5-2: Structures of gold(III) alkynyl complexes **1-*n*** to **8-*n***. *n* = 8, 10, 12, 14

The dominance of columnar mesophases for these gold(III) complexes (**1-*n*** to **8-*n***) is unsurprising given the disc-like geometry of the majority of species. In series **1-*n*** to **4-*n***, having two chains on the cyclometallating ligand resulted in a half-disc geometry, in which two complexes arranged in an anti-parallel arrangement to form a coherent column within the mesophase. With more intense functionalisation, *i.e.* in complexes **5-*n*** to **8-*n***, the incorporation of four dodecyloxy chains on the C^N^C backbone resulted in a full-disc geometry in which the discoid shape was satisfied purely by one molecule. The increase in the stability between the two organisational modes was striking, with clearing points for the four chain species significantly higher, often as much as 100 °C: the more disc-like the constituent complex, the more stable the phase.

Tuning of the liquid-crystallinity of these species was predominantly achieved through the modification of the alkynyl ligand, both in terms of the number of appended alkoxy chains (from one to three) and the length of these chains. Modifications such as these are unexplored in the literature for *bis*-cyclometallated, square-planar metallomesogens, where the majority of structural alteration has occurred through the functionalisation of the pincer ligand, typically a platinum(II) species with an N^C^N ligand.[11-13] Alteration of the alkynyl ligand in these gold(III)

complexes resulted in a range of phases, including Col_h, Col_r and lamellar phases, with number and length of chain contributing to the effectiveness of space-filling and therefore the effectiveness of column formation.

While the presence of two or four chains on the C^N^C pincer ligand had a pronounced effect on the mesomorphism of the complexes, it also had a significant influence on the photophysical properties. Conversely, while the liquid-crystallinity of the complexes was highly dependent on the functionalisation of the alkynyl ligand, this played a very small role in the variation of emissive behaviour.

In comparison to the platinum(IV) complexes detailed in Chapter 2, the thermally stable gold(III) alkynyl complexes were such more suited to incorporation as the emitter in an OLED device. The lifetimes of emission (in solution) for complexes with two chains on the cyclometallating ligand were all under 13 μs, which reduces the rate of triplet-triplet annihilation in a doped device matrix, although the quantum yields were poor. For the analogous four-chain complexes, the quantum yields were substantially higher, as much as 25%, although the lifetimes of emission ranged up to the hundreds of microseconds. The addition of two further alkoxy substituents to the pincer ligand resulted in a red-shift of approximately 50 nm in addition to the previously outlined changes. This was a result of a reduction in energy of the triplet excited state, lowering the energy of emission and increasing the energy gap between the emissive state and the deactivating *d-d* states.

Many of these complexes were utilised as emitters in proof-of-concept OLED devices fabricated in order to investigate general device performance and the ability of these devices to show polarised emission. The devices functioned well when the gold(III) complexes were included as dopants in a polymer host matrix, with devices becoming less efficient as the concentration of emissive complex was increased; indeed emission was quenched entirely when the complexes were used as the neat emissive layer. Interestingly, there was no significant difference in device performance between complexes with two chains and those with four chains, which was in great contrast to the solution phase measurements.

Significant effort was expended to synthesise semi-perfluorinated analogues of the above gold(III) complexes, exchanging the fully hydrocarbon alkoxy chains on the alkynyl ligand for semi perfluorinated chains (1H,1H,2H,2H-perfluoroalkyoxy chains) (Figure 5-3). The result of this was a new family of potentially amphiphilic emissive metallomesogens whose liquid-crystalline behaviour was influenced by the fluorophobic effect, where the fluorinated chains on the alkynyl ligand and the hydrocarbon chains on the C^N^C ligand were preferentially segregated.

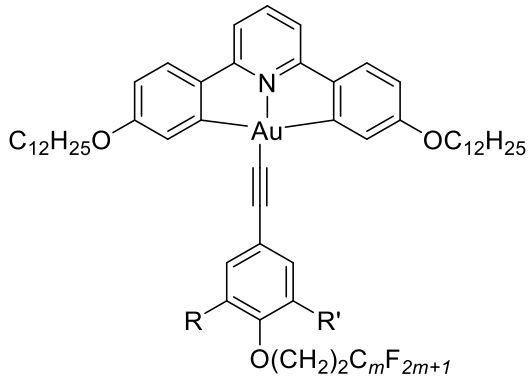

11-*n*: R = R' =H
12-*n*: R = H, R' = $O(CH_2)_2C_mF_{2m+1}$
13-*n*: R = R' = $O(CH_2)_2C_mF_{2m+1}$

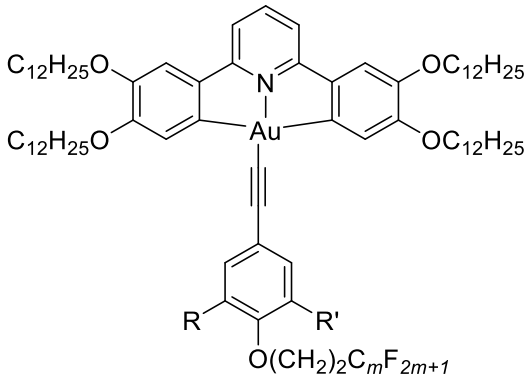

14-*n*: R = R' =H
15-*n*: R = H, R' = $O(CH_2)_2C_mF_{2m+1}$
16-*n*: R = R' = $O(CH_2)_2C_mF_{2m+1}$

Figure 5-3: Structures of semi-perfluorinated gold(III) alkynyl complexes **11-*n*** to **16-*n***. *n* = 8, 10, 12; *m* = 6, 8, 10

The result of this microsegregation was a significant change to the liquid-crystalline properties of the complexes with respect to the hydrocarbon equivalents, including an increase in the observation of Col_r phases. There was also a large impact on the stability of the mesophases formed, with phase destabilisation or even destruction observed when segregation was less favourable (as in the case of **14-*n*** and **13-*n***), and significant phase stabilisation when a favourable conformation was achievable.

Without a doubt the most staggering difference was the observation of a formally re-entrant nematic phase for **15-12** which occurs out of thermodynamic sequence between the Col_r and Col_h phases. This is the first example of a re-entrant nematic phase thought to be induced by amphiphilic frustration driven by the fluorophobic effect and is a very exciting development.

The emission profile of the complexes with semi-perfluorinated chains, in comparison to the fully hydrocarbon parent compounds, did not differ due to the electronic isolation of the fluorinated portions of the chains from the involved orbitals of the aromatic system by two $-CH_2-$ groups; this was expected. However, these chains did have a significant impact on both the solution-phase quantum yield and lifetime of emission values between the two families. This has been attributed to the difference in vibrational deactivation pathways arising from the differences between C−H and C−F bonds, as well as the extent of physical shielding of the metal centre by the chains, as to minimise interaction with both the solvent and neighbouring complexes.

Future research pathways for the gold(III) alkynyl complexes are perhaps not so obvious as for the platinum(IV) complexes. The proposed avenues of future work with respect to these compounds all involve structural modification of the ligand architecture in order to enhance the emissive

properties of the complexes, with a retention or modification of the liquid-crystallinity. Such modifications could include the use of a tetradentate ligand coordination mode, as proposed by Wong *et al.*[14] (shown in Chapter 4, Scheme 4-1), in which the quantum yields of the complexes were significantly increased due to the rigidity of the tetradentate species in comparison to the tridentate species. This may also have a positive impact on the liquid-crystalline properties of the proposed complexes due to the increase in planarity when tetradentate. Quantum yields have also been significantly improved through the use of aryl ligands in place of alkynyl ligands. These are also strongly σ-donating ligands, and therefore allow triplet emission by rendering the metal centre more electron rich and increasing the energy of deactivating *d-d* states. Such ligands have been investigated thoroughly in the work of Che, Yam and others,[15-19] although there have not been any reports of liquid-crystalline species at the time of writing. Complexes with aryl ligands often show higher quantum yields than the equivalent alkynyl complexes due to the reduction in energy of the HOMO, resulting in a reduction of the population of a non-emissive, competing ^{3}LLCT state.[19]

It is clear that more investigation should be carried out to probe the existence of the re-entrant nematic phase of **15-12**. Currently, this complex is the only one to show this phase progression, and therefore the information that can be gleaned with respect to the causes of this behaviour are limited. It is proposed that further complexes should be targeted which could potentially show this phase behaviour. This could be achieved through alteration of the proportion of fluorinated carbon atoms in the chain, or slight modification to the chain lengths of the hydrocarbon chains on the C^N^C ligand. Failing this, mixture studies between **15-12** and other complexes may yield useful information on the formation of the phase and should be performed even if other complexes which show the phase are found. Such studies may also be able to induce the phase in the chosen mixtures. Also of importance is the identification of the phase as a N_{col} or a N_D phase, which may be done by confocal microscopy or by studying the interference colours with reference to the Michel-Lévy chart.

It would be interesting to investigate how the fluorinated complexes perform in an OLED device. From the results of the hydrocarbon species, it is clear that the solution phase measurements are not transferable to the device, and therefore devices would have to be fabricated, as it is difficult to predict how these complexes would perform. Much of the efficiency of the device is due to interactions between emissive centres with each other and with the host matrix. Because of the inherent differences when including the perfluorinated chains, it would be worthwhile investigating what impact this has on the performance of the devices, and whether in this case it would be possible to generate polarised emission.

All outlined future areas of investigation for the work presented in this thesis either include generating data or synthesising complexes which would add to the research, or altering the promising emissive systems from the literature to induce liquid-crystallinity, with the aim of fabricating aligned devices which show efficient, polarised emission. This stepwise, scientific approach is deemed necessary to investigate the viability of this technology. It is obvious that a breakthrough to produce highly efficient emitters, such as those currently based on iridium(III), for platinum(IV) and gold(III) would be needed for these to be competitive with both the current commercial technologies and academic forefront. It cannot be stated at this point whether commercial displays with emissive metallomesogens will ever be state of the art for device technology, but investigating the properties and potential of multi-functional materials such as these is a worthy pursuit in trying to make that goal possible.

5.1 References

1. N. Giménez, E. Lalinde, R. Lara and M. T. Moreno, *Chem. Eur. J.*, 2019, **25**, 5514-5526.
2. D. M. Jenkins and S. Bernhard, *Inorg. Chem.*, 2010, **49**, 11297-11308.
3. F. Julia, D. Bautista, J. M. Fernandez-Hernandez and P. Gonzalez-Herrero, *Chem. Sci.*, 2014, **5**, 1875-1880.
4. F. Juliá, D. Bautista and P. Gonzalez-Herrero, *Chem. Comm.*, 2016, **52**, 1657-1660.
5. F. Juliá, M.-D. García-Legaz, D. Bautista and P. González-Herrero, *Inorg. Chem.*, 2016, **55**, 7647-7660.
6. F. Juliá and P. González-Herrero, *Dalton Trans.*, 2016, **45**, 10599-10608.
7. Á. Vivancos, D. Bautista and P. González-Herrero, *Chem. Eur. J.*, 2019, **25**, 6014-6025.
8. A. Santoro, A. M. Prokhorov, V. N. Kozhevnikov, A. C. Whitwood, B. Donnio, J. A. G. Williams and D. W. Bruce, *J. Am. Chem. Soc.*, 2011, **133**, 5248-5251.
9. A. Santoro, PhD Thesis, University of York, 2010.
10. A. Santoro, A. C. Whitwood, J. A. G. Williams, V. N. Kozhevnikov and D. W. Bruce, *Chem. Mater.*, 2009, **21**, 3871-3882.
11. V. N. Kozhevnikov, B. Donnio and D. W. Bruce, *Angew. Chem. Int. Ed.*, 2008, **47**, 6286-6289.
12. V. N. Kozhevnikov, B. Donnio, B. Heinrich and D. W. Bruce, *Chem. Comm.*, 2014, **50**, 14191-14193.
13. V. N. Kozhevnikov, B. Donnio, B. Heinrich, J. A. G. Williams and D. W. Bruce, *J. Mat. Chem. C.*, 2015, **3**, 10177-10187.
14. B. Y.-W. Wong, H.-L. Wong, Y.-C. Wong, M.-Y. Chan and V. W.-W. Yam, *Angew. Chem. Int. Ed.*, 2017, **56**, 302-305.
15. D.-A. Roşca, D. A. Smith and M. Bochmann, *Chem. Comm.*, 2012, **48**, 7247-7249.
16. M.-C. Tang, W.-K. Kwok, S.-L. Lai, W.-L. Cheung, M.-Y. Chan and V. Wing-Wah Yam, *Chem. Sci.*, 2019, **10**, 594-605.
17. M.-C. Tang, C.-H. Lee, S.-L. Lai, M. Ng, M.-Y. Chan and V. W.-W. Yam, *J. Am. Chem. Soc.*, 2017, **139**, 9341-9349.
18. M.-C. Tang, M.-Y. Leung, S.-L. Lai, M. Ng, M.-Y. Chan and V. Wing-Wah Yam, *J. Am. Chem. Soc.*, 2018, **140**, 13115-13124.
19. W.-P. To, D. Zhou, G. S. M. Tong, G. Cheng, C. Yang and C.-M. Che, *Angew. Chem. Int. Ed.*, 2017, **56**, 14036-14041.

Chapter 6: Experimental

6.1 General Considerations

6.1.1 Synthesis

Unless stated otherwise, reactions were carried out at room temperature under ambient conditions. All reagents were procured through common commercial sources and used without further purification. $PhICl_2$[1] and 2,5-di(4-dodecyloxyphenyl)pyridine[2] were prepared according to established literature procedures.

For any reactions carried out under inert atmosphere conditions, such as the in the coupling reactions to form the final [Au(C^N^C)(C≡CR)] products, dry solvents were used. These were dried in an Innovative Technologies SPS-7 system over alumina columns. Solvents were degassed by sparging with nitrogen or standard drying reagents within the system.

A CEM Discover S-class microwave was used in the synthesis of **Pt-1**.

6.1.2 Analysis

^{1}H NMR spectra were measured on a Jeol ECS400 spectrometer operating at 400 MHz with chemical shifts referred to residual non-deuterated $CHCl_3$ signals. ^{19}F NMR spectra were measured Jeol ECS400 spectrometer operating at 376 MHz. $^{195}Pt\{^{1}H\}$ NMR spectra were measured on Bruker 500 AVANCE II spectrometer operating at 107 MHz.

Concentration dependent ^{1}H and ^{19}F NMR spectra (Chapter 3) were measured on a Bruker 500 AVANCE II spectrometer operating at 500 and 470 MHz, respectively.

Mass spectra (ESI and APCI) were collected on Bruker compact time of flight mass spectrometer; spectra were internally calibrated using sodium formate as the calibrant. Samples were transferred to the spectrometer an Agilent 1260 Infinity LC system.

Cyclic Voltammetry was performed using an EmStat3+. A glassy carbon working electrode and platinum wire counter electrode were used to study solutions containing 1 mM of [Au], where [Au] is the gold complex in question, and 0.1 M NBu_4PF_6 in a CH_2Cl_2 solution. Ferrocene was used as an internal reference. Cyclic voltammetry was performed between +0.7 and -2.5 V for 3 scans at a scan rate of (100 mV s^{-1}).

CHN elemental analysis was carried out using an Exeter Analytical Inc. CE-440 Analyser and Sartorius S2 analytical balance; calibration was performed against acetanilide standards and checked by the use of *S*-benzyl thiouronium chloride as internal standard.

Polarising optical microscopy was carried out using an Olympus BX50 polarizing microscope equipped with a Linkam scientific LTS350 heating stage, Linkam LNP2 cooling pump, and Linkam TMS92 controller, differential scanning calorimetry was performed on a Mettler DSC822^e using Mettler STAR-E software, which was calibrated before use against indium and zinc standards under an atmosphere of dry nitrogen. Small angle X-ray scattering was recorded using a Bruker D8 Discover equipped with a temperature controlled, bored graphite rod furnace, custom built at the University of York. Cu-K_α (λ = 0.154056 nm) radiation was used, generated from a 1 µS microfocus source. Diffraction patterns were recorded on a 2048 × 2048 pixel Bruker VANTEC 500 area detector set at a distance of 121 mm from the sample, allowing simultaneous collection of small angle and wide angle scattering data. Samples were measured in 1 mm capillary tubes in a magnetic field of *ca* 1 T.

The absorption spectra of the complexes were measured in solution in CH_2Cl_2 in 1 cm pathlength quartz cuvettes using a Biotek Instruments XS spectrometer. Emission spectra were recorded using a Jobin Yvon Fluoromax-2 spectrometer equipped with a Hamamatsu R928 photomultiplier tube (PMT). For the measurements at 298 K, the solutions were contained within 1 cm pathlength quartz cuvettes modified for connection to a vacuum line. Degassing was achieved via a minimum of three freeze-pump-thaw cycles whilst connected to the vacuum manifold; final vapour pressure at 77 K was < 5 x 10^{-2} mbar, as monitored using a Pirani gauge. Luminescence quantum yields were determined using aqueous $[Ru(bipy)_3]Cl_2$ as the standard (ϕ = 0.028 in air-equilibrated aqueous solution).[3] Emission spectra at 77 K were recorded in a glass of EPA (= diethyl ether / isopentane / ethanol, 2:2:1 v/v) in 4 mm diameter tubes held within a liquid-nitrogen-cooled quartz dewar. The emission spectrum of complex **Pt-3** in the solid state was recorded by means of an integrating sphere attached to a Jobin Yvon Fluorolog instrument through optical fibres. The powdered sample was contained within a Spectralon holder of 1 cm diameter. The quantum yield was evaluated using a sample of finely powdered $BaSO_4$ as a non-emissive blank. Scattered light at the excitation wavelength for sample and blank was measured using a neutral density filter of O.D. = 2, whilst the emission region was monitored in the absence of the filter. The luminescence lifetimes of the complexes in deoxygenated solution and at 77 K were measured by multi-channel scaling following excitation into the lowest-energy absorption band using a microsecond pulsed xenon lamp or PicoBright pulsed diode laser of appropriate excitation wavelength. The emitted light was detected at 90˚ using a Peltier-cooled R928 PMT after passage through a monochromator. The lifetimes in

air-equilibrated solution (< 10 μs) were measured by time-correlated single photon counting (TCSPC), following excitation at 374 nm with a pulsed laser diode.

Diffraction data were collected at 110 K on an Oxford Diffraction SuperNova dual-source X-ray diffractometer with Mo-K_α radiation (λ = 0.71073 Å) (**Pt-1 and Pt-5**) or CuKα (λ = 1.54184) (**Pt-3^{Me}**, **Au-Cl-1**, **1-H**, **1-5** and **9-N**) using a EOS CCD camera. The crystal was cooled with an Oxford Instruments Cryojet. Diffractometer control, data collection, initial unit cell determination, frame integration and unit-cell refinement was carried out with 'Crysalis'.[4] Face-indexed absorption corrections were applied using spherical harmonics, implemented in SCALE3 ABSPACK scaling algorithm.[5] OLEX2[6] was used for overall structure solution, refinement and preparation of computer graphics and publication data. Within OLEX2, the algorithms used for structure solution were Superflip charge-flipping (**Pt-1**) and ShelXT (all others). Refinement by full-matrix least-squares used the SHELXL-97[7] algorithm within OLEX2.[6] All non-hydrogen atoms were refined anisotropically. Hydrogen atoms were placed using a 'riding model' and included in the refinement at calculated positions.

6.2 Synthesis of Platinum(IV) Complexes (Chapter 2)

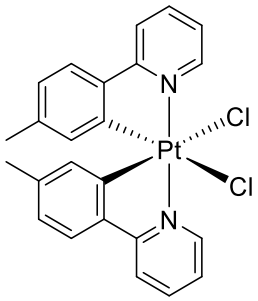

[Pt(tolpy)$_2$Cl$_2$], **Pt-1**: $K_2[PtCl_4]$ (30.5 mg, 73.1 μmol) dissolved in the minimum volume of hot water was added to a mixture of 2-*p*-tolylpyridine (24.2 μL, 0.419 mmol) and DMSO (15.1 μL, 0.213 mmol) in 2-ethoxyethanol (10 mL). The reaction mixture was heated with stirring at 80 ^oC for 6 hours under microwave conditions. The resulting precipitate was isolated by filtration and washed with water and cold methanol to afford the pure product. 13.0 mg (29 %).

^{1}H NMR (400 MHz, $CDCl_3$): δ = 10.00 (2H, d, $^3J_{HH}$ = 6.0 Hz, $^3J_{HPt}$ = 29.0 Hz), 8.06 (2H, td, $^3J_{HH}$ = 7.6 Hz, $^4J_{HH}$ = 1.2 Hz), 7.92 (2H, d, $^3J_{HH}$ = 8.0 Hz), 7.48 (2H, d, $^3J_{HH}$ = 8.0 Hz), 7.45 (2H, td, $^3J_{HH}$ = 6.4 Hz, $^4J_{HH}$ = 1.2 Hz), 6.92 (2H, d, $^3J_{HH}$ = 8.0 Hz), 5.83 (2H, s, $^3J_{HPt}$ = 33 Hz), 2.10 (6H, Me, s) ppm; CHN elemental analysis: observed (calculated): %C 47.6 (47.9), %H 3.3 (3.4), %N 4.6 (4.7).

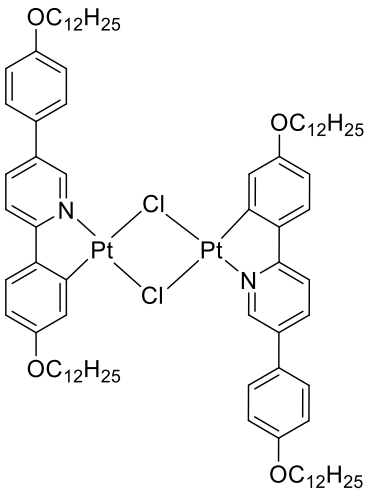

[Pt(κ^2-N^C-L)(μ-Cl)]$_2$, **Pt-2**: Prepared following literature procedure.[2] $K_2[PtCl_4]$ (150 mg, 0.361 mmol) was dissolved in a minimum amount of warm water and was added to a solution of **HL-1** (233 mg, 0.360 mmol) in acetic acid (75 cm^3) and heated at reflux for 16 hours. The solution was cooled to room temperature and the resulting precipitate was isolated *via* filtration and washed with water (45 cm^3), ethanol (75 cm^3) and diethyl ether (35 cm^3). The product was insoluble in common NMR solvents and was used without further purification. 205 mg (47 %).

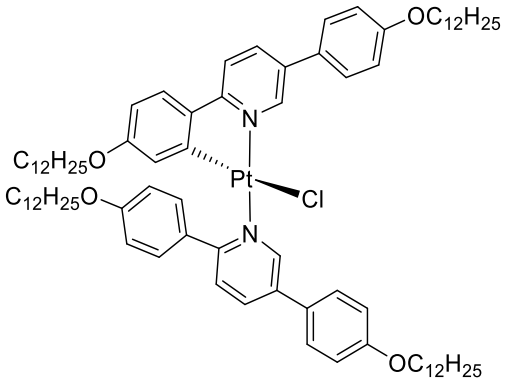

[Pt(κ^2-N^C-L)Cl(κ^1-N^C-LH)], **Pt-3**: $CHCl_3$ (70 mL) was added to compound **Pt-2** (450 mg, 0.293 mmol) and 2,5-di(4-dodecyloxyphenyl)-pyridine (334 mg, 0.584 mmol). The resulting reaction mixture heated at reflux for 24 hours. The solution was cooled to room temperature, filtered through Celite® to remove any residual compound **Pt-2** and the solvent removed under reduced pressure. The residue was washed with ice-cold $CHCl_3$, the filtrate collected and the solvent removed under reduced pressure. The residue was recrystallized from $CHCl_3$/propanone to yield the pure product. 285 mg (68 %).

^{1}H NMR (400 MHz, $CDCl_3$): δ = 9.84 (1H, d, $^{4}J_{HH}$ = 2.0 Hz), 9.45 (1H, d, $^{4}J_{HH}$ = 2.0 Hz), 8.14 (2H, d, $^{3}J_{HH}$ = 8.8 Hz), 8.03 (1H, dd, $^{3}J_{HH}$ = 8.4 Hz, $^{4}J_{HH}$ = 2.0 Hz), 7.86 (1H, dd, $^{3}J_{HH}$ = 8.4 Hz, $^{4}J_{HH}$ = 2.0 Hz), 7.63 (1H, d, $^{3}J_{HH}$ = 8.4 Hz), 7.56 (4H, dd, $^{3}J_{HH}$ = 8.8 Hz, $^{4}J_{HH}$ = 1.6 Hz), 7.42 (1H, d, $^{3}J_{HH}$ = 8.4 Hz), 7.28 (1H, d, $^{3}J_{HH}$ = 8.4 Hz), 6.97 (2H, d, $^{3}J_{HH}$ = 8.8 Hz), 6.96 (2H, d, $^{3}J_{HH}$ = 8.4 Hz), 6.86 (2H, d, $^{3}J_{HH}$ = 8.8 Hz), 6.55 (1H, dd, $^{3}J_{HH}$ = 8.4 Hz, $^{4}J_{HH}$ = 2.4 Hz), 5.77 (1H, d, $^{4}J_{HH}$ = 2.4 Hz), 3.98 (4H, t, $^{3}J_{HH}$ = 6.8 Hz), 3.89 (2H, t, $^{3}J_{HH}$ = 6.8 Hz), 3.75 (2H, m), 1.79 (4H, m), 1.71 (2H, m), 1.65 (2H, m), 1.46 (4H, m), 1.25 (64 H, broad m), 0.87 (12H, m) ppm; ^{195}Pt NMR (107 MHz, $CDCl_3$): δ = -3167 ppm; CHN elemental analysis: observed (calculated): %C 68.6 (68.9), %H 8.4 (8.5), %N 1.9 (2.0).

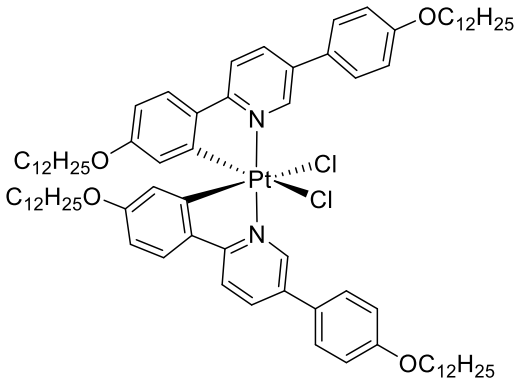

[Pt(κ^2-N^C-L)$_2$$Cl_2$], **Pt-4**: Compound **3** (100 mg, 0.681 mmol) and $PhICl_2$ (37.5 mg, 1.36 mmol) were dissolved in CH_2Cl_2 (60 mL) and stirred for 24 hours. The solvent was subsequently removed under reduced pressure and the residue recrystallized from toluene/methanol to yield the pure product. 71.8 mg (70 %).

^{1}H NMR (400 MHz, $CDCl_3$): δ = 10.18 (2H, d, $^{4}J_{HH}$ = 2.4 Hz, $^{3}J_{HPt}$ = 29.6 Hz), 8.17 (2H, dd, $^{3}J_{HH}$ = 8.8 Hz, $^{4}J_{HH}$ = 2.0 Hz), 7.82 (2H, d, $^{3}J_{HH}$ = 8.8 Hz), 7.66 (4H, d, $^{3}J_{HH}$ = 8.8 Hz), 7.51 (2H, d, $^{3}J_{HH}$ = 8.8 Hz), 7.01 (4H, d, $^{3}J_{HH}$ = 8.8 Hz), 6.62 (2H, dd, $^{3}J_{HH}$ = 8.8 Hz, $^{4}J_{HH}$ = 2.4 Hz), 5.64 (2H, d, $^{4}J_{HH}$ = 2.4 Hz, $^{3}J_{HPt}$ = 36.8 Hz), 4.0 (4H, t, $^{3}J_{HH}$ = 6.8 Hz), 3.68 (4H, m), 1.81 (4H. m), 1.47 (8H, m), 1.21 (64H, broad m), 0.87 (12H, t, $^{3}J_{HH}$ = 7.2 Hz) ppm; ^{195}Pt NMR (107 MHz, $CDCl_3$): δ = -1740 ppm; CHN elemental analysis: observed (calculated): %C 67.0 (67.2), %H 8.1 (8.3), %N 1.9 (1.9).

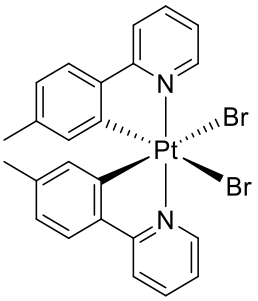

[Pt(tolpy)$_2$Br$_2$], **Pt-5**: Synthesised by modification of a literature procedure.[8] To a suspension **Pt-1** (67.9 mg, 0.111 mmol) in acetone (40 mL) was added AgOTf (72.8 mg, 0.278 mmol). The mixture was stirred in the dark at reflux for 5 hours. The reaction mixture was cooled, and the resulting suspension was filtered through Celite®, and the filtrate concentrated *in vacuo*. The [Pt(tolpy)$_2$OTf$_2$] intermediate was used without further purification. To this was added NaBr (0.288 g, 2.82 mmol) and the mixture heated at 50 °C for 1.5 hours in acetone (35 mL). The reaction mixture was cooled to room temperature and the solid isolated by filtration, then washed with water (50 mL) and acetone (50 mL). 44.0 mg (57 %).

^{1}H NMR (400 MHz, CD_2Cl_2): δ = 10.09 (2H, d, $^3J_{HH}$ = 6.0 Hz, $^3J_{HPt}$ = 29.5 Hz), 8.10 (2H, td, $^3J_{HH}$ = 7.7 Hz, $^4J_{HH}$ = 1.5 Hz), 7.97 (2H, d, $^3J_{HH}$ = 8.1 Hz), 7.54 (2H, d, $^3J_{HH}$ = 8.0 Hz), 7.47 (2H, td, $^3J_{HH}$ = 6.0 Hz, $^4J_{HH}$ = 1.5 Hz), 6.97 (2H, d, $^3J_{HH}$ = 8.0 Hz), 5.79 (2H, s, $^3J_{HPt}$ = 33 Hz), 2.10 (6H, Me, s) ppm.

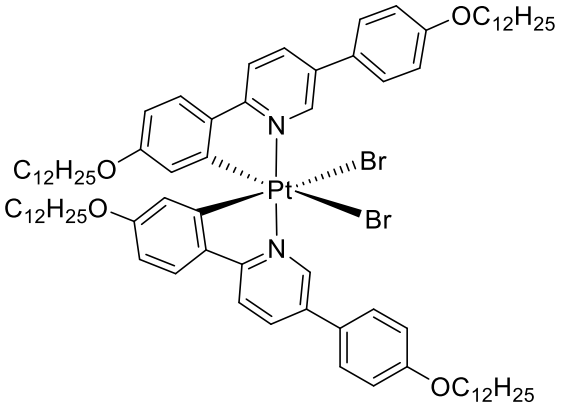

[Pt(κ^2-N^C-L)$_2$Br$_2$], **Pt-6**: Synthesised by modification of a literature procedure.[8] To a suspension **Pt-4** (500 mg, 0.342 mmol) in acetone (150 mL) was added AgOTf (220 mg, 0.861 mmol). The mixture was stirred in the dark at reflux for 5 hours. The reaction mixture was cooled, the solvent reduced to approx. 30 ml and the solution cooled in the fridge for 16 hours. The resulting suspension was filtered through Celite®, and the filtrate concentrated *in vacuo*. The [Pt(L)$_2$OTf$_2$] intermediate was used without further purification. To this was added NaBr (1.01 g, 9.72 mmol) and the mixture heated at 50 °C for 1.5 hours in acetone (60 mL). The reaction mixture was cooled to room temperature and the solid isolated by filtration, then washed with water (50 mL) and

acetone (50 mL). The solid was recrystallized from CH_2Cl_2 and hexane to give the pure product. 90.1 mg (17 %)

^{1}H NMR (400 MHz, $CDCl_3$): δ = 10.42 (2H, d, $^4J_{HH}$ = 2.0 Hz, $^3J_{HPt}$ = 29.6 Hz), 8.14 (2H, dd, $^3J_{HH}$ = 8.4 Hz, $^4J_{HH}$ = 1.6 Hz), 7.81 (2H, d, $^3J_{HH}$ = 8.8 Hz), 7.68 (4H, d, $^3J_{HH}$ = 8.8 Hz), 7.49 (2H, d, $^3J_{HH}$ = 8.4 Hz), 7.02 (4H, d, $^3J_{HH}$ = 8.8 Hz), 6.60 (2H, dd, $^3J_{HH}$ = 8.4 Hz, $^4J_{HH}$ = 2.0 Hz), 5.56 (2H, d, $^4J_{HH}$ = 2.0 Hz, $^3J_{HPt}$ = 36.8 Hz), 4.0 (4H, t, $^3J_{HH}$ = 6.8 Hz), 3.66 (4H, m), 1.81 (4H. m), 1.47 (8H, m), 1.21 (64H, broad m), 0.87 (12H, t, $^3J_{HH}$ = 7.2 Hz) ppm; ^{195}Pt NMR (107 MHz, $CDCl_3$): δ = -1928 ppm; CHN elemental analysis: observed (calculated): %C 63.4 (63.2), %H 7.8 (7.8), %N 1.8 (1.8).

6.3 Synthesis of Gold(III) Complexes and Associated Ligands (Chapter 3)

6.3.1 Synthesis of Cyclometallating Ligands

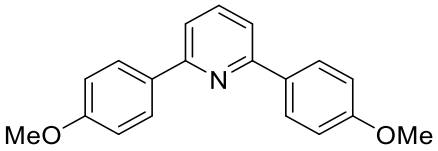

2,6-Bis(4-methoxyphenyl)pyridine: 2,6-dibromopyridine (2.59 g, 10.9 mmol) and 4-methoxyphenyl boronic acid (5.01 g, 32.9 mmol) were added to a flask containing $Pd(OAc)_2$ (13.1 mg, 0.5 mol-%) and K_3PO_4 (6.99 g, 32.9 mmol). Ethylene glycol (80 cm^3) was added, and the reaction mixture heated to 80 °C for 1.5 hours with vigorous stirring. The reaction mixture was cooled to room temperature, isolated by filtration and washed with water (150 cm^3), after which it was air dried. The resulting grey solid was dissolved in CH_2Cl_2 and filtered through Celite®. The filtrate was collected and the solvent removed under reduced pressure. The solid, off-white residue was recrystallized from ethanol to give the pure product as colourless crystals. 2.16 g (68 %).

^{1}H NMR (400 MHz, $CDCl_3$): δ = 8.09 (4H, AA'XX'), 7.73 (1H, t, $^3J_{HH}$ = 7.6 Hz), 7.56 (2H, d, $^3J_{HH}$ = 8.0 Hz), 7.0 (4H, AA'XX'), 3.87 (6H, s) ppm; CHN elemental analysis: observed (calculated): %C 78.0 (78.3), %H 5.9 (5.9), %N 4.8 (4.8).

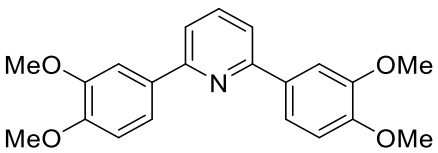

2,6-Bis(3,4-dimethoxyphenyl)pyridine: Synthesised as for 2,6-bis(4-methoxyphenyl)pyridine, using 2,6-dibromopyridine (2.21 g, 9.21 mmol), 3,4-dimethoxyphenyl boronic acid (5.02 g, 27.4 mol) and recrystallized from ethanol to give colourless crystals. 2.94 g (91 %).

^{1}H NMR (400 MHz, $CDCl_3$): δ = 7.82 (2H, d, $^4J_{HH}$ = 2.0 Hz), 7.74 (1H, t, $^3J_{HH}$ = 7.2 Hz), 7.64 (2H, dd, $^3J_{HH}$ = 8.4 Hz, $^4J_{HH}$ = 1.6 Hz), 7.67 (2H, d, $^3J_{HH}$ = 7.6 Hz), 6.97 (2H, d, $^3J_{HH}$ = 8.4 Hz), 4.01 (6H, s), 3.96 (6H, s) ppm. CHN elemental analysis: observed (calculated): %C 71.8 (71.8), %H 6.1 (6.0), %N 4.0 (4.0).

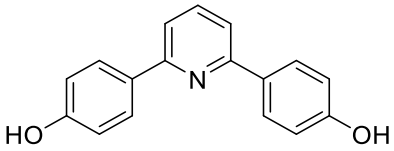

2,6-Bis(4-hydroxyphenyl)pyridine: 2,6-bis(4-methoxyphenyl)pyridine (1.52 g, 5.13 mmol) was added to molten pyridinium chloride (7.47 g, 64.6 mmol) at 200 °C and stirred for 16 hours. The still molten mixture was added to distilled water (100 cm^3) and the resulting yellow precipitate was isolated by filtration and air-dried. It was used without further purification. 952 mg (71 %).

^{1}H NMR (400 MHz, d_6-DMSO): δ = 9.74 (2H, s), 7.99 (4H, AA'XX'), 7.77 (1H, t, $^3J_{HH}$ = 7.6 Hz), 7.64 (2H, d, $^3J_{HH}$ = 7.6 Hz), 6.85 (4H, AA'XX') ppm.

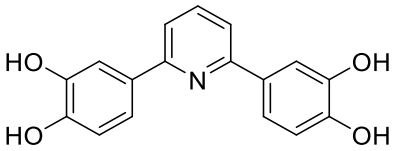

2,6-Bis(3,4-dihydroxyphenyl)pyridine: Synthesised as for 2,6-bis(4-hydroxyphenyl)pyridine using 2,6-bis(3,4-dimethoxyphenyl)pyridine (1.21 g, 3.40 mmol). 743 mg (73 %).

^{1}H NMR (400 MHz, d_6-DMSO): δ = 9.20 (2H, s), 9.06 (2H, s), 7.72 (1H, t, $^3J_{HH}$ = 7.6 Hz), 7.63 (2H, d, $^4J_{HH}$ = 2.0 Hz), 7.55 (2H, d, $^3J_{HH}$ = 8.0 Hz), 7.41 (2H, dd, $^3J_{HH}$ = 8.4 Hz, $^4J_{HH}$ = 2.0 Hz), 6.82 (2H, d, $^3J_{HH}$ = 8.0 Hz) ppm.

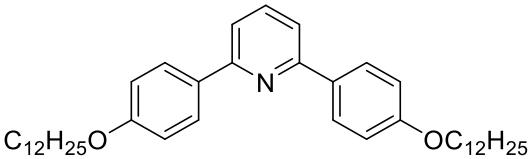

2,6-bis(4-dodecyloxyphenyl)pyridine: 2,6-bis(4-hydroxyphenyl)pyridine (0.903 g, 3.42 mmol), 1-bromododecane (2.06 cm^3, 8.63 mmol), K_2CO_3 (1.41 g, 10.2 mmol) were heated to 90 °C in DMF (50 cm^3) for 16 hours. The reaction mixture was cooled to room temperature and the solid isolated

by filtration and washed with water (150 cm^3) and acetone (60 cm^3) and left to air dry. 1.67 g (82 %).

^{1}H NMR (400 MHz, $CDCl_3$): δ = 8.06 (4H, AA'XX'), 7.71 (1H, t, $^3J_{HH}$ = 7.6 Hz), 7.55 (2H, d, $^3J_{HH}$ = 7.6 Hz), 6.98 (4H, AA'XX'), 4.0 (4H, t, $^3J_{HH}$ = 6.8 Hz), 1.79 (4H, m), 1.47 (4H, m), 1.21 (32H, broad m), 0.87 (6H, t, $^3J_{HH}$ = 7.2 Hz) ppm; CHN elemental analysis: observed (calculated): %C 82.0 (82.0), %H 10.1 (10.3), %N 2.3 (2.3)

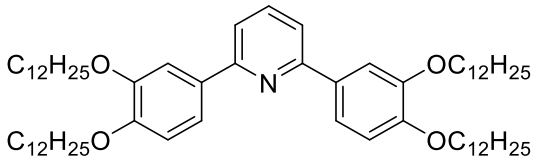

2,6-Bis(3,4-bis-dodecyloxyphenyl)pyridine: Synthesised as for 2,6-bis(4-dodecyloxyphenyl)pyridine using 2,6-bis(3,4-dihydroxyphenyl)pyridine (1.02 g, 3.41 mmol), 1-bromododecane (5.22 cm^3, 21.6 mmol), K_2CO_3 (5.91 g, 42.6 mmol). 2.27 g (70 %).

^{1}H NMR (400 MHz, $CDCl_3$): δ = 7.79 (2H, d, $^4J_{HH}$ = 2.0 Hz), 7.71 (1H, t, $^3J_{HH}$ = 7.6 Hz), 7.61 (2H, dd, $^3J_{HH}$ = 8.4 Hz, $^4J_{HH}$ = 2.4 Hz), 7.55 (2H, d, $^3J_{HH}$ = 8.0 Hz), 6.95 (2H, d, $^3J_{HH}$ = 8.4 Hz), 4.11 (4H, t, $^3J_{HH}$ = 6.4 Hz), 4.05 (4H, t, $^3J_{HH}$ = 6.4 Hz) 1.84 (8H, m), 1.47 (8H, m), 1.24 (64H, broad m), 0.87 (6H, t, $^3J_{HH}$ = 6.8 Hz), 0.87 (6H, t, $^3J_{HH}$ = 7.2 Hz) ppm; CHN elemental analysis: observed (calculated): %C 80.4 (80.6), %H 11.2 (11.3), %N 1.5 (1.5)

6.3.2 Synthesis of Alkynyl Ligands

4-ethynyl-1,2-bisalkoxybenzene ligands were synthesised *via* literature procedure, 4-ethynyl-1-alkoxybenzene and 5-ethynyl-1,2,3-trisalkoxybenzene ligands synthesised partially by modification of the same.[9]

General Procedure for the Synthesis of 4-Octyloxybenzaldehyde:

Under at atmosphere of nitrogen, the appropriate 1-bromoalkane (1.1 eq.) was added to a flask of 4-hydroxybenzaldehyde (1.0 eq.) and K_2CO_3 (1.1 eq.), along with a catalytic amount of KI. DMF (70 cm^3) was added and the reaction mixture was heated to 90 °C for 16 hours. The reaction mixture was then cooled to room temperature and insoluble salts were removed *via* by filtration and the solvent removed *in vacuo* from the filtrate. The residue was extracted into hexane and washed with 2M NaOH(aq) solution, brine and saturated $LiCl_{(aq)}$ solution, dried over $MgSO_4$ and

concentrated *in vacuo*. The residue was purified by column chromatography on silica gel using CH_2Cl_2 as the eluent.

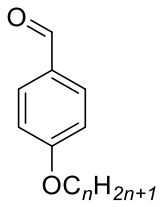

4-Octyloxybenzaldehyde: As above, with 4-hydroxybenzaldehyde (2.99 g, 24.5 mmol), 1-bromooctane (5.95 cm^3, 6.71 g, 34.7 mmol) and K_2CO_3 (4.43 g, 32.0 mmol). 4.71 g. (82%).

^{1}H NMR (400 MHz, $CDCl_3$): δ = 9.88 (1H, s), 7.82 (2H, AA'XX'), 6.99 (2H, AA'XX'), 4.03 (2H, t, $^3J_{HH}$ = 6.4 Hz), 1.81 (2H, m), 1.46 (2H, m), 1.24 (8H, m), 0.89 (3H, t, $^3J_{HH}$ = 6.8 Hz) ppm.

4-Decyloxybenzaldehyde: As above, with 4-hydroxybenzaldehyde (3.00 g, 24.5 mmol), 1-bromodecane (7.62 cm^3, 8.12 g, 36.7 mmol) and K_2CO_3 (6.79 g, 49.1 mmol). 4.81 g. (74%).

^{1}H NMR (400 MHz, $CDCl_3$): δ = 9.87 (1H, s), 7.82 (2H, AA'XX'), 6.99 (2H, AA'XX'), 4.03 (2H, t, $^3J_{HH}$ = 6.4 Hz), 1.81 (2H, m), 1.46 (2H, m), 1.24 (10H, m), 0.89 (3H, t, $^3J_{HH}$ = 6.8 Hz) ppm.

4-Dodecyloxybenzaldehyde: As above, with 4-hydroxybenzaldehyde (2.92 g, 23.7 mmol), 1-bromododecane (8.85 cm^3, 9.19 g, 36.9 mmol) and K_2CO_3 (6.74 g, 48.8 mmol). 3.6 g. (50%).

^{1}H NMR (400 MHz, $CDCl_3$): δ = 9.87 (1H, s), 7.82 (2H, AA'XX'), 6.99 (4H, AA'XX'), 4.03 (2H, t, $^3J_{HH}$ = 6.4 Hz), 1.81 (2H, m), 1.46 (2H, m), 1.24 (12H, m), 0.88 (3H, t, $^3J_{HH}$ = 6.8 Hz) ppm.

4-Tetradecyloxybenzaldehyde: As above, with 4-hydroxybenzaldehyde (3.02 g, 24.5 mmol), 1-bromotetradecane (11.0 cm^3, 10.3 g, 37.0 mmol) and K_2CO_3 (6.74 g, 48.8 mmol). 4.83 g. (62%).

^{1}H NMR (400 MHz, $CDCl_3$): δ = 9.87 (1H, s), 7.82 (2H, AA'XX'), 6.99 (2H, AA'XX'), 4.03 (2H, t, $^3J_{HH}$ = 6.4 Hz), 1.81 (2H, m), 1.46 (2H, m), 1.24 (14H, m), 0.88 (3H, t, $^3J_{HH}$ = 6.8 Hz) ppm.

General Procedure for the Synthesis of 3,4-Bis(alkyloxy)benzaldehyde:

Under at atmosphere of nitrogen, the appropriate 1-bromoalkane (2.2 eq.) was added to a flask of 4-hydroxybenzaldehyde (1.0 eq.) and K_2CO_3 (2.2 eq.), along with a catalytic amount of KI. DMF (70 cm^3) was added and the reaction mixture was heated to 90 °C for 16 hours. The reaction mixture was then cooled to room temperature and poured into aqueous 1M HCl**.** The product was extracted into CH_2Cl_2, washed with brine, dried over $MgSO_4$ and the solution concentrated *in vacuo*. The residue was purified by column chromatography on silica gel.

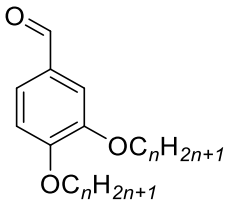

3,4-Bis(octyloxy)benzaldehyde: As above, using 3,4-dihydroxybenzaldehyde (1.52 g, 10.9 mmol), 1-bromooctane (4.21 cm^3, 23.3 mmol) and potassium carbonate (3.32 g, 23.9 mmol), using CH_2Cl_2 as the eluent. 2.50 g. (63 %).

^{1}H NMR (400 MHz, $CDCl_3$): δ = 9.83 (1H, s), 7.41 (1H, dd, $^3J_{HH}$ = 8.2, $^4J_{HH}$ = 2.0), 7.39 (1H, m), 6.95 (1H, d, $^3J_{HH}$ = 8.2), 4.08 (2H, t, $^3J_{HH}$ = 6.5 Hz), 4.05 (2H, t, $^3J_{HH}$ = 6.5 Hz), 1.81 (4H, m), 1.46 (4H, m), 1.28 (16H, m), 0.89 (6H, t, $^3J_{HH}$ = 6.8 Hz) ppm.

3,4-Bis(decyloxy)benzaldehyde: As above, using 3,4-dihydroxybenzaldehyde (1.98 g, 14.5 mmol), 1-bromooctane (7.32 cm^3, 35.2 mmol) and potassium carbonate (4.50 g, 32.6 mmol), using petroleum ether(40-60):ethyl acetate as the eluent. 5.91 g. (97 %).

^{1}H NMR (400 MHz, $CDCl_3$): δ = 9.82 (1H, s), 7.41 (1H, dd, $^3J_{HH}$ = 8.2, $^4J_{HH}$ = 2.0), 7.39 (1H, m), 6.95 (1H, d, $^3J_{HH}$ = 8.2), 4.08 (2H, t, $^3J_{HH}$ = 6.5 Hz), 4.05 (2H, t, $^3J_{HH}$ = 6.5 Hz), 1.81 (4H, m), 1.46 (4H, m), 1.28 (32H, m), 0.89 (6H, t, $^3J_{HH}$ = 6.8 Hz) ppm.

3,4-Bis(dodecyloxy)benzaldehyde*: As above, using 3,4-dihydroxybenzaldehyde (2.01 g, 14.5 mmol), 1-bromododecane (7.92 cm^3, 31.9 mmol) and potassium carbonate (4.42 g, 31.9 mmol), using hexane:ethyl acetate (85 : 15) as the eluent. 6.71 g. (97 %).

^{1}H NMR (400 MHz, $CDCl_3$): δ = 9.82 (1H, s), 7.41 (1H, dd, $^3J_{HH}$ = 8.2, $^4J_{HH}$ = 2.0), 7.39 (1H, m), 6.95 (1H, d, $^3J_{HH}$ = 8.2), 4.08 (2H, t, $^3J_{HH}$ = 6.5 Hz), 4.05 (2H, t, $^3J_{HH}$ = 6.5 Hz), 1.81 (4H, m), 1.46 (4H, m), 1.28 (40H, m), 0.89 (6H, t, $^3J_{HH}$ = 6.8 Hz) ppm.

3,4-Bis(tetradecyloxy)benzaldehyde*: As above, using 3,4-dihydroxybenzaldehyde (2.00 g, 14.5 mmol), 1-bromotetradecane (9.50 cm^3, 31.9 mmol), and potassium carbonate (4.41 g, 31.9 mmol), using hexane– ethyl acetate (85 : 15) as the eluent. 6.20 g (77 %).

^{1}H NMR (400 MHz, $CDCl_3$): δ = 9.82 (1H, s), 7.41 (1H, dd, $^3J_{HH}$ = 8.2, $^4J_{HH}$ = 2.0), 7.39 (1H, m), 6.95 (1H, d, $^3J_{HH}$ = 8.2), 4.08 (2H, t, $^3J_{HH}$ = 6.5 Hz), 4.05 (2H, t, $^3J_{HH}$ = 6.5 Hz), 1.81 (4H, m), 1.46 (4H, m), 1.28 (48H, m), 0.89 (6H, t, $^3J_{HH}$ = 6.8 Hz) ppm.

*Synthesised by MChem Project Student Rebecca Howarth

Synthesis of 3,4,5-Tris(alkoxy)benzaldehyde- Routes A and B

Route A:

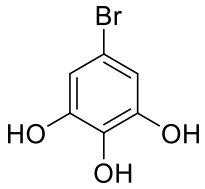

5-Bromo-1,2,3-trihydroxybenzene: 5-bromo-1,2,3-trimethoxybenzene (15.0 g, 60.7 mmol) in CH_2Cl_2 (50 cm^3) was cooled to -78 °C under an atmosphere of nitrogen. BBr_3 (1M in CH_2Cl_2, 200 cm^3, 200 mmol) was added dropwise and stirred at -78 °C for 1 hour. The solution was warmed to room temperature and stirred for 24 hours. The reaction was quenched with water, and the resulting precipitate removed *via* filtration and washed with CH_2Cl_2. The filtrate was separated and the aqueous layer washed with ethyl acetate (2 x 35 cm^3), brine (35 cm^3) and a further portion of ethyl acetate (35 cm^3). The organic layers were combined, dried over $MgSO_4$ and concentrated *in vacuo* to give the product. 12.1 g (97 %).

^{1}H NMR (400 MHz, CD_3OD): δ = 6.43 (2H, s) ppm; CHN elemental analysis: observed (calculated): %C 35.6 (35.2), %H 2.4 (2.5).

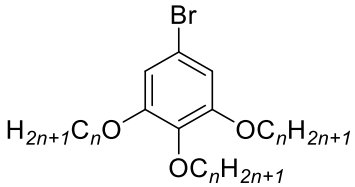

1-Bromo-3,4,5-trioctyloxybenzene: Under an atmosphere of nitrogen, 5-bromo-1,2,3-trihydroxybenzene (2.01 g, 9.80 mmol), 1-bromododecane (9.21 cm^3, 53.2 mmol) and K_2CO_3 (12.4 g, 89.7 mmol) in DMF was heated to 90 °C for 16 hours. The solution was cooled to room temperature and the product extracted into hexane, dried over $MgSO_4$ and the solution concentrated *in vacuo* to give a brown oil. The residue was purified flash chromatography on silica gel with CH_2Cl_2/petroleum ether (40-60) as eluent (7:3). 2.89 g (55 %).

^{1}H NMR (400 MHz, $CDCl_3$): δ = 6.67 (2H, s), 3.92 (4H, t, $^3J_{HH}$ = 6.6 Hz), 3.91 (2H, t, $^3J_{HH}$ = 7.2 Hz), 1.78 (4H, m), 1.72 (2H, m), 1.45 (6H, m), 1.26 (24H, broad m), 0.88 (9H, t, $^3J_{HH}$ = 7.1 Hz) ppm.

1-Bromo-3,4,5-tridodecyloxybenzene: Under an atmosphere of nitrogen, 5-bromo-1,2,3-trihydroxybenzene (2.00 g, 9.81 mmol), 1-bromododecane (14.0 cm^3, 47.9 mmol) and K_2CO_3 (12.3 g, 88.9 mmol) in DMF was heated to 90 °C for 16 hours. The solution was cooled to room temperature and the solid isolated by filtration. The solid was washed with water (100 cm^3) and

acetone (50 cm^3) to give the product as an off-white solid which was used without further purification. 6.74 g (95 %).

^{1}H NMR (400 MHz, $CDCl_3$): δ = 6.67 (2H, s), 3.93 (4H, t, $^3J_{HH}$ = 6.6 Hz), 3.91 (2H, t, $^3J_{HH}$ = 7.2 Hz), 1.78 (4H, m), 1.72 (2H, m), 1.45 (6H, m), 1.26 (48H, broad m), 0.88 (9H, t, $^3J_{HH}$ = 7.1 Hz) ppm.

Route B:

General Procedure for Synthesis of Methyl 3,4,5-Tris(alkoxy)benzoate

Methyl 3,4,5-trihydroxybenzoate and K_2CO_3 (3.3 equiv.) were heated to reflux in 2-pentanone (80 cm^3). 1-bromoalkane was added and the mixture heated for 24 hours at reflux. The reaction mixture was cooled to room temperature, filtered through a pad of Celite® and the filtrate concentrated *in vacuo*.

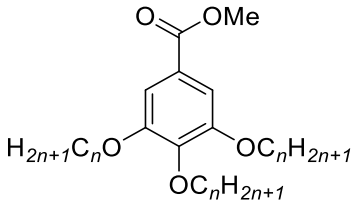

Methyl 3,4,5-tris(decyloxy)benzoate: As above, using methyl 3,4,5-trihydroxybenzoate (3.09 g, 16.8 mmol), 1-bromodecane (11.9 cm^3, 56.8 mmol) and K_2CO_3 (13.5 g, 96.9 mmol). The brown residue was purified by column chromatography on silica gel with CH_2Cl_2 as the eluent to give a colourless oil. 6.02 g (46 %).

^{1}H NMR (400 MHz, $CDCl_3$): δ = 7.25 (2H, s), 4.01 (2H, t, $^3J_{HH}$ = 6.6 Hz), 4.01 (4H, t, $^3J_{HH}$ = 6.6 Hz), 1.80 (4H, m), 1.74 (2H, m), 1.46 (6H, m), 1.26 (36H, broad m), 0.88 (9H, t, $^3J_{HH}$ = 6.9 Hz) ppm.

Methyl 3,4,5-tris(tetradecyloxy)benzoate: As above, using methyl 3,4,5-trihydroxybenzoate (3.10 g, 16.8 mmol), 1-bromotetradecane (16.5 cm^3, 55.4 mmol) and K_2CO_3 (13.4 g, 97.8 mmol). The brown residue was crystallised from ethanol to give a colourless solid. 3.31 g (34 %) ppm.

^{1}H NMR (400 MHz, $CDCl_3$): δ = 7.25 (2H, s), 4.00 (6H, t, $^3J_{HH}$ = 6.6 Hz), 1.80 (4H, m), 1.73 (2H, m), 1.46 (6H, m), 1.26 (60H, broad m), 0.88 (9H, t, $^3J_{HH}$ = 6.9 Hz).

General Procedure for Synthesis of 3,4,5-Trialkoxybenzyl Alcohol

Under at atmosphere of dinitrogen, methyl 3,4,5-trialkoxybenzoate was dissolved in dry THF and the mixture cooled to 0 °C. Lithium aluminium hydride (1M in THF, 1 equiv.) was added dropwise with stirring and the mixture was allowed to slowly warm to room temperature and stirred for 16

hours. The reaction was quenched with ethyl acetate (20 cm^3), followed by ethanol (20 cm^3) and water (20 cm^3). The volatiles were removed *in vacuo*, the product extracted with CH_2Cl_2, washed with water and dried over $MgSO_4$. The solvent was removed *in vacuo* to give a light brown oil.

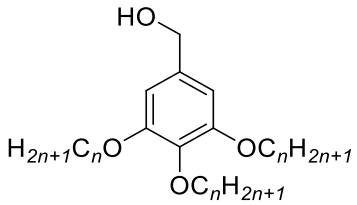

3,4,5-Tris(decyloxy)benzyl alcohol: As above, with methyl 3,4,5-tris(decyloxy)benzoate (5.87 g, 9.68 mmol) and lithium aluminium hydride (1M in THF, 10.0 cm^3, 10.0 mmol) in THF (100 cm^3). The residue was crystallised from hexane to give a colourless solid. 2.86 g (52 %).

^{1}H NMR (400 MHz, $CDCl_3$): δ = 6.56 (2H, s), 4.59 (2H, d, $^3J_{HH}$ = 6.0 Hz) 3.97 (4H, t, $^3J_{HH}$ = 6.6 Hz), 3.93 (2H, t, $^3J_{HH}$ = 6.6 Hz), 1.80 (4H, m), 1.74 (2H, m), 1.46 (6H, m), 1.26 (36H, broad m), 0.88 (9H, t, $^3J_{HH}$ = 6.9 Hz) ppm.

3,4,5-Tris(tetradecyloxy)benzyl alcohol: As above, with methyl 3,4,5-tris(tetradecyloxy)benzoate (2.27 g, 2.91 mmol) and lithium aluminium hydride (1M in THF, 2.90 cm^3, 2.89 mmol) in THF (50 cm^3). The residue was crystallised from ethanol to give a colourless solid. 1.05 g (49 %).

^{1}H NMR (400 MHz, $CDCl_3$): δ = 6.56 (2H, s), 4.59 (2H, d, $^3J_{HH}$ = 6.0 Hz) 3.97 (4H, t, $^3J_{HH}$ = 6.6 Hz), 3.93 (2H, t, $^3J_{HH}$ = 6.6 Hz), 1.80 (4H, m), 1.74 (2H, m), 1.46 (6H, m), 1.26 (60H, broad m), 0.88 (9H, t, $^3J_{HH}$ = 6.9 Hz) ppm.

Synthesis of 3,4,5-Tris(alkoxy)benzaldehyde- Routes A and B

Route A:

General Procedure for Synthesis of 3,4,5-Tris(alkyloxy)benzaldehyde

1-Bromo-3,4,5-trisalkoxybenzene in diethyl ether was cooled to -15 °C under a nitrogen atmosphere. n-BuLi (2.7 M in hexane, 1.0 equiv.) was added dropwise and the solution stirred at -15 °C for 15 minutes. DMF (1.3 equiv.) was added and the reaction mixture warmed to room temperature and stirred for 1 hour, after which HCl (10 %) was added. The solution was separated and the aqueous layer washed with diethyl ether. The organic layers were combined, dried over $MgSO_4$ and concentrated to give a brown oil.

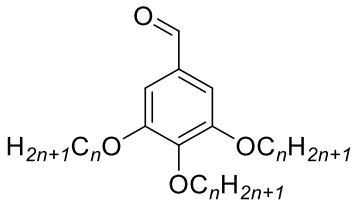

3,4,5-Tris(octyloxy)benzaldehyde: As above, using 1-bromo-3,4,5-tris(octyloxy)benzene (2.11 g, 3.88 mmol), n-BuLi (2.7 M in hexane, 1.50 cm^3, 3.90 mmol), DMF (0.5 cm^3, 6.51 mmol) and HCl (10 %, 6.79 cm^3) in diethyl ether (70 cm^3). The residue was purified by column chromatography on silica gel with petroleum ether (40-60)/ethyl acetate (9:1) as eluent to give a colourless oil. 911 mg (46 %).

^{1}H NMR (400 MHz, $CDCl_3$): δ = 9.83 (1H, s), 7.08 (2H, s), 4.05 (2H, t, $^3J_{HH}$ = 6.6 Hz), 4.03 (4H, t, $^3J_{HH}$ = 6.6 Hz), 1.82 (4H, m), 1.75 (2H, m), 1.47 (6H, m), 1.26 (24H, broad m), 0.87 (9H, m) ppm.

3,4,5-Tris(dodecyloxy)benzaldehyde: As above, using 1-bromo-3,4,5-tris(dodecyloxy)benzene (3.68 g, 5.10 mmol), n-BuLi (2.7 M in hexane, 1.9 cm^3, 5.13 mmol), DMF (0.7 cm^3, 9.0 mmol) and HCl (10 %, 9.0 cm^3) in diethyl ether (100 cm^3). The brown oil crystallised on standing. The residue was purified by column chromatography on silica gel with petroleum ether (40-60)/ethyl acetate (95:5) as eluent to give a colourless oil which crystallised on standing to give a white amorphous solid. 2.61 g (76 %).

^{1}H NMR (400 MHz, $CDCl_3$): δ = 9.82 (1H, s), 7.08 (2H, s), 4.05 (2H, t, $^3J_{HH}$ = 6.8 Hz), 4.03 (4H, t, $^3J_{HH}$ = 6.5 Hz), 1.82 (4H, m), 1.75 (2H, m), 1.47 (6H, m), 1.26 (48H, broad m), 0.87 (9H, m) ppm; CHN elemental analysis: observed (calculated): %C 78.2 (78.4), %H 11.9 (11.9).

Route B:

General Procedure for Synthesis of 3,4,5-Tris(alkoxy)benzaldehyde-

3,4,5-Trialkoxybenzyl alcohol was dissolved in CH_2Cl_2. Manganese dioxide (10.0 equiv.), was added and the mixture stirred at room temperature for 36 hours. $MgSO_4$ was added and the mixture stirred for 15 minutes. The solution was filtered through Celite® and the filtrate concentrated *in vacuo* to give a light yellow oil.

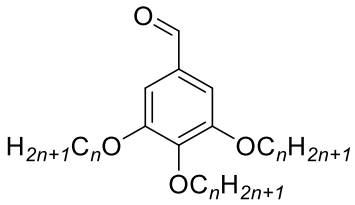

3,4,5-Tris(decyloxy)benzaldehyde: As above, using 3,4,5-tris(decyloxy)benzyl alcohol (2.77 g, 4.81 mmol) and manganese dioxide (4.21 g, 48.3 mmol) in CH_2Cl_2 (130 cm^3). The residue was purified by column chromatography on silica gel using CH_2Cl_2 as the eluent to give a colourless oil. 2.41 g (88 %).

^{1}H NMR (400 MHz, $CDCl_3$): δ = 9.83 (1H, s), 7.08 (2H, s), 4.05 (2H, t, $^3J_{HH}$ = 6.8 Hz), 4.03 (4H, t, $^3J_{HH}$ = 6.5 Hz), 1.82 (4H, m), 1.75 (2H, m), 1.47 (6H, m), 1.26 (36H, broad m), 0.88 (9H, t, $^3J_{HH}$ = 6.9 Hz).

3,4,5-Tris(tetradecyloxy)benzaldehyde: As above, using 3,4,5-tris(tetradecyloxy)benzyl alcohol (952 mg, 1.31 mmol) and manganese dioxide (1.11 g, 12.7 mmol) in CH_2Cl_2 (100 cm^3). The residue was crystallised from acetone to give a colourless, waxy solid. 923 mg (97 %).

^{1}H NMR (400 MHz, $CDCl_3$): δ = 9.83 (1H, s), 7.08 (2H, s), 4.05 (2H, t, $^3J_{HH}$ = 6.8 Hz), 4.03 (4H, t, $^3J_{HH}$ = 6.5 Hz), 1.82 (4H, m), 1.75 (2H, m), 1.47 (6H, m), 1.26 (60H, broad m), 0.88 (9H, t, $^3J_{HH}$ = 6.9 Hz) ppm.

General Procedure for Synthesis of 4-(2,2-dibromovinyl)-1-(alkyloxy)benzene, 4-(2,2-dibromovinyl)-1,2-bis(alkyloxy)benzene and 5-(2,2-dibromovinyl)-1,2,3-tris(alkyloxy)benzene:

Under a nitrogen atmosphere and cooled in an ice bath to 0 °C, a solution of tetrabromomethane (1.3 equiv.) in CH_2Cl_2 (20 cm^3) was added to a solution of triphenylphosphine (2.6 equiv.) in CH_2Cl_2 (60 cm^3), with the temperature maintained below 15 °C. After full addition the mixture was cooled again to 0 °C. A solution of the appropriate (alkyloxy)benzaldehyde and triethylamine (1.0 equiv.) in CH_2Cl_2 was added dropwise and the mixture stirred for 30 minutes. The mixture was warmed to room temperature and poured into hexane (100 cm^3). The mixture was filtered through a Celite® plug and the filtrate concentrated *in vacuo* to give a brown oil which was purified by column chromatography on silica gel.

4-(2,2-Dibromovinyl)-1-(alkyloxy)benzene:

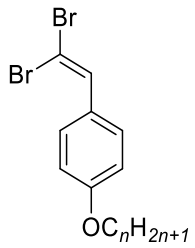

4-(2,2-Dibromovinyl)-1-(octyloxy)benzene: As above, with 4-octyloxybenzaldehyde (4.38 g, 18.8 mmol) in CH_2Cl_2 (40 cm^3), triphenylphosphine (12.9 g, 49.2 mmol) and tetrabromomethane (8.09 g, 24.4 mmol), purified with 7:3 petroleum ether(40-60):DCM as eluent. 3.36 g. (46%).

^{1}H NMR (400 MHz, $CDCl_3$): δ = 7.50 (2H, AA'XX'), 7.40 (1H, s), 6.87 (2H, AA'XX'), 3.96 (2H, t, $^3J_{HH}$ = 6.4 Hz), 1.81 (2H, m), 1.46 (2H, m), 1.24 (8H, m), 0.89 (3H, t, $^3J_{HH}$ = 6.8 Hz) ppm.

4-(2,2-Dibromovinyl)-1-(decyloxy)benzene: As above, with 4-decyloxybenzaldehyde (4.47 g, 17.2 mmol) in CH_2Cl_2 (40 cm^3), triphenylphosphine (12.1 g, 46.1 mmol) and tetrabromomethane (7.61 g, 22.9 mmol), purified with 7:3 petroleum ether(40-60):DCM as eluent. 5.87 g. (82%).

^{1}H NMR (400 MHz, $CDCl_3$): δ = 7.49 (4H, AA'XX'), 7.40 (1H, s), 6.87 (4H, AA'XX'), 3.96 (2H, t, $^3J_{HH}$ = 6.4 Hz), 1.81 (2H, m), 1.46 (2H, m), 1.24 (10H, m), 0.89 (3H, t, $^3J_{HH}$ = 6.8 Hz) ppm.

4-(2,2-Dibromovinyl)-1-(dodecyloxy)benzene: As above, with 4-dodecyloxybenzaldehyde (3.59 g, 12.4 mmol) in CH_2Cl_2 (30 cm^3), triphenylphosphine (8.50 g, 32.4 mmol) and tetrabromomethane (5.28 g, 16.0 mmol), purified with 7:3 petroleum ether(40-60):DCM as eluent. 4.90 g. (89%).

^{1}H NMR (400 MHz, $CDCl_3$): δ = 7.49 (2H, AA'XX'), 7.40 (1H, s), 6.87 (2H, AA'XX'), 3.96 (2H, t, $^3J_{HH}$ = 6.4 Hz), 1.81 (2H, m), 1.46 (2H, m), 1.24 (12H, m), 0.89 (3H, t, $^3J_{HH}$ = 6.8 Hz) ppm.

4-(2,2-Dibromovinyl)-1-(tetradecyloxy)benzene: As above, with 4-tetradecyloxybenzaldehyde (4.81 g, 15.2 mmol) in CH_2Cl_2 (40 cm^3), triphenylphosphine (10.3 g, 39.3 mmol) and tetrabromomethane (6.58 g, 20.0 mmol), purified with 7:3 petroleum ether(40-60):DCM as eluent. 5.39 g. (76%).

^{1}H NMR (400 MHz, $CDCl_3$): δ = 7.49 (2H, AA'XX'), 7.40 (1H, s), 6.87 (2H, AA'XX'), 3.96 (2H, t, $^3J_{HH}$ = 6.4 Hz), 1.81 (2H, m), 1.46 (2H, m), 1.24 (14H, m), 0.89 (3H, t, $^3J_{HH}$ = 6.8 Hz) ppm.

4-(2,2-Dibromovinyl)-1,2-bis(octyloxy)benzene:

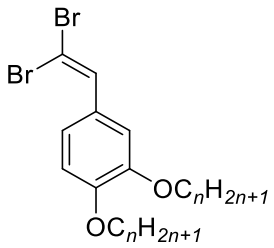

4-(2,2-Dibromovinyl)-1,2-bis(octyloxy)benzene: As above, with 3,4-bis(octyloxy)benzaldehyde (3.40 g, 9.39 mmol) in CH_2Cl_2 (40 cm^3), triphenylphosphine (6.51 g, 24.8 mmol) and carbon tetrabromide (4.09 g, 12.4 mmol), purified using petroleum ether:CH_2Cl_2 (1:1) as the eluent. Yield: 4.28 g (88%).

^{1}H NMR (400 MHz, $CDCl_3$): δ = 7.38 (1H, s), 7.19 (1H, d, $^4J_{HH}$ = 2.0), 7.06 (1H, dd, $^3J_{HH}$ = 8.4, $^4J_{HH}$ = 2.0), , 6.84 (1H, d, $^3J_{HH}$ = 8.4), 4.00 (2H, t, $^3J_{HH}$ = 6.6 Hz), 3.99 (2H, t, $^3J_{HH}$ = 6.6 Hz), 1.81 (4H, m), 1.46 (4H, m), 1.28 (16H, m), 0.89 (6H, t, $^3J_{HH}$ = 6.8 Hz) ppm.

4-(2,2-Dibromovinyl)-1,2-bis(decyloxy)benzene: As above, with 3,4-bis(decyloxy)benzaldehyde (6.01 g, 14.3 mmol) in CH_2Cl_2 (40 cm^3), triphenylphosphine (9.79 g, 37.4 mmol) and carbon tetrabromide (6.21 g, 18.7 mmol), purified using petroleum ether:CH_2Cl_2 (1:1) as the eluent. Yield: 6.34 g (77 %).

^{1}H NMR (400 MHz, $CDCl_3$): δ = 7.38 (1H, s), 7.18 (1H, d, $^4J_{HH}$ = 2.0), 7.05 (1H, dd, $^3J_{HH}$ = 8.4, $^4J_{HH}$ = 2.0), , 6.84 (1H, d, $^3J_{HH}$ = 8.4), 4.00 (2H, t, $^3J_{HH}$ = 6.6 Hz), 3.99 (2H, t, $^3J_{HH}$ = 6.6 Hz), 1.81 (4H, m), 1.46 (4H, m), 1.28 (24H, m), 0.89 (6H, t, $^3J_{HH}$ = 6.8 Hz) ppm.

4-(2,2-Dibromovinyl)-1,2-bis(dodecyloxy)benzene*: As above, with 3,4-bis(dodecyloxy)benzaldehyde (5.01 g, 10.5 mmol) in CH_2Cl_2 (40 cm^3), triphenylphosphine (7.17 g, 27.4 mmol) and carbon tetrabromide (4.50 g, 13.7 mmol), purified using petroleum ether:CH_2Cl_2 (1:1) as the eluent. Yield: 5.46 g (82 %).

^{1}H NMR (400 MHz, $CDCl_3$): δ = 7.38 (1H, s), 7.18 (1H, d, $^4J_{HH}$ = 2.0), 7.05 (1H, dd, $^3J_{HH}$ = 8.4, $^4J_{HH}$ = 2.0), , 6.84 (1H, d, $^3J_{HH}$ = 8.4), 4.00 (2H, t, $^3J_{HH}$ = 6.6 Hz), 3.99 (2H, t, $^3J_{HH}$ = 6.6 Hz), 1.81 (4H, m), 1.46 (4H, m), 1.28 (32H, m), 0.89 (6H, t, $^3J_{HH}$ = 6.8 Hz) ppm.

4-(2,2-Dibromovinyl)-1,2-bis(tetradecyloxy)benzene*: As above, with 3,4-bis(decyloxy)benzaldehyde (5.01 g, 9.42 mmol) in CH_2Cl_2 (40 cm^3), triphenylphosphine (6.42 g, 24.5 mmol) and carbon tetrabromide (4.06 g, 12.2 mmol), purified using petroleum ether:CH_2Cl_2 (1:1) as the eluent. The residue was recrystallised from ethyl acetate to give a colourless solid. Yield: 4.04 g (24 %).

^{1}H NMR (400 MHz, $CDCl_3$): δ = 7.38 (1H, s), 7.18 (1H, d, $^4J_{HH}$ = 2.0), 7.05 (1H, dd, $^3J_{HH}$ = 8.4, $^4J_{HH}$ = 2.0), , 6.84 (1H, d, $^3J_{HH}$ = 8.4), 4.00 (2H, t, $^3J_{HH}$ = 6.6 Hz), 3.99 (2H, t, $^3J_{HH}$ = 6.6 Hz), 1.81 (4H, m), 1.46 (4H, m), 1.28 (40H, m), 0.89 (6H, t, $^3J_{HH}$ = 6.8 Hz) ppm.

*Synthesised by MChem Project Student Rebecca Howarth

5-(2,2-Dibromovinyl)-1,2,3-tris(alkyloxy)benzene:

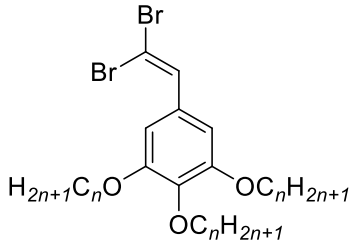

5-(2,2-Dibromovinyl)-1,2,3-tris(octyloxy)benzene: As above, using tetrabromomethane (527 mg, 1.60 mmol), triphenylphosphine (837 mg, 3.21 mmol) and 3,4,5-tris(octyloxy)benzaldehyde (602 mg, 1.21 mmol) in CH_2Cl_2 (25 cm^3). The residue was purified by column chromatography on silica gel using CH_2Cl_2/ petroleum ether (40-60) (1:1) to give a colourless solid. 650 mg (82 %).

^{1}H NMR (400 MHz, $CDCl_3$): δ = 7.37 (1H, s), 6.76 (2H, s), 3.96 (2H, t, $^3J_{HH}$ = 6.6 Hz), 3.96 (4H, t, $^3J_{HH}$ = 6.6 Hz), 1.79 (4H, m), 1.73 (2H, m), 1.46 (6H, m), 1.26 (24H, broad m), 0.88 (9H, t, $^3J_{HH}$ = 7.0 Hz) ppm.

5-(2,2-Dibromovinyl)-1,2,3-tris(decyloxy)benzene: As above, using tetrabromomethane (1.65 g, 5.01 mmol), triphenylphosphine (2.61 g, 10.0 mmol) and 3,4,5-tris(decyloxy)benzaldehyde (2.21 g, 3.19 mmol) in CH_2Cl_2 (30 cm^3). The residue was purified by column chromatography on silica gel using petroleum ether (40-60)/ethyl acetate (9:1) to give a colourless solid. 2.28 g (82 %).

^{1}H NMR (400 MHz, $CDCl_3$): δ = 7.37 (1H, s), 6.76 (2H, s), 3.97 (2H, t, $^3J_{HH}$ = 6.6 Hz), 3.96 (4H, t, $^3J_{HH}$ = 6.6 Hz), 1.79 (4H, m), 1.73 (2H, m), 1.46 (6H, m), 1.26 (36H, broad m), 0.88 (9H, t, $^3J_{HH}$ = 7.0 Hz) ppm.

5-(2,2-Dibromovinyl)-1,2,3-tris(dodecyloxy)benzene: As above, using tetrabromomethane (3.21 g, 9.59 mmol), triphenylphosphine (5.09 g, 19.4 mmol) and 3,4,5-tris(dodecyloxy)benzaldehyde (2.00 g, 4.20 mmol) in CH_2Cl_2 (30 cm^3). The residue was purified by column chromatography on silica gel using CH_2Cl_2/ petroleum ether (40-60) (1:1) to give a colourless solid. 1.19 g (48 %).

^{1}H NMR (400 MHz, $CDCl_3$): δ = 7.37 (1H, s), 6.76 (2H, s), 3.96 (2H, t, $^3J_{HH}$ = 6.5 Hz), 3.96 (4H, t, $^3J_{HH}$ = 6.5 Hz), 1.79 (4H, m), 1.73 (2H, m), 1.46 (6H, m), 1.26 (48H, broad m), 0.88 (9H, t, $^3J_{HH}$ = 7.0 Hz). CHN elemental analysis: observed (calculated) ppm: %C 64.7 (64.9), %H 9.7 (9.7).

5-(2,2-Dibromovinyl)-1,2,3-tris(tetradecyloxy)benzene: As above, using tetrabromomethane (506 mg, 1.50 mmol), triphenylphosphine (809 mg, 3.12 mmol) and 3,4,5-tris(tetradecyloxy)benzaldehyde (882 mg, 1.22 mmol) in CH_2Cl_2 (25 cm^3). The residue was purified by column chromatography on silica gel using CH_2Cl_2/ petroleum ether (40-60) (1:1) to give a colourless solid. 854 mg (81 %).

^{1}H NMR (400 MHz, $CDCl_3$): δ = 7.37 (1H, s), 6.76 (2H, s), 3.96 (2H, t, $^3J_{HH}$ = 6.5 Hz), 3.96 (4H, t, $^3J_{HH}$ = 6.5 Hz), 1.79 (4H, m), 1.73 (2H, m), 1.46 (6H, m), 1.26 (60H, broad m), 0.88 (9H, t, $^3J_{HH}$ = 7.0 Hz) ppm.

General Procedure for Synthesis of 1-alkoxy-4-ethynylbenzene, 1,2,-bis(alkoxy)-4-ethynylbenzene and 1,2,3-tris(alkoxy)-5-ethynylbenzene:

Under an atmosphere of nitrogen, ethylmagnesium bromide (3M solution in THF) was added dropwise to a solution of the appropriate 2,2-dibromovinyl(alkoxy)benzene in dry THF (60 cm^3). The mixture was stirred for 30 minutes at room temperature, followed by addition of solid ammonium chloride (excess). The solution was poured into hexane (50 cm^3) and filtered through a pad of Celite®. The solvent was removed from the filtrate *in vacuo* and the residue purified by column chromatography on silica gel.

1-Alkoxy-4-ethynylbenzene:

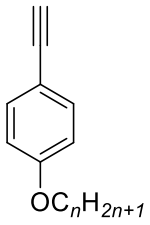

4-Ethynyl-1-(octyloxy)benzene: As above, using 4-(2,2-dibromovinyl)-1-(octyloxy)benzene (3.21 g, 8.21 mmol) and ethylmagnesium bromide (3M solution in THF) (5.3 cm^3, 15.9 mmol), purified using 1:1 petroleum ether(40-60):CH_2Cl_2. 1.62 g. (86%).

^{1}H NMR (400 MHz, $CDCl_3$): δ = 7.41 (4H, AA'XX'), 6.82 (4H, AA'XX'), 3.95 (2H, t, $^3J_{HH}$ = 6.4 Hz), 2.99 (1H, s), 1.81 (2H, m), 1.46 (2H, m), 1.24 (8H, m), 0.89 (3H, t, $^3J_{HH}$ = 6.8 Hz); CHN elemental analysis: observed (calculated): %C 83.5 (83.4), %H 9.7 (9.6) ppm.

4-Ethynyl-1-(decyloxy)benzene: As above, using 4-(2,2-dibromovinyl)-1-(decyloxy)benzene (5.61 g, 13.4 mmol) and ethylmagnesium bromide (3M solution in THF) (8.9 cm^3, 26.7 mmol), purified using 1:1 petroleum ether(40-60):CH_2Cl_2. 2.71 g. (62%).

^{1}H NMR (400 MHz, $CDCl_3$): δ = 7.41 (4H, AA'XX'), 6.82 (4H, AA'XX'), 3.95 (2H, t, $^3J_{HH}$ = 6.4 Hz), 2.99 (1H, s), 1.81 (2H, m), 1.46 (2H, m), 1.24 (10H, m), 0.89 (3H, t, $^3J_{HH}$ = 6.8 Hz); CHN elemental analysis: observed (calculated) ppm: %C 83.3 (83.7), %H 10.1 (10.1)

4-Ethynyl-1-(dodecyloxy)benzene: As above, using 4-(2,2-dibromovinyl)-1-(dodecyloxy)benzene (4.09 g, 9.20 mmol) and ethylmagnesium bromide (3M solution in THF) (6.2 cm^3, 18.6 mmol), purified using 1:1 petroleum ether(40-60):CH_2Cl_2. 2.52 g. (96%).

^{1}H NMR (400 MHz, $CDCl_3$): δ = 7.41 (4H, AA'XX'), 6.82 (4H, AA'XX'), 3.95 (2H, t, $^3J_{HH}$ = 6.4 Hz), 2.99 (1H, s), 1.81 (2H, m), 1.46 (2H, m), 1.24 (12H, m), 0.89 (3H, t, $^3J_{HH}$ = 6.8 Hz) ppm; CHN elemental analysis: observed (calculated): %C 83.6 (83.9), %H 10.4 (10.6).

4-Ethynyl-1-(tetradecyloxy)benzene: As above, using 4-(2,2-dibromovinyl)-1-(tetradecyloxy)benzene (4.90 g, 10.4 mmol) and ethylmagnesium bromide (3M solution in THF) (6.9 cm^3, 20.7 mmol), purified using 1:1 petroleum ether(40-60):CH_2Cl_2. 2.91 g. (89%).

^{1}H NMR (400 MHz, $CDCl_3$): δ = 7.41 (4H, AA'XX'), 6.82 (4H, AA'XX'), 3.95 (2H, t, $^3J_{HH}$ = 6.4 Hz), 2.99 (1H, s), 1.81 (2H, m), 1.46 (2H, m), 1.24 (14H, m), 0.89 (3H, t, $^3J_{HH}$ = 6.8 Hz) ppm; CHN elemental analysis: observed (calculated): %C 84.1 (84.0), %H 11.2 (10.9).

4-Ethynyl-1,2-bis(alkyloxy)benzene:

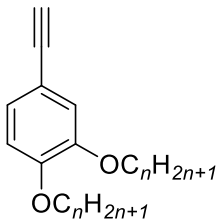

4-Ethynyl-1,2-bis(octyloxy)benzene: As above, using 4-(2,2-dibromovinyl)-1,2-bis(octyloxy)benzene (3.01 g, 5.82 mmol) and EtMgBr (3 M solution in ether) (3.9 cm^3, 11.7 mmol), purified using CH_2Cl_2 as eluent. 1.50 g (72%).

^{1}H NMR (400 MHz, $CDCl_3$): δ = 7.05 (1H, dd, $^3J_{HH}$ = 8.2, $^4J_{HH}$ = 2.0), 6.99 (1H, d, $^4J_{HH}$ = 2.0), 6.79 (1H, d, $^3J_{HH}$ = 8.2), 3.99 (2H, t, $^3J_{HH}$ = 6.7 Hz), 3.97 (2H, t, $^3J_{HH}$ = 6.7 Hz), 2.98 (1H, s), 1.81 (4H, m), 1.46 (4H, m), 1.28 (16H, m), 0.89 (6H, t, $^3J_{HH}$ = 6.8 Hz) ppm.

4-Ethynyl-1,2-bis(decyloxy)benzene: As above, using 4-(2,2-dibromovinyl)-1,2-bis(decyloxy)benzene (5.99 g, 10.4 mmol) and EtMgBr (3 M solution in ether) (7.0 cm^3, 20.9 mmol), purified using 7:3 petroleum ether (40-60):CH_2Cl_2 as eluent. 3.61 g (83%).

^{1}H NMR (400 MHz, $CDCl_3$): δ = 7.05 (1H, dd, $^3J_{HH}$ = 8.2, $^4J_{HH}$ = 2.0), 6.99 (1H, d, $^4J_{HH}$ = 2.0), 6.79 (1H, d, $^3J_{HH}$ = 8.2), 3.99 (2H, t, $^3J_{HH}$ = 6.7 Hz), 3.97 (2H, t, $^3J_{HH}$ = 6.7 Hz), 2.98 (1H, s), 1.81 (4H, m), 1.46 (4H, m), 1.28 (24H, m), 0.89 (6H, t, $^3J_{HH}$ = 6.8 Hz) ppm.

4-Ethynyl-1,2-bis(dodecyloxy)benzene*: As above, using 4-(2,2-dibromovinyl)-1,2-bis(dodecyloxy)benzene (4.51 g, 7.12 mmol) and EtMgBr (3 M solution in ether) (4.8 cm^3, 14.4 mmol), purified using CH_2Cl_2 as eluent. 3.10 g (93%).

^{1}H NMR (400 MHz, $CDCl_3$): δ = 7.05 (1H, dd, $^3J_{HH}$ = 8.2, $^4J_{HH}$ = 2.0), 6.99 (1H, d, $^4J_{HH}$ = 2.0), 6.79 (1H, d, $^3J_{HH}$ = 8.2), 3.99 (2H, t, $^3J_{HH}$ = 6.7 Hz), 3.97 (2H, t, $^3J_{HH}$ = 6.7 Hz), 2.98 (1H, s), 1.81 (4H, m), 1.46 (4H, m), 1.28 (32H, m), 0.89 (6H, t, $^3J_{HH}$ = 6.8 Hz) ppm.

4-Ethynyl-1,2-bis(tetradecyloxy)benzene*: As above, using 4-(2,2-dibromovinyl)-1,2-bis(tetradecyloxy)benzene (3.00 g, 4.37 mmol) and EtMgBr (3 M solution in ether) (2.9 cm^3, 8.69 mmol), purified using CH_2Cl_2 as eluent. 2.21 g (93%).

^{1}H NMR (400 MHz, $CDCl_3$): δ = 7.05 (1H, dd, $^3J_{HH}$ = 8.2, $^4J_{HH}$ = 2.0), 6.99 (1H, d, $^4J_{HH}$ = 2.0), 6.79 (1H, d, $^3J_{HH}$ = 8.2), 3.99 (2H, t, $^3J_{HH}$ = 6.7 Hz), 3.97 (2H, t, $^3J_{HH}$ = 6.7 Hz), 2.98 (1H, s), 1.81 (4H, m), 1.46 (4H, m), 1.28 (40H, m), 0.89 (6H, t, $^3J_{HH}$ = 6.8 Hz) ppm.

*Synthesised by MChem Project Student Rebecca Howarth

5-Ethynyl-1,2,3-tris(alkyloxy)benzene:

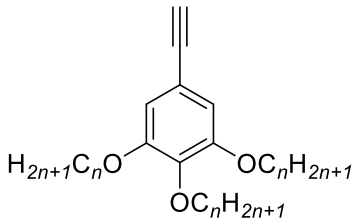

5-Ethynyl-1,2,3-tris(octyloxy)benzene: As above, using 5-(2,2-dibromovinyl)-1,2,3-tris(octyloxy)benzene (452 mg, 703 μmol) and ethylmagnesium bromide (3M solution in ether) (0.6 cm^3, 1.80 mmol), purified using petroleum ether(40-60)/CH_2Cl_2 (7:3) as eluent to give a light yellow oil. 254 mg (75 %).

^{1}H NMR (400 MHz, $CDCl_3$): δ = 6.69 (2H, s), 3.95 (2H, t, $^3J_{HH}$ = 6.5 Hz), 3.94 (4H, t, $^3J_{HH}$ = 6.5 Hz), 2.99 (1H, s), 1.79 (4H, m), 1.73 (2H, m), 1.46 (6H, m), 1.26 (24H, broad m), 0.88 (9H, t, $^3J_{HH}$ = 7.0 Hz) ppm.

5-Ethynyl-1,2,3-tris(decyloxy)benzene: As above, using 5-(2,2-dibromovinyl)-1,2,3-tris(decyloxy)benzene (1.89 g, 2.61 mmol) and ethylmagnesium bromide (3M solution in ether)

(0.86 cm^3, 2.60 mmol), purified using petroleum ether(40-60)/CH_2Cl_2 (9:1) as eluent to give a colourless solid. 1.10 g (76 %).

^{1}H NMR (400 MHz, $CDCl_3$): δ = 6.69 (2H, s), 3.95 (2H, t, $^3J_{HH}$ = 6.5 Hz), 3.94 (4H, t, $^3J_{HH}$ = 6.5 Hz), 2.99 (1H, s), 1.79 (4H, m), 1.73 (2H, m), 1.46 (6H, m), 1.26 (36H, broad m), 0.88 (9H, t, $^3J_{HH}$ = 7.0 Hz) ppm.

5-Ethynyl-1,2,3-tris(dodecyloxy)benzene: As above, using 5-(2,2-dibromovinyl)-1,2,3-tris(dodecyloxy)benzene (1.32 g, 2.11 mmol) and ethylmagnesium bromide (3M solution in ether) (0.8 cm^3, 2.40 mmol), purified using petroleum ether(40-60)/CH_2Cl_2 (7:3) as eluent to give a colourless solid. 292 mg (34 %).

^{1}H NMR (400 MHz, $CDCl_3$): δ = 6.69 (2H, s), 3.95 (2H, t, $^3J_{HH}$ = 6.5 Hz), 3.94 (4H, t, $^3J_{HH}$ = 6.5 Hz), 2.99 (1H, s), 1.79 (4H, m), 1.73 (2H, m), 1.46 (6H, m), 1.26 (48H, broad m), 0.88 (9H, t, $^3J_{HH}$ = 7.0 Hz) ppm. CHN elemental analysis: observed (calculated): %C 80.5 (80.7), %H 12.1 (12.0)

5-Ethynyl-1,2,3-tris(tetradecyloxy)benzene: As above, using 5-(2,2-dibromovinyl)-1,2,3-tris(tetradecyloxy)benzene (893 mg, 1.02 mmol) and ethylmagnesium bromide (3M solution in ether) (0.66 cm^3, 2.02 mmol), purified using petroleum ether(40-60)/CH_2Cl_2 (7:3) as eluent to give a colourless solid. 411 mg (57 %).

^{1}H NMR (400 MHz, $CDCl_3$): δ = 6.69 (2H, s), 3.95 (2H, t, $^3J_{HH}$ = 6.5 Hz), 3.94 (4H, t, $^3J_{HH}$ = 6.5 Hz), 2.99 (1H, s), 1.79 (4H, m), 1.73 (2H, m), 1.46 (6H, m), 1.26 (60H, broad m), 0.88 (9H, t, $^3J_{HH}$ = 7.0 Hz) ppm.

6.3.1 Synthesis of Semi-Perfluoronated Ligands

General Procedure for 1H,1H,2H,2H-perfluoro(alkyl)trifluoromethanesulfonate: Triflic anhydride was taken into dry CH_2Cl_2 and the solution degassed with N_2 and cooled to 0 °C. 1H,1H,2H,2H-perfluoroalkan-1-ol and pyridine were added (in varying solvents) and the reaction mixture was stirred under a flow of N_2 for 1 hour. The resulting precipitate was removed by filtration and volatiles removed from the filtrate *in vacuo*. The residue was then purified by flash column chromatography on silica gel.

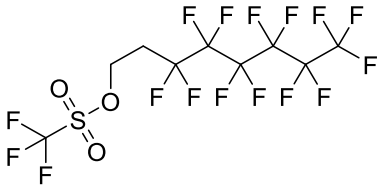

1H,1H,2H,2H-Perfluoro(octyl)trifluoromethanesulfonate†: As above, with triflic anhydride (5.1 cm^3, 30.2 mmol), 1H,1H,2H,2H- perfluorooctan-1-ol (11.0 g, 30.2 mmol) and pyridine (2.9 cm^3, 28.6 mmol), which were added in CH_2Cl_2:dioxane (1:1). The product was purified using petroleum ether(40-60):CH_2Cl_2 (8:2) as eluent. 10.7 g. (71%).

^{1}H NMR (400 MHz, $CDCl_3$): δ = 4.77 (2H, t, $^{3}J_{HH}$ = 6.3 Hz), 2.67 (2H, m) ppm. ^{19}F NMR (376 MHz, MeOD-d_4): δ = -74.6 (3F, s), -80.8 (3F, t,$^{3}J_{FF}$ = 9.7 Hz), -113.6 (2F, m), -121.8 (2F, m), -122.9 (2F,m), -123.4 (2F,m), -126.2 (2F,m) ppm.

†Synthesised by MChem student Rachel Stracey

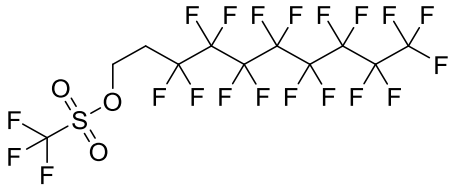

1H,1H,2H,2H-Perfluoro(decyl)trifluoromethanesulfonate: As above, with triflic anhydride (3.62 cm^3, 21.6 mmol), 1H,1H,2H,2H- perfluorodecan-1-ol (10.1 g, 21.8 mmol) and pyridine (1.73 cm^3, 21.3 mmol), which were added in CH_2Cl_2:dioxane (1:1). The product was purified using 8:2 petroleum ether(40-60):ethyl acetate as eluent. 8.80 g. (68%).

^{1}H NMR (400 MHz, $CDCl_3$): δ = 4.77 (2H, t, $^{3}J_{HH}$ = 6.3 Hz), 2.67 (2H, m) ppm. ^{19}F NMR (376 MHz, MeOD-d_4): δ = -74.63 (3F, s), -82.26 (3F, t, $^{3}J_{FF}$ = 10.0 Hz), -114.3 (2F, m), -122.6 (2F, m), -122.8 (4F, m), -123.7 (2F, m), -124.5 (2F, m), -127.2 (2F, m) ppm.

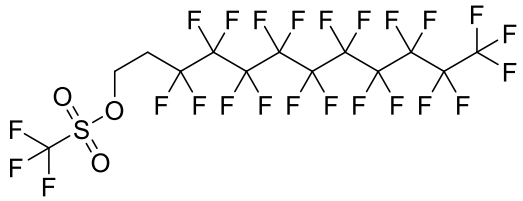

1H,1H,2H,2H-Perfluoro(dodecyl)trifluoromethanesulfonate: As above, with triflic anhydride (1.55 cm^3, 9.22 mmol), 1H,1H,2H,2H- perfluorododecan-1-ol (4.98 g, 8.91 mmol) and pyridine (0.75 cm^3, 9.32 mmol), which were added in dioxane:trifluoromethylbenzene (2:1). The product was purified using 8:2 CH_2Cl_2:petroleum ether(40-60) as eluent. 5.21 g. (85%).

^{1}H NMR (400 MHz, $CDCl_3$): δ = 4.77 (2H, t, $^{3}J_{HH}$ = 6.3 Hz), 2.67 (2H, m). ^{19}F NMR (376 MHz, MeOD-d_4): δ = -74.5 (3F, s), - 80.6 (3F, t, $^{3}J_{FF}$ = 9.8 Hz), -113.4 (2F, m), -121.7 (10F, m), -122.6 (2F, m), -123.3 (2F, m), -126.0 (2F, m) ppm.

General Procedure for Synthesis of 4-(1H,1H,2H,2H-Perfluoro(alkoxy))benzaldehyde:

4-Hydroxybenzaldehyde and K_2CO_3 (1.1 eq. per hydroxy group) were dissolved in acetonitrile (20 cm^3) and stirred at room temperature. The appropriate perfluorinated triflate (1.1 eq. per hydroxy group) was dissolved in acetonitrile (40 cm^3) and added to the benzaldehyde solution. The resulting

reaction mixture was stirred at room temperature for 16 hours. The K_2CO_3 was removed *via* filtration and the filtrate concentrated *in vacuo*. The residue was dissolved ethyl acetate and washed with aqueous 1M NaOH, dried over $MgSO_4$ and concentrated *in vacuo*. The residue was purified by column chromatography on silica gel using petroleum ether(40-60):ethyl acetate (8:2) as the eluent.

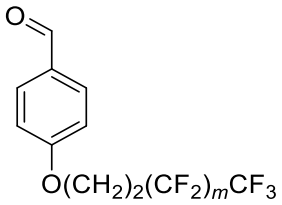

4-(1H,1H,2H,2H-Perfluoro(octyloxy))benzaldehyde†: As above, using 1H,1H,2H,2H-perfluoro(octyl)trifluoromethanesulfonate (2.50 g, 5.01 mmol), 4-hydroxybenzaldehyde (563 mg, 4.58 mmol) and K_2CO_3 (402 mg, 2.87 mmol). 1.62 g. (75%).

^{1}H NMR (400 MHz, $CDCl_3$): δ = 9.88 (1H, s), 7.90 (2H, AA'XX'), 7.14 (2H, AA'XX'), 4.43 (2H, t, $^3J_{HH}$ = 6.1 Hz), 2.77 (2H, m) ppm. ^{19}F NMR (376 MHz, MeOD-d_4): δ = -80.6 (3F, t, $^3J_{FF}$ = 9.7 Hz), -113.6 (2F, m), -121.8 (2F, m), -122.9 (2F,m), -123.4 (2F,m), -126.2 (2F,m) ppm.

4-(1H,1H,2H,2H-Perfluoro(decyloxy))benzaldehyde†: As above, using 1H,1H,2H,2H-perfluoro(decyl)trifluoromethanesulfonate (3.01 g, 5.03 mmol), 4-hydroxybenzaldehyde (564 mg, 4.58 mmol) and K_2CO_3 (633 mg, 4.57 mmol). 1.23 g. (47%).

^{1}H NMR (400 MHz, MeOH-d_4): δ = 9.86 (1H, s), 7.90 (2H, AA'XX'), 7.14 (2H, AA'XX'), 4.43 (2H, t, $^3J_{HH}$ = 6.1 Hz), 2.77 (2H, m) ppm. ^{19}F NMR (376 MHz, MeOD-d_4): δ = -82.3 (3F, t, $^3J_{FF}$ = 10.0 Hz), -114.3 (2F, m), -122.6 (2F, m), -122.8 (4F, m), -123.7 (2F, m), -124.5 (2F, m), -127.2 (2F, m) ppm.

4-(1H,1H,2H,2H-Perfluoro(dodecyloxy))benzaldehyde†: As above, using 1H,1H,2H,2H-perfluoro(dodecyl)trifluoromethanesulfonate (2.50 g, 3.59 mmol), 4-hydroxybenzaldehyde (403 mg, 3.26 mmol) and K_2CO_3 (500 mg, 3.59 mmol). 1.66 g. (76%).

^{1}H NMR (400 MHz, $CDCl_3$): δ = 9.91 (1H, s), 7.86 (2H, AA'XX'), 7.02 (2H, AA'XX'), 4.36 (2H, t, $^3J_{HH}$ = 6.7 Hz), 2.68 (2H, m) ppm. ^{19}F NMR (376 MHz, $CDCl_3$): δ = - 80.6 (3F, t, $^3J_{FF}$ = 9.5 Hz), -113.2 (2F, m), -121.7 (8F‡, m), -122.6 (2F, m), -123.4 (2F, m), -126.0 (2F, m) ppm.

†Synthesised by MChem student Rachel Stracey; ‡low integration due to impure commercial starting materials, if pure would equal 10F

General Procedure for Synthesis of 3,4-bis(1H,1H,2H,2H-perfluoro(alkoxy))benzaldehyde:

4-Hydroxybenzaldehyde and K_2CO_3 (1.1 eq. per hydroxy group) were dissolved in acetonitrile (20 cm^3) and stirred at room temperature. The appropriate perfluorinated triflate (1.1 eq. per hydroxy

group) was dissolved in acetonitrile (50 cm^3) and added to the benzaldehyde solution. The resulting reaction mixture was stirred at room temperature for 16 hours, after which the precipitate which formed was isolated by filtration and washed with water and acetonitrile and air dried. The product was used without further purification.

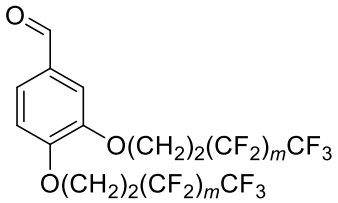

3,4-Bis(1H,1H,2H,2H-perfluoro(octyloxy))benzaldehyde: As above, using 1H,1H,2H,2H-perfluoro(octyl)trifluoromethanesulfonate (7.08 g, 14.3 mmol), 3,4-di(hydroxy)benzaldehyde (891 mg, 6.44 mmol) and K_2CO_3 (2.21 g, 15.9 mmol). 2.66 g. (50%).

^{1}H NMR (400 MHz, $CDCl_3$): δ = 9.87 (1H, s), 7.52 (1H, dd, $^3J_{HH}$ = 8.2, $^4J_{HH}$ = 1.8), 7.45 (1H, d, $^4J_{HH}$ = 1.8), 7.02 (1H, d, $^3J_{HH}$ = 8.2), 4.39 (2H, t, $^3J_{HH}$ = 6.5 Hz), 4.35 (2H, t, $^3J_{HH}$ = 6.5 Hz), 2.68 (4H, m) ppm; ^{19}F NMR δ_F (376 MHz, $CDCl_3$): - 80.7 (6F, t, $^3J_{FF}$ = 9.8 Hz), -113.2 (4F, m), -121.8 (4F, m), -122.8 (4F, m), -123.5 (4F, m), -126.1 (4F, m) ppm

3,4-Bis(1H,1H,2H,2H-perfluoro(decyloxy))benzaldehyde: As above, using 1H,1H,2H,2H-perfluoro(decyl)trifluoromethanesulfonate (7.39 g, 12.4 mmol), 3,4-di(hydroxy)benzaldehyde (781 mg, 5.70 mmol) and K_2CO_3 (1.72 g, 12.4 mmol). 5.14g. (87%).

^{1}H NMR (400 MHz, $CDCl_3$): δ = 9.87 (1H, s), 7.52 (1H, dd, $^3J_{HH}$ = 8.2, $^4J_{HH}$ = 1.8), 7.45 (1H, d, $^4J_{HH}$ = 1.8), 7.02 (1H, d, $^3J_{HH}$ = 8.2), 4.38 (2H, t, $^3J_{HH}$ = 6.5 Hz), 4.36 (2H, t, $^3J_{HH}$ = 6.5 Hz), 2.69 (4H, m) ppm; ^{19}F NMR δ_F (376 MHz, $CDCl_3$): - 80.7 (6F, t, $^3J_{FF}$ = 9.8 Hz), -113.2 (4F, m), -121.8 (4F, m), -121.9 (8F, m), -122.7 (4F, m), -123.5 (4F, m), -126.1 (4F, m) ppm

3,4-Bis(1H,1H,2H,2H-perfluoro(dodecyloxy))benzaldehyde: As above, using 1H,1H,2H,2H-perfluoro(dodecyl)trifluoromethanesulfonate (4.48 g, 6.46 mmol), 3,4-di(hydroxy)benzaldehyde (410 mg, 2.97 mmol) and K_2CO_3 (903 mg, 6.52 mmol). 2.89 g. (79%).

^{1}H NMR (400 MHz, $CDCl_3$): δ = 9.87 (1H, s), 7.52 (1H, dd, $^3J_{HH}$ = 8.2, $^4J_{HH}$ = 1.8), 7.45 (1H, d, $^4J_{HH}$ = 1.8), 7.02 (1H, d, $^3J_{HH}$ = 8.2), 4.38 (2H, t, $^3J_{HH}$ = 6.5 Hz), 4.35 (2H, t, $^3J_{HH}$ = 6.5 Hz), 2.69 (4H, m) ppm; ^{19}F NMR δ_F (376 MHz, $CDCl_3$): - 80.7 (6F, t, $^3J_{FF}$ = 9.8 Hz), -113.2 (4F, m), -121.8 (16F‡, m), -122.7 (4F, m), -123.5 (4F, m), -126.1 (4F, m) ppm.

‡low integration due to impure commercial starting materials, if pure would equal 20F

General Procedure for the Synthesis of Methyl 3,4,5-tri(1H,1H,2H,2H-perfluoro(alkoxy)benzoate:

Methyl 3,4,5-tri(hydroxy)benzoate and K_2CO_3 (3.3 eq) were dissolved in either acetone or acetonitrile (specified for individual reactions below) and stirred at room temperature. A solution of 1H,1H,2H,2H-perfluoro(alkyl)trifluoromethanesulfonate in the same solvent was added and the reaction mixture stirred at room temperature for 48 hours. The resultant precipitate was isolated *via* filtration and washed with water and acetonitrile and air dried. The product was used without further purification.

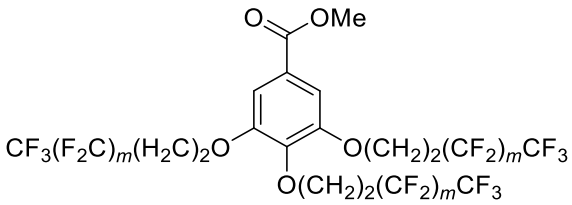

Methyl 3,4,5-tris(1H,1H,2H,2H-perfluoro(octyloxy))benzoate: As above, using 1H,1H,2H,2H-perfluoro(octyl)trifluoromethanesulfonate (10.0 g, 20.2 mmol), methyl 3,4,5-tri(hydroxy)benzoate (804 mg, 4.41 mmol) and K_2CO_3 (1.94 g, 14.0 mmol), using acetonitrile (200 cm^3) as the reaction solvent. 4.31 g. (81%).

^1H NMR (400 MHz, $CDCl_3$): δ = 7.33 (2H, s), 4.35 (4H, t, $^3J_{HH}$ = 6.3 Hz), 4.27 (2H, t, $^3J_{HH}$ = 6.8 Hz), 3.93 (3H, s), 2.64 (6H, m) ppm; ^{19}F NMR δ_F (376 MHz, $CDCl_3$): - 80.7 (6F, t, $^3J_{FF}$ = 9.9 Hz), - 80.9 (3F, t, $^3J_{FF}$ = 9.8 Hz), -113.3 (4F, m), -113.5 (2F, m), -121.8 (4F, m), -122.0 (2F, m), -122.8 (4F, m), -123.0 (2F, m), -123.6 (4F, m), -123.7 (2F, m), -126.1 (4F, m) -126.2 (2F, m) ppm

Methyl 3,4,5-tris(1H,1H,2H,2H-perfluoro(decyloxy))benzoate: As above, using 1H,1H,2H,2H-perfluoro(decyl)trifluoromethanesulfonate (11.6 g, 16.7 mmol), methyl 3,4,5-tri(hydroxy)benzoate (1.13 mg, 8.02 mmol) and K_2CO_3 (2.70 g, 19.5 mmol), using acetone (400 cm^3) as the reaction solvent. 3.91 g. (32%).

^1H NMR (400 MHz, $CDCl_3$): δ = 7.32 (2H, s), 4.35 (4H, t, $^3J_{HH}$ = 6.3 Hz), 4.26 (2H, t, $^3J_{HH}$ = 6.8 Hz), 3.92 (3H, s), 2.64 (6H, m) ppm; ^{19}F NMR δ_F (376 MHz, $CDCl_3$): - 80.8 (6F, t, $^3J_{FF}$ = 9.8 Hz), - 80.9 (3F, t, $^3J_{FF}$ = 9.8 Hz), -113.4 (4F, m), -113.6 (2F, m), -121.7 (4F, m), -122.0 (14F, m), -122.8 (6F, m), -123.5 (4F, m), -123.7 (2F, m), -126.1 (4F, m) -126.3 (2F, m) ppm

Methyl 3,4,5-tris(1H,1H,2H,2H-perfluoro(dodecyloxy))benzoate: As above, using 1H,1H,2H,2H-perfluoro(dodecyl)trifluoromethanesulfonate (18.7 g, 26.9 mmol), methyl 3,4,5-tri(hydroxy)benzoate (1.50 g, 8.11 mmol) and K_2CO_3 (3.71 g, 26.8 mmol), using a 2:1 mixture of acetonitrile (300 cm^3) and hexafluorobenzene (150 cm^3) as the reaction solvent. 1H,1H,2H,2H-perfluoro(dodecyl)trifluoromethanesulfonate was added in acetone only. 3.90 g. (26%).

^{1}H NMR (400 MHz, $CDCl_3$): δ = 7.35 (2H, s), 4.36 (4H, t, $^{3}J_{HH}$ = 6.3 Hz), 4.26 (2H, t, $^{3}J_{HH}$ = 6.8 Hz), 3.92 (3H, s), 2.64 (6H, m) ppm; ^{19}F NMR δ_F (376 MHz, $CDCl_3$): - 80.8 (6F, t, $^{3}J_{FF}$ = 9.9 Hz), - 80.8 (3F, t, $^{3}J_{FF}$ = 9.8 Hz), -112.9 (4F, m), -113.2 (2F, m), -122.0 (30F, m), -122.5 (6F, m), -123.3 (4F, m), -123.5 (2F, m), -125.9 (9F, m) ppm

General Procedure for the Synthesis of 3,4,5-tris(1H,1H,2H,2H-perfluoro(alkoxy))benzyl alcohol:

Under an atmosphere of nitrogen at room temperature, methyl 3,4,5-tris(1H,1H,2H,2H-perfluoro(alkoxy))benzoate was dissolved in THF (130 cm^3). $LiAlH_4$ (1M solution in THF) was added dropwise and the resultant solution was stirred at room temperature for 16 hours, after which time ethyl acetate was added to quench the reaction. The reaction mixture was concentrated *in vacuo* and dissolved in boiling hexane; insoluble impurities were isolated *via* filtration. The filtrate was concentrated *in vacuo* and recrystallised from $CHCl_3$.

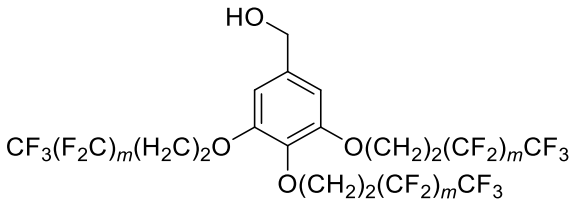

3,4,5-Tris(1H,1H,2H,2H-perfluoro(octyloxy))benzyl alcohol: As above, using methyl 3,4,5-tris(1H,1H,2H,2H-perfluoro(octyloxy))benzoate (4.10 g, 3.35 mmol) and $LiAlH_4$ (1M in THF) (4.0 cm^3, 12.0 mmol). 3.71 g. (90%).

^{1}H NMR (400 MHz, $CDCl_3$): δ = 6.65 (2H, s), 4.65 (2H, $^{4}J_{HH}$ = 4.0 Hz) 4.31 (4H, t, $^{3}J_{HH}$ = 6.4 Hz), 4.20 (2H, t, $^{3}J_{HH}$ = 6.9 Hz), 2.63 (6H, m) ppm; ^{19}F NMR δ_F (376 MHz, $CDCl_3$): - 80.7 (6F, t, $^{3}J_{FF}$ = 9.9 Hz), - 80.9 (3F, t, $^{3}J_{FF}$ = 9.8 Hz), -113.3 (4F, m), -113.5 (2F, m), -121.9 (4F, m), -122.0 (2F, m), -122.9 (6F, m), -123.6 (4F, m), -123.7 (2F, m), -126.1 (4F, m) -126.3 (2F, m) ppm.

3,4,5-Tris(1H,1H,2H,2H-perfluoro(decyloxy))benzyl alcohol: As above, using methyl 3,4,5-tris(1H,1H,2H,2H-perfluoro(decyloxy))benzoate (3.71 g, 2.40 mmol) and $LiAlH_4$ (1M in THF) (2.9 cm^3, 8.72 mmol). 2.50 g. (69%).

^{1}H NMR (400 MHz, $CDCl_3$): δ = 6.66 (2H, s), 4.65 (2H, $^{4}J_{HH}$ = 4.7 Hz) 4.32 (4H, t, $^{3}J_{HH}$ = 6.4 Hz), 4.22 (2H, t, $^{3}J_{HH}$ = 6.9 Hz), 2.62 (6H, m) ppm; ^{19}F NMR δ_F (376 MHz, $CDCl_3$): - 80.8 (6F, t, $^{3}J_{FF}$ = 9.8 Hz), - 80.9 (3F, t, $^{3}J_{FF}$ = 9.9 Hz), -112.9 (4F, m), -113.1 (2F, m), -121.3 (4F, m), -121.6 (14F, m), -122.5 (6F, m), -123.3 (4F, m), -123.5 (2F, m), -125.9 (6F, m) ppm.

General Procedure for the Synthesis of 3,4,5-tris(1H,1H,2H,2H-perfluoro(dodecyloxy))benzaldehyde:

3,4,5-Tris(1H,1H,2H,2H-perfluoro(alkoxy))benzyl alcohol and MnO_2 (excess) were taken into CH_2Cl_2 and stirred it either room temperature or 45 °C (specified below) for 36 hours. The reaction mixture was filtered through Celite to remove the MnO_2 and the filtrate was concentrated *in vacuo*. The residue was purified by column chromatography on silica gel.

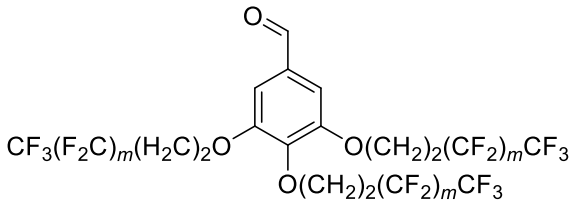

3,4,5-Tris(1H,1H,2H,2H-perfluoro(octyloxy))benzaldehyde: As above, with 3,4,5-tris(1H,1H,2H,2H-perfluoro(octyloxy))benzyl alcohol (3.69 g, 3.09 mmol) and MnO_2 (2.69 g, 31.0 mmol) in CH_2Cl_2 (200 cm^3), at room temperature, residue purified using petroleum ether(40-60):ethyl acetate (7:3) as the eluent. 3.10 g. (84%).

^{1}H NMR (400 MHz, $CDCl_3$): δ = 9.88 (1H, s), 7.16 (2H, s), 4.38 (4H, t, $^3J_{HH}$ = 6.3 Hz), 4.30 (2H, t, $^3J_{HH}$ = 6.8 Hz), 2.65 (6H, m) ppm; ^{19}F NMR δ_F (376 MHz, $CDCl_3$): - 80.8 (6F, t, $^3J_{FF}$ = 9.9 Hz), - 80.9 (3F, t, $^3J_{FF}$ = 9.8 Hz), -113.4 (4F, m), -113.6 (2F, m), -121.9 (4F, m), -122.0 (2F, m), -122.9 (4F, m), -123.0 (2F, m), -123.6 (4F, m), -123.7 (2F, m), -126.2 (4F, m) -126.3 (2F, m) ppm.

3,4,5-Tris(1H,1H,2H,2H-perfluoro(decyloxy))benzaldehyde: As above, with 3,4,5-tris(1H,1H,2H,2H-perfluoro(octyloxy))benzyl alcohol (2.31 g, 1.51 mmol) and MnO_2 (1.31 g, 15.1 mmol), at 45 °C, using a reaction solvent of 1:1 trifluoromethylbenzene:CH_2Cl_2 (200 cm^3), residue purified using petroleum ether(40-60):ethyl acetate (1:1) as the eluent. 1.04 g (51%)**.**

^{1}H NMR (400 MHz, $CDCl_3$): δ = 9.88 (1H, s), 7.17 (2H, s), 4.38 (4H, t, $^3J_{HH}$ = 6.1 Hz), 4.30 (2H, t, $^3J_{HH}$ = 6.8 Hz), 2.65 (6H, m) ppm; ^{19}F NMR δ_F (376 MHz, $CDCl_3$): - 80.8 (6F, t, $^3J_{FF}$ = 9.7 Hz), - 80.8 (3F, t, $^3J_{FF}$ = 9.9 Hz), -113.3 (4F, m), -113.5 (2F, m), -121.4 (4F, m), -122.0 (14F, m), -122.8 (6F, m), -123.5 (4F, m), -123.7 (2F, m), -126.2 (6F, m) ppm.

General Procedure for the Synthesis of 4-(2,2-dibromovinyl)-1-(1H,1H,2H,2H-perfluoro(alkoxy))benzene, 4-(2,2-dibromovinyl)-1,2-bis(1H,1H,2H,2H-perfluoro(alkoxy))benzene and 5-(2,2-dibromovinyl)-1,2,3-tris(1H,1H,2H,2H-perfluoro(alkoxy))benzene:

Under a nitrogen atmosphere and cooled in an ice bath to 0 °C, a solution of tetrabromomethane (1.3 equiv.) in CH_2Cl_2 (50 cm^3) was added to a solution of triphenylphosphine (2.6 equiv.) in CH_2Cl_2 (20 cm^3), with the temperature maintained below 15 °C. After full addition the mixture was cooled again to 0 °C. A solution of the appropriate 1H,1H,2H,2H-perfluoro(alkoxy)benzaldehyde and triethylamine (1.0 equiv.) in CH_2Cl_2 was added dropwise and the mixture stirred for 30 minutes. The mixture was warmed to room temperature and stirred for 1 hour and then poured into hexane. The resulting precipitate was removed *via* filtration and the filtrate was concentrated *in vacuo* to give a residue which was purified by column chromatography on silica gel using CH_2Cl_2:petroleum ether(40-60) (1:1) as eluent.

4-(2,2-Dibromovinyl)-1-(1H,1H,2H,2H-perfluoro(alkoxy))benzene:

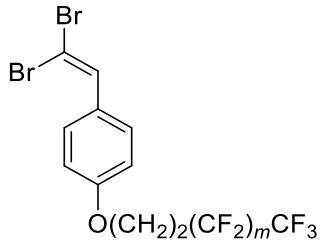

4-(2,2-Dibromovinyl)-1-(1H,1H,2H,2H-perfluoro(octyloxy))benzene: As above, using 4-(1H,1H,2H,2H-perfluoro(octyloxy))benzaldehyde (1.14 g, 2.43 mmol) in CH_2Cl_2 (30 cm^3), triphenylphosphine (1.66 g, 6.32 mmol) and tetrabromomethane (1.05 g, 3.16 mmol). 1.21 g. (79%).

^{1}H NMR (400 MHz, $CDCl_3$): δ = 7.52 (2H, AA'XX'), 7.41 (1H, s), 6.90 (2H, AA'XX'), 4.29 (2H, t, $^3J_{HH}$ = 6.8 Hz), 2.64 (2H, m) ppm. ^{19}F NMR (376 MHz, $CDCl_3$): δ =-80.6 (3F, t, $^3J_{FF}$ = 9.7 Hz), -113.6 (2F, m), -121.8 (2F, m), -122.9 (2F, m), -123.4 (2F, m), -126.2 (2F, m) ppm.

4-(2,2-Dibromovinyl)-1-(1H,1H,2H,2H-perfluoro(decyloxy))benzene†: As above, using 4-(1H,1H,2H,2H-perfluoro(decyloxy))benzaldehyde (1.37 g, 2.48 mmol) in CH_2Cl_2 (30 cm^3), triphenylphosphine (1.79 g, 6.84 mmol) and tetrabromomethane (1.13 g, 3.41 mmol). 562 mg. (31%).

^{1}H NMR (400 MHz, $CDCl_3$): δ = 7.52 (2H, AA'XX'), 7.41 (1H, s), 6.89 (2H, AA'XX'), 4.29 (2H, t, $^{3}J_{HH}$ = 6.8 Hz), 2.64 (2H, m) ppm. ^{19}F NMR (376 MHz, $CDCl_3$): δ = -82.3 (3F, t, $^{3}J_{FF}$ = 10.0 Hz), -114.3 (2F, m), -122.6 (2F, m), -122.8 (4F, m), -123.7 (2F, m), -124.5 (2F, m), -127.2 (2F, m) ppm.

4-(2,2-Dibromovinyl)-1-(1H,1H,2H,2H-perfluoro(dodecyloxy))benzene: As above, using 4-(1H,1H,2H,2H-perfluoro(dodecoxy))benzaldehyde (1.41 g, 2.11 mmol) in CH_2Cl_2 (30 cm^3), triphenylphosphine (1.53 g, 5.83 mmol) and tetrabromomethane (981 mg, 2.92 mmol). 1.63 g. (94%).

^{1}H NMR (400 MHz, $CDCl_3$): δ = 7.52 (2H, AA'XX'), 7.41 (1H, s), 6.90 (2H, AA'XX'), 4.29 (2H, t, $^{3}J_{HH}$ = 6.8 Hz), 2.64 (2H, m) ppm. ^{19}F NMR (376 MHz, $CDCl_3$): δ = -82.3 (3F, t, $^{3}J_{FF}$ = 10.0 Hz), -114.3 (2F, m), -122.6 (2F, m), -122.8 (6F‡, m), -123.7 (2F, m), -124.5 (2F, m), -127.2 (2F, m) ppm.

†Synthesised by MChem student Rachel Stracey; ‡low integration due to impure commercial starting materials, if pure would equal 8F

4-(2,2-Dibromovinyl)-1,2-bis(1H,1H,2H,2H-perfluoro(alkoxy))benzene:

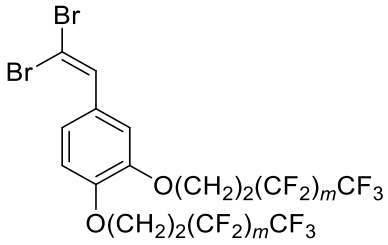

4-(2,2-Dibromovinyl)-1,2-bis(1H,1H,2H,2H-perfluoro(octyloxy))benzene: As above, using 3,4-bis(1H,1H,2H,2H-perfluoro(octyloxy))benzaldehyde (2.18 g, 2.65 mmol) in CH_2Cl_2 (30 cm^3), triphenylphosphine (1.81 g, 6.86 mmol) and tetrabromomethane (1.14 g, 3.44 mmol), purified using CH_2Cl_2 as eluent. 2.59 g. (99%).

^{1}H NMR (400 MHz, $CDCl_3$): δ = 7.40 (1H, s), 7.23 (1H, d, $^{4}J_{HH}$ = 2.0), 7.15 (1H, dd, $^{3}J_{HH}$ = 8.3, $^{4}J_{HH}$ = 2.0), 6.91 (1H, d, $^{3}J_{HH}$ = 8.3), 4.31 (2H, t, $^{3}J_{HH}$ = 6.6 Hz), 4.30 (2H, t, $^{3}J_{HH}$ = 6.6 Hz), 2.65 (4H, m) ppm; ^{19}F NMR (376 MHz, $CDCl_3$): δ = - 80.7 (6F, t, $^{3}J_{FF}$ = 9.8 Hz), -113.2 (4F, m), -121.8 (4F, m), -122.8 (4F, m), -123.5 (4F, m), -126.1 (4F, m) ppm.

4-(2,2-Dibromovinyl)-1,2-bis(1H,1H,2H,2H-perfluoro(decyloxy))benzene: As above, using 3,4-bis(1H,1H,2H,2H-perfluoro(decyloxy))benzaldehyde (4.52 g, 4.37 mmol) in CH_2Cl_2 (40 cm^3), triphenylphosphine (2.98 g, 11.4 mmol) and tetrabromomethane (1.88 g, 5.67 mmol); benzaldehyde was added in $CHCl_3$ due to increased solubility. Purified using CH_2Cl_2 as eluent. 4.22 g. (81%).

^{1}H NMR (400 MHz, $CDCl_3$): δ = 7.40 (1H, s), 7.23 (1H, d, $^{4}J_{HH}$ = 2.0), 7.15 (1H, dd, $^{3}J_{HH}$ = 8.3, $^{4}J_{HH}$ = 2.0), 6.91 (1H, d, $^{3}J_{HH}$ = 8.3), 4.31 (2H, t, $^{3}J_{HH}$ = 6.6 Hz), 4.30 (2H, t, $^{3}J_{HH}$ = 6.6 Hz), 2.65 (4H, m) ppm; ^{19}F NMR (376 MHz, $CDCl_3$): δ = - 80.7 (6F, t, $^{3}J_{FF}$ = 9.8 Hz), -113.2 (4F, m), -121.8 (4F, m), -121.9 (8F, m), -122.7 (4F, m), -123.5 (4F, m), -126.1 (4F, m) ppm.

4-(2,2-Dibromovinyl)-1,2-bis(1H,1H,2H,2H-perfluoro(dodecyloxy))benzene: As above, using 3,4-bis(1H,1H,2H,2H-perfluoro(dodecyloxy))benzaldehyde (2.62 g, 2.13 mmol) in CH_2Cl_2 (30 cm^3), triphenylphosphine (1.44 g, 5.49 mmol) and tetrabromomethane (909 mg, 2.74 mmol); benzaldehyde was added in 1:1 trifluoromethylbenzene:$CHCl_3$ due to increased solubility. Purified using petroleum ether(40-60):ethyl acetate (7:3) as eluent. 2.23 g. (76%).

^{1}H NMR (400 MHz, $CDCl_3$): δ = 7.40 (1H, s), 7.23 (1H, d, $^{4}J_{HH}$ = 2.0), 7.15 (1H, dd, $^{3}J_{HH}$ = 8.3, $^{4}J_{HH}$ = 2.0), 6.91 (1H, d, $^{3}J_{HH}$ = 8.3), 4.31 (2H, t, $^{3}J_{HH}$ = 6.6 Hz), 4.30 (2H, t, $^{3}J_{HH}$ = 6.6 Hz), 2.65 (4H, m) ppm; ^{19}F NMR (376 MHz, $CDCl_3$): δ = - 80.7 (6F, t, $^{3}J_{FF}$ = 9.8 Hz), -113.2 (4F, m), -121.8 (16F‡, m), -122.7 (4F, m), -123.5 (4F, m), -126.1 (4F, m) ppm.

‡low integration due to impure commercial starting materials, if pure would equal 20F

5-(2,2-Dibromovinyl)-1,2,3-tris(1H,1H,2H,2H-perfluoro(alkoxy))benzene:

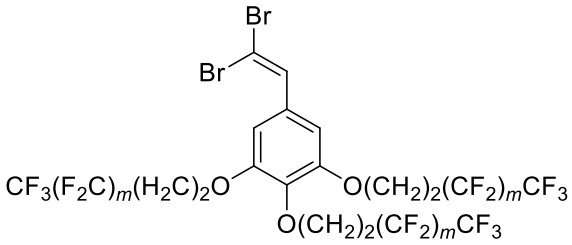

Note: for these two complexes, the reaction mixture was not poured into hexane, but rather the whole reaction mixture was concentrated *in vacuo* and this residue purified by column chromatography.

5-(2,2-Dibromovinyl)-1,2,3-tris(1H,1H,2H,2H-perfluoro(octyloxy))benzene: As above, using 3,4,5-tris(1H,1H,2H,2H-perfluoro(octyloxy))benzaldehyde (2.46 g, 2.06 mmol) in CH_2Cl_2 (40 cm^3), triphenylphosphine (1.41 g, 5.40 mmol) and tetrabromomethane (892 mg, 2.69 mmol), purified using petroleum ether(40-60):CH_2Cl_2 (1:1) as eluent. 2.11 g. (76%).

^{1}H NMR (400 MHz, $CDCl_3$): δ = 7.40 (1H, s), 6.82 (2H, s), 4.30 (4H, t, $^{3}J_{HH}$ = 6.3 Hz), 4.23 (2H, t, $^{3}J_{HH}$ = 6.9 Hz), 2.62 (6H, m) ppm; ^{19}F NMR (376 MHz, $CDCl_3$): δ = - 80.9 (6F, t, $^{3}J_{FF}$ = 9.9 Hz), - 81.0 (3F, t, $^{3}J_{FF}$ = 9.7 Hz), -113.4 (4F, m), -113.6 (2F, m), -121.9 (4F, m), -122.1 (2F, m), -122.9 (4F, m), -123.0 (2F, m), -123.6 (4F, m), -123.8 (2F, m), -126.2 (4F, m) -126.3 (2F, m) ppm

5-(2,2-Dibromovinyl)-1,2,3-tris(1H,1H,2H,2H-perfluoro(decyloxy))benzene: As above, using 3,4,5-tris(1H,1H,2H,2H-perfluoro(octyloxy))benzaldehyde (802 mg, 5.41 mmol), triphenylphosphine (374 mg, 1.43 mmol) and tetrabromomethane (232 mg, 6.92 mmol); benzaldehyde was dissolved and added in trifluoromethylbenzene (40 cm^3) instead of CH_2Cl_2 as outlined above. Purified using petroleum ether(40-60):CH_2Cl_2 (7:3) as eluent. 754 mg. (85%).

^{1}H NMR (400 MHz, $CDCl_3$): δ = 7.40 (1H, s), 6.82 (2H, s), 4.30 (4H, t, $^{3}J_{HH}$ = 6.2 Hz), 4.23 (2H, t, $^{3}J_{HH}$ = 6.9 Hz), 2.62 (6H, m) ppm; ^{19}F NMR (376 MHz, $CDCl_3$): δ = - 80.7 (6F, t, $^{3}J_{FF}$ = 9.7 Hz), - 80.8 (3F, t, $^{3}J_{FF}$ = 9.8 Hz), -113.3 (4F, m), -113.5 (2F, m), -121.4 (4F, m), -122.0 (14F, m), -122.8 (6F, m), -123.5 (4F, m), -123.7 (2F, m), -126.1 (4F, m), -126.2 (2F, m) ppm

General Procedure for 1-(1H,1H,2H,2H-perfluoro(alkoxy))-4-ethynylbenzene, 1,2,-bis(1H,1H,2H,2H-perfluoro(alkoxy))-4-ethynylbenzene and 1,2,3-tris(1H,1H,2H,2H-perfluoro(alkoxy))-5-ethynylbenzene:

The appropriate (2,2-dibromovinyl)-(1H,1H,2H,2H-perfluoro(alkoxy)benzene was dissolved in THF (50 cm^3) under an atmosphere of dinitrogen. A solution of EtMgBr (3M in diethyl ether) was added dropwise, with stirring at room temperature, and the resulting reaction mixture was stirred for 2 hours. Solid NH_4Cl (excess) was then added to quench the reaction. Excess and resultant salts were removed *via* filtration, and the filtrate concentrated *in vacuo*. The residue was purified by column chromatography on silica gel.

1-(1H,1H,2H,2H-Perfluoro(alkoxy))-4-ethynylbenzene:

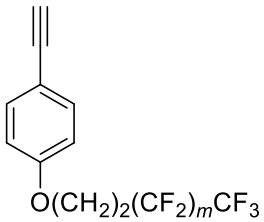

1-(1H,1H,2H,2H-Perfluoro(octyloxy))-4-ethynylbenzene: As above, using 4-(2,2-dibromovinyl)-1-(1H,1H,2H,2H-perfluoro(octyloxy))benzene (440 mg, 0.712 mmol) and EtMgBr (3M in ether) (0.3 cm^3, 0.902 mmol), purified using petroleum ether(40-60):ethyl acetate (6:4) as the eluent. 162 mg. (49%).

^{1}H NMR δ_H (400 MHz, $CDCl_3$): 7.43 (2H, AA'XX'), 6.84 (2H, AA'XX'), 4.26 (2H, t, $^{3}J_{HH}$ = 6.8 Hz), 3.00 (1H, s), 2.62 (2H, m) ppm. ^{19}F NMR (376 MHz, $CDCl_3$): δ = -80.6 (3F, t, $^{3}J_{FF}$ = 9.8 Hz), -113.2 (2F, m), -121.8 (2F, m), -122.8 (2F, m), -123.4 (2F, m), -126.0 (2F, m) ppm.

1-(1H,1H,2H,2H-Perfluoro(decyloxy))-4-ethynylbenzene: As above, using 4-(2,2-dibromovinyl)-1-(1H,1H,2H,2H-perfluoro(decyloxy))benzene (875 mg, 1.23 mmol) and EtMgBr (3M in ether) (0.5 cm^3, 1.51 mmol), purified using petroleum ether(40-60):ethyl acetate (6:4) as the eluent. 571 mg. (84%).

(^{1}H NMR δ_H (400 MHz, $CDCl_3$): 7.44 (2H, AA'XX'), 6.84 (2H, AA'XX'), 4.28 (2H, t, $^{3}J_{HH}$ = 6.8 Hz), 3.01 (1H, s), 2.63 (2H, m) ppm. ^{19}F NMR (376 MHz, $CDCl_3$): δ = -82.3 (3F, t, $^{3}J_{FF}$ = 10.0 Hz), -114.3 (2F, m), -122.6 (2F, m), -122.8 (4F, m), -123.7 (2F, m), -124.5 (2F, m), -127.2 (2F, m) ppm; CHN elemental analysis: observed (calculated): %C 38.4 (38.3), %H 1.3 (1.6)

1-(1H,1H,2H,2H-Perfluoro(dodecyloxy))-4-ethynylbenzene: As above, using 4-(2,2-dibromovinyl)-1-(1H,1H,2H,2H-perfluoro(dodecyloxy))benzene (1.18 g, 1.43 mmol) and EtMgBr (3M in ether) (0.7 cm^3, 2.12 mmol), purified using petroleum ether(40-60):ethyl acetate (6:4) as the eluent. 840 mg. (88%).

^{1}H NMR δ_H (400 MHz, $CDCl_3$): 7.44 (2H, AA'XX'), 6.84 (2H, AA'XX'), 4.28 (2H, t, $^{3}J_{HH}$ = 6.8 Hz), 3.01 (1H, s), 2.63 (2H, m) ppm. ^{19}F NMR (376 MHz, $CDCl_3$): δ = - 80.6 (3F, t, $^{3}J_{FF}$ = 9.5 Hz), -113.2 (2F, m), -121.7 (8F‡, m), -122.6 (2F, m), -123.4 (2F, m), -126.0 (2F, m) ppm.

‡low integration due to impure commercial starting materials, if pure would equal 10F

1,2,-Bis(1H,1H,2H,2H-perfluoro(alkoxy))-4-ethynylbenzene:

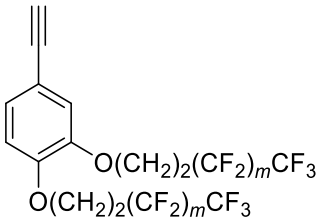

1,2,-Bis(1H,1H,2H,2H-perfluoro(octyloxy))-4-ethynylbenzene: As above, using 3,4-bis(2,2-dibromovinyl)-1-(1H,1H,2H,2H-perfluoro(octyloxy))benzene (1.72 g, 1.74 mmol) and EtMgBr (3M in ether) (0.97 cm^3, 2.90 mmol), purified using CH_2Cl_2:petroleum ether(40-60) (3:2) as the eluent. 1.22 g. (83%).

^{1}H NMR (400 MHz, $CDCl_3$): δ = 7.15 (1H, dd, $^{3}J_{HH}$ = 8.4, $^{4}J_{HH}$ = 2.0), 7.05 (1H, d, $^{4}J_{HH}$ = 2.0), 6.86 (1H, d, $^{3}J_{HH}$ = 8.5), 4.30 (2H, t, $^{3}J_{HH}$ = 6.6 Hz), 4.28 (2H, t, $^{3}J_{HH}$ = 6.6 Hz), 3.03 (1H, s), 2.65 (4H, m) ppm; ^{19}F NMR (376 MHz, $CDCl_3$): δ = - 80.7 (6F, t, $^{3}J_{FF}$ = 9.8 Hz), -113.2 (4F, m), -121.8 (4F, m), -122.8 (4F, m), -123.5 (4F, m), -126.1 (4F, m) ppm; CHN elemental analysis: observed (calculated): %C 34.7 (34.9), %H 1.5 (1.5)

1,2,-Bis(1H,1H,2H,2H-perfluoro(decyloxy))-4-ethynylbenzene: As above, using 3,4-bis(2,2-dibromovinyl)-1-(1H,1H,2H,2H-perfluoro(decyloxy))benzene (4.02 g, 3.37 mmol) and EtMgBr (3M in ether) (2.2 cm^3, 6.62 mmol), purified using CH_2Cl_2:petroleum ether(40-60) (3:2) as the eluent. 1.97 g. (57%).

^{1}H NMR (400 MHz, $CDCl_3$): δ = 7.15 (1H, dd, $^{3}J_{HH}$ = 8.4, $^{4}J_{HH}$ = 2.0), 7.05 (1H, d, $^{4}J_{HH}$ = 2.0), 6.86 (1H, d, $^{3}J_{HH}$ = 8.5), 4.30 (2H, t, $^{3}J_{HH}$ = 6.6 Hz), 4.28 (2H, t, $^{3}J_{HH}$ = 6.6 Hz), 3.03 (1H, s), 2.65 (4H, m) ppm; ^{19}F NMR (376 MHz, $CDCl_3$): δ = - 80.7 (6F, t, $^{3}J_{FF}$ = 9.8 Hz), -113.2 (4F, m), -121.8 (4F, m), -121.9 (8F, m), -122.7 (4F, m), -123.5 (4F, m), -126.1 (4F, m) ppm; CHN elemental analysis: observed (calculated): %C 32.6 (32.8), %H 1.2 (1.2)

1,2,-Bis(1H,1H,2H,2H-perfluoro(dodecyloxy))-4-ethynylbenzene: As above, using 3,4-bis(2,2-dibromovinyl)-1-(1H,1H,2H,2H-perfluoro(dodecyloxy))benzene (1.43 g, 1.00 mmol) and EtMgBr (3M in ether) (0.38 cm^3, 1.14 mmol), purified using petroleum ether(40-60):CH_2Cl_2 (7:3) as the eluent. 813 mg. (64%).

^{1}H NMR (400 MHz, $CDCl_3$): δ = 7.15 (1H, dd, $^{3}J_{HH}$ = 8.4, $^{4}J_{HH}$ = 2.0), 7.05 (1H, d, $^{4}J_{HH}$ = 2.0), 6.86 (1H, d, $^{3}J_{HH}$ = 8.5), 4.30 (2H, t, $^{3}J_{HH}$ = 6.6 Hz), 4.28 (2H, t, $^{3}J_{HH}$ = 6.6 Hz), 3.03 (1H, s), 2.65 (4H, m) ppm; ^{19}F NMR (376 MHz, $CDCl_3$): δ = - 80.7 (6F, t, $^{3}J_{FF}$ = 9.8 Hz), -113.2 (4F, m), -121.8 (16F‡, m), -122.7 (4F, m), -123.5 (4F, m), -126.1 (4F, m) ppm.

‡low integration due to impure commercial starting materials, if pure would equal 20F

1,2,3-Tris(1H,1H,2H,2H-perfluoro(alkoxy))-5-ethynylbenzene

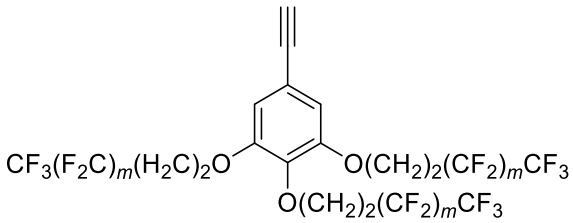

1,2,3-Tris(1H,1H,2H,2H-perfluoro(octyloxy))-5-ethynylbenzene: As above, using 3,4,5-tris(2,2-dibromovinyl)-1-(1H,1H,2H,2H-perfluoro(octyloxy))benzene (1.86 g, 1.38 mmol) and EtMgBr (3M in ether) (1.8 cm^3, 5.42 mmol), purified using petroleum ether(40-60):CH_2Cl_2 (7:3) as the eluent. 1.45 g. (88%).

^{1}H NMR (400 MHz, $CDCl_3$): δ = 6.76 (2H, s), 4.29 (4H, t, $^3J_{HH}$ = 6.3 Hz), 4.22 (2H, t, $^3J_{HH}$ = 6.9 Hz), 3.07 (1H, s), 2.62 (6H, m) ppm; ^{19}F NMR (376 MHz, $CDCl_3$): δ = - 80.8 (6F, t, $^3J_{FF}$ = 9.8 Hz), - 80.8 (3F, t, $^3J_{FF}$ = 10.0 Hz), -113.3 (4F, m), -113.5 (2F, m), -121.8 (4F, m), -122.0 (2F, m), -122.9 (4F, m), -123.0 (2F, m), -123.6 (4F, m), -123.7 (2F, m), -126.1 (4F, m) -126.2 (2F, m) ppm; CHN elemental analysis: observed (calculated): %C 32.4 (32.3), %H 1.1 (1.3).

1,2,3-Tris(1H,1H,2H,2H-perfluoro(decyloxy))-5-ethynylbenzene: As above, using 3,4,5-bis(2,2-dibromovinyl)-1-(1H,1H,2H,2H-perfluoro(dodecyloxy))benzene (752 mg, 4.55 mmol) and EtMgBr (3M in ether) (0.64 cm^3, 1.92 mmol), purified using petroleum ether(40-60):CH_2Cl_2 (7:3) as the eluent. 641 mg. (95%).

^{1}H NMR (400 MHz, $CDCl_3$): δ = 6.76 (2H, s), 4.29 (4H, t, $^3J_{HH}$ = 6.3 Hz), 4.21 (2H, t, $^3J_{HH}$ = 6.9 Hz), 3.07 (1H, s), 2.62 (6H, m) ppm; ^{19}F NMR (376 MHz, $CDCl_3$): δ = - 80.7 (6F, t, $^3J_{FF}$ = 9.8 Hz), - 80.8 (3F, t, $^3J_{FF}$ = 9.9 Hz), -113.3 (4F, m), -113.5 (2F, m), -121.6 (4F, m), -122.0 (14F, m), -122.8 (6F, m), -123.5 (4F, m), -123.7 (2F, m), -126.1 (4F, m), -126.2 (2F, m) ppm; CHN elemental analysis: observed (calculated): %C 30.9 (30.7), %H 0.6 (1.0).

6.3.2 Synthesis of 4-ethynylpyridine

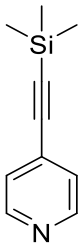

4-(Trimethylsilyl)ethynylpyridine[10]: Zinc bromide (22.6 g, 100 mmol), was added to THF (45 cm^3) cooled to between 0 and 10 °C. 4-Bromopyridine hydrochloride (9.01 g, 46.2 mmol) was added, followed by triphenylphosphine (2.43 g, 9.33 mmol) and palladium(II) chloride (405 mg, 2.30 mmol, 5 mol%). Triethylamine (51.2 cm^3, 369 mmol) was added at a rate to keep the temperature below 10 °C, followed by the dropwise addition of trimethylsilylacetylene (13.2 cm^3, 92.7 mmol). The reaction mixture was heated to 60 °C for 4.5 hours, after which it was cooled to -5 °C, and hexane (50 cm^3) and ammonium hydroxide (7 M, 60 cm^3) were added, forming a precipitate. The solution was washed with water, removing the solids as much as possible, dried of $MgSO_4$ and concentrated *in vacuo*. The product was purified by vacuum distillation at 80 °C to give a colourless oil. 3.11 g (38%).

^{1}H NMR (400 MHz, $CDCl_3$): δ = 8.58 (2H, AA'XX'), 7.30 (2H, AA'XX'), 0.26 (9H, s) ppm.

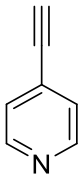

4-Ethynylpyridine: 4-(trimethylsilyl)ethynylpyridine (2.20 g, 12.5 mmol) was dissolved in a mixture of 2:1 MeOH:CH_2Cl_2 (37.5 cm^3 total) under an atmosphere of N_2. Potassium hydroxide (1.41 g, 25.1 mmol) was dissolved in the minimum amount of MeOH and added slowly at room temperature and the resulting reaction mixture was stirred for 2 hours. The reaction was quenched with water, extracted with CH_2Cl_2 (30 cm^3), dried over $MgSO_4$ and concentrated *in vacuo* (product is volatile-care was taken upon concentration). The residue was purified by column chromatography on silica gel using an eluent of 1:1 petroleum ether (40-60):ethyl acetate to give a colourless solid. 801 mg (62%).

^{1}H NMR (400 MHz, $CDCl_3$): δ = 8.59 (2H, AA'XX'), 7.35 (2H, AA'XX'), 3.29 (1H, s) ppm.

6.3.3 Synthesis of Gold(III) Chloride Complexes

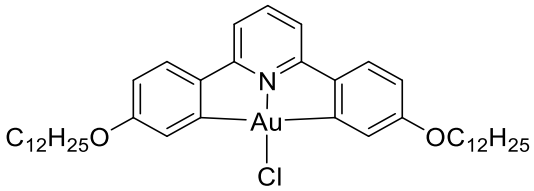

Au-Cl-1: $Hg(OAc)_2$ (5.02 g, 15.7 mmol) and 2,6-bis(4-(dodecyloxy)phenyl)pyridine (1.88 g, 3.31 mmol) were heated under vigorous reflux in ethanol (500 cm^3) for 24 hours. The solution was cooled to 50 °C and a solution of LiCl (265 mg, 6.20 mmol) in methanol (50 cm^3) was added. The resulting mixture was allowed to stir for 15 min. The reaction mixture cooled to room temperature and was then added to distilled water (200 cm^3) and filtered. The precipitate was washed with copious amounts of water and air-dried. The dried precipitate was dissolved in the minimum amount of boiling $CHCl_3$ and filtered through Celite®, after which the solvent was removed from the filtrate under reduced pressure. The residue was recrystallised from $CHCl_3$ and acetone, the resulting precipitate removed *via* filtration and the filtrate concentrated *in vacuo*. The residue used without further purification. $K[AuCl_4]$ (800 mg, 2.12 mmol) and the mixed product (2.81 g, 73.5% estimated [Hg(C^N^CH)Cl]) were heated in acetonitrile (400 cm^3) under reflux for 24 hours. The reaction mixture was then cooled and added to distilled water (150 cm^3) and isolated by filtration. The solid was washed with acetone (50 cm^3) and air-dried. The product was further purified by flash chromatography on silica gel using petroleum ether/chloroform as eluent (3:2), and recrystallised from CH_2Cl_2/ethyl acetate. 674 mg (26%).

^1H NMR (400 MHz, $CDCl_3$): δ = 7.69 (1H, t, $^3J_{HH}$ = 8.0 Hz), 7.43 (2H, d, $^4J_{HH}$ = 2.8 Hz), 7.42 (2H, d, $^3J_{HH}$ = 8.4 Hz), 7.16 (2H, d, $^3J_{HH}$ = 8.0 Hz), 6.7 (2H, dd, $^3J_{HH}$ = 8.4 Hz, $^4J_{HH}$ = 2.4 Hz), 4.05 (4H, t, $^3J_{HH}$ = 6.4 Hz), 1.79 (4H, m), 1.47 (4H, m), 1.21 (32H, broad m), 0.87 (6H, t, $^3J_{HH}$ = 7.2 Hz) ppm; CHN elemental analysis: observed (calculated): %C 59.0 (59.3), %H 7.1 (7.2), %N 1.5 (1.7).

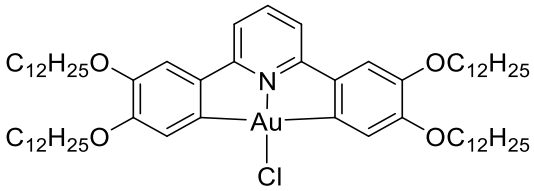

Au-Cl-2: $Hg(OAc)_2$ (10.5 g, 32.9 mmol) and 2,6-bis(3,4-bis(dodecyloxy)phenylpyridine (8.02 g, 8.19 mmol) were heated under vigorous reflux in ethanol (500 cm^3) for 24 hours. The solution was cooled to 50 °C and a solution of LiCl (265 mg, 6.21 mmol) in methanol (50 cm^3) was added. The resulting mixture was allowed to stir for 15 min. The reaction mixture was then cooled to room temperature and added to distilled water (200 cm^3) and filtered. The precipitate was washed with

copious amounts of water and air-dried. The mercurated complex, **Hg-Cl-2**, was used without further purification. $K[AuCl_4]$ (720 mg, 2.11 mmol) and the mixed product (2.40 g) were heated in an acetonitrile/chloroform (1:1) mixture (400 cm^3) under reflux for 24 hours. The reaction mixture was cooled and concentrated *in vacuo*. The residue was treated with acetonitrile and the insoluble material isolated *via* filtration. The solid was recrystallised from CH_2Cl_2 and the resulting solid isolated by filtration, then further recrystallised from CH_2Cl_2 and hexane resulting in the pure product as a vibrantly yellow solid. 1.29 g (13%).

^{1}H NMR (400 MHz, $CDCl_3$): δ = 7.65 (1H, t, $^3J_{HH}$ = 8.0 Hz), 7.38 (2H, s), 7.06 (2H, d, $^3J_{HH}$ = 8.0 Hz), 6.99 (2H, s), 4.13 (4H, t, $^3J_{HH}$ = 6.4 Hz), 3.98 (4H, t, $^3J_{HH}$ = 6.8 Hz), 1.79 (8H, m), 1.47 (8H, m), 1.21 (64H, broad m), 0.87 (12H, t, $^3J_{HH}$ = 7.2 Hz) ppm; CHN elemental analysis: observed (calculated): %C 65.1 (64.8), %H 9.2 (9.0), %N 1.1 (1.2).

6.3.4 Synthesis of Gold(III) Alkynyl Complexes

General Procedure for Gold(III) Alkynyl Complexes

The [Au(C^N^C)Cl] precursor (**Au-Cl-1** or **Au-Cl-2**) and CuI (10 mol%) were added to a 3-necked flask which was placed under N_2. Dry, degassed dichloromethane (40 cm^3) was added, followed by the appropriate acetylene (2.5 eq.) and triethylamine (45 mol%). The reaction mixture was stirred at room temperature for 5 h under a N_2 atmosphere, after which the reaction mixture was filtered through a pad of Celite and the solvent was removed *in vacuo*. The residue was purified by flash chromatography on silica gel and subsequently recrystallized from acetone or $CHCl_3$/acetonitrile.

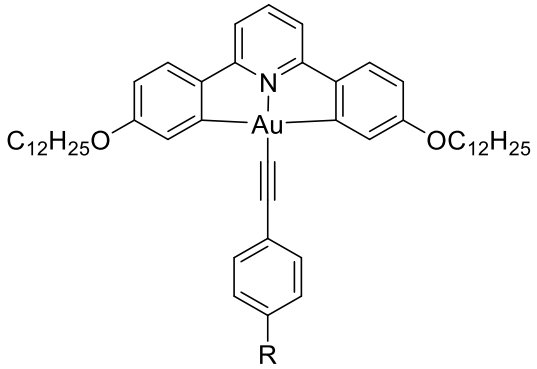

R = H or C_nH_{2n+1}

1-H: As above, using **Au-Cl-1** (302 mg, 63 μmol) and phenylacetylene (0.06 cm^3, 542 μmol), purified using petroleum ether/ethyl acetate as eluent (4:1), recrystallised from $CHCl_3$/acetonitrile. 247 mg (77%).

^{1}H NMR (400 MHz, $CDCl_3$): δ = 7.70 (1H, t, $^3J_{HH}$ = 8.0 Hz), 7.66 (2H, d, $^4J_{HH}$ = 2.8 Hz), 7.60 (2H, m), 7.48 (2H, d, $^3J_{HH}$ = 8.4 Hz), 7.31 (3H, m), 7.21 (2H, d, $^3J_{HH}$ = 8.0 Hz), 6.71 (2H, dd, $^3J_{HH}$ = 8.4 Hz, $^4J_{HH}$ = 2.4 Hz), 4.05 (4H, t, $^3J_{HH}$ = 6.4 Hz), 1.79 (4H, m), 1.47 (4H, m), 1.21 (32H, broad m), 0.87 (6H, t, $^3J_{HH}$ = 7.2 Hz) ppm. MS m/z (APCI+): 896.47 (calculated 896.0). CHN elemental analysis: observed (calculated): %C 65.2 (65.7), %H 7.0 (7.2), %N 1.6 (1.6)

1-5: As above, using **Au-Cl-1** (201 mg, 263 μmol) and 1-ethynyl-4-pentylbenzene (0.07 cm^3, 362 μmol), purified using petroleum ether/ethyl acetate as eluent (4:1), recrystallised from $CHCl_3$/acetonitrile. 154 mg (66%).

^{1}H NMR (400 MHz, $CDCl_3$): δ = 7.70 (1H, t, $^3J_{HH}$ = 8.0 Hz), 7.67 (2H, d, $^4J_{HH}$ = 2.8 Hz), 7.51 (2H, d, $^3J_{HH}$ = 8.0 Hz), 7.48 (2H, d, $^3J_{HH}$ = 8.4 Hz), 7.21 (2H, d, $^3J_{HH}$ = 8.0 Hz), 7.14 (2H, d, $^3J_{HH}$ = 8.0 Hz), 6.71 (2H, dd, $^3J_{HH}$ = 8.4 Hz, $^4J_{HH}$ = 2.4 Hz), 4.05 (4H, t, $^3J_{HH}$ = 6.4 Hz), 2.61 (2H, t, $^3J_{HH}$ = 8.0 Hz) 1.80 (4H, m), 1.63 (2H, m), 1.47 (4H, m), 1.33 (4H, m), 1.21 (32H, broad m), 0.87 (6H, t, $^3J_{HH}$ = 7.2 Hz), 0.87 (3H, m) ppm. MS m/z (APCI+): 966.54 (calc. 966.14); CHN elemental analysis: observed (calculated): %C 67.1 (67.1), %H 7.8 (7.7), %N 1.4 (1.5).

1-8: As above, using **Au-Cl-1** (203 mg, 264 μmol) and 1-ethynyl-4-octylbenzene (0.09 cm^3, 362 μmol), purified using petroleum ether/ethyl acetate as eluent (4:1), recrystallised from $CHCl_3$/acetonitrile. 172 mg (71%).

^{1}H NMR (400 MHz, $CDCl_3$): δ = 7.70 (1H, t, $^3J_{HH}$ = 8.0 Hz), 7.67 (2H, d, $^4J_{HH}$ = 2.8 Hz), 7.51 (2H, d, $^3J_{HH}$ = 8.0 Hz), 7.48 (2H, d, $^3J_{HH}$ = 8.4 Hz), 7.21 (2H, d, $^3J_{HH}$ = 8.0 Hz), 7.14 (2H, d, $^3J_{HH}$ = 8.0 Hz), 6.71 (2H, dd, $^3J_{HH}$ = 8.4 Hz, $^4J_{HH}$ = 2.4 Hz), 4.05 (4H, t, $^3J_{HH}$ = 6.4 Hz), 2.61 (2H, t, $^3J_{HH}$ = 8.0 Hz), 1.80 (4H, m), 1.63 (2H, m), 1.47 (4H, m), 1.31 (10H, m), 1.21 (32H, broad m), 0.87 (6H, t, $^3J_{HH}$ = 7.2 Hz), 0.87 (3H, m) ppm. MS m/z (APCI+): 1008.59 (Calc. 1008.22). CHN elemental analysis: observed (calculated): %C 67.5 (67.90), %H 7.9 (8.0), %N 1.3 (1.4).

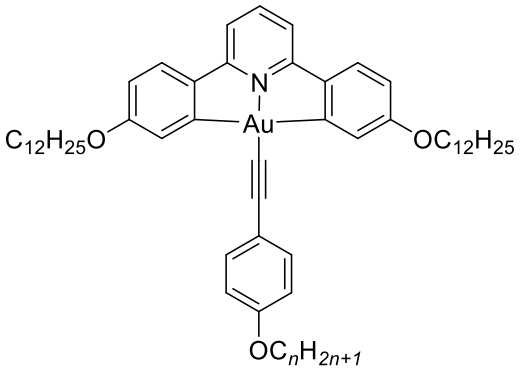

2-8: Synthesised as above using **Au-Cl-1**, (79.1 mg, 102 μmol) and 4-ethynyl-1-(octyloxy)benzene (44.1 mg, 192 μmol), purified using petroleum ether/CH_2Cl_2 (initially 7:3, followed by 1:1) as eluent, recrystallised from $CHCl_3$/acetonitrile. 64.2 mg (66 %).

^{1}H NMR (400 MHz, $CDCl_3$): δ = 7.67 (1H, t, $^3J_{HH}$ = 8.0 Hz), 7.63 (2H, d, $^4J_{HH}$ = 2.7 Hz), 7.52 (2H, AA'XX', $^3J_{HH}$ = 8.6 Hz), 7.45 (2H, d, $^3J_{HH}$ = 8.5 Hz), 7.18 (2H, d, $^3J_{HH}$ = 8.0 Hz), 6.85 (2H, AA'XX', $^3J_{HH}$ = 8.6 Hz), 6.68 (2H, dd, $^3J_{HH}$ = 8.5 Hz, $^4J_{HH}$ = 2.6 Hz), 4.04 (4H, t, $^3J_{HH}$ = 6.7 Hz), 3.97 (2H, t, $^3J_{HH}$ = 6.5 Hz), 1.80 (6H, m), 1.46 (6H, m), 1.27 (40H, broad m), 0.88 (9H, m) ppm; MS m/z (APCI+): 1024.58 (calc. 1024.22); CHN elemental analysis: observed (calculated): %C 66.6 (66.8), %H 7.7 (7.9), %N 1.2 (1.4).

2-10: Synthesised as above using **Au-Cl-1**, (69.4 mg, 82.1 μmol) and 4-ethynyl-1-(decyloxy)benzene (44.1 mg, 152 μmol), purified using petroleum ether/CH_2Cl_2 (initially 7:3, followed by 1:1) as eluent, recrystallised from $CHCl_3$/acetonitrile. 84.2 mg (95 %).

^{1}H NMR (400 MHz, $CDCl_3$): δ = 7.68 (1H, t, $^3J_{HH}$ = 8.0 Hz), 7.65 (2H, d, $^4J_{HH}$ = 2.7 Hz), 7.52 (2H, AA'XX', $^3J_{HH}$ = 8.6 Hz), 7.46 (2H, d, $^3J_{HH}$ = 8.5 Hz), 7.19 (2H, d, $^3J_{HH}$ = 8.0 Hz), 6.86 (2H, AA'XX', $^3J_{HH}$ = 8.6 Hz), 6.69 (2H, dd, $^3J_{HH}$ = 8.5 Hz, $^4J_{HH}$ = 2.6 Hz), 4.05 (4H, t, $^3J_{HH}$ = 6.7 Hz), 3.97 (2H, t, $^3J_{HH}$ = 6.5 Hz), 1.80 (6H, m), 1.46 (6H, m), 1.27 (44H, broad m), 0.88 (9H, m) ppm; MS m/z (APCI+): 1052.62 (calc. 1052.27); CHN elemental analysis: observed (calculated): %C 67.5 (67.3), %H 7.6 (8.0), %N 1.5 (1.3).

2-12: Synthesised as above using **Au-Cl-1**, (62.5 mg, 803 μmol) and 4-ethynyl-1-(dodecyloxy)benzene (41.9 mg, 132 μmol), purified using petroleum ether/CH_2Cl_2 (initially 7:3, followed by 1:1) as eluent, recrystallised from $CHCl_3$/acetonitrile. 79.1 mg (97 %).

^{1}H NMR (400 MHz, $CDCl_3$): δ = 7.68 (1H, t, $^3J_{HH}$ = 8.0 Hz), 7.65 (2H, d, $^4J_{HH}$ = 2.7 Hz), 7.52 (2H, AA'XX', $^3J_{HH}$ = 8.6 Hz), 7.46 (2H, d, $^3J_{HH}$ = 8.5 Hz), 7.19 (2H, d, $^3J_{HH}$ = 8.0 Hz), 6.85 (2H, AA'XX', $^3J_{HH}$ = 8.6 Hz), 6.70 (2H, dd, $^3J_{HH}$ = 8.5 Hz, $^4J_{HH}$ = 2.6 Hz), 4.05 (4H, t, $^3J_{HH}$ = 6.7 Hz), 3.97 (2H, t, $^3J_{HH}$ = 6.5 Hz), 1.80 (6H, m), 1.46 (6H, m), 1.27 (48H, broad m), 0.88 (9H, m) ppm; MS m/z (APCI+): 1080.65 (calc. 1080.32); CHN elemental analysis: observed (calculated): %C 67.8 (67.4), %H 8.1 (8.2), %N 1.4 (1.3).

2-14: Synthesised as above using **Au-Cl-1**, (80.2 mg, 105 μmol) and 4-ethynyl-1-(tetradecyloxy)benzene (60.1 mg, 183 μmol), purified using petroleum ether/CH_2Cl_2 (initially 7:3, followed by 1:1) as eluent, recrystallised from $CHCl_3$/acetonitrile. 83.2 mg (78 %).

^{1}H NMR (400 MHz, $CDCl_3$): δ = 7.68 (1H, t, $^3J_{HH}$ = 8.0 Hz), 7.65 (2H, d, $^4J_{HH}$ = 2.7 Hz), 7.52 (2H, AA'XX', $^3J_{HH}$ = 8.6 Hz), 7.46 (2H, d, $^3J_{HH}$ = 8.5 Hz), 7.19 (2H, d, $^3J_{HH}$ = 8.0 Hz), 6.85 (2H, AA'XX', $^3J_{HH}$ = 8.6 Hz), 6.70 (2H, dd, $^3J_{HH}$ = 8.5 Hz, $^4J_{HH}$ = 2.6 Hz), 4.05 (4H, t, $^3J_{HH}$ = 6.7 Hz), 3.97 (2H, t, $^3J_{HH}$ = 6.5 Hz), 1.80 (6H, m), 1.46 (6H, m), 1.27 (52H, broad m), 0.88 (9H, m) ppm; MS m/z (APCI+): 1108.68 (calc. 1108.38); CHN elemental analysis: observed (calculated): %C 67.9 (68.3), %H 8.3 (8.4), %N 1.2 (1.3).

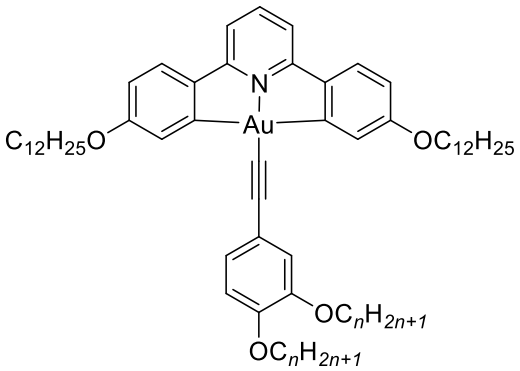

3-8: Synthesised as above using **Au-Cl-1** (118 mg, 142 μmol) and 4-ethynyl-1,2-bisoctyloxybenzene (132 mg, 368 μmol), purified using petroleum ether/CH_2Cl_2 as eluent (1:1), recrystallised from acetone. 128 mg (75%).

^{1}H NMR (400 MHz, $CDCl_3$): δ = 7.67 (1H, t, $^3J_{HH}$ = 8.0 Hz), 7.64 (2H, d, $^4J_{HH}$ = 2.2 Hz), 7.45 (2H, d, $^3J_{HH}$ = 8.6 Hz), 7.18 (2H, d, $^3J_{HH}$ = 8.0 Hz), 7.15 (2H, m), 6.83 (1H, d, $^3J_{HH}$ = 8.0 Hz), 6.69 (2H, dd, $^3J_{HH}$ = 8.5 Hz, $^4J_{HH}$ = 2.6 Hz), 4.04 (4H, t, $^3J_{HH}$ = 6.6 Hz), 4.02 (2H, t, $^3J_{HH}$ = 6.7 Hz), 4.01 (2H, t, $^3J_{HH}$ = 6.7 Hz), 1.81 (8H, m), 1.46 (8H, m), 1.25 (48H, broad m), 0.88 (12H, m) ppm. MS m/z (APCI+): 1152.71 (calc. 1152.43). CHN elemental analysis: observed (calculated): %C 67.4 (67.7), %H 8.7 (8.4), %N 1.4 (1.2).

3-10: Synthesised as above using **Au-Cl-1** (117 mg, 141 μmol) and 4-ethynyl-1,2-bisdecyloxybenzene (151 mg, 362 μmol), purified using petroleum ether/ethyl acetate as eluent (4:1), followed by a second column with CH_2Cl_2 as the eluent, recrystallised from acetone. 103 mg (61%).

^{1}H NMR (400 MHz, $CDCl_3$): δ = 7.68 (1H, t, $^3J_{HH}$ = 8.0 Hz), 7.65 (2H, d, $^4J_{HH}$ = 2.5 Hz), 7.46 (2H, d, $^3J_{HH}$ = 8.5 Hz), 7.19 (2H, d, $^3J_{HH}$ = 8.0 Hz), 7.15 (2H, m), 6.82 (1H, d, $^3J_{HH}$ = 8.0 Hz), 6.70 (2H, dd, $^3J_{HH}$ = 8.5 Hz, $^4J_{HH}$ = 2.6 Hz), 4.05 (4H, t, $^3J_{HH}$ = 6.6 Hz), 4.02 (2H, t, $^3J_{HH}$ = 6.7 Hz), 4.01 (2H, t, $^3J_{HH}$ = 6.7 Hz), 1.81 (8H, m), 1.46 (8H, m), 1.25 (56H, broad m), 0.88 (12H, m) ppm; MS m/z (APCI+): 1208.77 (calc. 1208.53); CHN elemental analysis: observed (calculated): %C 67.7 (68.6), %H 8.6 (8.7), %N 1.0 (1.2).

3-12: Synthesised as above using **Au-Cl-1** (98.1 mg, 110 μmol) and 4-ethynyl-1,2-bisdodecyloxybenzene (141 mg, 303 μmol), purified using petroleum ether/CH_2Cl_2 as eluent (1:1), recrystallised from acetone. 93.1 mg (66 %).

^{1}H NMR (400 MHz, $CDCl_3$): δ = 7.70 (1H, t, $^3J_{HH}$ = 8.0 Hz), 7.67 (2H, d, $^4J_{HH}$ = 2.6 Hz), 7.48 (2H, d, $^3J_{HH}$ = 8.6 Hz), 7.21 (2H, d, $^3J_{HH}$ = 8.1 Hz), 7.15 (2H, m), 6.82 (1H, d, $^3J_{HH}$ = 8.2 Hz), 6.72 (2H, dd, $^3J_{HH}$ = 8.6 Hz, $^4J_{HH}$ = 2.7 Hz), 4.06 (4H, t, $^3J_{HH}$ = 6.6 Hz), 4.02 (2H, t, $^3J_{HH}$ = 6.6 Hz), 4.01 (2H, t, $^3J_{HH}$ = 6.6 Hz), 1.81 (8H, m), 1.46 (8H, m), 1.25 (64H, broad m), 0.88 (12H, m) ppm. MS m/z (APCI+): 1264.83 (calc. 1264.64); CHN elemental analysis: observed (calculated): %C 69.2 (69.3), %H 9.1 (8.9), %N 1.0 (1.1).

3-14: Synthesised as above using **Au-Cl-1** (97.2 mg, 113 μmol) and 4-ethynyl-1,2-bistetradecyloxybenzene (158 mg, 302 μmol), purified using petroleum ether/CH_2Cl_2 as eluent (1:1), recrystallised from acetone. 99.1 mg (65 %)**.**

^{1}H NMR (400 MHz, $CDCl_3$): δ = 7.71 (1H, t, $^3J_{HH}$ = 8.1 Hz), 7.67 (2H, d, $^4J_{HH}$ = 2.5 Hz), 7.48 (2H, d, $^3J_{HH}$ = 8.5 Hz), 7.22 (2H, d, $^3J_{HH}$ = 8.1 Hz), 7.15 (2H, m), 6.82 (1H, d, $^3J_{HH}$ = 8.1 Hz), 6.72 (2H, dd, $^3J_{HH}$ = 8.6 Hz, $^4J_{HH}$ = 2.7 Hz), 4.06 (4H, t, $^3J_{HH}$ = 6.6 Hz), 4.02 (2H, t, $^3J_{HH}$ = 6.6 Hz), 4.01 (2H, t, $^3J_{HH}$ = 6.6 Hz), 1.81 (8H, m), 1.46 (8H, m), 1.25 (72H, broad m), 0.88 (12H, m) ppm. MS m/z (APCI+): 1320.90 (calc. 1320.75); CHN elemental analysis: observed (calculated): %C 69.5 (70.0), %H 9.2 (9.2), %N 1.0 (1.1)

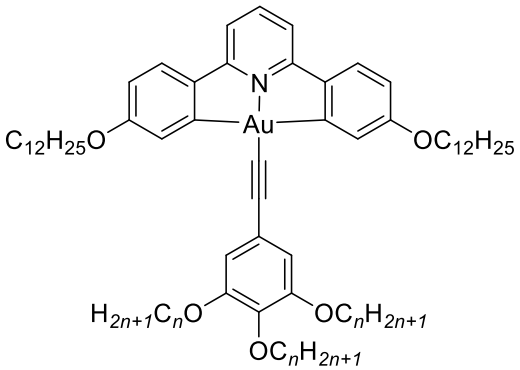

4-8: Synthesised as above using **Au-Cl-1** (113 mg, 142 μmol) and 5-ethynyl-1,2,3-trisoctyloxybenzene (98.2 mg, 201 μmol), purified using petroleum ether/ethyl acetate as eluent (7:3), recrystallised from acetone. 110 mg (64%).

^{1}H NMR (400 MHz, $CDCl_3$): δ = 7.72 (1H, t, $^3J_{HH}$ = 8.0 Hz), 7.65 (2H, d, $^4J_{HH}$ = 2.3 Hz), 7.49 (2H, d, $^3J_{HH}$ = 8.7 Hz), 7.22 (2H, d, $^3J_{HH}$ = 7.8 Hz), 6.81 (2H, s, $^3J_{HH}$ = 8.0 Hz), 6.72 (2H, dd, $^3J_{HH}$ = 8.7 Hz, $^4J_{HH}$ = 2.6 Hz), 4.05 (4H, t, $^3J_{HH}$ = 6.4 Hz), 3.99 (4H, t, $^3J_{HH}$ = 6.4 Hz), 3.97 (2H, t, $^3J_{HH}$ = 6.4 Hz), 1.79 (10H, m), 1.47 (10H, m), 1.25 (56H, broad m), 0.87 (15H, m) ppm. MS m/z (APCI+): 1280.83 (calc. 1280.64). CHN elemental analysis: observed (calculated): %C 68.1 (68.5), %H 8.7 (8.8), %N 1.0 (1.1).

4-10: Synthesised as above using **Au-Cl-1** (132 mg, 159 μmol) and 5-ethynyl-1,2,3-trisdecyloxybenzene (225 mg, 389 μmol), purified using petroleum ether/ethyl acetate as eluent (4:1), recrystallised from acetone. 156 mg (72 %).

^{1}H NMR (400 MHz, $CDCl_3$): δ = 7.71 (1H, t, $^3J_{HH}$ = 8.0 Hz), 7.65 (2H, d, $^4J_{HH}$ = 2.7 Hz), 7.49 (2H, d, $^3J_{HH}$ = 8.5 Hz), 7.22 (2H, d, $^3J_{HH}$ = 7.9 Hz), 6.81 (2H, s, $^3J_{HH}$ = 8.0 Hz), 6.72 (2H, dd, $^3J_{HH}$ = 8.6 Hz, $^4J_{HH}$ = 2.7 Hz), 4.05 (4H, t, $^3J_{HH}$ = 6.4 Hz), 3.99 (4H, t, $^3J_{HH}$ = 6.4 Hz), 3.97 (2H, t, $^3J_{HH}$ = 6.4 Hz), 1.79 (10H, m), 1.47 (10H, m), 1.25 (68H, broad m), 0.87 (15H, m) ppm; MS m/z (APCI+): 1364.92 (calc. 1364.80); CHN elemental analysis: observed (calculated): %C 69.1 (69.5), %H 9.3 (9.2), %N 1.2 (1.0).

4-12: Synthesised as above using **Au-Cl-1** (85.2 mg, 100 μmol) and 5-ethynyl-1,2,3-trisdodecyloxybenzene (102 mg, 152 μmol), purified using petroleum ether/ethyl acetate as eluent (4:1), recrystallised from acetone. 92.4 mg (62%).

^{1}H NMR (400 MHz, $CDCl_3$): δ = 7.72 (1H, t, $^3J_{HH}$ = 8.0 Hz), 7.65 (2H, d, $^4J_{HH}$ = 2.3 Hz), 7.49 (2H, d, $^3J_{HH}$ = 8.7 Hz), 7.22 (2H, d, $^3J_{HH}$ = 7.8 Hz), 6.81 (2H, s), 6.72 (2H, dd, $^3J_{HH}$ = 8.7 Hz, $^4J_{HH}$ = 2.6 Hz), 4.05 (4H, t, $^3J_{HH}$ = 6.4 Hz), 3.99 (4H, t, $^3J_{HH}$ = 6.4 Hz), 3.97 (2H, t, $^3J_{HH}$ = 6.4 Hz), 1.80 (10H, m), 1.47 (10H, m), 1.25 (80H, broad m), 0.87 (15H, m) ppm. MS m/z (APCI+): 1449.01 (calc. 1448.96). CHN elemental analysis: observed (calculated): %C 70.4 (70.5), %H 9.4 (9.5), %N 0.9 (1.0)

4-14: Synthesised as above using **Au-Cl-1** (102 mg, 121 μmol) and 5-ethynyl-1,2,3-tristetradecyloxybenzene (222 mg, 299 μmol), purified using petroleum ether/ethyl acetate as eluent (4:1), recrystallised from acetone. 165 mg (89 %).

^{1}H NMR (400 MHz, $CDCl_3$): δ = 7.70 (1H, t, $^3J_{HH}$ = 8.0 Hz), 7.64 (2H, d, $^4J_{HH}$ = 2.5 Hz), 7.48 (2H, d, $^3J_{HH}$ = 8.6 Hz), 7.21 (2H, d, $^3J_{HH}$ = 8.0 Hz), 6.81 (2H, s), 6.71 (2H, dd, $^3J_{HH}$ = 8.4 Hz, $^4J_{HH}$ = 2.6 Hz), 4.04 (4H, t, $^3J_{HH}$ = 6.4 Hz), 3.99 (4H, t, $^3J_{HH}$ = 6.4 Hz), 3.97 (2H, t, $^3J_{HH}$ = 6.4 Hz), 1.80 (10H, m), 1.47 (10H, m), 1.25 (92H, broad m), 0.87 (15H, m) ppm.; MS m/z (APCI+): 1533.10 (calc. 1533.12); CHN elemental analysis: observed (calculated): %C 70.8 (71.3), %H 9.5 (9.7), %N 0.7 (0.9).

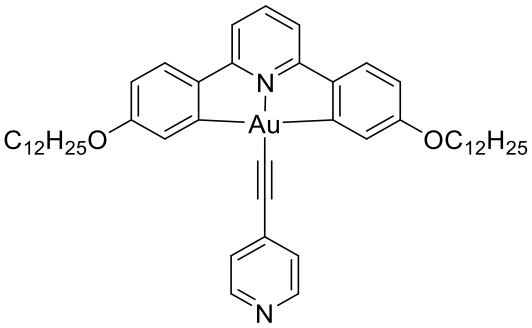

9-N: Synthesised as above using **Au-Cl-1** (400 mg, 482 μmol) and 4-ethynylpyridine (75.3 mg, 723 μmol), purified by recrystallisation from acetone. 425 mg (98 %).

^{1}H NMR (400 MHz, $CDCl_3$): δ = 8.56 (2H, s, broad) 7.72 (1H, t, $^3J_{HH}$ = 8.1 Hz), 7.55 (2H, d, $^4J_{HH}$ = 2.6 Hz), 7.48 (2H, d, $^3J_{HH}$ = 8.4 Hz), 7.43 (2H, s, broad), 7.21 (2H, d, $^3J_{HH}$ = 8.0 Hz), 6.72 (2H, dd, $^3J_{HH}$ = 8.4 Hz, $^4J_{HH}$ = 2.4 Hz), 4.03 (4H, t, $^3J_{HH}$ = 6.6 Hz), 1.79 (4H, m), 1.47 (4H, m), 1.21 (32H, broad m), 0.87 (6H, t, $^3J_{HH}$ = 7.0 Hz); CHN elemental analysis: observed (calculated): %C 63.3 (64.3), %H 6.9 (7.1), %N 3.7 (3.1).

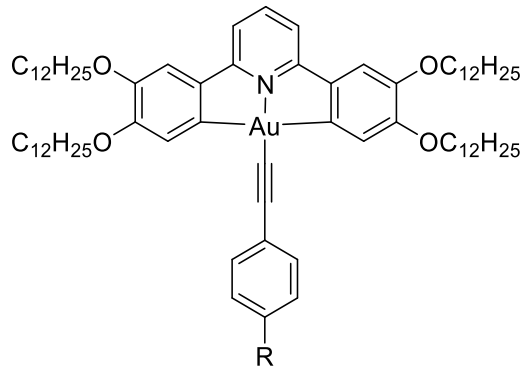

R = H or C_nH_{2n+1}

5-H: Synthesised as above using **Au-Cl-2**, (201 mg, 161 μmol) and phenylacetylene (0.03 cm^3, 273 μmol), purified using petroleum ether/ethyl acetate as eluent (1:4), recrystallised from $CHCl_3$/acetonitrile. 169 mg (80%).

^{1}H NMR (400 MHz, $CDCl_3$): δ = 7.68 (1H, t, $^3J_{HH}$ = 8.0 Hz), 7.61 (2H, s), 7.57 (2H, m), 7.31 (3H, m), 7.14 (2H, d, $^3J_{HH}$ = 8.0 Hz), 7.06 (2H, s), 4.14 (4H, t, $^3J_{HH}$ = 6.4 Hz), 3.99 (4H, t, $^3J_{HH}$ = 6.8 Hz), 1.79 (8H, m), 1.47 (8H, m), 1.21 (64H, broad m), 0.87 (12H, t, $^3J_{HH}$ = 7.2 Hz) ppm. MS m/z (APCI+): 1264.84 (calc. 1264.64). CHN elemental analysis: observed (calculated): %C 68.9 (69.3), %H 8.8 (8.9), %N 1.1 (1.1).

5-5: Synthesised as above using **Au-Cl-2**, (150 mg, 132 μmol) and 1-ethynyl-4-pentylbenzene (0.04 cm^3, 203 μmol), purified using petroleum ether/ethyl acetate as eluent (1:4), recrystallised from $CHCl_3$/acetonitrile. 135 mg (81%).

^1H NMR (400 MHz, $CDCl_3$): δ = 7.66 (1H, t, $^3J_{HH}$ = 8.0 Hz), 7.61 (2H, s), 7.48 (2H, d, $^3J_{HH}$ = 8.0 Hz), 7.13 (2H, d, $^3J_{HH}$ = 8.0 Hz), 7.12 (2H, d, $^3J_{HH}$ = 8.0 Hz), 7.05 (2H, s), 4.14 (4H, t, $^3J_{HH}$ = 6.4 Hz), 3.99 (4H, t, $^3J_{HH}$ = 6.8 Hz), 2.60 (2H, t, $^3J_{HH}$ = 7.6 Hz), 1.79 (8H, m), 1.47 (8H, m), 1.61 (2H, m), 1.31 (4H, m), 1.21 (64H, broad m), 0.87 (15H, t, $^3J_{HH}$ = 7.2 Hz), ppm. MS m/z (APCI+): 1334.91 (calc. 1334.91). CHN elemental analysis: observed (calculated): %C 70.1 (70.2), %H 9.4 (9.2), %N 0.9 (1.1)

5-8: Synthesised as above using **Au-Cl-2**, (198 mg, 164 μmol) and 1-ethynyl-4-octylbenzene (0.06 cm^3, 242 μmol), purified using petroleum ether/ethyl acetate as eluent (1:4), recrystallised from $CHCl_3$/acetonitrile. 198 mg (86%).

^1H NMR (400 MHz, $CDCl_3$): δ = 7.67 (1H, t, $^3J_{HH}$ = 8.0 Hz), 7.62 (2H, s), 7.48 (2H, d, $^3J_{HH}$ = 8.0 Hz), 7.13 (2H, d, $^3J_{HH}$ = 8.4 Hz), 7.12 (2H, d, $^3J_{HH}$ = 8.4 Hz), 7.06 (2H, s), 4.14 (4H, t, $^3J_{HH}$ = 6.4 Hz), 3.99 (4H, t, $^3J_{HH}$ = 6.8 Hz), 2.60 (2H, t, $^3J_{HH}$ = 7.6 Hz), 1.79 (8H, m), 1.47 (8H, m), 1.61 (2H, m), 1.31 (10H, m), 1.21 (64H, broad m), 0.87 (15H, t, $^3J_{HH}$ = 7.2 Hz) ppm; MS m/z (APCI+): 1376.96 (calc. 1376.85); CHN elemental analysis: observed (calculated): %C 70.26 (70.66), %H 9.25 (9.37), %N 0.91 (1.02).

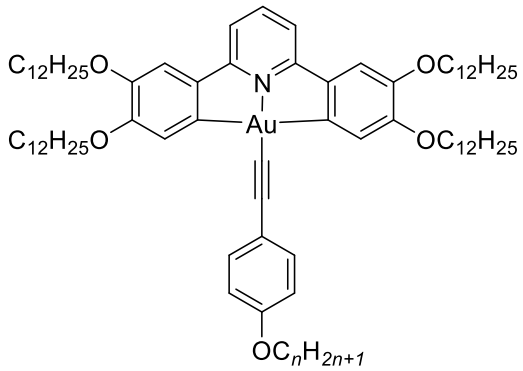

6-8: Synthesised as above using **Au-Cl-2**, (130 mg, 124 μmol) and 4-ethynyl-1-(octyloxy)benzene (63.0 mg, 272 μmol), purified using petroleum ether/ethyl acetate as eluent (9:1) and recrystallised from acetone. 121 mg (80 %).

^1H NMR (400 MHz, $CDCl_3$): δ = 7.67 (1H, t, $^3J_{HH}$ = 8.0 Hz), 7.6 (2H, s), 7.49 (2H, AA'XX', $^3J_{HH}$ = 8.7 Hz), 7.13 (2H, d, $^3J_{HH}$ = 8.0 Hz), 7.06 (2H, s), 6.84 (2H, AA'XX', $^3J_{HH}$ = 8.7 Hz), 4.15 (4H, t, $^3J_{HH}$ = 6.4 Hz), 4.00 (2H, t, $^3J_{HH}$ = 6.5 Hz), 3.96 (2H, t, $^3J_{HH}$ = 6.7 Hz), 1.82 (10H, m), 1.46 (10H, m), 1.25 (72H, broad m), 0.87 (15H, m) ppm. MS m/z (APCI+): 1392.95 (calc. 1392.85). CHN elemental analysis: observed (calculated): %C 69.6 (69.9), %H 9.6 (9.3), %N 1.0 (0.9).

6-10: Synthesised as above using **Au-Cl-2**, (131 mg, 121 μmol) and 4-ethynyl-1-(decyloxy)benzene (70.0 mg, 271 μmol), purified using petroleum ether/ethyl acetate as eluent (9:1) and recrystallised from acetone. 135 mg (87 %).

^{1}H NMR (400 MHz, $CDCl_3$): δ = 7.67 (1H, t, $^3J_{HH}$ = 8.0 Hz), 7.62 (2H, s), 7.49 (2H, AA'XX', $^3J_{HH}$ = 8.7 Hz), 7.13 (2H, d, $^3J_{HH}$ = 8.0 Hz), 7.06 (2H, s), 6.84 (2H, AA'XX', $^3J_{HH}$ = 8.7 Hz), 4.15 (4H, t, $^3J_{HH}$ = 6.4 Hz), 4.00 (2H, t, $^3J_{HH}$ = 6.5 Hz), 3.96 (2H, t, $^3J_{HH}$ = 6.7 Hz), 1.82 (10H, m), 1.46 (10H, m), 1.25 (78H, broad m), 0.87 (15H, m) ppm; MS m/z (APCI+): 1420.98 (calc. 1420.91). CHN elemental analysis: observed (calculated): %C 70.0 (70.2), %H 9.8 (9.4), %N 0.9 (1.0).

6-12: Synthesised as above using **Au-Cl-2**, (129 mg, 121 μmol) and 4-ethynyl-1-(dodecyloxy)benzene (78.0 mg, 271 μmol), purified using petroleum ether/ethyl acetate as eluent (9:1) and recrystallised from acetone. 135 mg (87 %).

^{1}H NMR (400 MHz, $CDCl_3$): δ = 7.68 (1H, t, $^3J_{HH}$ = 8.0 Hz), 7.63 (2H, s), 7.49 (2H, AA'XX', $^3J_{HH}$ = 8.7 Hz), 7.14 (2H, d, $^3J_{HH}$ = 8.0 Hz), 7.07 (2H, s), 6.84 (2H, AA'XX', $^3J_{HH}$ = 8.7 Hz), 4.15 (4H, t, $^3J_{HH}$ = 6.4 Hz), 4.00 (2H, t, $^3J_{HH}$ = 6.5 Hz), 3.96 (2H, t, $^3J_{HH}$ = 6.7 Hz), 1.83 (10H, m), 1.46 (10H, m), 1.25 (82H, broad m), 0.88 (15H, m) ppm. MS m/z (APCI+): 1449.02 (calc. 1448.96). CHN elemental analysis: observed (calculated): %C 70.3 (70.5), %H 9.6 (9.5), %N 1.0 (1.0).

6-14: Synthesised as above using **Au-Cl-2**, (131 mg, 110 μmol) and 4-ethynyl-1-(tetradecyloxy)benzene (85.1 mg, 272 μmol), purified using petroleum ether/ethyl acetate as eluent (9:1) and recrystallised from acetone. 141 mg (88 %).

^{1}H NMR (400 MHz, $CDCl_3$): δ = 7.67 (1H, t, $^3J_{HH}$ = 8.0 Hz), 7.62 (2H, s), 7.49 (2H, AA'XX', $^3J_{HH}$ = 8.7 Hz), 7.13 (2H, d, $^3J_{HH}$ = 8.0 Hz), 7.06 (2H, s), 6.84 (2H, AA'XX', $^3J_{HH}$ = 8.7 Hz), 4.15 (4H, t, $^3J_{HH}$ = 6.4 Hz), 4.00 (2H, t, $^3J_{HH}$ = 6.5 Hz), 3.96 (2H, t, $^3J_{HH}$ = 6.7 Hz), 1.83 (10H, m), 1.46 (10H, m), 1.25 (86H, broad m), 0.88 (15H, m) ppm. MS m/z (APCI+): 1477.05 (calc. 1477.01); CHN elemental analysis: observed (calculated): %C 70.51 (70.75), %H 9.14 (9.55), %N 0.86 (0.95).

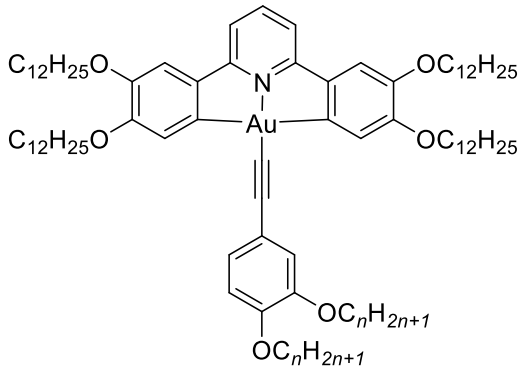

7-8: Synthesised as above using **Au-Cl-2**, (118 mg, 101 μmol) and 4-ethynyl-1,2-bis(octyloxy)benzene (92.1 mg, 262 μmol), purified using petroleum ether/ethyl acetate as eluent (95:5) and recrystallised from acetone. 87.0 mg (59 %).

^{1}H NMR (400 MHz, $CDCl_3$): δ = 7.65 (1H, t, $^3J_{HH}$ = 8.0 Hz), 7.60 (2H, s), 7.11 (2H, d, $^3J_{HH}$ = 8.0 Hz), 7.11 (1H, m), 7.04 (2H, s), 6.81 (2H, d, $^3J_{HH}$ = 8.2Hz), 4.14 (4H, t, $^3J_{HH}$ = 6.4 Hz), 4.00 (2H, t, $^3J_{HH}$ = 6.5 Hz), 3.99 (4H, t, $^3J_{HH}$ = 6.5 Hz), 1.81 (12H, m), 1.46 (12H, m), 1.25 (80H, broad m), 0.87 (18H, m) ppm. MS m/z (APCI+): 1521.07 (calc. 1521.07). CHN elemental analysis: observed (calculated): %C 70.0 (70.3), %H 9.7 (9.5), %N 0.9 (0.9).

7-10: Synthesised as above using **Au-Cl-2**, (117 mg, 102 μmol) and 4-ethynyl-1,2-bis(decyloxy)benzene (102 mg, 250 μmol), purified using petroleum ether/ethyl acetate as eluent (95:5) and recrystallised from acetone. 104 mg (67%).

^{1}H NMR (400 MHz, $CDCl_3$): δ = 7.67 (1H, t, $^3J_{HH}$ = 8.0 Hz), 7.61 (2H, s), 7.13 (2H, d, $^3J_{HH}$ = 8.0 Hz), 7.12 (1H, m), 7.07 (2H, s), 6.81 (2H, d, $^3J_{HH}$ = 8.2Hz), 4.14 (4H, t, $^3J_{HH}$ = 6.4 Hz), 4.00 (6H, t, $^3J_{HH}$ = 6.5 Hz), 3.99 (2H, t, $^3J_{HH}$ = 6.5 Hz), 1.81 (12H, m), 1.46 (12H, m), 1.25 (88H, broad m), 0.87 (18H, m). MS m/z (APCI+): 1577.13 (calc. 1577.17)**.** CHN elemental analysis: observed (calculated): %C 70.4 (70.8), %H 9.9 (9.7), %N 0.8 (0.9)**.**

7-12: Synthesised as above using **Au-Cl-2**, (117 mg, 101 μmol) and 4-ethynyl-1,2-bis(dodecyloxy)benzene (72.1 mg, 150 μmol), purified using petroleum ether/ethyl acetate as eluent (95:5) and recrystallised from acetone. 133 mg (84%).

^{1}H NMR (400 MHz, $CDCl_3$): δ = 7.66 (1H, t, $^3J_{HH}$ = 8.0 Hz), 7.60 (2H, s), 7.12 (2H, d, $^3J_{HH}$ = 8.0 Hz), 7.10 (1H, m), 7.05 (2H, s), 6.81 (2H, d, $^3J_{HH}$ = 8.2Hz), 4.14 (4H, t, $^3J_{HH}$ = 6.4 Hz), 4.00 (2H, t, $^3J_{HH}$ = 6.5 Hz), 3.99 (6H, t, $^3J_{HH}$ = 6.5 Hz), 1.81 (12H, m), 1.46 (12H, m), 1.25 (96H, broad m), 0.87 (18H, m) ppm. MS m/z (APCI+): 1633.20 (calc. 1633.28). CHN elemental analysis: observed (calculated): %C 71.2 (71.3), %H 10.1 (9.8), %N 0.8 (0.9).

7-14: Synthesised as above using **Au-Cl-2**, (118 mg, 102 μmol) and 4-ethynyl-1,2-bis(tetradecyloxy)benzene (82.1 mg, 162 μmol), purified using petroleum ether/ethyl acetate as eluent (95:5) and recrystallised from acetone. 128 mg (78%).

^{1}H NMR (400 MHz, $CDCl_3$): δ = 7.67 (1H, t, $^3J_{HH}$ = 8.0 Hz), 7.61 (2H, s), 7.13 (2H, d, $^3J_{HH}$ = 8.0 Hz), 7.12 (1H, m), 7.06 (2H, s), 6.81 (2H, d, $^3J_{HH}$ = 8.2Hz), 4.14 (4H, t, $^3J_{HH}$ = 6.5 Hz), 4.0 (6H, t, $^3J_{HH}$ = 6.6 Hz), 3.99 (2H, t, $^3J_{HH}$ = 6.6 Hz), 1.81 (12H, m), 1.46 (12H, m), 1.25 (104H, broad m), 0.87 (18H, m) ppm. MS m/z (APCI+): 1689.26 (calc. 1689.38)**.** CHN elemental analysis: observed (calculated): %C 71.6 (71.8), %H 10.4 (10.0), %N 0.9 (0.8)**.**

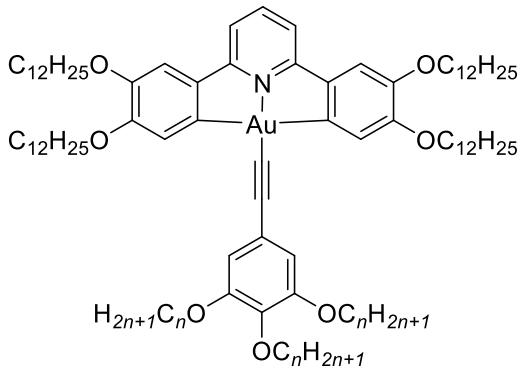

8-8: Synthesised as above using **Au-Cl-2**, (98.2 mg, 80.3 μmol) and 5-ethynyl-1,2,3-tris(octyloxy)benzene (61.1 mg, 130 μmol), purified using petroleum ether/ethyl acetate as eluent (95:5) and recrystallised from acetone. 110 mg (82 %)**.**

^{1}H NMR (400 MHz, $CDCl_3$): δ = 7.69 (1H, t, $^3J_{HH}$ = 8.0 Hz), 7.60 (2H, s), 7.14 (2H, d, $^3J_{HH}$ = 8.0 Hz), 7.07 (2H, s), 6.78 (2H, s), 4.13 (4H, t, $^3J_{HH}$ = 6.4 Hz), 4.00 (4H, t, $^3J_{HH}$ = 6.5 Hz), 3.96 (6H, t, $^3J_{HH}$ = 6.5 Hz), 1.81 (14H, m), 1.46 (14H, m), 1.25 (88H, broad m), 0.87 (21H, m) ppm. MS m/z (APCI+): 1649.19 (calc. 1649.28)**.** CHN elemental analysis: observed (calculated): %C 70.4 (70.6), %H 9.6 (9.9), %N 0.8 (0.9)

8-10: Synthesised as above using **Au-Cl-2**, (131 mg, 111 μmol) and 5-ethynyl-1,2,3-tris(decyloxy)benzene (156 mg, 270 μmol), purified using petroleum ether/ethyl acetate as eluent (95:5) and recrystallised from acetone. 159 mg (84 %)**.**

^{1}H NMR (400 MHz, $CDCl_3$): δ = 7.67 (1H, t, $^3J_{HH}$ = 8.0 Hz), 7.59 (2H, s), 7.13 (2H, d, $^3J_{HH}$ = 8.1 Hz), 7.06 (2H, s), 6.78 (2H, s), 4.13 (4H, t, $^3J_{HH}$ = 6.4 Hz), 3.99 (4H, t, $^3J_{HH}$ = 6.4 Hz), 3.96 (6H, t, $^3J_{HH}$ = 6.8 Hz), 1.81 (14H, m), 1.46 (14H, m), 1.25 (100H, broad m), 0.87 (21H, m) ppm. MS m/z (APCI+): 1733.29 (calc. 1733.44)**.** CHN elemental analysis: observed (calculated): %C 71.3 (71.4), %H 10.0 (10.0), %N 0.8 (0.8).

8-12: Synthesised as above using **Au-Cl-2**, (94.1 mg, 80.2 μmol) and 5-ethynyl-1,2,3-tris(dodecyloxy)benzene (77.0 mg, 120 μmol), purified using petroleum ether/ethyl acetate as eluent (95:5) and recrystallised from acetone. 81.1 mg (58 %).

^{1}H NMR (400 MHz, $CDCl_3$): δ = 7.69 (1H, t, $^3J_{HH}$ = 8.0 Hz), 7.60 (2H, s), 7.14 (2H, d, $^3J_{HH}$ = 8.1 Hz), 7.07 (2H, s), 6.78 (2H, s), 4.13 (4H, t, $^3J_{HH}$ = 6.1 Hz), 4.00 (4H, t, $^3J_{HH}$ = 6.4 Hz), 3.96 (6H, t, $^3J_{HH}$ = 6.8 Hz), 1.81 (14H, m), 1.46 (14H, m), 1.25 (112H, broad m), 0.87 (21H, m) ppm. MS m/z (APCI+): 1817.38 (calc. 1817.60). CHN elemental analysis: observed (calculated): %C 71.8 (72.0), %H 10.2 (10.2), %N 0.8 (0.8).

8-14: Synthesised as above using **Au-Cl-2**, (129 mg, 113 μmol) and 5-ethynyl-1,2,3-tris(tetradecyloxy)benzene (205 mg, 280 μmol), purified using petroleum ether/ethyl acetate as eluent (95:5) and recrystallised from acetone. 138 mg (71 %).

^{1}H NMR (400 MHz, $CDCl_3$): δ = 7.68 (1H, t, $^3J_{HH}$ = 8.0 Hz), 7.60 (2H, s), 7.14 (2H, d, $^3J_{HH}$ = 8.1 Hz), 7.07 (2H, s), 6.78 (2H, s), 4.13 (4H, t, $^3J_{HH}$ = 6.4 Hz), 4.00 (4H, t, $^3J_{HH}$ = 6.4 Hz), 3.96 (6H, t, $^3J_{HH}$ = 6.8 Hz), 1.81 (14H, m), 1.46 (14H, m), 1.25 (124H, broad m), 0.87 (21H, m) ppm. MS m/z (APCI+): 1901.48 (calc. 1901.76). CHN elemental analysis: observed (calculated): %C 72.4 (72.6), %H 10.3 (10.4), %N 0.9 (0.7).

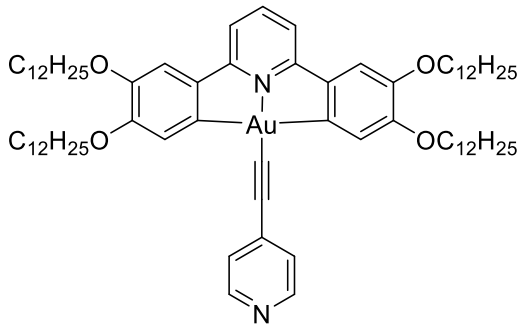

10-N: Synthesised as above, with an increase in reaction temperature to 40 °C, using **Au-Cl-2**, (131 mg, 110 μmol) and 4-ethynylpyridine (38.2 mg, 373 μmol), purified by recrystallisation from acetone. 133 mg (98 %).

^{1}H NMR (400 MHz, $CDCl_3$): δ = 8.55 (2H, d, $^3J_{HH}$ = 4.4 Hz), 7.69 (1H, t, $^3J_{HH}$ = 8.0 Hz), 7.50 (2H, s), 7.40 (2H, d, $^3J_{HH}$ = 4.6 Hz), 7.14 (2H, d, $^3J_{HH}$ = 8.0 Hz), 7.06 (2H, s), 4.11 (4H, t, $^3J_{HH}$ = 6.6 Hz), 4.0 (4H, t, $^3J_{HH}$ = 6.6 Hz), 1.79 (8H, m), 1.47 (8H, m), 1.21 (64H, broad m), 0.87 (12H, t, $^3J_{HH}$ = 7.2 Hz); CHN elemental analysis: observed (calculated): %C 66.8 (68.3), %H 8.7 (8.8), %N 3.3 (2.2).

6.3.5 Synthesis of Gold(III) Semi-Perfluorinated-Alkynyl Complexes

General Procedure for Synthesis of Gold(III) Semi-Perfluorinated-Alkynyl Complexes

The [Au(C^N^C)Cl] precursor (**Au-Cl-1** or **Au-Cl-2**) and CuI (10 mol%) were added to a 3-necked flask which was placed under N_2. Dry, degassed dichloromethane (40 cm^3) was added, followed by the appropriate acetylene (2.5 eq.) and triethylamine (45 mol%). The reaction mixture was stirred at reflux for 5 h under a N_2 atmosphere, after which the reaction mixture was filtered through a pad of Celite and the solvent was removed *in vacuo*. The residue was purified by flash chromatography on silica gel using petroleum ether/CH_2Cl_2 (initially 7:3, followed by 1:1) as eluent and subsequently recrystallized from hexane, CH_2Cl_2/acetonitrile or $CHCl_3$/acetonitrile.

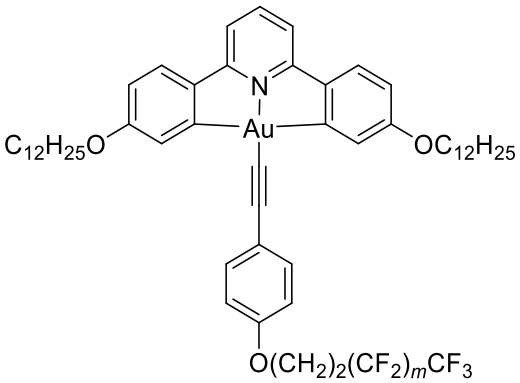

11-8†: Synthesised as above using **Au-Cl-1** (102 mg, 121 μmol) and 4-(*1H,1H,2H,2H*-perfluorooctyloxy)ethynylbenzene (82.1 mg, 182 μmol) and was recrystallised from CH_2Cl_2/acetonitrile. 130 mg (86%).

^{1}H NMR δ_H (400 MHz, $CDCl_3$): 7.71 (1H, t, $^3J_{HH}$ = 8.1 Hz), 7.67 (2H, d, $^4J_{HH}$ = 2.6 Hz), 7.55 (2H, AA'XX'), 7.49 (2H, d, $^3J_{HH}$ = 8.6 Hz), 7.22 (2H, d, $^3J_{HH}$ = 8.2 Hz), 6.87 (2H, AA'XX'), 6.72 (2H, dd, $^3J_{HH}$ = 8.6 Hz, $^4J_{HH}$ = 2.7 Hz), 4.30 (2H, t, $^3J_{HH}$ = 6.8 Hz), 4.06 (4H, t, $^3J_{HH}$ = 6.6 Hz), 2.67 (4H, m), 1.81 (4H, m), 1.47 (4H, m), 1.21 (32H, broad m), 0.87 (6H, t, $^3J_{HH}$ = 7.0 Hz) ppm; ^{19}F NMR (376 MHz, $CDCl_3$): δ = -80.64 (3F, t, $^3J_{FF}$ = 9.8 Hz), -113.20 (2F, m), -121.75 (2F, m), -122.75 (2F, m), -123.44 (2F, m), -126.02 (2F, m) ppm; MS m/z (APCI+): 1258.47 (calc. 1258.11); CHN elemental analysis: observed (calculated): %C 54.8 (54.4), %H 5.4 (5.4), %N 1.0 (1.1)

11-10†: Synthesised as above using **Au-Cl-1** (101 mg, 120 μmol) and 4-(*1H,1H,2H,2H*-perfluorodecyloxy)ethynylbenzene (100 mg, 181 μmol) and was recrystallised from CH_2Cl_2/acetonitrile. 160 mg (98%).

^{1}H NMR δ_H (400 MHz, $CDCl_3$): 7.71 (1H, t, $^{3}J_{HH}$ = 8.1 Hz), 7.67 (2H, d, $^{4}J_{HH}$ = 2.6 Hz), 7.55 (2H, AA'XX'), 7.49 (2H, d, $^{3}J_{HH}$ = 8.6 Hz), 7.22 (2H, d, $^{3}J_{HH}$ = 8.2 Hz), 6.87 (2H, AA'XX'), 6.72 (2H, dd, $^{3}J_{HH}$ = 8.6 Hz, $^{4}J_{HH}$ = 2.7 Hz), 4.30 (2H, t, $^{3}J_{HH}$ = 6.8 Hz), 4.06 (4H, t, $^{3}J_{HH}$ = 6.6 Hz), 2.67 (4H, m), 1.81 (4H, m), 1.47 (4H, m), 1.21 (32H, broad m), 0.87 (6H, t, $^{3}J_{HH}$ = 7.0 Hz) ppm; ^{19}F NMR (376 MHz, $CDCl_3$): δ = -82.26 (3F, t, $^{3}J_{FF}$ = 10.0 Hz), -114.28 (2F, m), -122.55 (2F, m), -122.81 (4F, m), -123.65 (2F, m), -124.47 (2F, m), -127.20 (2F, m) ppm; MS m/z (APCI+): 1358.13 (calc. 1358.46); CHN elemental analysis: observed (calculated): %C 52.3 (52.2), %H 4.8 (5.0), %N 0.9 (1.0)

11-12†: Synthesised as above using **Au-Cl-1** (100 mg, 120 μmol) and 4-(*1H,1H,2H,2H*-perfluorododecyloxy)ethynylbenzene (117 mg, 182 μmol), and was recrystallised from CH_2Cl_2/acetonitrile. 100 mg (57%).

^{1}H NMR δ_H (400 MHz, $CDCl_3$): 7.71 (1H, t, $^{3}J_{HH}$ = 8.1 Hz), 7.67 (2H, d, $^{4}J_{HH}$ = 2.6 Hz), 7.55 (2H, AA'XX'), 7.49 (2H, d, $^{3}J_{HH}$ = 8.6 Hz), 7.22 (2H, d, $^{3}J_{HH}$ = 8.2 Hz), 6.87 (2H, AA'XX'), 6.72 (2H, dd, $^{3}J_{HH}$ = 8.6 Hz, $^{4}J_{HH}$ = 2.7 Hz), 4.30 (2H, t, $^{3}J_{HH}$ = 6.8 Hz), 4.06 (4H, t, $^{3}J_{HH}$ = 6.6 Hz), 2.67 (4H, m), 1.81 (4H, m), 1.47 (4H, m), 1.21 (32H, broad m), 0.87 (6H, t, $^{3}J_{HH}$ = 7.0 Hz) ppm; ^{19}F NMR (376 MHz, $CDCl_3$): δ = - 80.61 (3F, t, $^{3}J_{FF}$ = 9.5 Hz), -113.18 (2F, m), -121.65 (8F‡, m), -122.58 (2F, m), -123.38 (2F, m), -125.98 (2F, m) ppm; MS m/z (APCI+): 1458.14 (M^+, calc. 1458.45), 1358.46 (M^+ with C10 chain (**11-10**); CHN elemental analysis: observed (calculated): %C 51.8 (50.3), %H 4.8 (4.6), %N 1.2 (1.0)

†Synthesised by MChem student Rachel Stracey; ‡low integration due to impure commercial starting materials, if pure would equal 10F

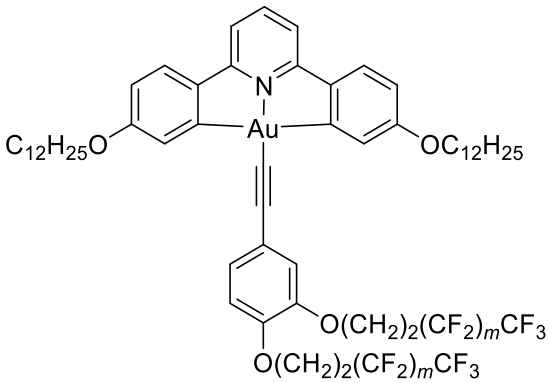

12-8: Synthesised as above using **Au-Cl-1** (61.2 mg, 70.1 μmol) and 3,4-bis(*1H,1H,2H,2H*-perfluorooctyloxy)ethynylbenzene (82.1 mg, 104 μmol) and was recrystallised from hexane. 70.2 mg (60%).

^{1}H NMR δ_H (400 MHz, $CDCl_3$): 7.72 (1H, t, $^{3}J_{HH}$ = 7.9 Hz), 7.64 (2H, d, $^{4}J_{HH}$ = 2.6 Hz), 7.49 (2H, d, $^{3}J_{HH}$ = 8.7 Hz), 7.23 (1H, dd, $^{3}J_{HH}$ = 8.4 Hz), 7.23 (2H, d, $^{3}J_{HH}$ = 7.9 Hz, $^{4}J_{HH}$ = 1.8 Hz), 7.18 (1H, d, $^{4}J_{HH}$ = 1.8 Hz), 6.89 (1H, d, $^{3}J_{HH}$ = 8.1 Hz), 6.73 (2H, dd, $^{3}J_{HH}$ = 8.5 Hz, $^{4}J_{HH}$ = 2.6 Hz), 4.31 (2H, t, $^{3}J_{HH}$ = 6.6 Hz), 4.30 (2H, t, $^{3}J_{HH}$ = 6.6 Hz), 4.05 (4H, t, $^{3}J_{HH}$ = 6.5 Hz), 2.67 (4H, m), 1.79 (4H, m), 1.44 (4H, m), 1.25 (32H, m), 0.87 (6H, t, $^{3}J_{HH}$ = 7.0 Hz) ppm. ^{19}F NMR (376 MHz, $CDCl_3$): δ = - 80.7 (6F, m), -113.3 (4F, m), -121.8 (4F, m), -122.8 (4F, m), -123.5 (4F, m), -126.1 (4F, m) ppm; MS m/z (APCI+): 1620.26 (calc. 1620.20); CHN elemental analysis: observed (calculated): %C 48.3 (48.2), %H 4.1 (4.4), %N 0.7 (0.9)

12-10: Synthesised as above using **Au-Cl-1** (62.0 mg, 70.5 μmol) and 3,4-bis(*1H,1H,2H,2H*-perfluorodecyloxy)ethynylbenzene (126 mg, 123 μmol) and was recrystallised from hexane. 116 mg (89%).

^{1}H NMR δ_H (400 MHz, $CDCl_3$): 7.71 (1H, t, $^{3}J_{HH}$ = 7.9 Hz), 7.64 (2H, d, $^{4}J_{HH}$ = 2.6 Hz), 7.48 (2H, d, $^{3}J_{HH}$ = 8.7 Hz), 7.23 (1H, dd, $^{3}J_{HH}$ = 8.4 Hz), 7.21 (2H, d, $^{3}J_{HH}$ = 7.9 Hz, $^{4}J_{HH}$ = 1.8 Hz), 7.18 (1H, d, $^{4}J_{HH}$ = 1.8 Hz), 6.89 (1H, d, $^{3}J_{HH}$ = 8.1 Hz), 6.71 (2H, dd, $^{3}J_{HH}$ = 8.5 Hz, $^{4}J_{HH}$ = 2.6 Hz), 4.31 (2H, t, $^{3}J_{HH}$ = 6.6 Hz), 4.30 (2H, t, $^{3}J_{HH}$ = 6.6 Hz), 4.05 (4H, t, $^{3}J_{HH}$ = 6.5 Hz), 2.67 (4H, m), 1.79 (4H, m), 1.44 (4H, m), 1.25 (32H, m), 0.87 (6H, t, $^{3}J_{HH}$ = 7.0 Hz) ppm; ^{19}F NMR (376 MHz, $CDCl_3$): δ = - 80.7 (6F, m), -113.3 (4F, m), -121.8 (4F, m), -121.9 (8F, m), -122.8 (4F, m), -123.5 (4F, m), -126.1 (4F, m) ppm; MS m/z (APCI+): 1820.45 (calc. 1820.23); CHN elemental analysis: observed (calculated): %C 44.8 (45.5), %H 3.7 (3.9), %N 0.6 (0.8).

12-12: Synthesised as above using **Au-Cl-1** (80.1 mg, 101 μmol) and 3,4-bis(*1H,1H,2H,2H*-perfluorododecyloxy)ethynylbenzene (177 mg, 140 μmol) and was recrystallised from hexane. 148 mg (76%).

^{1}H NMR δ_H (400 MHz, $CDCl_3$): 7.70 (1H, t, $^{3}J_{HH}$ = 7.9 Hz), 7.64 (2H, d, $^{4}J_{HH}$ = 2.6 Hz), 7.48 (2H, d, $^{3}J_{HH}$ = 8.7 Hz), 7.23 (1H, dd, $^{3}J_{HH}$ = 8.4 Hz), 7.21 (2H, d, $^{3}J_{HH}$ = 7.9 Hz, $^{4}J_{HH}$ = 1.8 Hz), 7.18 (1H, d, $^{4}J_{HH}$ = 1.8 Hz), 6.89 (1H, d, $^{3}J_{HH}$ = 8.1 Hz), 6.71 (2H, dd, $^{3}J_{HH}$ = 8.5 Hz, $^{4}J_{HH}$ = 2.6 Hz), 4.31 (2H, t, $^{3}J_{HH}$ = 6.6 Hz), 4.30 (2H, t, $^{3}J_{HH}$ = 6.6 Hz), 4.05 (4H, t, $^{3}J_{HH}$ = 6.5 Hz), 2.67 (4H, m), 1.79 (4H, m), 1.44 (4H, m), 1.25 (32H, m), 0.87 (6H, t, $^{3}J_{HH}$ = 7.0 Hz) ppm; ^{19}F NMR (376 MHz, $CDCl_3$): δ = - 80.7 (6F, m), -113.3 (4F, m), -121.8 (4F, m), -121.9 (12F[‡], m), -122.8 (4F, m), -123.5 (4F, m), -126.1 (4F, m) ppm; MS m/z (APCI+): 2020.44 (M^+ calc. 2020.27), 1920.45 (M^+ with 1x C10 chain), 1820.45 (M^+ with 2x C10 chain); CHN elemental analysis: observed (calculated): %C 44.1 (43.4), %H 3.6 (3.5), %N 0.6 (0.7).

[‡]low integration due to impure commercial starting materials, if pure would equal 16F

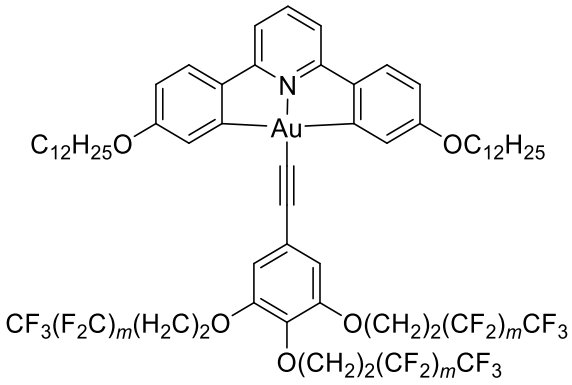

13-8: Synthesised as above using **Au-Cl-1** (81.1 mg, 104 μmol) and 3,4,5-tris(*1H,1H,2H,2H*-perfluorooctyloxy)ethynylbenzene (172 mg, 141 μmol) and was recrystallised from hexane. 144 mg (75%).

^{1}H NMR δ_H (400 MHz, $CDCl_3$): 7.72 (1H, t, $^{3}J_{HH}$ = 7.9 Hz), 7.61 (2H, d, $^{4}J_{HH}$ = 2.6 Hz), 7.50 (2H, d, $^{3}J_{HH}$ = 8.7 Hz), 7.23 (2H, d, $^{3}J_{HH}$ = 8.1 Hz), 6.87 (2H, s), 6.72 (2H, dd, $^{3}J_{HH}$ = 8.5 Hz, $^{4}J_{HH}$ = 2.6 Hz), 4.33 (4H, t, $^{3}J_{HH}$ = 6.5 Hz), 4.24 (2H, t, $^{3}J_{HH}$ = 6.8 Hz), 4.05 (4H, t, $^{3}J_{HH}$ = 6.5 Hz), 2.65 (6H, m), 1.79 (4H, m), 1.44 (4H, m), 1.25 (32H, m), 0.87 (6H, t, $^{3}J_{HH}$ = 7.0 Hz) ppm. ^{19}F NMR (376 MHz, $CDCl_3$): δ = - 80.7 (6F, t, $^{3}J_{HH}$ = 9.9 Hz), -80.9 (3F, t,), -113.3 (6F, m), -121.8 (4F, m), -122.0 (2F, m), -122.8 (6F, m), -123.5 (4F, m), -123.7 (2F, m), -126.2 (6F, m) ppm; MS m/z (APCI+): 1982.46 (calc. 1982.29); CHN elemental analysis: observed (calculated): %C 43.9 (44.2), %H 3.6 (3.7), %N 0.7 (0.7)

13-10: Synthesised as above using **Au-Cl-1** (80.0 mg, 101 μmol) and 3,4,5-tris(*1H,1H,2H,2H*-perfluorodecyloxy)ethynylbenzene (216 mg, 143 μmol) and was recrystallised from hexane. 135 mg (61%).

^{1}H NMR δ_H (400 MHz, $CDCl_3$): 7.74 (1H, t, $^{3}J_{HH}$ = 7.9 Hz), 7.61 (2H, d, $^{4}J_{HH}$ = 2.6 Hz), 7.50 (2H, d, $^{3}J_{HH}$ = 8.7 Hz), 7.25 (2H, d, $^{3}J_{HH}$ = 8.1 Hz), 6.87 (2H, s), 6.72 (2H, dd, $^{3}J_{HH}$ = 8.5 Hz, $^{4}J_{HH}$ = 2.6 Hz), 4.33 (4H, t, $^{3}J_{HH}$ = 6.5 Hz), 4.24 (2H, t, $^{3}J_{HH}$ = 6.8 Hz), 4.05 (4H, t, $^{3}J_{HH}$ = 6.5 Hz), 2.65 (6H, m), 1.79 (4H, m), 1.44 (4H, m), 1.25 (32H, m), 0.87 (6H, t, $^{3}J_{HH}$ = 7.0 Hz) ppm. ^{19}F NMR (376 MHz, $CDCl_3$): δ = - 80.7 (6F, t, $^{3}J_{HH}$ = 9.9 Hz), -80.9 (3F, t,), -113.3 (6F, m), -121.8 (18F, m), -122.8 (6F, m), -123.5 (6F, m), -126.2 (6F, m) ppm; MS m/z (APCI+): 2282.44 (calc. 2282.34); CHN elemental analysis: observed (calculated): %C 41.8 (41.6), %H 3.3 (3.2), %N 1.3 (0.6)

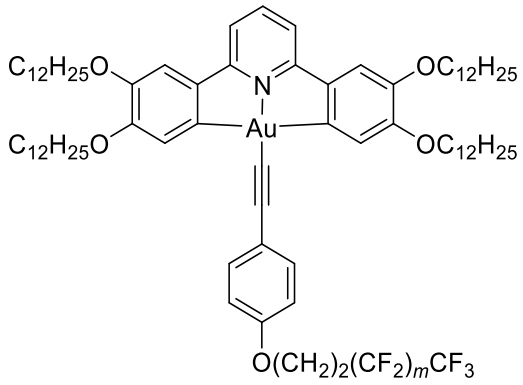

14-8†: Synthesised as above using **Au-Cl-2,** (101 mg, 83.2 μmol) and 4-(*1H,1H,2H,2H*-perfluorooctyloxy)ethynylbenzene (56.3 mg, 131 μmol) and was recrystallised from hexane. 113 mg (84%).

^{1}H NMR δ_H (400 MHz, $CDCl_3$): 7.66 (1H, t, $^{3}J_{HH}$ = 8.0 Hz), 7.59 (2H, s), 7.51 (2H, AA'XX'), 7.11 (2H, d, $^{3}J_{HH}$ = 8.1 Hz), 7.05 (2H, s), 6.86 (2H, AA'XX'), 4.29 (2H, t, $^{3}J_{HH}$ = 6.9 Hz), 4.14 (4H, t, $^{3}J_{HH}$ = 6.7 Hz), 3.99 (4H, t, $^{3}J_{HH}$ = 6.7 Hz), 2.65 (2H, m), 1.84 (8H, m), 1.47 (8H, m), 1.25 (64H, broad s), 0.88 (12H, m) ppm; ^{19}F NMR (376 MHz, $CDCl_3$): δ = -80.64 (3F, t, $^{3}J_{FF}$ = 9.8 Hz), -113.20 (2F, m), -121.75 (2F, m), -122.75 (2F, m), -123.44 (2F, m), -126.02 (2F, m) ppm; MS m/z (APCI+): 1626.76 (calc. 1626.83); CHN elemental analysis: observed (calculated): %C 60.7(59.8), %H 7.0 (7.1), %N 1.1 (0.9)

14-10: Synthesised as above using **Au-Cl-2** (84.2 mg, 70.0 μmol) and 4-(*1H,1H,2H,2H*-perfluorodecyloxy)ethynylbenzene (59.2 mg, 131 μmol) and was recrystallised from hexane. 98.1 mg (82%).

^{1}H NMR δ_H (400 MHz, $CDCl_3$): 7.66 (1H, t, $^{3}J_{HH}$ = 7.9 Hz), 7.59 (2H, s), 7.51 (2H, AA'XX'), 7.11 (2H, d, $^{3}J_{HH}$ = 8.1 Hz), 7.05 (2H, s), 6.86 (2H, AA'XX'), 4.29 (2H, t, $^{3}J_{HH}$ = 6.9 Hz), 4.14 (4H, t, $^{3}J_{HH}$ = 6.6 Hz), 3.99 (4H, t, $^{3}J_{HH}$ = 6.7 Hz), 2.65 (2H, m), 1.84 (8H, m), 1.47 (8H, m), 1.25 (64H, broad s), 0.88 (12H, m) ppm; ^{19}F NMR (376 MHz, $CDCl_3$): δ = -82.26 (3F, t, $^{3}J_{FF}$ = 10.0 Hz), -114.28 (2F, m), -122.55 (2F, m), -122.81 (4F, m), -123.65 (2F, m), -124.47 (2F, m), -127.20 (2F, m); MS m/z (APCI+): 1726.82 (calc. 1726.77); CHN elemental analysis: observed (calculated): %C 58.2 (57.7), %H 6.8 (6.7), %N 1.3 (0.8)

14-12†: Synthesised as above using **Au-Cl-2** (102 mg, 83.1 μmol) and 4-(*1H,1H,2H,2H*-perfluorododecyloxy)ethynylbenzene (76.7 mg, 133 μmol) and was recrystallised from hexane. 110 mg (73%).

^{1}H NMR δ_H (400 MHz, $CDCl_3$): 7.67 (1H, t, $^{3}J_{HH}$ = 8.0 Hz), 7.60 (2H, s), 7.51 (2H, AA'XX'), 7.13 (2H, d, $^{3}J_{HH}$ = 8.1 Hz), 7.06 (2H, s), 6.86 (2H, AA'XX'), 4.29 (2H, t, $^{3}J_{HH}$ = 6.9 Hz), 4.15 (4H, t, $^{3}J_{HH}$ = 6.6 Hz), 3.99 (4H, t, $^{3}J_{HH}$ = 6.7 Hz), 2.64 (2H, m), 1.84 (8H, m), 1.47 (8H, m), 1.25 (64H, broad s), 0.87 (12H, m) ppm; ^{19}F NMR (376 MHz, $CDCl_3$): δ = - 80.61 (3F, t, $^{3}J_{FF}$ = 9.5 Hz), -113.18 (2F, m), -121.65 (8F‡, m), -122.58 (2F, m), -123.38 (2F, m), -125.98 (2F, m); MS m/z (APCI+): 1826.82 (M^+, calc. 1826.79); CHN elemental analysis: observed (calculated): %C 57.4 (55.9), %H 6.7 (6.4), %N 1.3 (0.8).

†Synthesised by MChem student Rachel Stracey; ‡low integration due to impure commercial starting materials, if pure would equal 10F

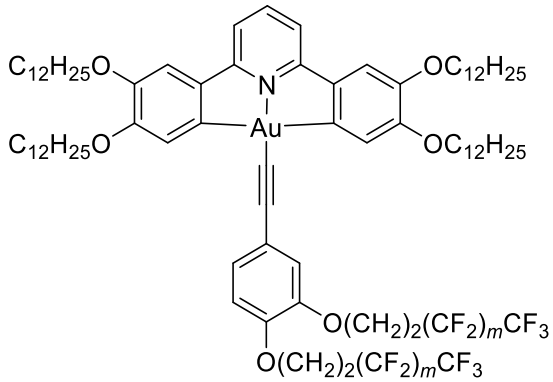

15-8: Synthesised as above using **Au-Cl-2,** (129 mg, 111 μmol) and 3,4-bis(*1H,1H,2H,2H*-perfluorooctyloxy)ethynylbenzene (224 mg, 272 μmol) and was recrystallised from hexane. 167 mg (78%).

^{1}H NMR δ_H (400 MHz, $CDCl_3$): 7.68 (1H, t, $^{3}J_{HH}$ = 8.0 Hz), 7.58 (2H, s), 7.21 (1H, dd, $^{3}J_{HH}$ = 8.1 Hz, $^{4}J_{HH}$ = 1.8 Hz), 7.15 (1H, d, $^{4}J_{HH}$ = 2.4 Hz), 7.13 (2H, d, $^{3}J_{HH}$ = 8.5 Hz), 7.06 (2H, s), 6.87 (2H, d, $^{3}J_{HH}$ = 8.2 Hz), 4.31 (2H, t, $^{3}J_{HH}$ = 6.6 Hz), 4.30 (2H, t, $^{3}J_{HH}$ = 6.6 Hz), 4.13 (4H, t, $^{3}J_{HH}$ = 6.6 Hz), 4.00 (4H, t, $^{3}J_{HH}$ = 6.6 Hz), 2.66 (4H, m), 1.84 (8H, m), 1.47 (8H, m), 1.25 (64H, broad s), 0.87 (12H, m) ppm; ^{19}F NMR (376 MHz, $CDCl_3$): δ = - 80.7 (6F, t, $^{3}J_{FF}$ = 9.9 Hz), -113.18 (4F, m), -121.8 (4F, m), -122.8 (4F, m), -123.5 (4F, m), -126.1 (4F, m) ppm; MS m/z (APCI+): 1988.83 (M+H, calc. 1987.82); CHN elemental analysis: observed (calculated): %C 53.6 (53.8), %H 6.1 (6.0), %N 0.6 (0.7).

15-10: Synthesised as above using **Au-Cl-2,** (129 mg, 112 μmol) and 3,4-bis(*1H,1H,2H,2H*-perfluorodecyloxy)ethynylbenzene (278 mg, 270 μmol) and was recrystallised from hexane. 146 mg (62%).

^{1}H NMR δ_H (400 MHz, $CDCl_3$): 7.68 (1H, t, $^{3}J_{HH}$ = 8.0 Hz), 7.58 (2H, s), 7.21 (1H, dd, $^{3}J_{HH}$ = 8.1 Hz, $^{4}J_{HH}$ = 1.8 Hz), 7.15 (1H, d, $^{4}J_{HH}$ = 2.0 Hz), 7.13 (2H, d, $^{3}J_{HH}$ = 8.5 Hz), 7.06 (2H, s), 6.87 (2H, d, $^{3}J_{HH}$ = 8.2 Hz), 4.31 (2H, t, $^{3}J_{HH}$ = 6.6 Hz), 4.30 (2H, t, $^{3}J_{HH}$ = 6.6 Hz), 4.13 (4H, t, $^{3}J_{HH}$ = 6.6 Hz), 4.00 (4H, t, $^{3}J_{HH}$ = 6.6 Hz), 2.66 (4H, m), 1.84 (8H, m), 1.47 (8H, m), 1.25 (64H, broad s), 0.87 (12H, m) ppm; ^{19}F NMR (376 MHz, $CDCl_3$): δ = - 80.7 (6F, t, $^{3}J_{FF}$ = 9.9 Hz), -113.18 (4F, m), -121.8 (4F, m), -121.9 (8F, m), -122.8 (4F, m), -123.5 (4F, m), -126.1 (4F, m); MS m/z (APCI+): 2188.82 (M+H, calc. 2187.81); CHN elemental analysis: observed (calculated): %C 50.9 (51.0), %H 5.3 (5.4), %N 0.5 (0.6).

15-12: Synthesised as above using **Au-Cl-2,** (91 mg, 80.2 μmol) and 3,4-bis(*1H,1H,2H,2H*-perfluorododecyloxy)ethynylbenzene (138 mg, 114 μmol) and was recrystallised from hexane. 110 mg (61%).

^{1}H NMR δ_H (400 MHz, $CDCl_3$): 7.68 (1H, t, $^{3}J_{HH}$ = 8.0 Hz), 7.58 (2H, s), 7.21 (1H, dd, $^{3}J_{HH}$ = 8.1 Hz, $^{4}J_{HH}$ = 1.8 Hz), 7.15 (1H, d, $^{4}J_{HH}$ = 2.0 Hz), 7.13 (2H, d, $^{3}J_{HH}$ = 8.5 Hz), 7.06 (2H, s), 6.87 (2H, d, $^{3}J_{HH}$ = 8.2 Hz), 4.31 (2H, t, $^{3}J_{HH}$ = 6.6 Hz), 4.30 (2H, t, $^{3}J_{HH}$ = 6.6 Hz), 4.13 (4H, t, $^{3}J_{HH}$ = 6.6 Hz), 4.00 (4H, t, $^{3}J_{HH}$ = 6.6 Hz), 2.66 (4H, m), 1.84 (8H, m), 1.47 (8H, m), 1.25 (64H, broad s), 0.87 (12H, m) ppm; ^{19}F NMR (376 MHz, $CDCl_3$): δ = - 80.7 (6F, m), -113.18 (4F, m), -121.7 (4F, m), -121.9 (12F‡, m), -122.8 (4F, m), -123.5 (4F, m), -126.1 (4F, m); MS m/z (APCI+): 2389.80 (M+H, calc. 2388.91), 2289.81 (M+H with 1x C10 chain), 2189.81 (M+H with 2x C10 chain, **15-10**); CHN elemental analysis: observed (calculated): %C 49.7 (49.8), %H 5.1 (5.0), %N 0.5 (0.6).

‡low integration due to impure commercial starting materials, if pure would equal 16F

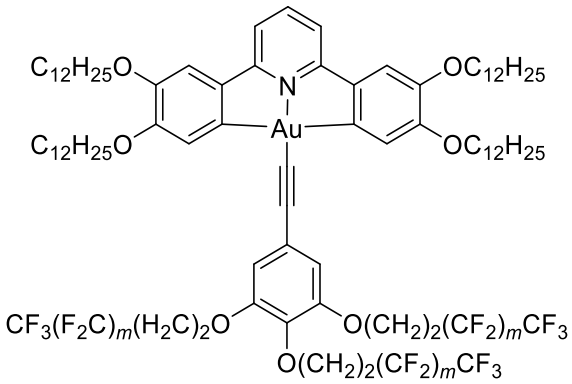

16-8: Synthesised as above using **Au-Cl-2,** (92.2 mg, 80.1 μmol) and 3,4,5-tris(*1H,1H,2H,2H*-perfluorooctyloxy)ethynylbenzene (134 mg, 114 μmol) and was recrystallised from hexane. 144 mg (82%).

^{1}H NMR δ_H (400 MHz, $CDCl_3$): 7.70 (1H, t, $^{3}J_{HH}$ = 8.0 Hz), 7.54 (2H, s), 7.15 (2H, d, $^{3}J_{HH}$ = 8.3 Hz), 7.07 (2H, s), 6.85 (2H, s), 4.30 (4H, t, $^{3}J_{HH}$ = 6.6 Hz), 4.23 (2H, t, $^{3}J_{HH}$ = 6.6 Hz), 4.11 (4H, t, $^{3}J_{HH}$ = 6.6 Hz), 4.00 (4H, t, $^{3}J_{HH}$ = 6.6 Hz), 2.66 (4H, m), 1.84 (8H, m), 1.47 (8H, m), 1.25 (64H, broad s), 0.87 (12H, m) ppm; ^{19}F NMR (376 MHz, $CDCl_3$): δ = - 80.7 (6F, m), -80.9 (3F, m), -113.4 (6F, m), -121.8 (4F, m), -122.0 (2F, m), -122.9 (6F, m), -123.5 (6F, m), -126.1 (6F, m); MS m/z (APCI+): 2350.82 (calc. 2350.94); CHN elemental analysis: observed (calculated): %C 50.0 (49.6), %H 5.3 (5.2), %N 1.3 (0.6)

16-10: Synthesised as above using **Au-Cl-2,** (91.1 mg, 80.3 μmol) and 3,4,5-tris(*1H,1H,2H,2H*-perfluorodecyloxy)ethynylbenzene (168 mg, 112 μmol) and was recrystallised from hexane. 161 mg (81%).

^{1}H NMR δ_H (400 MHz, $CDCl_3$): 7.70 (1H, t, $^{3}J_{HH}$ = 8.0 Hz), 7.54 (2H, s), 7.15 (2H, d, $^{3}J_{HH}$ = 8.3 Hz), 7.07 (2H, s), 6.85 (2H, s), 4.30 (4H, t, $^{3}J_{HH}$ = 6.6 Hz), 4.23 (2H, t, $^{3}J_{HH}$ = 6.6 Hz), 4.11 (4H, t, $^{3}J_{HH}$ = 6.6 Hz), 4.00 (4H, t, $^{3}J_{HH}$ = 6.6 Hz), 2.66 (4H, m), 1.84 (8H, m), 1.47 (8H, m), 1.25 (64H, broad s), 0.87 (12H, m) ppm; ^{19}F NMR (376 MHz, $CDCl_3$): δ = - 80.7 (6F, m), -80.9 (3F, m), -113.4 (6F, m), -121.8 (18F, m), -122.8 (6F, m), -123.5 (6F, m), -126.1 (6F, m); MS m/z (APCI+): 2650.81 (calc. 2650.99); CHN elemental analysis: observed (calculated): %C 46.8 (46.7), %H 4.4 (4.6), %N 0.5 (0.5).

6.4 Sample Preperation, Concentration and Associated Error in Concentration Dependent NMR (Chapter 3)

Solutions of specific concentrations for analysis by ^{1}H and ^{19}F NMR spectroscopy were prepared by successive dilution using volumetric glassware. The absolute concentrations (and associated errors) of the samples prepared are outlined in Table 6-1. The solvent in all cases was CD_2Cl_2.

Table 6-1: Concentrations and associated errors of solutions of **8-8**, **16-8** and **16-10** prepared for study by NMR spectroscopy.

Complex	8-8	16-8	16-10
Concentration (mmol dm^{-3})	0.050 ± 0.007	0.051 ± 0.007	0.051 ± 0.007
	0.099 ± 0.013	0.102 ± 0.013	0.102 ± 0.013
	0.50 ± 0.06	0.51 ± 0.06	0.51 ± 0.06
	0.99 ± 0.10	0.10 ± 0.10	0.10 ± 0.10
	3.0 ± 0.3	3.1 ± 0.3	3.0 ± 0.3
	5.1 ± 0.4	5.1 ± 0.4	5.0 ± 0.4
	8.1 ± 0.4	8.1 ± 0.4	7.8 ± 0.4
	14.2 ± 0.2	14.2 ± 0.2	13.7 ± 0.2

6.5 Device Fabrication and Testing (Chapter 4)

6.5.1 Doped Devices

ITO-coated glass substrates were washed by acetone, neutral detergent, deionised water and isopropanol. The substrates were then cured with ozone under UV irradiation for 15 minutes at 100 °C. PEDOT:PSS was spin coated onto the ITO glad substrate and annealed at 150 °C for 10 minutes in a glovebox with a nitrogen atmosphere; all subsequent fabrication was carried out within the glovebox. The appropriate gold(III) complexes, denoted as [Au] for general clarity, at increasing dopant levels (5, 10, 15 wt%), were blended with PVK:OXD-7 (or other host materials such as MCP or CzAcSF as described in Chapter 4) and dissolved in chlorobenzene to form a 1% w/v solution, which was spin-coated onto the device structure to form the emissive layer, which was annealed at 100 °C for 20 minutes.

Subsequently, DPEPO, TmPyPb, CsF and Al were successively deposited onto the device by resistive thermal evaporation in a vacuum chamber with a base pressure of 5 $x10^{-5}$ torr. Finally, the device was encapsulated with a final glass substrate, which was secured with a UV-curable epoxy resin.

6.5.2 Polarised Devices

Devices fabricated to induce polarised emission were fundamentally fabricated by the same methods outlined above. For those devices in which the emitter was not doped in a polymer matrix, the solution which was spin-coated onto the substrate to form the emissive layer contained only the relevant gold complex.

To align the emissive layer, an extra step was added to the procedure from Section 6.5.1. The hole injection layer of PEDOT:PSS was annealed at 150 °C for 10 minutes in the glove box, after which it was uniaxially rubbed with a dust-free cloth. After rubbing, the emissive layer was spin-coated onto the rubbed substrate and annealed at a temperature in which it was in the mesophase; for the selected complex (**6-8**) this was done at 100 °C, as above. The remaining layers were added to the device as above.

6.5.3 Device Characterisation

The current–voltage–luminance characteristics were collected with a PR735 Spectrascan spectrometer and a Keithley 2400 programmable source meter. The external quantum efficiency

was calculated from the luminance, current density, and EL spectrum, assuming a Lambertian distribution.

The polarized EL spectra were recorded by an Ocean Optics USB2000 spectrometer. The electroluminescence intensities parallel and perpendicular to the rubbed direction (along the ITO stripe) could be distinguished by aligning a linear polarizer inserted between the OLED and the spectrometer in two perpendicular orientations

6.6 Computational Chemistry (Chapters 2 and 4)

All calculations were performed by Dr Jason Lynam using the TURBOMOLE V6.4 package using the resolution of identity (RI) approximation.[11-18]

Initial optimisations were performed at the (RI-)BP86/SV(P) level, followed by frequency calculations at the same level. All minima were confirmed as such by the absence of imaginary frequencies. Single-point and TD-DFT calculations on the (RI-)BP86/SV(P) optimised geometries were performed using the hybrid PBE0 functional and the flexible def2-TZVPP basis set with a 60-electron effective core potential. The TD-DFT calculations determined the energy of the first 50 singlet excitations. Calculations on the Pt systems were performed with an m3 grid, whereas those on the Au complexes employed a finer m5 grid.

The triplet states of the gold complexes **1'-H** and **5'-H** were calculated using an unrestricted Hartree-Fock method with an imposed triplet spin state. Geometry optimisations and single-point energies were performed as described above. Predicted triplet emission energies for a given complex were corrected for zero-point energy and calculated by subtracting the energy of the singlet state from the corresponding triplet.

6.7 References

1. D. M. Jenkins and S. Bernhard, *Inorg. Chem.*, 2010, **49**, 11297-11308.
2. A. Santoro, A. C. Whitwood, J. A. G. Williams, V. N. Kozhevnikov and D. W. Bruce, *Chem. Mater.*, 2009, **21**, 3871-3882.
3. K. Nakamaru, *Bull. Chem. Soc. Jpn*, 1982, **55**, 2697-2705.
4. *CrysAlisPro, Oxford Diffraction Ltd. Version 1.171.34.41*.
5. *Empirical absorption correction using spherical harmonics, implemented in SCALE3 ABSPACK scaling algorithm within CrysAlisPro software, Oxford Diffraction Ltd. Version 1.171.34.40*.
6. O. V. Dolomanov, L. J. Bourhis, R. J. Gildea, J. A. K. Howard and H. Puschmann, *J. Appl. Crystallogr.*, 2009, **42**, 339-341.
7. G. Sheldrick, *Acta Crystallogr. A*, 2008, **64**, 112-122.
8. F. Juliá, M.-D. García-Legaz, D. Bautista and P. González-Herrero, *Inorg. Chem.*, 2016, **55**, 7647-7660.
9. T. Cardinaels, J. Ramaekers, P. Nockemann, K. Driesen, K. Van Hecke, L. Van Meervelt, G. Wang, S. De Feyter, E. F. Iglesias, D. Guillon, B. Donnio, K. Binnemans and D. W. Bruce, *Soft Matter*, 2008, **4**, 2172-2185.
10. *US Pat.*, US20180237433A1, 2018
11. P. Császár and P. Pulay, *J. Mol. Struct.*, 1984, **114**, 31-34.
12. R. Ahlrichs, M. Bär, M. Häser, H. Horn and C. Kölmel, *Chem. Phys. Lett*, 1989, **162**, 165-169.
13. P. Deglmann, F. Furche and R. Ahlrichs, *Chem. Phys. Lett*, 2002, **362**, 511-518.
14. P. Deglmann, K. May, F. Furche and R. Ahlrichs, *Chem. Phys. Lett*, 2004, **384**, 103-107.
15. K. Eichkorn, O. Treutler, H. Öhm, M. Häser and R. Ahlrichs, *Chem. Phys. Lett.*, 1995, **242**, 652-660.
16. K. Eichkorn, F. Weigend, O. Treutler and R. Ahlrichs, *Theor. Chem. Acc.*, 1997, **97**, 119-124.
17. O. Treutler and R. Ahlrichs, *J. Chem. Phys.*, 1995, **102**, 346-354.
18. M. von Arnim and R. Ahlrichs, *J. Chem. Phys.*, 1999, **111**, 9183-9190.

List of Common Abbreviations

acac	acetylacetonate	MCP	1,3-bis(carbazole-9-yl)benzene
AIE	aggregation induced emission	MLCT	metal to ligand charge transfer
bpy	bipyridine	MMLCT	metal-metal-ligand charge transfer
CE	current efficiency	N	nematic phase
CIE	Commission Internationale de l'Elcairage coordinates	NMR	nuclear magnetic resonance
Col	columnar phase, e.g. Col_h, Col_r	OLED	organic light emitting diode
Cr	crystal	OXD-7	1,3-bis[2-tert-butylphenyl)-1,3,5-oxadiazo-5-yl]benzene
CV	cyclic voltammetry/cyclic voltammogram	PC	poly(carbonate)
d	doublet	PE	power efficiency
dd	doublet of doublets	PLQY	photoluminescence quantum yield
DFT	density functional theory	PMMA	poly(methyl methacrylate)
DMF	dimethyl formamide	POM	polarising optical microscopy
DMSO	dimethyl sulfoxide	ppy	phenylpyridine
DSC	differential scanning calorimetry	PVK	poly(9-vinyl carbazole)
ΔH	enthalpy change	S	singlet e.g. S_0 singlet ground state, S_1 singlet excited state
EBL	electron-blocking layer	s	singlet
EIL	electron-injecting layer	SAXS	small-angle X-ray scattering
EL	electroluminescence	Sm	smectic phase, *e.g.* SmA
EML	emissive layer	SOC	spin orbit coupling
EPA	diethyl ether – isopentane – ethanol (2:2:1 v/v)	T	triplet e.g. T_1 triplet excited state
EQE	external quantum efficiency	t	triplet
ETL	electron-transport layer	TADF	thermally activated delayed fluorescence
HBL	hole-blocking later	TCSPC	time-correlated single photon counting
HIL	hole-injection layer	TD-DFT	time-dependant density functional theory
HOMO	highest occupied molecular orbital	tolpy	2-p-tolylpyridine
HTL	hole-transport layer	XRD	X-ray diffraction
IC	integral conversion		
ISC	intersystem crossing		
k_{nr}	non-radiative rate constant		
k_r	radiative rate constant		
Lam	lamellar phase		
LC	ligand centred		
LCD	liquid crystal display		
LLCT	ligand to ligand charge transfer		
LMCT	ligand to metal charge transfer		
LUMO	lowest unoccupied molecular orbital		
m	multiplet		